

**HANDBOOK OF BIOLOGICAL EFFECTS OF
ELECTROMAGNETIC FIELDS**

THIRD EDITION

Bioengineering and Biophysical Aspects of Electromagnetic Fields

EDITED BY

**Frank S. Barnes
Ben Greenebaum**



Taylor & Francis
Taylor & Francis Group

HANDBOOK OF BIOLOGICAL EFFECTS OF
ELECTROMAGNETIC FIELDS

THIRD EDITION

Bioengineering and Biophysical Aspects of Electromagnetic Fields

**HANDBOOK OF BIOLOGICAL EFFECTS OF
ELECTROMAGNETIC FIELDS**

THIRD EDITION

**Bioengineering
and Biophysical
Aspects of
Electromagnetic
Fields**

EDITED BY

Frank S. Barnes

University of Colorado-Boulder
Boulder, CO, U.S.A.

Ben Greenebaum

University of Wisconsin-Parkside
Kenosha, WI, U.S.A.



Taylor & Francis

Taylor & Francis Group
Boca Raton London New York

CRC is an imprint of the Taylor & Francis Group,
an Informa business

CRC Press
Taylor & Francis Group
6000 Broken Sound Parkway NW, Suite 300
Boca Raton, FL 33487-2742

© 2007 by Taylor & Francis Group, LLC
CRC Press is an imprint of Taylor & Francis Group, an Informa business

No claim to original U.S. Government works
Printed in the United States of America on acid-free paper
10 9 8 7 6 5 4 3 2 1

International Standard Book Number-10: 0-8493-9539-9 (Hardcover)
International Standard Book Number-13: 978-0-8493-9539-0 (Hardcover)

This book contains information obtained from authentic and highly regarded sources. Reprinted material is quoted with permission, and sources are indicated. A wide variety of references are listed. Reasonable efforts have been made to publish reliable data and information, but the author and the publisher cannot assume responsibility for the validity of all materials or for the consequences of their use.

No part of this book may be reprinted, reproduced, transmitted, or utilized in any form by any electronic, mechanical, or other means, now known or hereafter invented, including photocopying, microfilming, and recording, or in any information storage or retrieval system, without written permission from the publishers.

For permission to photocopy or use material electronically from this work, please access www.copyright.com (<http://www.copyright.com/>) or contact the Copyright Clearance Center, Inc. (CCC) 222 Rosewood Drive, Danvers, MA 01923, 978-750-8400. CCC is a not-for-profit organization that provides licenses and registration for a variety of users. For organizations that have been granted a photocopy license by the CCC, a separate system of payment has been arranged.

Trademark Notice: Product or corporate names may be trademarks or registered trademarks, and are used only for identification and explanation without intent to infringe

Visit the Taylor & Francis Web site at
<http://www.taylorandfrancis.com>

and the CRC Press Web site at
<http://www.crcpress.com>

Preface

We are honored to have been asked to carry on the tradition established by Dr. Postow and the late Dr. Polk in the first two editions of the *Handbook of Biological Effects of Electromagnetic Fields*. Their editions of this handbook were each recognized as the authoritative standards of their time for scientists working in bioelectromagnetics, the science of electromagnetic field effects on biological systems, and for others seeking information about this field of research.

In revising and updating this edition of the *Handbook of Biological Effects of Electromagnetic Fields*, we have expanded the coverage to include more material on diagnostic and therapeutic applications. At the same time, in updating and expanding the previous editions' coverage of the basic science and studies related to the possible biological effects of the electromagnetic fields, we have added new material on the related physics and chemistry as well as reviews of the recent developments in the setting standards for exposure limits. Following the previous edition's lead, we have charged the authors of the individual chapters with providing the reader, whom we imagine is fairly well founded in one or more of the sciences underlying bioelectromagnetics but perhaps not in the others or in the interdisciplinary subject of bioelectromagnetics itself, with both an introduction to their topic and a basis for further reading. We asked the chapter authors to write what they would like to be the first thing they would ask a new graduate student in their laboratory to read. We hope that this edition, like its two predecessors, will be useful to many as a reference book and to others as a text for a graduate course that introduces bioelectromagnetics or some of its aspects.

As a "handbook" and not an encyclopedia, this work does not intend to cover all aspects of bioelectromagnetics. Nevertheless, taking into account the breadth of topics and growth of research in this field since the last edition, we have expanded the number of topics and the number of chapters. Unavoidably, some ideas are duplicated in chapters, sometimes from different viewpoints that could be instructive to the reader; and different aspects of others are presented in different chapters. The increased amount of material has led to the publication of the handbook as two separate, but inter-related volumes: *Biological and Medical Aspects of Electromagnetic Fields* (BMA) and *Bioengineering and Biophysical Aspects of Electromagnetic Fields* (BBA). Because there is no sharp dividing line, some topics are dealt with in parts of both volumes. The reader should be particularly aware that various theoretical models, which are proposed for explaining how fields interact with biological systems at a biophysical level, are distributed among a number of chapters. No one model has become widely accepted, and it is quite possible that more than one will in fact be needed to explain all observed phenomena. Most of these discussions are in the *Biological and Medical* volume, but the *Bioengineering and Biophysics* volume's chapters on electroporation and on mechanisms and therapeutic applications, for example, also have relevant material. Similarly, the chapters on biological effects of static magnetic fields and on endogenous electric fields in animals could equally well have been in the *Biological and Medical* volume. We have tried to use the index and cross-references in the chapters to direct the reader to the most relevant linkages, and we apologize for those we have missed.

Research in bioelectromagnetics stems from three sources, all of which are important; and various chapters treat both basic physical science and engineering aspects and the biological and medical aspects of these three. Bioelectromagnetics first emerged as a

separate scientific subject because of interest in studying possible hazards from exposure to electromagnetic fields and setting exposure limits. A second interest is in the beneficial use of fields to advance health, both in diagnostics and in treatment, an interest that is as old as the discovery of electricity itself. Finally, the interactions between electromagnetic fields and biological systems raise some fundamental, unanswered scientific questions and may also lead to fields being used as tools to probe basic biology and biophysics. Answering basic bioelectromagnetic questions will not only lead to answers about potential electromagnetic hazards and to better beneficial applications, but they should also contribute significantly to our basic understanding of biological processes. Both strong fields and those on the order of the fields generated within biological systems may become tools to perturb the systems, either for experiments seeking to understand how the systems operate or simply to change the systems, such as by injecting a plasmid containing genes whose effects are to be investigated. These three threads are intertwined throughout bioelectromagnetics. Although any specific chapter in this work will emphasize one or another of these threads, the reader should be aware that each aspect of the research is relevant to a greater or lesser extent to all three.

The reader should note that the chapter authors have a wide variety of interests and backgrounds and have concentrated their work in areas ranging from safety standards and possible health effects of low-level fields to therapy through biology and medicine to the fundamental physics and chemistry underlying the biology. It is therefore not surprising that they have different and sometimes conflicting points of view on the significance of various results and their potential applications. Thus authors should only be held responsible for the viewpoints expressed in their chapters and not in others. We have tried to select the authors and topics so as to cover the scientific results to date that are likely to serve as a starting point for future work that will lead to the further development of the field. Each chapter's extensive reference section should be helpful for those needing to obtain a more extensive background than is possible from a book of this type.

Some of the material, as well as various authors' viewpoints, are controversial, and their importance is likely to change as the field develops and our understanding of the underlying science improves. We hope that this volume will serve as a starting point for both students and practitioners to come up-to-date with the state of understanding of the various parts of the field as of late 2004 or mid-2005, when authors contributing to this volume finished their literature reviews.

The editors would like to express their appreciation to all the authors for the extensive time and effort they have put into preparing this edition, and it is our wish that it will prove to be of value to the readers and lead to advancing our understanding of this challenging field.

**Frank S. Barnes
Ben Greenebaum**

Editors

Frank Barnes received his B.S. in electrical engineering in 1954 from Princeton University and his M.S., engineering, and Ph.D. degrees from Stanford University in 1955, 1956, and 1958, respectively. He was a Fulbright scholar in Baghdad, Iraq, in 1958 and joined the University of Colorado in 1959, where he is currently a distinguished professor. He has served as chairman of the Department of Electrical Engineering, acting dean of the College of Engineering, and in 1971 as cofounder/director with Professor George Coding of the Political Science Department of the Interdisciplinary Telecommunications Program (ITP).

He has served as chair of the IEEE Electron Device Society, president of the Electrical Engineering Department Heads Association, vice president of IEEE for Publications, editor of the *IEEE Student Journal* and the *IEEE Transactions on Education*, as well as president of the Bioelectromagnetics Society and U.S. Chair of Commission K—International Union of Radio Science (URSI). He is a fellow of the AAAS, IEEE, International Engineering Consortium, and a member of the National Academy of Engineering.

Dr. Barnes has been awarded the Curtis McGraw Research Award from ASEE, the Leon Montgomery Award from the International Communications Association, the 2003 IEEE Education Society Achievement Award, Distinguished Lecturer for IEEE Electron Device Society, the 2002 ECE Distinguished Educator Award from ASEE, The Colorado Institute of Technology Catalyst Award 2004, and the Bernard M. Gordon Prize from National Academy of Engineering for Innovations in Engineering Education 2004. He was born in Pasadena, CA, in 1932 and attended numerous elementary schools throughout the country. He and his wife, Gay, have two children and two grandchildren.

Ben Greenebaum retired as professor of physics at the University of Wisconsin-Parkside, Kenosha, WI, in May 2001, but was appointed as emeritus professor and adjunct professor to continue research, journal editing, and university outreach projects. He received his Ph.D. in physics from Harvard University in 1965. He joined the faculty of UW-Parkside as assistant professor in 1970 following postdoctoral positions at Harvard and Princeton Universities. He was promoted to associate professor in 1972 and to professor in 1980. Greenebaum is author or coauthor of more than 50 scientific papers. Since 1992, he has been editor in chief of *Bioelectromagnetics*, an international peer-reviewed scientific journal and the most cited specialized journal in this field. He spent 1997–1998 as consultant in the World Health Organization's International EMF Project in Geneva, Switzerland. Between 1971 and 2000, he was part of an interdisciplinary research team investigating the biological effects of electromagnetic fields on biological cell cultures. From his graduate student days through 1975, his research studied the spins and moments of radioactive nuclei. In 1977 he became a special assistant to the chancellor and in 1978, associate dean of faculty (equivalent to the present associate vice chancellor position). He served 2 years as acting vice chancellor (1984–1985 and 1986–1987). In 1989, he was appointed as dean of the School of Science and Technology, serving until the school was abolished in 1996.

On the personal side, he was born in Chicago and has lived in Racine, WI, since 1970. Married since 1965, he and his wife have three adult sons.

Contributors

Frank S. Barnes Department of Electrical and Computer Engineering, University of Colorado, Boulder, Colorado

Paolo Bernardi Department of Electronic Engineering, University of Rome, Rome, Italy

Martin Bier Department of Physics, East Carolina University, Greenville, North Carolina

Jon Dobson Institute for Science and Technology, Keele University, Stoke-on-Trent, U.K. and Department of Materials Science and Engineering, University of Florida, Gainesville, Florida

Stefan Engström Department of Neurology, Vanderbilt University, Nashville, Tennessee

Camelia Gabriel Microwave Consultants Ltd, London, U.K.

Ben Greenebaum University of Wisconsin–Parkside, Kenosha, Wisconsin

Kjell Hansson Mild National Institute for Working Life, Örebro University, Örebro, Sweden

William T. Joines Department of Electrical and Computer Engineering, Duke University, Durham, North Carolina

Sven Kühn Foundation for Research on Information Technologies in Society (IT'IS Foundation), Swiss Federal Institute of Technology (ETH), Zurich, Switzerland

Niels Kuster Foundation for Research on Information Technologies in Society (IT'IS Foundation), Swiss Federal Institute of Technology (ETH), Zurich, Switzerland

A.R. Liboff Center for Molecular Biology and Biotechnology, Florida Atlantic University, Boca Raton, Florida

James C. Lin Department of Electrical and Computer Engineering and Department of Bioengineering, University of Illinois, Chicago, Illinois

Qing H. Liu Department of Electrical and Computer Engineering, Duke University, Durham, North Carolina

Richard Nuccitelli Department of Electrical and Computer Engineering, Old Dominion University, Norfolk, Virginia

Tsukasa Shigemitsu Department of Biomedical Engineering, University of Tokyo, Tokyo, Japan

Shoogo Ueno Department of Biomedical Engineering, University of Tokyo, Tokyo, Japan

James C. Weaver Massachusetts Institute of Technology, Cambridge, Massachusetts

Gary Ybarra Department of Electrical and Computer Engineering, Duke University, Durham, North Carolina

Table of Contents

Introduction

- 1 Environmental and Occupationally Encountered Electromagnetic Fields**
Kjell Hansson Mild and Ben Greenebaum
- 2 Endogenous Electric Fields in Animals**
Richard Nuccitelli
- 3 Dielectric Properties of Biological Materials**
Camelia Gabriel
- 4 Magnetic Properties of Biological Material**
Jon Dobson
- 5 Interaction of Direct Current and Extremely Low-Frequency Electric Fields with Biological Materials and Systems**
Frank S. Barnes
- 6 Magnetic Field Effects on Free Radical Reactions in Biology**
Stefan Engström
- 7 Signals, Noise, and Thresholds**
James C. Weaver and Martin Bier
- 8 Biological Effects of Static Magnetic Fields**
Shoogo Ueno and Tsukasa Shigemitsu
- 9 The Ion Cyclotron Resonance Hypothesis**
A.R. Liboff
- 10 Computational Methods for Predicting Field Intensity and Temperature Change**
James C. Lin and Paolo Bernardi
- 11 Experimental EMF Exposure Assessment**
Sven Kühn and Niels Kuster
- 12 Electromagnetic Imaging of Biological Systems**
William T. Joines, Qing H. Liu, and Gary Ybarra

Introduction

Charles Polk*

Revised for the 3rd Edition by Ben Greenebaum

Much has been learned since this handbook's first edition, but a full understanding of biological effects of electromagnetic fields has yet to be achieved. The broad range of what must be studied has to be a factor in the apparent slow progress toward this ultimate end. The broad range of disciplines involved includes basic biology, medical science and clinical practice, biological and electrical engineering, basic chemistry and biochemistry, and fundamental physics and biophysics. The subject matter ranges over characteristic lengths and timescales from, at one extreme, direct current (dc) or $\sim 10^4$ km-wavelengths, multimillisecond ac fields and large, long-lived organisms to, at the other extreme, submillimeter wavelength fields with periods below 10^{-12} s and subcellular structures and molecules with subnanometer dimensions and characteristic times as short as the 10^{-15} s or less of biochemical reactions.

This chapter provides an introduction and overview of the research and the contents of this handbook.

0.1 Near Fields and Radiation Fields

In recent years it has become, unfortunately, a fairly common practice—particularly in nontechnical literature—to refer to the entire subject of interaction of electric (E) and magnetic (H) fields with organic matter as biological effects of nonionizing radiation, although fields that do not vary with time and, for most practical purposes, slowly time-varying fields do not involve radiation at all. The terminology had its origin in an effort to differentiate between relatively low-energy microwave radiation and high-energy radiation, such as UV and x-rays, capable of imparting enough energy to a molecule or an atom to disrupt its structure by removing one or more electrons with a single photon. However, when applied to dc or extremely low-frequency (ELF), the term “nonionizing radiation” is inappropriate and misleading.

A structure is capable of efficiently radiating electromagnetic waves only when its dimensions are significant in comparison with the wavelength λ . But in free space $\lambda = c/f$, where c is the velocity of light in vacuum (3×10^8 m/s) and f is the frequency in hertz (cycles/s); therefore the wavelength at the power distribution frequency of 60 Hz, e.g., is 5000 km, guaranteeing that most available human-made structures are much smaller than one wavelength.

The poor radiation efficiency of electrically small structures (i.e., structures whose largest linear dimension $L \ll \lambda$) can be illustrated easily for linear antennas. In free space the radiation resistance, R_r of a current element, i.e., an electrically short wire of length ℓ carrying uniform current along its length [1], is

$$R_r = 80\pi^2 \left(\frac{\ell}{\lambda}\right)^2 \quad (0.1)$$

*Deceased.

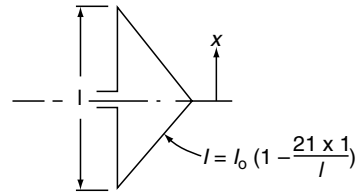


FIGURE 0.1

Current distribution on short, thin, center-fed antenna.

whereas the R_r of an actual center-fed radiator of total length ℓ with current going to zero at its ends, as illustrated in Figure 0.1, is

$$R_r = 20\pi^2 \left(\frac{\ell}{\lambda}\right)^2 \quad (0.2)$$

Thus, the R_r of a 0.01λ antenna, 50 km long at 60 Hz, would be 0.0197Ω . As the radiated power $P_r = I^2 R_r$ where I is the antenna terminal current, whereas the power dissipated as heat in the antenna wire is $I^2 R_d$; when I is uniform, the P_r will be very much less than the power used to heat the antenna, given that the ohmic resistance R_d of any practical wire at room temperature will be very much larger and R_r . For example, the resistance of a 50-km long, 1/2-in. diameter solid copper wire could be 6.65Ω . At dc, of course, no radiation of any sort takes place, as acceleration of charges is a condition for radiation of electromagnetic waves.

The second set of circumstances, which guarantees that any object subjected to low-frequency E and H fields usually does not experience effects of radiation, is that any configuration that carries electric currents sets up E and H field components which store energy without contributing to radiation. A short, linear antenna in free space (short electric dipole) generates, in addition to the radiation field E_r , an electrostatic field E_s and an induction field E_i . Neither E_s nor E_i contribute to the P_r [2,3]. Whereas E_r varies as $1/r$, where r is the distance from the antenna, E_i varies as $1/r^2$, and E_s as $1/r^3$. At a distance from the antenna of approximately one sixth of the wavelength ($r = \lambda/2\pi$), the E_i equals the E_r , and when $r \ll \lambda/6$ the E_r quickly becomes negligible in comparison with E_i and E_s . Similar results are obtained for other antenna configurations [4]. At 60 Hz the distance $\lambda/2\pi$ corresponds to about 800 km and objects at distances of a few kilometers or less from a 60-Hz system are exposed to nonradiating field components, which are orders of magnitude larger than the part of the field that contributes to radiation.

A living organism exposed to a static (dc) field or to a nonradiating near field may extract energy from it, but the quantitative description of the mechanism by which this extraction takes place is very different than at higher frequencies, where energy is transferred by radiation:

1. In the near field the relative magnitudes of E and H are a function of the current or charge configuration and the distance from the electric system. The E field may be much larger than the H field or vice versa (see [Figure 0.2](#)).
2. In the radiation field the ratio the E to H is fixed and equal to 377 in free space, if E is given in volt per meter and H in ampere per meter.
3. In the vicinity of most presently available human-made devices or systems carrying static electric charges, dc, or low-frequency (<1000 Hz) currents, the E and H fields will only under very exceptional circumstances be large enough to produce heating effects inside a living object, as illustrated by [Figure 0.3](#). (This statement assumes that the living object does not form part of a conducting path

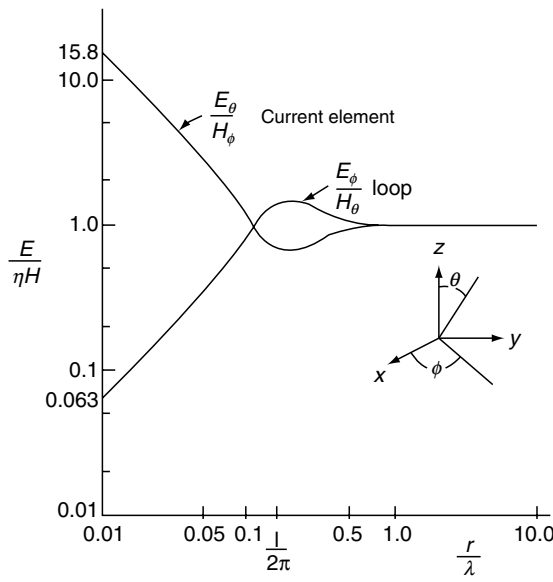


FIGURE 0.2

Ratio of E to H field (divided by wave impedance of free space $\eta = 377 \Omega$) at $\theta = 90^\circ$; for electric current element at origin along z -axis and for electrically small loop centered at the origin in $x-y$ plane.

that permits direct entrance of current from a wire or conducting ground.) However, nonthermal effects are possible; thus an E field of sufficient magnitude may orient dipoles, or translate ions or polarizable neutral particles (see Chapter 3 and Chapter 4 in *BBA**).

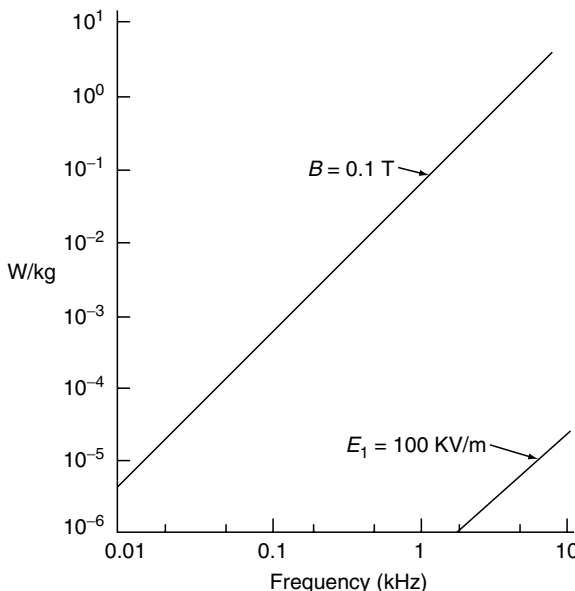


FIGURE 0.3

Top line: Eddy current loss produced in cylinder by sinusoidally time-varying axial H field. Cylinder parameters are conductivity $\sigma = 0.1 \text{ S/m}$, radius 0.1 m, density $D = 1100 \text{ kg/m}^3$, RMS magnetic flux density $0.1 \text{ T} = 1000 \text{ G}$. Watt per kilogram $= \sigma B^2 r^2 w^2 / 8D$; see Equation 0.15 and use power per volume $= J^2 / \sigma$. Lower line: Loss produced by 60-Hz E field in Watt per kilogram $= \sigma E_{\text{int}}^2 / D$, where external field E_1 is related to E_{int} by Equation 0.9 with $\epsilon_2 = \epsilon_0 \times 10^5$ at 1 kHz and $\epsilon_0 = 8 \times 10^4$ at 10 kHz.

*BBA: *Bioengineering and Biophysical Aspects of Electromagnetic Fields* (ISBN 0-8493-9539-9); BMA: *Biological and Medical Aspects of Electromagnetic Fields* (ISBN 0-8493-9538-0).

4. With radiated power it is relatively easy to produce heating effects in living objects with presently available human-made devices (see [Chapter 10](#) in *BBA* and [Chapter 5](#) in *BMA*). This does not imply, of course, that all biological effects of radiated radio frequency (RF) power necessarily arise from temperature changes.

The results of experiments involving exposure of organic materials and entire living organisms to static E and ELF E fields are described in *BBA*, [Chapter 3](#). Various mechanisms for the interaction of such fields with living tissue are also discussed there and in *BBA*, Chapter 5. In the present introduction, we shall only point out that one salient feature of static (dc) and ELF E field interaction with living organisms is that the external or applied E field is always larger by several orders of magnitude than the resultant average internal E field [5,6]. This is a direct consequence of boundary conditions derived from Maxwell's equations [1–3].

0.2 Penetration of Direct Current and Low-Frequency Electric Fields into Tissue

Assuming that the two materials illustrated schematically in Figure 0.4 are characterized, respectively, by conductivities σ_1 and σ_2 and dielectric permittivities ϵ_1 and ϵ_2 , we write E -field components parallel to the boundary as E_P and components perpendicular to the boundary as E_{\perp} . For both static and time-varying fields

$$E_{P1} = E_{P2} \quad (0.3)$$

and for static (dc) fields

$$\sigma_1 E_{\perp 1} = \sigma_2 E_{\perp 2} \quad (0.4)$$

as a consequence of the continuity of current (or conservation of charge). The orientations of the total E fields in media 1 and 2 can be represented by the tangents of the angles between the total fields and the boundary line

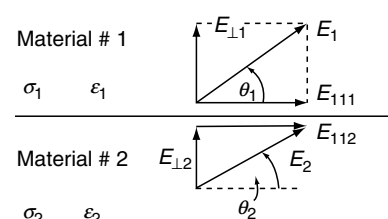
$$\tan \theta_1 = \frac{E_{\perp 1}}{E_{P1}}, \quad \tan \theta_2 = \frac{E_{\perp 2}}{E_{P2}} \quad (0.5)$$

From these equations it follows that

$$\tan \theta_1 = \frac{\sigma_2}{\sigma_1} \frac{E_{\perp 1}}{E_{P1}} = \frac{\sigma_2}{\sigma_1} \frac{E_{\perp 2}}{E_{P2}} = \frac{\sigma_2}{\sigma_1} \tan \theta_2 \quad (0.6)$$

FIGURE 0.4

Symbols used in description of boundary conditions for E -field components.



If material 1 is air with conductivity [7] $\sigma_1 = 10^{-13}$ S/m and material 2 a typical living tissue with $\sigma_2 \approx 10^{-1}$ S/m (compare Chapter 3 in *BBA*), $\tan \theta_1 = 10^{12} \tan \theta_2$, and therefore even if the field in material 2 (the inside field) is almost parallel to the boundary so that $\theta_2 \cong 0.5^\circ$ or $\tan \theta_2 \approx (1/100)$, $\tan \theta_1 = 10^{10}$ or $\theta_1 = (\pi/2 - 10)^{-10}$ radians. Thus an electrostatic field in air, at the boundary between air and living tissue, must be practically perpendicular to the boundary. The situation is virtually the same at ELF although Equation 0.4 must be replaced by

$$\sigma_1 E_{\perp 1} - \sigma_2 E_{\perp 2} = -j\omega\rho_s \quad (0.7)$$

and

$$\varepsilon_1 E_{\perp 1} - \varepsilon_2 E_{\perp 2} = \rho_s \quad (0.8)$$

where $j = \sqrt{-1}$, ω is the radian frequency ($= 2\pi \times$ frequency), and ρ_s is the surface charge density. In Chapter 3 in *BBA* it is shown that at ELF the relative dielectric permittivity of living tissue may be as high as 10^6 so that $\varepsilon_2 = 10^6 \varepsilon_0$, where ε_0 is the dielectric permittivity of free space ($1/36 \pi$) 10^{-9} F/m; however, it is still valid to assume that $\varepsilon_2 \leq 0^{-5}$. Then from Equation 0.7 and Equation 0.8

$$E_{\perp 1} = \frac{\sigma_2 + j\omega\varepsilon_2}{\sigma_1 + j\omega\varepsilon_1} E_{\perp 2} \quad (0.9)$$

which gives at 60 Hz with $\sigma_2 = 10^1$ S/m, $\sigma_1 = 10^{-13}$ S/m, $\varepsilon_2 \approx 10^{-5}$ F/m, and $\varepsilon_1 \approx 10^{-11}$ F/m

$$E_{\perp 1} = \frac{10^{-1} + j_4 10^{-3}}{10^{-13} + j_4 10^{-9}} E_{\perp 2} \approx \frac{\sigma_2}{j\omega\varepsilon_1} = -j(2.5 \times 10^7) E_{\perp 2} \quad (0.10)$$

This result, together with Equation 0.3 and Equation 0.5, shows that for the given material properties, the field in air must still be practically perpendicular to the boundary of a living organism: $\tan \theta_1; 2.5(10^7) \tan \theta_2$.

Knowing now that the living organism will distort the E field in its vicinity in such a way that the external field will be nearly perpendicular to the boundary surface, we can calculate the internal field by substituting the total field for the perpendicular field in Equation 0.4 (dc) and Equation 0.9 (ELF). For the assumed typical material parameters we find that in the static (dc) case

$$\frac{E_{\text{internal}}}{E_{\text{external}}} \approx 10^{-12} \quad (0.11)$$

$$\rho_f = \frac{3(\sigma_2\varepsilon_1 - \sigma_1\varepsilon_2)E_0}{2\sigma_1 + \sigma_2} \cos \vartheta \text{ C/m}^2$$

and for 60 Hz

$$\frac{E_{\text{internal}}}{E_{\text{external}}} \approx 4(10^{-8}) \quad (0.12)$$

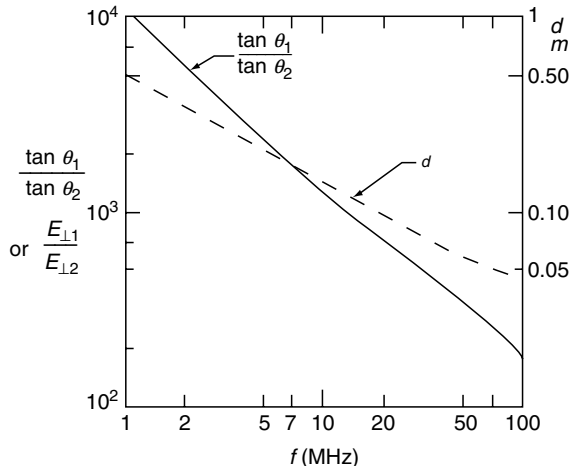


FIGURE 0.5

Orientation of E -field components at air–muscle boundary (or ratio of fields perpendicular to boundary); depth (d) at which field component parallel to boundary surface decreases by approximately 50% ($d = 0.6938$).

Thus, a 60-Hz external field of 100 kV/m will produce an average E_{internal} field of the order of 4 mV/m.

If the boundary between air and the organic material consists of curved surfaces instead of infinite planes, the results will be modified only slightly. Thus, for a finite sphere (with ϵ and σ as assumed here) embedded in air, the ratios of the internal field to the undisturbed external field will vary with the angle θ and distance r as indicated in Figure 0.5, but will not deviate from the results indicated by [Equation 0.7](#) and [Equation 0.8](#) by more than a factor of 3 [3,8]. Long cylinders ($L \ll r$) aligned parallel to the external field will have interior fields essentially equal to the unperturbed external field, except near the ends where the field component perpendicular to the membrane surface will be intensified approximately as above (see [Chapter 9](#) and [Chapter 10](#) in this volume).

0.3 Direct Current and Low-Frequency Magnetic Fields

Direct current H fields are considered in more detail in the [Chapter 3](#), [Chapter 5](#), and [Chapter 8](#) in *BBA*. ELF H fields are considered in various places, including Chapter 5 and [Chapter 7](#) in *BBA* and [Chapter 2](#) and [Chapter 11](#) in *BMA*. As the magnetic permeability μ of most biological materials is practically equal to the magnetic permeability μ_0 of free space, $4\pi(10^{-7})$ H/m, the dc or ELF H field “inside” will be practically equal to the H field “outside.” The only exceptions are organisms such as the magnetotactic bacteria, which synthesize ferromagnetic material, discussed in Chapter 8 of *BBA*. The known and suggested mechanisms of interaction of dc H fields with living matter are:

1. Orientation of ferromagnetic particles, including biologically synthesized particles of magnetite.
2. Orientation of diamagnetically or paramagnetically anisotropic molecules and cellular elements [9].
3. Generation of potential differences at right angles to a stream of moving ions (Hall effect, also sometimes called a magnetohydrodynamic effect) as a result of the magnetic force $F_m = qvB \sin \theta$, where q is the electric charge, v is the

velocity of the charge, B is the magnetic flux density, and $\sin \theta$ is the sine of the angle θ between the directions v and B . One well-documented result of this mechanism is a “spike” in the electrocardiograms of vertebrates subjected to large dc H fields.

4. Changes in intermediate products or structural arrangements in the course of light-induced chemical (electron transfer) reactions, brought about by Zeeman splitting of molecular energy levels or effects upon hyperfine structure. (The Zeeman effect is the splitting of spectral lines, characteristic of electronic transitions, under the influence of an external H field; hyperfine splitting of electronic transition lines in the absence of an external H field is due to the magnetic moment of the nucleus; such hyperfine splitting can be modified by an externally applied H field.) The magnetic flux densities involved not only depend upon the particular system and can be as high as 0.2 T (2000 G) but also <0.01 mT (100 G). Bacterial photosynthesis and effects upon the visual system are prime candidates for this mechanism [10,11].
5. Induction of E fields with resulting electrical potential differences and currents within an organism by rapid motion through a large static H field. Some magnetic phosphenes are due to such motion [12].

Relatively slow time-varying H fields, which are discussed in the basic mechanisms and therapeutic uses chapters ([Chapter 5](#) of BBA and [Chapter 11](#) in BMA), among others, may interact with living organisms through the same mechanisms that can be triggered by static H fields, provided the variation with time is slow enough to allow particles of finite size and mass, located in a viscous medium, to change orientation or position where required (mechanism 1 and 2) and provided the field intensity is sufficient to produce the particular effect. However, time-varying H fields, including ELF H fields, can also induce electric currents into stationary conducting objects. Thus, all modes of interaction of time-varying E fields with living matter may be triggered by time-varying, but not by static, H fields.

In view of Faraday’s law, a time-varying magnetic flux will induce E fields with resulting electrical potential differences and “eddy” currents through available conducting paths. As very large external ELF E fields are required (as indicated by [Equation 0.9](#) through [Equation 0.12](#)) to generate even small internal E fields, many human-made devices and systems generating both ELF E and H fields are more likely to produce physiologically significant internal E fields through the mechanism of *magnetic induction*.

The induced voltage V around some closed path is given by

$$V = \oint E \cdot d\ell = - \iint \frac{\partial B}{\partial t} ds \quad (0.13)$$

where E is the induced E field. The integration $\oint E \cdot d\ell$ is over the appropriate conducting path, $\partial B/\partial t$ is the time derivative of the magnetic flux density, and the “dot” product with the surface element, ds , indicates that only the component of $\partial B/\partial t$ perpendicular to the surface, i.e., parallel to the direction of the vector ds , enclosed by the conducting path, induces an E field. To obtain an order-of-magnitude indication of the induced current that can be expected as a result of an ELF H field, we consider the circular path of radius r , illustrated by [Figure 0.6](#). Equation 0.13 then gives the magnitude of the E field as

$$E = \frac{\omega Br}{2} \quad (0.14)$$

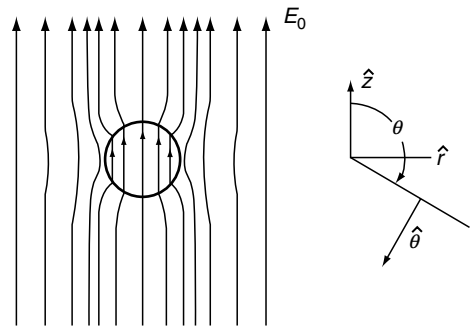


FIGURE 0.6

E field when sphere of radius R , conductivity σ_2 , and dielectric permittivity ϵ_2 is placed into an initially uniform static field ($E = 2E_0$) within a medium with conductivity σ_1 and permittivity ϵ_1 . The surface charge density is $\rho_r = \frac{3(\sigma_2\epsilon_1 - \sigma_1\epsilon_2)E_0}{2\sigma_1 + \sigma_2} \cos\theta \text{ C/m}^2$.

$$r < R \quad \bar{E} = \frac{3\sigma_1 E_0}{2\sigma_1 + \sigma_2} \hat{z} \quad \epsilon_2, \sigma_2$$

$$r < R \quad \bar{E} = E_0 \cos\theta \left[1 + \frac{2R^3(\sigma_2\epsilon_1)}{r^3(2\sigma_1 + \sigma_2)} \right] \hat{r} \quad \epsilon_1, \sigma_1$$

$$- E \sin\theta \left[1 - \frac{R^3(\sigma_2\epsilon_1)}{r^3(2\sigma_1 + \sigma_2)} \right] \hat{\theta}$$

where ω is the $2\pi f$ and f is the frequency. The magnitude of the resulting electric current density J in ampere per square meter is*

$$J = \sigma E = \frac{\sigma \omega B r}{2} \quad (0.15)$$

where σ is the conductivity along the path in Siemens per meter. In the SI (Système Internationale) units used throughout this book, B is measured in tesla ($T = 10^4 \text{ G}$) and r in meters. Choosing for illustration a circular path of 0.1 m radius, a frequency of 60 Hz, and a conductivity of 0.1 S/m, Equation 0.14 and Equation 0.15 give $E = 18.85 \text{ B}$ and $J = 1.885 \text{ B}$. The magnetic flux density required to obtain a current density of 1 mA/m^2 is 0.53 mT or about 5 G. The E field induced by that flux density along the circular path is 10 mV/m. To produce this same 10 mV/m E_{internal} field by an external 60 Hz E_{external} field would require, by Equation 0.12, a field intensity of 250 kV/m.

As the induced voltage is proportional to the time rate of change of the H field (Equation 0.13), implying a linear increase with frequency (Equation 0.14), one would expect that the ability of a time-varying H field to induce currents deep inside a conductive object would increase indefinitely as the frequency increases; or conversely, that the magnetic flux density required to induce a specified E field would decrease linearly with frequency, as indicated in Figure 0.7. This is not true however, because the displacement current density $\partial D / \partial t$, where $D = \epsilon E$, must also be considered as the frequency increases. This leads to the wave behavior discussed in Part III, implying that at sufficiently high frequencies the effects of both external E and H fields are limited

*Equation 0.15 neglects the H field generated by the induced eddy currents. If this field is taken into account, it can be shown that the induced current density in a cylindrical shell of radius r and thickness Δ is given by $\Delta r < 0.01 \text{ m}^2/[1 + j\Delta r/\delta^2]$, where $H_0 = B_0/\mu_0$ and δ is the skin depth defined by Equation 0.17 below. However, for conductivities of biological materials ($\sigma < 5 \text{ s/m}$) one obtains at audio frequencies $\delta > 1 \text{ m}$ and as for most dimensions of interest $\Delta r < 0.01 \text{ m}^2$ the term $j\Delta r/\delta^2$ becomes negligible. The result $-jrH_0/\delta^2$ is then identical with Equation 0.15.

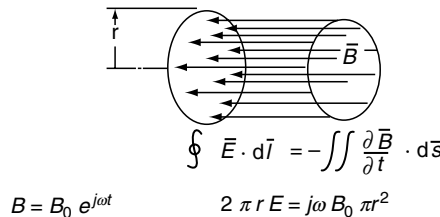


FIGURE 0.7

Circular path (loop) of radius r enclosing uniform magnetic flux density perpendicular to the plane of the loop. For sinusoidal time variation $B = B_0 e^{j\omega t}$.

by reflection losses (Figure 0.8 through Figure 0.10) as well as by skin effect [13], i.e., limited depth of penetration d in Figure 0.5.

0.4 RF Fields

At frequencies well below those where most animals and many field-generating systems have dimensions of the order of one free space wavelength, e.g., at 10 MHz where $\lambda = 30$ m, the skin effect limits penetration of the external field. This phenomenon is fundamentally different from the small ratio of internal to external E fields described in Equation 0.4 (applicable to dc) and Equation 0.9.

Equation 0.9 expresses a “boundary condition” applicable at all frequencies, but as the angular frequency ω increases (and in view of the rapid decrease with frequency of the dielectric permittivity ϵ_2 in biological materials—see Chapter 3 of *BBA*, the ratio of the normal component of the external to the internal E field at the boundary decreases

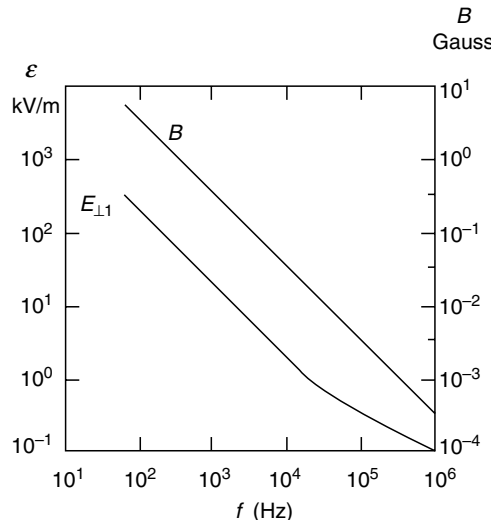


FIGURE 0.8

External E and H field required to obtain an internal E field of 10 mV/m (conductivity and dielectric permittivity for skeletal muscle from Foster, K.R., Schepps, J.L., and Schwan, H.P. 1980. *Biophys. J.*, 29:271–281. H -field calculation assumes a circular path of 0.1-m radius perpendicular to magnetic flux).

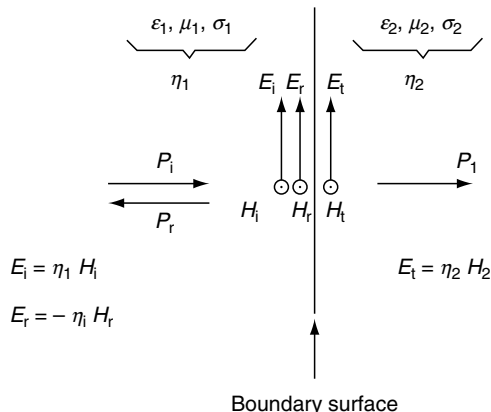


FIGURE 0.9

Reflection and transmission of an electromagnetic wave at the boundary between two different media, perpendicular incidence; P_i = incident power, P_r = reflected power, P_t = transmitted power.

with increasing frequency. This is illustrated by Figure 0.10 where $\tan \theta_1 / \tan \theta_2$ is also equal to $E_{\perp 1} / E_{\perp 2}$ in view of [Equation 0.3](#), [Equation 0.5](#), and [Equation 0.9](#). However, at low frequencies the total field inside the boundary can be somewhat larger than the perpendicular field at the boundary; and any field variation with distance from the boundary is not primarily due to energy dissipation, but in a homogeneous body is a consequence of shape. At RF, on the other hand, the E and H fields of the incoming

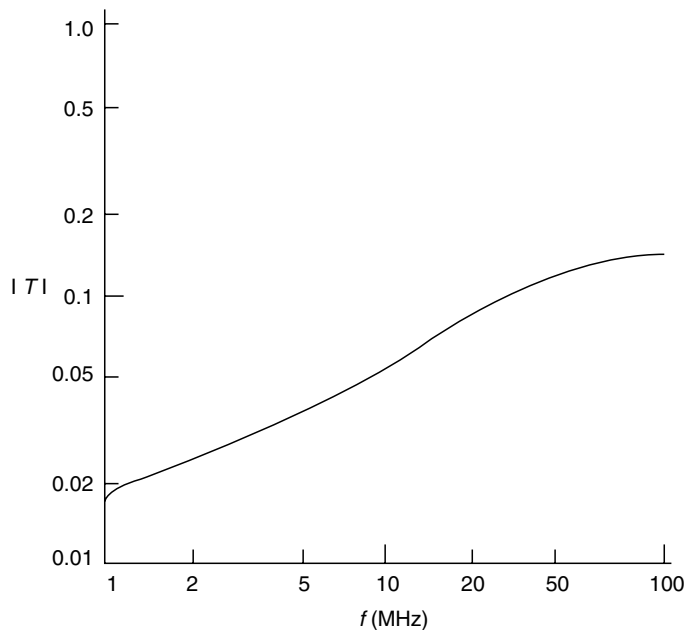


FIGURE 0.10

Magnitude of transmission coefficient T for incident E field parallel to boundary surface. $T = E_t / E_i$; reflection coefficient $r = E_r / E_i = T - 1$. Γ and T are complex numbers; ϵ_r and σ for skeletal muscle from [Chapter 3](#) in *BBA*.

electromagnetic wave, after reflection at the boundary, are further decreased due to energy dissipation. Both E and H fields decrease exponentially with distance from the boundary

$$g(z) = Ae^{-\frac{z}{\delta}} \quad (0.16)$$

where $g(z)$ is the field at the distance z and A is the magnitude of the field just *inside* the boundary.

As defined by Equation 0.16 the skin depth δ is the distance over which the field decreases to $1/e$ ($= 0.368$) of its value just *inside* the boundary. (Due to reflection, the field A just inside the boundary can already be very much smaller than the incident external field; see [Figure 0.8](#) and [Figure 0.9](#).)

Expressions for δ given below were derived [2,3,13,14] for plane boundaries between infinite media. They are reasonable accurate for cylindrical structures if the ratio of radius of curvature to skin depth (r_0/δ) is larger than about five [13]. For a good conductor

$$\delta = \frac{1}{\sqrt{\pi f \mu \sigma}} \quad (0.17)$$

where a good conductor is one for which the ratio p of conduction current, $J = \sigma E$, to displacement current, $\partial D / \partial t = \epsilon (\partial E / \partial t) = j \omega \epsilon E$ is large:

$$p = \frac{\sigma}{\omega \epsilon} \gg 1 \quad (0.18)$$

Since for most biological materials p is of the order of one ($0.1 < p < 10$) over a very wide frequency range (see [Chapter 3](#) of *BBA*), it is frequently necessary to use the more general expression [13]

$$\delta = \frac{1}{\omega \left[\frac{\mu \epsilon}{2} \left(\sqrt{1 + p^2} - 1 \right) \right]^{1/2}} \quad (0.19)$$

The decrease of field intensity with distance from the boundary surface indicated by Equation 0.16 becomes significant for many biological objects at frequencies where $r_0/\delta \geq 5$ is not satisfied. However, the error resulting from the use of Equation 0.16 and Equation 0.17 or Equation 0.19 with curved objects is less when $z < \delta$. Thus at $z = 0.693 \delta$, where $g(z) = 0.5 A$ from Equation 0.16 and Equation 0.17, the correct values of $g(z)$, obtained by solving the wave equation in cylindrical coordinates, differs only by 20% (it is 0.6 A) even when r_0/δ is as small as 2.39 [14]. Therefore, [Figure 0.10](#) shows the distance $d = 0.693 \delta$, at which the field decreases to half of its value just inside the boundary surface, using Equation 0.19 with typical values for σ and ϵ for muscle from [Figure 0.11](#). It is apparent that the skin effect becomes significant for humans and larger vertebrates at frequencies > 10 MHz.

Directly related to skin depth, which is defined for fields varying sinusoidally with time, is the fact that a rapid transient variation of an applied magnetic flux density constitutes an exception to the statement that the dc H field inside the boundary is equal to the H field outside. Thus, from one viewpoint one may consider the rapid application or removal of a dc H field as equivalent to applying a high-frequency field during the switching period, with the highest frequencies present of the order of $1/\tau$, where τ is the rise time of the applied step function. Thus, if $\tau < 10^{-8}$ s, the skin effect will be important during the transient period, as d in [Figure 0.5](#) is < 5 cm above 100 MHz. It is also possible to calculate directly the magnetic flux density inside a conducting cylinder as a function of radial position r and time t when a magnetic pulse is applied in the axial

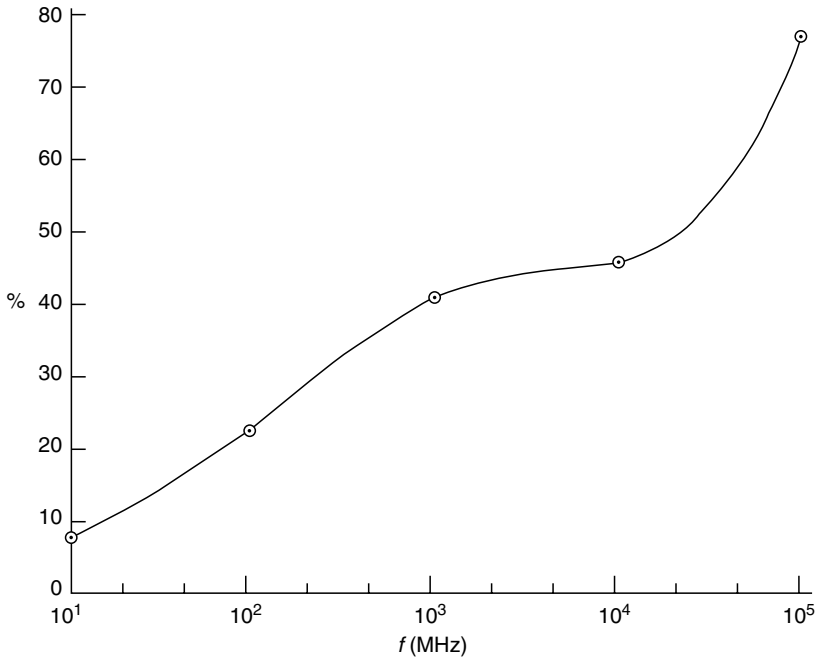


FIGURE 0.11

Ratio of transmitted to incident power expressed as percent of incident power. Air-muscle interface, perpendicular incidence (Equation 0.31, Table 0.1).

direction [15,16]. Assuming zero rise time of the applied field B_0 , i.e., a true step function, one finds that the field inside a cylinder of radius a is

$$B = B_0 \left[1 - \sum_{k=1}^{\infty} J_0\left(r \frac{v_k}{a}\right) e^{-t/T_k} \right] \quad (0.20)$$

where $J_0(r v_k/a)$ is the zero-order Bessel function of argument $r v_k/a$ and the summation is over the nulls of J_0 designated v_k (the first four values of v_k are 2.405, 5.520, 8.654, and 11.792).* T_k is the rise time of the k th term in the series and is given by

$$T_k = \frac{\mu_0 \sigma a^2}{v_k} \quad (0.21)$$

As v_k increases, the rise time decreases and therefore the longest delay is due to the first term in the summation with $k = 1$

$$T_1 = \frac{\mu_0 \sigma a^2}{2.405} \quad (0.22)$$

For a cylinder with 0.1 m radius and a conductivity $\sigma \approx 1 \text{ S/m}$, which is a typical value for muscle between 100 and 1000 MHz, Equation 0.22 gives $T_1 = 2.6 \times 10^{-8} \text{ s}$. This finite rise time (or decay time in case of field removal) of the internal H field may be of some importance when pulsed H fields are used therapeutically [17]. It might also be used

*This result is based on solution of $\partial B / \partial t = (1/\mu_0) \nabla^2 B$, which is a consequence of Ampere's and Faraday's laws when displacement is disregarded. Equations 0.20 to 0.22 are therefore only correct when $p \gg 1$.

to measure noninvasively the conductivity of biological substances *in vivo* through determination of the final decay rate of the voltage induced into a probe coil by the slowly decaying internal field after the applied field is removed [16].

The properties of biological substances in the intermediate frequency range, above ELF (>300 Hz), and below the higher RFs, where wave behavior and skin effect begin to be important (~ 20 MHz), are discussed in [Chapter 3](#) of *BBA*. However, many subsequent chapters are concerned with biological effects at dc and ELF frequencies below a few kilohertz, while others deal primarily with the higher RFs, >50 MHz. One reason for this limited treatment of the intermediate frequency range is that very little animal data are available for this spectral region in comparison with the large number of experiments performed at ELF and microwave frequencies in recent years.* Another reason is that most electrical processes known to occur naturally in biological systems—action potentials, EKG, EEG, ERG, etc.—occur at dc and ELF frequencies. Therefore, one might expect some physiological effects from external fields of appropriate intensity in the same frequency range, even if the magnitude of such fields is not large enough to produce thermal effects. As illustrated by [Figure 0.3](#) and [Figure 0.7](#), most *E* fields below 100 kHz set up by currently used human-made devices, and most *H* fields below 10 kHz except the very strongest, are incapable of producing thermal effects in living organisms, excluding, of course, fields accompanying currents directly introduced into the organism via electrodes. Thus, the frequencies between about 10 and 100 kHz have been of relatively little interest because they are not very likely to produce thermal or other biological effects. On the other hand, the higher RFs are frequently generated at power levels where enough energy may be introduced into living organisms to produce local or general heating. In addition, despite skin effect and the reflection loss to be discussed in more detail below, microwaves modulated at an ELF rate may serve as a vehicle for introducing ELF fields into a living organism of at least the same order of magnitude as would be introduced by direct exposure to ELF. Any effect of such ELF-modulated microwaves would, of course, require the existence of some amplitude-dependent demodulation mechanism to extract the ELF from the microwave carrier.

Among the chapters dealing with RF, [Chapter 10](#) and [Chapter 11](#) of *BBA* give the necessary information for establishing the magnitude of the fields present in biological objects: (1) experimental techniques and (2) analytical methods for predicting field intensities without construction of physical models made with “phantom” materials, i.e., dielectric materials with properties similar to those of living objects which are to be exposed. As thermal effects at microwave frequencies are certainly important, although one cannot assume *a priori* that they are the only biological effects of this part of the spectrum, and as some (but not all) thermal effects occur at levels where the thermoregulatory system of animals is activated, thermoregulation in the presence of microwave fields is discussed in [Chapter 5](#) of *BMA*, as well as in Chapter 10 of *BBA*. Not only are the therapeutic applications of microwaves based upon their thermal effects, but also the experimental establishment of possible nonthermal effects at the threshold of large scale tissue heating in particular living systems and also requires thorough understanding of thermoregulatory mechanisms. The vast amount of experimental data obtained on animal systems exposed to microwave is discussed in [Chapter 3](#) and [Chapter 4](#) in *BMA*. Both nonmodulated fields and modulated fields, where the type of modulation had no apparent effect other than modification of the average power level, are considered. These chapters and the [Chapter 9](#) in *BMA* are considered to be very new extension of experiments into exposures to ultra-short and to ultra-high power pulses.

*Though this statement was written in for the second edition in 1995, it continues to be true in 2005—Ben Greenebaum.

At the higher RFs, the external E field is not necessarily perpendicular to the boundary of biological materials (see Figure 0.4 and Figure 0.10), and the ratio of the total external E field to the total internal field is not given by Equation 0.9. However, the skin effect (Equation 0.16 through Equation 0.19) and reflection losses still reduce the E field within any biological object below the value of the external field. As pointed out in Chapter 3, dielectric permittivity and electrical conductivity of organic substances both vary with frequency. At RF, most biological substances are neither very good electrical conductors nor very good insulators, with the exception of cell membranes, which are good dielectrics at RF but at ELF can act as intermittent conductors or as dielectrics and are ion-selective [18–20]. The ratio p (Equation 0.18) is neither much smaller nor very much larger than values shown for typical muscle tissue [21,22] in Table 0.1.

Reflection loss at the surface of an organism is a consequence of the difference between its electrical properties and those of air. Whenever an electromagnetic wave travels, from one material to another with different electrical properties, the boundary conditions (Equation 0.3 and Equation 0.8) and similar relations for the H field require the existence of a reflected wave. The expressions for the reflection coefficient

$$\Gamma = \frac{E_r}{E_i} \quad (0.23)$$

and the transmission coefficient

$$T = \frac{E_t}{E_i} \quad (0.24)$$

become rather simple for loss-free dielectrics ($p \ll 1$) and for good conductors ($p \gg 1$). As biological substances are neither the most general expressions for Γ and T , applicable at plane boundaries, are needed [3,13]. For perpendicular incidence, illustrated by Figure 0.8,

$$\Gamma = \frac{\eta_2 - \eta_1}{\eta_2 + \eta_1} \quad (0.25)$$

$$T = \frac{2\eta_2}{\eta_2 + \eta_1} = 1 + \Gamma \quad (0.26)$$

TABLE 0.1

Ratio p of Conduction Current to Displacement as a Function of Frequency

f (MHz)	σ	ϵ_r	$p = \frac{\sigma}{\omega\epsilon_0\epsilon_r}$
1	0.40	2000	3.6
10	0.63	160	7.1
100	0.89	72	2.2
10^3	1.65	50	0.59
10^4	10.3	40	0.46
10^5	80	6	2.4

where η_1 and η_2 are the wave impedances, respectively, of mediums 1 and 2. The wave impedance of a medium is the ratio of the E to the H field in a plane wave traveling through that medium; it is given by [13]

$$\eta = \left(\frac{j\omega\mu}{\sigma + j\omega\epsilon} \right)^{1/2} \quad (0.27)$$

Clearly Γ and T are in general complex numbers, even when medium 1 is air for which Equation 0.27 reduces to the real quantity $\eta_0 = \sqrt{\mu_0/\epsilon_0}$, because medium 2, which here is living matter, usually has a complex wave impedance at RFs.

The incident, reflected, and transmitted powers are given by [13]

$$P_i = R_1 |E_i|^2 \frac{1}{\eta_1^*} = \frac{|E_i|^2}{|\eta_1|^2} R_1 \quad (0.28)$$

$$P_r = R_1 |E_r|^2 \frac{1}{\eta_1^*} = \frac{|E_r|^2}{|\eta_1|^2} R_1 \quad (0.29)$$

$$P_t = R_1 |E_t|^2 \frac{1}{\eta_2^*} = \frac{|E_t|^2}{|\eta_2|^2} R_2 \quad (0.30)$$

where the E fields are effective values ($E_{\text{eff}} = E_{\text{peak}}/\sqrt{2}$) of sinusoidal quantities, R_1 signifies “real part of,” η^* is the complex conjugate of η , and R_1 and R_2 are the real parts of η_1 and η_2 . If medium 1 is air, $\eta_1 = R_1 = 377 \Omega$, it follows from [Equation 0.23](#), [Equation 0.24](#), and Equation 0.28 through Equation 0.30 and conservation of energy that the ratio of the transmitted to the incident real power is given by

$$\frac{P}{P_i} = |T|^2 \frac{\eta_1 \eta_2^* + \eta_1^* \eta_2}{2|\eta_2|^2} = 1 - \frac{P_r}{P_i} = 1 - |\Gamma|^2 \quad (0.31)$$

The magnitude of the transmission coefficient T for the air–muscle interface over the 1- to 100-MHz frequency range is plotted in [Figure 0.9](#), which shows that the magnitude of the transmitted E field in muscle tissue is considerably smaller than the E field in air. The fraction of the total incident power that is transmitted (Equation 0.31) is shown in [Figure 0.11](#), indicating clearly that reflection loss at the interface decreases with frequency. However, for deeper lying tissue this effect is offset by the fact that the skin depth δ ([Equation 0.19](#)) also decreases with frequency ([Figure 0.12](#)) so that the total power penetrating beyond the surface decreases rapidly.

In addition to reflection at the air–tissue boundary, further reflections take place at each boundary between dissimilar materials. For example, the magnitude of the reflection coefficient at the boundary surface between muscle and organic materials with low-water content, such as fat or bone, is shown in [Table 0.2](#).

The situation is actually more complicated than indicated by [Figure 0.9](#) and [Figure 0.11](#), because the wave front of the incident electromagnetic wave may not be parallel to the air–tissue boundary. Two situations are possible: the incident E field may be polarized perpendicular to the plane of incidence defined in [Figure 0.13](#) (perpendicular polarization, [Figure 0.13a](#)) or parallel to the plane of incidence (parallel polarization, [Figure 0.13b](#)). The transmission and reflection coefficients [8] are different for the two types of polarization and also become functions of the angle of incidence α_1 :

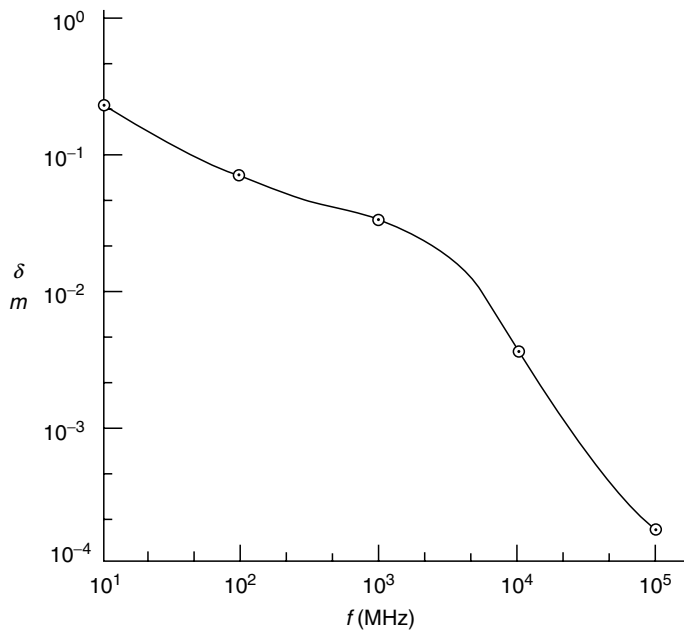


FIGURE 0.12

Electromagnetic skin depth in muscle tissue from plane wave expression (Equation 0.19, Table 0.1).

$$\text{Perpendicular polarization} \begin{cases} T_{\perp} = \frac{2\eta_2 \cos \alpha_1}{\eta_2 \cos \alpha_1 + \eta_1 \cos \alpha_2} \\ \Gamma_{\perp} = \frac{\eta_2 \cos \alpha_1 - \eta_1 \cos \alpha_2}{\eta_2 \cos \alpha_1 + \eta_1 \cos \alpha_2} \end{cases} \quad (0.32), (0.33)$$

$$\text{Parallel polarization} \begin{cases} T_p = \frac{2\eta_2 \cos \alpha_1}{\eta_2 \cos \alpha_2 + \eta_1 \cos \alpha_1} \\ \Gamma_p = \frac{\eta_1 \cos \alpha_1 - \eta_2 \cos \alpha_2}{\eta_2 \cos \alpha_2 + \eta_1 \cos \alpha_1} \end{cases} \quad (0.34), (0.35)$$

where α_2 is given by the generalized Snell's law (when both the media have the magnetic permeability of free space) by

TABLE 0.2

Reflection Coefficient "Capital Gamma" for Low-Water-Content Materials

f (MHz)	Fat or Bone		Muscle ^a -Fat (Γ)
	σ (S/m)	ϵ_r	
10^2	0.048	7.5	0.65
10^3	0.101	5.6	0.52
10^4	0.437	4.5	0.52

^a σ and ϵ_r for muscle from Table 0.1.

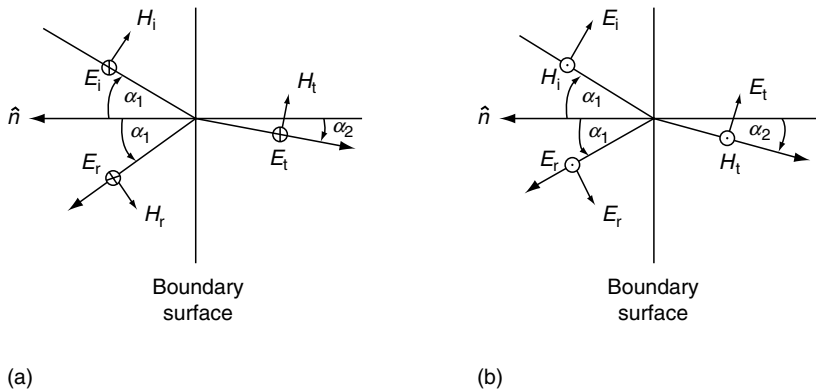


FIGURE 0.13
Oblique incidence of an electromagnetic wave at the boundary between two different media. (a) Perpendicular polarization (E vector perpendicular to plane of incidence); (b) parallel polarization (E vector parallel to plane of incidence). The plane of incidence is the plane formed by the surface normal (unit vector \hat{n}) and the direction of the incident wave; \otimes indicates a vector into the plane of the paper; \odot indicates a vector out of the plane of the paper. The orientation of the field vectors in the transmitted field is shown for loss-free dielectrics. For illustration of the transmitted wave into a medium with finite conductivity, where the wave impedance η_2 becomes a complex number, see Stratton, J.A., *Electromagnetic Theory*, McGraw-Hill, New York, 1941, p. 435.

$$\sin \alpha_2 = \frac{\sqrt{\epsilon_1}}{\sqrt{\epsilon_2 - j\sigma_2/\omega}} \quad (0.36)$$

so that $\cos \alpha_2 = \sqrt{1 - \sin^2 \alpha_2}$ is a complex number unless $\rho_2 = (\sigma_2/\omega\epsilon_2) = 1$.

As illustration, the variation with angle of incidence of the transmission coefficient for parallel polarization at the air–muscle interface at 10 MHz, is shown in Figure 0.14. It is apparent that the transmitted field is not necessarily maximized by perpendicular incidence in the case of parallel polarization. Furthermore, whenever $p \approx 1$ or $p > 1$ (see Table 0.1, above), α_2 is complex, which causes the waves entering the tissue to be inhomogeneous—they are not simple plane waves, but waves where surfaces of constant phase and constant amplitude do not coincide [3,23]; only the planes of constant amplitude are parallel to the boundary surface.

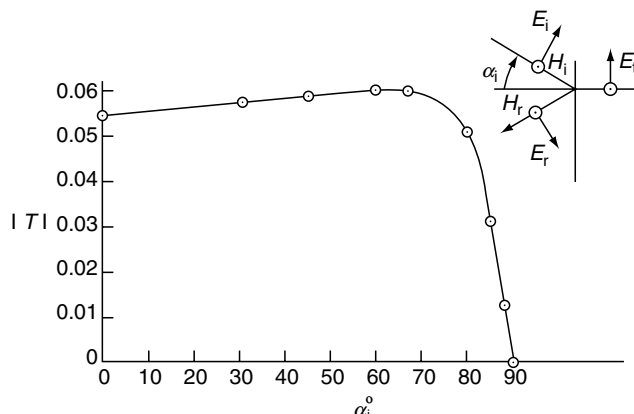


FIGURE 0.14
Magnitude of complex transmission coefficient for parallel polarization versus angle of incidence α_1 at 10 MHz (E field in plane of incidence, H field parallel to boundary plane; $\sigma_2 = 0.7 \text{ S/m}$, $\epsilon_{r2} = 150$, $T = E_t/E_r$).

Analytical solutions for nonplanar structures taking into account size and shape of entire animals have been given [24] and are also described in the RF modeling [Chapter 10](#) of *BBA*.

0.5 Biophysical Interactions of Fields: Ionization, Ionizing Radiation, Chemical Bonds, and Excitation

RF fields can be characterized as nonionizing radiation. By this we mean that there is not enough energy in a single quantum of energy, hf , to ionize an atom or a molecule at RFs, where h is Planck's constant and f is the frequency. By comparison radiation in the UV or x-rays often lead to ionization. It is desirable to begin by reviewing the differences between ionizing and nonionizing radiations, to explain ionization phenomena and also to discuss related excitation phenomena, which require less energy than ionization. Then a number of the proposed models concerning atomic or molecular-level interactions of fields will be introduced. A number of these theories will be discussed and their predictions compared with experimental results in later chapters, including [Chapter 5](#) through [Chapter 7](#) and [Chapter 9](#) in *BBA*; Chapter 9 and [Chapter 11](#) in *BMA*. Heating, cell excitation, electroporation, and other results of high-intensity fields have been accepted as explanations for many bioelectromagnetic phenomena. For low-intensity exposure, however, no theory is widely accepted as a general explanation for bioelectromagnetic phenomena, and few specific phenomena have accepted explanations. It is quite possible that no general explanation exists and that more than one mechanism of interaction between fields will be found to be operating, depending on the situation. Binihi's book [25] contains a good summary of most recent theoretical proposals, including comparisons with data and critiques of their strong and weak points, as well as his own theory.

We note first that the energy of electromagnetic waves is quantized with the quantum of energy (in joules) being equal to Planck's constant ($h = 6.63 \times 10^{-34}$ J s) times the frequency. This energy can also be expressed in electron volts, i.e., in multiples of the kinetic energy acquired by an electron accelerated through a potential difference of 1 eV ($1 \text{ eV} \approx 1.6 \times 10^{-19}$ J). Energy quanta for a few frequencies are listed in [Table 0.3](#).

Quantized energy can "excite" molecules; appropriate frequencies can couple to vibrational and rotational oscillation; and if the incident energy quantum has sufficient magnitude it can excite other changes in the electron configuration, such as changing an electron to another (unoccupied) energy level or tearing an electron away from one of the constituent atoms, the latter process called as ionization. The energy required to remove one electron from the highest energy orbit of a particular chemical element is called its "ionization potential." Typical ionization potentials are of the order 10 eV; for example, for the hydrogen atom it is 13.6 eV and for gaseous sodium it is 5.1 eV. As chemical binding forces are essentially electrostatic, ionization implies profound chemical changes. Therefore ionization by any outside agent of the complex compounds that make up a living system leads to profound and often irreversible changes in the operation of that system.

Table 0.3 shows that even the highest RF (millimeter waves) has quantum energies well below the ionization potential of any known substance; thus one speaks of nonionizing radiation when referring to electromagnetic waves below UV light frequencies. Ionizing radiation includes UV and higher frequency electromagnetic waves (x-rays, γ -rays).

TABLE 0.3

Wave and Quantum Characteristics of Various Types of Radiation

Name of Radiation or Application	Frequency (Hz)	Wavelength (m)	Energy of 1 Quantum of Radiation (eV)
UHF TV	7×10^8	0.43	2.88×10^{-6}
Microwave radar	10^{10}	3×10^{-2}	4.12×10^{-5}
Millimeter wave	3×10^{11}	1×10^{-3}	1.24×10^{-3}
Visible light	6×10^{14}	5×10^{-7}	2.47
Ionizing UV	10^{16}	3×10^{-4}	41.2
Soft x-ray	10^{18}	3×10^{-10}	4120
Penetrating x-ray	10^{20}	3×10^{-12}	4.12×10^5

This explanation of the difference between ionizing and nonionizing radiation should not imply that nonionizing electromagnetic radiation cannot have profound effects upon inorganic and organic substances. As excitation of coherent vibrational and rotational modes requires considerably less energy than ionization, it could occur at RF; this will be discussed in later chapters. In addition, many other possible biological effects require energies well below the level of ionizing potentials. Examples are tissue heating, dielectrophoresis, depolarization of cell membranes, mechanical stress due to piezoelectric transduction, or dielectric saturation, resulting in the orientation of the polar side chains of macromolecules and leading to the breaking of hydrogen bonds. These and other mechanisms will be discussed by the authors of several chapters (see especially [Chapter 5](#) through [Chapter 7](#) of *BBA* and [Chapter 9](#) of *BMA*), who will also give estimates of rates at which energy must be delivered to produce particular effects.

Returning to the discussion of ionization, it is important to note that ionization of a chemical element can be brought about not only by absorption of electromagnetic energy, but also by collision either with foreign (injected) atoms, molecules, or subatomic particles of the requisite energy, or by sufficiently violent collision among its own atoms. The latter process constitutes ionization by heating, or thermal breakdown of a substance, which will occur when the kinetic energy of the colliding particles exceeds the ionization potential. As the average thermal kinetic energy of particles is related to temperature [26] by $W = kT$ where k is Boltzmann's constant ($= 1.38 \times 10^{-23} \text{ J/K}$), we find that the required temperature is

$$1.38(10^{-23})T \approx 5 \text{ eV} \approx (5)1.6(10^{-19})\text{J}$$

$$T \approx 5(10^4) \text{ K}$$

which is about twice the temperature inside a lightning stroke [27] and orders of magnitude higher than any temperature obtainable from electromagnetic waves traveling through air.

Actually, initiation of lightning strokes is an example of ionization by collision with injected energetic particles. The few free electrons and ions always present in the air due to ionization by cosmic rays are accelerated by the E fields generated within clouds to velocities corresponding to the required ionization energy. Only when the field is large enough to impart this energy over distances shorter than the mean free path of the free electrons or ions at atmospheric pressure can an avalanche process take place: an accelerated electron separates a low-energy electron from the molecule with which it collides and in the process loses most of its own energy; thus, one high-energy free electron is exchanged for two free low-energy electrons and one positive ion. Both the

electrons are in turn accelerated again by the field, giving them high kinetic energy before they collide with neutral molecules; their collision produces four free electrons and the multiplication process continues. The breakdown field strength for air at atmospheric pressure is approximately 3×10^6 V/m, implying a mean free path of electrons

$$\Delta\ell \approx [5 \text{ eV}/3 \times 10^6 \text{ V/m}] \approx 10^{-6} \text{ m}$$

However, this model is not entirely accurate because the actual mean free path corresponds to energies of the order of 0.1 eV, which is only sufficient to excite vibrational modes in the target molecule. Apparently such excitation is sufficient to cause ionization if the collision process lasts long enough [28].

Except for some laboratory conditions where a sufficiently high potential difference can be applied directly across a biological membrane to bring about its destruction, collisional ionization is generally not a factor in the interaction of electromagnetic waves with tissue: The potential difference required for membrane destruction [29] is between 100 nV and 300 mV, corresponding to a field strength of the order of 2×10^7 V/m, assuming a membrane thickness ($d = 100 \text{ \AA}$; $E = V/d$). However, there is a third mechanism of ionization that is particularly important in biological systems. When a chemical compound of the type wherein positive and negative ions are held together by their electrostatic attraction, such as the ionic crystal NaCl, is placed in a suitable solvent, such as H₂O, it is separated into its ionic components. The resulting solution becomes an electrolyte, i.e., an electrically conducting medium in which the only charge carriers are ions.

In this process of chemical ionization, the Na⁺ cations and Cl⁻ anions are separated from the original NaCl crystal lattice and individually surrounded by a sheet of solvent molecules, the "hydration sheath." If the solvent is H₂O, this process is called "hydration," or more generally, for any solvent, "solvation."

A dilute solution of NaCl crystals in H₂O is slightly cooler than the original constituents before the solvation process, indicating that some internal energy of the system was consumed. Actually energy is consumed in breaking up the original NaCl bonds and some, but less, is liberated in the interaction between the dipole moment of the solvent molecule (H₂O in our example) and the electric charges on the ions. Thus, solvents with higher relative dielectric constant ϵ_r , indicating higher inherent electric dipole moment per unit volume (P), solvate ions more strongly ($\epsilon_r = 1 + P/[\epsilon_0 E]$, where E is the electric field applied during the measurement of ϵ_r). For example, H₂O with $\epsilon_r \approx 80$ solvates more strongly than methanol with $\epsilon_r \approx 33$. For biological applications it is worth noting that solvation may affect not only ionic substances, but also polar groups, i.e., molecular components which have an inherent dipole moment, such as—C=O, —NH, or —NO₂. Details of the process are discussed in texts on electrochemistry [30,31].

In biological processes not only chemical ionization and solvation of ionic compounds, but also all kinds of chemical reaction take place. One of the central questions in the study of biological effects of E and H fields is therefore not only whether they can cause or influence ionization, but also whether they can affect—speed up, slow down, or modify—any naturally occurring biologically important chemical reaction.

In Table 0.4 typical energies for various types of chemical bonds are listed. For comparison the thermal energy per elementary particle at 310 K is also shown. Complementing the numbers in Table 0.4 one should also point out that:

1. The large spread in the statistical distribution of energies of thermal motion guarantees that at physiological temperatures some molecules always have sufficient energy to break the strongest weak bonds [32].

TABLE 0.4

Bond and Thermal Energies

Type of Bond	Change in Free Energy (Binding Energy) kcal/mol	eV/Molecule
Covalent	50–100	2.2–4.8
Van der Waals	1–2	0.04–0.08
Hydrogen	3–7	0.13–0.30
Ionic ^a	5	0.2
Avg. thermal energy at 310 K	0.62	0.027

^aFor ionic groups of organic molecules such as COO^- , NH_3^+ in aqueous solution.

2. The average lifetime of a weak bond is only a fraction of a second.
3. The weak binding forces are effective only between the surfaces in close proximity and usually require complementary structures such as a (microscopic) plug and hole, such as are thought to exist, for instance, between antigen and antibody [33].
4. Most molecules in aqueous solution form secondary bonds.
5. The metabolism of biological systems continuously transforms molecules and therefore also changes the secondary bonds that are formed.

Comparison of the last columns in [Table 0.3](#) and Table 0.4 shows that millimeter waves have quantum energies, which are only about one order of magnitude below typical Van der Waals energies (waves at a frequency of 10^{12} Hz with a quantum energy of 0.004 eV have a wavelength of 0.3 mm and can still be classified as millimeter waves). One might expect therefore that such waves could initiate chemically important events, such as configurational changes, by e.g., multiple transitions between closely spaced vibrational states at successively high-energy levels [46].

Energies associated with transition from one to another mode of rotation of a diatomic molecule are given by $W = \ell(\ell + 1)A$ [26,33], where $\ell = 0, 1, 2, 3 \dots$ and $A = 6 \times 10^{-5}$ eV; thus an electromagnetic wave with a frequency as low as 29 GHz—still in the microwave region—can excite a rotational mode. Vibrational modes of diatomic molecules [26,33] correspond to energies of the order of 0.04 eV, requiring excitation in the IR region. Vibrational frequencies in a typical H-bonded system [34] are of the order of 3000 GHz; however, attenuation at this frequency by omnipresent free H_2O may prevent any substantial effect [34].

Kohli et al. [34] predict that longitudinal and torsional modes of double helical DNA should not be critically damped at frequencies > 1 GHz, although relaxation times are of the order of picoseconds, and Kondepudi [36] suggests the possibility of an influence of millimeter waves at approximately 5×10^{11} Hz upon oxygen affinity of hemoglobin due to resonant excitation of heme plane oscillations. Although Furia et al. [37] did not find resonance absorption at millimeter waves in yeast, such was reported by Grundler et al. [38,47]. The latter experiment has been interpreted [39,40] as supporting Fröhlich's theory of cooperative phenomena in biological systems. That theory postulates "electric polarization waves" in biological membranes which are polarized by strong biologically generated [18] fields (10^7 V/m). Fröhlich [41,42] suggests that metabolically supplied energy initiates mechanical vibrations of cell membranes. The frequency of such vibrations is determined by the dimensions and the elastic constants of the membranes;

based on an estimate of the sound velocity in the membrane of 10^3 m/s and a membrane thickness of 100 \AA (equal to one half wavelength) one obtains a frequency of $5(10^{10})$ Hz. Individual molecules within and outside the membrane may also oscillate, and frequency estimates vary between 10^9 Hz for helical RNA [43] and 5×10^{13} Hz for hydrogen-bonded amide structures [44]. As the membranes and molecules involved are strongly polarized, the mechanically oscillating dipole electromagnetic fields that are able to transmit energy, at least in some situations, over distances much larger than the distance to the next adjacent molecule.

Electromagnetic coupling of this type may produce long-range cooperative phenomena. In particular, Fröhlich [45] has shown that two molecular systems may exert strong forces upon each other when their respective oscillation frequencies are nearly equal, provided the dielectric permittivity of the medium between them is strongly dispersive or excitation is supplied by pumping, i.e., by excitation at the correct frequency from an external source. The mechanism is nonlinear in the sense that it displays a steplike dependence on excitation intensity. Possible long-range effects may be, for example, attraction between enzyme and substrate [42]. These and related topics have been discussed in detail by Illinger [34] and are reviewed in the present volume in [Chapter 11](#) and [Chapter 5](#) of *BBA*.

References

1. Jordan, E.C., *Electromagnetic Waves and Radiating Systems*. Prentice-Hall, Englewood Cliffs, NJ, 1950.
2. Schelkunoff, S.A., *Electromagnetic Waves*, D Van Nostrand, New York, 1943, p. 133.
3. Stratton, J.A., *Electromagnetic Theory*, McGraw-Hill, New York, 1941, p. 435.
4. Van Bladel, J., *Electromagnetic Fields*, McGraw-Hill, New York, 1964, p. 274.
5. Kaune, W.T. and Gillis, M.F., General properties of the interaction between animals and ELF electric fields, *Bioelectromagnetics*, 2, 1, 1981.
6. Bridges, J.E. and Preache, M., Biological influences of power frequency electric fields—a tutorial review from a physical and experimental viewpoint, *Proc. IEEE*, 69, 1092, 1981.
7. Iribarne, J.V. and Cho, H.R., *Atmospheric Physics*, D. Reidel, Boston, 1980, p. 134.
8. Zahn, M., *Electromagnetic Field Theory, A Problem Solving Approach*, John Wiley & Sons, New York, 1979.
9. Raybourn, M.S., The effects of direct-current magnetic fields on turtle retina in vitro, *Science*, 220, 715, 1983.
10. Schulten, K., Magnetic field effects in chemistry and biology, *Festkörperprobleme/Advances in Solid State Physics*, Vol. 22, Heyden, Philadelphia, 1982, p. 61.
11. Blankenship, R.E., Schaafsma, T.J., and Parson, W.W., Magnetic field effects on radical pair intermediates in bacterial photosynthesis, *Biochim. Biophys. Acta*, 461, 297, 1977.
12. Sheppard, A.R., Magnetic field interactions in man and other mammals: an overview, in *Magnetic Field Effect on Biological Systems*, Tenforde, T.S., Ed., Plenum Press, New York, 1979, p. 33.
13. Jordan, E.C., *Electromagnetic Waves and Radiating Systems*, Prentice-Hall, Englewood Cliffs, NJ, 1950, p. 132.
14. Ramo, S., Whinnery, J.R., and Van Duzer, T., *Fields and Waves in Communication Electronics*, John Wiley & Sons, New York, 1965, p. 293.
15. Smyth, C.P., *Static and Dynamic Electricity*, McGraw-Hill, New York, 1939.
16. Bean, C.P., DeBlois, R.W., and Nesbitt, L.B., Eddy-current method for measuring the resistivity of metals, *J. Appl. Phys.*, 30(12), 1959, 1976.
17. Bassett, C.A.L., Pawluk, R.J., and Pilla, A.A., Augmentation of bone repair by inductively coupled electromagnetic fields, *Science*, 184, 575, 1974.

18. Plonsey, R. and Fleming, D., *Bioelectric Phenomena*, McGraw-Hill, New York, 1969, p. 115.
19. Houslay, M.D. and Stanley, K.K., *Dynamics of Biological Membranes*, John Wiley & Sons, New York, 1982, p. 296.
20. Wilson, D.F., Energy transduction in biological membranes, in *Membrane Structure and Function*, Bittar, E.D., Ed., John Wiley & Sons, New York, 1980, p. 182.
21. Johnson, C.C. and Guy, A.W., Nonionizing electromagnetic wave effects in biological materials and systems, *Proc. IEEE*, 60, 692, 1972.
22. Schwan, H.P., Field interaction with biological matter, *Ann. NY Acad. Sci.*, 303, 198, 1977.
23. Kraichman, M.B., *Handbook of Electromagnetic Propagation in Conducting Media*, NAVMAT P-2302, U.S. Superintendent of Documents, U.S. Government Printing Office, Washington, D.C., 1970.
24. Massoudi, H., Durney, C.H., Barber, P.W., and Iskander, M.F., Postresonance electromagnetic absorption by man and animals, *Bioelectromagnetics*, 3, 333, 1982.
25. Binhi, V.N., *Magnetobiology: Understanding Physical Problems*, Academic Press, London, 473 pp.
26. Sears, F.W., Zemansky, M.W., and Young, H.D., *University Physics*, 5th ed., Addison-Wesley, Reading, MA, 1976, p. 360.
27. Uman, M.A., *Lightning*, McGraw-Hill, New York, 1969, p. 162.
28. Coelho, R., *Physics of Dielectrics for the Engineer*, Elsevier, Amsterdam, 1979, p. 155.
29. Schwan, H.P., Dielectric properties of biological tissue and biophysical mechanisms of electromagnetic field interaction, in *Biological Effects of Nonionizing Radiation*, Illinger, K.H., Ed., ACS Symposium Series 157, American Chemical Society, Washington, D.C., 1981, p. 121.
30. Koryta, J., *Ions, Electrodes and Membranes*, John Wiley & Sons, New York, 1982.
31. Rosenbaum, E.J., *Physical Chemistry*, Appleton-Century-Crofts, Education Division, Meredith Corporation, New York, 1970, p. 595.
32. Watson, J.D., *Molecular Biology of the Gene*, W.A. Benjamin, Menlo Park, CA, 1976, p. 91.
33. Rosenbaum, E.J., *Physical Chemistry*, Appleton-Century-Crofts, Education Division, Meredith Corporation, New York, 1970, p. 595.
34. Illinger, K.H., Electromagnetic-field interaction with biological systems in the microwave and far-infrared region, in *Biological Effects of Nonionizing Radiation*, Illinger, K.H., Ed., ACS Symposium Series 157, American Chemical Society, Washington, D.C., 1981, p. 1.
35. Kohli, M., Mei, W.N., Van Zandt, L.L., and Prohofsky, E.W., Calculated microwave absorption by double-helical DNA, in *Biological Effects of Nonionizing Radiation*, Illinger, K.H., Ed., ACS Symposium Series 157, American Chemical Society, Washington, D.C., 1981, p. 101.
36. Kondepudi, D.K., Possible effects of 10^{11} Hz radiation on the oxygen affinity of hemoglobin, *Bioelectromagnetics*, 3, 349, 1982.
37. Furia, L., Gandhi, O.P., and Hill, D.W., Further investigations on resonant effects of mm-waves on yeast, Abstr. 5th Annu. Sci. Session, Bioelectromagnetics Society, University of Colorado, Boulder, June 12 to 17, 1983, 13.
38. Grundler, W., Keilman, F., and Fröhlich, H., Resonant growth rate response of yeast cells irradiated by weak microwaves, *Phys. Lett.*, 62A, 463, 1977.
39. Fröhlich, H., Coherent processes in biological systems, in *Biological Effects of Nonionizing Radiation*, Illinger, K.H., Ed., ACS Symposium Series 157, American Chemical Society, Washington, D.C., 1981, p. 213.
40. Fröhlich, H., What are non-thermal electric biological effects? *Bioelectromagnetics*, 3, 45, 1982.
41. Fröhlich, H., Coherent electric vibrations in biological systems and the cancer problem, *IEEE Trans. Microwave Theory Tech.*, 26, 613, 1978.
42. Fröhlich, H., The biological effects of microwaves and related questions, in *Advances in Electronics and Electron Physics*, Marton, L. and Marton, C., Eds., Academic Press, New York, 1980, p. 85.
43. Prohofsky, E.W. and Eyster, J.M., Prediction of giant breathing and rocking modes in double helical RNA, *Phys. Lett.*, 50A, 329, 1974.
44. Careri, J., Search for cooperative phenomena in hydrogen-bonded amide structures, in *Cooperative Phenomena*, Haken, H. and Wagner, W., Eds., Springer-Verlag, Basel, 1973, p. 391.
45. Fröhlich, H., Selective long range dispersion forces between large systems, *Phys. Lett.*, 39A, 153, 1972.

46. Barnes, F.S. and Hu, C.-L.J., Nonlinear Interactions of electromagnetic waves with biological materials, in *Nonlinear Electromagnetics*, Uslenghi, P.L.E., Ed., Academic Press, New York, 1980, p. 391.
47. Grundler, W., Keilmann, F., Putterlik, V., Santo, L., Strube, D., and Zimmermann, I., Nonthermal resonant effects of 42 GHz microwaves on the growth of yeast cultures, in *Coherent Excitations of Biological Systems*, Frölich, H. and Kremer, F., Eds., Springer-Verlag, Basel, 1983, p. 21.

1

Environmental and Occupationally Encountered Electromagnetic Fields

Kjell Hansson Mild and Ben Greenebaum

CONTENTS

1.1	Introduction	1
1.2	Direct Current and ELF (0–3000 Hz) EM Fields	2
1.2.1	Naturally Occurring Fields	2
1.2.2	Artificial DC and Power Frequency EM Fields in the Environment	3
1.2.2.1	DC Fields	3
1.2.2.2	High-Voltage AC Power Lines	4
1.2.2.3	Exposure in Homes	8
1.2.2.4	Electrical Appliances	11
1.2.2.5	ELF Fields in Occupational Settings	14
1.2.2.6	Internal ELF Fields Induced by External and Endogenous Fields	17
1.3	EM Fields at Intermediate and Radio Frequencies (3 kHz to 300 MHz)	19
1.3.1	Electronic Article Surveillance	19
1.3.2	EM Fields from Video Display Terminals	20
1.3.3	RF Transmissions	22
1.3.3.1	Shortwave Transmission	22
1.3.3.2	FM Radio and TV Transmission	22
1.3.3.3	Wireless Communication Systems (Base Stations, Personal Wireless Devices Such as Cellular Telephones and Pagers)	23
1.3.4	RF EM Fields in Industrial Settings (RF Dielectric Heaters, Worker Exposure to Broadcast Systems)	27
1.3.4.1	RF Sealers	27
1.3.4.2	Occupational Exposure from Broadcasting and Radars	27
1.3.4.3	Exposure in Medical Applications	28
1.4	Conclusion	29
	References	29

1.1 Introduction

We encounter electromagnetic (EM) fields every day, both naturally occurring and man-made fields. This leads to exposure both in our homes as well as in our various

workplaces, and the intensity of the fields varies substantially with the situation. Quite high exposure can occur in some of our occupations as well as our personal activities, for instance, in trains, where the extremely low-frequency (ELF) magnetic field can reach rather high levels. The frequency of the fields we are exposed to covers a wide range, from slowly changing static fields to the gigahertz range.

In this chapter, we give an overview of the fields we encounter in various situations.

1.2 Direct Current and ELF (0–3000 Hz) EM Fields

1.2.1 Naturally Occurring Fields

The most obvious naturally occurring field is the Earth's magnetic field, known since ancient times. The total field intensity diminishes from the poles, with a high of $67 \mu\text{T}$ at the south magnetic pole and a low of about $30 \mu\text{T}$ near the equator. In South Brazil, an area with flux densities as low as about $24 \mu\text{T}$ can be found. Indeed, the angle of the Earth's field to the horizontal (inclination) varies, primarily with latitude, ranging from very small near the equator to almost vertical at high latitudes. More information is available in textbooks (see, e.g., Dubrov [1]) and in databases available on the Web (see, e.g., the U.S. National Geophysical Data Center [2]).

However, the geomagnetic field is not constant, but is continuously subject to more or less strong fluctuations. There are diurnal variations, which may be more pronounced during the day and in summer than at night and in winter (see, e.g., König et al. [3]). There are also short-term variations associated with ionospheric processes. When the solar wind brings protons and electrons toward the Earth, phenomena like the Northern Lights and rapid fluctuations in the geomagnetic field intensity occur. The variation can be rather large; the magnitude of the changes can sometimes be up to $1 \mu\text{T}$ on a timescale of several minutes. The variation can also be very different in two fairly widely separated places because of the atmospheric conditions. There is also a naturally occurring direct current (DC) electric field at the surface of the Earth in the order of $100\text{--}300 \text{ V/m}$ (Earth's surface negative) in calm weather and can be 100 kV/m in thunderstorms, caused by atmospheric ions [4].

EM processes associated with lightning discharges are termed as atmospherics or "sferics" in short. They consist mostly of waves in the ELF (strictly speaking $30\text{--}300 \text{ Hz}$ but usually taken in the bioelectromagnetics literature to extend from 0 to 3000 Hz) and very low-frequency (VLF) ranges ($3\text{--}30 \text{ kHz}$) (see König et al. [3]). Each second about 100 lightning discharges occur globally, and in the United States one cloud-to-ground flash occurs about every second, averaged over the year [3]. The ELF and VLF signals travel efficiently in the waveguide formed by the Earth and the ionosphere and can be detected many thousands of kilometers from the initiating stroke. Since 1994, several experiments studying the effects of short-term exposure to simulated 10-kHz sferics have been performed at the Department of Clinical and Physiological Psychology at the University of Giessen, Germany [5,6]. In the ELF range, very low-intensity signals, called Schumann resonances, also occur. These are caused by the ionosphere and the Earth's surface acting as a resonant cavity, excited by lightning [3,7] (see also <http://www.oulu.fi/~spaceweb/textbook/schumann.html>). These cover the low-frequency spectrum, with broad peaks of diminishing amplitude at $7.8, 14, 20,$ and 26 Hz and higher frequencies. Higher-frequency fields, extending into the microwave region, are also present in atmospheric or intergalactic sources. These fields are much weaker, usually by many

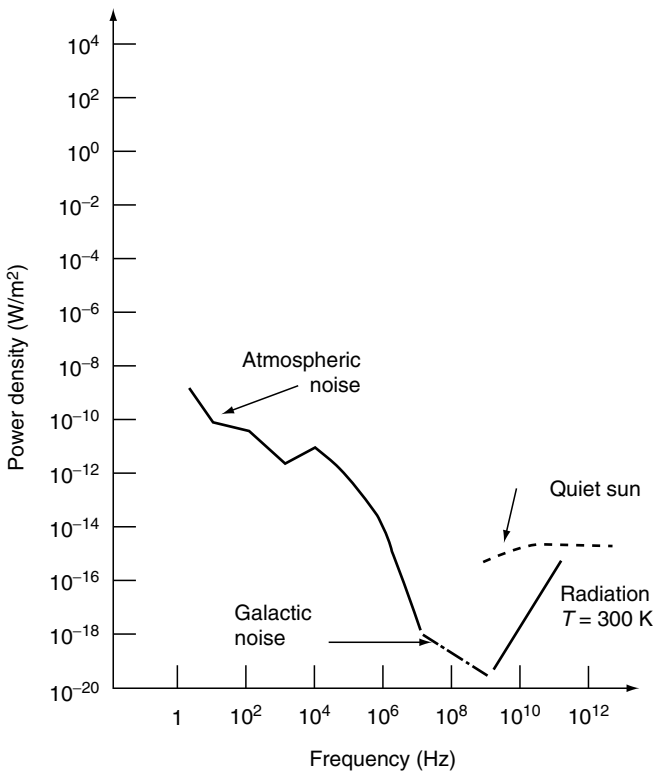


FIGURE 1.1

Power density from natural sources as a function of frequency. (Data from Smith, E. *Proceedings of the IEEE Symposium on Electromagnetic Compatibility*. Institute of Electrical and Electronic Engineering, Piscataway, NJ, 1982. Graph adapted from Barnes, F.S. *Health Phys.* 56, 759–766, 1989. With permission.)

orders of magnitude, than those caused by human activity (compare Figure 1.1 and subsequent tables and figures in this chapter).

1.2.2 Artificial DC and Power Frequency EM Fields in the Environment

1.2.2.1 DC Fields

Although alternate current (AC) power transmission is facilitated by the availability of transformers to change voltages, DC is also useful, especially since high-power, high-efficiency solid-state electronic devices have become available. Overland high-voltage DC lines running at up to ± 1100 kV are found in Europe, North America, and Asia [8] (see also, e.g., <http://www.answers.com/topic/high-voltage-direct-current>, accessed on August 17, 2005). Electric and magnetic fields near these lines are essentially the same as those for AC lines running at the same voltages and currents, which are discussed below. Because potentials on the cables do not vary in time and there are only two DC conductors (+ and -) instead of the three AC phases, the DC electric fields and space charge clouds of air ions that partially screen them are somewhat different from those near AC transmission lines, though the general features are the same, especially for positions away from the lines. Electric fields, corona, and air ions are discussed further in the AC transmission line section below; see also Refs. [9,10].

For transfer of electric power between countries separated by sea, undersea power cables are especially useful, since their higher capacity causes increased losses in AC.

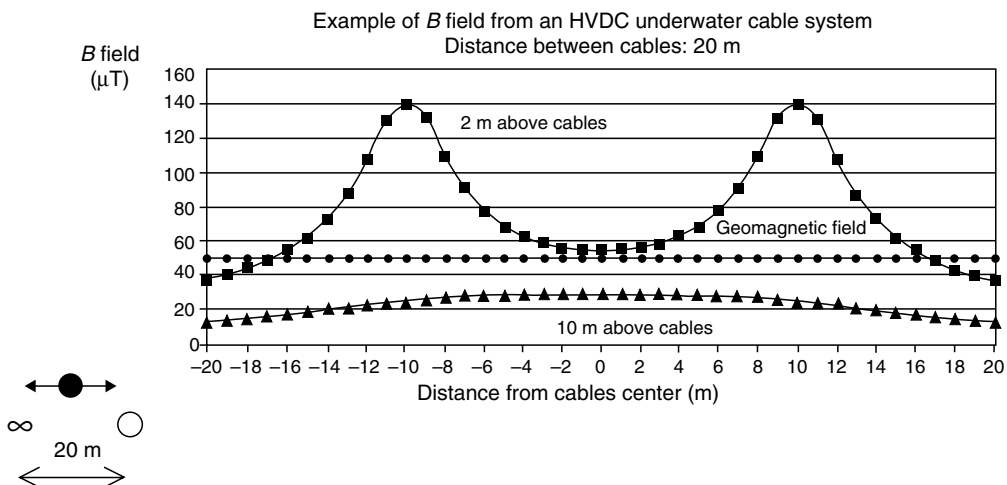


FIGURE 1.2

Predicted DC magnetic field from a high-voltage DC cable with the return cable placed at a distance of 20 m. The current in the cable was assumed to be 1333 A, which is the maximum design current. (From Hansson Mild, K. In Matthes, R., Bernhardt, J.H., and Repacholi, M.H., Eds. Proceedings from a joint seminar, *International Seminar on Effects of Electromagnetic Fields on the Living Environment*, of ICNIRP, WHO, and BfS, Ismaning, Germany, October 4–5, 1999, pp. 21–37. With permission.)

Examples are cables between Sweden and Finland, Denmark, Germany, and Gotland, a Swedish island in the Baltic Sea. Under construction at present is a cable from Sweden to Poland (SwePol). In these cables DC is used, and the ELF component of the current is less than a few tenths of a percent. The maximum current in these cables is slightly above 1000 A, and the estimated normal load is about 30% or 400 A. Depending on the location of the return path, the DC magnetic field will range from a maximum disturbance of the geomagnetic field (with a return through water) to a minimal disturbance (with a return through a second cable as close as possible to the feed cable). With a closest distance of 20 m between the cables, the predicted field distribution can be seen in Figure 1.2, immediately above the cables (2 m), practically the same value as that obtained for a single wire. When the distance between cables is increased beyond 20 m, the distortion at a given distance rises above that of Figure 1.2. Since the cables are shielded, no electric field will be generated outside the cable. For a more detailed discussion of the fields associated with this technique, the reader is referred to the paper by Koops [11].

Few other DC fields from human activity are broadly present in the environment, though very short-range DC fields are found near permanent magnets, usually ranging from a few tenths of a millitesla to a few millitesla at the surface of the magnet and decreasing very rapidly as one moves away. Occupationally encountered DC fields are discussed below.

1.2.2.2 High-Voltage AC Power Lines

The electric and magnetic fields from high-voltage power lines have been figuring for a long time in the debate on the biological effects of EM fields. Although the AC power systems in the Americas, Japan, the island of Taiwan, Korea, and a few other places are 60 Hz, while most of the rest of the world is 50 Hz, the frequency difference has no effect on high-voltage transmission line fields. In the early days of bioelectromagnetics research, the electric field was considered the most important part, and measurements of field strengths were performed in many places. Figure 1.3 shows an example of such

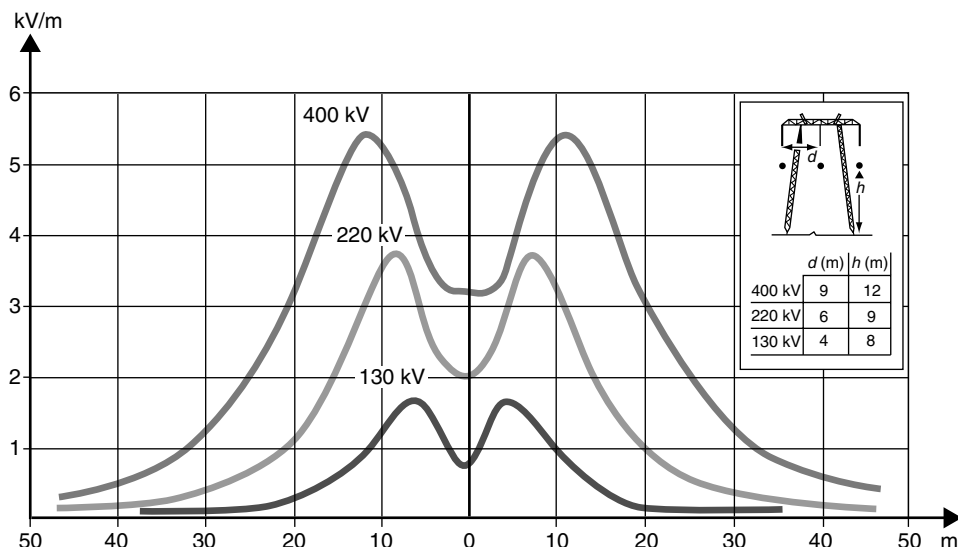


FIGURE 1.3

Electric field from three different high-voltage power lines as a function of the distance from the center of the line. In the inset the distance between the phases as well as the height above ground of the lines are given. (From Hansson Mild, K. In Matthes, R., Bernhardt, J.H., and Repacholi, M.H., Eds. Proceedings from a joint seminar, *International Seminar on Effects of Electromagnetic Fields on the Living Environment*, of ICRNIRP, WHO, and BfS, Ismaning, Germany, October 4–5, 1999, pp. 21–37. With permission.)

measurements from three different types of lines: 400, 220, and 130 kV lines, respectively. The field strength depends not only on the voltage of the line but also on the distance between the phases and the height of the tower. The strongest field can be found where the lines are closest to the ground, and this usually occurs midway between two towers. Here, field strengths up to a few kilovolts per meter can be found. Since the guidelines of the International Commission on Non-Ionizing Radiation Protection (ICNIRP) [12] limit public exposure to 5 kV/m and there is no time averaging for low-frequency fields, people walking under high-voltage power lines may on some occasions be exposed in excess of existing international guidelines.

Because electric fields are well shielded by trees, buildings, or other objects, research in the 1970s and 1980s did not turn up any major health effects (see, e.g., Portier and Wolf [13]), and because of the epidemiological study by Wertheimer and Leeper [14] (see also Chapter 6 on ELF epidemiology in this volume), attention turned from electric to magnetic fields in the environment. The magnetic field from a transmission line or any other wire depends on the current load carried by the line, as well as the distance from the conductors; in Figure 1.4 calculations of the magnetic flux density from several different types of transmission lines are shown. There is a very good agreement between the theoretical calculation and the measured flux density in most situations. The flux density from two-wire power lines is directly proportional to the electric current, generally inversely proportional to the square of the distance to the power line for distances greater than several times the distance between the phase lines, and directly proportional to the distance between the phase wires. For three and six-wire systems the fields decrease more rapidly with distance at a rate that is dependent on the phase sequences and the spacing between the wires. For most lower-voltage lines, around 10–20 kV, the distance at which the B field falls below 0.2 µT is generally less than 10 m; this distance still depends on current and the spacing of the wires.

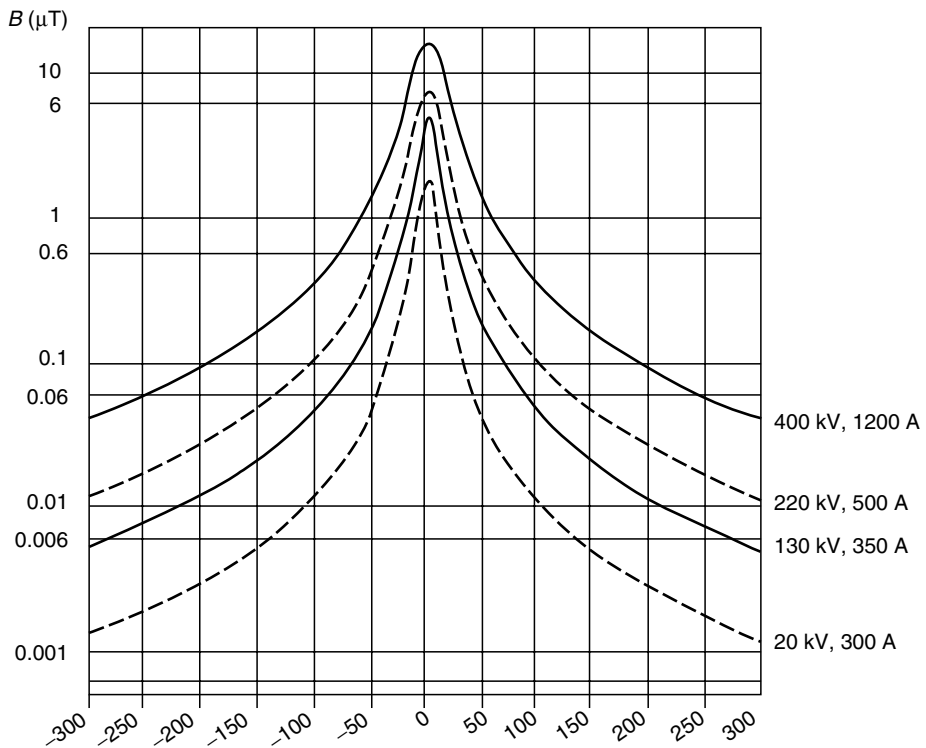


FIGURE 1.4

Magnetic flux density from different high-voltage power lines at a distance (in meters) from the center of the line. The currents in the lines are the maximum values allowed and are given to the right in the figure. (Figure courtesy of Swedish National Institute for Working Life.)

The electric or magnetic field vector from a single AC conductor displays a sinusoidal waveform, oscillating back and forth through zero intensity in a single direction determined by the observation position with respect to the wire, ignoring any small distortions due to harmonics, etc. However, near a three-phase high-voltage transmission line, the electric and magnetic field vectors from the group of conductors, which are at some distance from each other and whose individual sinusoidal variations are out of phase, rotate in space as well as change in magnitude, but their magnitude never decreases exactly to zero [15]. This so-called elliptical polarization may or may not have a different biological significance than the single conductor's "plane polarization."

Several approaches have been used for reducing the magnetic field from a line, and in Figure 1.5 some examples are given. Instead of hanging the three phases at the same height and in parallel, the lines can be arranged in a triangular form, thereby reducing the distance between the phases and thus also the flux density. The reduction is of the order of about 1.6. An even greater reduction is obtained if the so-called split phase arrangement is used. Here, five lines are used. One phase is placed in the center, and the other two phases are split into two lines each, which are placed diagonally (see Figure 1.4). The reduction is almost tenfold.

When high voltage is present, there is a possibility of the insulation breaking down, causing a catastrophic discharge—a spark; lightning is an obvious example. There is also the more common possibility of very minor discharges occurring, in which one or a relatively small number of molecules near the high-voltage element become

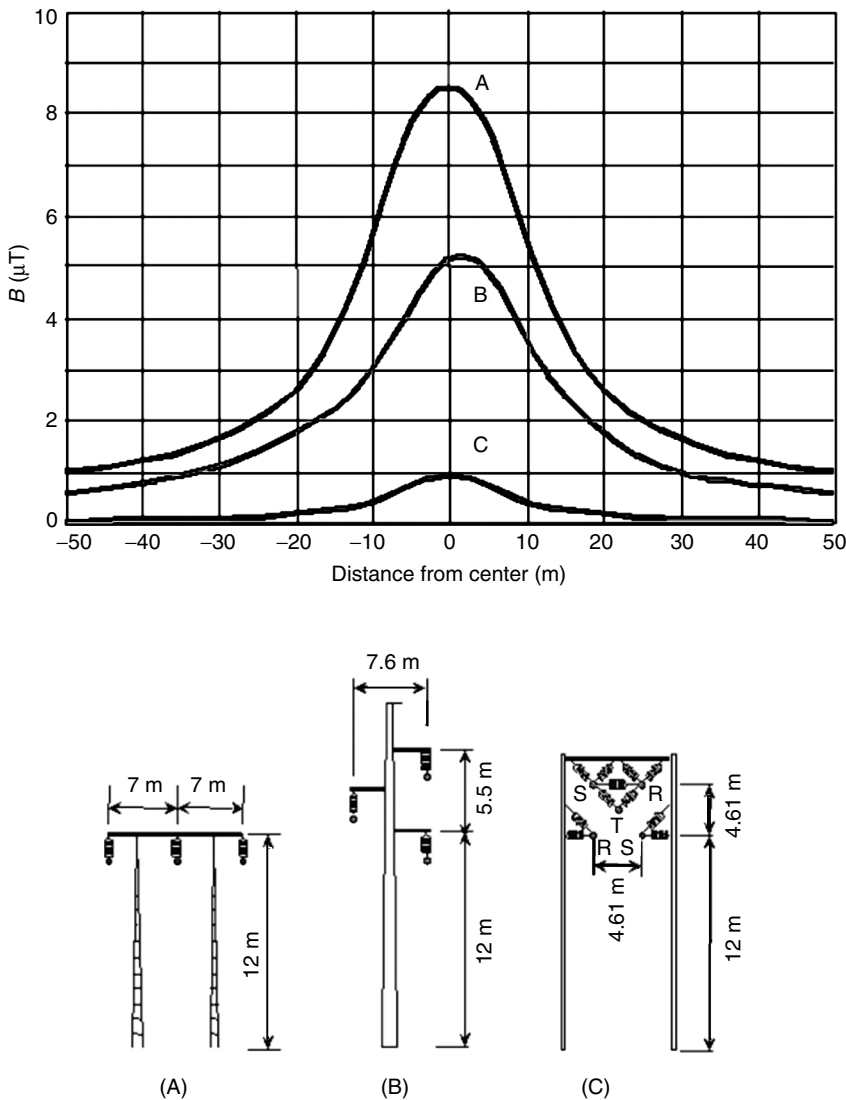


FIGURE 1.5

Examples of reduction of the magnetic flux density from a 220-kV line with a maximum phase current of 500 A. In (A) the normal configuration is used and the maximum flux density is about $8 \mu\text{T}$, and in (B) a delta arrangement is used which gives a reduction to about $5 \mu\text{T}$ maximum under the line. In (C) the split-phase arrangement is used leading to a maximum value of only $1 \mu\text{T}$. (Figure courtesy of Swedish National Institute for Working Life.)

ionized; this is often called a *corona*, since in extreme cases a small glow can be seen near parts of the high-voltage system. Corona discharge can also occur at grounded objects near a high voltage and is more likely to occur at more pointed objects; this is the principle of the lightning rod. Minor corona damage has been observed on pine tree needles very close to a 1200 V transmission line [16]. (No other environmental damage to plants or animals from either fields or corona has been found [17].) The resulting ions screen the electric field of the transmission line cables to varying extents, because their number depends on a variety of factors, including humidity, dust, rain, and wind [9,10]. While a hypothesis has been put forward that ions from power lines make small airborne

particles, particularly those carrying naturally occurring radioactive atoms, more likely to enter and remain in the lungs and cause cancer or various other diseases [18], it has not found much acceptance.

1.2.2.3 Exposure in Homes

Although Wertheimer and Leeper [14] initially used transmission and distribution line sizes and configurations as surrogates for estimating magnetic field exposure from transmission lines, it quickly became apparent that the correlation was not very good and that sources of exposure inside the home were at least as important, unless the home was very close to a transmission line [13]. Several studies have explored the exposure to ELF electric and magnetic fields in homes in different countries. Deadman et al. [19] investigated the exposure of children in Canada. A logging device was used, which recorded the fields during two consecutive 24-h periods. For 382 children up to the age of 15 they found an arithmetic mean (AM) of the magnetic field of $0.121 \mu\text{T}$ with a range of $0.01\text{--}0.8 \mu\text{T}$. The corresponding values for the electric field were AM 14.4 V/m , range $0.82\text{--}64.7 \text{ V/m}$. Hansson Mild et al. [20] compared the ELF fields in Swedish and Norwegian residential buildings. The overall mean values were as follows: E fields 54 V/m ($SD = 37$) and 77 V/m ($SD = 58$) in Sweden and Norway, respectively; the corresponding values for B fields were 40 nT ($SD = 37$) and 15 nT ($SD = 17$). Table 1.1 shows additional comparisons.

McCurdy et al. [21] measured women's exposure in the United States by using personal magnetic field exposure meters that were worn during a working day or a day at home. The geometric mean of the time-weighted average for the working day was $0.138 \mu\text{T}$ with a range of $0.022\text{--}3.6 \mu\text{T}$, and for the homemakers the corresponding values were $0.113 \mu\text{T}$, range $0.022\text{--}0.403 \mu\text{T}$.

In the meta-analysis by Ahlbom et al. [22] on childhood cancer and residential magnetic fields, it was stated that 99.2% of the population resided in homes with $B \leq 0.4 \mu\text{T}$.

Exposure varies widely in time, according to the time of day and the season. One may be outdoors, far from any field sources at one time, indoors near an operating appliance at another, riding in an electric transit vehicle at some other time, and so forth. Sample exposure values for an individual, recorded as a function of time over a 24-h period in spring and summer, are shown in Figure 1.6.

TABLE 1.1

Comparison of Personal Exposure and Background Fields

Country		Geometric Mean of Personal Exposure (nT)	Geometric Mean of Long-Term Background Field (nT)	Ratio, Personal Mean to Background Mean
United States	Adults at home	134	58	2.3
	Adults at home, not in bed	111	74	1.5
	Children, residential	96	99	1.0
	Children, at home	96	67	1.4
Canada	Children at home	117	107	1.1
	Adults at home	133		1.2
U.K.	Adults at home	54	37	1.5
	Adults	42	29	1.5

Source: From Swanson, J. and Kaune, W.T. *Bioelectromagnetics* 20, 244–254, 1999.

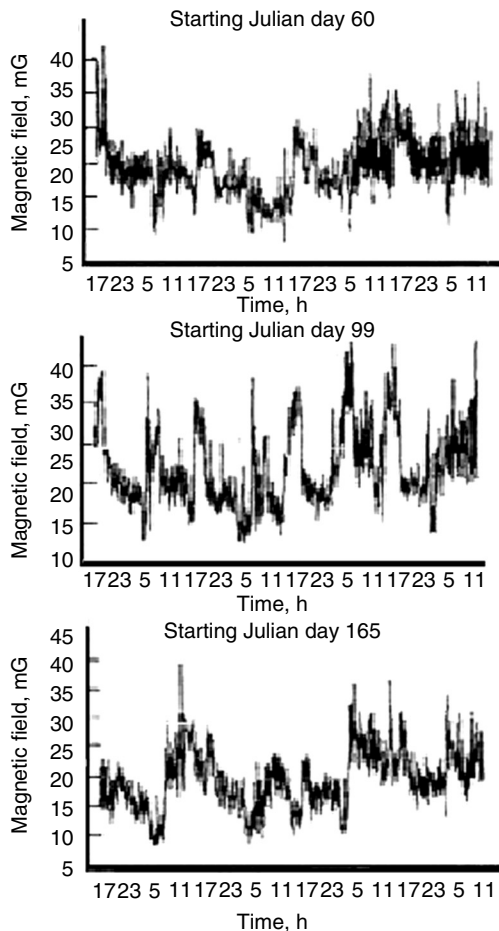


FIGURE 1.6

An individual's measured magnetic field exposure over the course of a day. Note that $1\text{ mG} = 0.1\text{ }\mu\text{T}$. (From Koontz, M.D., Mehegan, L.L., Dietrich, F.M., and Nagda, N.L. Assessment of Children's Long Term Exposure to Magnetic Fields [The Geomet Study]. Final Report TR-101406, Research Project 2966-04, Electric Power Research Institute, Palo Alto, CA, 1992. With permission.)

Since the three-phase systems used for electrical distribution are dimensioned for sinusoidal fields, the harmonic content can create problems. Today we may find large stray currents, usually resulting from unbalanced currents between phases, in water pipes, ventilation systems, concrete reinforcement mesh, etc., and the current flowing also contains these harmonics. [Figure 1.7](#) gives an example of a measurement of a current flowing in a cable in a large apartment building, and [Figure 1.8](#) shows the corresponding Fourier frequency analysis. The magnetic field in the building thus also has these harmonic components. Often, the largest stray currents, which generate large domestic fields, are due to errors in wiring that violate the building code [23] or to a poorly planned wiring layout that has currents flowing in open loops instead of both wires of a circuit being laid next to each other in the same conduit [24].

From Figure 1.6 through Figure 1.8, as well as the data in the rest of this chapter, it is easy to see that average field strength is far from being the only parameter that is needed to characterize electric or magnetic field exposure. Other parameters include frequency or frequencies present (or the related parameters, the rise and fall times of up-and-down excursions or "transients"), numbers and height of transients, number of

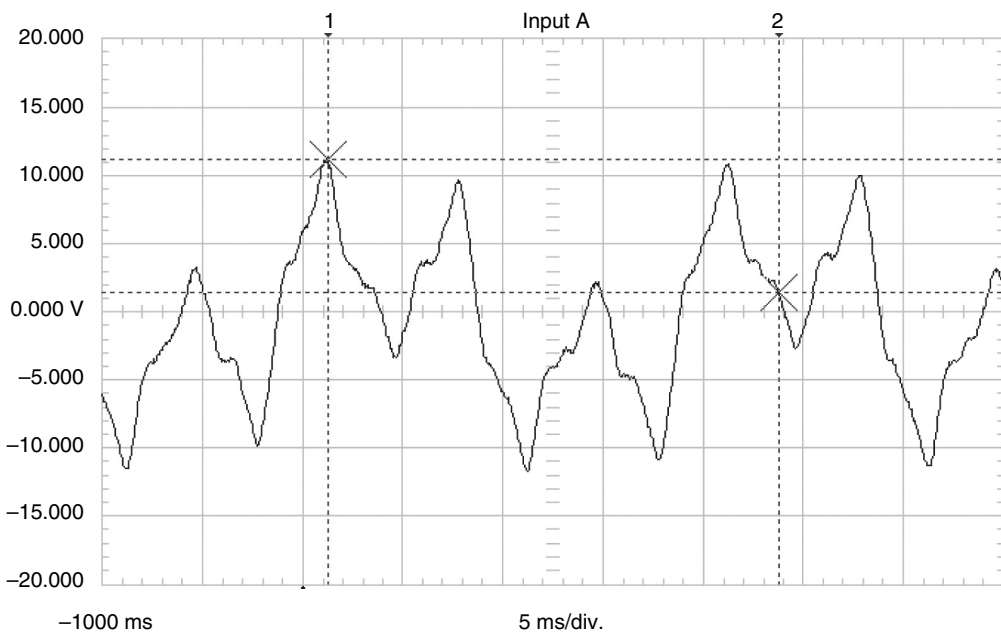


FIGURE 1.7

Stray current wave shape in the 50 Hz power delivery cable in an office building. The peak to peak current is of the order 20 A. (Figure courtesy of Swedish National Institute for Working Life.)

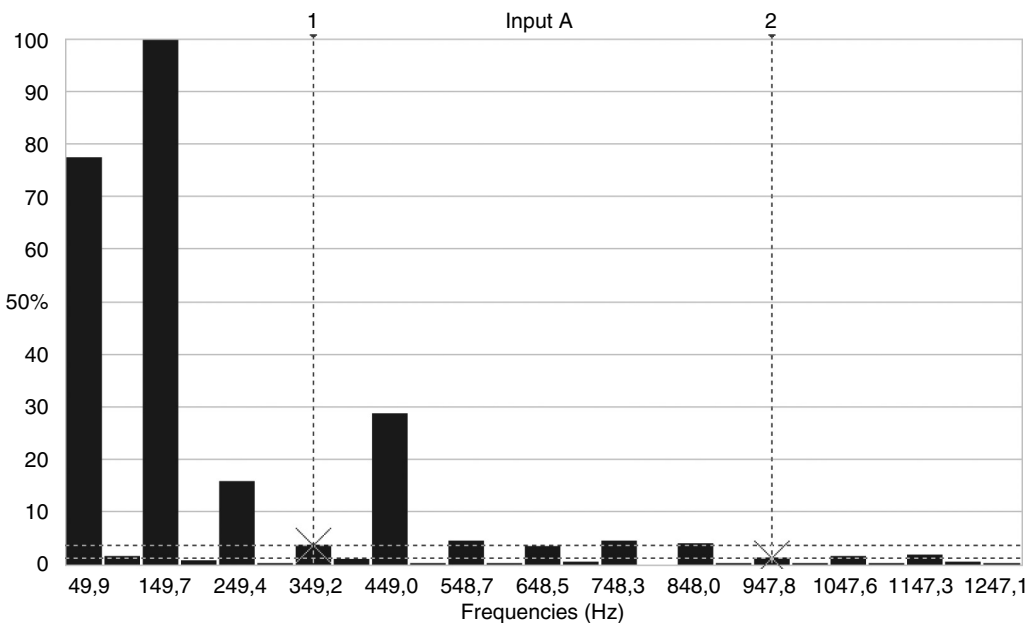


FIGURE 1.8

The Fourier spectrum of the wave shape in Figure 1.5. Note the high 150 Hz (third harmonic) component. (Figure courtesy of Swedish National Institute for Working Life.)

times the field exceeds or falls below a certain fraction of its average value, whether both DC and time-varying fields are present, relative direction of multiple fields, etc. As discussed elsewhere (e.g., the Introduction and chapters such as [Chapter 5](#), [Chapter 6](#), and [Chapter 9](#) in this volume and Chapter 5 through [Chapter 8](#) and [Chapter 11](#) in *BMA*), it is not clear, in most cases, which one or group of these parameters is related to a particular biological effect. To date, average field strength is the most commonly used parameter, partly because it is the most easily obtainable summary of exposure over an extended period. For a given frequency range, average field strength is related to some other parameters, such as fraction of time over a certain threshold, but not to others, such as number of transients per hour. For further discussion of various parameters and their interrelationships, see, for example, Refs. [25,26].

Most measurements have been done in detached houses, even though many city dwellers live in apartment buildings. In apartment buildings, the current in the wiring in the ceiling of one unit, for instance, for ceiling lamps, may most strongly affect the magnetic field level of the unit above. Also, some apartment buildings have an electric substation in the basement, where a transformer reduces the medium-voltage distribution line power to 110 or 220 V for domestic use. The low-voltage conductors of the substation may carry substantial currents and create magnetic fields up to several tens of microtesla directly above the substation; reduction through placing conductors away from the substation ceiling and shielding with aluminum plates is possible [27].

In the United States and Canada, though not in other countries, the neutral wire of the AC power distribution system is required to be physically connected to the earth (grounded) at regular intervals to avoid injury from electric shocks; building wiring systems' neutral wires must also be grounded, often by connection to the buried water pipe as it enters the building. Unbalanced loading of the system can produce currents in the ground system, sometimes including currents that leave one residence through the grounding system and return to the power grid through another, which further contributes to the residential magnetic fields [28,29].

Kavet and colleagues [30–32] have proposed that effects observed in children, which epidemiology has associated with domestic magnetic fields, are in fact due to small shocks that arise due to potential differences that build up between the water tap and the grounded drain of a tub. Shocks received in the bath can still induce in a small child's body current densities of a magnitude known to induce a biological effect. This alternative hypothesis is still under investigation.

1.2.2.4 Electrical Appliances

The United States, Japan, Canada, and some other countries use 110 V_{rms} AC for basic electrical power, while most of the rest of the world uses 230 V. Since transmission and distribution voltages in the two types of system are about the same, only differences due to appliances or building wiring would be expected. For a given power consumption and similar design, 110 V appliances draw twice as much current and create twice as strong a local magnetic field, although their local electric fields are half as strong. However, because both types of field fall off rapidly with increasing distance from the appliance and metal appliance cabinets shield electric fields, measurements of exposure to magnetic fields have not yielded great differences between the two systems ([see Table 1.1](#)). Measurements of magnetic fields from a sample of various appliances show that the fields have a rapid falloff with distance from the device [33]. Very close, the values may exceed international guidelines, but at a distance of 0.5–1 m the fields are seldom higher than few tenths of a microtesla. In general, it can be said that the more power the equipment uses, the higher the magnetic field. [Table 1.2](#) presents some representative values from 110 V appliances.

TABLE 1.2Ratios ($B_{\text{on}}/B_{\text{off}}$) of Magnetic Fields Measured with Appliances Turned On and Off

Appliance	Measurement Location	6–54 Hz	$B_{\text{on}}/B_{\text{off}}$ 54–606	606–3066 Hz	8–200 kHz
Hair dryer	5 cm from nozzle	8.3	57	76	11
	10 cm from nozzle	3.2	17	31	—
	15 cm from nozzle	2.1	7.9	16	—
	25 cm from nozzle	1.4	3.1	6.1	—
Headset playing music	Forehead	1.5	1.0	1.2	—
	Center of head	<1.0	1.0	1.2	1.1
	Above ear	2.0	1.0	2.5	—
	Sternum	1.4	1.0	1.1	—
	Hip	2.7	1.0	2.6	—
Home sewing machines	Front of abdomen	2.7	2.8	2.4	1.5
	Left side of abdomen	1.7	2.0	1.8	—
	Right side of abdomen	1.7	1.6	1.5	—
Motorized clock	10 cm from clock	<1.0	13	4.3	1.1
	25 cm from clock	<1.0	4.0	<1.0	—
	50 cm from clock	<1.0	1.7	<1.0	—
	100 cm from clock	<1.0	1.0	1.0	—
	At subject's head	<1.0	1.4	1.0	—
Electronic clock	10 cm from clock	<1.0	4.7	1.5	1.5
	25 cm from clock	<1.0	1.8	1.0	—
	50 cm from clock	<1.0	1.1	<1.0	—
	100 cm from clock	1.1	1.0	1.0	—
	At subject's head	1.1	1.1	1.0	—

Note: B_{off} was estimated using linear interpolation at those measurement locations where it was not directly measured.

Source: From Kaune, W.T., Miller, M.C., Linet, M.S., Hatch, E.E., Kleinerman, R.A., Wacholder, S., Mohr, A.H., Tarone, R.E., and Haines, C. *Bioelectromagnetics* 23, 14–25, 2002.

Vistnes [34] recently gave some examples of flux densities near 220 V appliances. Of special interest may be a clock radio, which because of bad electrical design may give rise to exposure of the order of 100 μT close to the equipment. Since people are likely to place a clock radio very close to the pillow, the head may be exposed to quite a large magnetic field, exceeding the normal levels in the house.

The general range of magnetic and electric field magnitudes at various distances from transmission lines, local distribution lines, and appliances is shown in Figure 1.9.

Most modern electrical appliances are equipped with an electronically switched power supply in which an electronic circuit replaces the old-style transformer. This means that the current is no longer a pure sinusoidal 50- or 60-Hz signal but contains harmonics. The current used by a low-energy 50-Hz fluorescent lamp is illustrated in Figure 1.10, and the Fourier analysis is shown in Figure 1.11 indicating all the harmonics. Higher harmonics and transients (fast spikelike excursions) are also generated by motor-driven appliances and those run by vibrating mechanisms using make-and-break switching contacts, such as older electric shavers or doorbells (Table 1.2).

The magnetic field in different infant incubators used in hospital nurseries varied between 0.23 and 4.4 μT , with an arithmetic average of 1.0 μT [35]. Most of these values are considerably higher than the exposure that can be measured in residential areas close to transmission lines. The technology to reduce the exposure is at hand and can be easily applied.

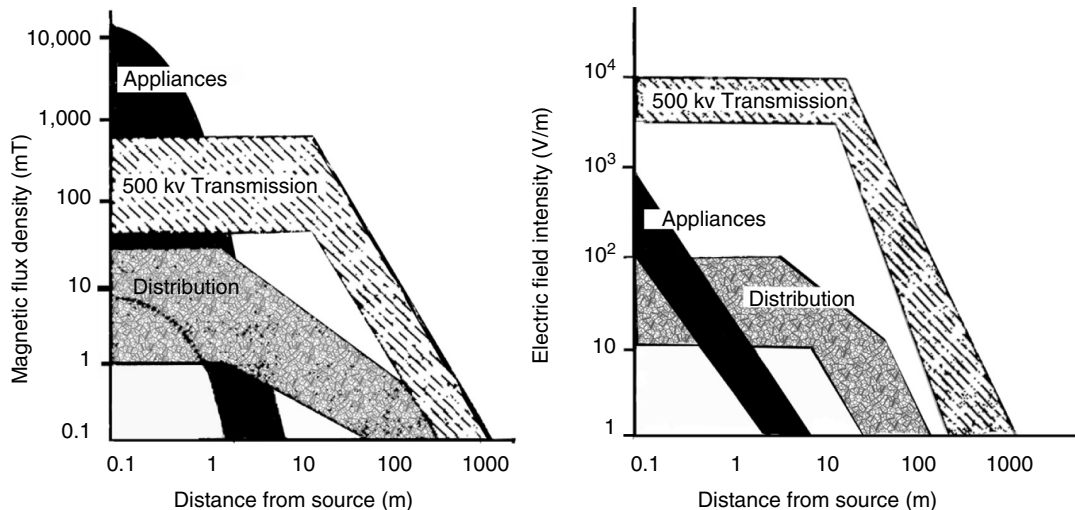


FIGURE 1.9

Magnetic flux density (left) and electric field strength (right) as a function of distance from transmission lines, local distribution lines, and appliances. (From U.S. Office of Technology Assessment. Biological Effects of Power Frequency Electric and Magnetic Fields. U.S. Government Printing Office, Washington, DC, Background Paper OTA-BP-E-53, 1989.)

Occupational exposure from handheld electrical appliances can be quite high. This is mainly equipment that is held close to the body and that uses high power, such as drills and circle saws. These devices usually have adjustable speed, which is done through the switched power supply. Values for the magnetic field of the order 100–200 µT are not uncommon, and in order to show compliance with standards the measurements have to take into account the harmonic contents of the waveform.

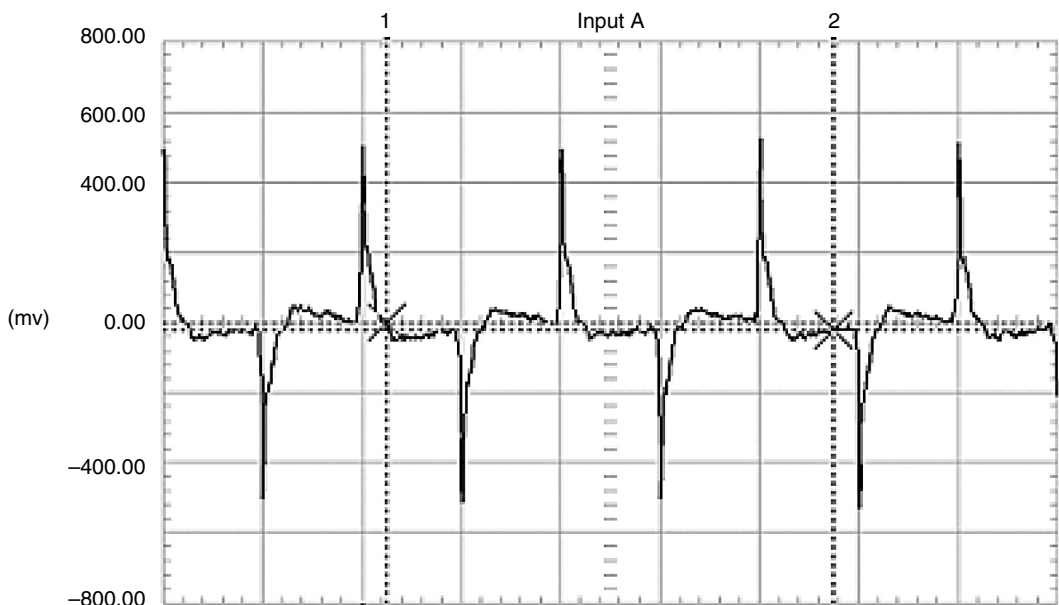


FIGURE 1.10

Wave shape of the current to a low-energy fluorescent lamp. The timescale is 10 ms/div. (Figure courtesy of Swedish National Institute for Working Life.)

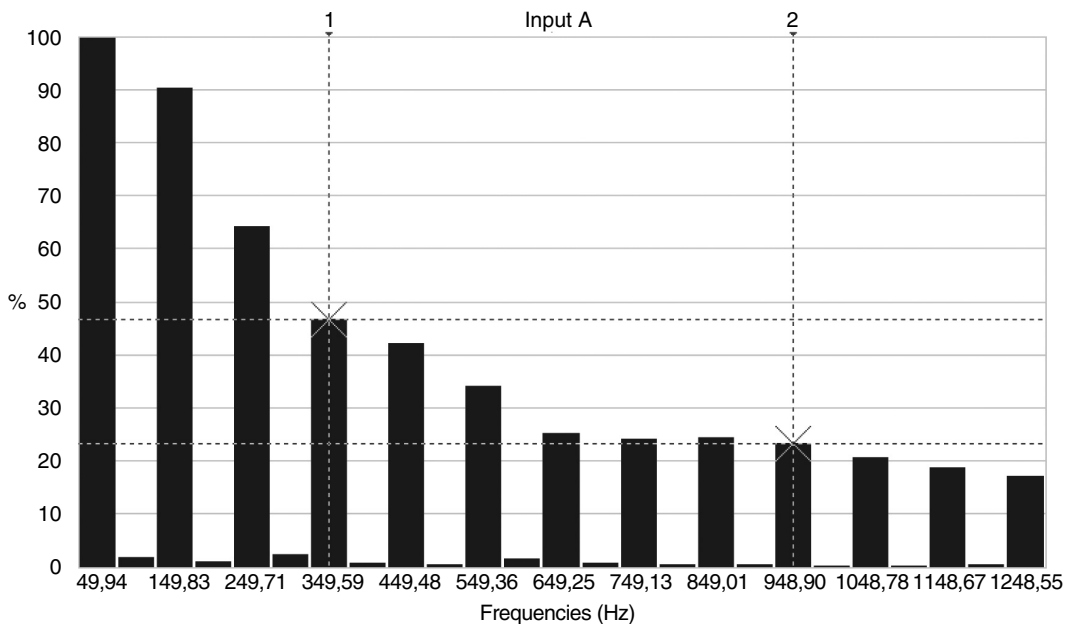


FIGURE 1.11

The Fourier spectrum of the wave shape in Figure 1.7. Note the high 150-Hz component. (Figure courtesy of Swedish National Institute for Working Life.)

1.2.2.5 ELF Fields in Occupational Settings

Wertheimer and Leeper [14] were not only the first to publish evidence in support of increased childhood cancer risk with magnetic field exposure, but they also pointed to increased cancer risk in occupations with high magnetic field exposure. Since then, hundreds of studies have looked into this problem, and the assessment of workers' exposure has been debated. There are studies where individual estimates of the exposure have been made for male [36] and females [37]. For workday means, the 25th, 50th, and 75th percentiles were 0.13, 0.17, and 0.27 μT , respectively, for males, and the corresponding values for females were almost similar: 0.14, 0.17, and 0.23 μT . The study on exposure of males investigated the 1000 most common occupations in Sweden, and the study on female exposure included 61 job categories. Table 1.3 shows additional estimates for various professions.

Sewing machines—Near sewing machines increased magnetic fields can be found, and depending on the type of machines used the values differ. The mean average value logged during some working hours is of the order of several tenths of a microtesla [38].

Welders—Among the occupations where quite high exposure exists, electric arc welders are a prominent example. They handle cables carrying hundreds of amperes very close to their bodies. The welder normally grasps the cable, and it sometimes also is in contact with other parts of the body, for instance, it might be draped over the shoulder. Depending on the technique used—DC or AC, type of rectification, etc.—the ELF magnetic field varies, but several studies report values in the range of tens to hundreds of microtesla [39]. Skotte and Hjøllund [40] found a mean of 21 μT for a full-shift average workday of manual metal arc welders. During the actual welding, the B field can be up to several millitesla.

The frequency content of the signal can be rather complex. In one of the most common situations the welding equipment is connected to a three-phase outlet, and the current for the weld is thus three-phase full-wave rectified. This means that we have first a DC

TABLE 1.3
EMF Exposures in Common Environments

Environment	Median ^a Exposure	Top 5th Percentile	Environment	Median ^a Exposure	Top 5th Percentile
<i>Office Building</i>			<i>Machine Shop</i>		
Support staff	0.6	3.7	Machinist	0.4	6.0
Professional	0.5	2.6	Welder	1.1	24.6
Maintenance	0.6	3.8	Engineer	1.0	5.1
Visitor	0.6	2.1	Assembler	0.5	6.4000
<i>School</i>			<i>Office staff</i>	0.7	4.7
Teacher	0.6	3.3	<i>Grocery Store</i>		
Student	0.5	2.9	Cashier	2.7	11.9
Custodian	1.0	4.9	Butcher	2.4	12.8
Administrative staff	1.3	6.9	<i>Office staff</i>	2.1	7.1
<i>Hospital</i>			Customer	1.1	7.7
Patient	0.6	3.6	—	—	—
Medical staff	0.8	5.6			
Visitor	0.6	2.4			
Maintenance	0.6	5.9			

Note: Magnetic fields are measured in milligauss (mG); 1 mG = 0.1 µT.

^aThe median of four measurements. For this table, the median is the average of the two middle measurements.

Source: National Institute for Occupational Safety and Health. From Portier, C.J. and Wolfe, M.S., Eds. Assessment of Health Effects from Exposure to Power-Line Frequency Electric and Magnetic Fields. NIH Publication 98-3981, National Institute of Health Sciences, Research Triangle Park, NC, 1998 (accessed April 7, 2005, at <http://www.niehs.nih.gov/emfrapid/html/WGReport/WorkingGroup.html>).

component and on that a large AC ripple with main frequency 300 Hz (50 Hz power system), but it also has harmonics at 600, 900, 1200 Hz, etc. A newer type of equipment has a pulsed DC (50–200 Hz pulse frequency) as a base with a 53 kHz current applied between the pulses. This leads to frequencies in the current equal to the pulse frequency and its harmonics and also 53 kHz and harmonics. It is a very complex situation to evaluate with respect to compliance with guidelines, because of the complexity of the signal.

Since in many cases, high exposure results from the cables being very close to the body, much can be done to reduce the exposure of the welder by carefully arranging the workstation to keep the cables away from the body. By placing the welding machine on the right-hand side of the worker (if right-handed) and seeing that the return cable is as close as possible to the current cable, the exposure can be reduced by one order of magnitude.

Induction heaters—Induction heating is used for heating metals for purposes that include surface or deep hardening, welding, melting, soft soldering, brazing, annealing, tempering, and relieving stress. The frequency can be from 50 Hz to the low megahertz range, depending on the desired skin depth and purpose. Since high currents are used, the leakage magnetic field can be substantial. At the operator's position, values of the order of 0.5–8 µT are common, and the maximum field near the coil, where, for instance, the hands can be exposed, can reach several hundreds of microtesla. The field strength is in many cases high compared with recommended limits [12].

Railway workers—Engine drivers of AC electric engines experience rather high magnetic field exposure. The intensity depends of several factors, one of them being the age of the engine. Nordensson et al. [41] (see also Refs. [42,43]) found that drivers of Swedish model RC engines were exposed to flux densities of the order of 10–100 µT. The older

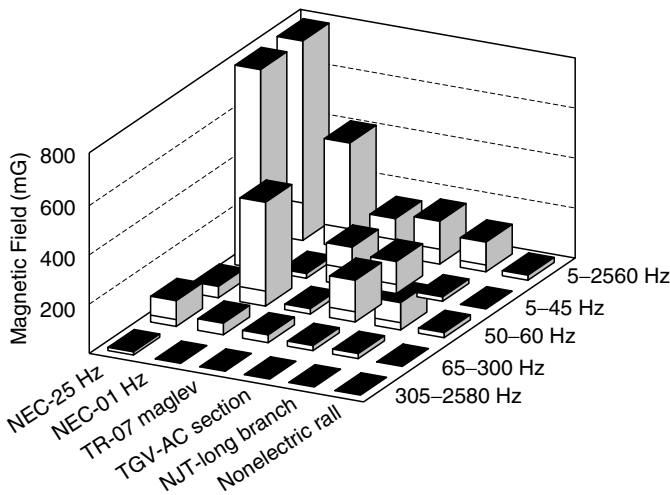


FIGURE 1.12

Maximum (top of bar) and average (horizontal bar) magnetic fields in various frequency bands in the passenger compartment of several intercity rail systems. NEC = U.S. Amtrak Northeast Corridor (Washington, DC, to Boston, MA), which has both 25- and 60-Hz segments; TR-07 = German Transrapid maglev system; TGV = French “Train a Grande Vitesse,” AC-powered segment of Paris-Tours line; NJT = New Jersey Transit, NJ Coast Line Long Branch section. (From Bernardi, A., Fraser-Smith, A.C., and Villard, O.G., Jr. *IEEE Trans. Electromagn. Compat.* 31, 413–417, 1989.)

models of engines had the higher values. The mean average values for a full workday ranged from 2 to 15 μT . The main input power frequency is $16\frac{2}{3}\text{Hz}$, and this frequency was dominant at idle, but at full power, harmonics up to 150 Hz existed. Wenzl [44] measured the exposure of rail maintenance workers in the United States and found peak values ranging from 3.4 to 19 μT , and the time-weighted average was in the range 0.3–1.8 μT . Chadwick and Lowes [45] have examined the exposure of passengers on trains in the U.K., and they found static magnetic flux densities up to several microtesla. The alternating field was also substantial in some locations and reached up to 15 mT at floor level. However, none of the whole-body alternating magnetic flux densities approached the National Radiological Protection Board (NRPB) investigation levels.

Trains operating on DC, such as in the Washington, DC, and San Francisco, CA, transit systems, also produce time-varying fields in the passenger compartments, particularly below 5 Hz [46,47]. Figure 1.12 shows field intensity in various frequency bands in the passenger compartment of several representative electric rail systems and a nonelectric one. Interestingly, the figure shows that an experimental magnetic levitation (maglev) system does not exhibit substantially different field levels [48].

Electrochemical plants—In factories producing, for instance, aluminum, copper, or chloride through electrochemical processes, very high DC currents are used, often of the order of tens of kiloamperes. The DC current is obtained through rectification of the incoming three-phase AC power. Often there is still a substantial AC component of the current and hence an AC magnetic field. Measurements have shown broadband ELF measurements of the order of 10–50 μT , with many different frequencies present that need to be taken into account in the evaluation of the exposure situation. Typically, a 50 Hz component can be present, because of unbalance between the three phases, and the full-wave rectification gives 300, 600, and 900 Hz components. The exposure guidelines can often be exceeded in some locations in the plants, and special requirements may be needed to reduce the exposure. DC fields in these smelters are often on the order of several millitesla, with peaks of at least 20–30 mT; up to 70 mT has been reported [49,50].

1.2.2.6 Internal ELF Fields Induced by External and Endogenous Fields

Because the bodies of humans, other animals, and even plants contain ionic solutions and because cell cultures, as well as many one-celled and other organisms such as fish or the roots of plants, live in conductive media, external exposure to electric or time-varying magnetic fields can produce internal fields, which can be quite different than the unperturbed external fields.

In an electric field, as discussed in [Chapter 3](#) and [Chapter 4](#) in this volume on properties of materials, the conductivity and dielectric constants of tissue are quite different from those of air or vacuum, creating a layer of charge due to polarization at the surface of the body, which decreases the internal field, often by many orders of magnitude. For a human standing in the ELF electric field below a high-voltage transmission line, the field inside the body may be only 10^{-6} of the external field. The shape of the body also affects the amount of polarization. Since a standing human's body has more of a "lightning rod" shape than a crouching rat, a rat must be exposed to a much lower external field to achieve an equivalent internal electric field. A squatting human will experience lower and the rearing rat, higher fields. The body shape and foot area also affect the average current densities in various body locations because of the external electric field. Figure 1.13 illustrates these differences [51]. As shown in the figure, current densities increase in areas of smaller cross section, for example, the human neck or leg, and closer to the ground, for example, the upper and lower human torso. When calculated without averaging across a cross section, current densities are higher near a junction point; for instance, they are higher and more horizontal at the armpit than in the middle of the chest area [52].

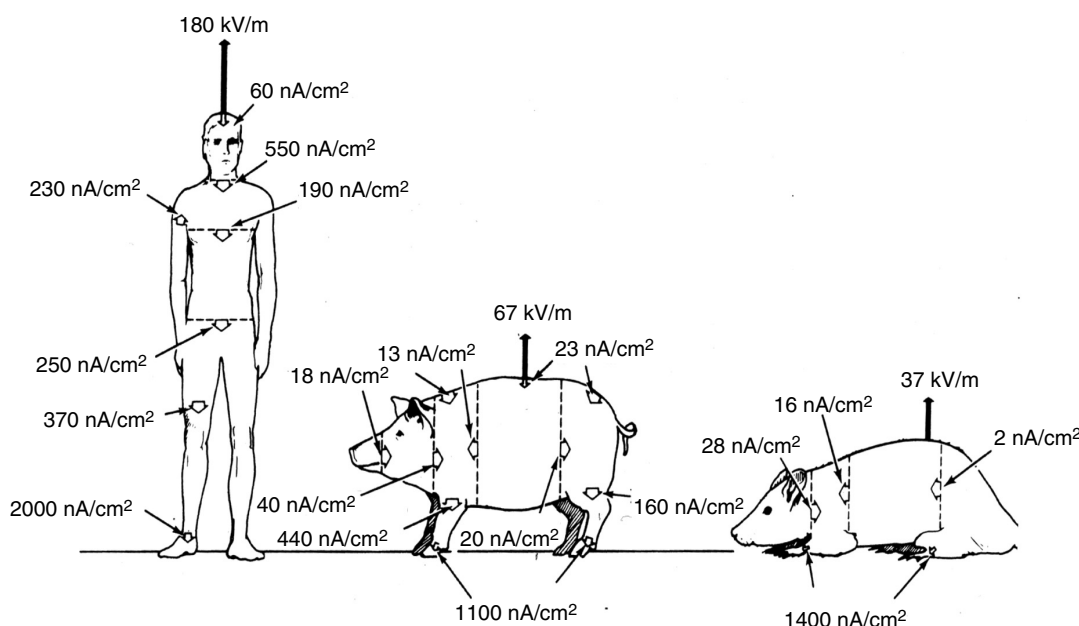


FIGURE 1.13

Estimated external electric field and current densities of a grounded man, pig, and rat exposed to a vertical 0-Hz, 6-kV/m electric field. Calculated internal current densities are averaged over sections through bodies as shown; calculated current densities perpendicular to the body surface are shown for man and pig. (From Figure 4 in Kaune, W.T. and Phillips, R.D. *Bioelectromagnetics* 1, 117–129, 1980; Copyright John Wiley & Sons, reproduced With permission.)

It is important to recognize that electric fields and current densities such as those in [Figure 1.13](#) are averages, whether across the whole cross section of the body or a limb or across a localized region. Fields vary greatly across very small distances when one examines them at dimensions on the order of a cell or a molecule; this is called *microdosimetry*. Forming a good picture at this level of fields from either endogenous or external sources is an unsolved but very important problem. [Chapter 5](#) in this volume on basic mechanisms discusses this issue further.

An external magnetic field's value is little changed as it enters a biological system, whether the human body or cells in culture, since the average biological magnetic susceptibilities are very close to those of air or vacuum ([see Chapter 3 and Chapter 4](#) in this volume on magnetic properties of materials). However, the internal electric fields and currents induced in the body according to Faraday's Law are strongly determined by body's (or specimen) shape, electric conductivity, and orientation with respect to the field. Table 1.4 gives some comparisons between the current induced in a human by the ELF magnetic fields generated in various situations and the external vertical 60 Hz electric field needed to produce the same current densities.

As discussed further in several chapters in this volume, especially [Chapter 2](#) on endogenous fields, Chapter 5 on the basic interactions of fields and biological systems, and [Chapter 7](#) on noise, as well as in the various discussions of models of field–biological system interaction, an externally applied field is unlikely to cause a biological effect unless the part of the biological system with which the field interacts is able to distinguish the external field from the internal electric fields and currents that are an integral part of the system. Exactly how to formulate the aspects of the endogenous field or current

TABLE 1.4

Magnetically Induced Total Body Current and Current Densities and Vertical 60-Hz Electric Field Inducing Equivalent Currents

Source	Current (μA)	Current Density (A/m^2)	Electric Field (kV/m)
<i>Sinusoidal waveforms</i>			
Cord-connected household appliance	20–500	0.5–12 ^a	1.5–38
Man in 8-kV/m electric field	120	3 ^a	8
Electric blanket (not low field)	7–25	2–40 ^b	0.5–1.7
Man in 0.16-kV/m electric field	2.2	0.05 ^a	0.16
<i>Nonsinusoidal waveforms—medical devices</i>			
Electric anesthesia device (100-Hz square wave)	10,000	71,000 ^c	670
Pacemaker electrode in myocardium ^{d,e}	6,000	20,000	400
Pacemaker electrode implanted in abdomen ^{d,f}	6,000	300	400

^aThrough 40-cm² ankle.

^b0.63 cm from electric wire in blanket.

^cNext to electrode.

^dPeak pulse current $\sim 10^{-3}$ -s duration, repeated every 0.8 s.

^eElectrode area, 0.3 cm².

^fElectrode area, 20 cm².

Source: After Bridges, J.E. and Preache, M. *Proc. IEEE* 69, 1092–1120, 1981. (Slightly modified from [Table 1.3](#), [Chapter 2](#) of second edition.)

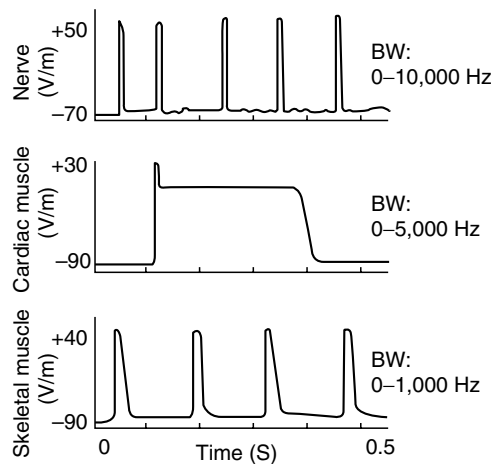


FIGURE 1.14

Typical time course and amplitudes of time-varying membrane potentials (V_m) of various cells. BW is the equivalent frequency bandwidth containing the main Fourier components of each voltage excursion. (From H. Wachtel, University of Colorado, private communication, copyright 1992; reprinted with permission.)

density that should be compared with the local field or currents in a particular situation is still an open research question; for example, over what region (how many molecules or cells) and over what range of frequencies (very narrow or broad) does the biological system average?

These endogenous fields range from the normal \sim 50–100 mV DC transmembrane potentials of most cells (negative in animals, sometimes positive in plants) to the relatively rapid pulses of nerve cell depolarization or repolarization spikes and the less rapid pulses of, for instance, muscle cells (see Figure 1.14 for examples). They also include the very large and often highly local and hence very nonuniform fields because of local charge densities on some macromolecules or changes in the double ion layer next to a membrane because of the inclusion of a protruding structure, such as a channel, at a particular location (see, e.g., diagrams in [Chapter 5](#) in this volume on basic interactions of fields and biological systems).

1.3 EM Fields at Intermediate and Radio Frequencies (3 kHz to 300 MHz)

1.3.1 Electronic Article Surveillance

Many libraries and stores are currently equipped with electronic article surveillance systems, which generate EM fields ranging from ELF to radio frequencies (RFs). Sometimes, employees spend long periods of time close to parts of these systems, and they might therefore be exposed to strong EM fields, well in excess of the reference levels (RLs). RLs are the levels of easily measured fields in air that exposure-limiting regulations or guidelines state may, but do not necessarily, create health questions in those exposed to them. Above RLs, more precise measurements or calculations are needed for each specific situation to determine whether limits for the actual fields inside the body, the basic restrictions (BRs), are exceeded (for a discussion of RLs and BRs, see [Chapter 8](#) in *BMA* on standards in [82]).

Kjellsson et al. [53] made measurements on two different systems, one used in a shop and one in a library. The coils in the library at the exit were working at 920 Hz, and the

flux density at the center of the coils was of the order of $10 \mu\text{T}$, compared with the RL for the general public of $6.25 \mu\text{T}$. When the books are returned to the library, the electronic tag in the book has to be activated before the book is put back into the library. The system used for deactivating operates at 50 Hz, and at close range the flux densities were of the order of some millitesla, thus again above the RL for occupational exposure at $500 \mu\text{T}$. In the store the signal was a mixture of 17 Hz and 6.25 kHz. The flux densities at the lower frequency were of the order of 200–300 μT , and at the higher frequency the values were well in excess of $100 \mu\text{T}$. The RLs at 6.25 kHz for the general public is $6.25 \mu\text{T}$, so the RLs are clearly exceeded, and more in-depth analysis is needed to see if the BRs are still not violated. See also Harris et al. [54] for a technical description of these devices.

Both at the shop and in the library there are situations and places where the general public as well as the employees are exposed to magnetic fields that exceed the RL. Logging the exposure during a work shift at the shop also showed that the cashiers are exposed to magnetic fields generated by the transmitter signal of the detection gates, which were often activated by customers during the work shift studied. The cashiers are therefore a highly exposed category of personnel and hence are of interest to include in epidemiological studies. Eskelinen et al. [55] have published similar results and conclusions in a previous study.

In the library not only the detection gates but also the activators and deactivators contribute to the high magnetic fields. One problem is the handheld activator used by the employees. Because of its small size, it is possible to hold the activator against almost every part of the body. If for example, a user is wearing a pacemaker and is not aware of the magnetic fields, the worst case could lead to disturbances in the pacemaker.

1.3.2 EM Fields from Video Display Terminals

A very commonly used appliance emitting EM fields is the computer video display terminal (VDT). Flat panel displays are increasingly replacing the cathode ray tube (CRT)-based VDTs at present, but a great many CRTs are still in use. There are five different types of fields present in the vicinity of the CRT: an electrostatic field, VLF electric and magnetic fields at the horizontal sweep frequencies, and various ELF electric and magnetic fields at the screen refreshing rate, related to the power frequency. These are considered separately in the next few sections. Measurements show that the equivalent electrostatic surface potential on the screen can reach up to 20 kV for some VDTs, and the ELF electric fields in front of the VDT at a distance of 0.5 m range from a few to tens of volts per meter, although most of the time it is not distinguishable from the office background 50 or 60 Hz electric field. The ELF magnetic field can reach a few tenths of a microtesla, and close to the tube the values are up to a few microtesla. The VLF electric fields range from a few to tens of volts per meter, and the corresponding magnetic field is of the order of a few tenths of a microtesla at 0.5 m in front of the VDT. The VLF B field time derivative ranges from a few to a few hundreds of millitesla per second (see Ref. [56]).

In Figure 1.15 a schematic drawing of a CRT-based VDT is shown with the deflection coils. Since these coils are to move the electron beam horizontally, from left to right, the magnetic field affecting the electrons has to be vertically directed; therefore, the coils are in horizontal planes above and below the neck of the tube as shown in Figure 1.15. The stray field from these coils at the operator's position is mainly vertical. The sawtooth wave shape of the magnetic field is also schematically shown in Figure 1.10. The times, 3 and $30 \mu\text{s}$, given in the figure are typical examples of values found on some VDTs. Also shown in the figure is the time derivative of the signal. Since the vertical deflection requires a horizontal magnetic field, the coils for the vertical deflection (omitted in the drawing in

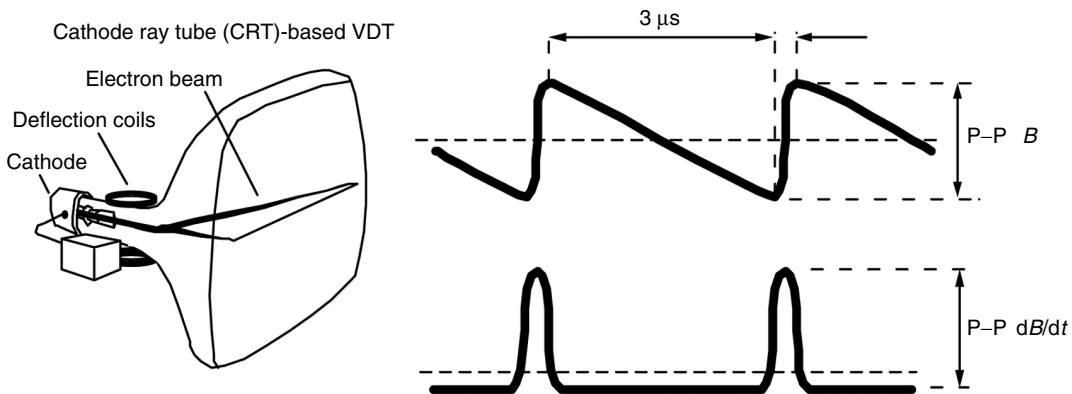


FIGURE 1.15

Schematic drawing of CRT-based VDT. To the right, examples of an idealized waveform of the VLF magnetic field and its time derivative are given. (Figure courtesy of Swedish National Institute for Working Life.)

Figure 1.15) lie in vertical planes on each side of the neck of the tube, giving a horizontal field and, thus, a corresponding stray field. The field from these coils has a frequency equal to the refresh rate, usually equal to or a small harmonic of the line frequency, and has a sawtooth wave shape. The electric field experienced by the operator is usually due to charge accumulating on the screen and is directed between the screen and the operator's body.

The time derivative, dB/dt , is usually measured only for the maximum field component in front of the VDTs. The median values found are 0.63 and 15 mT/s for the ELF and VLF frequency ranges, respectively. The corresponding maximum values are 1.9 and 101 mT/s for the ELF and VLF fields. For the ELF magnetic field in front of the VDT the median value was 0.21 μT. This is then a combination of the general magnetic field level in the office (median value 0.07 μT) and the emission from the VDT [56].

Flat panel displays for computers are presently based primarily on liquid crystal technology, particularly in portable computers. Compared with VDTs they use much lower internal voltages and currents and do not use magnetic field deflection, leading to the presumption that users' exposures are quite low. Even with a flat panel display, it or various sources inside the computer may expose portions of an operator's body to some fields that can approach few tenths of a microtesla in the ELF and VLF regions, especially for a portable computer that is held on the knees. At the time of writing, any values of the fields from laptop computers or other flat panel displays do not seem to have been published in the peer-reviewed literature. Swedish and Australian trade union tests on several laptop computers have shown magnetic field emissions below their internal certification limits for exposure (see Swedish levels in Table 1.5), initially established for VDTs. The Australians found two exceptions: a peak of up to 10 mG for up to 5 s during the program loading and a 0.01–0.16-μT fluctuating field at 30 cm, emanating from the computer transformer (frequencies not given) [57]. Computers with flat panel displays that have ungrounded power supplies, including laptops running either on batteries or on an ungrounded charger, can generate considerable static charges on their screens, producing DC potentials that exceed the Swedish unions' specifications. Older displays using cold-cathode backlighting sometimes also exceed the specifications for ELF or intermediate RF electric fields (Y. Hamnerius, Chalmers University, private communication, 2005).

Computers equipped for local area RF networking, such as "Wi-Fi" systems, and hubs for such networks emit and receive fields in the same general ranges of frequency and

TABLE 1.5

Swedish Tjänstemännens Central Organisation (TCO) Certification Limits for Computer Display Terminal Fields

Frequency Band	Quantity	Field Strength	Measurement Distance From Screen
DC	Electric potential	$\pm 0.5 \text{ kV}$	0
Band I 5 Hz–2 kHz	Electric field	$\leq 10 \text{ V/m}$	30 and 50 cm
	Magnetic field	$\leq 200 \text{ nT}$	30 and 50 cm
Band II 20–400 kHz	Electric field	$\leq 1 \text{ V/m}$	30 and 50 cm
	Magnetic field	$\leq 25 \text{ nT}$	30 and 50 cm

Source: TCO'03 Displays Flat Panel Displays, version 2.01 (translated by Y. Hamnerius), January. 2, 2004 (<http://www.tcodevelopment.com>).

intensity and are subject to the same sorts of limits as other portable RF devices, such as portable or cell phones. These are discussed later.

CRT-based VDTs use magnetic deflection of the electron beam, and therefore an external magnetic field can cause jitter and flicker on the screen. Sandström et al. [58] applied both 50 and 60 Hz magnetic fields to monitors with different refresh rates. The distortion was detectable from 0.6 up to $1.1 \mu\text{T}$ for seven monitors investigated. Background magnetic fields higher than $0.5 \mu\text{T}$ are not uncommon in offices; Sandström et al. [56] found that 5% of the workplaces measured exceeded this value. The ability to detect jitter depends, among other things, on the frequency of the disturbance. Since the frequency of the jitter oscillation is equal to the difference between the frequency of applied magnetic field and the refresh rate, the sensitivity to the external magnetic field will be different with different frequencies of the applied magnetic field.

1.3.3 RF Transmissions

1.3.3.1 Shortwave Transmission

High-power shortwave transmitters (approximately 2–25 MHz) are used for international broadcasts. Often the power supplied to the antenna system can be several hundreds of kilowatts. The antenna systems used are most often movable log-periodic or steerable curtain-type antennas.

Measurements of field strengths from such transmitters have been recently presented by Altpeter et al. [59] in connection with their study on health effects on people living near a station. The magnetic field values ranged from tens of milliamperes per meter for those at a distance of 500 m from the antenna to some tenths of a millampere per meter for those at a distance of a few kilometers. In a study of leukemia and residence near a high-power shortwave transmitter in Italy, Michelozzi et al. [60] reported spot measurements of the electric field in some of the closest houses to be between 3 and 20 V/m. (Under far-field conditions 3 V/m corresponds to a magnetic field of 8 mA/m and 20 V/m to 53 mA/m.) For a review of measured field strengths see also Mantiply et al. [61].

1.3.3.2 FM Radio and TV Transmission

Exposures to RF fields have been occurring for as long as we have had radio broadcasting. Since the antenna towers are usually quite high and the emissions are directed for reaching a long distance, exposure levels near the towers are minimal. The Environmental Protection Agency has done field strength measurements in the United States, and an

TABLE 1.6

Electric Field Strengths

Source	Distance		
	1 km	10 km	50 km
(a) Combined electric field strengths from large radio and TV transmitters and one type of base station for mobile phones ^a			
Radio	1	0.1	0.02
UHF TV	5	0.5	0.1
(b) Electric field strengths from radio base stations for Mobile Communication			
	10 m	100 m	1000 m
Base station	7	0.7	0.07

Note: E field in V/m.

^aRadio: 60 kW ERP; TV1: 60 kW ERP; TV2: 1000 kW ERP. $S = PG/(4\pi R^2) = E^2/120\pi$. (ERP is the effective radiated power, also expressed as PG, where P is the total power to the antenna and G is the gain; R is the distance to the antenna.)

overview is given by Mantiply et al. [61]. At a distance, the fields can be estimated from calculations using the far-field formula, and some examples are given in Table 1.6. The input power is often highest for UHF TV broadcasting. The TV signal consists of an amplitude-modulated video signal and a frequency-modulated audio signal. In Sweden, for instance, 30 kW of power is used for the video signal and about 5 kW for the audio. With the antenna gain this gives an effective radiated power (ERP) of 1000 kW.

There have not been many radio and TV towers built during the last 10 y or so, although a number have been moved or upgraded, e.g., moved to taller buildings for greater range, but we have seen an increase in the number of terrestrial channels available. New ways of transmitting information have also come into play with digital radio and TV. However, with these the output RF power may be lower; instead, this technique uses a much larger frequency bandwidth.

The total power density of RF exposure of the public has undeniably increased during the last 10 y. Tell and Mantiply [62] reported in 1980 that the average level in the United States from FM radio and TV transmitters was about $50 \mu\text{W}/\text{m}^2$. Today, exposure due to such sources is about the same [50], but with mobile phone base stations added, the total power density is now often found to be on the order of $100 \mu\text{W}/\text{m}^2$ or so (see Figure 1.16). Despite the proliferation of mobile telephone systems, most of the power is still due to broadcasting (Figure 1.11). Although the total level of RF exposure of the general public has increased during the last few years, it should be clearly stated that at all distances the RF field levels on the ground from base stations are well within the international guidelines for RF exposure of the general public.

1.3.3.3 Wireless Communication Systems (Base Stations, Personal Wireless Devices Such as Cellular Telephones and Pagers)

1.3.3.3.1 Mobile Phone Base Stations

Current mobile telephone systems operate at frequencies between 800 and 2100 MHz, but some older systems operating near 450 MHz are still in use (see Table 1.7). With the rapid increase in the use of mobile phones, the number of base stations has also increased. The phones operate by communicating with a nearby base station, which is a low-powered

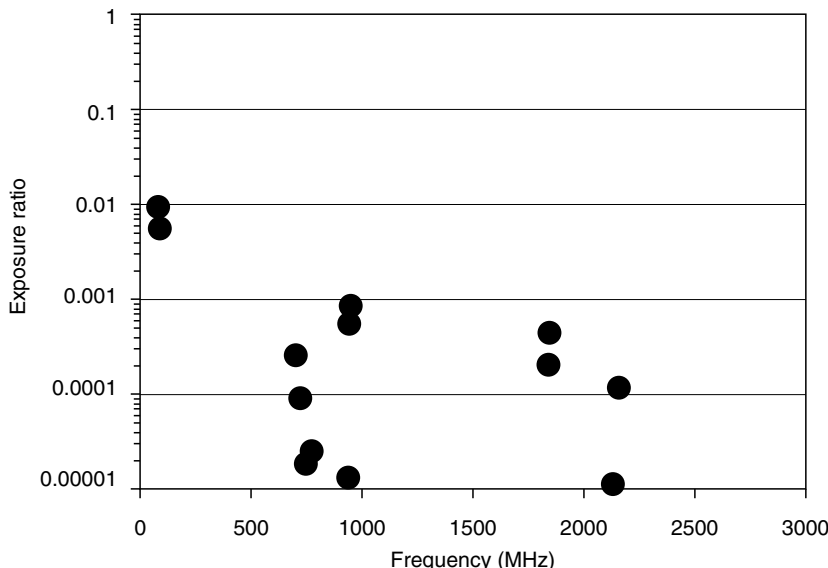


FIGURE 1.16

Power and frequency of environmental RF fields at a sample urban location in Sweden, plotted at each frequency as a comparison to the ICNIRP guideline power limit for personal exposure at the same frequencies, which is set equal to 1 (for plot of limits as a function of frequency, see Chapter 8 in BMA on standards in Ref. [82]). (From Hamnerius, Y. COST 281 Workshop 2004/09, Workshop on RF Exposure Assessment, Paris, September 20–21, 2004. With permission.)

radio transmitter, typically mounted on a tower or the roof of a building, that relays calls between the user and the telephone system. In Nordic countries the market penetration is over 100%; that is, there are more mobile phone subscriptions than people; many have more than one phone, and practically everyone in the working population has access to a mobile phone. The number of base stations in Sweden is estimated at over 20,000. In 2000,

TABLE 1.7

Frequencies and Modulation Characteristics of Various Mobile Telephone Systems

System	Carrier Frequency	Modulation	Multiplexing Type
TETRA	380–470 MHz	17 Hz	TDMA
MIRS	806–821 MHz	11.1 Hz	TDMA
NADC	824–849 MHz	50 Hz	TDMA
CDMA	824–849 MHz	800 Hz	Multichannel
Analog	824–849 MHz	FM	None
GSM	890–915 MHz	217 Hz	TDMA
PDC	929.2 MHz/1.5 GHz	50 Hz	TDMA
Iridium	1616–1626 MHz	11 Hz	TDMA
CDMA	1765 MHz	800 Hz	Multichannel
PCS	1805–1880 MHz	217 Hz	TDMA
GSM	1800 MHz	217 Hz	TDMA
GSM	1900 MHz	217 Hz	TDMA
NMTS	1920–2170 MHz	100 Hz–1.5 kHz FDD	

Notes: TDMA = Time division multiple access; conversations use different time slices of shared channels. CDMA = code division multiple access; digital identifiers signal phone when the conversation is using one of many closely spaced channels.

Source: Data courtesy of M. Swicord, private communication, 2005.

the United States had more than 82,000 cellular base station sites, some with more than one base station in operation, while there were some 20,000 base stations sites in the U.K. [63].

The antenna system used for base stations comprises often either omnidirectional (whip) antennas, which radiate in all directions in the horizontal plane, or directional (panel) antennas, which radiate energy primarily from their front surfaces. Most commonly employed is a sectorized panel arrangement with three sets of directional transmitting and receiving antennas, oriented 120° apart.

The antennas have a high gain, giving a narrow beam in the vertical direction but a quite wide one in the horizontal direction. In the main beam of the antenna, that is, several meters or more directly in front of and at the same height as the antenna, the intensity of the beam (i.e., the power density) decreases as the inverse square of the distance from it. The RF exposure a person receives from a base station thus depends both on the distance from the antenna and on the angle with respect to the direction of the main beam. At ground level, the signal is relatively weak near the base of the antenna tower since the main beam is passing directly overhead. The ground level signal characteristically increases with distance from the tower to a maximum at between 10 and 100 m from the base of the tower and then decreases at still greater distances. Panel antennas only radiate significant amounts of energy in the forward direction. Thus, for panel antennas mounted facing outward on building parapets, the exposure is low for people on the rooftop or in rooms below the antenna. (See further the 1999 report on cellular telephones and health by the U.K. House of Commons Committee on Science and Technology [64].)

In rural areas, where there is a lower user density, base stations are typically a couple of kilometers apart. In towns and cities where there are more users the cells are smaller and transmitter base stations can be as little as a few hundred meters apart. The actual levels of transmitted power vary widely between urban and rural areas. Since a longer reaching distance is wanted in rural areas, the output power tends to be greater, whereas the large increase in the number and density of base stations within the cities will make the cells smaller and thereby also permit a reduction of output power from the surrounding base stations. Therefore, the levels of public exposure to RF energy from any system will not increase in proportion to the number of its base stations in an area.

In Table 1.6b an example is given of the calculation of electric field strength under far-field conditions. The values given are for the main beam, and since the beam would not be aimed at the ground in the near zone, the theoretical values are presumably overestimating the field strength for close distances. Measurements of field strength from base stations have recently been reported by Thuroczy et al. [65] and Hamnerius and Uddmar [66]. They found levels encountered within about 20 m from the antenna in the range of a few to some tens of volts per meter. However, at distances where most people would be exposed, the field strength is down to tens of millivolts per meter within cities, and in rural area values as low as a few millivolts per meter can be measured. For an estimation of maximum encountered levels, the formula used in Table 1.6b above may be used, and as can be seen from this table values in the range of tens of millivolts per meter are estimated for a distance of 1000 m from the station.

1.3.3.3.2 Handheld Mobile Phones

The technical details of analog and digital systems used for mobile phones have been described in detail [67,68], and only a short background is given here. The Nordic Mobile Telephone (NMT) system operates at 900 MHz with a continuous carrier wave. The maximum output from the handheld NMT900 phones is 1 W. The NMT phones have their output power regulated through the base station in two levels, 0.1 or 1 W; the closer to the station, the lower is the output power likely to be.

To make more efficient use of the available frequencies, various schemes that take advantage of the relatively slow way speech transmits information have allowed more than one conversation to occur in the same frequency channel. Some of these systems include pulsing the RF signal at various frequencies, often in the ELF frequency region, or otherwise modulating it. The result is a departure from a pure, continuous sinusoidal field. In the digital Global System for Mobile Communications (GSM), which is in very common use worldwide, the information is sent in pulses with a repetition rate of 217 Hz. The pulse length and repetition frequency give a duty cycle of 1/8. The maximum output power is 2 W, which gives a time-averaged value of 0.25 W maximum. The GSM system also provides a battery-saving function, which in practice reduces the output power to about half of the maximum. The output power is also regulated from the base station, from a maximum of 2 W down to a minimum of 20 mW, depending on the strength of the signal received at the phone; with the newest phones sold today an even lower value of 5 mW is used. The mean output power is thus normally well below 0.1 W. Frequencies and coding patterns of some other current or proposed mobile telephone signal systems are indicated in [Table 1.7](#).

Different models of phones have different specifications for the antenna design position and physical dimensions, for instance, a dipole antenna or a helical antenna. Kuster [69] measured 16 different European digital phones and found a very wide variation in the SAR values. The phone giving the lowest value, when averaged over time and 10 g of tissue, had a specific absorption rate (SAR) of 0.28 W/kg in the user's head, and the one with the highest value had an SAR of 1.33 W/kg, all normalized to an antenna input power of 0.25 W, which is the maximal value for a GSM phone. If the averaging was done over 1 g of tissue, the span was from a low of 0.42 W/kg to a high of 2.0 W/kg. Anger [70] reported the measurement of SAR on 21 different phones, and his result is similar. The SAR ranged from 0.3 to 1.7 W/kg over 10-g tissues. He also reported the telephone communication power value, that is, how much of the output power can be used for communication, and he found values ranging from only about 5% in the lowest phone to just less than 50% in the "best" phone. Thus, more than half of the output power from the phone is lost because of mismatch between the phone and the antenna, and some is deposited as SAR in the user.

These SAR measurements were done under normal user conditions. However, when the phone is slightly tilted toward the head, Kuster [69] shows that the value can go up from 0.2 to 3.5 W/kg. Thus, for different phones under maximal output, we have a factor of about 5 between the extremes, and to this the personal handling of the phone gives a factor of tenfold or more. It should be noted that all given values are the maximum SAR values found, regardless of the anatomical location. An equal weight is given to the values, independent of whether they are obtained on the external ear, in the middle or inner ear, or behind the ear. In the future, it will be necessary to make the comparison at the same anatomical location. Presumably then, the values as given by Kuster [69] might differ even more.

Taken together there is a rather large uncertainty in estimating the actual SAR that depends on the specific situation, including a factor of 100 from the distance to the base station and at least a factor 10–50 depending on the make and model of the telephone and the personal style of use.

The currents from the battery also give rise to magnetic fields near the phone. For GSM phones magnetic flux densities of a few microtesla near the phone have been measured [66,71]. The fields are pulsed DC fields with a frequency of 217 Hz. For the NMT phones the magnetic field from the battery current can be regarded as pure DC. Jokela et al. [72] recently measured seven different GSM phones and examined the frequency content of the magnetic pulse, and he found that a considerable amount is found in the low kilohertz range. It was even found that some phones exceeded the ICNIRP guideline reference values when the multiple frequency formula was applied, but calculations show that the BRs were not exceeded.

1.3.4 RF EM Fields in Industrial Settings (RF Dielectric Heaters, Worker Exposure to Broadcast Systems)

1.3.4.1 RF Sealers

Operators of RF plastic sealers (RF operators) are an occupational category highly exposed to RF with frequencies around 27 MHz. RFs are used to produce heat to seal, for instance, plastics for tarpaulins, tents, rain clothes, and covers. Around an RF plastic sealer (RF sealer), both a magnetic and an electric field will be present, and close to the machine the coupling between the two is complex since far-field conditions are not at hand.

During RF exposure, a current is induced in the body, the magnitude of which is dependent on many factors such as the electric and magnetic field strength, the polarization of the field, and the grounding conditions. See further Wilén et al. [73], who tested different techniques to measure the induced current in grounded as well as ungrounded conditions.

Within the category of RF sealer operators, many different exposure situations exist, which can roughly be divided into two main types: tarpaulin workers and readymade clothing workers. Tarpaulin workers often stand in front of the RF sealer and will experience whole-body exposure, which often causes a high current to pass through the ankles. Readymade clothing workers often sit down in front of the RF sealer, often without perfect contact with the ground, but with their hands close to the electrode.

To get a good weld, both the welding time and the total power can be adjusted. The combination of the two will produce enough energy to seal the plastic. Typical welding times range from 1 to 10 s, depending on the material being sealed. The total exposure time will also vary between different RF-sealing processes; in the same amount of time, more welds are made in the readymade clothing industry than in the tarpaulin industry. For more information about the welding process see Refs. [74–76].

In a recent study, Wilén et al. [77] studied the exposure among RF sealer operators. The mean values of the calculated 6-min spatially averaged field strengths, in line with ICNIRP recommendations, are 107 V/m and 0.24 A/m, respectively. The maximum measured field strengths were 2 kV/m and 1.5 A/m, respectively. The induced current in ankles varied depending on the work situation, with a mean value of 101 mA and a maximum measured value of 1 A. In total, 16 out of the 46 RF plastic sealers measured exceeded the ICNIRP guidelines.

1.3.4.2 Occupational Exposure from Broadcasting and Radars

Workers in the fields of communication and radar are only exposed to low-level field strength in most situations. However, when climbing FM or TV towers, for instance, accidental exposure can be intense if proper safety precautions are not taken to keep exposure below the regulated limits. The same is true when someone is working near transmitter cabinets with the interlocks defeated and doors open. In these instances, the exposure, usually inadvertent, can be substantial.

Radar is used to detect the presence and directions of aircraft, ships, or other usually movable objects. The systems usually operate in the frequency range from 300 MHz to 15 GHz depending on the purpose of their use. The output power can range from a few milliwatts from police radar to several kilowatts for large air surveillance systems. A short description of various systems can be found, for example, on the WHO Fact Sheet No. 226 [78]. Here, as an example, a short description is given of one usual system where environmental exposure may occur. For civilian air traffic control, radars operating at 1305 MHz are used. The systems use a pulsed field with pulse duration of 2 μ s and

repetition rate of 625 pps. The peak power is 1.8 MW, and with the antenna gain this gives 3590 MW peak ERP in the maximum direction. Calculations using the far-field formula then give a peak electric field at 5 km of 65 V/m (equivalent power density of 11 W/m²). However, with the pulsing this comes down to a time-averaged power density of 1.4 μW/cm², and since the antenna is rotating at 9 rpm and the lobe width is 1.2° this is then further reduced to 3×10^{-5} μW/cm². For a review of measurements on different systems see Mantiply et al. [61].

In all known exposure situations of exposure of the general public to EMF from radar systems, the level is below the limiting values given in international guidelines. However, occupational exposure in the near field can occur, and strict adherence to safety instructions is needed, in form of both engineering controls, for example, interlocks, and administrative controls, for instance, strong training and enforcement of safety policies.

1.3.4.3 *Exposure in Medical Applications*

When medical uses of EM devices are considered, a distinction is made between exposure of patients and medical workers operating the equipment. The balance between any possible risks and the anticipated benefit of exposure of the patient has to be considered by consultation between the patient and the prescribing physician; as a result, exposures are often in excess of limits for workers or the general public. However, operator exposure is governed by the usual rules for occupational exposures; hence, only operator exposure is considered here.

One of the earliest applications of RF energy was shortwave diathermy, which usually operates at 27 MHz. Usually, unshielded electrodes are used, and this may lead to high stray fields. The person operating the equipment, therefore, may be exposed to high field strengths, and the time-averaged guideline for exposure may be exceeded for both RF electric (*E*) and magnetic (*H*) fields, depending on the working conditions at hand. Microwave diathermy at 2.45 GHz is also being used in therapy. In this case, the antenna is such that the beam can be directed toward the area to be treated, but the microwave beam may easily be directed toward the patients. Although the beam may not be exposed to the therapist, it may be exposed to the people in the immediate vicinity, including people waiting in the next room. It is therefore necessary to take this into account when planning the space where the microwave diathermy treatment is to be performed.

Electrosurgical units are commonly used in operating suites. They employ RF energy for cutting and coagulation and typically operate at frequencies from about 0.5 MHz to a few megahertz. The energy is supplied to the cutting tool via unshielded cable, which may pass close to the arm and hand of the surgeon, resulting in exposure of operating room personnel to RF energy. The electric and magnetic field near the active lead may be quite high, from a few hundred volts per meter to several kilovolts per meter [79,80]. The induced current in the tissue is of the same order of magnitude as the basic guideline limit for these frequencies, about 5 A/m². Since the exposure is rather high, precautionary action would be wise, and shielded wires should be used for the active lead.

Operator and general public exposure to static and RF fields may occur in connection with the use of magnetic resonance imaging (MRI) and nuclear magnetic resonance spectrometers. MRI systems use strong DC magnets, typically from 0.05 to about 3 T, as well as rapidly changing gradient magnetic fields with time derivatives (dB/dt) typically from 1 to 3 mT/ms (1–3 T/s). The RF fields (10–100 MHz) are low and almost fully contained within the patient enclosure, and the RF exposure of the operators is negligible. Inside treatment rooms, near MRI equipment, the maximum exposure level is about 1 T in front of the magnet, and nurses and technicians staying with patients can be exposed to magnetic flux densities up to 200 mT, approaching the protection guideline. When professional activities

take place very close to or inside the magnet's tube, workers can be exposed to higher fields (up to 1–2 T), for example, when assisting the patient, plugging in RF cables of treatment coils, or device cleaning. Reduction of the workers' exposure level is possible if MRI device design is required to include operation with workers no less than 0.5 m from the magnet. Workers' training should also include methods for exposure reduction.

Transcranial magnetic stimulation (TMS) has been introduced recently as a noninvasive and focal stimulation tool for the study of connectivity of brain regions, localization of functions, and pathophysiology of neuropsychiatric disorders and a therapeutic intervention method in the treatment of chronic depression. A high-intensity, fast magnetic field pulse produces a cortical stimulus through the induction of locally confined eddy currents; therefore, tailored coil arrangements can be used to achieve controlled local levels of stimulus. The TMS makes use of magnetic fields that can have intensities of up to 1 T with pulse durations in the range of ~0.05 to 0.2 ms. The resulting time derivative of the field can be several tens of kilotesla per second. This impulsive field transient is able to induce a rapid depolarization of the nerve cells within a volume of about 5 mm³ at the cortical level.

In some instances, the operator holds the TMS transducer coil in place during exposure. Measurements of the leakage magnetic field at different distances from the coils of the transducer show that the intensity of the field decays proportionally to $1/r^3$ (r = distance). The regulations set limits aimed at avoiding excitation of the central nervous system, while TMS or repetitive TMS aims at just reaching the level of local exposure high enough to produce cortical excitations in patients. For the pulse trains in use, one group found a pulse spacing of ~0.3 ms and about 72-μs active pulse width, which gives an equivalent frequency of about 3.5 kHz. For this the limit value is about 1 T/s, and this is transgressed at distances of about 0.7 m from the surface of the transducer's coils under normal treatment conditions [81].

1.4 Conclusion

EM fields, both natural and of human origin, are ubiquitous. Fields of human origin are primarily a result of technological developments that did not begin until late in the 19th century. In general, the natural fields in the environment are much smaller than those inside organisms; natural environmental fields are also usually smaller than fields of human origin at the same frequency. Inside an organism, naturally occurring charges, currents, and fields in cells, tissues, and organs are very important physiologically, and electric charges and magnetic moments are crucial factors in determining molecular structure and chemical reaction rates. Since organisms, including humans, evolved in the natural fields alone, it is not clear how their adaptation to artificial ones might affect them. The other chapters of this handbook explore this question.

References

1. Dubrov, A.P. *The Geomagnetic Field and Life. Geomagnetobiology*. Plenum Press, New York, 1978.
2. U.S. National Geophysical Data Center. <http://www.ngdc.noaa.gov>

3. König, H.L., Krueger, A.P., Lang, S., and Sönnig, W. *Biologic Effects of Environmental Electromagnetism*. Springer-Verlag, New York, 1981.
4. National Academy Press. *Studies in Geophysics: The Earth's Electrical Environment*. National Academy Press, Washington, DC, 1986.
5. Schienle, A., Stark, R., Kulzer, R., Klöpper, R., and Vaitl, D. Atmospheric electromagnetism: individual differences in brain electrical response to simulated sferics. *Int. J. Psychophysiol.* 21, 177–188, 1996.
6. Schienle, A., Stark, R., and Vaitl, D. Electrocortical responses of headache patients to the simulation of 10 kHz sferics. *Int. J. Neurosci.* 97, 211–224, 1999.
7. Campbell, W.C. Geomagnetic pulsations. In Matsushita, S. and Campbell, W.H., Eds. *Physics of Geomagnetic Phenomena*. Academic Press, New York, 1967, pp. 822–909.
8. Hingorani, N.G. High-voltage DC transmission: a power electronics workhorse. *IEEE Spectr.* 33(4): 63–72, 1996.
9. Kaune, W.T., Gilis, M.F., and Weigel, R.J. Analysis of air ions in biological exposure systems, including HVDC electric power transmission lines, in rooms containing generators, and near exposed humans and animals. *J. Appl. Phys.* 54, 6274–6283, 1983.
10. Fews, A.P., Wilding, R.J., Keitch, P.A., Holden, N.K., and Henshaw, D.L. Modification of atmospheric DC fields by space charge from high-voltage power lines. *Atmos. Res.* 63, 271–289, 2002.
11. Koops, F.B.J. Electric and magnetic fields in consequence of undersea power cables. In Matthes, R., Bernhardt, J., and Repacholi, M., Eds. *Effects of Electromagnetic Fields on the Living Environment*. Proceedings from International Seminar, Ismaning, Germany, October 4–5, 1999, ICNIRP 10/2000, pp. 189–210.
12. ICNIRP. Guidelines for limiting exposure to time-varying electric, magnetic, and electromagnetic fields (up to 300 GHz). *Health Phys.* 74(4), 494–522, 1998.
13. Portier, C.J. and Wolfe, M.S., Eds. Assessment of Health Effects from Exposure to Power-Line Frequency Electric and Magnetic Fields. NIH Publication 98-3981, National Institute of Health Sciences, Research Triangle Park, NC, 1998 (accessed April 7, 2005, at <http://www.niehs.nih.gov/emfrapid/html/WGReport/WorkingGroup.html>).
14. Wertheimer, N. and Leeper, E. Electrical wiring configurations and childhood cancer. *Am. J. Epidemiol.* 109, 273–284, 1979.
15. Deno, D.W. Transmission line fields. *IEEE Trans. Power Appl. Syst.* PAS-95, 1600–1611, 1976.
16. Rogers, L.E., Beedlow, P.A., Carlile, D.W., Ganok, K.A., and Lee, J.M. Environmental Studies of a 1100-kV Prototype Transmission Line: An Annual Report for the 1984 Study Period. Prepared by Battelle Pacific Northwest Laboratories for Bonneville Power Administration, Portland, OR, 1984.
17. Lee, J.M., Pierce, K.S., Spiering, C.A., Stearns, R.D., and VanGinhoven, G. *Electrical and Biological Effects of Transmission Lines: A Review*. Bonneville Power Administration, Portland, OR, 1996.
18. Fews, A.P., Henshaw, D.L., Keitch, P.A., Close, J.J., and Wilding, R.J. Increased exposure to pollutant aerosols under high voltage powerlines. *Int. J. Radiat. Biol.* 75, 1505–1521, 1999.
19. Deadman, J.E., Armstrong, B.G., McBride, M.L., Gallagher, R., and Thériault, G. Exposures of children in Canada to 60 Hz magnetic and electric fields. *Scand. J. Work Environ. Health* 1999, 25(4), 368–375.
20. Hansson Mild, K., Sandström, M., and Johnsson, A. Measured 50 Hz electric and magnetic fields in Swedish and Norwegian residential buildings. *IEEE Trans. Instrum. Meas.* 45(3), 710–714, 1996.
21. Mccurdy, A.L., Wijnberg, L., Loomis, D., Savitz, D., and Nylander-French, L. Exposure to extremely low frequency magnetic fields among working women and homemakers. *Ann. Occup. Hyg.* 45, 643–650, 2001.
22. Ahlbom, A., Day, N., Feychtig, M., Roman, E., Skinner, J., Dockerty, J., Linet, M., McBride, M., Michaelis, J., Olsen, J.H., Tynes, T., and Verkasalo, P.K. A pooled analysis of magnetic fields and childhood leukemia. *Br. J. Cancer* 83, 692–698, 2000.
23. Adams, J., Bitler, S., and Riley, K. Importance of addressing National Electrical Code® violations that result in unusual exposure to 60 Hz magnetic fields. *Bioelectromagnetics* 25, 102–106, 2004.

24. Moriyama, K. and Yoshitomi, K. Apartment electrical wiring: a cause of extremely low frequency magnetic field exposure in residential areas. *Bioelectromagnetics* 26, 238–241, 2005.
25. Zhang, J., Nair, I., and Morgan, M.G. Effects function simulation of residential appliance field exposures. *Bioelectromagnetics* 18, 116–124, 1997.
26. Verrier, A., Souques, M., and Wallet, F. Characterization of exposure to extremely low frequency magnetic fields using multidimensional analysis techniques. *Bioelectromagnetics* 26, 266–274, 2005.
27. Forsgren, P.G., Berglund, A., and Hansson Mild, K. Reduktion av lågfrekventa magnetiska fält i nya och befintliga anläggningar för eldistribution. Arbetsmiljöinstitutets undersökningsrapport 35, 1994 (in Swedish), 20 pp.
28. von Winterfeldt, D. and Trauger, T. Managing electromagnetic fields from residential electrode grounding systems: a predecision analysis. *Bioelectromagnetics* 17, 71–84, 1996.
29. Kaune, W.T., Dovan, T., Kavet, R.I., Savitz, D.A., and Neutra, R.R. Study of high- and low-current-configuration homes from the 1988 Denver childhood cancer study. *Bioelectromagnetics* 23, 177–188, 2002.
30. Kavet, R. and Zaffanella, L.E. Contact voltage measured in residences: implications to the association between magnetic fields and childhood leukemia. *Bioelectromagnetics* 23, 464–474, 2002.
31. Bridges, J.E. Non-perceptible body current ELF effects as defined by electric shock safety data. *Bioelectromagnetics* 23, 542–544, 2002.
32. Kavet, R., Zaffanella, L.E., Pearson, R.L., and Dallapiazza, J. Association of residential magnetic fields with contact voltage. *Bioelectromagnetics* 25, 530–536, 2004.
33. Kaune, W.T., Miller, M.C., Linet, M.S., Hatch, E.E., Kleinerman, R.A., Wacholder, S., Mohr, A.H., Tarone, R.E., and Haines, C. Magnetic fields produced by hand held hair dryers, stereo headsets, home sewing machines, and electric clocks. *Bioelectromagnetics* 23, 14–25, 2002.
34. Vistnes, A.I. Electromagnetic fields at home. In Brune, D., Hellborg, R., Persson, B.R.R., and Pääkkönen, R., Eds. *Radiation at Home, Outdoors and in Workplace*. Scandinavian Science Publisher, Oslo, Norway, ISBN 82-91833-02-8, 2001, pp. 286–305.
35. Söderberg, K.C., Naumburg, E., Anger, G., Cnattingius, S., Ekbom, A., and Feychting, M. Childhood leukemia and magnetic fields in infant incubators. *Epidemiology* 13(1), 45–49, 2002.
36. Floderus, B., Persson, T., and Stenlund, C. Magnetic-field exposures in the workplace: reference distribution and exposures in occupational groups. *Int. J. Occup. Environ. Health* 2(3), 226–238, 1996.
37. Deadman, J.E. and Infante-Rivard, C. Individual estimation of exposures to extremely low frequency magnetic fields in jobs commonly held by women. *Am. J. Epidemiol.* 155(4), 368–378, 2002.
38. Kelsh, M.A., Bracken, T.D., Sahl, J.D., Shum, M., and Ebi, K.L. Occupational magnetic field exposures of garment workers: results of personal and survey measurements. *Bioelectromagnetics* 24, 316–326, 2003.
39. Stuchly, M.A. and Lecuyer, D.W. Exposure to electromagnetic fields in arc welding. *Health Phys.* 56, 297–302, 1989.
40. Skotte, J.H. and Hjøllund, H.I. Exposure to welders and other metal workers to ELF magnetic fields. *Bioelectromagnetics* 18, 470–477, 1997.
41. Nordensson, I., Hansson Mild, K., Järventaus, H., Hirvonen, A., Sandström, M., Wilén, J., Blix, N., and Norppa, H. Chromosomal aberrations in peripheral lymphocytes of train engine drivers. *Bioelectromagnetics* 22, 306–315, 2001.
42. Ptitsyna, N.G., Villoresi, G., Kopytenko, Y.A., Tyasto, M.I., Kopytenko, E.A., Iucci, N., Voronov, P.M., and Zaitsev, D.B. Magnetic field environment in ULF range (0–5 Hz) in urban areas: man-made and natural fields in St Petersburg (Russia). In Bersani, F., Ed. *Electricity and Magnetism in Biology and Medicine*. Kluwer Academic/Plenum Publishers, New York, 1999, pp. 279–282.
43. Ptitsyna, N.G., Kopytenko, Y.A., Villoresi, G., Pfluger, D.H., Ismaguilov, V., Iucci, N., Kopytenko, E.A., Zaitzev, D.B., Voronov, P.M., and Tyasto, M.I. Waveform magnetic field survey in Russian DC and Swiss AC powered trains: a basis for biologically relevant exposure assessment. *Bioelectromagnetics* 24, 546–556, 2003.
44. Wenzl, T.B. Estimating magnetic field exposures of rail maintenance workers. *Am. Ind. Hyg. Assoc. J.* 58, 667–671, 1997.

45. Chadwick, P. and Lowes, F. Magnetic fields on British trains. *Ann. Occup. Hyg.* 42, 331–335, 1998.
46. Fraser-Smith, A.C. and Coates, D.B. Large amplitude ULF electromagnetic fields from BART. *Radio Sci.* 13, 661–668, 1978.
47. Bernardi, A., Fraser-Smith, A.C., and Villard, O.G., Jr. Measurement of BART magnetic fields with an automatic geomagnetic pulsation index generator. *IEEE Trans. Electromagn. Compat.* 31, 413–417, 1989.
48. Dietrich, F.M., Feero, W.E., and Jacobs, W.L. Safety of High Speed Guided Ground Transportation Systems: Final Report to the U.S. Federal Railroad Administration. U.S. Government Printing Office, Washington, DC, DOT/FRA/ORDL-93-07, DOT-VNTSC-TRA-93-13, 1993.
49. NIOSH. NIOSH Health Hazard Evaluation Report: Alumax of South Carolina, Centers for Disease Control and Prevention. National Institute of Occupational Safety and Health, Cincinnati, OH, 1994.
50. Von Kaenel, R. et al. The determination of the exposure to electromagnetic fields in aluminum electrolysis. In Mannweiler, U., Ed. *Light Metals 1994*. The Minerals, Metals & Materials Society, Warrendale, PA, 1994, pp. 253–260.
51. Kaune, W.T. and Phillips, R.D. Comparison of the coupling of grounded humans, swine and rats to vertical, 60-Hz electric fields. *Bioelectromagnetics* 1, 117–129, 1980.
52. Tenforde, T.S. and Kaune, W.T. Interaction of extremely low frequency electric and magnetic fields with humans. *Health Phys.* 53, 585–606, 1987.
53. Kjellsson, N., Sandström, M., Stensson, O., and Hansson Mild, K. Measurements of magnetic fields generated by electronic article surveillance systems. In Kostarakis, P., Ed. *Proceedings of the 2nd International Workshop on Biological Effects of EMFs*, Rhodes, Greece, October 7–11, 2002, ISBN 960-86733-3-X, pp. 937–941.
54. Harris, C., Boivin, W., Boyd, S., Coletta, J., Kerr, L., Kempa, K., and Aronow, S. Electromagnetic field strength levels surrounding electronic article surveillance (EAS) systems. *Health Phys.* 78(1), 21–27, 2000.
55. Eskelinen, T., Toivonen, T., Jokela, K., Keskinen, K., and Juutilainen, J. Occupational exposure to magnetic fields from EAS devices. In Proceedings of the EBEA 2001 5th International Congress of the European BioElectromagnetics Association, Helsinki, Finland, September 6–8, 2002, pp. 147–148.
56. Sandström, M., Hansson Mild, K., Stenberg, B., and Wall, S. A survey of electric and magnetic fields among VDT operators in offices. *IEEE Trans. EMC* 35(8), 394–397, 1993.
57. ACTU. *ACTU Guidelines for Screen Based Work*. Publ. D. No. 40/1998ACTU OHS UNIT, Australian Council of Trade Unions, Melbourne, 1998 (accessed April 2005 at <http://www.ohsrep.org.au/data/files/general/SBW98.rtf>).
58. Sandström, M., Hansson Mild, K., Sandström, M., and Berglund, A. External power frequency magnetic field induced jitter on computer monitors. *Behav. Inf. Technol.* 12(6), 359–363, 1993.
59. Altpeter, E.S., Krebs, Th., Pfluger, D.H., von Känel, J., Blattmann, R., Emmenegger, D., Cloetta, B., Rogger, U., Gerber, H., Manz, B., Coray, R., Baumann, R., Staerk, K., Griot, Ch., and Abelin, Th. Study on Health Effects of the Shortwave Transmitter Station of Schwarzenburg, Berne, Switzerland. Major report on behalf of the Federal Office of Energy, BEW Publication Series Study No. 55, August. 1995.
60. Michelozzi, P., Capon, A., Kirchmayer, U., Fusco, D., and Ancona, C. Risk of leukemia and residence near high-power radio-transmitters in Italy. *Epidemiology* 10, S116, 1999.
61. Mantiply, E.D., Pohl, K.R., Poppell, S.W., and Murphy, J.A. Summary of measured radiofrequency electric and magnetic fields (10 kHz to 30 GHz) in general and work environment. *Bioelectromagnetics* 18, 563–577, 1997.
62. Tell, R.A. and Mantiply, E.D. Population exposure to VHF and UHF broadcast radiation in the United States. *Proc. IEEE* 80, 6–12, 1980.
63. World Health Organization. Electromagnetic Fields and Public Health: Mobile Telephones and Their Base Stations. WHO International EMF Project Fact Sheet 193, Geneva, June. 2000 (accessed September 30, 2005, at <http://www.who.int/mediacentre/factsheets/fs193/en>).
64. Clark, R., et al. Cellular Phones and Health. Report House of Commons, No. 489, U.K. House of Commons Committee on Science and Technology, London, September 22, 1999 (see also <http://www.parliament.uk/commons/selcom89/s&thome.htm>).

65. Thuroczy, G., Janossy, J., and Nagy, N. Radiofrequency (RF) exposure of mobile communications in Hungary and evaluation relevant to EU and national standard: base stations and handy devices. Manuscript for NATO Workshop, Slovenia, October. 1998.
66. Hamnerius, Y. and Uddmar, T. Microwave exposure from mobile phone and base stations. Presented at Mobile Telephones and Health, Mobitel conference, Gothenburg, Sweden, September 16–17, 1999.
67. Bach Andersen, J., Johansen, C., Frölund Pedersen, G., and Raskmark, P. On the Possible Health Effects Related to GSM and DECT Transmissions. Report to the European Commission, Aalborg University, Denmark, 1995.
68. McKinlay, A.F., Andersen, J.B., Bernhardt, J.H., Grandolfo, M., Hossman, K.-A., van Leeuwen, F.E., Hansson Mild, K., Swerdlow, A.J., Verschaeve, L., and Veyret, B. Possible health effects related to the use of radiotelephones. Proposal for a research programme by a European Commission Expert Group, 1996.
69. Kuster, N. Review of dosimetry and near-field measurement techniques for human exposure evaluations and bioexperiments. In Legris, C., Ed. *Communication Mobile-Effects*, Biologique. CADAS, Académie des Sciences, Paris, 2001, pp. 45–69.
70. Anger, G. SAR och utstrålad effekt för 21 mobiltelefoner. Statens Strålskyddsinstitut, SSI Rapport, 2002.
71. Linde, T. and Hansson Mild, K. Measurement of low frequency magnetic fields from digital cellular telephones. *Bioelectromagnetics* 18, 184–186, 1997.
72. Jokela, K., Puranen, L., and Sihvonen, A.-P. Assessment of the magnetic field exposure due to the battery current of digital mobile phones. *Health Phys.* 86, 56–66, 2004.
73. Wilén, J., Hansson Mild, K., Paulsson, L.E., and Anger, G. Induced current measurements in whole body exposure condition to radio frequency electric fields. *Bioelectromagnetics* 22(8), 560–567, 2001.
74. Eriksson, A. and Hansson Mild, K. Radiofrequency electromagnetic leakage fields from plastic welding machines. Measurements and reducing measures. *J. Microwave Power* 20, 95–107, 1985.
75. Williams, P. and Hansson Mild, K. *Guidelines for Measurement of RF Welders*. Arbetsmiljöinstitutet, Solna, Sweden, 1991.
76. International Labour Office. *Safety in the Use of Radiofrequency Dielectric Heaters and Sealers: A Practical Guide*. Occupational Safety and Health Series 71. International Labour Office Bureau of Publications, Geneva, 1998.
77. Wilén, J., Hörnsten, R., Sandström, M., Bjerle, P., Wiklund, U., Stensson, O., Lyskov, E., and Hansson Mild, K. Electromagnetic field exposure and health among RF plastic sealer operators. *Bioelectromagnetics* 25, 5–15, 2004.
78. World Health Organization. Electromagnetic Fields and Public Health: Radars and Human Health. Fact Sheet No. 226, World Health Organization, Geneva, 1999 (accessed May 2005 at <http://www.who.int/mediacentre/factsheets/fs226/en/>).
79. Paz, J.D., Milliken, R., Ingram, W.T., Frank, A., and Atkin, A. Potential ocular damage from microwave exposure during electrosurgery: dosimetric survey. *J. Occup. Med.* 29, 580–583, 1987.
80. Hansson Mild, K., Ly, C., Liljestrand, B., Sandström, M., and Foster, K.R. Dosimetric studies on electrosurgical units. Poster presentation at BEMS 23rd Annual Meeting, St. Paul, MN, 2001.
81. Figueira Karlström, E., Stensson, O., Lundström, R., and Hansson Mild, K. Therapeutic staff exposure to magnetic field pulses during TMS/rTMS treatments. *Bioelectromagnetics* 27, 156–158, 2006.
82. van Deventer, E., Simunic, D., Repacholi, M., EMF Standards for Human Health, In Barnes, F.S., and Greenebaum, B., Eds., *Biological and Medical Aspects*, Taylor & Francis, Boca Raton, FL, 2006, Chapter 8.

2

Endogenous Electric Fields in Animals

Richard Nuccitelli

CONTENTS

2.1	Introduction	35
2.1.1	Sources of Endogenous Electric Fields.....	36
2.1.2	Methods for Measuring Endogenous Electric Fields.....	38
2.1.2.1	Self-Referencing Probe	38
2.1.2.2	Microelectrode Techniques for Measuring Endogenous Electric Fields.....	38
2.1.2.3	Voltage-Sensitive Fluorescent Dyes for Measuring Endogenous Electric Fields	38
2.2	Measurements of Endogenous Extracellular Electric Fields	38
2.2.1	Amputated Limbs	38
2.2.2	Embryonic Electric Fields Beneath the Skin.....	39
2.2.3	Fields Associated with the Neural Tube	43
2.2.4	Fields Associated with Epithelial Wounds	43
2.3	Measurements of Endogenous Intracellular Electric Fields	46
2.3.1	Nurse Cell Complex in Insects.....	46
2.3.2	Development of Left-Right Polarity in Chick and Frog	46
2.4	Methods for Modifying Endogenous Electric Fields	47
2.4.1	Passing Current between Electrodes	47
2.4.2	Low-Resistance Shunts	48
2.4.3	Placing Tissues in an External Electric Field	48
2.5	Summary	48
	References	49

2.1 Introduction

In a volume presenting the biological effects of electromagnetic fields it is appropriate to review the information we have regarding endogenous electric fields in the body. After all, imposed electromagnetic fields may augment the naturally occurring ones, so a complete understanding of the possible effects of imposed fields requires consideration of those electric fields already present. Here, I will provide a brief overview of the direct current (DC) endogenous fields that have been best characterized in animals and will touch on the evidence that these electric fields are required for the function of various cellular and organ systems. Other well-known variable fields that are generated by various electrically excitable organs such as the heart (electrocardiogram), brain (electroencephalogram), and

eye (electrooculogram) will not be covered here. Another very comprehensive review of endogenous fields that will be of interest has appeared quite recently in *Physiological Reviews* by McCaig et al. (2005), and another review of the roles of such fields in development was presented by Levin (2003).

In order to put these endogenous fields in perspective for the reader, I would like to summarize here their main characteristics. Unlike much of the material considered in this volume, these endogenous fields are small and very slowly changing. Endogenous fields typically fall into the 10- to 100-V/m range and are generally very steady, DC fields generated by the flow of ionic currents through cells and embryos. This can be compared with the much higher fields required to electroporate cells (3 V/cell diameter or 3×10^5 V/m for a 10- μm -diameter cell), which are usually only applied for a short time on the order of a millisecond.

2.1.1 Sources of Endogenous Electric Fields

In order to generate an electric field in the body, a voltage generator or power source is required. There are two main sources of such a power source in living systems: (1) the plasma membrane surrounding every cell in the body and (2) the epithelium that surrounds every organ in the body as well as the entire body itself in the form of the skin. The plasma membrane forms the defining boundary for every cell and is a lipid bilayer with many embedded transporter proteins whose main function is to control the movement of molecules inside or outside of the cell. One of these transporter proteins is the Na^+/K^+ -ATPase, which is responsible for maintaining two ion concentration gradients across the plasma membrane (high internal $[\text{K}^+]$ and low internal $[\text{Na}^+]$). The K^+ concentration gradient, in combination with a large number of K^+ channels in the plasma membrane, results in the outward diffusion of K^+ . This outward movement of K^+ leaves behind the anion that was associated with maintaining electroneutrality and thereby separates charge across the membrane. This separation of charge generates a voltage difference or membrane potential (inside negative). This membrane potential is used for a wide variety of cellular functions, from capturing nutrients to signaling the occurrence of important events, such as sperm–egg fusion in many egg types or light absorption in retinal rods. Indeed, we expend more than half of our energy in maintaining this voltage across all of the cells in our brain and kidney, where excitatory events and Na^+ -dependent transport constitute major functions (Clausen et al., 1991).

Voltage differences are also found across all epithelial layers, and this is called the transepithelial potential (TEP). Both organs and embryos are surrounded by one or more monolayers of cells called an epithelium. The outer epithelium belongs to the organ while the plasma membrane to the cell, and epithelia pump ions across themselves to generate the TEP. One clear difference between these two voltage sources (plasma membrane and epithelial layer) is their opposite polarity. Whereas the plasma membrane potential is usually negative on the inside with respect to the outside, the TEP is usually positive on the inside or basal side of the epithelial monolayer with respect to the outside or apical side of the monolayer.

This polarity difference results from the opposite flow of charge across these layers. The plasma membrane of most animal cells generates a potential difference across itself that is negative on the interior. This results from the outward diffusion of K^+ that separates charge across the membrane. In contrast, most animal epithelia are composed of highly polarized cells in which Na^+ channels are localized to the apical end of the cell and both the K^+ channels and the Na^+/K^+ ATPases are localized at the basal end. This polarized distribution of these transport proteins leads to Na^+ influx at the apical end and both Na^+ and K^+ efflux at the basal end to drive positive charge to the interior of the epithelial

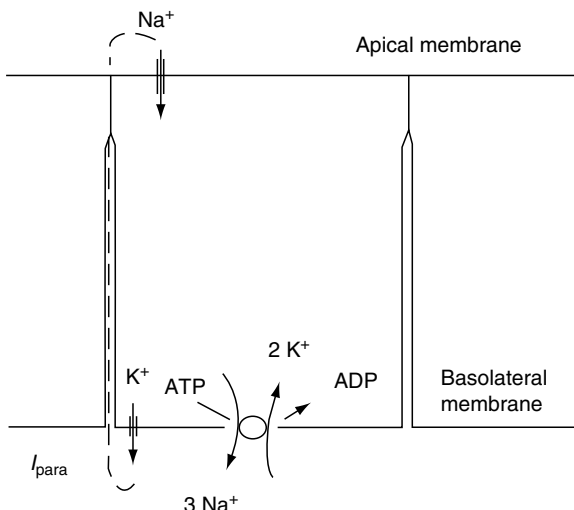


FIGURE 2.1

Diagram of a typical epithelial cell in a monolayer with Na^+ channels localized on the apical plasma membrane and K^+ channels localized on the basolateral membranes along with the Na^+/K^+ -ATPase. This asymmetric distribution of ion channels generates a transcellular flow of positive current that must flow back between the cells through the paracellular pathway (I_{para}). This current flow generates a TEP that is positive on the basolateral side of the monolayer.

layer. However, this current cannot flow freely in the extracellular medium because these polarized epithelial cells are attached to each other with both tight and adherent junctions. As the apical–basal transcellular current flows back extracellularly, it must follow a pathway between the cells called the paracellular pathway (Figure 2.1). Current flow through this pathway encounters a high-resistance region at the tight junctions near the apical end, and the current flow through this resistance leads to a TEP that is positive on the basal side of the monolayer with respect to the apical side. The TEP will be proportional to the resistance of this paracellular pathway, and typical values for this TEP range from 15 to 60 mV, basal side positive.

It is this TEP that is the driving force for most endogenous ionic currents in embryos and adults. This voltage across epithelia will drive current out of regions of low resistance where there has been a break in the epithelium (wounds) or where tight junction resistance is low, such as along the primitive streak (Jaffe and Stern, 1979; Winkel and Nuccitelli, 1989), the posterior intestinal portal (Hotary and Robinson, 1990) in chick or mouse embryos, or at the forming limb bud in amphibian, chick, and mouse embryos (Borgens et al., 1983; Robinson, 1983; Altizer et al., 2001). This “leakage current” will in-turn generate a lateral electric field along its path that will be proportional to the resistivity in that region. This electric field results from Ohm’s law in a conductive medium,

$$E = \rho J$$

where J is the current density and ρ is the local resistivity.

The earliest measurements of the leakage current associated with wounds were made more than a century ago. DuBois-Reymond (1843) used a unique galvanometer that he built himself with more than two miles of wire and measured about 1 μA flowing out of a cut in one of his fingers. This was confirmed in 1849 and 1910 by other investigators, and the history of these measurements is presented in a scholarly review by Venable (1991). More modern techniques have also been used to study this wound current as discussed. Direct measurements of electric fields *in situ* have been made, and I will discuss them next.

2.1.2 Methods for Measuring Endogenous Electric Fields

2.1.2.1 Self-Referencing Probe

Lionel Jaffe and I developed a technique for exploring transcellular ionic currents, called the vibrating or self-referencing probe (Jaffe and Nuccitelli, 1974). This instrument vibrates a small platinum sphere between two points about $10\text{ }\mu\text{m}$ apart at about 300 Hz and measures the voltage between those points using signal averaging to improve the signal-to-noise ratio. In a conducting medium where most cells find themselves, a voltage difference can exist only where there is a current flowing through the medium. Ionic currents entering or leaving cells can be readily detected by measuring the voltage they generate as they flow through the extracellular medium, and the past 30 years of research on more than 30 cell types has revealed that most cells have an asymmetrical distribution of ion channels that naturally leads to a transcellular current density on the order of $1\text{--}10\text{ }\mu\text{A}/\text{cm}^2$ (Nuccitelli, 1988, 1990). Most epithelia that have been studied exhibit extracellular current densities on the order of $10\text{--}100\text{ }\mu\text{A}/\text{cm}^2$ flowing through the organ or embryo with which they are associated. This technique detects the current that is flowing outside the cell or tissue, and the exact electric field that is generated by this current when it flows inside the cell or tissue can only be estimated based on tissue resistivity. It is more accurate to directly measure the electric fields in the tissue or cells as described here.

2.1.2.2 Microelectrode Techniques for Measuring Endogenous Electric Fields

The classic approach to these measurements is to use KCl-filled glass microelectrodes to penetrate the outer epithelium and measure the voltage just beneath it in several positions. Such electrodes are typically connected via a Ag–AgCl junction to a very high-input impedance preamplifier, so that they do not drain current from the system under study, and their tips are small (on the order of $0.1\text{--}1\text{ }\mu\text{m}$) to minimize tissue damage (Wallis, 1993). If ionic currents are flowing within a tissue, these currents will generate an electric field that can be detected as the difference in potential at various sites along the current path. We will see below that this is the most commonly used approach to measure intraembryonic electric fields.

2.1.2.3 Voltage-Sensitive Fluorescent Dyes for Measuring Endogenous Electric Fields

Another popular technique for measuring the voltage across lipid membranes uses lipophilic fluorescent dyes whose fluorescence is voltage sensitive (Loew, 1992; Loew et al., 2002). For some of these dyes, their fluorescence intensity is dependent on their position within the lipid bilayer, which is in turn influenced by the membrane potential drop across this region. Membrane potential changes can be monitored by measuring the fluorescence intensity of these dyes, and differences in the membrane potential of cells making up an organ or embryo can also be detected. One example of the use of this approach, which will be discussed below, is to provide information about electric fields within sheets of cells that are electrically coupled via gap junctions in the chick embryo.

2.2 Measurements of Endogenous Extracellular Electric Fields

2.2.1 Amputated Limbs

Among the earliest direct measurements of endogenous extracellular electric fields were those made in the regenerating amphibian limb (McGinnis and Vanable, 1986). Upon

amputation, the skin battery of the amphibian limb drives 10–100 $\mu\text{A}/\text{cm}^2$ out of the cut end of the limb stump. This current flow generates an electric field within the limb tissue that is 60 mV/mm near the lesion during the first hours after amputation, and this field drops to about 25 mV/mm within 6 h as the healing process leads to an increase in the resistance of the wound.

Electric fields of this magnitude have been found to stimulate the growth of neurons into the limb via galvanotropism, and the presence of enhanced nerve in limbs has been correlated with enhanced regeneration (Borgens et al., 1979). The study of nerve galvanotropism has a long and fascinating history that is thoroughly reviewed by McCaig et al. (2005). Briefly, most neurons exhibit sensitivity to imposed electric fields by either bending their outgrowth direction toward the negative pole of the field or in the case of a neural ganglion, exhibiting a higher density of outgrowths on the side of the ganglion facing the negative pole. This galvanotropism may play a role in the guidance of neurons to their targets during development and has also been found to play an important role in regeneration.

2.2.2 Embryonic Electric Fields Beneath the Skin

Direct measurements of electric fields have been made in both avian and amphibian embryos during normal development. Hotary and Robinson (1990) used both the self-referencing probe and microelectrodes to first detect the transemбриonic current in the 2- to 4-day-old chick embryo and then measure the electric field that the transemбриonic current generates beneath the epidermis. They measured current entering much of the epidermis during stage 14 of development with the outward current focused mainly at the posterior intestinal portal, where up to 105 $\mu\text{A}/\text{cm}^2$ was measured (Figure 2.2). One would expect that this large anterior–posterior current would generate an internal electric field, so they then used microelectrodes to measure the TEP along this axis. Here, they measured electric fields of 5–20 mV/mm.

They then proceeded to test the hypothesis that these fields are important for normal development by perturbing them (Figure 2.3). They implanted a glass capillary that was filled with either conductive saline agar or nonconducting glass, used as a control, through the ectoderm at the dorsal trunk of the embryo (Hotary and Robinson, 1992). The conductive capillary allowed large currents of about 5 $\mu\text{A}/\text{cm}^2$ to leak out of the embryo. While the control embryos developed quite normally, most embryos with the implanted conducting capillary exhibited abnormalities in posterior structures where the endogenous electric field is normally the largest but was reduced by the capillary shunt. Perturbing the normal voltage pattern within the embryo resulted in striking tail abnormalities; and an investigation of a genetic mutant, rumpless, that exhibits similar tail abnormalities led to a very interesting correlation. They found that most rumpless mutants exhibited a much lower transemбриonic current density and lower electric field within the embryo and those mutants that exhibited a normal electric field pattern also exhibited normal development. Therefore, they found a good correlation between the internal electric field and the normal posterior development. These observations certainly support the hypothesis that the endogenous field is important for the development of posterior structures.

Studies of endogenous fields have also been carried out on the stage 14–21 developing axolotl embryo (Metcalf et al., 1994; Shi and Borgens, 1995). Current is driven out of the lateral walls of the neural folds and the blastopore and enters most of the rest of the embryo's body surface (Figure 2.4). Measurements of the TEP indicate an internal, caudally negative electrical field beneath the neural plate ectoderm. The magnitude of the endogenous field is on the order of 10–20 mV/mm (Figure 2.5). When these embryos

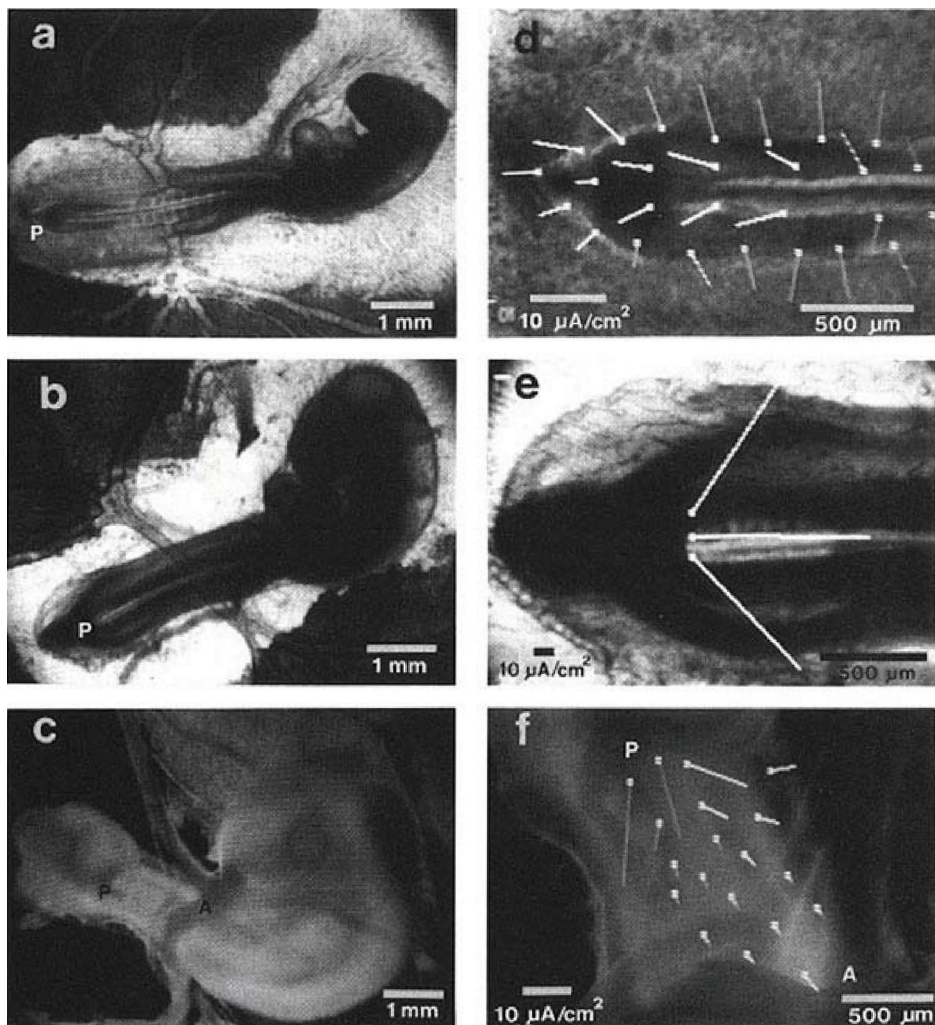


FIGURE 2.2

Ventral surface of three chick embryos at stages 14 (a and d), 17 (b and e), and 20 (c and f). Low-magnification views of the whole embryo are shown in (a)–(c), while (d)–(f) show the current pattern around the posterior intestinal portals of the embryos. Current vectors are represented by lines originating at a dot that indicates the position of the self-referencing probe when the measurement was made. The direction of the vector line away from the dot indicates the direction of current flow at that point, and the length of the line is proportional to the current density. At stage 14 (d), all vectors point toward the posterior intestinal portal or the lateral walls of the midgut. The three vectors shown at stage 17 (e) indicate large currents of about $100 \mu\text{A}/\text{cm}^2$ leaving the posterior intestinal portal. At stage 20 (f), outward currents were also found at the posterior intestinal portal. Current densities were much lower by this stage. Note the inward current at the anterior intestinal portal (A). (From Horaty, K.B. and Robinson, K.R. (1990). *Dev. Biol.* 140, 149–160. With permission.)

were placed into an external electric field designed to modify the internal field, abnormalities were observed that depended on the developmental stage (Metcalf and Borgens, 1994). Gastrula-stage embryos exhibited normal development after exogenous field exposure, indicating that the imposed field does not harm the embryo in some nonspecific way. In contrast, neurula-stage embryos exhibited developmental abnormalities when exposed to similar electric fields of 25–75 mV/mm. These data support the hypothesis that the natural electric field within the embryo influences normal morphogenesis.

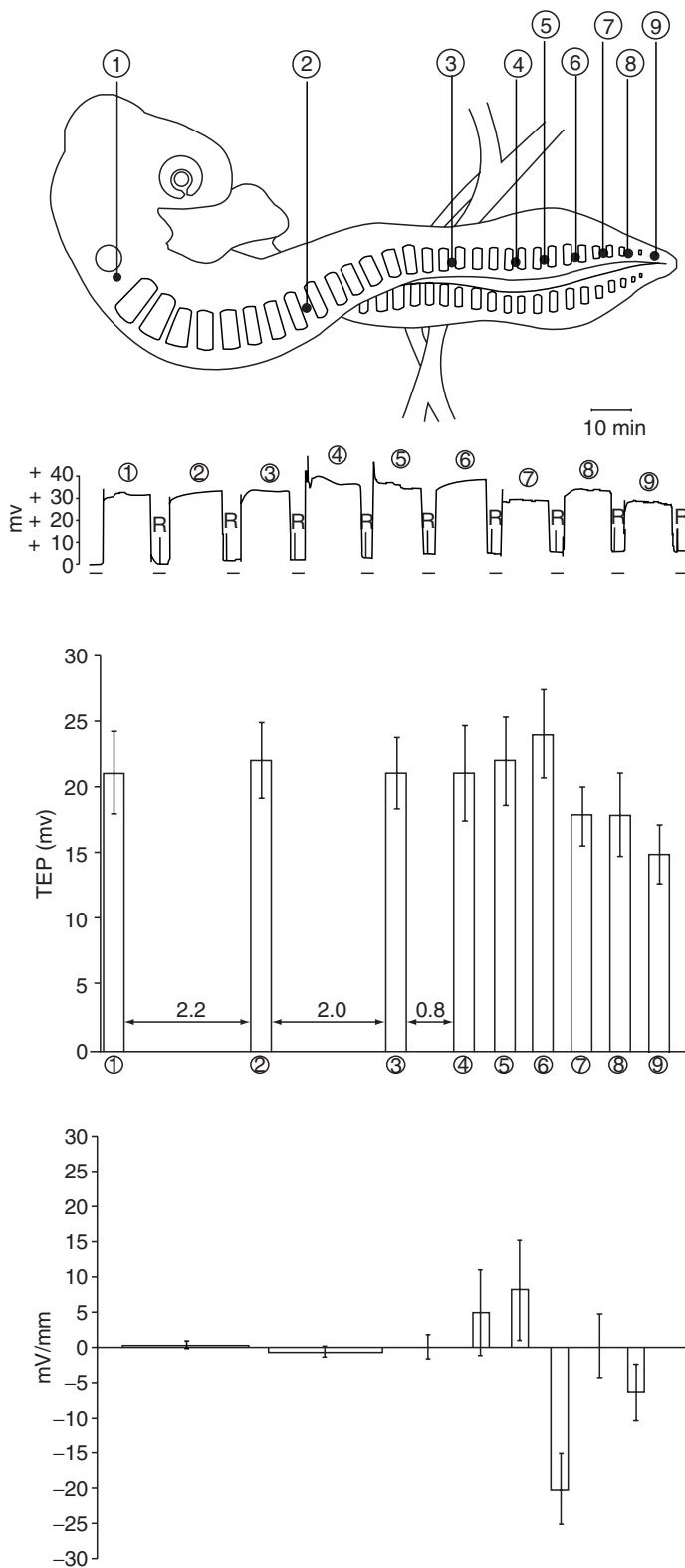


FIGURE 2.3

Stage 17 chick embryo TEP measured in nine rostral-caudal positions. Numbered measurement positions are shown in the drawing in the upper part of the figure. Below the drawing is a chart recording, tracing, and showing the TEP at the different measurement positions. At each numbered peak (corresponding to the positions shown in the drawing) the integument of the embryo was impaled and a stable positive potential was measured. Times at which the embryo was not impaled are indicated by a solid line below the recording. The upper bar chart shows the TEP at each position. The numbers below each bar correspond to the measurement positions indicated. The numbers between bars indicate the average distance (in mm) between each position. Where this is not indicated, the average distance is 0.3 mm. The lower chart shows the average voltage gradient between each consecutive position. Error bars indicate the standard error of the mean, $N = 6$. A steep voltage gradient was found between positions 6 and 7. (From Hotary, K.B. and Robinson, K.R. (1991). *Dev. Biol.* 140, 149. With permission.)

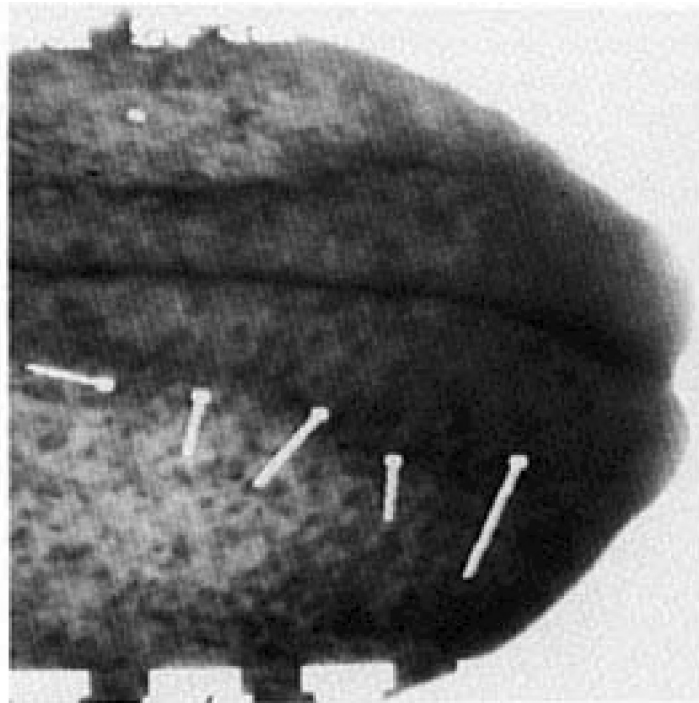


FIGURE 2.4

Neural fold currents in a stage 18 axolotl embryo measured with a two-dimensional self-referencing probe. Current vectors are displayed as a line originating at a dot that marks the measurement position. The direction of current flow from the dot is denoted by the line direction, and its length is proportional to the current density. Note the outwardly directed currents at the edge of the cranial neural folds. (From Metcalf, M.E.M., Shi, R.Y., and Borgens, R.B. (1994). *J. Exp. Zool.* 268, 307–322. With permission.)

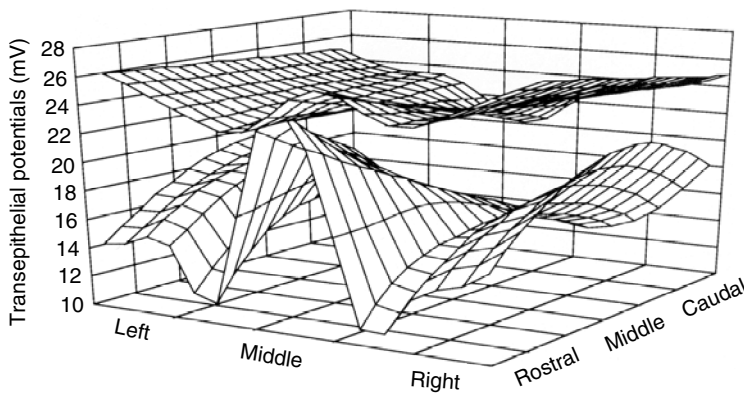


FIGURE 2.5

Summary of three-dimensional plot of TEPs at stage 15/16 (bottom) and stage 18/19 (top) axolotl embryos. The overall increase in the magnitude of TEPs at stage 18/19 is real, permitting these two views to be presented adjacent to each other. Note that only a hint of the characteristic voltage gradients beneath the ectoderm is evident at stage 18/19, and the potentials are not statistically different from one another. The embryo is essentially isopotential within the extracellular domain of the neural plate near the climax of neurulation. (Reproduced from Shi R.L and Borgens R.B. (1995) *Dev. Dyn.* 202, 101–114, 1995. With permission.)

2.2.3 Fields Associated with the Neural Tube

The neural tube forms during development as a folding over of neural plate epithelium, inverting the normal polarity of this layer. The apical end of the neural plate becomes the inside of the tube so that transport of Na^+ occurs from the inside to the outside of the tube and the trans-tube potential is inside negative. This potential has been measured in both frog and axolotl to be as large as -90 mV (Hotary and Robinson, 1991; Shi and Borgens, 1994). Neuroblasts within the wall of the tube are therefore exposed to very large electric fields, since the wall is only about $50\text{ }\mu\text{m}$ thick and the 90 mV across this distance generates a field of roughly 1800 mV/mm . There is little doubt that such a large field will influence the migration and sprouting of these neuroblasts.

2.2.4 Fields Associated with Epithelial Wounds

As noted above, the earliest measurements of the electrical phenomena associated with wounds did not measure the electric field itself but rather the current flowing out of the wound. More modern techniques have also been used to study this wound current. The leakage current that is driven out of epithelia in low-resistance regions has been measured using the vibrating probe technique (Jaffe and Nuccitelli, 1974) in several systems. One of the earliest such measurements was a current as large as $100\text{ }\mu\text{A/cm}^2$ leaving the stumps of regenerating newt limbs (Borgens et al., 1977). Similar measurements have also been made on fingertip amputation currents in humans (Illingworth and Barker, 1980), where up to $30\text{ }\mu\text{A/cm}^2$ was detected leaving the accidentally amputated stump for about 3 wk. These currents will certainly generate electric fields just beneath the epidermis that will be proportional to the resistivity encountered in the tissue. The range of human tissue resistivity spans $200\text{--}1000\text{ }\Omega\text{ cm}$ (Faes et al., 1999), so these currents would be expected to generate an electric field within the tissue of about $10\text{--}100\text{ mV/mm}$.

However, since this tissue resistivity can vary substantially as a function of cell density and tissue anatomy, it is always more reliable to measure these fields directly in the tissue rather than estimating them based on the transembryonic current density. This has been accomplished in four different wound types in skin and cornea. The classic approach to these measurements is to use KCl-filled glass microelectrodes to penetrate the outer epithelium and measure the voltage just beneath it in several positions along a line leading away from the wound. However, for skin measurements, another approach is more common. This method is to measure the potential gradient just beneath the stratum corneum on the surface of the epidermis, either with surface electrodes or by other means. The field generated by the current flowing between the upper surface of the epidermis and the stratum corneum is often larger than that generated below the epidermis because of the higher resistivity of that upper region. The range of field strengths measured in the four cases in the literature is surprisingly small, between 40 and 200 mV/mm ([Table 2.1](#)). The field direction is a function of position. Beneath and within the epidermis the field polarity has the negative pole at the wound center, and above the epidermis the wound current is flowing in the opposite direction so that the positive pole is at the wound ([Figure 2.6](#)).

These wound fields have some useful properties for signaling. First, they appear immediately upon wounding since the TEP is continuously present to drive current out of any low-resistance region as soon as it is formed. Second, the lateral electric field illustrated in Figure 2.6, that is generated by the wound current, will persist until the resistance increases as the wound heals. Thus, we have a signal that is immediate and persistent. These are ideal properties for a physiological signal to stimulate wound healing. If the epithelial cells forming the epidermis were able to detect such electric

TABLE 2.1

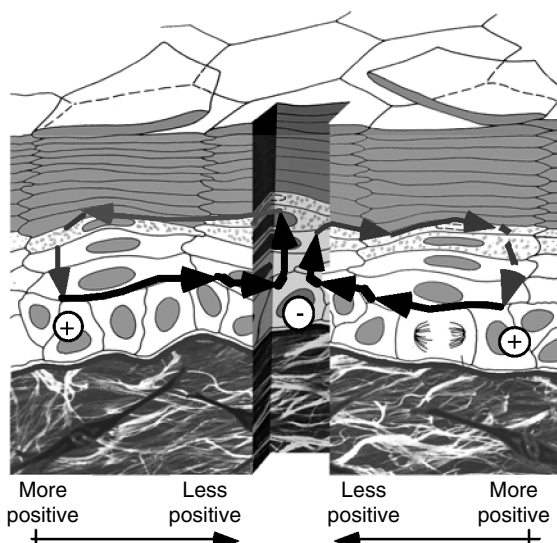
Endogenous Electric Fields Measured near Wounds

Species	Tissue	Wound Type	E Field (mV/mm)	Reference
Bovine	Cornea	Cut	42	Chiang et al., 1992; Sta Iglesia and Vanable, 1998
<i>Notophthalmus viridescens</i>	Digit	Digit tip amputation	40	McGinnis and Vanable, 1986; Chiang et al., 1989; Iglesia et al., 1996
<i>N. viridescens</i>	Limb stump	Amputation	7–50	McGinnis and Vanable, 1986
Guinea pig	Skin	Small cut	100–200	Barker et al., 1982

fields, they would be able to initiate wound healing immediately upon wounding. This is in fact the case, as discussed in the next section.

Measurements of endogenous electric fields near epithelial wounds have been made in three different systems. The first was a skin wound in the guinea pig (Barker et al., 1982). The transepidermal potential was measured in several locations lateral to a skin wound (Figure 2.7). At the wound itself, there is no epidermis, so the transcutaneous potential is zero, whereas about 1 mm away, the transcutaneous potential exhibited the normal value of 50–70 mV. The steepest voltage gradient was found immediately adjacent to the wound edge where values as high as 150 mV/mm were measured. The second direct measurement of the electric field near a wound was made in two regions of the newt limb. The electric field adjacent to an amputated digit was measured with microelectrodes and found to be about 40 mV/mm (McGinnis and Vanable, 1986; Chiang et al., 1989; Iglesia et al., 1996). This is very similar to the field near an amputated limb of the newt of 7–50 mV/mm (McGinnis and Vanable, 1986). The third direct measurement was made on the bovine cornea, and the magnitude of the electric field was 42 mV/mm (Chiang et al., 1992; Sta Iglesia and Vanable, 1998).

The fields in the cornea and the newt digit have been found to play a role in wound healing. When the field strength associated with the wound is modified, the rate of wound healing changes. The newt's wound healing rate can be optimized under normal

**FIGURE 2.6**

Generation of skin wound electric fields. Unbroken skin maintains a “skin battery” or TEP, generated by the apical influx of Na^+ and basolateral efflux of K^+ . When there is a wound, the potential drives current flow through the newly formed low-resistance pathway, generating an electric field whose negative vector points toward the wound center at the lower portion of the epidermis and away from the wound on the upper portion below the stratum corneum.

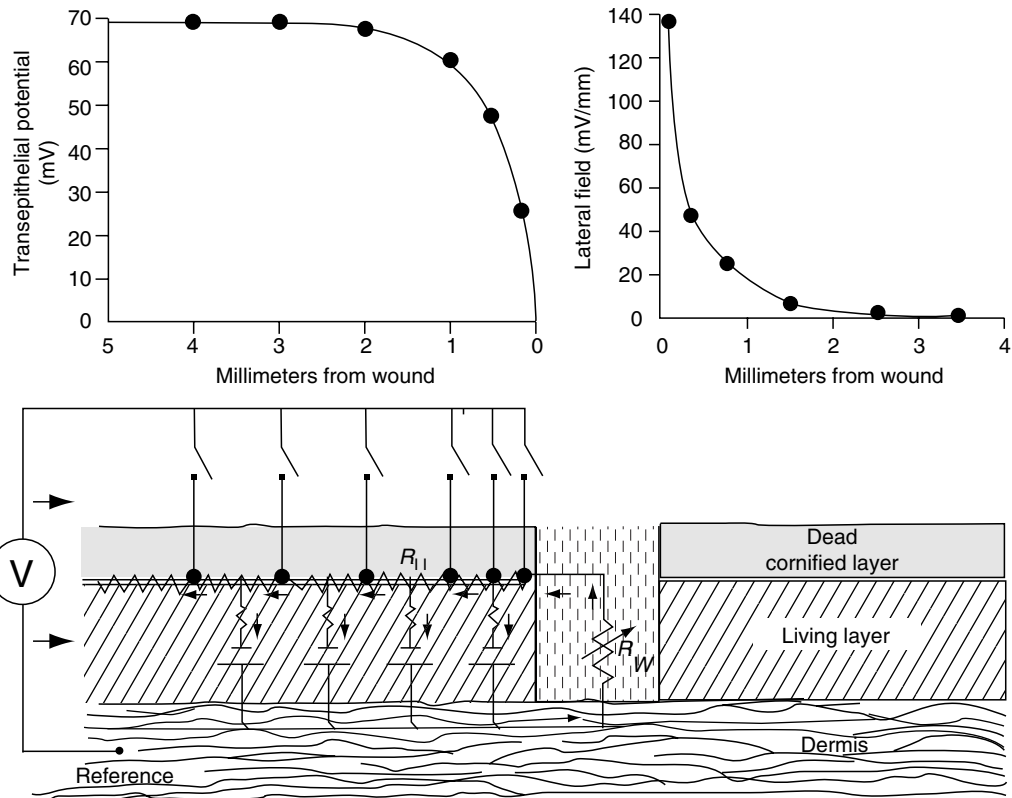


FIGURE 2.7

The electric field near a skin wound in a guinea pig. Bottom: diagram of the method used. A metal probe penetrated the stratum corneum to contact the epidermis at various distances from the wound site, and the surface voltage at each location was recorded with respect to the potential within the dermis. This voltage is the TEP and is plotted in the upper left of the figure. The voltage at the wound must be zero because the epidermal layer has been broken there, and far from that region, the TEP is 70 mV. The electric field at a given location is given by the voltage difference between sampling sites divided by the distance between those sites and is plotted on the upper right of the figure.

conditions but cannot be speeded up, removing the endogenous field does slow down the rate of wound healing by about 25%. However, the rate of bovine corneal wound healing can be enhanced by increasing the electric field strength. Epithelization was fastest in wounds with the field strength raised to 80 mV/mm, more than twice the normal field strength present in wounds maintained in Hanks' solution alone. Epithelization decreased, however, when the field strength was increased to 120 mV/mm. A similar pattern was also observed when the field's polarity was reversed. Decreasing the field strength by submersion of the lesions or by treating the lesions with the Na^+ channel blocker, benzamil, significantly retarded healing. In addition, an increase in the field strength of lesions treated with Na^+ -depleted Hanks' solution, by the addition of DC, increased the rate of epithelization. These observations suggest that the endogenous electric field plays a role in the normal wound healing process.

More recent studies of rat cornea have reported a similar correlation between the wound healing rate and the electric field strength. The mammalian cornea exhibits an internally positive TEP of 30–40 mV. Na^+ and K^+ are transported out of the tear fluid and into the epithelium while Cl^- is transported in the opposite direction. A wound in this

epithelium exhibits the same current pattern as skin (Figure 2.6), and a laterally oriented electric field is generated by this wound current with the cathode at the wound site. Recent work from McCaig, Zhao, and colleagues has indicated a strong correlation between the rate of wound healing in the rat cornea and the electric field strength lateral to the wound (Zhao et al., 1996; Song et al., 2004). They have used drugs to either increase the trans-corneal potential or decrease it. Drugs that increased this voltage difference also increased the rate of wound healing, while drugs that reduced this voltage difference also slowed down the rate of wound healing. In addition, when current was injected to restore and amplify the endogenous electric field in bovine cornea, the wound healing rate increased (Sta Iglesia and Venable, 1998). These data provide very strong support for the hypothesis that these electric fields near corneal wounds play an important role in influencing the healing of these wounds.

2.3 Measurements of Endogenous Intracellular Electric Fields

2.3.1 Nurse Cell Complex in Insects

In the silk moth oocyte-nurse cell complex or the ovarian follicle, the oocyte cytoplasm is about 10 mV more positive than that of the nurse cell cytoplasm despite their connection by a broad cytoplasmic bridge. Woodruff and Telfer have published several studies of this system in which they show that the polarized transport of fluorescently labeled proteins between nurse cells and oocyte depends on the charge of these proteins in a manner consistent with intercellular electrophoresis driven by the voltage gradient across the cytoplasmic bridge of the silk moth and other insects (Jaffe and Woodruff, 1979; Woodruff and Telfer, 1980; Woodruff and Cole, 1997; Cole and Woodruff, 2000). Since these nurse cell complexes arise from incomplete cell division they must be considered electrically as a single cell that is generating a significant voltage gradient across a small region.

2.3.2 Development of Left-Right Polarity in Chick and Frog

The most recent study of the role of electric fields in development utilized both frog and chick embryos. The generation of left-right asymmetry in these systems was found to depend on both functioning gap junctions and voltage difference between blastomeres in very early stages of development (Levin and Mercola, 1998, 1999; Levin et al., 2002). This work started with a pharmacological screen to identify drugs that interfered with the development of left-right patterning. The most effective drugs were the ones that interfered with K⁺ and H⁺ ion fluxes. Lansoprazole and chromanol 293B were the most effective and these block the H⁺ pump and a specific K⁺ channel (KvLQT-1), respectively. Next most effective was SCH28080 and omeprazole, which block the H⁺/K⁺-ATPase, followed by BaCl₂, which blocks all K⁺ channels.

They further tested the hypothesis that these ion fluxes were important for left-right patterning by injecting mRNA for either the alpha or beta subunits of the H⁺/K⁺-ATPase or the K⁺ channel into the frog egg. They found that heterotaxia was induced when either was injected but by far the largest increase, 37%, occurred when all three mRNAs were injected. This suggests that overexpression of these molecules, which can influence or perturb ion concentration gradients of K⁺ or H⁺, disrupted the normal left-right patterning of the embryo.

In order to learn more about the mechanism through which H^+/K^+ -ATPase influenced patterning, they used *in situ* hybridization to show an asymmetrical distribution of the K^+/H^+ -ATPase. It was concentrated in the right ventral blastomere of the 4-cell stage frog embryo. the addition of Both K^+ channels and K^+/H^+ -ATPase should hyperpolarize cells making them more negative than their neighbors. This voltage difference between the blastomeres of the 4-cell stage embryo could be used to segregate low molecular weight determinants through gap junctions to achieve asymmetric gene expression. They further tested this hypothesis by measuring the membrane potential of cells near the primitive streak during early chick development. They used an anionic fluorescent dye, DiBAC₄, whose distribution depended on membrane potential to show that the early chick embryo exhibited a voltage gradient across the primitive streak. The left side of the primitive streak was 10–20 mV more positive than right side and this difference was inhibited by the K^+ channel blocker, BaCl₂, and the H^+/K^+ -ATPase inhibitor, omeprazole. Since these drugs also partially inhibited the development of left-right patterning, the membrane potential difference appears to play a role in this aspect of development. This paper is the first to demonstrate a role for membrane potential differences between blastomeres in early vertebrate pattern formation.

2.4 Methods for Modifying Endogenous Electric Fields

Modifying endogenous fields within embryos or cells is really quite challenging. The only way to generate a relatively steady field in a conducting medium is to pass current through it. However, the outer membranes or epithelia surrounding the targets here make this very hard to accomplish. These structures have high resistance to current flow so that slowly varying fields placed outside the cell or embryo will not effectively penetrate to the inside but will mainly generate current flow around the outside of the cells or embryos. Because of this there have been precious few attempts to modify endogenous fields, but I will discuss some of them.

The only exception to this field penetration problem is the application of ultrashort pulses in the nanosecond domain that have risen times faster than the charging time of biological membranes (Schoenbach et al., 2004). These pulses penetrate beyond the plasma membrane into the interior of cells and tissues but are present only for very short times. It is conceivable that by combining millions of these short pulses per second, one could significantly modify the DC electric field within cells and tissues. This remains to be explored.

2.4.1 Passing Current between Electrodes

If two electrodes can be placed within a single cell or in different regions of an embryo, current can be passed between them and a well-defined electric field can be generated. However, this requires penetrating the outer membrane or epithelium and may damage this outer layer. The longer the field is applied, the more likely that some damage will occur due to vibrations or embryo movement. This approach has been used with some success in the regenerating tip of newt limbs (Chiang et al., 1991; Iglesia et al., 1996), where current was passed along the limb by inserting one electrode into a slit made at the knee and the current delivery electrode was placed distal to the wounded digit tip. The electric field at the newt limb could be manipulated in this way, and elimination of this field significantly slowed down the rate of wound healing.

2.4.2 Low-Resistance Shunts

One way to perturb the natural transembryonic current pattern is to place a low-resistance pathway or shunt into a resistive membrane or epithelium. The endogenous fields will drive current out through this shunt, and this new current flow will definitely perturb the endogenous field within the tissue. This technique was used with striking results by Robinson's group in the chick embryo as described above (Hotary and Robinson, 1994).

2.4.3 Placing Tissues in an External Electric Field

While DC electric fields cannot penetrate into the conducting cytoplasm of a cell or tissue, they have been found to perturb normal development at certain stages in amphibians (Metcalf and Borgens, 1994). In addition, there is a very extensive old literature in which the polarity of both development and regeneration could be strongly influenced by imposed DC electric fields (Jaffe and Nuccitelli, 1977; Levin, 2003). One interpretation of these observations is that the imposed field has its effective target along the exterior of the embryo via lateral electrophoresis of membrane glycoproteins.

The only external electric field that can penetrate into the interior of cells is the one that rises faster than the charges within the cell can redistribute (Schoenbach et al., 2004). Such a pulsed field could certainly modify internal electric fields for the extremely short duration of the pulse. Perhaps by using either a large field strength or multiple pulses, such brief pulsed fields might have a significant effect on endogenous fields. This relatively new area deserves future investigation.

2.5 Summary

All plasma membranes and epithelia generate voltage differences across themselves. These batteries are the power sources that drive ionic currents through cells, tissues, and organisms. These currents will generate internal electric fields as they traverse tissue, and such fields can do work through electrophoresis of charged molecules within and between cells as well as in the plane of the plasma membrane. Cases in which such fields have been measured include the following:

1. Two- to 4-day-old chick embryos generate a 20-mV/mm field near the posterior intestinal portal that is important for normal development of posterior structures.
2. Stage 14–21 amphibian embryos generate similar internal electric fields, and modifying these fields during neurulation but not gastrulation results in developmental abnormalities.
3. Neural tubes in amphibians generate an internally negative voltage difference of as much as 90 mV across the wall of the tube, and cells in this region are exposed to fields as large as 1800 mV/mm.
4. Mammalian skin wounds generate 150-mV/mm fields just below the stratum corneum, and corneal epidermal wounds exhibit fields of 40 mV/mm lateral to wounds.
5. The development of left-right asymmetry in frog and chick embryos utilizes an electric field between blastomeres that is generated by an asymmetrical distribution of the K^+/H^+ -ATPase among the blastomeres.

In nearly all of these well-documented examples, the electric field plays a critical role in either the development of the organism or the wound healing and regeneration of adult structures. Because of this, imposed electric fields may be utilized to perturb or influence normal development. One intriguing possible perturbation is the use of imposed electric fields to enhance the rate of wound healing, particularly in cases where the normal healing process is slower than normal, as observed in chronic wounds.

References

- Altizer, A.M., Moriarty, L.J., Bell, S.M., Schreiner, C.M., Scott, W.J., and Borgens, R.B. (2001). Endogenous electric current is associated with normal development of the vertebrate limb. *Dev. Dyn.* 221, 391–401.
- Barker, A.T., Jaffe, L.F., and Vanable, J.W., Jr. (1982). The glabrous epidermis of cavies contains a powerful battery. *Am. J. Physiol.* 242, R358–R366.
- Borgens, R.B., Vanable, J.W., Jr., and Jaffe, L.F. (1977). Bioelectricity and regeneration: large currents leave the stumps of regenerating newt limbs. *Proc. Natl. Acad. Sci. USA* 74, 4528–4532.
- Borgens, R.B., Vanable, J.W., Jr., and Jaffe, L.F. (1979). Small artificial currents enhance *Xenopus* limb regeneration. *J. Exp. Zool.* 207, 217–226.
- Borgens, R.B., Rouleau, M.F., and DeLaney, L.E. (1983). A steady efflux of ionic current predicts hind limb development. *J. Exp. Zool.* 228, 491–503.
- Chiang, M., Cragoe, E.J., Jr., and Vanable, J.W., Jr. (1989). Electrical fields in the vicinity of small wounds in *Notophthalmus viridescens* skin. *Biol. Bull.* 176(S), 179–183.
- Chiang, M., Cragoe, E.J., Jr., and Vanable, J.W., Jr. (1991). Intrinsic electric fields promote epithelialization of wounds in the newt, *Notophthalmus viridescens*. *Dev. Biol.* 146, 377–385.
- Chiang, M., Robinson, K.R., and Vanable, J.W., Jr. (1992). Electrical fields in the vicinity of epithelial wounds in the isolated bovine eye. *Exp. Eye Res.* 54, 999–1003.
- Clausen, T., Van, H.C., and Everts, M.E. (1991). Significance of cation transport in control of energy metabolism and thermogenesis. *Physiol Rev.* 71, 733–774.
- Cole, R.W. and Woodruff, R.I. (2000). Vitellogenesis ovarian follicles of *Drosophila* exhibit a charge-dependent distribution of endogenous soluble proteins. *J. Insect Physiol.* 46, 1239–1248.
- DuBois-Reymond, E. (1843). Vorlaufiger abrifs einer untersuchung über den sogenannten froschstrom und die electromotorischen fische. *Ann. Phys. U. Chem.* 58, 1.
- Faes, T.J., van der Meij, H.A., de Munck, J.C., and Heethaar, R.M. (1999). The electric resistivity of human tissues (100 Hz–10 MHz): a meta-analysis of review studies. *Physiol. Meas.* 20, R1–R10.
- Hotary, K.B. and Robinson, K.R. (1990). Endogenous electrical currents and the resultant voltage gradients in the chick embryo. *Dev. Biol.* 140, 149–160.
- Hotary, K.B. and Robinson, K.R. (1991). The neural tube of the *Xenopus* embryo maintains a potential difference across itself. *Dev. Brain Res.* 59, 65–73.
- Hotary, K.B. and Robinson, K.R. (1992). Evidence of a role for endogenous electrical fields in chick embryo development. *Development* 114, 985–996.
- Hotary, K.B. and Robinson, K.R. (1994). Endogenous electrical currents and voltage gradients in *Xenopus* embryos and the consequences of their disruption. *Dev. Biol.* 166, 789–800.
- Iglesia, D.D.S., Cragoe, E.J., Jr., and Vanable, J.W., Jr. (1996). Electric field strength and epithelialization in the newt (*Notophthalmus viridescens*). *J. Exp. Zool.* 274, 56–62.
- Illingworth, C.M. and Barker, A.T. (1980). Measurement of electrical currents emerging during the regeneration of amputated fingertips in children. *Clin. Phys. Physiol. Meas.* 1, 87–89.
- Jaffe, L.F. and Nuccitelli, R. (1974). An ultrasensitive vibrating probe for measuring extracellular currents. *J. Cell Biol.* 63, 614–628.
- Jaffe, L.F. and Nuccitelli, R. (1977). Electrical controls of development. *Annu. Rev. Biophys. Bioeng.* 6, 445–475.

- Jaffe, L.F. and Stern, C.D. (1979). Strong electrical currents leave the primitive streak of chick embryos. *Science* 206, 569–571.
- Jaffe, L.F. and Woodruff, R.I. (1979). Large electrical currents traverse developing Cecropia follicles. *Proc. Natl. Acad. Sci. USA* 76, 1328–1332.
- Levin, M. (2003). Bioelectromagnetics in morphogenesis. *Bioelectromagnetics* 24, 295–315.
- Levin, M. and Mercola, M. (1998). Gap junctions are involved in the early generation of left-right asymmetry. *Dev. Biol.* 203, 90–105.
- Levin, M. and Mercola, M. (1999). Gap junction-mediated transfer of left-right patterning signals in the early chick blastoderm is upstream of Shh asymmetry in the node. *Development* 126, 4703–4714.
- Levin, M., Thorlin, T., Robinson, K.R., Nogi, T., and Mercola, M. (2002). Asymmetries in H⁺/K⁺-ATPase and cell membrane potentials comprise a very early step in left-right patterning. *Cell* 111, 77–89.
- Loew, L.M. (1992). Voltage-sensitive dyes: measurement of membrane potentials induced by DC and AC electric fields. *Bioelectromagnetics* 13(Suppl. 1), 179–189.
- Loew, L.M., Campagnola, P., Lewis, A., and Wuskell, J.P. (2002). Confocal and nonlinear optical imaging of potentiometric dyes. *Methods Cell Biol.* 70, 429–452.
- McCaig, C.D., Rajnicek, A.M., Song, B., and Zhao, M. (2005). Controlling cell behavior electrically: current views and future potential. *Physiol. Rev.* 85, 943–978.
- McGinnis, M.E. and Vanable, J.W., Jr. (1986). Electrical fields in *Notophthalmus viridescens* limb stumps. *Dev. Biol.* 116, 184–193.
- Metcalf, M.E.M. and Borgens, R.B. (1994). Weak applied voltages interfere with amphibian morphogenesis and pattern. *J. Exp. Zool.* 268, 323–338.
- Metcalf, M.E.M., Shi, R.Y., and Borgens, R.B. (1994). Endogenous ionic currents and voltages in amphibian embryos. *J. Exp. Zool.* 268, 307–322.
- Nuccitelli, R. (1988). Ionic currents in morphogenesis. *Experientia* 44, 657–666.
- Nuccitelli, R. (1990). The vibrating probe technique for studies of ion transport. In *Noninvasive Techniques in Cell Biology*, J.K. Foskett and S. Grinstein, eds. New York: Wiley-Liss, pp. 273–310.
- Robinson, K.R. (1983). Endogenous electrical current leaves the limb and prelimb region of the *Xenopus* embryo. *Dev. Biol.* 97, 203–211.
- Schoenbach, K.H., Joshi, R.P., Kolb, J.F., Chen, N., Stacey, M., Buescher, E.S., Beebe, S.J., and Blackmon, P. (2004). Ultrashort electrical pulses open a new gateway into biological cells. *Proc. IEEE* 92, 1122–1137.
- Shi, R. and Borgens, R.B. (1994). Embryonic neuroepithelial sodium transport, the resulting physiological potential, and cranial development. *Dev. Biol.* 165, 105–116.
- Shi, R. and Borgens, R.B. (1995). Three-dimensional gradients of voltage during development of the nervous system as invisible coordinates for the establishment of embryonic pattern. *Dev. Dyn.* 202, 101–114.
- Song, B., Zhao, M., Forrester, J., and McCaig, C. (2004). Nerve regeneration and wound healing are stimulated and directed by an endogenous electrical field *in vivo*. *J. Cell Sci.* 117, 4681–4690.
- Sta Iglesia, D.D. and Vanable, J.W., Jr. (1998). Endogenous lateral electric fields around bovine corneal lesions are necessary for and can enhance normal rates of wound healing. *Wound Repair Regen.* 6, 531–542.
- Venable, J.W., Jr. (1991). A history of bioelectricity in development and regeneration. In *A History of Regeneration Research*, C.E. Dinsmore, ed. Cambridge: Cambridge University Press, pp. 151–177.
- Wallis, D.I. (1993). *Electrophysiology: A Practical Approach*. Dublin: IRL Press.
- Winkel, G.K. and Nuccitelli, R. (1989). Large ionic currents leave the primitive streak of the 7.5-day mouse embryo. *Biol. Bull.* 176, 110–117.
- Woodruff, R.I. and Cole, R.W. (1997). Charge dependent distribution of endogenous proteins within vitellogenetic ovarian follicles of *Actias luna*. *J. Insect Physiol.* 43, 275–287.
- Woodruff, R.I. and Telfer, W.H. (1980). Electrophoresis of proteins in intercellular bridges. *Nature* 286, 84–86.
- Zhao, M., Agius-Fernandez, A., Forrester, J.V., and McCaig, C.D. (1996). Directed migration of corneal epithelial sheets in physiological electric fields. *Invest. Ophthalmol. Vis. Sci.* 37, 2548–2558.

3

Dielectric Properties of Biological Materials

Camelia Gabriel

CONTENTS

3.1	Introduction	52
3.2	Dielectric Properties—Molecular Origin	53
3.2.1	Quasi-Static Response.....	53
3.2.2	Permittivity of Low-Pressure Gases	54
3.2.3	Permittivity of Liquids and Dense Gases.....	55
3.3	Time and Frequency Dependence of the Dielectric Response	56
3.3.1	Time-Dependent Polarization—Impulse Response—Kramers–Krönig Relations	56
3.3.2	Permittivity of a Polar Substance—The Debye Equation	57
3.3.3	Nonpolar Molecules.....	60
3.4	Observed Responses of Real Systems—Conduction—Multiple Relaxations—The Universal Law	60
3.4.1	Conduction	60
3.4.2	Multiple Relaxation Models—Distribution of Relaxation Times—Fractional Power Law Behavior	61
3.4.3	Universal Law of Dielectric Relaxation	66
3.4.4	Combined Response Model.....	67
3.5	Dielectric Properties of Biological Materials—Main Components	67
3.5.1	Water	68
3.5.2	Carbohydrates	70
3.5.3	Proteins and Other Macromolecules	70
3.5.4	Electrolytes.....	71
3.5.5	Dielectric Dispersions in Tissue	72
3.5.5.1	α Dispersion	73
3.5.5.2	β Dispersion	73
3.5.5.3	γ Dispersion	73
3.5.5.4	δ Dispersion	74
3.5.6	Effective Complex Permittivity of a Heterogenous System	75
3.6	Dielectric Relaxation Mechanisms in Heterogenous Media	77
3.6.1	Interfacial Polarization.....	77
3.6.1.1	Interface between Two Media.....	78
3.6.1.2	Suspension of Spheroids	79
3.6.2	Counterion Polarization Effects	81

3.7 Dielectric Properties of Tissue—State-of-Knowledge.....	82
3.7.1 1996 Database.....	82
3.7.2 Literature After 1996—A Brief Review.....	85
3.7.2.1 Brain Tissue: Gray and White Matter.....	85
3.7.2.2 Liver.....	87
3.7.2.3 Muscle	88
3.7.2.4 Skin	89
3.7.2.5 Bone.....	92
3.7.2.6 Dielectric Properties of Cancerous Tissue	92
3.7.2.7 Conductivity of Tissue at Low-Frequency.....	93
3.7.2.8 Nonlinear Dielectric Properties.....	94
References	94

3.1 Introduction

At some level of organization, all matter consists of charged entities held together by various atomic, molecular, and intermolecular forces. The effect of an externally applied electric field on the charge distribution is specific to the material; the dielectric properties are a measure of that effect; they are intrinsic properties of matter used to characterize nonmetallic materials. Biological matter has free and bound charges; an applied electric field will cause them to drift and displace, thus inducing conduction and polarization currents. Dielectric spectroscopy is the science that relates the dielectric properties to the underlying microscopic mechanisms of polarization and conduction. These dielectric phenomena are determined by and are informative about the structure and composition of the material. Consequently, knowledge of the dielectric properties is of practical importance in all fields of science where electromagnetic fields impinge or are used to probe or process matter. It is equally important in biomedical fields such as electrophysiology, where endogenous bioelectric sources provide signals that are sensed through various body tissues and are affected by their dielectric properties.

The past decade has seen a dramatic increase in the exposure of people to electromagnetic fields from wireless telecommunication devices and infrastructure. This situation sparked large research programs on the assessment and quantification of exposure of people and on the biological effects resulting from the exposure. Information on the dielectric properties of tissues is vital to these studies, for the computation of exposure metrics and the provision of a mechanistic explanation for biological effects. To satisfy the need of current research activity, this chapter will review the dielectric data for body tissue and the underlying mechanisms of interaction at the cellular, subcellular, and molecular levels. In doing so, we will draw on the authoritative article by Foster and Schwan (1996), published in the second edition of this book, which goes a long way toward establishing dielectric spectroscopy as a powerful tool for mechanistic studies.

Another area of scientific activity in the last decade revolved around the formulation of standard procedures for the experimental assessment of human exposure from electromagnetic sources, mostly telecommunication radio transceivers and their accessories. This created the need to formulate and measure the dielectric properties of tissue equivalent material and made dielectric measurement and the assessment of the associated uncertainty part of the compliance testing procedure. This chapter will deal with the fundamental issues that need to be established if dielectric measurement is to become a routine but accurate laboratory procedure.

It is not possible to review the dielectric properties and the polarization mechanisms in biological material without singling out the contribution to this field of Herman P. Schwan, whose name is associated with all the major findings over the past 50 years (Foster, 2002). Indeed, his 1957 review of the bulk electrical properties of cells and cell suspensions is one of the earliest and most studied texts on the subject. There are other reviews by Pethig (1979), Stuchly (1979), Schwan and Foster (1980), Pethig and Kell (1987), and Foster and Schwan (1989). The fundamental aspects and a more extensive treatment of the theoretical aspects of this subject can be found in books by Cole (1972), Grant et al. (1978), Schanne and Ceretti (1978), Pethig (1979), and more recently, Craig (1995), Roussy and Pearce (1995), and Grimnes and Martinsen (2000).

For most biological materials, the magnetic permeability is close to that of free space (i.e., diamagnetic), which implies that there is no direct interaction with the magnetic component of electromagnetic fields at low field strengths. However, this position is now changing following relatively recent reports of the presence of magnetite in human nervous tissue (see, e.g., Dobson and Grassi, 1996), which suggest that magnetite may provide a mechanism for direct interaction of external magnetic fields with the human central nervous system. The role of these strongly magnetic materials in organisms is only just beginning to be unraveled. This subject is elaborated in the second part of next chapter.

3.2 Dielectric Properties—Molecular Origin

From a historical perspective, the dielectric properties of materials were first observed experimentally by Faraday in the 1830s as a change in the capacity of an empty capacitor when a material is introduced inside it. Faraday introduced the term *specific inductive capacity* to describe the ratio of the capacities of the filled and empty capacitor. This quantity is now known as the permittivity and is denoted by ϵ . It is a fundamental property of nonmetallic or dielectric materials. Under quasistatic conditions, the capacitance C_0 of a perfect capacitor of area A and plate separation d changes to $C > C_0$:

$$C = \epsilon\epsilon_0 = \epsilon \frac{\epsilon_0 A}{d} \quad (3.1)$$

where ϵ is the relative permittivity of the material (dimensionless), ϵ_0 is the permittivity of free space (8.8542×10^{-12} F/m), and the product $\epsilon\epsilon_0$ is the absolute permittivity. The increase in capacity is due to the additional charge density induced by the field in the material. The field is said to have polarized the medium; polarizability or the ability of the material to polarize is the main determinant of its dielectric properties.

This section will start with the fundamental concepts of the interaction of homogenous matter with static fields and proceed, in steps, to heterogenous mixtures and their dynamic response to time-varying fields leading to the dielectric properties of tissues.

3.2.1 Quasi-Static Response

Considering the simple case of a monomolecular material, three main interaction mechanisms are possible: electronic, atomic, and molecular polarization. Electronic polarization is the shift of electrons, in the direction of the field, from their equilibrium position with respect to the positive nuclei. Atomic polarization is the relative displacement of

atoms or atom groups relative to each other. The orientation of permanent or induced molecular dipoles, when present, is known as molecular polarization. The total polarizability α_T is the sum of the contribution of, in this case, all three processes, termed α_e , α_a , and α_d .

In view of the relative importance of molecular orientation processes in defining the total polarization ($\alpha_e + \alpha_a < \alpha_d$) and hence the dielectric properties, it is usual to differentiate between the polar and nonpolar materials when these properties are considered.

For ideal nonpolar materials, the relationship $\varepsilon = n^2$, where n is the optical refractive index, holds true. When a dielectric material becomes polarized by the application of an external electric field E , the dipole moment of the constituent molecules is given by

$$\bar{m} = \alpha_T \bar{E}_l \quad (3.2)$$

where E_l is the local field acting on the molecules. The dipole moment per unit volume of the material P increases the total displacement flux density D , defined from the relationship $D = \varepsilon_0 E$ in vacuum and $D = \varepsilon_0 \varepsilon E$ in a medium of relative permittivity ε . The latter expression may also be written as

$$D = \varepsilon_0 E + P \quad (3.3)$$

The dependence of P on E can take several forms, the simplest and most common being a scalar proportionality:

$$P = \varepsilon_0 \chi E \quad (3.4)$$

where $\chi = \varepsilon - 1$ is the relative dielectric susceptibility. This simple relationship is valid for a perfect isotropic dielectric, at low or moderate field intensities and at static or quasi-static field frequencies.

If the material contains N dipoles per unit volume, then

$$P = N \alpha_T E_l \quad (3.5)$$

and

$$\varepsilon - 1 = \frac{N \alpha_T}{\varepsilon_0} \frac{E_l}{E} \quad (3.6)$$

The molecular description of the permittivity requires that the relationship between the microscopic and the macroscopic field intensities be known. In most cases, there is no exact solution to this problem, only more or less good approximations that hold within the confines of the assumptions and simplifications made, as will be briefly illustrated for typical classes of materials.

3.2.2 Permittivity of Low-Pressure Gases

At low pressures the molecules are far apart from each other, and their interaction with each other may be assumed to be negligible in comparison with the macroscopic field intensity E . Under these conditions $E_l \approx E$ and

$$\varepsilon - 1 = \frac{N \alpha_T}{\varepsilon_0} \quad (3.7)$$

The relative permittivity of a nonpolar gas is very close to 1, typically of the order of 1.0001 at atmospheric pressure.

3.2.3 Permittivity of Liquids and Dense Gases

When the intermolecular interactions are such that $E_l \neq E$, the local field must be estimated. One approach is to consider a spherical region inside the dielectric that is large compared to the size of a molecule; the field inside it is estimated for nonpolar materials to be

$$E_l = \left(\frac{\varepsilon + 2}{3} \right) E \quad (3.8)$$

which yields

$$\frac{3(\varepsilon - 1)}{\varepsilon + 2} = \frac{N}{\varepsilon_0} \alpha_T \quad (3.9)$$

The above expression is known as the Claussius–Mossoti–Lorentz formulation. It is not always valid, such as when the density of the material corresponds to $N = 3 \varepsilon_0 / \alpha_T$. An alternative formulation, valid when the molecules are polarizable point dipoles of permanent moment μ , was provided by Onsager:

$$\frac{(\varepsilon - n^2)(2\varepsilon + n^2)}{\varepsilon(n^2 + 2)^2} = \frac{N\mu^2}{9kT\varepsilon_0} \quad (3.10)$$

where k is the Boltzman constant and T is the absolute temperature.

Debye separated out the contribution to the total polarization of the permanent dipole from those associated with electronic and atomic displacements and arrived at the following relationship

$$\frac{\varepsilon - 1}{\varepsilon + 2} = \frac{N}{3\varepsilon_0} (\alpha + \mu^2 / 3kT) \quad (3.11)$$

While Onsager and Debye used semistatistical techniques to estimate the local field, others like Kirkwood, and later Fröhlich, used statistical methods to obtain a rigorous expression of the permittivity after taking local interactions into consideration and obtained

$$\frac{(\varepsilon - 1)(2\varepsilon + 1)}{3\varepsilon} = \frac{N}{\varepsilon_0} (\alpha + g\mu^2 / 3kT) \quad (3.12)$$

This is Kirkwood's equation for permittivity in which g is known as the Kirkwood correlation parameter, introduced to account for the effect of local ordering in the material. Fröhlich's theory gives

$$\frac{(\varepsilon - n^2)(2\varepsilon + n^2)}{\varepsilon(n^2 + 2)^2} = \frac{Ng\mu^2}{9kT\varepsilon_0} \quad (3.13)$$

which, except for the correlation parameter g , is identical to Onsager's equation.

This brief outline of the dielectric theory gives an idea of the nature of the electric field interaction problems and of the various techniques used to partially solve them under static field conditions. The solutions hold for slow time-varying fields as long as there is a quasistatic state. References to the original work by Debye (1929), Kirkwood (1936), Onsager (1936), and Fröhlich (1955) are given in Böttcher and Bordewijk (1978) and other well-known texts (Hill et al., 1969; Jonscher, 1983).

3.3 Time and Frequency Dependence of the Dielectric Response

Much of the interest in the dielectric properties of biological materials is concerned with their response to time-varying electric fields. This can be explained by the same macroscopic variables used for the quasi-static state except for the introduction of a time dependence for the excitation and response. The general discussion will assume sinusoidal fields and linear and isotropic responses, nonsinusoidal fields and material anisotropy, and nonlinearity being special cases.

3.3.1 Time-Dependent Polarization—Impulse Response—Kramers–Krönig Relations

The following relationship holds irrespective of the polarization mechanism:

$$P(t) = D(t) - \varepsilon_0 E(t) \quad (3.14)$$

For an ideal dielectric material with no free charge, the polarization follows the pulse with a delay determined by the time constant of the polarization mechanism. Assuming a rate process, which is that the rate of polarization is proportional to the constantly decreasing number of unpolarized units, the simplest expression for the polarization is obtained from the solution of the first-order differential rate equation with constant coefficients and time constant τ , giving

$$P(t) = P(1 - e^{-t/\tau}) \quad (3.15)$$

The decay of polarization is also an exponential function

$$P(t) = e^{-t/\tau} \quad (3.16)$$

For a linear system, the response to a unit-step electric field is the impulse response $f(t)$ of the system. The response of the system to a time-dependent field can be obtained from summation in a convolution integral of the impulses corresponding to a sequence of elements making up the electric field. For a harmonic field and a causal, time-independent system, the Fourier transform exists and yields

$$P(\omega) = \varepsilon_0 \chi(\omega) E(\omega) \quad (3.17)$$

indicating that the dielectric susceptibility $\chi(\omega)$ is the Fourier transform of $f(t)$. In general, the susceptibility is a complex function reflecting the fact that it informs on the magnitude and phase of the polarization with respect to the polarizing field

$$\chi(\omega) = \chi' - j\chi'' \quad (3.18)$$

The real and imaginary parts of $\chi(\omega)$ can be obtained from the separate parts of the Fourier transform:

$$\begin{aligned}\chi'(\omega) &= \int_{-\infty}^{+\infty} f(t) \cos(\omega t) dt = \int_0^{+\infty} f(t) \cos(\omega t) dt \\ \chi''(\omega) &= \int_{-\infty}^{+\infty} f(t) \sin(\omega t) dt = \int_0^{+\infty} f(t) \sin(\omega t) dt\end{aligned}\quad (3.19)$$

The limit of integration can be changed from $-\infty$ to 0 since $f(t)$ is causal.

The impulse response $f(t)$ defines the dielectric response, and conversely, knowledge of the complex susceptibility allows the determination of the impulse response by carrying out the reverse transformation, which gives $f(t)$ in terms of either $\chi'(\omega)$ or $\chi''(\omega)$:

$$\begin{aligned}f(t) &= (2/\pi) \int_0^{+\infty} \chi'(\omega) \cos(\omega t) d\omega \\ f(t) &= (2/\pi) \int_0^{+\infty} \chi''(\omega) \sin(\omega t) d\omega\end{aligned}\quad (3.20)$$

Eliminating $f(t)$ from the above equations gives an expression of $\chi'(\omega)$ in terms of $\chi''(\omega)$ and vice versa. Thus, there is a relationship between the real and imaginary parts of the complex susceptibility of any material, such that knowledge of either enables the other to be calculated. The expressions of real and imaginary parts of the susceptibility or permittivity in terms of each other are known as the Kramers–Krönig relations and have been derived as

$$\begin{aligned}\chi'(\omega) &= \chi'(\infty) + \frac{2}{\pi} \int_0^{\infty} \frac{u\chi''(u) - \omega\chi''(\omega)}{u^2 - \omega^2} du \\ \chi''(\omega) &= \frac{2}{\pi} \int_0^{\infty} \frac{\chi'(u) - \chi'(\omega)}{u^2 - \omega^2} du\end{aligned}\quad (3.21)$$

where u is a variable of integration. Recalling the relationship between relative dielectric susceptibility and relative permittivity $\chi = \varepsilon - 1$, the permittivity is a complex function given by

$$\hat{\varepsilon}(\omega) = \varepsilon'(\omega) - j\varepsilon''(\omega) = (1 + \chi'(\omega) - j\chi''(\omega)) \quad (3.22)$$

Thus, the Kramers–Krönig relations relate ε' to the complete spectrum of ε'' and vice versa. A clear account of their derivation can be found in Jonscher (1983).

3.3.2 Permittivity of a Polar Substance—The Debye Equation

When a step field E is applied to a polar dielectric material, the electronic and atomic polarizations are established almost instantaneously compared to the time scale of the

molecular orientation; the total polarization reaches a steady state as a first-order process characterized by the time constant of the dipolar rotation. When the field is removed, the process is reversed; electronic and atomic polarizations subside first, followed by a relatively slow decay in dipolar polarization (Figure 3.1). The time constant τ depends on the physical process, in this case the rotational dynamics of the dipole determined by the size, shape, and intermolecular relations of the molecules. If P_∞ and P_0 are the instantaneous and steady-state polarization, respectively, then the total polarization for a first-order process characterized by a time constant τ is

$$P = P_\infty + (P_0 - P_\infty)(1 - e^{-t/\tau}) \quad (3.23)$$

In time-varying fields the permittivity is a complex function originating from the magnitude and phase shift of the polarization with respect to the polarizing field:

$$\hat{\epsilon} = \epsilon' - j\epsilon'' = \epsilon' - j\sigma/\omega\epsilon_0 \quad (3.24)$$

The real part ϵ' is a measure of the induced polarization per unit field and the imaginary part ϵ'' is the out-of-phase loss factor associated with it. The loss factor can also be represented by a conductivity term $\sigma = \omega\epsilon_0\epsilon''$ where ω is the angular frequency. The SI unit of conductivity is siemens per meter (S/m).

The frequency response of the first-order system is obtained from the Laplace transformation, which provides the relationship known as the Debye equation:

$$\hat{\epsilon} = \epsilon_\infty + \frac{(\epsilon_0 - \epsilon_\infty)}{1 + j\omega\tau} = \epsilon' - j\epsilon'' \quad (3.25)$$

The limiting values of the permittivity, ϵ_s and ϵ_∞ , are known as static and infinite permittivity, respectively. The relaxation time τ corresponds to a relaxation frequency $f_r = 1/2\pi\tau$. For a highly associated liquid such as water, the static permittivity can be expressed in terms of molecular parameters in accordance with the discussions in the previous section as

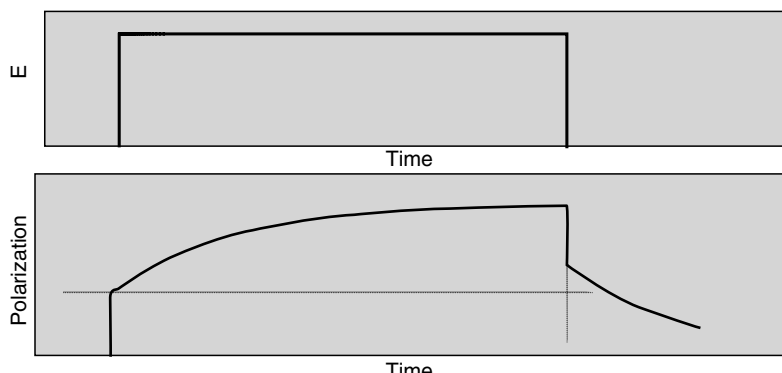


FIGURE 3.1

Schematic graph of dielectric response of a polar material expressed as polarization in the time domain in response to the step onset and removal of a polarizing electric field E . The nearly instantaneous rise in polarization, indicated by the horizontal dotted line, is P_∞ ; the vertical dotted line marks the instant and equivalent drop in polarization occurs when the field is removed.

$$\epsilon_s = \epsilon_\infty + \frac{Ng\mu^2}{2kT\epsilon_0} \quad (3.26)$$

The relaxation time may be identified with the time constant of the molecular polarization and expressed in terms of molecular parameters. If η is the viscosity, then for a spherical molecule of radius a

$$\tau = 4\pi a^3 \eta / kT \quad (3.27)$$

For most polar materials, though not for water, ϵ_∞ corresponds to the optical permittivity and is equal to the square of optical refractive index n of the medium:

$$\epsilon_\infty = n^2 \quad (3.28)$$

The dielectric properties of polar molecules vary with temperature; in general, both ϵ_s and τ decrease with increasing temperature.

As with the charge density and polarization, the time dependence of the current density J and σ , the current density per unit field, also follows a first-order law such that

$$J/E = \sigma_\infty + (\sigma_s - \sigma_\infty)(1 - e^{-t/\tau}) \quad (3.29)$$

This transforms into the conductivity equivalent of the Debye equation:

$$\hat{\sigma} = \sigma_\infty + \frac{(\sigma_s - \sigma_\infty)}{1 + j\omega\tau} \quad (3.30)$$

Figure 3.2 shows the variation in the permittivity, loss factor, and conductivity with frequency for a single time constant relaxation; such behavior pertains to an idealized monomolecular polar substance with no residual frequency-independent conductivity, that is $\sigma_s = 0$. The best, if not the only, example of such material is pure water as will be discussed later.

At the relaxation frequency, the permittivity is halfway between its limiting values and the loss factor at its highest. In the case of a single time constant as described in Figure 3.2, the conductivity is halfway between its limiting values at the relaxation frequency.

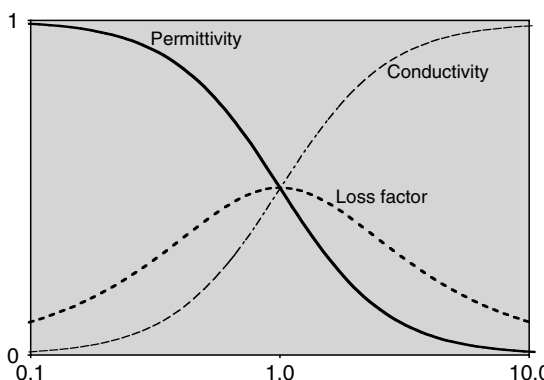


FIGURE 3.2

Normalized permittivity $(\epsilon' - \epsilon_\infty)/(\epsilon_s - \epsilon_\infty)$, loss factor $\epsilon''/(\epsilon_s - \epsilon_\infty)$, and conductivity $\omega\epsilon_0\epsilon''/(\epsilon_s - \epsilon_\infty)$ for a single time constant relaxation plotted against f/f_r .

3.3.3 Nonpolar Molecules

The permittivity of nonpolar materials is virtually constant throughout the frequency range. In general, the temperature dependence is not significant. The static and optical values of the permittivity are almost identical, hence the Maxwell relation $\epsilon = n^2$ holds true throughout the frequency and temperature range.

3.4 Observed Responses of Real Systems—Conduction—Multiple Relaxations—The Universal Law

In the previous section we described the expected behavior of idealized materials; we now need to deal with the observed responses of real systems. Few materials exhibit single relaxation time dispersions as in the Debye model; real materials depart from this ideal behavior to a greater or lesser extent depending on the complexity of the underlying mechanisms. To describe these responses we need to introduce the concepts of multiple dispersions and distribution of relaxation time. Moreover, biological materials exhibit conduction as well as polarization mechanisms; this needs to be taken into consideration in describing their dielectric response.

3.4.1 Conduction

The Debye expression does not include the effect of conduction currents as would arise from, for example, the drift of free ions in static fields. If σ_s is the static conductivity, the Debye expression becomes

$$\hat{\epsilon} = \epsilon_\infty + \frac{(\epsilon_s - \epsilon_\infty)}{1 - j\omega\tau} - \frac{j\sigma_s}{\omega\epsilon_0} \quad (3.31)$$

In terms of real and imaginary parts we have

$$\begin{aligned} \epsilon' &= \epsilon_\infty + \frac{(\epsilon_s - \epsilon_\infty)}{1 + (\omega\tau)^2} \\ \epsilon'' &= \frac{\sigma_s}{\omega\epsilon_0} + \frac{(\epsilon_s - \epsilon_\infty)\omega\tau}{1 + (\omega\tau)^2} \end{aligned} \quad (3.32)$$

The total conductivity σ is given by

$$\sigma = \omega\epsilon_0\epsilon'' = \sigma_s + \frac{(\epsilon_s - \epsilon_\infty)\epsilon_0\omega^2\tau}{1 + (\omega\tau)^2} \quad (3.33)$$

The total conductivity is thus made of two terms corresponding to the residual static conductivity and polarization losses. In practice, it is only possible to measure the total conductivity of a material; σ_s is obtained from data analysis or by measurement at frequencies corresponding to $\omega\tau \ll 1$ where the dipolar contribution to the total conductivity is negligible.

3.4.2 Multiple Relaxation Models—Distribution of Relaxation Times—Fractional Power Law Behavior

The occurrence of multiple interaction processes or the presence of more than one molecular conformational state or type of polar molecule may cause the dielectric behavior of a substance to exhibit multiple relaxation time dispersions. Deviation from Debye behavior may also indicate a polarization process whose kinetics are not first order or the presence of a complex intermolecular interaction. Models are needed to analyze the dielectric spectra of complex systems to unravel the underlying interaction mechanisms.

The simplest case is that of a dielectric response arising from multiple first-order processes; in this case the dielectric response will consist of multiple Debye terms to correspond to the polarization processes such that

$$\hat{\epsilon} = \epsilon_{\infty} + \frac{\Delta\epsilon_1}{1 - j\omega\tau_1} + \frac{\Delta\epsilon_2}{1 - j\omega\tau_2} + \dots \quad (3.34)$$

where $\Delta\epsilon_n$ corresponds to the limits of the dispersion characterized by time constant τ_n . If the relaxation times are well separated such that $\tau_1 \ll \tau_2 \ll \tau_3 \ll \dots$, a plot of the dielectric properties as a function of frequency will exhibit clearly resolved dispersion regions.

If, as is quite often the case, the relaxation times are not well separated, the material will exhibit a broad dispersion encompassing all the relaxation times. In the limit of a continuous distribution of relaxation times, the multiple Debye expression would be

$$\hat{\epsilon} = \epsilon_{\infty} + (\epsilon_s - \epsilon_{\infty}) \int_0^{\infty} \frac{\rho(\tau) d\tau}{1 - j\omega\tau} \quad (3.35)$$

where

$$\int_0^{\infty} \rho(\tau) d\tau = 1 \quad (3.36)$$

The above equations can be used to represent all dielectric dispersion data, provided an appropriate distribution function $\rho(\tau)$ is available. Conversely, it should also be possible, at least in principle, to invert dielectric relaxation spectra to determine $\rho(\tau)$ directly; however, this is not easily achievable in practice. More commonly, one has to assume a distribution to describe the frequency dependence of the dielectric properties observed experimentally. The choice of distribution function should depend on the cause of the multiple dispersions in the material. For example, one can assume a Gaussian distribution as is known to occur for other physical characteristics ([Figure 3.3](#)) would be

$$\rho(t/\tau) = \frac{b}{\sqrt{\pi}} e^{-b^2 [\ln(t/\tau)]^2} \quad (3.37)$$

where τ is the mean relaxation time. The shape of the Gaussian function depends on the parameter b ; it reduces to the delta function when b tends to infinity and becomes very broad when b decreases; the area under the curve remains the same as required by the normalization condition. Incorporated into the expression for complex permittivity, it produces an expression that cannot be solved analytically, which makes it impractical for experimental data analysis.

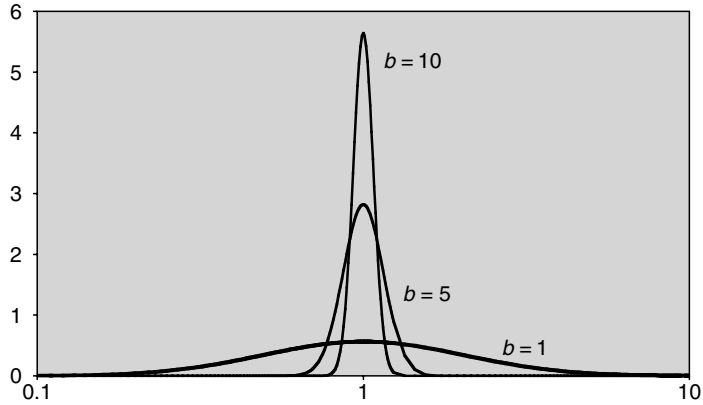


FIGURE 3.3

Gaussian distribution function as a function of t/τ .

Numerous empirical distribution functions or models have been proposed to model the experimental data without elaboration of the underlying mechanisms. One of the most commonly used models, a modified version of the Debye expression, was proposed in 1941 by Cole and Cole and is widely known as the Cole–Cole model:

$$\hat{\varepsilon} = \varepsilon_\infty + \frac{(\varepsilon_s - \varepsilon_\infty)}{1 - (j\omega\tau)^{1-\alpha}} = \varepsilon' - j\varepsilon'' \quad (3.38)$$

In it, α is a distribution parameter in the range $1 > \alpha \geq 0$; for $\alpha = 0$, the model reverts to the Debye equation. The real and imaginary parts are

$$\begin{aligned} \varepsilon' &= \varepsilon_\infty + \frac{(\varepsilon_s - \varepsilon_\infty)[1 - (\omega\tau)^{1-\alpha} \sin(\alpha\pi/2)]}{1 + (\omega\tau)^{2(1-\alpha)} + 2(\omega\tau)^{1-\alpha} \sin(\alpha\pi/2)} \\ \varepsilon'' &= \frac{(\varepsilon_s - \varepsilon_\infty)(\omega\tau)^{1-\alpha} \cos(\alpha\pi/2)}{1 + (\omega\tau)^{2(1-\alpha)} + 2(\omega\tau)^{1-\alpha} \sin(\alpha\pi/2)} \end{aligned} \quad (3.39)$$

Eliminating $\omega\tau$ from the above equations gives

$$\left(\varepsilon' - \frac{(\varepsilon_s + \varepsilon_\infty)}{2}\right)^2 + \left(\varepsilon'' + \frac{(\varepsilon_s + \varepsilon_\infty)}{2} \cot\frac{(1-\alpha)\pi}{2}\right)^2 = \left(\frac{\varepsilon_s - \varepsilon_\infty}{2} \cosec\frac{(1-\alpha)\pi}{2}\right)^2 \quad (3.40)$$

indicating that a plot of ε' against ε'' is a semicircle with its center below the real axis. For $\alpha = 0$, the Debye equivalent of the above equation is

$$\left(\varepsilon' - \frac{(\varepsilon_s + \varepsilon_\infty)}{2}\right)^2 + \varepsilon''^2 = \left(\frac{\varepsilon_s - \varepsilon_\infty}{2}\right)^2 \quad (3.41)$$

which indicates that ε' against ε'' is a semicircle with its center on the real axis ([Figure 3.4](#)); these semicircle plots are known as Cole–Coles.

The distribution function that corresponds to the Cole–Cole model is

$$\rho(t/\tau) = \frac{1}{2\pi} \frac{\sin(\alpha\pi)}{\cosh[(1-\alpha)\ln(t/\tau)] - \cos(\alpha\pi)} \quad (3.42)$$

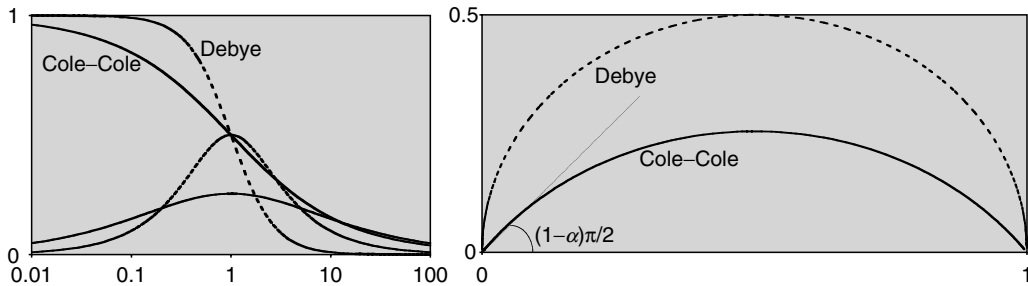


FIGURE 3.4

Left: Frequency dependence of normalized permittivity $(\varepsilon' - \varepsilon_\infty)/(\varepsilon_s - \varepsilon_\infty)$ and loss factor $\varepsilon''/(\varepsilon_s - \varepsilon_\infty)$ against frequency, normalized to the relaxation frequency, for a Debye and Cole–Cole with $\alpha = 0.4$. Right: Plot of normalized permittivity against loss factor showing a semicircle with its center on the real axis in the case of the Debye and an arc of a semicircle with its center below the real axis in the case of the Cole–Cole; the apex of the arc corresponds to the mean relaxation frequency.

Here again, τ is the mean relaxation time. As with the Gaussian, this distribution is logarithmically symmetrical about t/τ (Figure 3.5).

In 1951, Davidson and Cole proposed another variant of the Debye equation in which an exponent β is applied to the whole denominator:

$$\hat{\varepsilon} = \varepsilon_\infty + \frac{(\varepsilon_s - \varepsilon_\infty)}{(1 - j\omega\tau)^\beta} \quad (3.43)$$

which gives

$$\begin{aligned} \varepsilon' &= \varepsilon_\infty + (\varepsilon_s - \varepsilon_\infty) \cos(\beta\phi)(\cos\phi)^\beta \\ \varepsilon'' &= (\varepsilon_s - \varepsilon_\infty) \sin(\beta\phi)(\cos\phi)^\beta \end{aligned} \quad (3.44)$$

where $\phi = \arctan(\omega\tau)$. The corresponding distribution of relaxation times is

$$\rho(t/\tau) = \frac{1}{\pi} \left(\frac{t}{\tau - t} \right)^\beta \sin(\pi\beta) \quad (3.45)$$

When $\beta = 1$, the model reverts to the Debye equation. A plot of the real and imaginary parts of the model presents a skewed arc, similar to the Debye plot at low-frequencies, where it intercepts the abscissa at $\pi/2$, but at high frequencies the tangent to the arc is $\pi/2$ (Figure 3.6).

The distribution function is shown graphically in Figure 3.7. It has a singularity at $t/\tau = 1$ and returns zero at $t > \tau$.

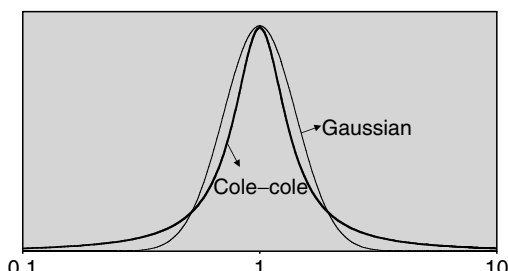


FIGURE 3.5

Gaussian distribution with $b = 2$ and Cole–Cole distribution with $\alpha = 0.09$ as a function of t/τ .

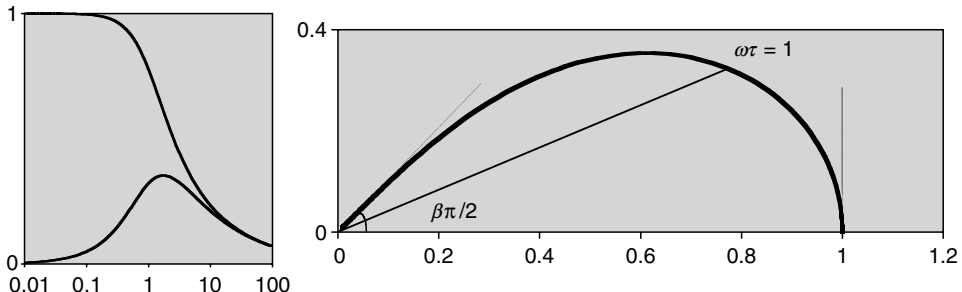


FIGURE 3.6

Left: Frequency dependence of normalized permittivity $(\epsilon' - \epsilon_\infty)/(\epsilon_s - \epsilon_\infty)$ and loss factor $\epsilon''/(\epsilon_s - \epsilon_\infty)$ for a Cole–Davidson model with $\beta = 0.5$. Right: Plot of normalized loss factor against permittivity showing the characteristic Cole–Davidson skewed arc where the maximum in ϵ'' does not correspond with $\omega\tau = 1$; this point is found at the intersection of the bisector of the high-frequency limiting angle with the data plot.

Another expression, sometimes used to model dielectric data, is the Havriliak–Negami relation (Havriliak and Negami, 1966). It combines the variations introduced in both the Cole–Cole and the Cole–Davidson models, giving

$$\hat{\epsilon} = \epsilon_\infty + \frac{(\epsilon_s - \epsilon_\infty)}{(1 - (j\omega\tau)^{1-\alpha})^\beta} \quad (3.46)$$

with real and imaginary parts:

$$\begin{aligned} \epsilon' &= \epsilon_\infty + \frac{(\epsilon_s - \epsilon_\infty) \cos(\beta\phi)}{1 + 2(\omega\tau)^{1-\alpha} \sin(\alpha\pi/2) + (\omega\tau)^{2(1-\alpha)} \beta^{1/2}} \\ \epsilon'' &= \frac{(\epsilon_s - \epsilon_\infty) \sin(\beta\phi)}{1 + 2(\omega\tau)^{1-\alpha} \sin(\alpha\pi/2) + (\omega\tau)^{2(1-\alpha)} \beta^{1/2}} \end{aligned} \quad (3.47)$$

in which $\phi = \arctan \{[(\omega\tau)^{1-\alpha} \cos(\alpha\pi/2)]/[1 + (\omega\tau)^{1-\alpha} \sin(\alpha\pi/2)]\}$ and the corresponding distribution of relaxation times is

$$\rho(t/\tau) = \frac{1}{\pi} \frac{(t/\tau)^{\beta(1-\alpha)} \sin(\beta\theta)}{(t/\tau)^{2(1-\alpha)} + 2(t/\tau)^{1-\alpha} \cos(\pi(1-\alpha)) + 1} \quad (3.48)$$

where $\theta = \arctan \{[(\sin(1-\alpha)\pi)/((t/\tau) + \cos(1-\alpha)\pi)]\}$.

The Cole–Cole plot of the Havriliak–Negami model is an asymmetric curve intercepting the real axis at different angles at high and low-frequencies (Figure 3.8). The distribution of relaxation times is also asymmetric (Figure 3.9).

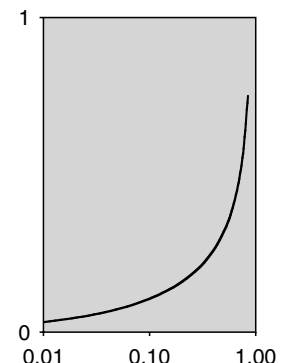


FIGURE 3.7

Cole–Davidson distribution with $\beta = 0.5$ as a function of t/τ .

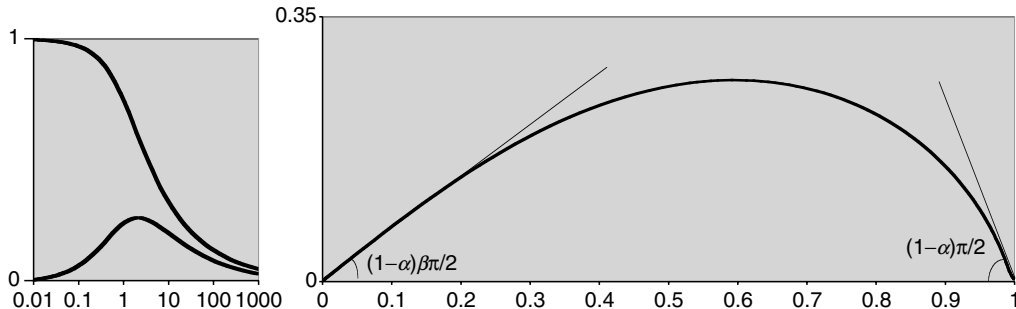


FIGURE 3.8

Left: frequency dependence of normalized permittivity $(\epsilon' - \epsilon_\infty)/(\epsilon_s - \epsilon_\infty)$ and loss factor $\epsilon''/(\epsilon_s - \epsilon_\infty)$ for a Havriliak-Negami model with $\alpha = 0.2$ and $\beta = 0.5$. Right: Cole-Cole plot of the same data. As with the Cole-Davidson plot, the $\omega\tau = 1$ point is found at the intersection of the bisector of the high-frequency limiting angle with the data plot.

Havriliak-Negami expressions revert to their Cole-Cole, Cole-Davidson, and Debye equivalents at the limiting values of β , α , and α and β , respectively. In principle, this should be the model of choice for dielectric data analysis. In practice, it is not widely used to describe the dielectric properties of biological material, as will be discussed later. It is important to recall that these empirical distribution functions lack mechanistic justification; however, they do serve a useful purpose in enabling the parametrization of the experimental data, albeit with very limited clarification of the underlying mechanisms.

Another limitation of this type of analysis is the possibility of obscuring multirelaxation processes, particularly the presence of a small amplitude dispersion following in the high-frequency tail end of a much larger principal one. This point is well illustrated by Wei and Sridhar (1993); they point out that a graphical representation of the parameter $\sigma'' = \omega\epsilon_0(\epsilon' - \epsilon_\infty)$ versus $\sigma' = \omega\epsilon_0\epsilon''$ provides a more sensitive visualization of multirelaxation processes.

The Debye model and its many variations, including those described in this section, have been widely used over more than half a century primarily because they lend themselves to simple curve-fitting procedures. In particular, the Cole-Cole model is

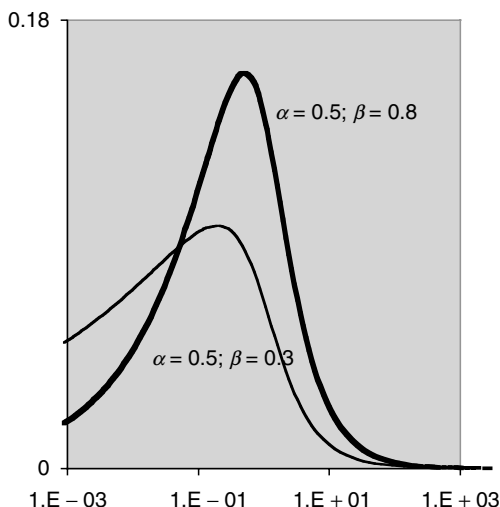


FIGURE 3.9

Havriliak-Negami distribution as a function of t/τ showing the effect of β for a given value of α .

used almost as a matter of course in the analysis of the dielectric properties of biological materials. Mathematically, at the limit of high frequencies, the Cole–Cole function simplifies to a fractional power law, that is, both ϵ' and ϵ'' are proportional to $(\omega\tau)^{(\alpha-1)}$. This fractional power law behavior is at the basis of what is known as the universal law of dielectric phenomena developed by Jonscher, Hill, and Dissado (Jonscher, 1983) for the analysis of the frequency dependence of dielectric data.

3.4.3 Universal Law of Dielectric Relaxation

Jonscher and his collaborators (Hill and Jonscher, 1983; Dissado and Hill, 1989) collated and analyzed extensive dielectric data obtained from numerous sources, pertaining to a wide range of materials, measured over a broad range of temperatures and frequencies. Their aim was to observe how dielectrics behave rather than presume a model for their frequency dependence; they studied the data on a log–log scale to better recognize the presence of a power law dependence, if present. Figure 3.10 shows plots for Debye and non-Debye responses where ω_p is the loss peak radial frequency.

Very few materials exhibit a pure Debye behavior where, at frequencies in excess of ω_p , the logarithmic slopes for $\epsilon'(\omega)$ and $\epsilon''(\omega)$ are -2 and -1 , respectively, which is a Kramers–Krönig compatible result. However, for most materials a power law dependence of the type ω^{n-1} , with $n \neq 0$, applies for both $\epsilon'(\omega)$ and $\epsilon''(\omega)$. This is in compliance with the Kramers–Krönig relations, which require that at frequencies exceeding ω_p , both parameters follow the same frequency dependence, making the ratio $\epsilon''(\omega)/\epsilon'(\omega)$ frequency independent. Under such conditions, the ratio of energy dissipated to energy stored per radian of sinusoidal excitation is constant. The universal law can be summarized by the following frequency dependencies for the normalized complex permittivity:

$$\text{for } \omega < \omega_p, \quad \epsilon''(\omega) \approx \omega^m \quad \text{and} \quad \epsilon'(\omega) \approx 1 - \epsilon''(\omega) \quad (3.49)$$

$$\text{for } \omega > \omega_p, \quad \epsilon''(\omega) \approx \omega^{n-1} \quad \text{and} \quad \epsilon'(\omega) \approx \epsilon''(\omega) \approx \omega^{n-1} \quad (3.50)$$

Observation of the experimental data showed that ω_p is temperature dependent and follows an Arrhenius function:

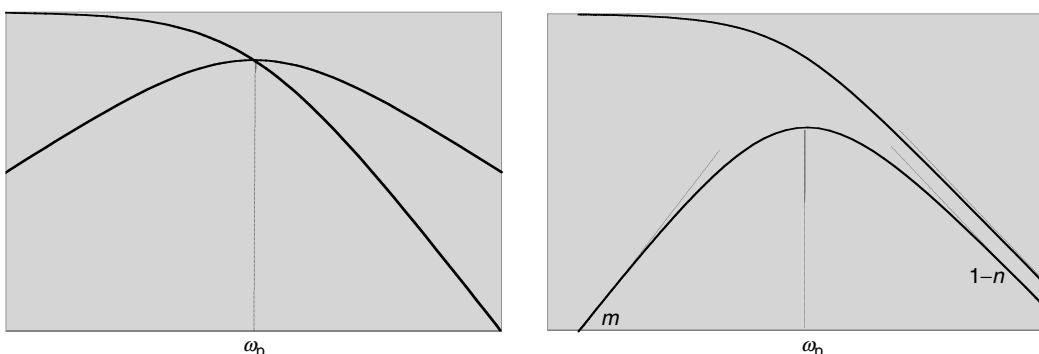


FIGURE 3.10

Log–log plot of the normalized permittivity and loss factor against frequency for a Debye-type behavior (left) and a non-Debye response (right).

$$\omega_p = A e^{-W/kT} \quad (3.51)$$

and the functional form for $\epsilon''(\omega)$ is

$$\epsilon''(\omega) = \frac{A}{(\omega/\omega_p)^{1-n} + (\omega_p/\omega)^m} \quad (3.52)$$

The values for $\epsilon'(\omega)$ can then be determined numerically from the Kramer–Krönig relations.

Although the features of the dielectric spectra of most materials can be described using this approach, there is no theoretical justification for it. This makes it yet another empirical model, albeit a very general and mathematically elegant one.

3.4.4 Combined Response Model

A model that combines features from Debye-type and universal dielectric response behavior was proposed by Raicu (1999). In the course of modeling broad dielectric dispersions, as is often observed in the dielectric spectrum of biological materials, Raicu found that neither approach was good enough over a wide frequency range. He proposed the following very general function

$$\hat{\epsilon} = \epsilon_\infty + \frac{\Delta}{[(j\omega\tau)^\alpha + (j\omega\tau)^{1-\beta}]^\gamma} \quad (3.53)$$

where α , β , and γ are real constants in the range [0,1], τ is the characteristic relaxation time, and Δ is a dimensional constant, which becomes the dielectric increment ($\epsilon_s - \epsilon_\infty$) when $\alpha = 0$, and the above expression reverts to the Havriliak–Negami model, which further reduces to the Debye, Cole–Cole, or Cole–Davison models with an appropriate choice of the α , β , and γ parameters. For $\gamma = 1$, it reverts to Jonsher's universal response model; in the special case where $\gamma = 1$ and $\alpha = 1 - \beta$, it becomes

$$\hat{\epsilon} = \epsilon_\infty + \left(j\frac{\omega}{S}\right)^{\beta-1} \quad (3.54)$$

which is known as the constant phase angle model (Dissado, 1990). In this expression S is a scaling factor given by $S = (\Delta/2)^{1/(1-\beta)}\tau^{-1}$. The above expression was successfully used to model the dielectric spectrum of a biological material over five frequency decades from 10^3 Hz to 10^8 Hz.

3.5 Dielectric Properties of Biological Materials—Main Components

Tissue is a heterogenous material containing water, dissolved organic molecules, macromolecules, ions, and insoluble matter. The constituents are highly organized in cellular and subcellular structures forming macroscopic elements and soft and hard tissues. The presence of ions plays an important role in the interaction with an electric field, providing means for ionic conduction and polarization effects. Ionic charge drift creates conduction currents and also initiates polarization mechanisms through charge accumulation at

structural interfaces, which occur at various organizational levels. Their dielectric properties will thus reflect contributions to the polarization from both structure and composition. In this section, the contribution of each of the components will be determined individually and then collectively, leading to the formulation of models for the dielectric response of biological tissue.

3.5.1 Water

Water is a constituent of all living things; it is the environment in which body electrolytes and biomolecules reside and interact. Knowledge of its properties must precede the study of the more complex system. Many of the physical properties peculiar to water are due to its molecular asymmetry, polar nature, and ability to hydrogen bond, which are all interrelated. Water is described as an associated liquid because of its intermolecular hydrogen bonding. One practical reason for emphasizing the study of water in this chapter is its increasing use as a reference liquid, that is, a material of well-known dielectric properties. Consequently, it is often used as a standard for the calibration and testing of dielectric measuring procedures.

The dielectric properties of water are among the most studied and reported in the literature. Over the past decades, many experimental studies have been carried out to determine the dielectric properties of water over wide frequency and temperature ranges. These include Haggis et al. (1952), Lane and Saxton (1952), Hasted and El Sabeh (1953), Grant et al. (1957), Grant and Shack (1967), Grant and Sheppard (1974), Schwan et al. (1976), Grant et al. (1981), Hasted et al. (1985), Kaatze (1986, 1988), Buckmaster (1990), and Buchner et al. (1998). A comprehensive list of references and a historical overview of the subject can be found in Ellison et al. (1996). Other notable reviews were carried out by Kaatze (1989) and Liebe et al. (1991).

Data up to 100 GHz exhibit a near-perfect Debye dispersion with fairly well-defined parameters. Table 3.1 gives the Debye parameters for water at 20°C from three relatively recent reviews. Kaatze (1989) used a Debye expression to model his own extensive experimental data covering -4°C to 60°C and 1 to 57 GHz in addition to what he considered to be credible data from other sources.

Liebe et al. (1991) gathered extensive static and high-frequency data. For frequencies up to 100 GHz and temperatures from 0°C to 30°C, the data were a very good fit to the Debye function. However, including data at higher frequency somewhat reduced the goodness of the fit, suggesting the possible presence of a much smaller secondary dispersion in the hundreds of gigahertz range. The next logical step was then to use a two-Debye model. This proved a good fit to all experimental data up to 1 THz, thus confirming the presence of a small, high-frequency dispersion, probably due to some subtle molecular mechanism.

TABLE 3.1

Debye Parameters for Pure Water at 20°C

Review	ϵ_s	τ (ps)	ϵ_∞
Kaatze (1989)	80.2	9.47	5.2
Liebe et al. (1991)	80.1	9.35–9.39	5.3–5.4
Buchner et al. (1998)	80.2	9.32–9.52	5.9–6.0

Notes: For Liebe et al. (1991), τ and ϵ_∞ values are those of the single-Debye model (<100 GHz) and of the principal dispersion in the two-Debye model (up to 1 THz). Buchner et al. (1998) provide upper and lower bounds for τ and ϵ_∞ of the principal relaxation of a two-Debye model.

This secondary dispersion, centered around 670 GHz, brought down the high-frequency permittivity from 5.4 to 3.3 and made practically no impact on the characteristics of the principal dispersion, which were almost unchanged (Table 3.1). Liebe et al. (1991) extended the model to the far infrared (30 THz) by accounting for two near-infrared resonance absorption terms.

The most recent and comprehensive analysis of the dielectric properties of water is provided by Ellison et al. (1996), who critically reviewed the literature spanning the late 19th and most of the 20th centuries. With respect to the static permittivity, they obtained a function $\varepsilon_s = a e^{-b}$ with $a = 87.85306$ and $b = 0.00456992$, which predicts the value of ε_s at a given temperature to well within the limits of experimental accuracy for the range $-35^\circ\text{C} < t < 100^\circ\text{C}$. All high-frequency data (up to 1 THz) that met their selection criteria are tabulated. They stopped short of formulating models for the frequency dependence of the data; instead, they invited comments from the scientific community prior to the determination of what would probably be the ultimate model and spectral parameters for the dielectric properties of pure water, a finding that will greatly benefit this field of study. Already, other researchers have used this extensive survey. For example, Buchner et al. (1998) reported values for τ and ε_∞ of the principal water dispersion (Table 3.1) by fitting a two-Debye model to combined experimental data from Ellison et al. (1996) and other, more recent, studies (Barthel et al., 1995).

It is evident from Table 3.1 that the static permittivity and the relaxation time are fairly well-defined, less so the infinite permittivity. Fortunately, this parameter has little impact on the dielectric data in the gigahertz range because its value is only a small percentage of the permittivity in that frequency range. This relatively large uncertainty highlights the fact that even this most studied, pure substance is not a perfect reference liquid and that much remains to be done in the characterization of the dielectric properties of water at terahertz frequencies. Figure 3.11 is a plot of the dielectric properties of water at 20° tabulated by Ellison et al. (1996).

In biological materials, water is a solvent for salts, protein, nucleic acids, and smaller molecules. It is therefore important to study the effect of solutes on its dielectric response.

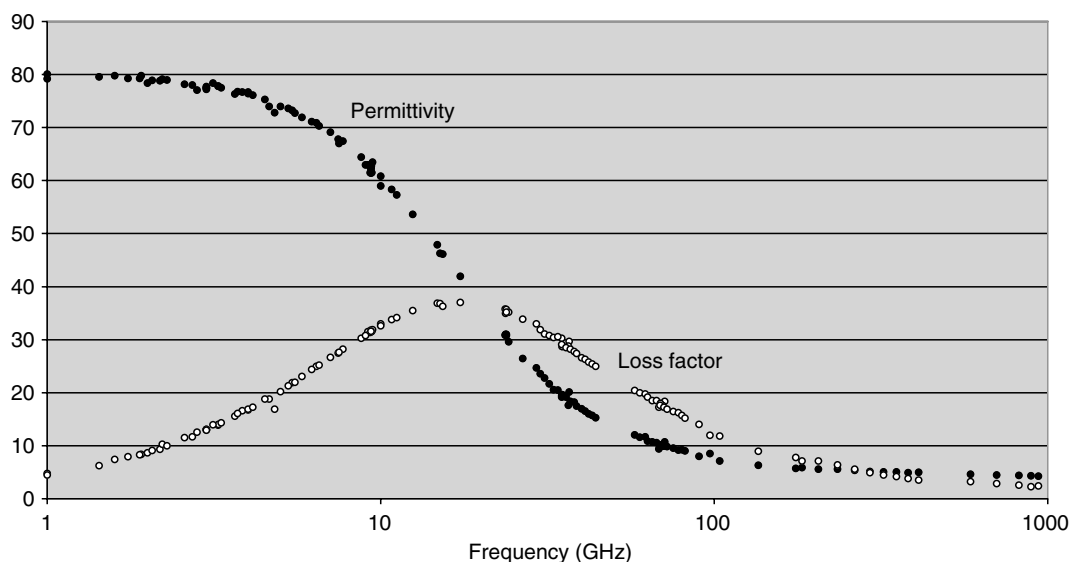


FIGURE 3.11

Experimental data from numerous sources reviewed and tabulated by Ellison et al. (1996).

3.5.2 Carbohydrates

In quantitative terms carbohydrates are not major constituents of animal cells; they are present at the surface of the cell membrane and are known to play a role in cellular communications. They are responsible for the gel consistency that gives certain body fluids such as vitreous humor and synovial fluid cushioning or lubricating properties. They are important constituents of certain tissues such as cartilage, tendon, and ligament. In terms of molecular structure, they vary in complexity and molecular size; they have in common the presence of one or more hydroxyl groups and the ability to hydrogen bond with each other or with water molecules. In aqueous solution they modify the principal dispersion of water to an extent that depends on the nature and concentration of the organic radical. In general, the dispersion is likely to be broader than a Debye, the static permittivity lower, and the relaxation time longer than for pure water, as observed and reported by Bateman and Gabriel (1987).

3.5.3 Proteins and Other Macromolecules

Protein constitutes the bulk of the organic matter in the body. Proteins are described as biopolymers, each molecule being a sequence of amino acids folded into a specific three-dimensional structure enclosing its hydrophobic sites within it. The surface has polar, hydrophilic groups with an affinity to bind water molecules from its surrounding aqueous environment. Part of the function of a protein resides in its structure; if the structure unfolds the protein is said to be denatured and is no longer functional. A good model for a globular protein in solution is that of a cluster of organic matter surrounded by a layer of strongly bound water; the solvent is referred to as free water to differentiate it from bound water. The size of the cluster depends on the molecular weight of the protein, which is typically of the order of tens or hundreds of thousands, that is, significantly larger than a water molecule. In an aqueous environment, most biological macromolecules including proteins act like polar molecules with permanent or induced dipole moment the magnitude of which depends on the molecular structure, configuration, and size.

Dielectric spectroscopy is therefore an important tool in the study of these molecular properties (Bateman et al., 1990, 1992). Typically, the dielectric dispersion of a protein will be in the megahertz frequency range, corresponding to a time constant of the order of microseconds. The dielectric spectrum of an aqueous globular protein solution will have two dispersion regions corresponding to the polarization of the protein and water molecules; the larger the protein the more clearly defined they will be. Conventionally, they are referred to as β and γ dispersions, respectively ([Figure 3.12](#)). Figure 3.12 shows a conceptual spectrum of a binary, protein–water system. In practice, to maintain the conformational stability of the biological molecules, inorganic ions, in the form of dissolved salts, must also be present. [Table 3.2](#) has actual data, gathered from the literature, on the magnitude of the dielectric increment and the relaxation time for proteins of different shapes, sizes, and dipole moments. Many authors have reported the presence of a small dispersion that is attributed to bound water, described as molecules that are more or less strongly bound or otherwise affected by the presence of organic matter. When present, the spectral region of the bound water is termed δ dispersion. The book by Grant et al. (1978) is a good introduction to this important topic.

Larger biopolymers such as DNA, whose molecular weight may be of the order of several million, have more complex dielectric spectra with dispersions extending from kilohertz to megahertz. The elucidation of the polarization mechanisms responsible for

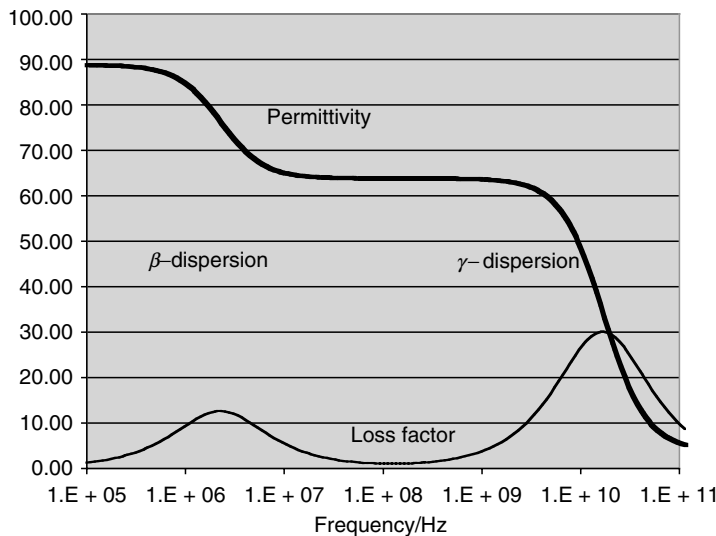


FIGURE 3.12

Conceptual representation of the dielectric spectrum of an aqueous protein solution. In practice, the two dispersions may overlap. The nearest to this picture is the complex permittivity spectrum of an aqueous solution of 1,2-dimyristoyl-*l*-3-phosphatidylcholine reported by Kaatze and Giese (1980).

the dielectric spectrum of aqueous DNA solution is an area of active research. A good introduction to the subject is the book on biopolymers by Takashima (1989).

There is more than just academic interest in the study of biopolymers. Advances in nanotechnology are such that biological macromolecules are being considered as possible nanoscale electronic devices for fast information processing and transfer, a quest that will keep theoreticians and experimentalists busy for a long time.

3.5.4 Electrolytes

Electrolytes in the form of sodium, potassium, calcium, magnesium, chloride, and other ions play an important role in the function of biological systems. Many vital processes depend on a subtle balance being established between the concentration of electrolytes

TABLE 3.2

Dielectric Parameters of Various Proteins at 25°C

Protein	Mol wt. ($\times 10^3$)	$\Delta\epsilon$	μ (D)	$\tau \times 10^8$ (s)	a/b
Myoglobin	17	0.15	170	2.9	—
β -Lactoglobulin (in 0.25 M glycine)	40	1.51	730	15, 5.1	4
Ovalbumin	44	0.10	250	18, 4.7	5
Horse carboxyhemoglobin	67	0.33	480	8.4	1.6
Horse serum albumin	70	0.17	380	36, 7.5	6
Horse serum pseudoglobulin	142	1.08	1100	250, 28	9

Notes: a/b is the axial ratio that determines the shape of the molecule. Where the shape deviates significantly from the spherical, two relaxation times are observed. The dielectric increment is $\Delta\epsilon$, the dipole moment μ is given in Debye unit (1 D = 3.33×10^{-30} cm)

Source: From Foster KR, Schwan HP. 1989. *Crit Rev Biomed Eng* 17(1): 25–104. With permission.

inside and outside the cell. The cell membrane is, to a great extent, impermeable to the passive exchange of ions but allows directed movement under physiological control. In terms of dielectric properties, electrolytes have two effects. The direct effect, already mentioned, is the production of ohmic currents and energy loss in the system. This has the effect of making the static conductivity finite with a value commensurate with the ionic concentration and mobility. There are also important indirect effects whereby ionic charges contribute to the polarization of a biological system. One is interfacial polarization, whereby charge accumulation occurs at interfaces that are impermeable to ions. Another polarization mechanism is the ionic diffusion in electrical double layers adjacent to charged surfaces. Conduction, interfacial, and ion diffusion phenomena contribute significantly to the dielectric spectra of tissue.

3.5.5 Dielectric Dispersions in Tissue

The dielectric spectrum of a biological tissue (spleen at 37°C) is given in Figure 3.13 as an example of the response of a high water content tissue. Three main dispersion regions are immediately obvious and are referred to as α , β , and γ dispersions. The dispersions are rather broad, indicating the possible overlap of discrete relaxations arising from the polarization mechanisms encountered in the complex biological environment. Ionic conductivity contributes significantly to the loss factor, obliterating its features, and it is more

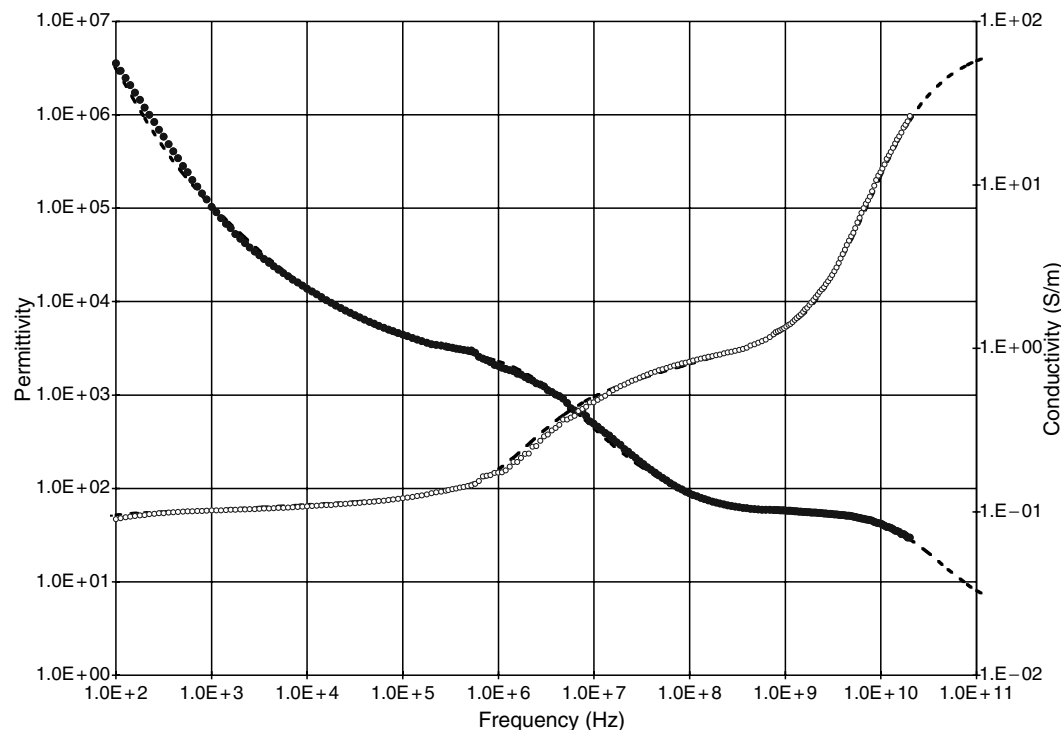


FIGURE 3.13

Dielectric spectrum of a high water content tissue (spleen at 37°C); experimental data are from Gabriel et al. (1996); dotted line is a best fit to a model of four Cole–Coles and a conductivity term.

informative to express the dielectric properties of tissues as permittivity and conductivity as in [Figure 3.13](#).

3.5.5.1 α Dispersion

The α or low-frequency dispersion is characterized by very high permittivity values and can be ascribed, at least partially, to counterion diffusion effects. Such large dispersions are predicted by theories of ionic diffusion in heterogeneous media. While it is not possible to model the complexity of a tissue, simpler mixture models predict dielectric increments of the right order of magnitude. Other mechanisms were postulated to contribute to the α dispersion; many relate to interactions in the vicinity of the cell membrane. The cell membrane is a complex, dynamic structure comprising a phospholipid bilayer. The lipid, hydrophobic ends of the phospholipids form a middle layer; the hydrophilic groups cover the inner and outer surfaces. Embedded in the bilayer are proteins, transport organelles, and ionic channels that operate under physiological control. The ionic balance between the intra- and extracellular media maintains a 60- to 70-mV potential difference between them of about 10 kV/mm across the membrane, assuming a 6- to 7-nm thickness. Membrane-related mechanisms that are thought to contribute to the α dispersion include the charging of intracellular membrane-bound organelles and a frequency dependence in the impedance of the cell membrane itself. An important reason for the uncertainty in the understanding of this dispersion is the paucity of error-free dielectric data in its frequency range. The α dispersion has a very large permittivity increment. The corresponding decrement in conductivity is small; this, however, does not contravene the principle of causality and the Kramers–Kronig relations, which predict a change in conductivity of about 0.005 S/m for a 10^6 increment in permittivity and relaxation frequency of 100 Hz.

3.5.5.2 β Dispersion

The β dispersion occurs at intermediate frequencies and originates mostly from the capacitive charging of the cellular membranes and those of membrane-bound intracellular bodies. This phenomenon, also known as interfacial polarization, has been studied theoretically and experimentally. It was established experimentally that damage to the cell membrane changes the features of the β dispersion. Numerous biomedical applications are based on the variation of the parameters of the β dispersion with pathological conditions involving changes in cell physiology and morphology. Tissue with directed, anisotropic cellular structure would exhibit an anisotropic dielectric response in the frequency range of the β dispersion.

Modeling the electrodynamics of a simplified tissue-like system, for example, suspensions of spherical inclusions in conductive media, has established theoretical grounds for the presence of the β dispersions. It enables the computation of an effective permittivity of similar order of magnitude to the β dispersion. For a system of concentric shells in conductive media (Hanai et al., 1988; Irimajiri et al., 1991), it predicts the presence of dielectric dispersions equal in number to the number of interfaces. These interfacial polarizations are boundary effects that occur in addition to other polarizations that may occur in the components of the system. The multiplicity of mechanisms goes a long way toward explaining why the β dispersions in tissue are rather broad.

3.5.5.3 γ Dispersion

The γ dispersion is due to the dipolar polarization of tissue water. At frequencies in excess of a few hundred megahertz, where the response of tissue water is the dominant

TABLE 3.3

Dielectric Parameters of Water Dispersion in Tissues Obtained by Analysis of Experimental Results at 37°C

Tissue	ϵ_s	τ (ps)	α	σ (S/m)
Bone (cortex)	14.9	13.8	0.26	0.092
Bone (section)	22.1	14.4	0.22	0.208
Cartilage	43.6	12.8	0.27	0.58
Cornea	53.0	8.72	0.13	1.05
Lens (cortex)	52.1	9.18	0.11	0.72
Lens (nucleus)	38.1	11.3	0.20	0.33
Retina	67.3	7.25	0.05	1.42
Brain (gray)	55.5	7.76	0.12	1.03
Brain (white)	37.0	8.04	0.24	0.47
Cerebellum	50.2	8.52	0.09	0.89
Dura	49.2	9.63	0.14	0.77
Brain stem	34.6	8.45	0.20	0.47
Tongue (<i>in vivo</i>)	57.7	9.12	0.08	0.63
Aqueous humor	74.2	6.81	0.01	1.83
Water	74.1	6.2	0.0	>0.0001

Source: From Gabriel et al. (1996c).

mechanism, the complex permittivity may be expressed as Cole–Cole plus a conductivity term to simulate the dipolar dispersion of water and the contribution of the electrolytes; thus,

$$\hat{\epsilon}(\omega) = \epsilon_{\infty} + \frac{\epsilon_s - \epsilon_{\infty}}{1 + (j\omega\tau)^{1-\alpha}} + \frac{\sigma}{j\omega\epsilon_0}$$

where σ is the conductivity due to ionic currents and to the lower-frequency polarization mechanisms. Table 3.3 gives the parameters of the γ dispersion of tissues modeled to the above expression. The water content of the tissues considered ranges from >95% for vitreous humor and >85% for retina to <20% for cortical bone. The correlation between ϵ_s and tissue water content is an obvious and expected result. The value of the distribution parameter α is significant for most tissues and negligible for body fluids (as for aqueous humor, for example). The mean relaxation time τ is generally longer than the value for water, indicating a restriction in the rotational ability of at least some of the tissue water molecules. The lengthening of the relaxation time of water in biological material is a well-studied hypothesis; the effect is common to most organic solutes, is known to increase with solute concentration (Grant et al., 1981; Bateman et al., 1990), and has previously been observed in tissues (Gabriel et al., 1983).

3.5.5.4 δ Dispersion

Tissues and other biological materials may exhibit dispersions other than the three main ones. The δ dispersion, identified in some protein solutions between the β and γ , dispersions may also occur in tissue in the hundreds of megahertz range; when present, its magnitude is small compared to the adjacent ones. Possible mechanisms include the dipolar relaxation of bound water, relaxation of small dipolar segments or side chains of biological molecules, and counterion diffusion along small regions of the charged surface. Under these conditions it is difficult to isolate and, in view of the multiplicity of possible mechanisms, difficult to interpret. It is often treated as the tail end of the β dispersion or a broadening of the γ dispersion.

3.5.6 Effective Complex Permittivity of a Heterogenous System

Where adequate experimental data are available, the complex permittivity of a tissue can be quite adequately modeled with four Cole–Coles and a static conductivity term:

$$\hat{\epsilon}(\omega) = \epsilon_{\infty} + \sum_{n=1}^4 \frac{\Delta\epsilon_n}{1 + (j\omega\tau_n)^{1-\alpha_n}} + \sigma_s/j\omega\epsilon_0 \quad (3.55)$$

This is a descriptive model, imparting no definite information on the polarization mechanisms; the measured dielectric properties represent the bulk response of the tissue. Assigning effective parameters to a heterogenous medium is equivalent to treating it as homogenous where these parameters are concerned; in this case, its structural components are much finer than the wavelength of the field probing it.

The derivation of a general formula for the effective permittivity of a system in terms of those for its constituents is based on the theory of the transport properties of mixtures (Reynolds and Hough, 1957). For example, in the case of a binary mixture where a medium with permittivity ϵ_1 has inclusions of permittivity ϵ_2 and assuming that v_1 and v_2 are their respective volume fractions such that $v_1 + v_2 = 1$, then the average electric displacement D is given by

$$D = v_1 D_1 + v_2 D_2 \quad (3.56)$$

and the average electric field is given by

$$E = v_1 E_1 + v_2 E_2 \quad (3.57)$$

The effective permittivity ϵ of the mixture is given by

$$D = \epsilon \epsilon_0 E \quad (3.58)$$

and for each component, $D_1 = \epsilon_1 \epsilon_0 E_1$ and $D_2 = \epsilon_2 \epsilon_0 E_2$. Equation 3.56 and Equation 3.57 give

$$\epsilon = \epsilon_1 v_1 f_1 + \epsilon_2 v_2 f_2 \quad (3.59)$$

where $v_1 f_1 + v_2 f_2 = 1$, $f_1 = E_1/E$, and $f_2 = E_2/E$, which gives two general formulations for the effective permittivity of the mixture:

$$\epsilon = \epsilon_1 + (\epsilon_2 - \epsilon_1) v_2 f_2 \quad (3.60)$$

or

$$(\epsilon - \epsilon_1) v_1 f_1 + (\epsilon - \epsilon_2) v_2 f_2 = 0 \quad (3.61)$$

The theoretical problem that needs to be resolved for specific mixtures boils down to the determination of the field ratios f_2 or f_2 and f_1 . Theoretically, the two formulations are equivalent but, when approximations have to be made for the values of the field ratios, this is no longer true. Most of the published mixture equations differ from one another in the approximations considered appropriate. As for which of the two formulations to use as a starting point, it would seem reasonable to use Equation 3.60 for the case of sparse inclusions in a continuous medium and Equation 3.61 when the volume fractions of the

two components are comparable. In the general case, the dielectric properties (in [Equation 3.60](#) and [Equation 3.61](#)) are complex. However, under static or quasistatic conditions, the mixture equations hold for either permittivity or conductivity.

Maxwell (1891) was the first to characterize the field ratios for a system of sparse spherical inclusions in a homogenous medium under static field conditions and obtained:

$$\frac{\sigma - \sigma_1}{\sigma + 2\sigma_1} = \nu_2 \frac{\sigma_2 - \sigma_1}{\sigma_2 + 2\sigma_1} \quad (3.62)$$

where the subscripts 1 and 2 refer to the suspending medium and inclusions, respectively. In terms of permittivity, Equation 3.62 is known as the Rayleigh formula; in its complex form it is attributed to Wagner and commonly known as the Maxwell–Wagner equation. Other well-known mixture equations for spherical inclusions include:

Böttcher equation:

$$\frac{\varepsilon - \varepsilon_1}{3\varepsilon} = \nu_2 \frac{\varepsilon_2 - \varepsilon_1}{\varepsilon_2 + 2\varepsilon_1} \quad (3.63)$$

Bruggeman equation:

$$\left(\frac{\varepsilon - \varepsilon_1}{\varepsilon_2 - \varepsilon_1} \right)^3 + (1 - \nu_2) \frac{\varepsilon}{\varepsilon_1} = 1 \quad (3.64)$$

Looyenga equation:

$$\varepsilon^{1/3} = \nu_1 \varepsilon_1^{1/3} + \nu_2 \varepsilon_2^{1/3} \quad (3.65)$$

To first-order approximation, the above mixture equations revert to the same expression irrespective of the formulation of the problem and of the technique used to solve it. This is because the conditions of infinite dilution and the spherical shape enable an almost exact solution to the field ratio to be obtained.

Other formulations exist for different shape inclusions such as oblate and prolate spheroids. The subject has been reviewed by, among others, Van Beek (1967), Hanai (1968), Dukhin (1971), and more recently, Greffe and Grosse (1992), Sihvola and Lindell (1992), and Tinga (1992).

It is possible to extend mixture equations to multiple inclusions by using an iterative procedure (Tamasanis, 1992). For example, if $\varepsilon(\varepsilon_1, \varepsilon_2, \nu_2)$ is the effective permittivity of a binary mixture of background of permittivity ε_1 , inclusion of permittivity ε_2 , and volume fraction ν_2 , then a mixture with two types of inclusions identified with subscripts 2 and 3, respectively, can be described as a binary mixture of background permittivity $\varepsilon(\varepsilon_1, \varepsilon_2, \nu_2/1 - \nu_3)$ and inclusion of permittivity ε_3 and volume fraction ν_3 . The effective permittivity of such a mixture will be

$$\varepsilon(\varepsilon_1; \varepsilon_2, \nu_2; \varepsilon_3, \nu_3) \approx \varepsilon \left[\varepsilon \left(\varepsilon_1; \varepsilon_2, \frac{\nu_2}{1 - \nu_3} \right); \varepsilon_3, \nu_3 \right] \quad (3.66)$$

The contributions of the different types of inclusion are added recursively in order of increasing density.

Where the assumptions used in their derivation can be approximated in the tissue model, mixture equations can be used to analyze the dielectric properties of biological materials in terms of their constituents. A few examples are given here to illustrate their application.

If the ionic conductivities of the suspending phase and that of a protein solution are known, say, by measurement at a frequency below the protein β dispersion, and if an assumption is made about the conductivity of the protein molecules, an appropriate mixture equation can then be used to determine the volume fraction of the inclusions, which, in this case, is the hydrated protein. In turn, this enables the amount of bound water to be calculated given that the fraction of anhydrous protein is known. Bull and Breese (1969) followed this approach and calculated the bound water for a variety of proteins. They evaluated the water fraction to be 0.6 g/g of protein. Pauly and Schwan (1966), following a similar procedure, estimated the conductivity of the human erythrocyte to be 0.518 S/m at 25°C, compared to the value of 1.45 S/m calculated from the known ionic composition of the cell. They attributed the difference partly to excluded volume by the protein-bound water and partly to decreased ionic mobility due to hydrodynamic effects.

Bound water in biological systems including tissue was estimated by applying mixture equations in the near-plateau region between the β and γ dispersions of the permittivity spectrum. Assuming the tissue to be a suspension of hydrated organic matter in an electrolyte solution that is little affected by the presence of the organic matter, the measured permittivity at 1 GHz is a reasonable estimate of the effective static permittivity. Knowledge of the permittivity of the suspending medium and an estimate of the permittivity of the organic matter enables the volume fraction of the inclusion to be calculated. Comparison with the known organic content provides an estimate of bound water (e.g., Grant et al., 1984; Kaatze, 1990; Schaefer et al., 2003).

3.6 Dielectric Relaxation Mechanisms in Heterogenous Media

The description of a material as heterogenous is a matter of scale; in the context of dielectric relaxation, it refers to electrical heterogeneity or the presence of electrical boundaries or interfaces. Boundary conditions at and around the interfaces gives rise to dielectric dispersions quite apart from dipolar-type dispersions that occur in the surrounding media. In biological materials, cellular membranes provide such interfaces; their presence is associated with two major dispersion regions in the dielectric spectra of tissues, namely, α and β dispersions originating mainly from interfacial polarization and ionic diffusion effects. The main mechanisms giving rise to these phenomena will be briefly discussed in this section.

3.6.1 Interfacial Polarization

Interfacial polarization is due to the charging of interfaces between conducting media and is an important mechanism of interaction in biological material. The basic principles of this phenomenon are best illustrated in simple models first before discussing their occurrence in biological materials.

3.6.1.1 Interface between Two Media

The simplest model is that of an interface between two media, for example, two slabs of thickness d_1 and d_2 in contact with each other with their interface perpendicular to an external electric field (Figure 3.14a). If the static permittivity and conductivity of the two materials are ϵ_1, σ_1 and ϵ_2, σ_2 , respectively, the boundary condition on the electric field component normal to the interface gives

$$E_1\epsilon_1 = E_2\epsilon_2 \quad (3.67)$$

If the current densities j_1 and j_2 are equal, there will be no charge accumulation at the interface; this, however, is hardly ever the case. The ratio of current densities at the interface is

$$j_1/j_2 = \sigma_1 E_1 / \sigma_2 E_2 = \sigma_1 \epsilon_2 / \sigma_2 \epsilon_1 \quad (3.68)$$

Therefore, if $\sigma_1 \epsilon_2 \neq \sigma_1 \epsilon_1$, the interface will be charged at a rate that is proportional to the difference between j_1 and j_2 .

The effective permittivity ϵ and conductivity σ of the system are calculated from its effective capacitance. With the field across the interface, this is equivalent to capacitances in series combination; thus,

$$\frac{d_1 + d_2}{\epsilon - j\sigma/\omega\epsilon_0} = \frac{d_1}{\epsilon_1 - j\sigma_1/\omega\epsilon_0} + \frac{d_2}{\epsilon_2 - j\sigma_2/\omega\epsilon_0} \quad (3.69)$$

This can be rearranged into a Debye type expression with a relaxation time of

$$\tau = \epsilon_0 \frac{\epsilon_1 d_2 + \epsilon_2 d_1}{\sigma_1 d_2 + \sigma_2 d_1} \quad (3.70)$$

and limiting values for low and high frequencies

$$\epsilon_s = \frac{(\epsilon_2 \sigma_1 - \epsilon_1 \sigma_2)^2 (d_1 + d_2) d_1 d_2}{(\epsilon_1 d_2 + \epsilon_2 d_1) (\sigma_1 d_2 + \sigma_2 d_1)^2} + \epsilon_\infty \quad (3.71)$$

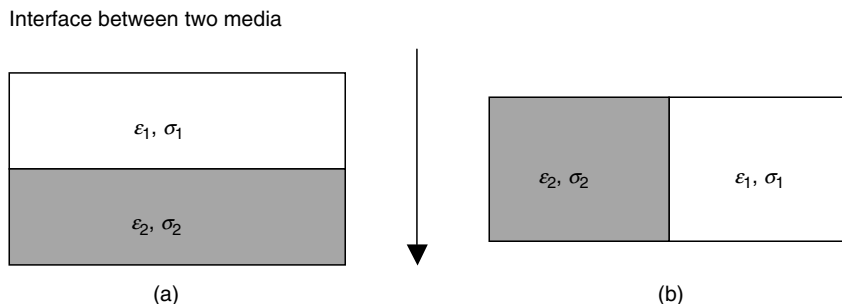


FIGURE 3.14

Two-media system; the arrow gives the direction of the electric field: (a) interface at right angle to the field and (b) interface along the field.

$$\sigma_s = (d_1 + d_2) \frac{\sigma_1 \sigma_2}{\sigma_1 d_2 + \sigma_2 d_1} \quad (3.72)$$

$$\epsilon_\infty = \frac{(d_1 + d_2) \epsilon_1 \epsilon_2}{(\epsilon_1 d_2 + \epsilon_2 d_1)} \quad (3.73)$$

The polarization of the effective capacitance occurs in addition to any polarization process within the constituent phase, in which case the dielectric spectrum of the composite system will reflect the multiple dispersions.

If the field is along the interface (Figure 3.14b), no interfacial dispersion is observed, the effective permittivity is $\hat{\epsilon} = (\hat{\epsilon}_1 + \hat{\epsilon}_2)/2$.

3.6.1.2 Suspension of Spheroids

The simplest system in this category is a dilute suspension of spherical inclusions in a continuum. Its effective complex permittivity is given by the formulation known as the Maxwell–Wagner equation, where the subscripts 1 and 2 refer to the suspending medium and inclusions, respectively:

$$\frac{\hat{\epsilon} - \hat{\epsilon}_1}{\hat{\epsilon} + 2\hat{\epsilon}_1} = v_2 \frac{\hat{\epsilon}_2 - \hat{\epsilon}_1}{\hat{\epsilon}_2 + 2\hat{\epsilon}_1} \quad (3.74)$$

This equation can be rearranged in the form of a dispersion equation with the following parameters:

$$\begin{aligned} \epsilon_\infty &= \epsilon_2 \frac{2\epsilon_2 + \epsilon_1 - 2v_2(\epsilon_2 - \epsilon_1)}{2\epsilon_2 + \epsilon_1 + v_2(\epsilon_2 - \epsilon_1)} \\ \epsilon_s - \epsilon_\infty &= \frac{9(\epsilon_2 \sigma_1 - \epsilon_1 \sigma_2)^2 v_2 (1 - v_2)}{[2\epsilon_2 + \epsilon_1 + v_2(\epsilon_2 - \epsilon_1)][2\sigma_2 + \sigma_1 + v_2(\sigma_2 - \sigma_1)]^2} \\ \sigma_s &= \sigma_2 \frac{2\sigma_s + \sigma_2 - 2v_2(\sigma_2 - \sigma_1)}{2\sigma_2 + \sigma_1 + v_2(\sigma_2 - \sigma_1)} \\ \sigma_s - \sigma_\infty &= \frac{9(\sigma_2 \epsilon_1 - \sigma_1 \epsilon_2)^2 v_2 (1 - v_2)}{[2\sigma_2 + \sigma_1 + v_2(\sigma_2 - \sigma_1)][2\epsilon_2 + \epsilon_1 + v_2(\epsilon_2 - \epsilon_1)]^2} \\ \tau &= \epsilon_0 \frac{2\epsilon_2 + \epsilon_1 - v_2(\epsilon_2 - \epsilon_1)}{2\sigma_2 + \sigma_1 + v_2(\sigma_2 - \sigma_1)} \end{aligned} \quad (3.75)$$

The dispersion will occur when $\sigma_1 \epsilon_2 \neq \sigma_2 \epsilon_1$, which is practically always the case. The magnitude of the dispersion depends on the differences in dielectric parameters between the two phases.

In the context of mixture theory, sparse means $v_2 \leq 0.2$; to model the effective permittivity of more concentrated suspensions, it is necessary to take into consideration interparticle interactions. This becomes a very complex model; there are no rigorous solutions even for the relatively simple case of identical spherical inclusions. The Bruggeman–Hanai Equation 3.64 was formulated taking account of some interaction between particles and is therefore better suited than the Maxwell–Wagner equation to model more concentrated suspension. In its complex form, it can be shown to predict the occurrence of a dispersion with the following limiting parameters:

$$\begin{aligned}
& \left(\frac{\varepsilon_\infty - \varepsilon_2}{\varepsilon_1 - \varepsilon_2} \right) \left(\frac{\varepsilon_1}{\varepsilon_s} \right)^{1/3} = 1 - v_2 \\
& \varepsilon_s \left(\frac{3}{\varepsilon_s - \sigma_2} - \frac{1}{\sigma_s} \right) = 3 \left(\frac{\varepsilon_1 - \varepsilon_2}{\sigma_1 - \sigma_2} + \frac{\varepsilon_2}{\sigma_s - \sigma_2} \right) - \frac{\varepsilon_2}{\sigma_2} \\
& \left(\frac{\varepsilon_s - \sigma_2}{\sigma_1 - \sigma_2} \right) \left(\frac{\sigma_1}{\sigma_s} \right)^{1/3} = 1 - v_2 \\
& \sigma_\infty \left(\frac{3}{\varepsilon_\infty - \varepsilon_2} - \frac{1}{\varepsilon_\infty} \right) = 3 \left(\frac{\sigma_1 - \sigma_2}{\varepsilon_1 - \varepsilon_2} + \frac{\sigma_2}{\varepsilon_\infty - \varepsilon_2} \right) - \frac{\sigma_1}{\varepsilon_1}
\end{aligned} \tag{3.76}$$

In these expressions ε_s , ε_∞ , σ_∞ are the limiting values of the corresponding parameters. The dispersion is characterized by a distribution of relaxation times.

The validity of the model has been verified experimentally for mixtures of known composition and geometry (Hanai et al., 1982; Ishikawa et al., 1982). The dispersion is broader than a single time constant because of the interactions between particles. Moreover, if the components of the heterogenous system exhibit molecular dielectric dispersion of their own, then these intrinsic dispersions will also appear, together with the interfacial dispersion, in the complete frequency spectrum of the system.

Fricke (1955), Sihvola and Kong (1988), Sihvola and Lindell (1992), and many others have extended the model to the more general case of a suspension of spheroids with any combination of axial ratios. Ultimately, the outcome is equivalent to introducing a parameter to account for the shape. The Maxwell-Wagner equation becomes

$$\frac{\hat{\varepsilon} - \hat{\varepsilon}_1}{\hat{\varepsilon} + F\hat{\varepsilon}_1} = v_2 \frac{\hat{\varepsilon}_2 - \hat{\varepsilon}_1}{\hat{\varepsilon}_2 + F\hat{\varepsilon}_1} \tag{3.77}$$

where F is the shape factor, equal to 2 for spheres, which reverts to [Equation 3.74](#). In cases where the shape of the inclusion is not known, limiting values for the effective permittivity can be obtained using the shape factors in the extreme cases of infinitely long thin rods and infinitely thin circular disks.

An interesting case is that of ellipsoids with their axes aligned in the same direction. The permittivity would be different depending on the direction of the field; the mixture would be electrically anisotropic and the effective permittivity is represented by a tensor.

Another case of practical interest is that of layered spherical inclusions. This situation is required when modeling cellular structures surrounded by a membrane of finite thickness. Solutions for the effective permittivity of this model were provided by many researchers in this field (e.g., Schwan, 1957; Zhang et al., 1983; Grosse, 1988). These authors applied two mixture models, once to the concentric bodies, thus obtaining an effective permittivity for the inclusions, and then treating the mixture as a suspension of homogenous spheres. The parameters of the dispersion could be expressed in terms of the physical dimensions and electrical characteristics of the cell and cell membrane; simplified versions of these expressions are reported by Foster and Schwan (1989). Sihvola (1989) and Irimajiri et al. (1991), among others, extended the treatment to several concentric shells by using a recursive technique. These complex models are more relevant to the study of biological systems and to the understanding of the interactions at the cellular level. They are not sufficiently developed for the quantitative characterization of the interfacial polarization in biological systems, but do provide an insight into the factors that determine its characteristics. An example from the recent literature is the modeling of the dielectric response of heart tissue by Schaefer et al. (2002). The model is a function of the cell shape, electrical cell coupling and

polarization of cell membranes, and intracellular structure. It describes heart cells and subcellular organelles as rotational ellipsoids filled with electrolyte enclosed by an isolating membrane and is capable of reproducing the main features of the dielectric spectrum of heart tissue.

In recent years, statistical methods using probabilistic descriptions of the physical mixture in terms of a spatial density function have been developed to provide realistic bounds for the effective permittivity of mixtures. This approach, developed by, among others, Bergman (1978) and Milton (2002), provides an analytic integral representation of the effective permittivity $\hat{\epsilon}$ of an arbitrary binary mixture in terms of a spatial density function $g(x)$:

$$\frac{\hat{\epsilon} - \hat{\epsilon}_1}{\hat{\epsilon}_1} = \int_0^1 \frac{g(x) dx}{x + \hat{\epsilon}_1/\hat{\epsilon}_2 - \hat{\epsilon}_1}$$

where, as before, the subscripts 1 and 2 refer to continuum and dispersed phases, respectively, and the integration is over all possible positions. Depending on the choice of distribution function $g(x)$, it is possible for the above equation to revert to some of the well-known binary mixture equations. Recursive application is possible; modeling biological systems remains challenging.

A new tool for the study of mixtures, including biological materials, has evolved with the development of increasingly powerful numerical modeling packages for the propagation of electromagnetic fields in complex structures from full solutions of Maxwell's equations. With structures being defined at the nanoscale, the characterization of fields within cells and subcellular structures appears to be within reach (Gimsa and Wachner, 1998, 1999, 2001a,b; Bianco et al., 2000; Sebastian et al., 2001; Munoz et al., 2003).

3.6.2 Counterion Polarization Effects

Another important polarization phenomenon in electrically biological materials originates from ionic diffusion effects near charged surfaces and the formation of counterion or electric double layers. The distribution of ions in the vicinity of charged interfaces is subject to concentration and electric field gradients; an equilibrium is reached with the ions continuously distributed over the volume of the electrolyte solution. The time constant associated with this mechanism is longer than that of the Maxwell-Wagner effect, it is of the form L^2/D , where L is the length over which diffusion occurs and D is a diffusion coefficient (Schwarz, 1962).

Counterion phenomena are difficult to analyze rigorously; they involve coupled electrodynamic and hydrodynamic mechanisms. The theories are complex, but good reviews are available as an introduction to the subject (Dukhin, 1971; Dukhin and Shilov, 1974; Fixman, 1980, 1983; Mandel and Odijk, 1984). Relatively simple models that provide exact solutions have been proposed (Grosse and Foster, 1987; Grosse, 1988), whereby coupled differential equations for the ion concentrations and current densities are obtained for a macroscopic sphere of radius a in an ionic medium. Their solution yields a broad, asymmetrical, low-frequency dispersion. The time constant of this dispersion is a^2/D , where D is the diffusion coefficient of ions in the bulk electrolyte.

To visualize the effect, consider the motion of an ion in the bulk electrolyte near the particle, it will be conducted away or excluded depending on whether its sign is the same or opposite that of the ions in the counterion layer. Thus, for an ion in the electrolyte, the particle acts either as a good conductor or as an insulator depending on its charge

compared to that of the counterion. A cloud of charge accumulates within a Debye length of the charged surface; for physiological saline (0.15 N NaCl) the Debye length is very small, <1 nm, resulting in a very large induced capacitance and hence a large permittivity dispersion.

3.7 Dielectric Properties of Tissue—State-of-Knowledge

Research into the dielectric properties of biological materials and their variation with frequency has been ongoing for most of the past century. Early studies went a long way toward understanding and establishing the principles of interaction and the corresponding features of the highly frequency-dependent spectrum of a tissue. In the last few decades, the research was driven, above all, by the need to establish a credible database of dielectric properties of all body tissues for use in electromagnetic dosimetry studies, where the object is to quantify the exposure of people to external electromagnetic fields from knowledge of the effective internal fields and currents induced in them. In these studies, tissues are characterized by their measured dielectric properties. In the last decade, most dosimetric studies drew on data published in the scientific literature in 1996 and made widely available on the Internet thereafter (Gabriel et al., 1996; Gabriel and Gabriel, 1997).

3.7.1 1996 Database

The backbone of the 1996 database is a large experimental study providing data pertaining, almost exclusively, to excised animal tissue at 37°C. For most tissues, the characterization was over a wide frequency range, 10 Hz to 20 GHz, using three previously established experimental setups with overlapping frequency ranges. The following are some of its characteristics:

- The data are presented in the context of a review covering all relevant publications in the preceding half-century. By and large, the experimental data were well within the confines of corresponding values from the literature.
- The data showed good internal consistency, that is, good agreement between data obtained with different experimental setups in a common frequency range.
- Finally, an element of great practical importance, the dielectric spectra were parametrized using a multidispersion model consisting of four Cole–Cole terms and one ionic conductivity term. For each tissue, the parameters of the model enable the reconstruction of its spectrum, a procedure that could easily be incorporated in numerical studies to provide dielectric data that are broadly in line with the vast body of literature on the subject.
- The fact that the complex permittivity data could be fitted to Cole–Cole dispersions implies that they also agree with the Kramers–Kronig relation in accordance with the principle of causality for a linear system. This imparts another level of consistency to the data.

Examples are given here to illustrate the extent of the available data in the literature for certain tissues at certain frequencies in contrast to the scarcity of data elsewhere

(Figure 3.15 through Figure 3.17). No attempt is made at a quantitative or mechanistic analysis.

While useful, the 1996 database has several limitations, as pointed out by its authors:

- Most measurements were carried out on excised tissue, while data pertaining to live tissue would have been more relevant in bioelectromagnetics studies.
- For most tissues, the predictions of the model can be used with confidence for frequencies above 1 MHz because of the availability of supporting data in the literature.
- At lower frequencies, where the literature values are scarce and have larger than average uncertainties, the model should be used with caution in the knowledge that it provides a “best estimate” based on the then available knowledge. This is particularly important for tissues where there are no data to support its predictions.
- Electrode polarization, an inevitable source of error at low-frequencies, was not totally accounted for. It affects the data at frequencies below 100 Hz.
- Because of the geometry of the sampling probe, it was not possible to orient the field along and across directed structure to demonstrate the anisotropy of the dielectric properties.

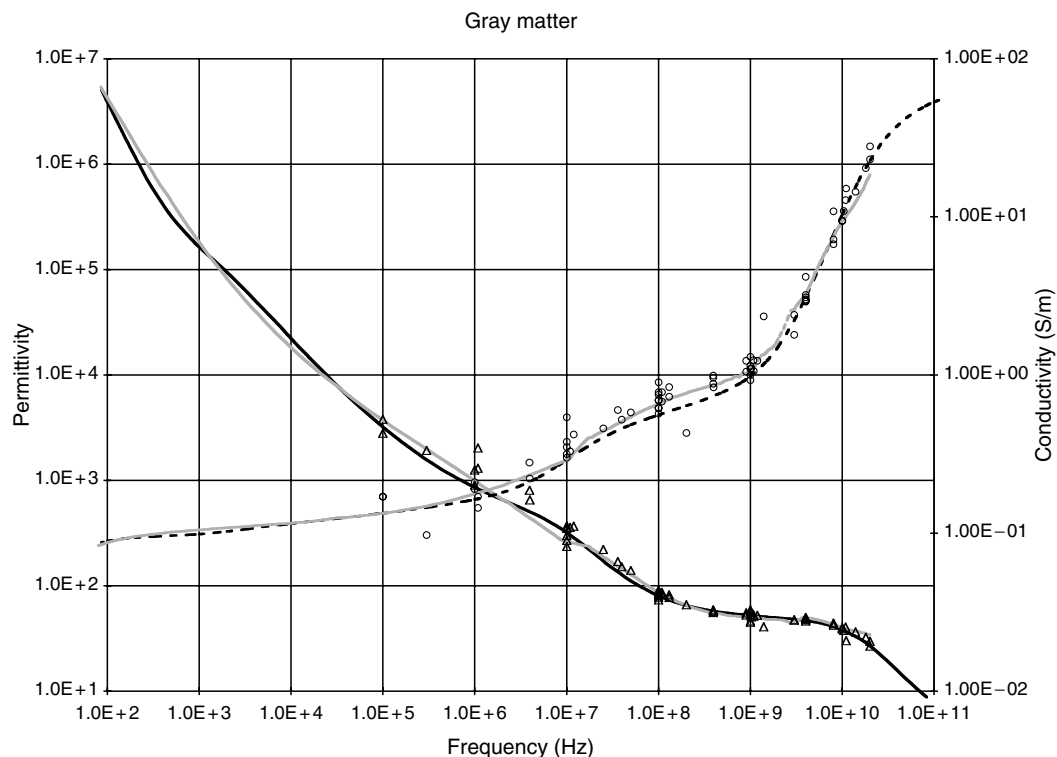


FIGURE 3.15

Permittivity and conductivity of gray matter at 37°C; gray lines are experimental data from Gabriel et al. (1996), triangles and circles are permittivity and conductivity values from the pre-1996 literature, black solid and dashed lines are the predictions of the model.

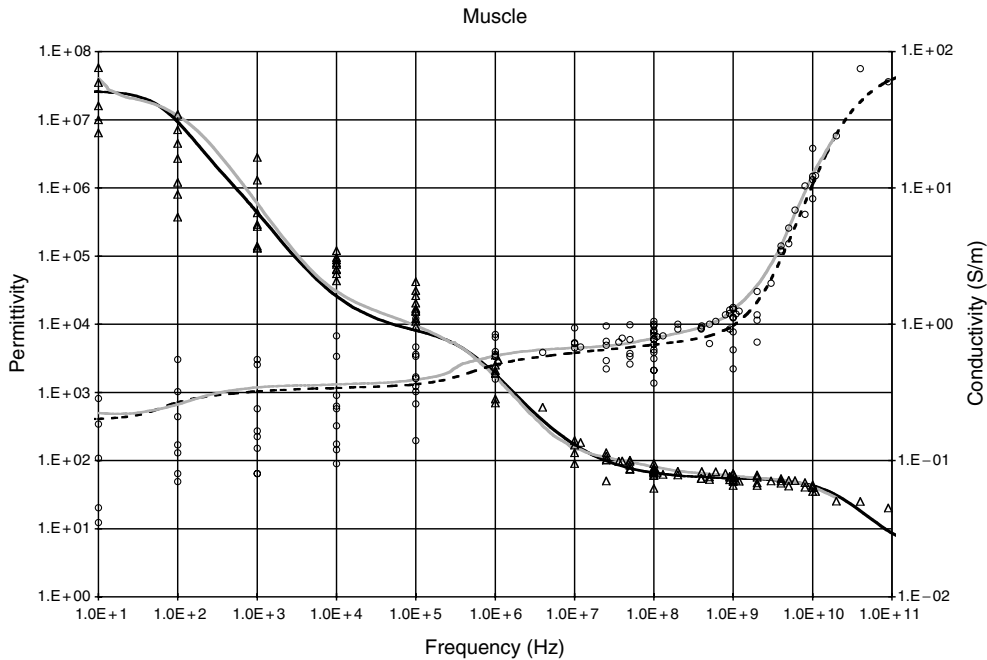


FIGURE 3.16

Permittivity and conductivity of skeletal muscle at 37°C; legend as in Figure 3.15. The very wide spectrum of data below 1 MHz is, at least partially, due to the anisotropy in the dielectric properties of muscle tissue. The literature data pertain to measurement along and across the muscle fibers and to measurements where the direction was not specified.

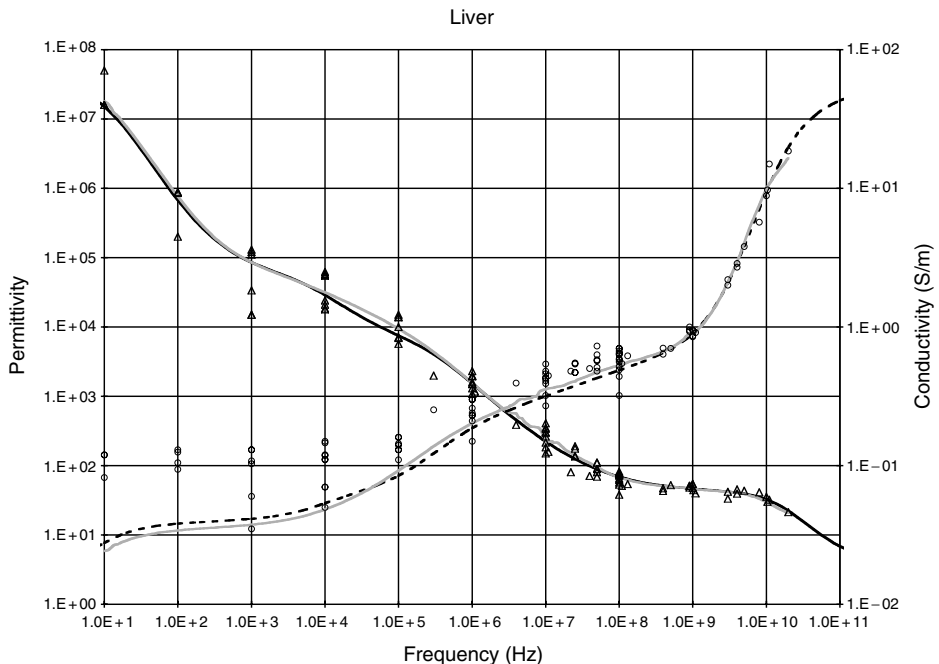


FIGURE 3.17

Permittivity and conductivity of liver tissue at 37°C; legend as in Figure 3.15. Liver tissue exhibits no significant anisotropy in its dielectric properties, but as with all tissue, the characteristics of the β dispersion and the static conductivity are sensitive to the viability and time after death when the measurements were made.

Evidently, much remains to be done, in particular with respect to reducing the uncertainty in the data and filling in the gaps identified. Ten years on, the recent literature is reviewed to update the state-of-knowledge on the subject.

3.7.2 Literature After 1996—A Brief Review

The review is carried out per tissue type or thematic underline. In some cases, data from recent studies are compared with the model in the 1996 database and with data from a recent study, where the dielectric properties of over 40 tissues were characterized *in vivo* and *in vitro* in the frequency range 10^2 to 10^4 MHz (Peyman et al., 2005).

3.7.2.1 Brain Tissue: Gray and White Matter

At microwave frequencies, three studies reported new data for brain tissue (Bao et al., 1997; Schmid et al., 2003a,b). Data tabulated by the authors are given in Figure 3.18. Data by Peyman et al. (2005) are in reasonable agreement with the database, while data by Bao and coworkers and Schmid and coworkers are higher for both permittivity and conductivity.

It is important to find a reason as to why carefully conducted studies, using adaptations of a conceptually similar experimental procedure, are still coming up with different results. In terms of explanation we note the handling of the sample by Bao et al., in which the whole brain is excised, immersed in saline, temperature regulated, and measured while immersed. The authors give good reasons for following this procedure.

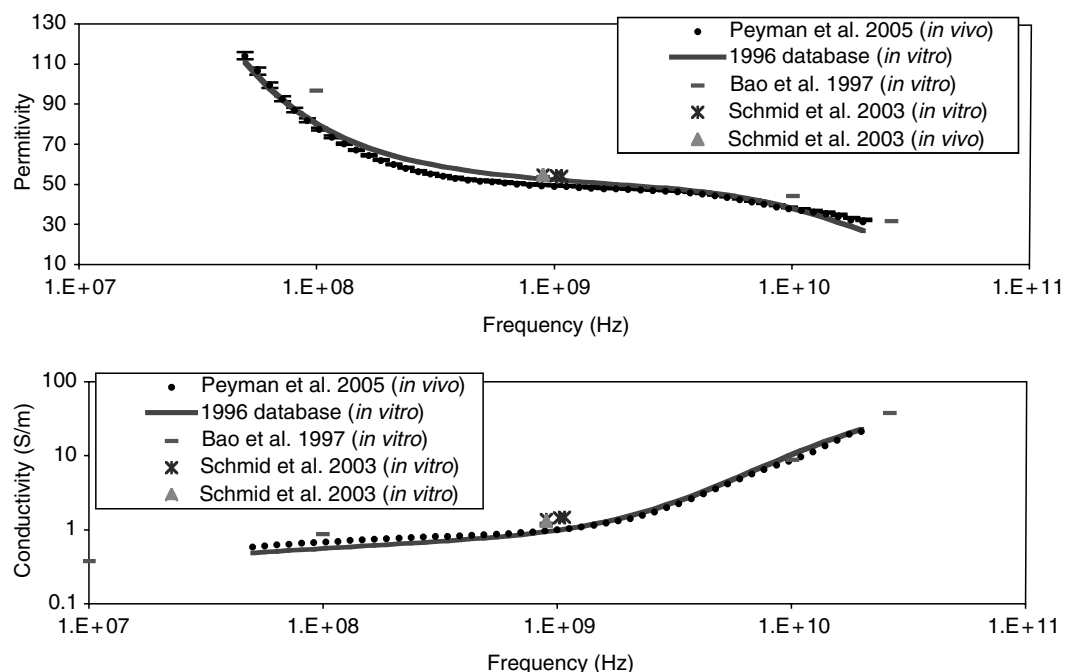


FIGURE 3.18

Dielectric properties of gray matter at 37°C . Data from recent studies compared to the prediction of the 1996 database.

It is inevitable, however, that one should expect their data to fall on the high side of average because of the presence of saline. Schmid et al. published data on porcine (*in vivo*) and human gray matter (*in vitro*). Their porcine gray matter data were obtained under conditions designed for the study of variation with time over a period spanning the time of death and beyond. Presumably, this is why their measurements were carried out over a narrow frequency range with the measurement probe held in position for the duration of the experiment (150 min). One might speculate that the amount of pressure used to maintain constant contact between the probe and the live brain could cause local oozing of fluid and higher conductivity values.

Conjecture apart, these data are valuable additions to the literature, but one must be cautious not to generalize on the basis of such limited data that measurement *in vitro* underestimates the dielectric properties of living tissues at microwave frequencies. Differences between tissue properties obtained *in vivo* and *in vitro* are to be expected at lower frequencies, in the range of α and β dispersions, in view of the sensitivity of their causal mechanism to the physiological state of the tissue. Differences between *in vivo* and *in vitro* data are much less likely in the frequency range of the γ dispersion, where water content is the most important determinant factor, and as recently reported by Stauffer et al. (2003), for liver tissue, and by Peyman et al. (2005), for many tissues including gray matter. Measurements *in vivo* are fraught with difficulties. For example, Burdette et al. (1986) measured the gray matter, *in vivo*, through the pia matter and directly beneath it. Of the two sets of data obtained, one is similar to that of Schmid et al., and the other is significantly lower.

In their human study, Schmid et al. measured the dielectric properties of gray matter in the frequency range of 800 MHz to 2450 MHz on 20 human brains immediately after excision. The measurements were carried out at room temperature in the range 18°C to 25°C and extrapolated to 37°C using experimentally determined thermal coefficients. Nevertheless, the dielectric properties at 900 MHz were in very good agreement with their data for porcine gray matter *in vivo*. It is understandably frustrating to realize that the bounds of uncertainty remain high when comparing data from different laboratories, even for those tissues that have been widely measured and reported.

Latikka et al. (2001) reported conductivity values at 50 kHz for gray matter (0.28 S/m), white matter (0.25 S/m), cerebrospinal fluid (1.25 S/m), and tumors (0.1 S/m to 0.43 S/m). They used a monopolar needle electrode during brain surgery on nine patients who had deep brain tumors. The technique is not geared toward making directed measurement and detecting anisotropy in the electrical properties, although those are anticipated on theoretical grounds and are known to be present in the hertz to kilohertz frequency range (Nicholson, 1965; Ranck et al., 1965; Yeldin et al., 1974; Nicholson and Freeman, 1975). Observed differences in the conductivity along and across the cellular structure were factors between 2 and 10 depending on the tissue. Clearly, this is an area of importance to electrophysiology, among other applications; it is also an area where data are scarce.

Peyman et al. (2001) reported variation in the dielectric properties of rat brain tissue as a function of age, at microwave frequencies. Their data pertained to the whole brain. The observed variation was ascribed, at least partially, to the change in the ratio of gray to white matter, which is known to occur throughout the developmental stage. In a recent study on porcine tissues (Peyman et al., 2005), they were able investigate gray and white matter separately. In this case, no variations were observed in the dielectric spectrum of gray matter, while statistically significant variations were observed in the dielectric spectrum of white matter (Figure 3.19). The observed variations are probably related to the process of myelination, which begins at birth and lasts to maturation. Similar variations were observed in the dielectric properties of the spinal cord.

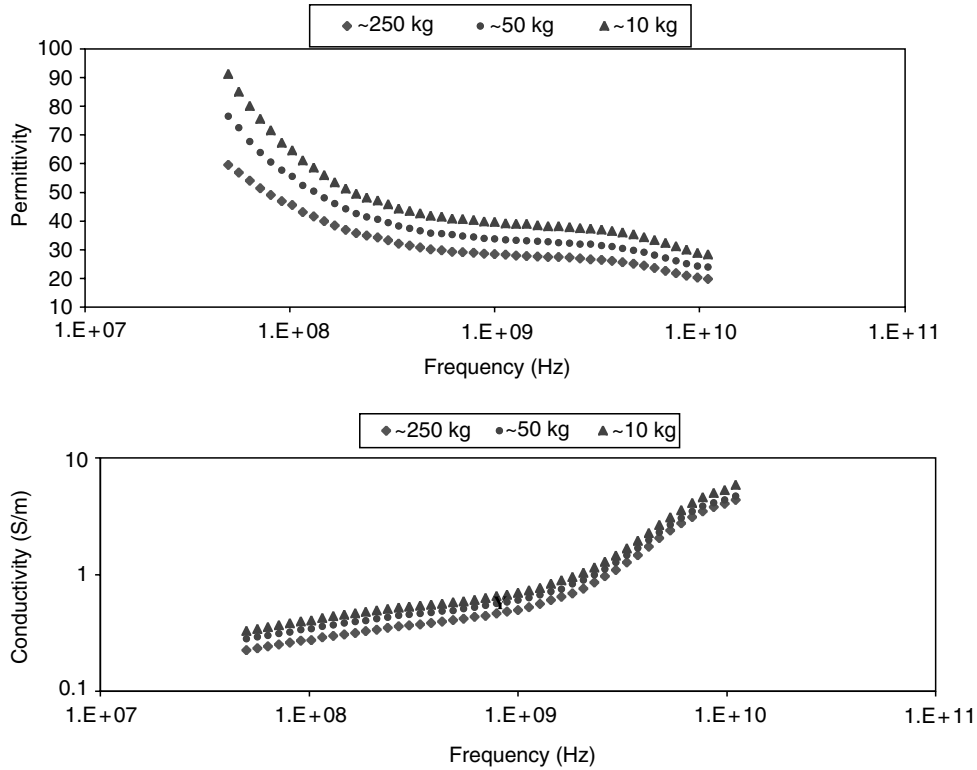


FIGURE 3.19
Permittivity and conductivity of white matter as a function of animal growth. The measurements were made *in vitro* at 37°C. The lowest permittivity and conductivity spectra pertain to a fully grown, 250-kg sow, the highest to a 10-kg piglet. (Data are from Peyman A, Holden S, Gabriel C. 2005. Dielectric Properties of Biological Tissues at Microwave Frequencies. Final technical report, MTHR Department of Health, U.K.)

3.7.2.2 Liver

Dielectric data for liver tissue were reported in several studies carried out under different conditions for a variety of reasons. For example, Riedel et al. (2003) developed a contact-free inductive measurement procedure and demonstrated the system by carrying out conductivity measurements on liver tissue between 50 and 400 kHz as a function of time after death. Stauffer et al. (2003) characterized the dielectric properties of normal and cancerous liver tissue in the frequency range of 0.3 to 3 GHz and reported higher permittivity and conductivity for tumor tissue. Chin and Sherar (2001) observed irreversible changes in the dielectric properties of liver tissue at 915 MHz because of excessive heating causing protein denaturation. Haemmerich et al. (2002) reported changes in the electrical resistivity of liver tissue during induced ischemia and postmortem. They observed increases in resistivity *in vivo* during occlusion. They analyzed the data in terms of intra- and extracellular resistance and cell membrane capacitance.

Valuable contributions by Raicu et al. (1998a,b) have provided data for rat liver tissue, measured *in vivo*, in the frequency range of 10^2 to 10^8 Hz. This is an eventful part of the dielectric spectrum of a tissue where contributions from interfacial and counterion interaction mechanisms occur. The measured data were corrected for electrode polarization and found to be in reasonable agreement with some previous studies (Surowiec et al., 1986; Foster and Schwan, 1996; Gabriel et al., 1996c). As expected, the data obtained traced a broad dielectric dispersion curve over the range of 10^3 to 10^8 Hz, suggestive of the

involvement of widely distributed relaxation times. In the second of their 1998 papers, they provide a mechanistic analysis. A simple application of the Maxwell–Wagner interfacial polarization theory could not fully explain the observed dielectric behavior, especially at frequencies below 1 MHz. The Bruggeman–Hanai-type effective medium theory (EMT) was better, but not perfect, at simulating the observation at low-frequencies. A better simulation of the effective permittivity was obtained when second-order corrections, for possible dipole–dipole interaction (DDI) effects, were introduced to the classical EMT for a concentrated suspension of particles. Application of the new EMT-DDI model enabled reasonable estimates to be made of the following: effective size and shape of hepatic cell; specific capacitance for the plasma, nuclear, and mitochondrial membranes associated with the hepatocyte; and cytosolic as well as nucleoplasmic conductivities of physiological interest.

3.7.2.3 Muscle

Muscle tissues, be it skeletal, myocardial, lingual, or other, exhibit large anisotropy in their electrical properties. This is to be expected from the tissue structure and was observed at frequencies below 1 MHz (Epstein and Foster, 1983; Fallert et al., 1993). The static conductivity value measured along the muscle fiber may be up to an order of magnitude higher than when measured across. The α dispersion is more prominent and the β dispersion less defined in the longitudinal direction in accordance with the predictions of effective permittivity modeling of elongated structures. For example, Semenov et al. (2002) evaluated anisotropy of the myocardium using a cellular model of the myocardial tissue and concluded that at frequencies lower than 10 MHz, myocardial dielectric properties are highly anisotropic (up to a factor of 10). Reliable, low-frequency data are very scarce, and there is a wide range in what is available in the literature, partly due to the fact that many authors do not specify the measurement orientation. The situation is not helped by the fact that the apparent anisotropy depends on the measurement procedure, in particular the interelectrode distance in relation to the size of the muscle fiber. Some of the problems associated with obtaining good data at frequencies below 1 MHz have been described by Tsai et al. (2000, 2002) in the context of their *in vivo* measurement of swine myocardial resistivity. In their study, they report changes in the myocardial resistivity as a function of time after death. The postmortem resistivity at 1, 10, and 100 Hz increased to about three times their original *in vivo* value and at 500 kHz and 1 MHz increased less than 15%, 6 h after death.

Most recent studies on the electrical properties of muscle tissue focused on the differences between normal and ischemic or hypoxic tissue. One of the drivers is to investigate the possibility of using *in situ* impedance measurements to map the histological changes in tissue *in vivo*. There is also potential for noninvasive imaging provided that the electrical characteristics of both normal and scar tissue are well-defined. Miyauchi et al. (1999) and Schaefer et al. (1999) observed changes in the α and β dispersions of normal and ischemic skeletal muscle. Ischemia in myocardial muscle is a matter of clinical importance in the assessment of myocardial infarction and has been the subject of many dielectric investigations. Schwartzman et al. (1999) investigated the properties of the border zone, which were found to be intermediate between healthy and infarcted tissue in the case of chronically infarcted ventricular myocardium. Semenov et al. (2002) observed the dielectric properties of canine myocardium during acute ischemia and hypoxia to explore the potential of these observations for the clinical assessment of myocardial tissue using electrical impedance and microwave tomography. One of the problems identified is the need to know and take into consideration the tissue electrical anisotropy.

3.7.2.4 Skin

Skin is the interface of the body with environmental agents including electromagnetic fields; knowledge of its dielectric properties is of importance in the assessment of human exposure and in numerous biomedical applications. Data from *in vivo* measurements are now available, obtained using noninvasive, open-ended coaxial probes (Gabriel et al., 1996c; Gabriel, 1997; Raicu et al., 2000). However, the interpretation of such topical measurements as effective permittivity of the skin is far from straightforward. Lahtinen et al. (1997) and Alanen et al. (1998) advocate an analysis based on a quasistatic approximation of the fringing field of the probe penetrating a layered structure. Gabriel (1997) drew attention to the effect on the dielectric spectrum of the degree of hydration of the stratum corneum (Figure 3.20), which also affects penetration of the field into the tissue. Joining the discussion, Raicu et al. (2000) carried out *in vivo* measurements on dry skin and on skin moistened with physiological saline, in the frequency range of 100 Hz to 100 MHz. They analyzed the data using the dispersion model comprising a Debye-type and “universal” responses (Equation 3.53) and a conductivity term. Comparing the parameters of the model for dry and saline-moistened skin, they noted a fivefold increase in the dispersion magnitude. One possible explanation they provide is that the “effective penetration depth” increases and contributions from the innermost skin layers become evident. This statement appears paradoxical; in fact, it is due to the reduction in the layering effect; when moistened, the skin appears more homogenous and behaves like a high water content tissue.

Raicu et al. (2000) further speculate that an interfacial polarization originating from the stratum corneum–epidermis interface occurs in the case of dry skin, as suggested by Alanen et al. (1999), but not in that of the saline-moistened skin. In support of this argument, they refer to the change in one of the distribution parameters, β , which decreases from 0.152 to 0.076 after the skin is hydrated with aqueous NaCl solution. It therefore appears that topical measurement on dry (normal) skin *in vivo* may not be proportionately representative of the inner layers. On the other hand, the use of an aqueous coupling agent that is likely to hydrate the stratum corneum affects the results of the measurements. In practice, the use of a coupling agent gives more reproducible results and leads to better agreement between data from the recent literature, as is evident in Figure 3.21 through Figure 3.23, which contain such data (Gabriel, 1997; Ghodgaonkar et al., 2000; Raicu et al., 2000; Sunaga et al., 2002; Hwang et al., 2003; Petaja et al., 2003) and collectively cover the frequency range of 100 Hz to 100 GHz.

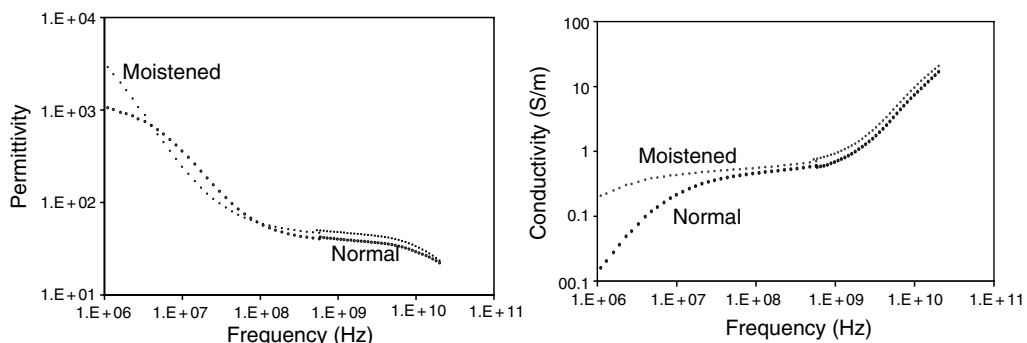


FIGURE 3.20

Permittivity and conductivity of skin (ventral forearm) illustrating the effect of moistening the skin on the dielectric spectra (Gabriel, 1996).

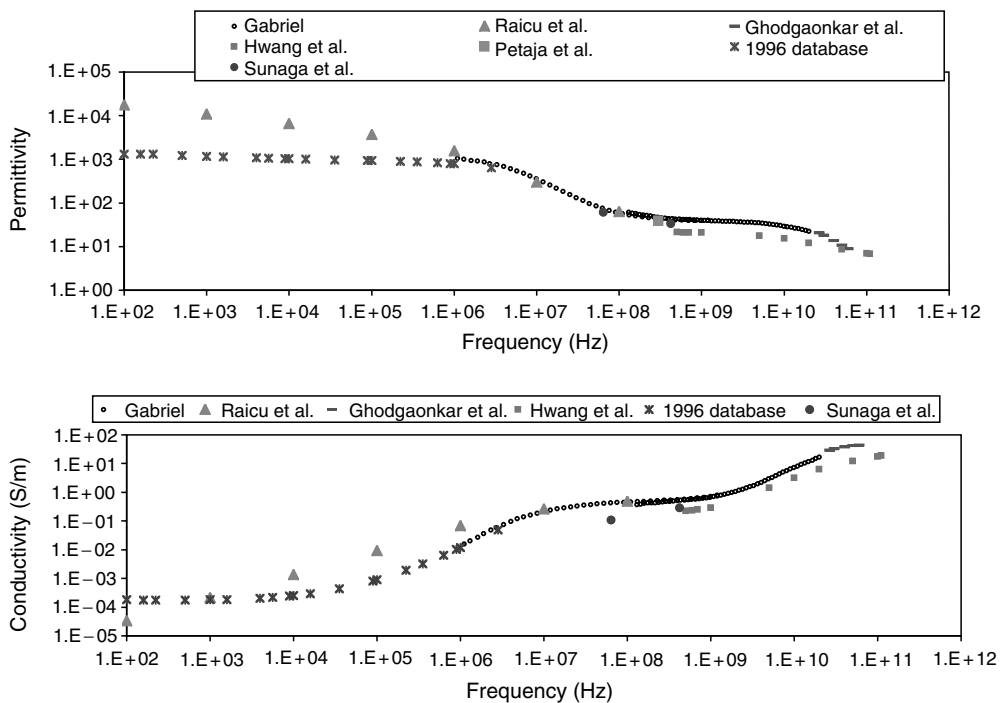


FIGURE 3.21

Permittivity and conductivity of skin (different parts of the body, excluding palms and soles). No moistening or contact gel was used. Different measurement techniques were used including open-ended coaxial probes of vastly different sizes.

The dielectric properties of skin have been widely investigated as monitors of various pathological conditions. Hayashi et al. (2005) investigated the dielectric properties of human skin *in vivo* at frequencies up to 10 GHz to monitor the progress of the healing process of skin burns using water content as the determinant factor. Their measurement technique, time domain spectroscopy and open-ended probe, is similar to that used by

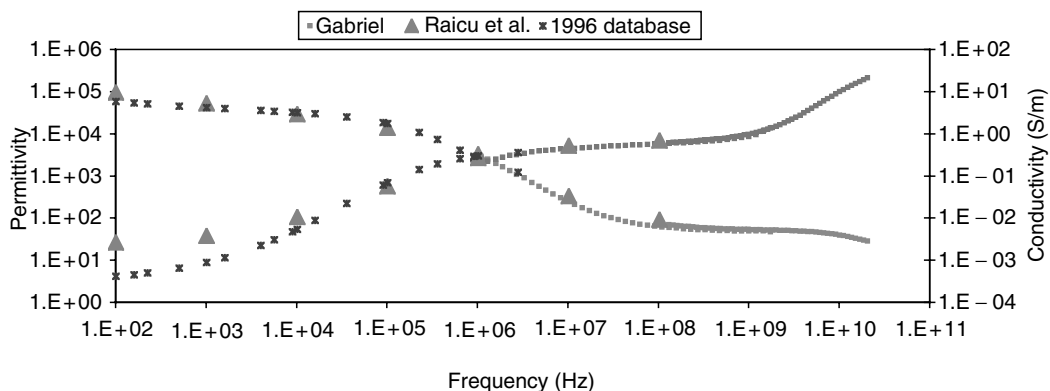


FIGURE 3.22

Permittivity and conductivity of skin (Raicu et al.: back of neck, moistened with physiological saline; Gabriel and database: ventral forearm, moistened with water). Open-ended coaxial probes of vastly different sizes were used.

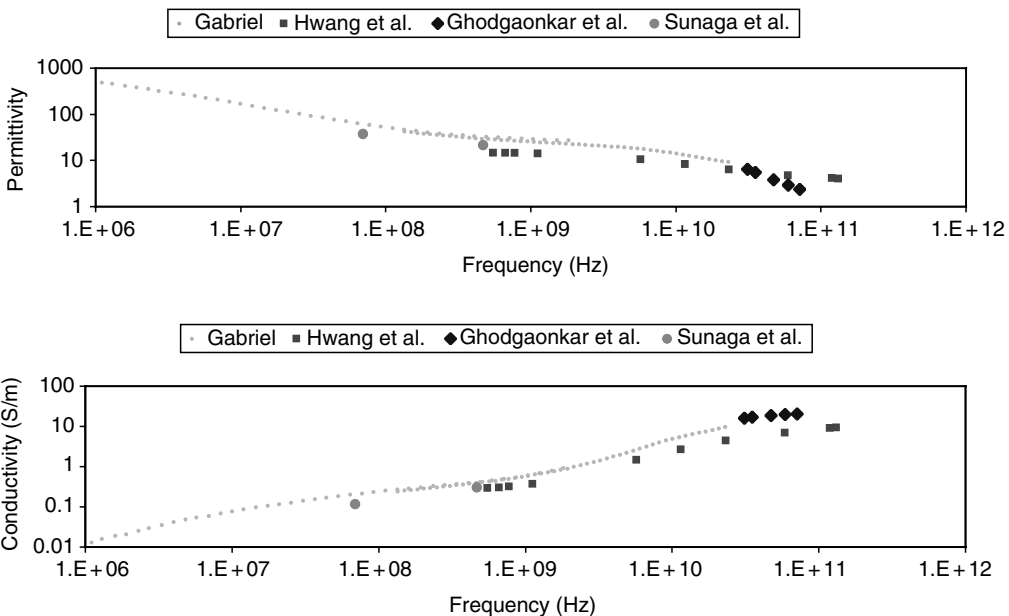


FIGURE 3.23
Permittivity and conductivity of palm, from recent studies.

Gabriel et al. (1997), who reported the dielectric spectra of normal and wounded tissue and ascribed the differences to water content.

Petaja et al. (2003) attempted to correlate the dielectric properties of skin at 300 MHz to body fluid changes after cardiac surgery and report limited success. Sunaga et al. (2002) investigated the variability in the dielectric properties of human skin of healthy volunteers, collagen disease patients, and dialysis patients over the frequency range of 1 to 450 MHz. No significant difference was detected in the dielectric properties among the three groups; some regional (abdomen, thigh, and forearm) dependence was observed. Marzec et al. (1999) measured the conductance and susceptance of soles and calves in leg skin from healthy controls and patients with ischemia in the frequency range of 100 Hz to 100 kHz. Ischemia was found to have no effect on the admittance at frequencies lower than 10 kHz, where the effect of the stratum corneum is dominant. Observed differences at frequencies in excess of 10 kHz are ascribed to ischemia in the underlying skin tissue.

Lindholm-Sethson et al. (1998) investigated the potential of using noninvasive skin impedance spectroscopy for the early detection of diabetic changes. They implemented a multivariate data analysis procedure to demonstrate how a regression model between the skin impedance and other diagnostic data for diabetic and control groups can be developed into a novel diagnostic tool for the early discovery of possible complications in diabetic patients. Statistical procedures are increasingly being applied to correlate dielectric parameters to structural or compositional elements of biological material, particularly in cases where there is a physical mechanism underpinning the effect that is obscured by noisy data (Kent et al., 2002).

The use of dielectric spectroscopy to monitor damage to the skin caused by ionizing radiation is an active field of research aiming at monitoring the side effects of clinical radiotherapy objectively and quantitatively. It appears that the changes to the skin during

the acute stage cause both permittivity and conductivity to decrease (Tamura et al., 1994; Nuutinen et al., 1998), while the reverse happens when radiation-induced fibrosis finally sets in (Lahtinen et al., 1999). The initial decrease in permittivity, which also means a decrease in skin water, may be due to damage to skin capillaries resulting in swelling of the cytoplasm, with narrowing or occlusion of capillaries and a reduction in the effective microcirculation of the skin. In the long term, an increase in collagen and collagen-bound water is a likely explanation for the observed increase in the permittivity in line with a clinical indicator of subcutaneous fibrosis (Nuntineu, 1998).

3.7.2.5 Bone

Peyman et al. (2001) observed variation in the dielectric properties of rat skull bone as a function of developmental stage from neonate to 70 days old. They reported lower permittivity and conductivity values across the spectrum (100 MHz to 20 GHz). Similar results were recently reported for porcine skull, cortical bone, and bone marrow (Peyman et al., 2005).

3.7.2.6 Dielectric Properties of Cancerous Tissue

The pathological differences between normal and cancerous cells affect their composition and morphology and shape their dielectric spectrum. Interest in this field of study is driven by biomedical applications where such differences can be exploited for the treatment or diagnosis of cancer. Most of the clinical applications are based on hyperthermia, whereby electromagnetic energy is preferentially applied to the cancerous tissue, usually as an adjunct to radiotherapy. Electromagnetic hyperthermia was an active field of study in the 1980s, and it remains the domain of specialist medical centers. In contrast, there is a growing interest in applications geared toward the detection of cancerous regions using three-dimensional microwave tomography procedures and signal analysis (Hagness et al., 1998, 1999; Bulyshev et al., 2001; Wersebe et al., 2002). In cases where the suspect region is accessible for dielectric measurements, the procedure relies on the characterization and comparative analysis of the dielectric spectrum (Walker et al., 2000). The ultimate goal is to detect changes at the precancerous stage prior to their visibility by x-rays and to the emergence of serious clinical symptoms.

There is evidence that tumors have higher water content than the corresponding normal tissue; for certain types of tumor, such as breast carcinoma surrounded by fatty tissue, the difference could be considerable. In terms of dielectric properties, one would expect cancerous tissue to have higher permittivity and conductivity at microwave frequencies compared to normal tissue, as observed and reported by Schepps and Foster (1980), Foster and Schepps (1981), Rogers et al. (1983), and more recently, Stauffer et al. (2003).

Morphological changes affect the dielectric properties in the frequency range of the β dispersion and can be quite significant (Smith et al., 1986). Walker et al. (2000) used a finite element analysis to model the differences in impedance between normal and precancerous cervical cells in the frequency range of 100 Hz to 10 MHz. Their results showed significant differences at frequencies lower than 10 kHz, basically in line with measurements carried out *in situ* with a four-electrode pencil probe. Polevaya et al. (1999) used time domain dielectric spectroscopy to study the differences between normal and malignant white blood cells. They used a Maxwell–Wagner mixture formulation and a double-shell cell model to determine differences in cellular and nuclear membrane characteristics between normal and malignant cells. Their detailed analysis reflects on some functional differences between membranes and provides some insight into the etiology of cancer.

The use of the electrical characteristics of tissue to understand, image, or treat cancerous tissue relies on the availability of good representative data across the spectrum but particularly in the frequency range of the β dispersion, where the changes are specific to the cellular transformation as well as the water content.

3.7.2.7 Conductivity of Tissue at Low-Frequency

There are limited, reliable dielectric data for body tissue at frequencies below 100 kHz. Some of the reasons relate to the dependence of the dielectric properties on the physiological state, degree of perfusion, time after death, and other biological parameters. There are also experimental difficulties, in particular electrode polarization, which is a major source of systematic error at frequencies below 100 Hz, even when precautions are taken to minimize its effects. Based on typical tissue dielectric data and a simple model for the electrode polarization, it is possible to estimate that it affects the permittivity more than the conductivity and that for body tissue, the conductive rather than the capacitive component dominates its electrical admittance (Schwan, 1992). For this reason, at extremely low-frequencies, the conductivity of tissue is considered real rather than complex, and the body is modeled as a resistive network the parameters of which are determined by the conductivity of the various tissues.

The conductivity of body tissue can be estimated by modeling on a cellular scale and applying appropriate mixture equations. Using this approach, Peters et al. (2001) evaluated the effective conductivity of several tissues such as cerebral cortex, liver, and blood. Such studies help to place upper and lower bounds on the conductivity values based on cellular parameters and knowledge of the conductivity of the phases.

Faes et al. (1999) carried out a meta-analysis of review studies (Geddes and Baker, 1967; Stuchly and Stuchly, 1980; Duck, 1990; Gabriel et al., 1996a,b) of tissue conductivity in the frequency range 100 Hz to 10 MHz. To make relative comparisons between different tissues, they calculated the mean and 95% confidence interval. They found large confidence intervals such that the conductivities of most high water content tissues (skeletal and cardiac muscle, kidney, liver, lung, and spleen) were not statistically different from one another at that level of significance. In contrast, blood has higher conductivity, while bone and fat have demonstrably lower conductivities. The insignificance of differences in high water content tissues could, of course, imply an equality of their conductivities, but it could also point at a large source of experimental variation that obscures real differences.

The conductivity of the body, or body parts, can be obtained by volume averaging using anatomical models and individual tissue conductivity as in Table 3.4, where the conductivity of the whole and the various parts of the body is given based on tissue conductivity in Gabriel (2000) and a voxel anatomical human model (Dimbylow, 1996).

At 50 Hz, the calculated conductivity values are comparable to the commonly used estimate of 0.2 S/m for the effective permittivity of a homogenous body model. When dielectric data become available, it would become imperative to reexamine the whole

TABLE 3.4

Conductivity (in S/m) of the Whole and Parts of the Body Obtained by Volume Averaging

Frequency	Whole Body	Head	Torso	Arm	Leg	Neck
50 Hz	0.22	0.25	0.22	0.19	0.20	—
10 kHz	0.28	0.28	0.26	—	0.24	0.22
100 kHz	0.29	0.30	0.33	—	0.24	0.24

Source: From Gabriel (2000).

question of whether or not there is sufficient justification for neglecting the contribution of the capacitive element of the body's electrical properties.

3.7.2.8 Nonlinear Dielectric Properties

The polarization mechanisms discussed so far occur from interactions with weak fields eliciting linear responses. At high field strength, nonlinear molecular and cellular polarization phenomena are predicted on theoretical grounds, on the basis of induced dipolar properties and classical electrodynamics. The threshold for initiating such effects is system and frequency dependent. As a general rule, as the frequency increases, so does the field level required to cause an effect. In general, at frequencies below the manifestation of the β dispersion, field strengths of the order of 10^6 V/m may be capable of initiating polarization mechanisms that affect the cellular function; higher fields may cause dielectric breakdown within the membrane, ultimately leading to cell destruction.

Under controlled conditions, high field strength, nonlinear effects are the focus of numerous applications in biotechnology. For example, dielectrophoresis, or the motion of particles caused by electrical polarization effects in nonuniform fields, is used to separate and manipulate cells. For a review of this subject, see Pethig (1996). Another nonlinear phenomenon, electroporation, is a consequence of the electrical breakdown of biological membranes, resulting in the formation of pores and a significant increase in the membrane permeability to external ions and molecules. Under controlled conditions, electroporation could be reversible and used to advantage in therapeutic, drug delivery applications. The basic principles can be found in mechanistic studies by Pickett and Weaver (1996), Prausnitz et al. (1999), and many others.

The hypothesis that weak fields may trigger nonlinear effects in cells has been investigated in theory and practice (Weaver and Astumian, 1990; Woodward and Kell, 1990). The generation of harmonics is one aspect that can be used to monitor their occurrence (Woodward and Kell, 1990); it also means that the dielectric properties are nonlinear, responding to harmonics as well as to the fundamental frequency. The study of harmonics is a subtle and clever tool; it has yet to prove its effectiveness in monitoring physiological responses to weak fields.

More recently, Balzano (2002) proposed to use a similar approach to test whether biological cells exhibit nonlinear responses to weak fields, at microwave frequencies. His idea hinges on the possibility of detecting a microwave signal at 1.8 GHz (second harmonic of 900 MHz) as weak as one microwave photon per cell per second. An experimental project based on this hypothesis is currently under way (see MTHR Web site: http://www.mthr.org.uk/research_projects/HO_funded_projects_excell.htm, accessed August 5, 2005). It will help to clarify the issue of nonlinear dielectric properties.

References

- Alanen E, Lahtinen T, Nuutinen J. 1998. Variational formulation of open-ended coaxial line in contact with layered biological medium. *IEEE Trans Biomed Eng* 45(10): 1241–1248.
- Alanen E, Lahtinen T, Nuutinen J. 1999. Penetration of electromagnetic fields of an open-ended coaxial probe between 1 MHz and 1 GHz in dielectric skin measurements. *Phys Med Biol* 44: N169–N176.

- Balzano Q. 2002. Proposed test for detecting nonlinear responses in biological preparations exposed to RF energy. *Bioelectromagnetics* 23(4): 278–287.
- Bao JZ, Lu ST, Hurt WD. 1997. Complex dielectric measurements and analysis of brain tissues in the radio and microwave frequencies. *IEEE Trans Microwave Theory Tech MTT* 45(10): 1730–1741.
- Barthel J, Buchner R, Munsterer M. 1995. The dielectric properties of water in aqueous electrolyte solutions. In: *Chemistry Data Series 12*, Kreysa G, Ed., DECHEMA, Frankfurt.
- Bateman JB, Gabriel C. 1987. Dielectric properties of aqueous glycerol and a model relating these to the properties of water. *J Chem Soc Faraday Trans 2*(83): 355–369.
- Bateman JB, Gabriel C, Grant EH. 1990. Permittivity at 70 GHz of water in aqueous solutions of some amino acids and related compounds. *J Chem Soc Faraday Trans 2*(86): 3577–3583.
- Bateman JB, Evans GF, Brown PR, Gabriel C, Grant EH. 1992. Dielectric properties of the system bovine albumin: urea: betaine in aqueous solutions. *Phys Med Biol* 37: 175.
- Bergman DJ. 1978. The dielectric constant of a composite material. *Phys Rep* C43: 377.
- Bianco B, Giordano S. 2003. Electrical characterization of linear and nonlinear random networks and mixtures. *Int J Circ Theor Appl* 31: 199–218.
- Bianco B, Chiabrera A, Giordano S. 2000. DC-ELF characterization of random mixtures of piecewise nonlinear media. *Bioelectromagnetics* 21: 145–149.
- Böttcher CJF, Bordewijk P. 1978. *Theory of Electric Polarization*. Elsevier, Amsterdam.
- Buchner R, Hefter GT, May PM. 1998. Dielectric relaxation of aqueous NaCl solutions. *J Phys Chem A* 103: 1–9.
- Buckmaster HA. 1990. Precision microwave complex permittivity measurements of high loss liquids. *J Electromagn Waves Appl* 4: 645–656.
- Bull HB, Breese K. 1969. Electrical conductance of protein solutions. *J Colloid Interface Sci* 29: 492.
- Bulyshev AE, Semenov SY, Souvorov AE, Svenson RH, Nazarov AG, Sizov YE, Tatsis GP. 2001. Computational modeling of three dimensional microwave tomography of breast cancer. *IEEE Trans Biomed Eng* 48(9): 1053–1056.
- Burdette EC, Friederich PG, Seaman RL, Larsen LE. 1986. *In situ* permittivity of canine brain: regional variations and postmortem changes. *IEEE Trans Microwave Theory Tech MTT* 34(1): 38–49.
- Chin L, Sherar M. 2001. Changes in dielectric properties of *ex vivo* bovine liver at 915 MHz during heating. *Phys Med Biol* 46: 197–211.
- Cole KS. 1972. *Membrane, Ions and Impulses*. University of California Press, Berkeley.
- Cole KS, Cole RH. 1941. Dispersion and absorption in dielectrics. I. Alternating current characteristics. *J Chem Phys* 9: 341–351.
- Craig DQM. 1995. *Dielectric Analysis of Pharmaceutical Systems*. Taylor & Francis, London.
- Davidson DW, Cole RH. 1951. Dielectric relaxation in glycerol, propylene glycol and *n*-propanol. *J Chem Phys* 19: 1484–1490.
- Debye, P., Polar Molecules, Dover, Mincola, N.Y., 1929.
- Dimbylow PJ. 1996. The development of realistic voxel phantoms for electromagnetic field dosimetry. In: *Proceedings of an International Workshop on Voxel Phantom Development*, National Radiological Protection Board, Chilton, U.K., 1–7.
- Dissado LA. 1990. A fractal interpretation of the dielectric response of animal tissues. *Phys Med Biol* 35(11): 1487–1503.
- Dissado LA, Hill RM. 1989. The fractal nature of the cluster model dielectric response functions. *J Appl Phys* 66(6): 2511–2524.
- Dobson J, Grassi P. 1996. Magnetic properties of human hippocampal tissue: evaluation of artefact and contamination sources. *Brain Res Bull* 39: 255–259.
- Duck FA. 1990. *Physical Properties of Tissue: A Comprehensive Reference Book*. Academic Press, London.
- Dukhin SS. 1971. Dielectric properties of disperse systems. *Surface Colloid Sci* 3: 83.
- Dukhin SS, Shilov VN. 1974. *Dielectric Phenomena and the Double Layer in Disperse Systems*. John Wiley & Sons, New York.
- Ellison WJ, Lamkaouchi K, Moreau J. 1996. Water: a dielectric reference. *J Mol Liq* 68: 171–279.
- Epstein BR, Foster KR. 1983. Anisotropy in the dielectric properties of skeletal muscle. *Med Biol Eng Comput* 21: 51–55.

- Faes TJC, Meij HA, Munk JC, Heethaar RM. 1999. The electric resistivity of human tissues (100 Hz–10 MHz) a meta-analysis of review studies. *Physiol Meas* 20: R1–R10.
- Fallert MA, Mirotznik MS, Bogen DK, Savage EB, Foster KR, Josephson ME. 1993. Myocardial electrical impedance mapping of ischemic sheep hearts and healing aneurisms. *Circulation* 87: 188.
- Fixman M. 1980. Charged macromolecules in external fields. 1. The sphere. *J Chem Phys* 72: 5177.
- Fixman M. 1983. Thin double layer approximation for electrophoresis and dielectric response. *J Chem Phys* 78: 1483.
- Foster KR. 2002. Herman P. Schwan: a scientist and pioneer in biomedical engineering. *Annu Rev Biomed Eng* 4: 1–27.
- Foster KR, Schepps JL. 1981. Dielectric properties of tumor and normal tissues at RF through microwave frequencies. *J Microwave Power* 16(2): 107–119.
- Foster KR, Schwan HP. 1989. Dielectric properties of tissues and biological materials: a critical review. *Crit Rev Biomed Eng* 17(1): 25–104.
- Foster KR, Schwan HP. 1996. Dielectric properties of tissues. In: *CRC Handbook of Biological Effects of Electromagnetic Fields*, Polk C, Postow E, Ed., CRC Press, Boca Raton, FL pp. 25–101.
- Fricke HA. 1955. A mathematical treatement of the electric conductivity and capacity of disperse systems. II. The capacity of a suspension of conducting spheroids surrounded by a nonconducting membrane for a current of low frequency. *Phys Rev* 26: 678.
- Fröhlich H. 1955. *Theory of Dielectrics*. Oxford University Press, Oxford.
- Gabriel C. 1997. Comments on “Dielectric properties of the skin.” *Phys Med Biol* 42: 1671–1674.
- Gabriel C. and Gabriel S. 1997. <http://www.brooks.af.mil/AFRL/HED/hedr/reports/dielectric/Report/Report.html>
- Gabriel C, Bentall RH, Grant EH. 1987. Comparison of the dielectric properties of normal and wounded human skin material. *Bioelectromagnetics* 8: 23–28.
- Gabriel C, Gabriel S, Corthout E. 1996a. The dielectric properties of biological tissues: I. Literature survey. *Phys Med Biol* 41: 2231–2249.
- Gabriel S, Lau RW, Gabriel C. 1996b. The dielectric properties of biological tissues: II. Measurements in the frequency range of 10 Hz to 20 GHz. *Phys Med Biol* 41: 2251–2269.
- Gabriel S, Lau RW, Gabriel C. 1996c. The dielectric properties of biological tissues: III. Parametric models for the dielectric spectrum of tissues. *Phys Med Biol* 41: 2271–2293.
- Gabriel C, Sheppard RJ, Grant EH. 1983. Dielectric properties of ocular tissues at 37°C. *Phys Med Biol* 28: 43–49.
- Gabriel C., 2000. The dielectric properties of tissues. In: Radiofrequency radiation dosimetry and its relationship to the biological effects of electromagnetic fields. Editors: Klaeugerg BJ and Miklavic D. Nato science series. *High Technology* (82): 75–84.
- Geddes LA, Barker LE. 1967. The specific resistance of biological material—a compendium of data for the biomedical engineer and physiologist. *Med Biol Eng* 5: 271–293.
- Ghodgaonkar DK, Gandhi Om P, Iskander MF. 2000. Complex permittivity of human skin *in-vivo* in the frequency band 26.5–60 GHz. *IEEE Antennas and Propagation Society Symposium Proceedings*, Salt Lake City, UT, USA, July 16–20, 2000, Vol. 2, pp. 1100–1103.
- Gimsa J, Wachner D. 1998. A unified resistor–capacitor model for impedance, dielectrophoresis, electrorotation, and induced transmembrane potential. *Biophys J* 75: 1107–1116.
- Gimsa J, Wachner D. 1999. A polarization model overcoming the geometric restrictions of the Laplace solution for spheroidal cells: obtaining new equations for field-induced forces and transmembrane potential. *Biophys J* 77: 1316–1326.
- Gimsa J, Wachner D. 2001a. Analytical description of the transmembrane voltage induced on arbitrarily oriented ellipsoidal and cylindrical cells. *Biophys J* 81: 1888–1896.
- Gimsa J, Wachner D. 2001b. On the analytical description of transmembrane voltage induced on spheroidal cells with zero membrane conductance. *Eur Biophys J* 30: 463–466.
- Grant E, Shack R. 1967. Complex permittivity measurements at 8.6 mm wavelength over the temperature range 1–60 degrees centigrade. *Br J Appl Phys* 18: 1807–1814.
- Grant EH, Sheppard RJ. 1974a. Dielectric relaxation in water in the neighbourhood of 4°C. *J Chem Phys* 60: 1792–1796.

- Grant E, Buchanan T, Cook H. 1957. Dielectric behaviour of water at microwave frequencies. *J Chem Phys* 26: 156–161.
- Grant EH, Sheppard RJ, South GP. 1978. *Dielectric Behaviour of Biological Molecules in Solution*. Clarendon Press, Oxford.
- Grant EH, Szwarnowski S, Sheppard RJ. 1981. Dielectric properties of water in the microwave and infrared regions. In: *Biological Effects of Nonionising Radiation*, Illinger KH, Ed., American Chemical Society Symposium Series, Washington, DC, 157: 47–56.
- Grant EH, McLean VER, Nightingale NRV and Gabriel C. 1984. Dielectric properties of water in biological solutions. In: *Interaction between Electromagnetic Fields and Cells*, Plessum Press, Newyork and London. Chiabrera A, Nicolini C, Schwan HP, Eds., NATO ASI Series, 97: 65–74.
- Greffé JL, Grosse C. 1992. Static permittivity of emulsions. *Prog Electromagn Res* 41.
- Grimnes S, Martinsen ØG, Eds. 2000. *Bioimpedance and Bioelectricity*. Academic Press, New York.
- Grosse C. 1988. Permittivity of a suspension of charged spherical particles in electrolyte solution. II. Influence of the surface conductivity and asymmetry of the electrolyte on the low and high frequency relaxations. *J Phys Chem* 92: 3905–3910.
- Grosse C, Foster KR. 1987. Permittivity of a suspension of charged spherical particle in electrolyte solution. *J Phys Chem* 91: 3073.
- Haggis GH, Hasted JB, Buchanan TJ. 1952. The dielectric properties of water in solutions. *J Chem Phys* 20: 1452–1465.
- Hagness SC, Taflove A, Bridges JE. 1998. Two-dimensional FDTD analysis of a pulsed microwave confocal system for breast cancer detection: fixed-focus and antenna-array sensors. *IEEE Trans Biomed Eng* 45(12): 1470–1479.
- Hagness SC, Taflove A, Bridges JE. 1999. Three-dimensional FDTD analysis of a pulsed microwave confocal system for breast cancer detection: design of an antenna-array element. *IEEE Trans Antennas Propagat* 47(5): 783–791.
- Hammerich D, Ozkan OR, Tsai JZ, Staelin ST, Tungjirkusolmun S, Mahvi DM, Webster JG. 2002. Changes in electrical resistivity of swine liver after occlusion and postmortem. *Med Biol Eng Comput* 40: 29–33.
- Hanai T, Imakita T, Koizumi N. 1982. Analysis of dielectric relaxations of w/o emulsions in the light of theories of interfacial polarization. *Colloid Polym Sci* 260(11): 1029.
- Hasted JB, El Sabeh. 1953. The dielectric properties of water in solutions. *Trans Faraday Soc* 49: 1003–1011.
- Hasted JB, Husain SK, Frescura FAM, Birch JR. 1985. Far-infrared absorption in liquid water. *Chem Phys Lett* 118(6): 622–625.
- Havriliak SJ, Negami S. 1966. A complete plane analysis of dispersion in some polymer systems. *J Polym Sci Polym Symp* 6: 99–117.
- Hayashi Y, Miura N, Shinyashiki N, Yagihara S. 2005. Free water content and monitoring of healing processes of skin burns studied by microwave dielectric spectroscopy *in vivo*. *Phys Med Biol* 50: 599–612.
- Hill NE, Vaughan WE, Price AH, Davies M. 1969. *Dielectric Properties and Molecular Behaviour*. Van Nostrand, London.
- Hill RM, Jonscher AK. 1983. The dielectric behaviour of condensed matter and its many-body interpretation. *Contemp Phys* 24(1): 75–110.
- Hwang H, Yim J, Cho J, Cheon C, Kwon Y. 2003. 110 GHz broadband measurement of permittivity on human epidermis using 1 mm coaxial probe. *IEEE MTT S Digest* 399–402.
- Irimajiri A, Suzuki T, Asami K, Hanai T. 1991. Dielectric modeling of biological cells. Models and algorithm. *Bull Inst Chem Res Kyoto Univ* 69(4): 421–438.
- Ishikawa A, Hanai T, Koizumi N. 1982. Dielectric properties of dextran gel Sephadex G-25 dispersed in aqueous phases. *Jpn J Appl Phys* 21(12): 1762.
- Jonscher AK. 1983. *Dielectric Relaxation in Solids*. Chelsea Dielectrics Press, London.
- Kaatze U. 1986. The dielectric spectrum of water in the microwave and near-millimetre wavelength region. *Chem Phys Lett* 132(3): 291–293.
- Kaatze U. 1988. Complex permittivity of water as a function of frequency and temperature. *J Chem Eng* 34: 371–374.
- Kaatze U. 1989. Complex permittivity of water as function of frequency and temperature. *J Chem Eng Data* 34: 371–374.

- Kaatze U. 1990. On the existence of bound water in biological systems as probed by dielectric spectroscopy. *Phys Med Biol* 35(12): 1663–1681.
- Kaatze U, Giese K. 1980. Dielectric relaxation spectroscopy of liquids: frequency domain and time domain experimental methods. *J Phys E: Sci Instrum* 13: 133–141.
- Kent M, Peyman A, Gabriel C, Knight A. 2002. Determination of added water in pork products using microwave dielectric spectroscopy. *Food Control* 13: 43–149.
- Kirkwood JG, 1936. On the Theory of Dielectric Polarization, *J Chem Phys-Vol 4(9)*, 592–601.
- Lahtinen T, Nuutinen J, Alanen E. 1997. Dielectric properties of the skin. *Phys Med Biol* 42: 1471–1472.
- Lahtineu T, Nuntineu J, Alanen E, Turunen M, Nuortio L, Usenius T, Hopewell JW: Quantitative assessment of protein content in irradiated human skin. *Int J Radiat Oncol Biol Phys* 43: 635–638, 1999.
- Lane JA, Saxton, JA. 1952. Dielectric dispersion in pure polar liquids at very high radio frequencies. *Proc R Soc Lond* 213: 400–408.
- Latikka J, Kuurne T, Skola H. 2001. Conductivity of living intracranial tissues. *Phys Med Biol* 46: 1611–1616.
- Liebe HJ, Hufford GA, Manabe T. 1991. A model for the complex permittivity of water at frequencies below 1 THz. *Int J Infrared Millimeter Waves* 12: 659–660.
- Lindholm-Setson B, Han S, Ollmar S, Nicander I, Jonsson G, Lithner F, Bertheim U, Geladi P. 1998. Multivariate analysis of skin impedance data in long term type 1 diabetic patients. *Chemom Intell Lab Syst* 44: 381–394.
- Mandel M, Odijk T. 1984. Dielectric properties of polyelectrolyte solutions. *Annu Rev Phys Chem* 35: 75.
- Marzec E, Wachal K. 1999. The electrical properties of leg skin in normal individuals and in-patients with ischemia. *Bioelectrochem Bioenerg* 49: 73–75.
- Maxwell JC. 1891. *A Treatise on Electricity and Magnetism*, 2nd ed., Vol. 1, chap. IX. Clarendon Press, Oxford.
- Milton GW. 2002. *Theory of Composites*, Cambridge University Press, Cambridge.
- Miyauchi T, Hirose H, Sasaki E, Hayashi M, Mori Y, Murakawa S, Takagi H, Yasuda H, Kumada Y, Iwata H. 1999. Predictability of dielectric properties for ischemic injury of the skeletal muscle before reperfusion. *J Surg Res* 86: 79–88.
- Munoz San Martín S, Sebastian JL, Sancho M, Miranda JM. 2003. A study of the electric field distribution in erythrocyte and rod shape cells from direct RF exposure. *Phys Med Biol* 48: 1649–1659.
- Nicholson PW. 1965. Specific impedance of cerebral white matter. *Exp Neurol* 13: 386–401.
- Nicholson C, Freeman JA. 1975. Theory of current source-density: analysis and determination of conductivity tensor for anuran cerebellum. *Neurophysiol* 38: 356–368.
- Nuutinen J, Lahtinen T, Turunen M, Alanen E, Tenhunen M, Usenius T, Kolle R. 1998. A dielectric method for measuring early and late reactions in irradiated human skin. *Radiother Oncol* 47: 249–254.
- Onsager L, 1936. Electric Moments of Molecules in Liquids *J. Am. Chem. Soc.* 58, 1486–1493.
- Pauly H, Schwan HP. 1966. Dielectric properties and ion mobility in electrocytes. *Biophys J* 6: 621.
- Petaja L, Nuutinen J, Uusaro A, Lahtinen T, Ruokonen E. 2003. Dielectric constant of skin and subcutaneous fat to assess fluid changes after cardiac surgery. *Physiol Meas* 24: 383–390.
- Peters MJ, Stinstra JG, Hendriks M. 2001. Estimation of the electrical conductivity of human tissue. *Electromagnetics* 21: 545–557.
- Pethig R. 1979. *Dielectric and Electronic Properties of Biological Materials*. John Wiley & Sons, New York.
- Pethig R, Kell DB. 1987. The passive electrical properties of biological systems: their significance in physiology, biophysics, and biotechnology. *Phys Med Biol* 32(8): 933–970.
- Pethig R. 1996. Dielectrophoresis: using inhomogeneous AC electrical fields to separate and manipulate cells. *Critical Reviews in Biotechnology* 16(4): 331–348.
- Peyman A, Rezazadeh AA, Gabriel C. 2001. Changes in the dielectric properties of rat tissue as a function of age at microwave frequencies. *Phys Med Biol* 46: 1617–1629.
- Peyman A, Holden S, Gabriel C. 2005. Dielectric Properties of Biological Tissues at Microwave Frequencies. Final technical report, MTHR Department of Health, U.K.

- Polevaya Y, Erunolina I, Schlesinger M, Ginzburg BZ, Feldman Y. 1999. Time domain dielectric spectroscopy study of human cells II. Normal and malignant white blood cells. *Biochim Biophysica Acta* 1419: 257–271.
- Prausnitz MR, Pliquett U and Vanbever R (1999) Mechanistic studies of skin electroporation using biophysical methods in Electrically Mediated Delivery of Molecules to cells – Electrochemotherapy, Electrogenetherapy, and Transdermal Delivery by Electroporation, MJ Jaroszeski, R Gilbert, and R Heller, eds., Humana Press, Totowa, NJ, pp. 214–235.
- Raicu 1999. Dielectric dispersion of biological matter: model combining Debye-type and “universal” response. *Phys Rev E* 60(4): 4677–4680.
- Raicu V, Saibara T, Enzan H, Irimajiri A. 1998a. Dielectric properties of rat liver *in vivo*: analysis by modeling hepatocytes in the tissue architecture. *Phys Med Biol* 47: 333–342.
- Raicu V, Saibara T, Irimajiri A. 1998b. Dielectric properties of rat liver *in vivo*: a non-invasive approach using an open-ended coaxial probe at audio/radio frequencies. *Phys Med Biol* 47: 325–332.
- Raicu V, Kitagawa N, Irimajiri A. 2000. A quantitative approach to the dielectric properties of the skin. *Phys Med Biol* 45: L1–L4.
- Ranck JB, BeMent SL. 1965. The specific impedance of the dorsal columns of cat: an anisotropic medium. *Exp Neurol* 11: 451–463.
- Reynolds JA, Hough JM. 1957. Formulae for dielectric constant of mixtures. *Proc Phys Soc* 70: 769–775.
- Riedel CH, Keppelen M, Nani S, Dössel O. 2003. Postmortem conductivity measurement of liver tissue using a contact free magnetic induction sensor. *EMBC IEEE* 3126–3129.
- Rogers JA, Sheppard RJ, Grant EH. 1983. The dielectric properties of normal and tumour mouse tissue between 50 MHz and 10 GHz. *Br J Radiol* 56: 335–338.
- Roussy G, Pearce JA. 1995. *Foundations and Industrial Applications of Microwaves and Radio Frequency Fields: Physical and Chemical Processes*. Wiley Publishers, New York.
- Schaefer M, Kirlum HJ, Schlegel C, Gebhard MM. 1999. Dielectric properties of skeletal muscle during ischemia in the frequency range from 50 Hz to 200 MHz. *Ann NY Acad Sci* 873: 59–64.
- Schaefer M, Gross W, Ackemann J, Gebhard MM. 2002. The complex dielectric spectrum of heart tissue during ischemia. *Bioelectrochemistry* 58: 171–180.
- Schaefer M, Gross W, Preuss M, Ackemann J, Gebhard MM. 2003. Monitoring of water content and water distribution in ischemic hearts. *Bioelectrochemistry* 61: 85–92.
- Schanne OF, Ceretti ERP. 1978. *Impedance Measurements in Biological Cells*. Wiley, New York.
- Schepps JL, Foster KR. 1980. UHF and microwave dielectric properties of normal and tumor tissues: variation in dielectric properties with tissue water content. *Phys Med Biol* 25: 1149–1159.
- Schmid G, Neubauer G, Illievich UM, Alesch F. 2003a. Dielectric properties of porcine brain tissue in the transition from life to death at frequencies from 800 to 1900 MHz. *Bioelectromagnetics* 24: 413–421.
- Schmid G, Neubauer G, Mazal PR. 2003b. Dielectric properties of human brain tissue measured less than 10 h post-mortem at frequencies from 800 to 2450 MHz. *Bioelectromagnetics* 24: 423–430.
- Schwan HP. 1957. Electrical properties of tissue and cell suspensions. In: *Advances in Biological and Medical Physics*, Lawrence JH, Tobias CA, Eds., Academic Press, New York, 5: 147–209.
- Schwan HP. 1992. Linear and nonlinear electrode polarization and biological materials. *Ann Biomed Eng* 20: 269–288.
- Schwan HP, Foster KR. 1980. RF-field interactions with biological systems: electrical properties and biophysical mechanisms. *Proc IEEE* 68: 104–13.
- Schwan HP, Sheppard RJ, Grant EH. 1976. Complex permittivity of water at 25°C. *J Chem Phys* 64: 2257–2258.
- Schwartzman D, Chang I, Michele JJ, Mirotznik MS, Foster KR. 1999. Electrical impedance properties of normal and chronically infarcted left ventricular myocardium. *J Interv Card Electrophysiol* 3: 213–224.
- Schwarz G. 1962. A theory of the low frequency dielectric dispersion of colloidal particles in electrolyte solution. *J Phys Chem* 66: 2636.
- Sebastian JL, Munoz S, Sancho M, Miranda JM. 2001. Analysis of the influence of the cell geometry, orientation and cell proximity effects on the electric field distribution from direct RF exposure. *Phys Med Biol* 46: 213–225.

- Semenov SY, Svenson RH, Posukh VG, Nazarov AG, Sizov YE, Bulyshev AE, Souvorov AE, Chen W, Kasell J, Tatsis GP. 2002. Dielectrical spectroscopy of canine myocardium during acute ischemia and hypoxia at frequency spectrum from 100 kHz to 6 GHz. *IEEE Trans Med Imaging* 21(6): 703–707.
- Sihvola AH. 1989. Self-consistency aspects of dielectric mixing theories. *IEEE Trans Geosci Remote Sensing* 27(4): 403.
- Sihvola AH, Kong JA. 1988. Effective permittivity of dielectric mixtures. *IEEE Trans Geosci Remote Sensing* 26(4): 420.
- Sihvola AH, Lindell IV. 1992. Polarizability modeling of heterogeneous media. *Prog Electromagn Res PIER* 06: 101–151.
- Smith SR, Foster R, Wolf GL. 1986. Dielectric properties of VX-2 carcinoma versus normal liver tissue. *IEEE Trans Biomed Eng* 33(5): 522–524.
- Stauffer PR, Rossetto F, Prakash M, Neuman DG, Lee T. 2003. Phantom and animal tissues for modelling the electrical properties of human liver. *Int J Hyperthermia* 19(1): 89–101.
- Stuchly M. 1979. Interaction of radiofrequency and microwave radiation with living systems. *Radiat Environ Biophys* 16: 1.
- Stuchly MA, Stuchly SS. 1980. Dielectric properties of biological substances—tabulated. *J Microwave Power* 15(1): 19–26.
- Sunaga T, Ikehira H, Furukawa S, Shinkai H, Kobayashi H, Matsumoto Y, Yoshitome E, Obata T, Tanada S, Murata H, Sasaki Y. 2002. Measurement of the electrical properties of human skin and the variation among subjects with certain skin conditions. *Phys Med Biol* 47: N11–N15.
- Suwowiec AJ, Stuchly SS, Keaney M, Swarup A. 1986. *In vivo* and *in vitro* dielectric properties of feline tissues at low radio-frequencies. *Phys Med Biol* 31(8): 901–909.
- Takashima S. 1989. Electrical properties of proteins. I. Dielectric relaxation. In: *Physical Principles and Techniques of Protein Chemistry*, Leach JS, Ed., Academic Press, New York.
- Tamasanis D. 1992. Application of volumetric multiple scattering approximation to foliage media. *Radio Science (USA)* 27(6): 797–812.
- Tamura T, Tenhunen M, Lahtinen T, Repo T, Schwan HP. 1994. Modelling of the dielectric properties of normal and irradiated skin. *Phys Med Biol* 39: 927–936.
- Tinga WR. 1992. Mixture laws and microwave material interactions. *Prog Electromagn Res* 6: 1–40.
- Tsai JZ, Cao H, Tungjitusolmun S, Woo EJ, Vorperian VR, Webster JG. 2000. Dependence of apparent resistance of four-electrode probes on insertion depth. *IEEE Trans Biomed Eng* 47(1): 41–48.
- Tsai JZ, Will JA, Stelle SHV, Cao H, Tungjitusolmun S, Choy YB, Haemmerich D, Vorperian VR, Webster JG. 2002. *In-vivo* measurements of swine myocardial resistivity. *IEEE Trans Biomed Eng* 49(5): 472–483.
- Van Beek LKH. 1967. Dielectric behaviour of heterogeneous systems, *Prog Dielectr* 7: 69–114.
- Walker DC, Brown BH, Hose DR, Smallwood RH. 2000. Modelling the electrical impedance of normal and prealignant cervical tissue. *Electron Lett.* 36(19): 1603–1604.
- Weaver JC, Astumian RD. 1990. The response of living cells to very weak electric fields: the thermal noise limit. *Science* 247(4941): 459–462.
- Wei YZ, Sridhar S. 1993. A new graphical representation for dielectric data. *J Chem Phys* 99(4): 3119–3124.
- Wersebe A, Siegmann K, Krainick U, Fersis N, Vogel U, Claussen CD, Muller-Schimpfle M. 2002. Diagnostic potential of targeted electrical impedance scanning in classifying suspicious breast lesions. *Invest Radiol* 37(2): 65–72.
- Woodward AM, Kell DB. 1990. On the nonlinear dielectric properties of biological systems *Saccharomyces cerevisiae*. *Bioelectrochem Bioenerg* 24: 83–100.
- Yeldin M, Kwan H, Murphy JT, Nguyen-Hou H, Wong YC. 1974. Electrical conductivity in cat cerebellar cortex. *Exp Neurol* 43: 533–569.
- Zaghoul H, Buckmaster HA. 1985. The complex permittivity of water at 9.356 GHz from 10 to 40 degrees C. *J Phys D: Appl Phys* 18: 2109–2118.
- Zhang ZH, Sekine K, Hanai T, Koizumi N. 1983. Dielectric observations on polystyrene microcapsules and the theoretical analysis with reference to interfractal polarization. *Colloid Polym Sci* 261: 381.

4

Magnetic Properties of Biological Material

Jon Dobson

CONTENTS

4.1	Introduction	101
4.2	Diamagnetic Materials	102
4.3	Paramagnetic Materials	102
4.4	Ferromagnetic Materials	103
4.4.1	Antiferromagnetism	104
4.4.2	Ferrimagnetism	105
4.4.3	Temperature Dependence of Ferromagnetism	105
4.5	Biological Magnets.....	106
4.6	Magnetic Iron Compounds Related to Pathogenesis.....	109
	References	111

4.1 Introduction

Magnetism arises from the movement of electrical charges, such as the oscillation of electrons in a conducting wire, the flow of ions in an organism or the orbital, and spin motions of electrons in an atom. Since all materials contain moving subatomic particles (electrons and protons), all materials are, in some sense, "magnetic." In order to understand more about the role of magnetic materials in organisms, it is first necessary to examine what is meant by the various types of magnetic behavior of materials.

The magnetic properties of materials are dominated by the electron spin motion. In quantum mechanical terms, electrons may assume two possible spin states: spin +1/2 or spin -1/2. These may also be referred to as "spin up" and "spin down." The Pauli exclusion principle states that no two electrons may occupy the same energy state in an atom. This means that no two electrons may have the same set of values for the quantum numbers as they would then be indistinguishable. As electrons are added, they fill up each possible state in a given shell before filling the shell associated with the next higher energy state. The filling of the shells is governed by Schrödinger's wave equation and the quantum numbers.

Electrons are added to subshells in parallel spin configurations first according to Hund's rule. If all electrons are paired, there is no "spin" magnetic moment. These materials are still magnetic though, because of the electron's orbital motion. In most materials of biological origin, however, electron spin motion is cancelled, allowing electron orbital motion to dominate.

The spin structure of the transition series elements (iron in particular) is most important for the magnetic properties of biological materials. This is due to the presence of uncompensated spins in the 3d orbital, which gives rise to a spin magnetic moment. The spin moment is much stronger than the orbital moment and is aligned parallel to an applied field.

All materials, including biological materials, fall into one of the three categories of magnetic materials based on the spin and orbital motion of electrons: (1) diamagnetic, (2) paramagnetic, and (3) ferromagnetic.

4.2 Diamagnetic Materials

Diamagnets are materials in which all electron spins are paired (i.e., there are no uncompensated spins). Therefore, the magnetic properties of diamagnets are determined by the electron orbital motion.

According to Faraday's law, in the presence of an applied magnetic field there is an electric field induced that is acting on the orbiting electron. The induced electric field produces a torque on the electron, which gives the electron extra angular momentum. This extra angular momentum produces a magnetic moment, the sign of which is negative (i.e., antiparallel to the induced or applied magnetic field). Therefore, diamagnetic materials are repelled in magnetic fields (they have weak, negative magnetic susceptibility).

4.3 Paramagnetic Materials

Paramagnetic materials are those in which individual atoms, ions, or molecules have some number of uncompensated spins and thus a permanent net spin magnetic moment. As we have stated before, the spin moment is much larger than the orbital moment, so we would therefore expect that the behavior of paramagnetic materials when placed in a magnetic field will be governed by the behavior of the spin magnetic moments. This is indeed the case.

When paramagnetic substances are placed in an external magnetic field, the uncompensated spin moments tend to align, to some degree, parallel to the applied field direction (Figure 4.1). The magnetic energies involved in this alignment are relatively

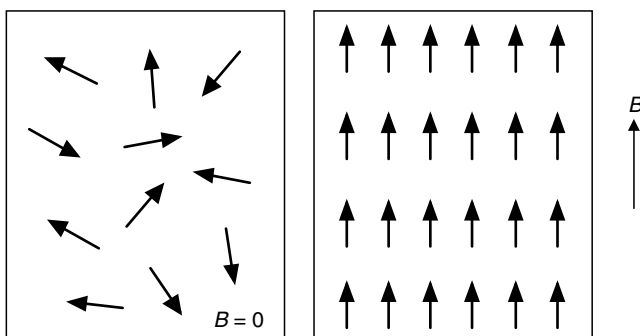


FIGURE 4.1

Orientation of spins in a paramagnet in the absence of a magnetic field ($B = 0$; left) and in the presence of a strong magnetic field (right)

small, and the energy associated with thermal agitation tends to work against the alignment, having a randomizing effect. The degree of alignment of the uncompensated spins with the applied magnetic field depends, therefore, on the strength of the field (the stronger the field, the greater the degree of alignment up to very high fields) and the temperature (the hotter the material, the lower the degree of alignment in the same applied field).

Since the spin moments in paramagnetic materials align with the applied field in this classical model, they add to it, so that the net effect is that these materials are attracted to a magnetic field (and they have a positive magnetic susceptibility). The linear temperature dependence of the magnetic susceptibility in paramagnetic materials was worked out by Pierre Curie and is known as Curie's law:

$$M/H = \chi = C/T$$

where M is the magnetization, H is the applied magnetic field, χ is the magnetic susceptibility, T is the temperature, and C is the Curie constant and is related to the magnetic properties of the material.

In paramagnetic materials, the individual dipole spin moments of the ions may be thought of as noninteracting (in other words, the magnetic moment of one atom has no effect on its neighboring atoms in the material). Because of the noninteraction of the magnetic moments, this fairly weak effect (paramagnetism) is lost upon removal of the external field. Therefore, when a paramagnetic material is not in an external magnetic field, the net magnetic moment in the material is zero because of the randomizing effects of thermal agitation.

4.4 Ferromagnetic Materials

As in paramagnets, in ferromagnetic materials, there are also uncompensated spins; however, these spins are coupled, giving rise to strong magnetic effects. Ferromagnetism may be thought of as a "group phenomenon," where groups of spin moments act in concert, whereas paramagnetism may be thought of as an "individual phenomenon," where the moment of one atom has little or no effect on the moment of neighboring atoms.

In ferromagnetic materials, as in paramagnets, the magnetic susceptibility is positive, and these materials acquire a positive magnetization when placed in an applied field because of alignment of the spin moments in the material with the field. Unlike paramagnets, however, the net magnetization is not lost upon removal of the field (as long as the material is below a certain temperature, which will be discussed in a moment), and the induced moment in the material may be very strong (Figure 4.2). This is to say that ferromagnetic materials exhibit "hysteresis."

The mechanism responsible for coupling of the spin magnetic moments in neighboring atoms in a material is due to quantum mechanical phenomena and is governed by the Pauli exclusion principle. The uncompensated spins in individual atoms of a ferromagnetic material may couple either directly (direct exchange) or through an intermediate anion—usually oxygen (superexchange). In ferromagnetic materials, this gives rise to a net magnetic moment because of the coupling of spins in a preferred orientation. Keep in mind that this coupling is quantum mechanical in nature and not purely due to magnetic forces acting between uncompensated spins in neighboring atoms.

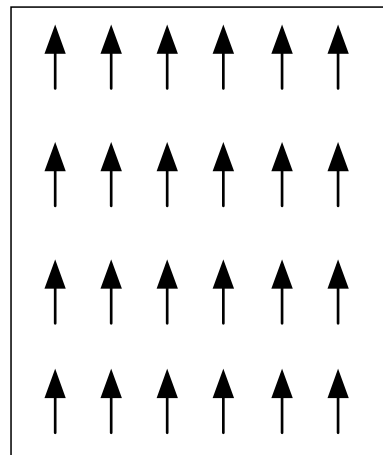


FIGURE 4.2

In ferromagnets, all spins are coupled and aligned, even in the absence of an applied field. This is the origin of remanent magnetization (i.e., hysteresis) in materials.

There are also special cases of ferromagnetism in which neighboring spins are coupled, but not necessarily in the same direction. We will examine two of these cases, antiferromagnetism and ferrimagnetism, as they are important to biological materials, though there are others.

4.4.1 Antiferromagnetism

For some ferromagnetic materials, the exchange coupling between neighboring lattice elements is such that the spins are aligned opposite to each other. This is called antiferromagnetism, and the exchange coupling arises from super exchange according to the Pauli exclusion principle and Hund's rule (Figure 4.3).

In this case the spin moments will still align themselves to an external applied field, only some will be parallel to the applied field and those exchange coupled to them will be antiparallel. This would normally give rise to a material with no net magnetic moment if for every spin up, it was coupled to a spin down. This is not, however, always the case. In some materials, there is a canted antiferromagnetic spin structure (Figure 4.3) or lattice defects and frustrated surface spins (in very fine particles), which can give rise to a net moment in the absence of an applied field.

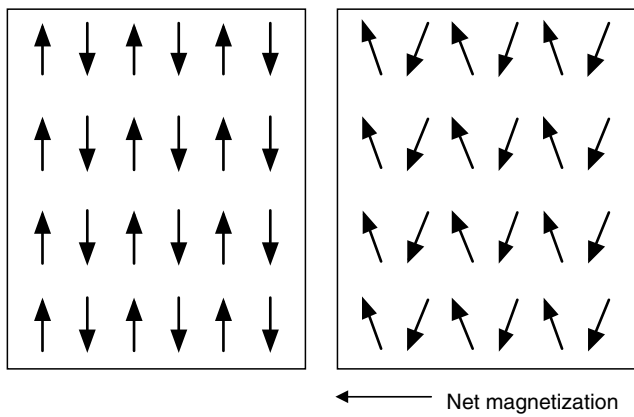


FIGURE 4.3

Pure antiferromagnetic behavior in which spins are coupled antiparallel to each other (left) and an antiferromagnet with a canted spin structure that gives rise to a net magnetization even in the absence of an applied field (right).

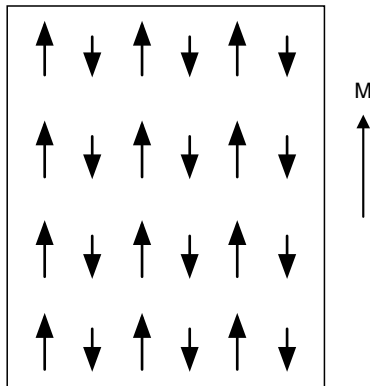


FIGURE 4.4

Electron spin configuration for a ferrimagnet. M = magnetization.

4.4.2 Ferrimagnetism

In addition to antiferromagnetic materials, it is also possible for the neighboring lattice subunits to have unequal numbers of uncompensated electrons coupled antiparallel to each other. This is the case for magnetite (Fe_3O_4), which contains both Fe^{2+} and Fe^{3+} in its lattice structure. The unequal distribution of the two neighboring iron ions gives rise to a net moment (again, even in the absence of an applied field) since one sublattice will have a magnetic moment of greater magnitude than the other, as shown in Figure 4.4. This type of material is called ferrimagnetic.

4.4.3 Temperature Dependence of Ferromagnetism

Since ferromagnetism results from the interaction of atomic moments in materials, there is an exchange energy associated with coupling of the spin moments. At room temperature, this exchange energy is much greater than the energy due to randomizing thermal effects (kT). If thermal energy exceeds the spin coupling (exchange) energy, the coupling breaks down, and the material behaves as a paramagnet. This temperature is dependent on the material and is called the Curie temperature (or, in the case of antiferromagnetic materials, the Néel temperature) (Figure 4.5).

Finally, materials that are superparamagnetic are generally very small (on the order of nanometers), and the electron spins may be coupled either parallel (ferromagnet) or

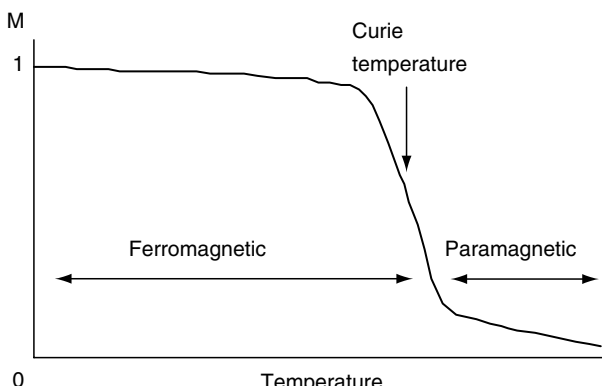
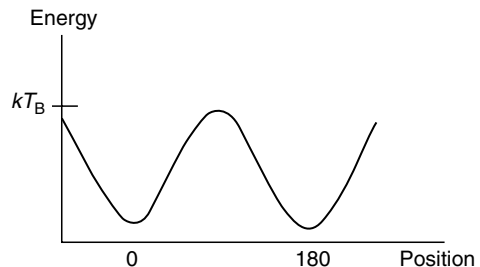


FIGURE 4.5

Magnetization as a function of temperature for a ferromagnet. Above the Curie temperature, spin coupling breaks down, and the material behaves as a paramagnet.

FIGURE 4.6

Schematic of the energy barriers in a superparamagnet. If thermal energy is above a given temperature—the blocking temperature (T_B)—the spins will be able to very rapidly flip between 0° and 180° along the easy axis of magnetization. If the particle becomes larger or the temperature is lowered, the height of the energy barrier constrains the orientation of the electron spins to one or the other of the easy axis energy wells.



antiparallel (ferri- or antiferromagnet). In the case of these materials, however, thermal considerations are dominant. Superparamagnetic materials are named as such because thermal energy causes them to behave—even though this is a special class of ferromagnetism—like a paramagnet. The difference is that, because of coupling of the spin moments, thermal energy causes the spins to flip rapidly as a group rather than individually, as is the case for paramagnetism. On a macroscopic level, the behavior of the two is very similar, except at low temperatures when the thermal energy is sufficiently reduced.

If the superparamagnetic particles are placed in an applied field, the energy of the field will cause the spins to align themselves parallel to it, just as with a normal ferromagnet or paramagnet (the degree of alignment depending on the strength of the field and the temperature—as with paramagnets). If the field is taken away, thermal fluctuation causes a “relaxation” of the spins, and they begin to flip rapidly between parallel and antiparallel orientations along the easy axis of magnetization (determined by magnetocrystalline or shape anisotropy). This has the effect of causing the material to appear paramagnetic when the magnetization is examined on timescales longer than the flipping frequency (generally $\sim 10^{-9}$ s). The remanent magnetization (which is the magnetization left in the material after removal of the field) decays with time according to the equation:

$$\tau = f_0 \exp\left(\frac{\nu M_s H_c}{2kT}\right)$$

where τ = relaxation time, f_0 = lattice vibration frequency, ν = grain volume, M_s = spontaneous magnetization, H_c = coercivity, k = Boltzmann's constant, and T = temperature.

The relaxation time depends on the height of the energy barrier—which is a function of grain volume and the magnetic properties of the material—and the amount of thermal energy (kT) required to overcome it (Figure 4.6). Using this equation, it is possible to calculate grain volumes above which the magnetization becomes stable or “blocked” (i.e., decays over very long periods of time at a given temperature).

4.5 Biological Magnets

For most biological materials, the magnetic permeability is close to that of free space (i.e., diamagnetic), which implies that there is no direct interaction with the magnetic component of electromagnetic fields at low field strengths. However, this is not the case for all biological materials.

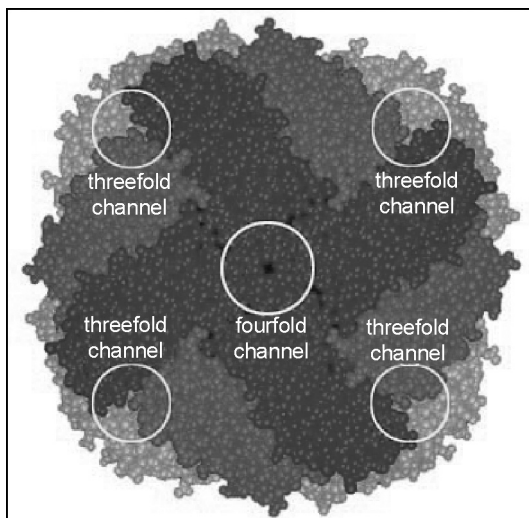


FIGURE 4.7 (See color insert following page 380.)
Model of the ferritin protein showing the peptide subunits and iron transport channels. (From www.chemistry.wustl.edu/~edudev/LabTutorials/Ferritin/FerritinTutorial.html. With permission.)

Most magnetic (paramagnetic and ferromagnetic) materials in organisms are compounds of iron—and in particular, iron oxides. Virtually all organisms require iron to function normally. This is mainly due to its redox activity, which allows it to play an important role in energetic biochemical reactions. In organisms, iron is stored as the mineral ferrihydrite ($5\text{Fe}_2\text{O}_3 \cdot 9\text{H}_2\text{O}$) within the iron storage protein ferritin. It consists of a 12-nm hollow spherical protein shell made up of 24 subunits (Figure 4.7). The core of ferritin protein is 8 nm in diameter, and it can hold up to 4500 iron atoms in the form of ferrihydrite. Iron is transported into and out of the core through three- and fourfold channels in the shell. During transport, highly toxic Fe(II) is oxidized to Fe(III) for storage as ferrihydrite (Harrison and Arosio, 1996). The specific iron biochemistry of ferritin is complex and is not completely understood (e.g., Yang et al., 1998; Zhao et al., 2001).

Ferrihydrite is a superparamagnetic antiferromagnet at body temperature, and as such, its magnetic properties are potentially important for understanding the environmental consequences of electromagnetic field exposure, including exposure to strong fields within magnetic resonance imaging (MRI) scanners. In fact, the development of pulse sequences for MRI of ferritin is leading to novel ways of assessing iron concentrations in the liver and examining iron associated with neurodegenerative disorders such as Alzheimer's and Parkinson's diseases (Clarke and St. Pierre, 2000; Bartzokis et al., 2004; St. Pierre et al., 2004, 2005). These techniques rely on the magnetic fields generated by ferritin to produce contrast in ferrihydrite-rich tissue in much the same way as synthetic superparamagnetic iron oxide contrast agents do (for a review, see Pankhurst et al., 2003).

In addition to ferrihydrite in ferritin, in 1992 Joseph Kirschvink's group at the California Institute of Technology discovered that biogenic magnetite is produced in the human brain (Kirschvink et al., 1992). Later work demonstrated that this magnetic iron biomimetic mineral is present in several organs in the human body, including the heart, liver, and spleen (Schultheiss-Grassi et al., 1997).

Magnetite (Fe_3O_4)—a ferromagnetic iron oxide—is also known as lodestone and is a mineral more commonly associated with sedimentary rocks and volcanics. However, it is also found in many organisms. Probably, the most well-known example is the magnetotactic bacterium. These bacteria use chains of single-domain, biogenic magnetite arranged in chains in order to sense the geomagnetic field and use it for navigation—much like a

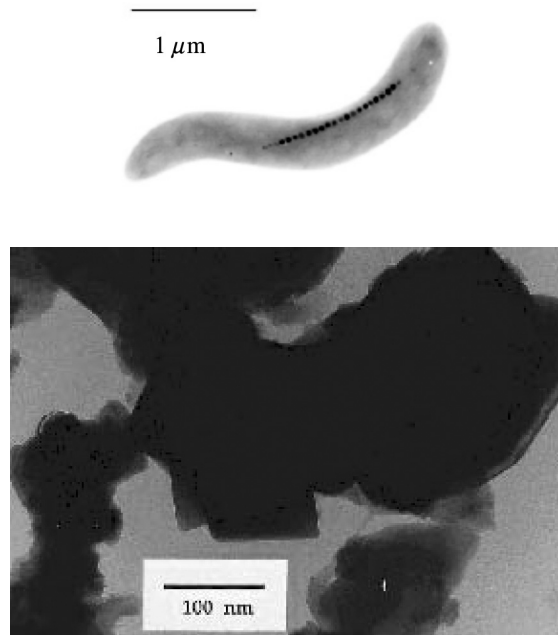


FIGURE 4.8

Transmission electron micrograph of the magnetotactic bacterium MS-1 (top). (From www.calpoly.edu/~rfrankel/mtbphoto.html) Biogenic magnetite extracted from the human hippocampus (bottom). (From Schultheiss-Grassi, PP, R Wessiken, and J Dobson (1999) *Biochim. Biophys. Acta* 1426: 212–216. With permission.)

compass needle (Blakemore, 1975) (Figure 4.8). Although the mechanism by which these organisms produce perfect magnetite crystals is not well understood, it has recently been shown that the process appears to be mediated by specific proteins (Arakaki et al., 2003). Since Blakemore's early discovery, magnetite has been found in a wide variety of animals from bacteria to humans, and in some cases, as with magnetotactic bacteria, it appears to be used for navigation (e.g., Walker and Bitterman, 1989; Walker et al., 1997; Wiltschko and Wiltschko, 2002; for a review, see Kirschvink and Hagadorn, 2000).

Although by 1992, magnetite was known to occur in many organisms, the discovery of biogenic magnetite in the human brain proved controversial. Further work in this area confirmed and extended Kirschvink's results, examining not only the occurrence of magnetite in the brain but also its potential role in neurophysiological processes (Dunn et al., 1995; Dobson and Grassi, 1996; Schultheiss-Grassi and Dobson, 1999; Dobson 2001, 2002, 2004; Hautot et al., 2003; Collingwood et al., 2005) (Figure 4.8).

One area of research where the presence of biogenic magnetite in the brain may provide answers to some controversial questions is in the examination of potential mechanisms for the interaction of environmental electromagnetic fields with humans. Two theoretical models have been proposed to demonstrate how biogenic magnetite could act as a transducer of both low-frequency magnetic fields and radio frequency (RF) fields emitted from mobile phones and base stations (Kirschvink, 1992, 1996; Dobson and St. Pierre, 1996). These models rely on the fact that magnetite will couple strongly to the magnetic fields from electrical devices and, either through ferromagnetic resonance effects or through mechanical effects on membrane ion channels, can disrupt the normal functioning of cells in the brain.

Early tests of these models indicate that low-frequency, pulsed magnetic fields from mobile phones may have an influence on cellular activity (including cell death), whereas effects due to ferromagnetic resonance in RF fields are less clear (Cranfield et al., 2003a,b). In addition, magnetite contamination and the presence of biogenic magnetite in model organisms have also been highlighted as potential confounders that could influence the results of studies on the effects of environmental magnetic fields on organisms (Kobayashi and Kirschvink, 1995; Cranfield et al., 2004).

Although magnetite and ferrihydrite are two of the most ubiquitous magnetic materials in organisms, they are not the only ones. Greigite (Fe_3S_8) is a ferrimagnetic iron sulfide found in some iron-reducing bacteria (Posfai et al., 1998). It has a strong magnetic moment similar to magnetite and is thought to be produced as a by-product of iron reduction. Hematite (Fe_2O_3) and wüstite-like (FeO) iron phases also have recently been found within human ferritin (Quintana et al., 2004). And hemosiderin (FeOOH) is a goethite-like iron oxyhydroxide that is antiferromagnetic and is found primarily in pathogenic liver tissue (St. Pierre et al., 1998). In addition to these ferromagnetic materials, other ions and iron compounds, such as hemoglobin, are paramagnetic.

4.6 Magnetic Iron Compounds Related to Pathogenesis

Though iron is an important component of normally functioning organisms, in some cases, it can also be toxic. Because of its redox potential, Fe(II) generally has the potential to do more damage than oxidized Fe(III). For this reason, iron is primarily stored as Fe(III) within ferritin in organisms.

Disruption of the body's normal mechanisms for iron storage can lead to iron overload diseases such as hemochromatosis and β -thalassemia and the deposition of significant amounts of magnetic iron compounds (St. Pierre et al., 1998; Chua-anusorn et al., 2000). These diseases result in the formation of significant iron deposits, predominantly in the liver, which consist mainly of the iron biominerals hemosiderin (FeOOH). Hemosiderin is antiferromagnetic, but can occur as large particles in the body. As with ferrihydrite, both these antiferromagnets contain only Fe(III) and as such have a relatively weak magnetic moment primarily due to lattice defects and, for very fine particles, to frustrated spins on the particle's surface. As mentioned earlier, the presence of these magnetic iron compounds is being exploited for the development of noninvasive MRI monitoring of liver iron in order to track the effectiveness of chelating compounds that are used to treat these diseases (Clarke and St. Pierre, 2000; St. Pierre et al., 2004, 2005). In the brain, disruption of normal iron metabolism results from either disease or trauma and can often lead to pathogenesis (Beard et al., 1993). The accumulation of excess iron is known to induce epileptic activity, primarily as a result of intracranial bleeding due to head trauma. The model of iron-induced epilepsy was first introduced by Willmore et al. (1978), and the electrophysiological responses have been characterized in many studies since then (e.g., Ueda and Willmore, 2000; Engstrom et al., 2001). More recently, evidence shows that iron overload diseases may even predispose a person to epilepsy (Ikeda, 2001).

Although the initial seizure response to trauma and excess iron is relatively swift (Ueda et al., 1998), the long-term consequences of intracranial bleeding on the formation of various magnetic iron compounds in the brain are unclear. Little is known about the formation of iron compounds in the brain of epileptic patients, other than that there appears to be a relationship with an increase in iron (e.g., Willmore et al., 1978; Ueda and

Willmore, 2000; Engstrom et al., 2001). This increase may lead to increased iron loading in the ferritin core or the sequestration of free iron in another form, which could have significant consequences for disease progression. A preliminary correlation between magnetite particle packing geometry and epileptogenic tissue has been demonstrated; however, there is as yet no indication of an increase in magnetite biomineratization associated with temporal lobe epilepsy (Schultheiss-Grassi and Dobson, 1999).

The association of abnormal accumulations of iron with neurodegenerative disorders such as Alzheimer's, Parkinson's, and Huntington's diseases has been known for over 50 y (Goodman, 1953). Although this relationship has been studied extensively, it is not yet clear which iron compounds are present and what their role in these diseases is; however, evidence is mounting that there are likely synergistic mechanisms related to iron and amyloid- β ($A\beta$, the principal component of Alzheimer's plaques) and other disease-related proteins (e.g., Sayre et al., 2000; Rottkamp et al., 2001; Atamna and Frey, 2004]. Recent work seems to confirm that iron plays a role in disease progression as iron chelators appear to have neuroprotective effects in rat models of Parkinson's disease (Ben Shachar et al., 2004).

Various forms of iron may play a significant role in the biochemical processes that lead to the progression of neurodegenerative diseases. Although there is much speculation on that role, the primary mechanism is thought to be the result of oxidative stress—the generation of free radicals via the Fenton reaction (Connor and Menzies, 1995; Markesberry, 1997; Koppenol, 2001). Recently, Floor (2000) demonstrated the connection between high levels of iron in the basal ganglia and oxidative stress in Parkinson's patients. A disruption of iron metabolism and increased iron in the same region of the brain also has been implicated in Alzheimer's and Huntington's diseases (Bartzokis and Tishler, 2000). Furthermore, iron accumulation has been associated with microgliosis and correlated with increased damage to the CA1 region of the hippocampus via iron–zinc interactions in models of neurodegenerative diseases (Shoham and Youdim, 2000).

It should be noted, however, that some results have shown that the presence of oxidized nucleosides in neurons does not appear to be related to senile plaque material or neurofibrillary tangles in Alzheimer's (Nunomura et al., 1999). In some cases, free radical damage has even been reported to be reduced by $A\beta$ deposition because of the inhibitory role of $A\beta$ -related Zn^{2+} in H_2O_2 -mediated toxicity (Cuajungco et al., 2000; Nunomura et al., 2000). More recently, it has been noted that in transgenic mouse models of Alzheimer's, neurogenesis was related to increased deposition of $A\beta$ (Jankowsky et al., 2003). It has been postulated that this may be due to a possible neuroprotective role of $A\beta$ in binding excess redox active iron, which is deposited because of the increased need for iron during neurogenesis (Dobson and Batich, 2004).

Recently, state-of-the-art superconducting quantum interference device (SQUID) magnetometry, nuclear forward scattering, and synchrotron x-ray fluorescence imaging have been employed to evaluate which specific iron compounds are present in these diseases and to map them to structures in the tissue (Hautot et al., 2003; Collingwood et al., 2005; Mikhailova et al., 2005). Early results of these studies indicate that several magnetic iron compounds are associated with these diseases—ferrihydrite (from ferritin), biogenic magnetite, α -iron, and hemosiderin. These results represent a major step toward our understanding of the origin and role of magnetic iron compounds in these diseases.

The role of the various magnetic materials in many organisms, particularly in humans, is only just beginning to be unraveled. After more than two decades of research on magnetic biominerals, it is clear that in many cases they play an important role in biological processes and may provide us with insights into mechanisms of interaction of environmental electromagnetic fields and organisms.

References

- Arakaki, A, J Webb, and T Matsunaga (2003) A novel protein tightly bound to bacterial magnetite particles in *Magnetospirillum magneticum* strain AMB-1. *J. Biol. Chem.* 278: 8745–8750.
- Atamna, H and WH Frey (2004) A role for heme in Alzheimer's disease: heme binds amyloid beta and has altered metabolism. *Proc. Natl. Acad. Sci. USA* 101: 11153–11158.
- Bartzokis, G and TA Tishler (2000) MRI evaluation of basal ganglia ferritin iron and neurotoxicity in Alzheimer's and Huntington's disease. *Cell. Mol. Biol.* 46: 821–834.
- Bartzokis, G, TA Tishler, IS Shin, PH Lu, and JL Cummings (2004) Brain ferritin iron as a risk factor for age at onset in neurodegenerative diseases. *Ann. NY Acad. Sci.* 1012: 224–236.
- Beard, JL, JR Connor, and BC Jones (1993) Iron in the brain. *Nutr. Rev.* 51: 157–170.
- Ben Shachar, D, N Kahana, V Kampel, A Warshawsky, and MBH Youdim (2004) Neuroprotection by a novel brain permeable iron chelator, VK-28, against 6-hydroxydopamine lesion in rats. *Neuropharmacology* 46: 254–263.
- Blakemore, RP (1975) Magnetotactic bacteria. *Science* 190: 377–379.
- Chua-anusorn, W, KC Tran, J Webb, DJ Macey, and TG St. Pierre (2000) Chemical speciation of iron deposits in thalassemic heart tissue. *Inorg. Chim. Acta* 300–302: 932–936.
- Clarke, P and TG St. Pierre (2000) Quantitative 1/T2 mapping of hepatic iron overload: a single spin echo imaging methodology. *Magn. Reson. Imaging* 18: 431–438.
- Collingwood, JF, A Mikhailova, M Davidson, C Batich, WJ Streit, J Terry, and J Dobson (2005) *In-situ* characterization and mapping of iron compounds in Alzheimer's tissue. *J. Alzheimers Dis.* In press.
- Connor, RJ and SL Menzies (1995) Cellular management of iron in the brain. *J. Neurol. Sci.* 134: 33–44.
- Cranfield, CG, HG Wieser, JM Al Madan, and J Dobson (2003a) Evaluation of ferromagnetic transduction mechanisms for mobile phone bioeffects. *IEEE Trans. NanoBiosci.* 2: 40–43.
- Cranfield, CG, HG Wieser, and J Dobson (2003b) Exposure of magnetic bacteria to simulated mobile phone type RF radiation has no impact on mortality. *IEEE Trans. NanoBiosci.* 2: 146–149.
- Cranfield, CG, A Dawe, V Karloukovski, RE Dunin-Borkowski, D de Pomerai, and J Dobson (2004) Biogenic magnetite in the nematode *Caenorhabditis elegans*. *Proc. R. Soc. B (Suppl.) Biol. Lett.* 271: S436–S439.
- Cuajungco, MP, LE Goldstein, A Nunomura, MA Smith, JT Lim, CS Atwood, X Huang, YW Farrag, G Perry, and AI Bush (2000) Evidence that the β -amyloid plaques of Alzheimer's disease represent the redox-silencing and entombment of A β by zinc. *J. Biol. Chem.* 275: 19439–19442.
- Dobson, J (2001) Nanoscale biogenic iron oxides and neurodegenerative disease. *FEBS Lett.* 496: 1–5.
- Dobson, J (2002) Investigation of age-related variations in biogenic magnetite levels in the human hippocampus. *Exp. Brain Res.* 144: 122–126.
- Dobson, J (2004) Magnetic iron compounds in neurological disorders. *Ann. NY Acad. Sci.* 1012: 183–192.
- Dobson, J and C Batich (2004) A potential iron-based mechanism for enhanced deposition of amyloid plaques due to cognitive stimulation in Alzheimer's disease. *J. Neuropathol. Exp. Neurol.* 63: 674–675.
- Dobson, J and P Grassi (1996) Magnetic properties of human hippocampal tissue: evaluation of artefact and contamination sources. *Brain Res. Bull.* 39: 255–259.
- Dobson, J and TG St. Pierre (1996) Application of the ferromagnetic transduction model to D.C. and pulsed magnetic fields: effects on epileptogenic tissue and implications for cellular phone safety. *Biochem. Biophys. Res. Commun.* 227: 718–723.
- Dunn, JR, M Fuller, J Zoeger, J Dobson, F Heller, E Caine, and BM Moskowitz (1995) Magnetic material in the human hippocampus. *Brain Res. Bull.* 36: 149–153.
- Engstrom, ER, L Hillered, R Flink, L Kihlstrom, C Lindquist, JX Nie, Y Olsson, and HC Silander (2001) Extracellular amino acid levels measured with intracerebral microdialysis in the model of posttraumatic epilepsy induced by intracortical iron injection. *Epilepsy Res.* 43: 135–144.
- Floor, E (2000) Iron as a vulnerability factor in nigrostriatal degeneration in aging and Parkinson's disease. *Cell. Mol. Biol.* 46: 709–720.

- Goodman, L (1953) Alzheimer's disease—a clinicopathologic analysis of 23 cases with a theory on pathogenesis. *J. Nerv. Ment. Dis.* 118: 97–130.
- Harrison, PM and P Arosio (1996) The ferritins: molecular properties, iron storage function and cellular regulation. *Biochim. Biophys. Acta* 1275: 161–203.
- Hautot, D, QA Pankhurst, N Khan, and J Dobson (2003) Preliminary evaluation of nanoscale biogenic magnetite and Alzheimer's disease. *Proc. R. Soc. Lond. B: Biol. Lett.* 270: S62–S64.
- Ikeda, M (2001) Iron overload without the C282Y mutation in patients with epilepsy. *J. Neurol. Neurosurg. Psychiatry* 70: 551–553.
- Jankowsky, JL, G Xu, D Fromholt, V Gonzales, and DR Borchelt (2003) Environmental enrichment exacerbates amyloid plaque formation in a transgenic mouse model of Alzheimer disease. *J. Neuropathol. Exp. Neurol.* 16: 1220–1227.
- Kirschvink, JL (1992) Comments on "Constraints on biological effects of weak extremely-low-frequency electromagnetic fields." *Phys. Rev. A* 46: 2178–2184.
- Kirschvink, JL (1996) Microwave absorption by magnetite: a possible mechanism for coupling non-thermal levels of radiation to biological systems. *Bioelectromagnetics* 17: 187–194.
- Kirschvink, JL and JW Hagadorn (2000) A grand unified theory of biomineratization. In Bäuerlein, E (ed.) *The Biomineratization of Nano- and Micro-Structures*. Wiley-VCH Verlag GmbH, Weinheim, Germany, pp. 139–149.
- Kirschvink, JL, A Kobayashi-Kirschvink, and BJ Woodford (1992) Magnetite biomineratization in the human brain. *Proc. Natl. Acad. Sci., USA* 89: 7683–7687.
- Kobayashi, AK, JL Kirschvink, and MH Nesson (1995) Ferromagnetism and EMFs. *Nature* 374: 123.
- Koppenol, WH (2001) The Haber–Weiss cycle 70 years later. *Redox Rep.* 6: 229–234.
- Markesberry, WR (1997) Oxidative stress hypothesis in Alzheimer's disease. *Free Radic. Biol. Med.* 23: 134–147.
- Mikhailova, A, M Davidson, JET Channel, Y Guyodo, C Batich, and J Dobson (2005) Detection, identification and mapping of iron anomalies in brain tissue using x-ray absorption spectroscopy. *J. R. Soc. Interface* 2: 33–37.
- Nunomura, A, G Perry, MA Pappolla, R Wade, K Hirai, S Chiba, and MA Smith (1999) RNA oxidation is a prominent feature of vulnerable neurons in Alzheimer's disease. *J. Neurosci.* 19: 1959–1964.
- Nunomura, A, G Perry, MA Pappolla, RP Friedland, K Hirai, S Chiba, and MA Smith (2000) Neuronal oxidative stress precedes amyloid-beta deposition in Down's syndrome. *J. Neuropathol. Exp. Neurol.* 59: 1011–1017.
- Pankhurst, QA, J Connolly, SK Jones, and J Dobson (2003) Applications of magnetic nanoparticles in biomedicine. *J. Phys. D* 36: R167–R181.
- Posfai, M, PR Buseck, DA Bazylinski, and RB Frankel (1998) Reaction sequence of iron sulfide minerals in bacteria and their use as biomarkers. *Science* 280: 880–883.
- Quintana, C, JM Cowley, and C Marhic (2004) Electron diffraction and high-resolution electron microscopy studies of the structure and composition of physiological and pathological ferritin. *J. Struct. Biol.* 147: 166–78.
- Rottkamp, CA, AK Raina, X Zhu, E Gaier, AI Bush, CS Atwood, M Chevion, G Perry, and MA Smith (2001) Redox-active iron mediates amyloid- β toxicity. *Free Radic. Biol. Med.* 30: 447–450.
- Sayre, LM, G Perry, PLR Harris, YH Liu, KH Schubert, and MA Smith (2000) *In situ* oxidative catalysis by neurofibrillary tangles and senile plaques in Alzheimer's disease: a central role for bound transition metals. *J. Neurochem.* 74: 270.
- Schlutheiss-Grassi, PP and J Dobson (1999) Magnetic analysis of human brain tissue. *BioMetals* 12: 67–72.
- Schlutheiss-Grassi, PP, F Heller, and J Dobson (1997) Analysis of magnetic material in the human heart, spleen and liver. *BioMetals* 10: 351–355.
- Schlutheiss-Grassi, PP, R Wessiken, and J Dobson (1999) TEM observation of biogenic magnetite extracted from the human hippocampus. *Biochim. Biophys. Acta* 1426: 212–216.
- Shoham, S and MBH Youdim (2000) Iron involvement in neuronal damage and microgliosis in models of neurodegenerative disease. *Cell. Mol. Biol.* 46: 743–750.
- St. Pierre, TG, W Chua-anusorn, J Webb, DJ Macey, and P Pootrakul (1998) The form of iron oxide deposits in thalassemic tissues varies between different groups of patients: a comparison

- between Thai β -thalassemia/hemoglobin E patients and Australian β -thalassemia patients. *Biochim. Biophys. Acta* 1407: 51–60.
- St. Pierre, TG, PR Clark, and W Chua-anusorn (2004) Single spin-echo proton transverse relaxometry of iron loaded liver. *NMR Biomed.* 17: 446–458.
- St. Pierre, TG, PR Clark, W Chua-anusorn, AJ Fleming, GP Jeffrey, JK Olynyk, P Pootrakul, E Robins, and R Lindeman (2005) Non-invasive measurement and imaging of liver iron concentrations using proton magnetic resonance. *Blood* 105: 855–861.
- Ueda, Y and LJ Willmore (2000) Sequential changes in glutamate transporter protein levels during Fe^{3+} -induced epileptogenesis. *Epilepsy Res.* 39: 201–209.
- Ueda, Y, LJ Willmore, and WJ Triggs (1998) Amygdalar injection of FeCl_3 causes spontaneous recurrent seizures. *Exp. Neurol.* 153: 123–137.
- Walker, MM and ME Bitterman (1989) Honeybees can be trained to respond to very small changes in geomagnetic field intensity. *J. Exp. Biol.* 145: 489–494.
- Walker, MM, CE Diebel, CV Haugh, PM Pankhurst, JC Montgomery, and CR Green (1997) Structure and function of the vertebrate magnetic sense. *Nature* 390: 371–376.
- Willmore, LJ, GW Sypert, and JB Munson (1978) Recurrent seizures induced by cortical iron injection—model of post-traumatic epilepsy. *Ann. Neurol.* 4: 329–336.
- Wiltschko W and R Wiltschko (2002) Magnetic compass orientation in birds and its physiological basis. *Naturwissenschaften* 89: 445–452.
- Yang, X, Y Chen-Barrett, P Arosio, and ND Chasteen (1998) Reaction paths of iron oxidation and hydrolysis in horse spleen and recombinant human ferritins. *Biochemistry* 37: 9743–9750.
- Zhao, G, F Bou-Abdallah, X Yang, P Arosio, and ND Chasteen (2001) Is hydrogen peroxide produced during iron(II) oxidation in mammalian apoferritins? *Biochemistry* 40: 10832–10838.

5

Interaction of Direct Current and Extremely Low-Frequency Electric Fields with Biological Materials and Systems

Frank S. Barnes

CONTENTS

5.1	Introduction	115
5.2	Maxwell's Equations and the Properties of Materials	116
5.3	Physics of the Interactions of Electric Fields with Biological Materials	117
5.4	Biological Amplification	127
5.5	Effects of Electric Fields on Cell Membranes	128
5.6	Nonlinear Effects of AC Fields on Cells	132
5.6.1	Introduction	132
5.6.2	Rectification by Cell Membranes	133
5.7	Thermal Effects	144
5.8	Natural Fields and Man-Made Fields	147
5.9	Discussion and Summary	152
	Acknowledgments	152
	References	152

5.1 Introduction

The fact that electrical currents can affect the behavior of biological systems has been known for more than 2000 years. Electric shocks have been used to treat a wide variety of ailments since the eighteenth century. However, our knowledge of how these fields and the resulting currents influence biological systems is surprisingly incomplete. Electrical signals are clearly important in the control of biological processes and in carrying information from one part of the body to another. Nerve cells propagate electrical signals from sensors of pressure, temperature, light, sound, etc., to the brain and return control signals to muscles and other tissue. Yet, if we choose to stimulate these processes with external electrical inputs, we have a relatively limited understanding of how a given electrical signal will affect various biological organs; what the safe limits of exposure are (particularly overextended periods of time); and how electrical signals are carried across cell membranes, are propagated along nerves, or affect growth processes and cell division.

The purpose of this review is to bring together some of the physical concepts that underlie the interaction between electric fields and biological materials with the objective of providing background for determining safe levels of exposure and new applications for the use of electricity in therapy. This is the first step in a long chain of events that lead from externally applied electric field forces to significant biological changes. An objective of this chapter is to provide a background for some of the other chapters that cover both possible health effects and some therapeutic applications of electric and magnetic fields.

The approach that will be taken is to start with Maxwell's equations and couple them to the bulk electric and magnetic properties of the materials. These equations allow us to calculate the values of the electric and magnetic fields as a function of time and space given the values for the dielectric constant and the conductivity. The techniques for the solution of these equations for a wide variety of biological systems are covered in [Chapter 10](#) in this volume by J. Lin and P. Bemardi and for imaging see [Chapter 12](#) in this volume by W.T. Joines, O.H. Liu and G. Ybarra. From the solutions of these equations for the electric and magnetic fields, the conservation of energy, and charge, expressions can be obtained for the current density and other parameters of interest.

Next, the force equations are used to develop equations for the conductivity and the dielectric constant. This section is organized to begin at the lowest level of complexity by examining some of the forces that are exerted on charged particles in fluids, and it then proceeds to some of the effects of electric fields on chemical reaction rates and membranes. At the next level of complexity, some effects of externally applied electric fields on currents through membranes and membrane nonlinearities are described. Some effects of high-level fields and electroporation are described in [Chapter 9](#) in *BMA* by Weaver and Chizmadzhev [112]. This is followed by a discussion of some long-term adaptive processes and secondary effects of current flow due to heating and by a description of a few effects on whole animals. This information is presented with the objective of specifying the general level or intensity of fields, currents, and temperatures where one can expect to observe a given class of biological responses. Much more data are presented in [Chapter 3](#) in *BMA* by Anderson et al. [113]. The next section contains data on the levels of typical naturally occurring and man-made fields. This section also includes a comparison of some externally applied fields, fundamental noise levels, and signals generated in the body. J. Weaver and M. Bier present a more complete treatment of some of the noise sources in biological cells in [Chapter 7](#) in this volume.

5.2 Maxwell's Equations and the Properties of Materials

Maxwell's equations can be written in both differential and integral form, and solutions to them under a variety of boundary conditions are extensively covered in Chapter 10 in this volume by James C. Lin and Paolo Bernardi. In differential form they are given by [1]

$$\vec{\nabla} \times \vec{H} = \vec{J} + \frac{\partial \vec{d}}{\partial t} \quad (5.1)$$

$$\vec{\nabla} \times \vec{E} = - \frac{\partial \vec{B}}{\partial t} \quad (5.2)$$

$$\vec{d} = \epsilon_0 \vec{E} + \vec{p} \quad (5.3)$$

$$\vec{B} = \mu_0 \vec{H} + \vec{M}_B \quad (5.4)$$

where \vec{H} is the magnetic field, \vec{J} is the current density, \vec{d} is the displacement vector, t is time, \vec{E} is the electric field, $\vec{\nabla}$ is the partial differential operator, del, \vec{B} is the magnetic flux density, ϵ_0 is the dielectric constant for free space, \vec{p} is the electrical polarization per unit volume, μ_0 is the magnetic permeability in vacuum, and \vec{M}_B is the magnetic polarization per unit volume. It is often convenient to expand the electrical polarization in a power series:

$$\vec{p} = \vec{p}_0 + \epsilon_0 X_e \vec{E} + \epsilon_0 X_2 \vec{E}^2 + \dots \quad (5.5)$$

where \vec{p}_0 is the permanent polarization, X_e is the linear electric susceptibility, and X_2 is the quadratic coefficient. X_2 is significant for nonlinear optics and very large values of the electric field. For most of the exposure conditions described in this volume it is convenient to express the induced polarization in terms of the dielectric constant ϵ

$$\epsilon = \epsilon_0(1 + X_e) \quad (5.6)$$

Note that in anisotropic materials, both ϵ and X_e may be tensors and complex numbers. The imaginary part of ϵ is associated with the loss or dissipation of energy by the bound charges. The solutions to Maxwell's equations for \vec{E} and \vec{B} are given for a variety of boundary conditions and under the assumption that values for \vec{J} , \vec{p} , and \vec{M}_B are known (given in [Chapter 10](#) in this volume by James C. Lin and Paolo Bernardi). These fields, in turn, determine the forces on the components of the biological material.

5.3 Physics of the Interactions of Electric Fields with Biological Materials

Biological systems consist of complex physical subsystems. In an attempt to understand them, we will start at the most elementary level. Perhaps the simplest level—which is already surprisingly complicated—is the effect of electric fields on biological fluids. These fluids contain a large number of components, including ions, polar molecules such as water, proteins, lipids, hormones, and colloidal particles. Current flow in these fluids is given by the sum of the drift and diffusion currents for each component. At low current densities the system is linear; however, at moderate to high current densities nonlinearities are observed [2]. In addition, the fields can change the orientation of molecules with dipole moments, induce dipoles by distorting electron orbits, and change the relative positions of some of the atoms within the molecule. This, in turn, leads to changes in the dielectric constant. The next level of complexity involves the interaction of the fields with membranes that behave like porous solids for fields applied perpendicularly to their surface and like viscous liquids for fields in the plane of the membrane [3,4]. Membranes are inhomogenous so that different portions of them may be affected differently by the perturbing fields. Additionally, membranes are involved in active chemical reactions that change their porosity to various ions selectively. Both electrical potentials and chemical signals may change the membranes' conductivity by orders of magnitude and transmit signals across membranes. The next level of complexity occurs in the interactions between

the biological fluids and the membranes in the presence of electric fields. Electric fields affect the selective transport of ions or molecules through the membrane. They change the buildup of charged ion layers at the surface and change the way new molecules are incorporated into the membrane or are bound to its surface. The result of changes in the transport of molecules or ions across cell membranes is changes in the performance of the cells and, in turn, of the organs of which they are a part. They can also lead to changes in the rate of exchange of electrons between molecules in the membrane and ions or molecules in the fluid [5]. For example, a biasing electric voltage across a pacemaker cell in the heart will change its firing rate and thus the pumping rate of the heart.

The fundamental law describing the forces on charged particles is given by

$$\vec{F} = q(\vec{E} + \vec{v} \times \vec{B}) \quad (5.7)$$

where \vec{F} is the force, q is the charge on the particle, and \vec{v} is the velocity of the particle. \vec{E} and \vec{B} are coupled by Maxwell's equations so that a time-varying magnetic field generates an \vec{E} field and vice versa. This force may lead to ion currents and changes in the orientation of dipoles in molecules, and it may also lead to transitions between energy levels, to shifts in their spacing and induced dipole moments, \vec{P} . Additionally, if nonlinearities or time-varying impedances are present, alternating current (AC) fields can be rectified to produce direct current (DC), frequencies at the second and higher harmonics, and sum and difference frequencies with biological or molecular oscillations. Direct magnetic field effects may occur through the term $\vec{v} \times \vec{B}$. For example, for a Na^+ moving at a thermal velocity of $4 \times 10^2 \text{ m/sec}$ in the earth's magnetic field of about $5 \times 10^{-5} \text{ T}$, this term has a magnitude of $2 \times 10^{-2} \text{ V/m}$, and the force is at right angles to the field and the velocity.

In addition to the forces on charged particles, electric fields can induce forces on polarizable atoms, molecules, ions, and molecules with dipole moments. To first order these forces are described by

$$\vec{F}_d = (\vec{P}_0 \cdot \vec{\nabla})\vec{E} \quad (5.8)$$

$$\vec{F}_L = \alpha V(\vec{E} \cdot \vec{\nabla})\vec{E} \quad (5.9)$$

where \vec{F}_d is the force on a molecule with a permanent dipole moment \vec{P}_0 , and $\vec{\nabla}\vec{E}$ is the gradient of the electric field. \vec{F}_L is the force on a molecule with an induced dipole moment $\vec{P}_i = \alpha V \vec{E}$, where α is the tensor polarizability and V is the volume [6]. Note that biological materials are highly inhomogeneous and that there are large electric field gradients at the boundaries between the fluids and membranes. Additionally, for induced dipole moments, when the sign of the dipole reverses with an alternating field the force along the gradient of the field can be in a constant direction.

The current flow \vec{J}_i of a given molecule or ion, in molecules or ions per second per meter square, has both drift and diffusion components that may be given by

$$\vec{J}_i = N_i \mu \vec{F} + q D \vec{\nabla} N_i \quad (5.10)$$

where N_i is the ion concentration, μ is the mobility in seconds per kilogram, D is the diffusion constant in meter square per second, and $\vec{\nabla} N_i$ is the gradient of the concentration. For charged particles, the force has two components [7]:

$$\vec{F} = q\vec{E} + (\vec{M} \cdot \vec{\nabla})\vec{E} \quad (5.11)$$

where \vec{M} is the sum of the permanent and induced dipole moments.

The drift portion of the ion currents takes the form

$$\vec{J} = \sum q_i N_i \mu_i \vec{E} + \sum N_i \mu_i (\vec{M} \cdot \vec{\nabla}) \vec{E} \quad (5.12)$$

The conductivity $\sigma = \sum q_i N_i \mu_i$, and N_i is the concentration of each ion, μ_i is the mobility, and \vec{M}_i is the dipole moment. Table 5.1 shows some typical values of mobility.

The conductivity of biological fluids such as blood, which contains cells, is in the vicinity of $\sigma = 0.6 \text{ S/m}$, while for physiological saline it is approximately 1.4 S/m . For more detailed material on the conductivities and dielectric constants of biological materials, see Chapter 3 in this volume by C. Gabriel. If the fluid channels between cells are relatively thick and the fluids are relatively good conductors, the channels tend to short circuit the voltages that might otherwise appear across membranes that typically have conductivities at least a thousand times smaller.

The total dielectric constant for a material includes the sum of the induced polarizabilities of the components and interaction terms between them. It is sometimes useful to think of the dielectric constant as a way of describing the fraction of the electric field that is shorted out by the bound charges. This can be shown by considering an ideal parallel plate capacitor where the outside plates are separated by a distance l . The capacity for these plates is given by

$$C_0 = \frac{\epsilon_0 A}{l} \quad (5.13)$$

If an ideal thin metal plate of thickness w is inserted halfway between these plates, then the resulting capacity is given by

$$C = \frac{C_0}{(1 - w/l)} = \frac{\epsilon A}{l} \quad (5.14)$$

The corresponding dielectric constant is given by

$$\epsilon = \frac{\epsilon_0}{(1 - w/l)} \quad (5.15)$$

In this example it is apparent that as the fraction of the field that is shorted out by the metal plate of thickness w increases, so does the effective dielectric constant. The electrons or ions forming an induced dipole moment can be thought of as doing the same thing. If there is a significant time lag for the movement of the charge, the effective value of w is reduced. The very large values of the dielectric constants of some tissues at low-frequencies can be thought of as the resulting motion of ions that are trapped inside highly

TABLE 5.1

Typical Values of Biological Ionic Mobilities

Particles	Mobilities	Ions	Mobilities
Proteins	$\mu = 10^{-10} \text{ to } 10^{-8} \text{ m}^2/\text{V sec}$	Ca^{2+}	$\mu = 6.2 \times 10^{-8} \text{ m}^2/\text{V sec}$
Na^+	$\mu = 5.2 \times 10^{-8} \text{ m}^2/\text{V sec}$	Mg^{2+}	$\mu = 5.4 \times 10^{-8} \text{ m}^2/\text{V sec}$
K^+	$\mu = 7.6 \times 10^{-8} \text{ m}^2/\text{V sec}$	Cr^{3+}	$\mu = 1.9 \times 10^{-8} \text{ m}^2/\text{V sec}$

resistive membranes. At higher frequencies, the ions can no longer move fast enough to fully charge the surfaces of the membranes, and the effective dielectric constant for the tissue decreases. If energy is absorbed in inducing the dipole moments, then the dielectric constant becomes a complex number.

The forces applied by an electric field superimpose a drift velocity on the much larger random thermal velocity in the opposite directions for positively and negatively charged particles. These forces can lead to a redistribution of ions or molecules as a result of the differential mobilities and to an increase in the concentration of ions at interfaces. The average drift velocity \vec{v} for a charged particle is given by

$$\vec{v} = \mu_i \vec{E} \quad (5.16)$$

The separation of molecules as a result of the different velocities in a DC electric field is known as electrophoresis and is frequently used to identify large molecules or charged colloidal particles [8]. The separation of particles in an AC field gradient is known as dielectrophoresis [5].

For a spherical particle in a homogenous insulating fluid the mobility μ_i is given by

$$\mu_i = q / 6\pi\eta a \quad (5.17)$$

provided that the particle is significantly larger than the background particles of the fluid, where η is the viscosity of the fluid and a is the radius of the particle. In a conducting medium, counterions, or ions with a charge opposite to that of the particle, and molecules with dipole moments are attracted to it. They change the effective radius of the particle and then partially shield its charge. Additionally, small counterions may flow in the direction opposite to the particle motion, exerting a viscous drag. The theory for motion of a rigid sphere through a conducting liquid is complicated if all these effects are taken into account. Often some of the parameters, including the charge on the sphere, are not measurable. However, a relatively simple expression for the electrophoretic mobility is often used:

$$\mu_i = \frac{\epsilon_i \zeta}{4\pi\eta} \quad (5.18)$$

where ϵ_i and η are the dielectric permittivity and the viscosity of the fluid (in kg/m sec), respectively, and ζ is the electrical potential drop from the particle surface across the bound fluid to the interface where the liquid begins to flow under the shear stress. Stated another way the "zeta potential," ζ , is the potential at the surface boundary between the stationary fluid and the liquid that is moving with the particle. It should be noted that ζ is less than the total potential ψ across the charge double layer surrounding the charged particle. Also, note that water molecules bind to the ions, increase the effective diameter, and reduce the effective charge. This, in turn, makes the mobility less than that which might be expected at first from the atomic size and Stokes' law.

In a uniform AC field a charged particle oscillates about its mean position, and the electrical energy added to the solution is largely converted to heat. If there is a gradient in the field, as is to be expected in biological materials that are highly inhomogenous, then the gradient of the field can lead to a net charge displacement if the fields are large enough to lead to nonlinearities in the mobility or induced dipole moments. For large \vec{E} the velocity saturates and mobility varies as

$$\mu_i = \frac{\mu'_0}{|\vec{E}|} \quad (5.19)$$

and [Equation 5.16](#) yields

$$|\vec{v}| = \mu'_0$$

Most biological systems are highly inhomogenous, and the induced currents will vary rapidly in space. For the case of an induced dipole moment and an ideal dielectric sphere with a permittivity ϵ_2 and a conductivity $\sigma_2 = 0$ in an ideal dielectric fluid with a dielectric permittivity ϵ_1 and a conductivity $\sigma_1 = 0$ and a nonuniform electric field prior to inserting the sphere, the force

$$\vec{F}_L = \alpha V (\vec{E} \cdot \vec{\nabla}) \vec{E} = 4\pi a^2 \epsilon_1 \left\{ \frac{\epsilon_2 - \epsilon_1}{\epsilon_2 + 2\epsilon_1} \right\} \{(\vec{E}_1 \cdot \vec{\nabla}) \vec{E}_1\} \quad (5.20)$$

where \vec{E}_1 is the field in the fluid prior to insertion of the sphere. Written another way

$$\vec{F}_L = (3/2) V \epsilon_1 \left\{ \frac{\epsilon_2 - \epsilon_1}{\epsilon_2 + 2\epsilon_1} \right\} \vec{\nabla} |\vec{E}_1|^2 \quad (5.21)$$

If we assume that the viscous drag on a spherical particle is given by Stokes' law, then

$$\vec{F}_d = 6\pi a \eta \vec{v} \quad (5.22)$$

and the mobility μ_i is given by

$$\mu_i = (2a^2/3\eta) \epsilon_1 \left\{ \frac{\epsilon_2 - \epsilon_1}{\epsilon_2 + 2\epsilon_1} \right\} \vec{\nabla} \vec{E}_1 \quad (5.23)$$

Dielectrophoresis may also be used for identifying molecules, and a more general treatment of the forces needs to take into account the conductivity or a complex dielectric constant for both the fluid and the particle [9].

For particles with dipole moments to change their distribution under the influence of an electric field gradient the force \vec{F} must be large enough to overcome other forces. One of these forces that frequently must be overcome is due to osmotic pressure or diffusion. The osmotic pressure can be thought of as the force per unit area arising from diffusion or the random motion of the particles and is given by

$$\Pi = N_i k T \quad (5.24)$$

where k is Boltzmann's constant and T is the absolute temperature [10]. The average differential force on a particle is proportional to the gradient of the osmotic pressure and is given by

$$\vec{F}_{os} = -\frac{1}{N_i} \vec{\nabla} \Pi = \frac{kT \vec{\nabla} N_i}{N_i - k \vec{\nabla} T} \quad (5.25)$$

If we consider the case of a spherical volume with a radial concentration gradient at constant temperature, the force is given by

$$\vec{F}_{os} = -kT \frac{\Delta N_i}{N_i} \cdot \frac{r_0}{\Delta r} \quad (5.26)$$

where r_0 is the unit vector, ΔN_i is the incremental change in concentration, and Δr is the incremental change in distance. The maximum change is given by

$$\frac{\Delta N_i}{N_i} = 1 \quad (5.27)$$

when the presence or absence of a particle occurs at a distance $\Delta r = 2a$, where a is the particle radius. In this case, we get the maximum force

$$|\vec{F}_{os(max)}| = -\frac{kT}{2a} \quad (5.28)$$

To get an idea of the size of these forces, consider a particle of fat with $a = 1 \mu\text{m}$ in water. The maximum osmotic pressure at $T = 300\text{K}$ is $|\vec{F}_{os(max)}| = 2 \times 10^{-13}\text{N}$. The dielectric constant for water is approximately $\epsilon_1 = 80\epsilon_0$ and for a fat particle, $\epsilon_2 = 2\epsilon_0$, where $\epsilon_0 = 8.854 \times 10^{-12}\text{F/m}$. To get a dielectric force greater than the maximum osmotic force, we need a value of $|\vec{\nabla} \cdot \vec{E}_1|^2 > 10^{12}\text{V}^2/\text{m}^3$. This is given approximately by a voltage of 100 V across a 5 mm gap when the \vec{E} field goes from zero to a peak value of $5 \times 10^4\text{V/m}$ over the same gap. For a particle with a single charge in a uniform field, we would need a field of $E = 1.3 \times 10^4\text{V/m}$ to get an equal force.

The electric current densities generated by a concentration gradient are given by

$$\vec{J}_d = -qD\vec{\nabla}N_i \quad (5.29)$$

where D is the diffusion constant and is given by

$$D = \nu kT \quad (5.30)$$

where ν is the hydrodynamic mobility with the dimensions of velocity/force and D has the dimensions of meter square per second. For rigid spherical particles of radius a , where $a \gg a_{H_2O}$, the Einstein–Stokes equation gives

$$D = \frac{kT}{6\pi\eta a} \quad (5.31)$$

This is only a first-order approximation because D varies slightly with concentration, departure of the molecule from a spherical shape, and other factors. η is the viscosity (in kg/m sec).

It is sometimes of interest to estimate the ratio of the drift to the diffusion current in order to estimate the level of the applied fields or the applied field gradients that lead to biological changes. This ratio is approximately given by [6]

$$\frac{\vec{J}_{i,diffusion}}{\vec{J}_{i,drift}} = \left(\frac{kT}{F_i}\right) \cdot \left(\frac{\Delta N_i}{N_i}\right) \quad (5.32)$$

where \vec{F}_i is the force on the particle due to both the charge on the particle and the gradient of the field on the dipole moment. If we now assume that the maximum change in N_i goes from N_i in the solution to 0 at the membrane surface over a distance of the diameter of the

molecule of N_i and that this is the same distance over which the field goes from the field in the fluid to the field in the membrane, then

$$\frac{\vec{J}_{i,\text{diffusion}}}{\vec{J}_{i,\text{drift}}} = \frac{kT}{W_i} \quad (5.33)$$

where W_i is the energy acquired by the particle moving through the field and its gradient. At room temperature the thermal energy $kT \cong 0.026 \text{ eV}$. A voltage drop from an externally applied source across the membrane liquid boundary on the order of $2 \times 10^{-3} \text{ V}$ would be required in order to make the drift current significant with respect to the total diffusion current under these assumptions. One way in which smaller drift currents and smaller voltages could be significant is if the ions with low velocities perpendicular to the membrane are the most important in binding to the membrane. Slow molecules stay close to the membrane for longer times, and these molecules are most affected by the applied forces [6].

For different boundary conditions the results will be quite different. If, for example, the boundary was nearly perfectly reflective, then the concentration gradient would be nearly 0, and so would the net diffusion current. Additionally, the gradient in the concentration may occur over a larger distance than the gradient of the electric field. At steady state the concentration at the membrane can be expected to increase until the diffusion current and the drift current balance each other so that the net current is equal to the rate at which the molecules are bound to the membrane or pass through it.

There are four forces that may become important when considering the interaction between two particles in a fluid. These are the osmotic diffusion force, the electrostatic force, the van der Waals force, and the hydration force [9]. These forces may all become important in considering the interaction between particles or bilipid membranes in an aqueous fluid. Electrostatic or coulomb forces between particles of like charge are repulsive. Because the charged particles attract free ions of the opposite sign—which produces a double layer—they are effectively shielded or are screened by the charged ions of the opposite sign when immersed in a conducting fluid. This force decays exponentially or

$$\vec{F}_c = \vec{F}_0 \exp - \frac{r}{\lambda_d} \quad (5.34)$$

where λ_d is known as the Debye screening length [11]

$$\lambda_d = \left[\frac{2q^2 n}{\epsilon k T} \right]^{1/2} \quad (5.35)$$

where n is the density of the ion species doing the shielding, q is the charge and ϵ is the dielectric constant of the solution, k is Boltzmann's constant, and T is the absolute temperature. For physiological saline solution of approximately 0.14 M, the Debye length is approximately 0.83 nm [12]. Thus, the electrostatic forces are important only at very short ranges.

For like particles, the forces are repulsive at short distances (0.1 to 0.2 nm) and attractive at longer ranges. These forces may be thought of as being generated by transient electromagnetic fields because of fluctuations that occur as a result of thermal agitation or natural uncertainties in the position and momentum of the electrons and atomic nuclei.

If one thinks of the local transient fluctuations in terms of the underlying contributions from oscillations at all possible frequencies, it can be shown that the strength of the contributions due to the local fluctuations at a given frequency is proportional to the absorption of light at that frequency by the material. For an individual atom these forces fall off very rapidly as $1/r^7$ [7]. However, when they are integrated over the surface of a membrane, which is thick compared to an atomic layer, they are correlated over many atoms, as the wavelengths are large compared to an atomic diameter.

A calculation of these fields has been performed starting with quantum field theory [13]. The size of the forces and the rate at which they decay depend on the distance between the membranes and the difference of the bulk polarizability of the membrane and the aqueous gap in a complex way. All frequencies of the charge fluctuations contribute to the attraction, and each gives rise to a different relationship between energy and the distance of separation. For many simple cases and for a classical explanation of these forces and potential distributions, see Ref. [14].

One case of interest is for two membranes with a distance d_w across the aqueous gap between them. The thickness of the membranes is assumed to be large compared to the spacing. The force between these two membranes is approximately given by

$$\vec{F}_w = \frac{H}{6d_w^3} \quad (5.36)$$

where H is the Hamaker coefficient [9]. In a typical situation, the distances over which the van der Waals force is estimated to be important extend out to separations of 10 to 20 nm, which is substantially longer than a Debye length or the rate of falloff for the electrostatic or coulomb forces. The hydration forces are repulsive forces that rise extremely rapidly as the membrane bilayers approach a separation distance of approximately an atomic spacing. Experimentally, these forces can be expressed in the form [9]

$$\vec{F}_H = \vec{F}_{H_0} \exp -d_w/\Lambda \quad (5.37)$$

where Λ is a scaling constant. In the case of egg phosphomonoesterase bilayers, $\vec{F}_{H_0} \approx 7 \times 10^{-13}$ N/m² and $\Lambda = 0.256$ nm. This force may be important up to about 2 nm and is assumed to come about as a consequence of the work required to remove water from the hydrophilic surface of the membrane.

Long-range attractive forces have been observed between hydrophobic surfaces [15]. These forces are proportional to the contact area and may be the orders of magnitude larger than the van der Waals forces. They may also have decay lengths up to 25 nm. The magnitude and range of these forces depends on the temperature and the length of the surfactant's chain, and they appear only when the chains are in a fixed ordered state. These forces appear to be generated when the fields emanating from one surface induce a larger polarization in the other surface layer than in the intervening medium. Some relatively complex expressions for these attractive forces have been worked out [14].

These forces are important in self-organizing processes such as protein folding, ligand binding to hydrophobic receptor sites, and transformation of membrane structures. All these forces act over relatively short ranges in typical biological fluids. The ion densities are so large that charge neutrality is maintained everywhere except very close to charged surfaces.

The effect of an electric field, or an electric field gradient in a fluid, is to superimpose a small drift velocity on a relatively large random thermal velocity. For example, if

we apply an electric field of 10^3 V/m to a Na^+ ion, we would expect a drift velocity of about 5×10^{-5} m/sec as compared to a thermal velocity of about 4×10^2 m/sec. For a protein, we would expect a drift velocity approximately one tenth of the speed of the Na^+ ion, although at higher fields. This means that if we are to transport proteins or other small charged particles over appreciable distances of a few millimeters, we can expect it to take minutes or longer. In the case of bacteria, we have measured drift velocities of 10^{-6} m/sec at 100 Hz in fields of about 10^4 V/m and gradients of 5×10^6 V/m² or about 0.2% of the velocity of the Na ions in the same field [5,16].

This drift velocity may also change chemical reaction rates if the rate is limited by the availability of one of the charged components. Consider the case of a chemical reaction that takes place in a homogenous fluid if the chemical reaction has the form



where (A) and (B) are the concentrations of the two input chemical reactants and k_1 is the reaction rate for A + B to C and k_2 is the rate for the back reaction of C to A and B. If we simplify the system and let k_2 be small, then the initial reaction rate may take the form [17,18]

$$k_1 = k(A)^n(B)^m \quad (5.39)$$

where n and m refer to the order of the reaction. In order to find the values of n and m , one can make the concentration of one of the reactants small so that it takes the form

$$k_1 = k(A_0)^n(B)^m \quad (5.40)$$

where we have made the concentration (A_0) large enough so that it is approximately constant, and the changes in the reaction rate can be measured by varying (B). The value of k is given by

$$k = zpe^{-\Psi/RT} \quad (5.41)$$

where z is the collision frequency and p is the steric factor, which is <1 and reflects the fact that not all collisions occur with the right orientation of the molecules to react. Ψ is the activation energy, R is the gas constant, and T is the absolute temperature. For many cases the collision frequency is proportional to the current density, and thus there are terms that are proportional to both the drift and the diffusion currents. For example, consider the case of an enzyme reaction on a charged substrate such as a biological membrane. The total current density for a given ion in the fluid incident on the membrane is given by [Equation 5.10](#).

If the chemical reaction rate is limited by the number of ions arriving at the membrane surface with enough energy to overcome the barrier required to initiate the reaction, then a DC drift current may either add to or subtract from the diffusion current. If the field direction is such that it prevents the ion from reaching the surface, then the chemical reaction is blocked. If the direction is reversed, the rate can grow exponentially. These changes in chemical reaction rates with the direction of the electric field are likely to be responsible for changes in the growth and reabsorption of neuritis [19]. They are also likely to be involved in the mobility of cells such as leukocytes and fibroblasts [20,21].

An AC drift current will add to the diffusion current. For the AC fields, the drift current can be thought of as increasing the volume covered by a particle executing a random walk as a result of Brownian motion. Thus, in an asymmetrical environment an electric field oscillating in the x direction may increase the number of particles that will strike the $y-z$ plane in a fixed period of time and can increase the chemical reaction rate for a catalytic reaction at the $y-z$ plane. Seto and Hsieh show that AC fields as low as 5 V/m can increase enzyme reaction rates by a factor of 5 [22]. For a 60 Hz field, the peak-to-peak displacement for Ca^{2+} resulting from this field is estimated to be about 1.6 nm or about twice the thickness of the Debye layer. AC magnetic fields have also been shown to change the growth rate of corn roots at fields levels of 5×10^{-3} T. It is likely that these fields are inducing significant currents [23].

An additional mechanism by which AC or DC electric or magnetic fields can effect chemical reactions is by shifting the energy level and the distribution of particles in them. DC electric fields can shift the energy level by an amount that is given by the change in the dipole moment, $\Delta\vec{M}$, and in the polarizability, $\Delta\alpha$, associated with the transition. A DC field can either stretch or compress a dipole depending on its orientation with respect to the field, thus increasing or decreasing the energy levels for atoms or molecules with different orientations. It also can modify its rate of rotation, speeding it up when the dipole is pointed in the direction of the field and slowing it down when it is pointed away from the field [24]. In a vacuum the modifications of the rotational states have been worked out from the quantum mechanics for relatively simple molecules and can lead to a relatively complex set of allowed energy states that are a function of the applied field [23]. In a solid or a membrane the energy levels between the states corresponding to the different orientations shift, by different amounts, for each state as a function of the applied field. This is known as the Stark effect [25]. The frequency corresponding to this energy shift with a fixed orientation is given by

$$h\Delta f = -\Delta\vec{M} \cdot \vec{E} - \frac{1}{2}\vec{E} \cdot \Delta\alpha \cdot \vec{E} \quad (5.42)$$

where Δf is the frequency splitting between levels, $\Delta\vec{M}$ is the change in the dipole moment, $\Delta\alpha$ is the change in polarizability, and h is Plank's constant. These terms give the linear and quadratic Stark effects for a transition in a uniaxially oriented system. These energy levels will be inhomogeneously broadened by the random orientation of the dipoles with respect to the applied field and by the thermal energy. Since the quantum of energy, hf , at microwave and lower frequencies is very much smaller than a quantum of thermal energy, low-lying energy levels are approximately equally populated. However, higher-energy states may be preferentially excited by chemical reactions or optical photons so that different excited states may contain different populations. These states may be further defined by the magnetic field and separated by a Zeeman splitting. Thus, radio- and low-frequency fields corresponding to energy separation between these states may excite transitions between levels that are separated by the Stark splitting and change the population distribution in these excited states. The transition rate between an excited molecule and its final product depends on the overlap between the energy levels of the two states. Thus, the application of an electric field can shift the energy levels so as to either increase or decrease this overlap and the transition rate. This has been discussed at length in Ref. [23] for the case of Zeeman splitting of the energy levels by a DC magnetic field and free radicals [26]. See also Chapter 6 in this volume by S. Engstrom.

5.4 Biological Amplification

Biological systems are not in a state of thermal equilibrium. In a typical cell, energy is supplied by hydrolysis of an ATP molecule, which leads to the pumping of three sodium ions out of a cell and two potassium ions into the cell. The net result is creation of potential difference between the inside and outside of a cell in the range of 50 to 100 mV so that the interior of the cell is at a negative potential with respect to the external environment [27]. This potential difference can be used to amplify a variety of external signals just as a typical electronic amplifier can use a small AC signal to convert DC energy into a larger AC signal. For example, the input from many dendritic junctions can be summed in a pyramidal cell to trigger an action potential that is larger than any of the input signals [28]. The input from a single synaptic junction might change the cell resting potential by 0.5 to 1 mV, and 10 to 20 inputs might be required to fire an action potential of 50 to 100 mV [27]. Additionally, subthreshold inputs can lead to the release of neural transmitters that, in turn, can release from 2 to 10,000 Ca^{2+} ions from internal stores. These neural transmitters may remain bound to the postsynaptic membrane for up to 4 sec and reduce the threshold for the firing of successive pulses [29]. Feedback from the postsynaptic membrane to the presynaptic membrane can further reduce the firing potential for the synaptic junction.

Another mechanism of amplification that may be of interest is the extraction of energy from a high-frequency signal. If a low-frequency electric field is added to a higher-frequency field and is incident on a nonlinear reactance, then the low-frequency signal may be amplified parametrically. This mechanism for amplification is valuable in the optical region for the generation of tunable signal sources and for low-noise microwave amplifiers [1,30]. In a biological system the low-frequency signal might be generated by an ongoing process such as the heart and amplified by mixing with an external signal from a power line field.

An additional mechanism for amplifications is stochastic resonance. Stochastic resonance differs from the foregoing mechanisms of amplification in that the energy is extracted from the noise. Consider, for example, a small, externally applied sinusoidal electric field incident on an ion in a potential well. If the energy acquired from the external signal is not large enough to exceed the potential barrier, the ion stays trapped in the potential well. However, if noise is added to the system, then when the sum of the applied electric field and the noise are large enough to provide enough energy to exceed the height of the potential barrier, the ion may escape the potential well. This happens most frequently at the peaks of the applied electric field so that the signal is amplified at the applied frequency. Gains on the order of 20 to 30 dB and increases in the signal-to-noise ratio of 18 dB have been observed for stochastic resonance amplifiers [31]. For an extensive review of this subject and some application neuronal systems, see Gammaitoni [32]. For a bistable system, such as a pacemaker cell that is driven by both noise and a periodic signal, it has been shown that the signal-to-noise ratio can be enhanced by the addition of noise to a weak periodic signal and that power can be extracted from the noise. A strong periodic signal can be generated at signal-to-noise ratios < 1 [31,33]. This phenomenon occurs when two energy states are separated by a barrier, and the probability of a transition increases exponentially with increasing noise power. For periodic signals that are insufficient to cause a transition over the barrier but periodically increase the energy of the particle, the transition rate at the signal frequency first increases with increased noise power up to some maximum. When the noise power is increased above this level, the output signal becomes more random (see also Chapter 9 in this volume by Weaver and Bier).

5.5 Effects of Electric Fields on Cell Membranes

Electric fields play a very important role in the normal biological functioning of membranes. Membranes are complex structures containing lipids, voltage-activated ion channels, and proteins. It would be surprising if externally applied fields did not affect the membrane behavior. First, an electric field exerts a mechanical force on a membrane by means of the force exerted on charges in the Debye layer on either side of it and on charged proteins that may protrude from the lipid bilayer. Note that although as a first approximation the membrane is often modeled as a smooth planar or spherical surface, it is highly inhomogeneous, and the charges are sparsely disturbed. Thus, the field on a protein may be widely different from the average field. See Figure 5.1a. and b for a partial indication of a membrane and cell complexity. The effects from fields in the plane of the membrane, where large molecules such as proteins are free to move as in a viscous fluid, are significantly different from the effects of fields in the transverse direction, where the membrane components are bound in a layer typically 5 to 15 nm thick.

The field distribution incident on a particular part of a cell membrane is a function of its geometry, frequency, and the cells around it. As can be seen from the models in Figure 5.1d, a wide variety of environments may exist. The currents that flow through and along the membranes are dependent on the geometry and frequency. A variety of equivalent circuits have been used to model both the impedance of the membrane and the extracellular fluids. The simplest of these are a resistor and capacitor in parallel. At very low-frequencies a collection of cells can be modeled with resistors as indicated in Figure 5.1c.

The interiors of cells are normally negatively biased in relation to the surrounding fluid by 50 to 150 mV, which leads to average transverse electric fields up to tens of millions of volts per meter [34]. The effective membrane resistance (R_m) per unit area takes on values of 0.14 to $15 \Omega/m^2$ in the transverse direction. This corresponds to resistivities in the range of $\rho_m = 10^7$ to $10^9 \Omega \cdot m$. The relative dielectric constant for the membrane is typically in the range of 2 to 4. Both the surrounding fluid and the interior of a cell have resistivities ρ_f of about $2 \Omega \cdot m$ and a relative dielectric constant of 50 to 80. This means that the cell membrane tends to shield the interior of a cell very effectively from externally applied fields at frequencies below a few kilohertz and becomes almost a short circuit in the multimegahertz region of the spectrum. In most cells the interior of the cell contains complex structures that are functions of time as the cell grows and divides. See Figure 5.1b.

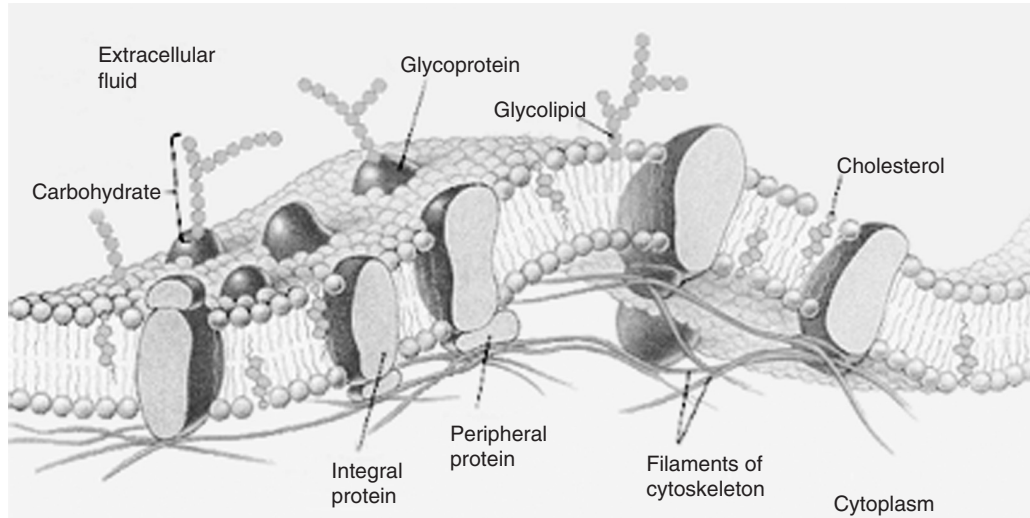
Consider the case of an oversimplified hypothetical rectangular cell as shown in Figure 5.1c. At low-frequencies, an external field \vec{E} causes a current density $\vec{J}_f = \vec{E}/\rho_f$ to flow in the external medium, where ρ_f is the resistivity of the fluid. The corresponding voltage drop is $V = \vec{E}L = \vec{J}_f\rho_f L$, which we can consider to be applied to the cell. This voltage is distributed across the cell length as

$$V = [\rho_m 2t + \rho_f(L - 2t)]|J_m| \quad (5.43)$$

where \vec{J}_m is the current density through the cell and ρ_m is the resistivity of the membranes. Typical cell membrane thicknesses are 6 to 10 nm, and typical dimensions are 10 to 150 μm . Setting $L = 100 \mu\text{m}$ and

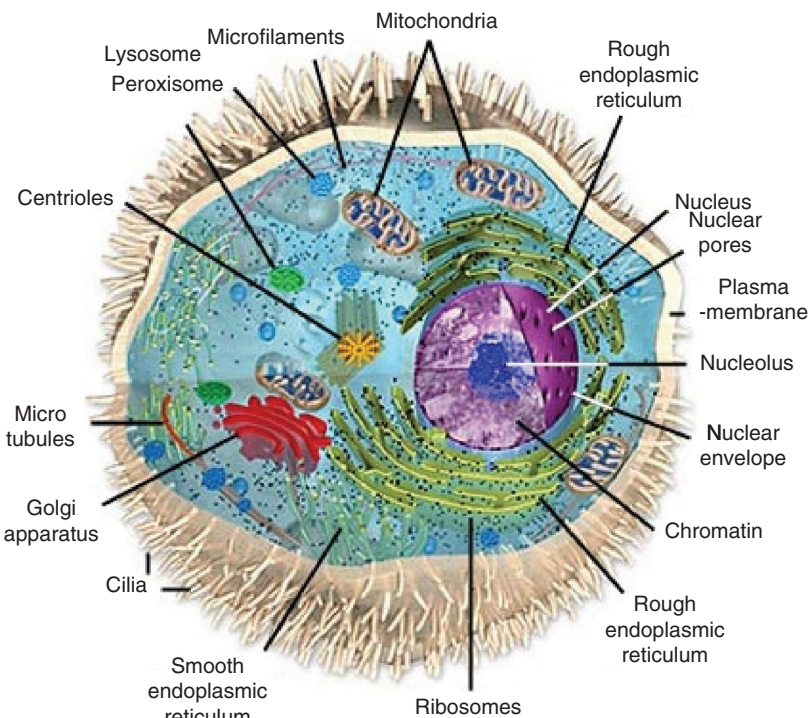
$$\rho_m 2t = 10 \Omega \cdot m^2 \quad (5.44)$$

$$V = (10 \Omega \cdot m^2 + 2 \times 10^{-6} \Omega \cdot m^2)|J_m| \quad (5.45)$$



(a)

Anatomy of the animal cell

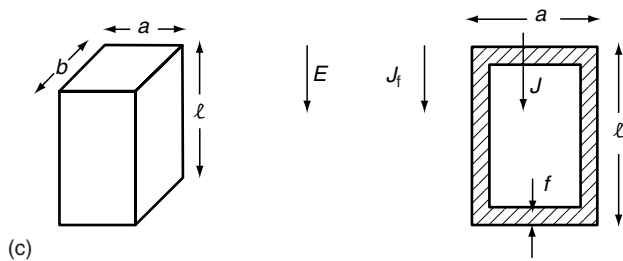


(b)

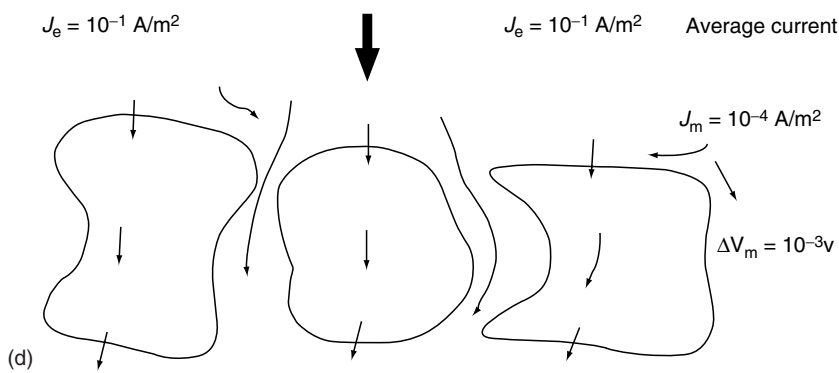
FIGURE 5.1 (See color insert following page 380.)

(a) Model of a cell membrane. (From Chiras, D., *Human Biology*, © 5th edition, 2006, Jones and Bartlett Publishers, Boston. With permission.) (b) Anatomy of the animal cell. (From Molecular Expressions, <http://microscopy.fsu.edu>, accessed Sep. 30, 2005; drawing © M.W. Davidson and Florida State University. With permission.)

(continued)



(c)

**FIGURE 5.1 (continued) (See color insert following page 380.)**

(c) Current distribution in a hypothetical rectangular cell. (d) Partition of 60-Hz currents through and around cells for an average current density $J = 10^2 \text{ A/m}^2$. J_c is the current density between cells, and J_m is the current density through the membrane. (From Wachtel, H., private communication. With permission.)

This shows that essentially all of the transverse voltage drop occurs across the membrane at low-frequencies and the interior of the cell is almost completely shielded from external fields. A more complete theory for long cells that accounts for the internal resistance of the cell is given by Cooper et al. [35]. See also Chapter 11 by Pila [114]. Note that muscles, nerves, and a number of other cells may be much longer than $100 \mu\text{m}$ and may have dimensions in centimeters. Additionally, blood vessels form long, low-resistance paths that may concentrate currents due to externally applied fields. The anisotropic characteristics of cells are reflected in an anisotropy of the dielectric and conductive properties of tissue, which may give variations of as much as 10 to 1 in conductivity, depending on the direction of measurement relative to cell orientation [36]. A number of fish, including sharks, have been shown to use very long cells and to sum signals in both series and parallel to increase the voltage drop across a sensitive membrane in order to sense fields as low as 10^{-6} V/m [37–39]. The long cell may be thought of as an antenna that concentrates the field across a very thin, voltage-sensitive detector membrane. This membrane appears to have a built-in amplifier that allows detection of signals that are only a little above the natural electrical noise.

Membranes are not just simple linear resistors, but they usually are nonlinear and, in the case of nerve cells, are time varying as well. For a passive membrane in which the membrane potential is primarily determined by the concentration gradient of a single ion such as K^+ , the Nernst equation predicts a diode-rectifying characteristic of the form [31]

$$I = I_0 \left[\exp\left(\frac{V_m}{\eta V_T}\right) - 1 \right] \quad (5.46)$$

where V_T is given by

$$V_T = \frac{kT}{q} = 0.026 \text{ V} \quad (5.47)$$

at $T = 300 \text{ K}$. q is the charge on the electron, V_m is the voltage across the membrane, I_o is the current for ideal back-biased current in amperes, and η is a dimensionless constant. Thus, for currents flowing through a membrane in one direction, the current is nearly constant, whereas for flow in the other direction the current increases exponentially with voltage. In addition to passive currents, cells also use the energy from metabolic processes for the active transport of ions against the fields established by the concentration gradients. These processes are usually modeled as current sources and described as pumps [31]. A thermodynamic approach to pumping shows that ions can be pumped if they form a compound with a material that can flow through the membrane and that is created on one side of the membrane and destroyed on the other [40]. A large variety of models have been generated to characterize the effects of externally applied fields on the transport of ions through membranes [41–43]. However, the details of the pumping process are not well understood. In addition to ion transport, electrical fields can change the binding of ions or molecules to the membrane surface.

In the case of pacemaker cells, there are also feedback processes that lead to an oscillating membrane potential and a membrane resistance that is a function of time. The current flow for these cells is described empirically by the Hodgkin–Huxley equation [31]. An alternate approach that treats the nerve pulse like a plasma instability has been proposed by Triffet and Green and Vaccaro and Green [44,45]. Na^+ and K^+ currents are the dominant carriers for the propagation of nerve impulses along a cell. It is generally believed that the Na^+ and K^+ currents that flow through the membrane in opposite directions are carried through separate channels. Ca^{2+} ion currents are involved in the activation of at least a portion of the K^+ currents and are voltage gated. By activating the K^+ currents, the Ca^{2+} ions shorten the length of time the cell is depolarized and thus speed up the firing cycle [46]. A statistical approach to the formation of protein channels in the membrane by Baumann and Easton predicts many of the observed characteristics [47–49].

During the firing of a nerve cell, the Na^+ current pulse precedes the K^+ current pulse, which returns the cell to its resting potential [31]. The overall concentration balances are maintained by active ion pumps. Cl^- , Mg^{2+} , and possibly OH^- and H^+ ions may also be involved in the current flow across a cell membrane.

The firing of a nerve cell typically involves voltage spikes of 10^{-1} V and peak current densities of 1.5 A/m^2 . Changes in the firing rate can be induced by the injection of charge through a microelectrode of $<10^{-9} \text{ A}$ for a few milliseconds. However, in cases where electrodes are used to stimulate muscles or to control epilepsy, the current is injected through a series of cell membrane fluid boundaries at a distance from the controlling nerve fiber. Thus, typical injected currents to produce behavioral changes in cells are in milliamperes, and current densities are 10 A/m^2 or higher.

For fields parallel to the plane of the membrane, it is possible to obtain electrophoresis or a rearrangement of charged particles. This has been shown by Poo in a striking fashion in cultured embryonic *Xenopus* myotomal muscle cells [50,51]. Receptors on the surface of the cell were labeled with a fluorescent dye and allowed to uniformly distribute themselves. Exposures to electric fields of 10^2 to 10^3 V/m were sufficient to concentrate the

fluorescent-labeled receptors on the side of the anode in about 10 min. After shutting off the field, diffusion returned the dye to its uniform distribution in about 2 h. This corresponds to an in-plane diffusion constant of about $3 \times 10^{-12} \text{ m}^2/\text{sec}$. The force on the receptor molecules or particles in the membrane includes not only $q\vec{E}$ but also any viscous drag that may be generated by the flow of ions of the opposite sign moving along the surface in the opposite direction. The direction of motion for a given charged particle seems to depend on whether it has a larger or smaller zeta (ζ) potential than the potential across the charged double layer at the interface between the cell surface and the fluid (see Equation 5.16).

Additional work has shown that the distribution of acetylcholine (ACh) receptors is changed by external fields [48,49]. These receptors are concentrated on the cathode-facing surface of the cell in fields of 10^3 V/m over a period of 30 min by literally rearranging channels already existing in the cell membrane. The concentration or clustering persists for at least 5 h after the field has been turned off, indicating that the clustering is relatively stable. Single-channel patch measurements show both a higher density of ACh channels in the clusters near the cathode and a longer mean duration of the pulses through the transmembrane channels. The length of the current pulse near the anode does not differ from the controls, indicating that the field itself does not have a direct effect on the channel kinetics. The lateral diffusion coefficient, D , of ACh receptors in the plasma membrane of cultured *Xenopus* embryonic muscle cells is estimated to be $2.6 \times 10^{-6} \text{ m}^2/\text{sec}$ at 22°C [48,49]. Lateral concentration gradients in lipid monolayers have been shown to be induced by externally applied electric field gradients. For binary mixtures of dihydrocholesterol and dimyristoylphosphatidylcholine, the application of an electric field gradient at pressures below the critical pressure produces a liquid–liquid phase separation in a monolayer that is otherwise homogenous [52]. This separation occurs at field levels on the order of 10^7 V/m and gradients of 10^9 to 10^{11} V/m^2 .

5.6 Nonlinear Effects of AC Fields on Cells

5.6.1 Introduction

The application of an AC electric field to nonlinear systems, which can be described by either a nonlinear resistance or capacitance, leads to at least partial rectification of the input signal and the generation of harmonics. If two or more signal frequencies are applied, it also leads to frequency mixing of the form

$$f_o = \pm mf_1 \pm nf_2 \quad (5.48)$$

where f_o is the output frequency, f_1 and f_2 are input frequencies, and m and n are integers. The rectified component of the AC current can, in turn, lead to ion accumulation at interfaces, which results in changes in ion concentration [53,54]. These changes in ion concentration, in turn, can affect biological function. Another important additional effect is the dependence of the dielectric constant on frequency. This leads to changes in the electric field distributions in tissue with frequency. Thus, both the electrophoretic and the dielectrophoretic forces become both size and frequency dependent. A third—possibly important—additional effect is the excitation of frequency-sensitive biological systems in a resonant manner. By driving systems near their resonant frequency, we may change the effective amplitude of the stimulating signal and change the frequency of the nerve cells firing.

In this section we will review the rectification process at the cell membrane in some detail. Additionally, we will show that cell nonlinearities lead to frequency-dependent effects such as injection phase locking of pacemaker cells. We will also briefly examine some problems associated with the exposure of cells to very low, extremely low-frequency (ELF) fields and the application of large ELF fields to biological systems.

5.6.2 Rectification by Cell Membranes

The rectification of currents flowing across membranes has been studied by many authors, beginning with Katz in 1949. Much of this work is referenced by Hayashi and Fishman in their paper on the inward rectifier K^+ channel kinetics [53].

For many passive cell membranes, an approximate relation for the transmembrane current can be derived from the Nernst equation as given in [Equation 5.41](#) [31]. If we apply an AC signal across the membrane of the form $V_M = V_0 + V_1 \cos \omega t$, the resulting current can be approximated for small values of V_M (i.e., $qV_M < \eta kT$) by a Taylor series yielding

$$I = \frac{I_0}{\eta V_T} \left(V_0 + \frac{V_1^2}{4\eta V_T} + V_1 \cos \omega t + \frac{1}{4\eta V_T} V_0 V_1 \cos \omega t + \frac{V_1^2}{4\eta V_T} \cos 2\omega t + \dots \right) \quad (5.49)$$

It is to be noted that the second term in the expression is the first approximation to the fraction of the applied AC voltage V_1 that yields a DC current component ΔI ,

$$\Delta I = \frac{I_0}{4} \left(\frac{V_1}{\eta V_T} \right)^2 \quad (5.50)$$

or an offset voltage V_{DC} given by

$$V_{DC} \approx \frac{I_0}{4} \left(\frac{V_1}{\eta V_T} \right)^2 R_m \quad (5.51)$$

where R_m is the membrane impedance. This predicted voltage offset for an applied AC current has been measured by Montaigne and Pickard [55]. In their experiments, an AC signal was applied to a large plant cell by a strip line, and the measured voltage shift was obtained through microelectrodes located outside the applied AC fields. For an applied AC field of about 0.2 V, they measured a DC offset of 1 to 2×10^{-4} V. For frequencies above 2.5 kHz, the effects of the membrane capacitance must be taken into account, and the effective driving voltage is reduced to

$$(V_1)_{eff} = [\sqrt{2} a \sigma_e \vec{E}_{1rms}] [(\sigma_e + aG)^2 + (a\omega C)^2]^{-1/2} \quad (5.52)$$

where a is the cell radius, σ_e is the conductivity of the medium \vec{E}_{1rms} is the electric field strength in the medium surrounding the cell, G is the membrane conductance per unit area, ω is the frequency, and C is the membrane capacitance per unit area [56]. This leads to the usual roll-off in the measured DC offset with increasing frequency. Note that the DC effect gets still smaller at higher frequencies (above 1 MHz) because of transit time limitations for ion flow across the membrane [57].

The relaxation times for a typical K^+ channel in an *Aplysia* membrane has been measured to be from 2 to 8 ms [51]. Rectification has also been demonstrated in thin lipid membranes [58]. In these systems, both the conductivity of the membrane and the ion concentration differences across it can be controlled. The Nernst equation was shown

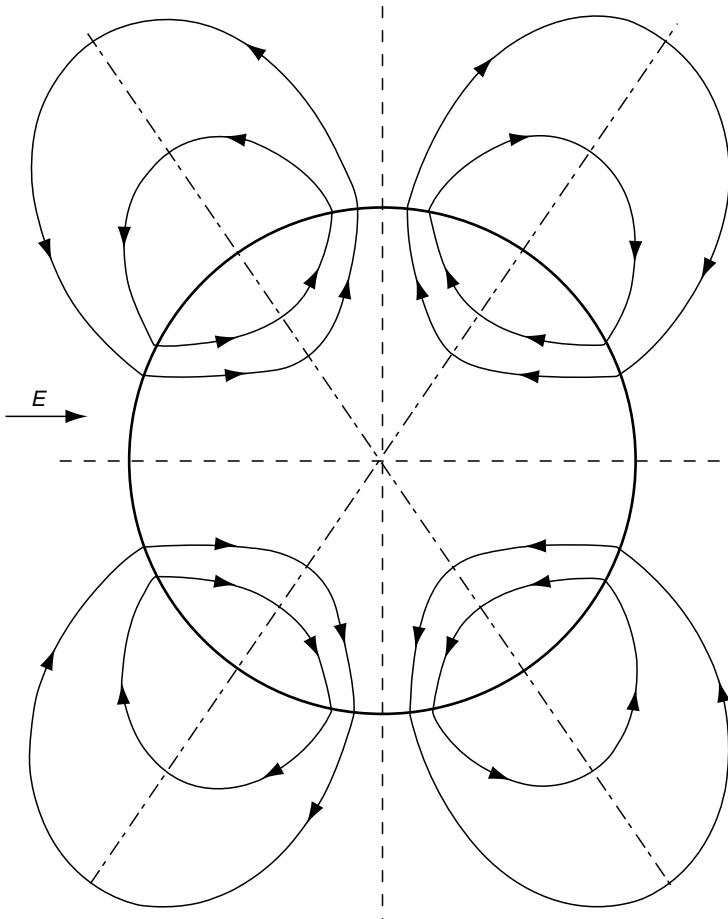


FIGURE 5.2

Induced DC current distribution in a spherical cell. (From Bisceglia and Pinto, I., personal communication, 1984. With permission.)

to apply to the I vs. V curve over a range of voltages from -60 to $+40$ mV. Depending on the ion concentration and membrane doping, the values of η ranged from 1 to 0.25.

A different treatment of the nonlinear response of passive cell membranes to an applied AC field has been carried out by Franceschetti and Pinto and by Casaleggio et al. [59,60]. Both these groups have expanded the Nernst equation in a Volterra series that takes into account memory of the preceding state of the cell. They have also treated the cell in spherical rather than planar geometry. The inclusion of a spherical cell requires that the total current into and out of the cell be equal to zero, and thus loops are formed circulating through the cell membrane (see Figure 5.2). All the theoretical treatments predict a DC component that varies as the square of the input signal V and tends to hyperpolarize the cell or make the interior of the cell more negative.

Cain has considered the effects of an AC field on nonlinearities of the nerve cell by numerical analysis of the Hodgkin-Huxley equation [61].* He applied a voltage

*Bisceglia and Pinto have applied a Volterra series expansion to the Hodgkin-Huxley equations. This approach gives an alternate method to Cain's of computing the current shifts resulting from applied AC signals [62].

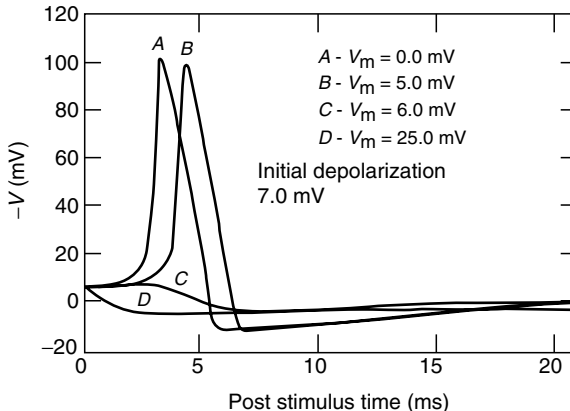


FIGURE 5.3

Computed membrane action potentials in response to an initial membrane depolarization of 7 mV for different values of V_m . Curves are solutions to the Hodgkin-Huxley equations. (From Cain, C.A., *Bioelectromagnetics*, 2, 23, 1981. With permission.)

$$V_m = V_0 + V_1 \cos \omega t [u(t) - u(t - \tau)] \quad (5.53)$$

across the membrane, where $u(t)$ and $u(t - \tau)$ are unit step functions that define an AC pulse of length τ . For the case where the AC frequency is large compared to the reciprocal of the pulse length, if a 7 mV depolarizing pulse is also applied to the membrane, the action potential is obtained as shown in Figure 5.3. Cain has assumed coefficients appropriate to the giant squid axon. Increasing V_1 first delays, and then suppresses, the action potential. If no depolarizing pulse is applied, the predicted changes in g_{Na} and g_K and the deviation V from the resting potential are as shown in Figure 5.4 for a 10 msec AC pulse with $V_1 = 25$ mV. Note that the applied AC frequency is assumed high enough not to be resolved in these figures. From these results, it is clear that AC signals can induce substantial changes in the operating characteristics of nerve cells at moderate to high levels of applied voltage. Although the appropriate coefficients were not measured in order to make a direct comparison between theory and experiments, Wachtel's results on *Aplysia* at frequencies above the lock-in range would appear to support Cain's theoretical predictions [63].

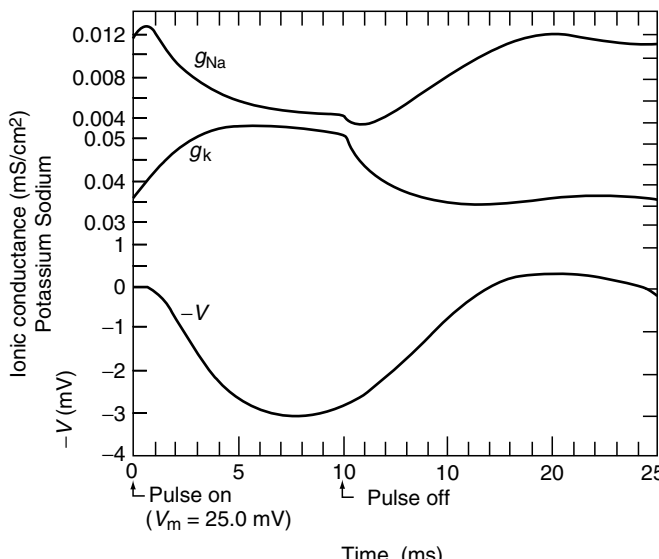


FIGURE 5.4

Response of model axon to a pulsed oscillating component of membrane electric field (10-ms pulse, $V_m = 25$ mV). The membrane potential and the sodium and potassium conductances are shown. These curves are solutions of the Hodgkin-Huxley equations. (Note: $1\text{mS}/\text{cm}^2 = 10 \text{ S}/\text{m}^2$.) (From Cain, C.A., *Bioelectromagnetics*, 2, 23, 1981. With permission.)

Wachtel has made a series of measurements that demonstrate the nonlinear characteristics of pacemaker cells from *Aplysia* [61]. First, he measured the current input through a microelectrode that changed the firing rate of the cell. The current threshold for a minimum detectable change was approximately 6×10^{-10} A at frequencies between 0.8 and 1 Hz (see Figure 5.5). The natural firing rate for this cell is about 0.8 Hz, and an increasing current is required to synchronize the cell to the injected signal as the frequency deviates from the natural firing rate. A theory for injection locking of electronic oscillators predicts that the signal required for locking an oscillator to an external signal increases linearly as the difference between the two frequencies $\Delta\omega$ increases [64]. The signal required for lock-in according to this theory is given by

$$I_t \approx |A\Delta\omega| I \quad (5.54)$$

where I_t is the injected signal current and I is the peak unperturbed oscillator current. $A = \partial\phi/\partial\omega$ is the rate of change of phase with respect to frequency in the unperturbed oscillator. $\Delta\omega_0$ is equal to the difference between the frequency of the free-running oscillator and the injected signal. This expression is applicable as long as

$$\Delta\omega_0 \leq \frac{2\pi}{\tau} \quad (5.55)$$

where τ is the time constant for adjusting the gain of the circuit. The time constant τ for the *Aplysia* cells varied between 0.1 and 0.5 sec, and this corresponds to a maximum measured lock-in frequency of about 10 Hz. The results in Figure 5.5 show the threshold for one-to-one locking up to about 2 Hz. In the range from 2 to 10 Hz, Wachtel observed a lower threshold for subharmonic locking than one-to-one locking. At frequencies above 80 Hz, he observed a constant shift in the firing rate of the neuron in response to the injected transmembrane AC signal. The natural firing rate would be restored by also injecting a transmembrane DC signal equal in amplitude to about 1% of the peak-to-peak value of the AC current. This DC current was in the depolarizing direction, making the exterior of the cell more negative with respect to the cell cytoplasm to increase the firing rate (i.e., to restore it to its natural value). Apparently, the applied transmembrane AC current was partially rectified so as to hyperpolarize the membrane (making the interior of the cell more negative with respect to the external fluid). The details of how the applied field modifies the ion flow are only partially understood, but one characteristic is an increase in the conductivity for K^+ , which increases its flow out of the cell. Wachtel also

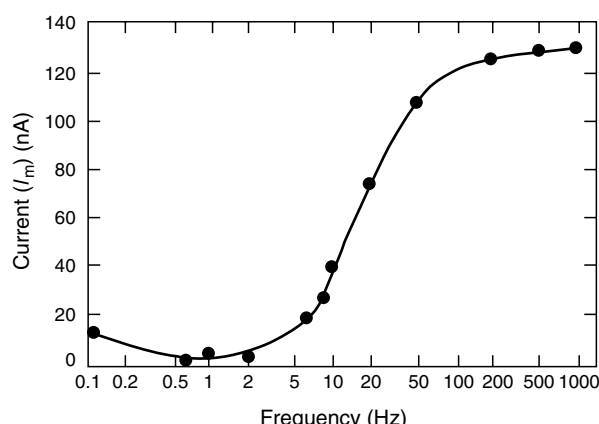


FIGURE 5.5

Intracellular (transmembrane) currents I_m (in nA) needed at different frequencies to produce firing-pattern changes (in a pacemaker neuron). Note that the detectable changes take on different forms at different frequencies. (From Wachtel, H., *Proceedings of the 18th Annual Hansford Life Science Symposium*, Technical Information Center, U.S. Department of Energy, Richland, WA, 132, 1978. With permission.)

injected low-frequency currents into the seawater surrounding the cell preparation through external electrodes [61]. In this case, the minimum current densities flowing in the vicinity of the cell preparation for injection locking were estimated to be about 10^{-2} A/m^2 , and there was about a 30 to 1 variation between the maximum and minimum sensitivities for changes in angle between the applied field and the cells. At frequencies above 100 Hz, a minimum of about 0.35 A/m^2 was necessary to obtain a detectable change in firing rate.

These studies have been extended by Barnes et al., and injection locking at harmonic and subharmonics has been shown to occur. It is suggested that phase locking may provide a mechanism for narrow banding or time averaging so that a weak coherent signal may be distinguished from noise by a cell. In an electronic circuit model we showed we could phase lock an oscillator at signal-to-noise ratios < 1 [65]. Extensive modeling of phase locking for a squid axon using two versions of the Hodgkin-Huxley equations has been carried out by Fohlmeister et al. [66]. They show that phase locking can occur for a wide variety of frequencies with AM-modulated signals at injected current densities greater than 0.1 A/m^2 [67]. For natural oscillation frequencies less than the externally applied signal, the system may be treated as a parametric process. For parametric amplification, a phase stability such that

$$\frac{d\Phi}{dt} < \Delta\omega - KV_s \quad (5.56)$$

is required for injection locking of the frequency of oscillation to an external signal, where $d\Phi/dt$ is the rate of change of the phase, $\Delta\omega$ is the frequency offset, K is the linear control characteristic in units of $(2\pi \text{ Hz/V})$ and is closely related to the loop gain, and V_s is the injected signal [68]. Stated in words, this equation requires that the amplified signal, KV_s be large enough to correct for the random frequency fluctuations $d\Phi/dt$ generated by the noise for the system to become phase locked to a signal that is displaced by $\Delta\omega$ (see Figure 5.6 for some examples of injection locking of pacemaker cells to an external signal) [65]. An increase in the sensitivity to electromagnetic fields has also been shown in isolated frog hearts for signals that approach the natural resonant frequency or firing rate [69]. In these experiments, the firing rate of the heart was shown to increase as much as 30% when a signal in the vicinity of 10 to 20 V/m was applied through Ringer's solution to the isolated frog hearts at a frequency between 0.5 and 1 Hz . The natural firing rate of these excised hearts started out at approximately 1 Hz and dropped to about 0.5 Hz .

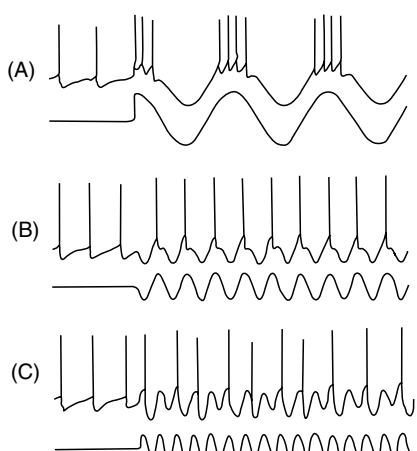


FIGURE 5.6

Examples of several modes of synchrony between an imposed ELF field and neuronal patterns. In each case the ELF current is shown below the transmembrane potential recording. (A) For ELF frequencies well below FR_0 , several nerve impulses (spikes) are locked to each ELF half cycle. (B) ELF frequencies slightly above FR_0 are effective in phase locking the rise of neuronal spikes on a one-to-one basis. (C) For ELF frequencies several times greater than FR_0 , phase locking can take the form of spikes occurring on alternate cycles (two-for-one synchrony). (From Barnes, F.S., *Bioelectromagn. Suppl.*, 1, 67–85, 1992. With permission.)

over a period of 2 h, where they remained stable for at least 5 h. To get a 30% increase in firing rate at 60 Hz, it was necessary to apply field strengths of 60 to 80 V/m. Thus, we have additional evidence that electric fields with repetition rates near the natural biological signaling frequencies are more likely to induce changes than those of higher frequencies and that signal strengths required for a given shift increase approximately linearly up to some cutoff, as shown in [Figure 5.5](#).

For weak fields, it has been shown that cells can respond differently to signals that are both space and time coherent than they do for signals that look like the background noise. Litovitz et al. have shown that the application of 10 μT magnetic fields at either 55 or 65 Hz doubles the specific activity of ornithine decarboxylase (ODC) in L929 cells if the signals are coherent for periods of 10 sec or longer during the course of a 4 h exposure [70]. The applied signal and the corresponding ODC response as a function of the coherence time are shown in [Figure 5.7](#). The ODC response of the cell can be fitted to an exponential curve of the form

$$(ODC) = 1 + 1.26 \left[1 - \exp \left(\frac{\tau_{coh}}{\tau_{cell}} \right) \right] \quad (5.57)$$

where τ_{coh} is the length of the time between shifts in frequency and the introduction of a random phase shift and τ_{cell} is the effective time constant of the cell [70]. τ_{cell} has a value of about 8 sec for these cells. If a spatially coherent noise signal with a power spectral density ranging from 30 to 90 Hz is superimposed on the coherent signal, the increased ODC response decreases with a decreasing signal-to-noise ratio and is less than 10% at a signal-to-noise ratio of 1 [71]. This work has been extended to show that temporally incoherent magnetic fields inhibit 60 Hz-induced changes in the ODC activity of developing chick embryos [72].

For the exposure geometry used in these experiments, the magnetic field induced a corresponding electric field of 4 $\mu\text{V}/\text{m}$. This signal is well below the calculated thermal noise field of 0.02 V/m for a 20 μm cell diameter. The combined results of the experiments cited above indicate that both space and time coherence may be used by cells to separate useful signals from larger natural background noise signals. For example, to get a significant biological response, some threshold number of channels or receptor molecules may need to be activated within a given period of time; this, in turn, requires nearly

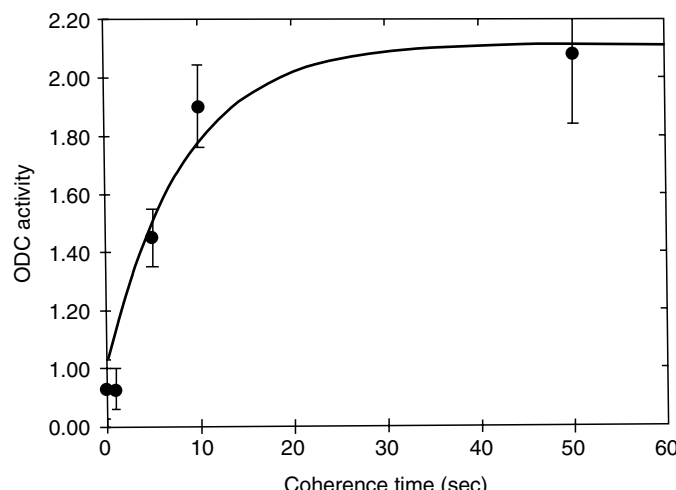


FIGURE 5.7
Plot of the enhancement of ODC activity (exposed/control) as a function of the coherence time, τ_{coh} , of the applied field. The solid line is the best fit to the mathematical function given by [Equation 5.44](#), where τ_{cell} is found to be 8.2 sec. The experimental points shown represent a minimum of six different exposures. (© Academic Press; From Litovitz, T.A., Krause, D., and Mullins, J.M., *Biochem. Biophys. Res. Commun.*, 178, 3, 862, 1991. With permission.)

simultaneous activation over a significant fraction of the cell surface. Similar results have been obtained for developing chick embryos, where weak coherent signals lead to an increased incidence of abnormalities [73]. In this work, Litovitz and his colleagues show an increase in the incidence of abnormalities of approximately a factor of 3 for White Leghorn chicken embryos incubated in periodic magnetic fields with peak field strength of $1 \mu\text{T}$ (100 Hz repetition rate, 500 μs pulse duration, 2 μs rise, and decay times) when compared with the controls. This increased rate of the incidence of abnormalities was nearly eliminated with the addition of band-filtered noise with a spectrum running from 30 to 100 Hz and a root mean square value of $1 \mu\text{T}$. Thus, Litovitz makes a strong case for a requirement of both space and time coherence for biological systems to detect signals below the natural noise environment.

A number of experiments indicate that at least two mechanisms are involved in the effects of low-level time-varying magnetic fields on membrane transport. The first of these is through Faraday's law or the induced electric field, which, in turn, induces electric currents. In these experiments, one would expect to get the same effects by introducing electric fields with electrodes at levels that induce the same current densities. The second group of experiments indicates that the background DC magnetic field is also important and that the combined effects of AC and DC magnetic fields are observed.

The initial experiments by Walleczek and Liburdy showed an enhanced uptake of Ca^{2+} in Con. A-activated rat thymocytes with exposures of 1 h to 60 Hz magnetic fields of 22 mT and induced current densities of 0.16 A/m^2 [74]. In this paper the exposure system consisted of concentric rings on cell culture plates, which, in turn, were placed in a water-cooled solenoid that produced a uniform magnetic field. This was followed by a group of experiments by Liburdy on Ca^{2+} transport across mitogen-activated lymphocyte membranes [75]. In these experiments, both the DC and the AC magnetic fields were controlled so that the DC geomagnetic field and the ambient 60 Hz fields were perpendicular to the exposed and control plates. The results show an increase in the Ca^{2+} influx during the plateau phase of the calcium signaling for Con. A-activated lymphocytes, which was a function of the induced electric field and which could be reproduced by applying the electric fields across the cells with a salt bridge at levels between 0.1 and 0.17 V/m . This corresponds to induced current levels of 0.168 to 0.28 A/m^2 in the fluid surrounding the cells, which had a conductivity, $\sigma = 1.68 \text{ S/m}$, that is approximately a hundred times larger than the current densities observed around growing cells. Thus, the approximately 20% to 25% increase in the initial Ca^{2+} uptake is the result of a relatively large external current. In other experiments it was also shown that the response is dependent on the age of the animals from which cells are taken [76].

Most other reported experiments have not been done in a way to sort out the differences between possible direct effects of the magnetic fields and the induced electric fields. Yost and Liburdy [77] have also conducted experiments in the same system that show a direct dependence of the calcium uptake on the DC magnetic field.

The experiments by McLeod et al. [78] show both a frequency dependence and a dependence on the electric field strength across the cell membrane. They exposed neonatal bovine fibroblast cells to electric fields in culture through a media bridge. The fibroblasts populated a collagen matrix that enabled the cells to be grown with a dominant orientation and exposed to a well-defined current. An estimate of newly synthesized protein was made by measuring the incorporation of (^3H) proline into macromolecules after a 12 h exposure to current densities ranging from 10^{-3} to 10 A/m^2 and frequencies from 0.1 Hz to 1 kHz. The results in Figure 5.8 show an approximately 30% reduction in the ^3H counts with current densities as low as 10^{-2} A/m^2 . This reduction is interpreted as a reduction in the incorporation of newly synthesized protein into the extracellular matrix rather than as a change in the cell number. The frequency specificity for this threshold is

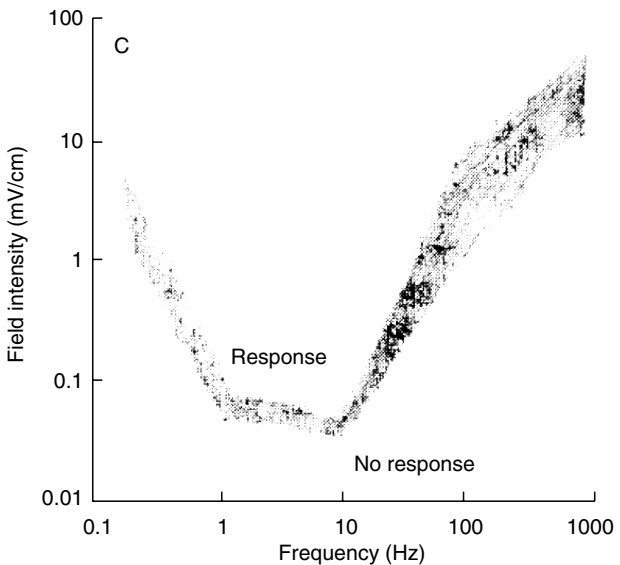


FIGURE 5.8

Minimum field intensity for a detectable response. Summary of results for all tested frequencies and current densities. Current densities were converted to peak field intensities by using the measured media resistivity of $65\ \Omega\text{ cm}$. The lower boundary of the gray region represents the highest field intensity at which no significant change in extracellular protein accumulation was detected; the upper boundary represents the lowest intensity evoking a statistically significant change ($n = 6$). (From McLeod, K.J., Lee, R.C., and Ehrlich, H.P., *Science*, 136, 1465–1469, 1987.)

shown in Figure 5.8; the peak sensitivity was recorded at $5 \times 10^{-3}\text{ A/m}^2$ and 10 Hz. The corresponding peak electric field intensity was 4.5 mV/m. The fractional change in the (^3H) proline was nearly independent of the current density for increases in current density up to two orders of magnitude above 10^{-2} A/m^2 . The cell membranes have a resistance many times higher than the resistance of the matrix as a whole. The cells are also asymmetric, with a ratio of major to minor axes of about 7 to 10. Thus, the current through the cell membranes would be expected to be at a maximum when the long axes of the cells are parallel to the applied field. For randomly oriented cells, current densities of 3 mA/m^2 produced no significant effect on the rate of proline incorporation. However, when the cells were oriented parallel to the electric field that was estimated at 2 mV/m and 10 Hz, a little more than a 30% reduction was observed. The estimated transmembrane potential was $0.5\ \mu\text{V}$. With the cell oriented perpendicular to the field, no significant change in proline incorporation was measured at 5 mA/m^2 .

In addition to the nonlinear conductances associated with Na^+ and K^+ currents, membranes also exhibit nonlinear (i.e., potential dependent) and frequency-dependent capacitances and inductances. It is sometimes useful to think of these effects in terms of a phasor diagram as shown in Figure 5.9, where the electric field vector \vec{E} is rotating at a velocity ω , and ϕ is the phase angle between \vec{E} and the current density \vec{j} . If there is, for example, a fixed time delay between the field activation of a current gate and the current flow, then, depending on the frequency, \vec{j} may be in any of the four quadrants and appear capacitive or inductive or even present a negative resistance to an external driving source.

Nonlinear inductive effects seem to be associated with the time delay for the onset of the K^+ currents under excitation in a typical excitable membrane, and they have been studied in the giant squid axon [79]. The nonlinear capacitive effects are difficult to measure at frequencies below a few kilohertz. Extra care needs to be exercised to minimize the series resistance and the end effects of the wire being used to measure the capacitance or inductance. Additionally, corrections must be made in the calculations of the membrane capacitance to take into account the appropriate variations in the frequency response that these terms introduce. However, when this is done, it can be shown that the membrane capacitance has both frequency- and voltage-dependent terms. The capacitance of giant squid axons is shown in Figure 5.10 and Figure 5.11 as a function of frequency and membrane voltage.

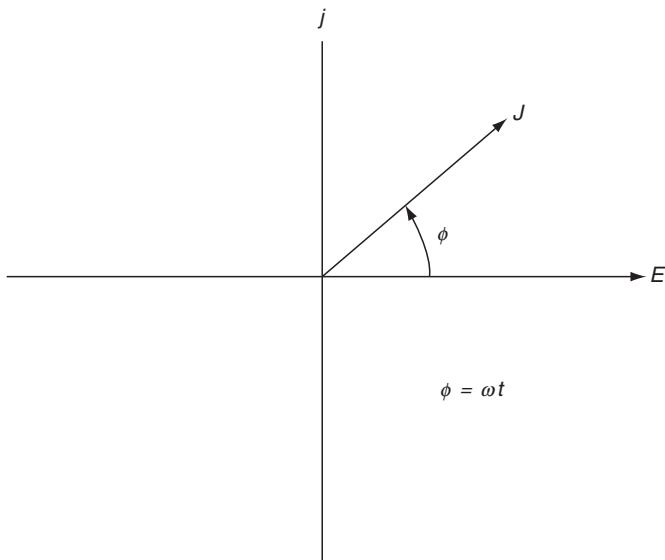


FIGURE 5.9

Steady-state vector characterization of electric fields \vec{E} vs. current density \vec{J} in polar form. ϕ is the phase angle between the sinusoidal electric field \vec{E} and the resulting current density \vec{J} .

Variation of the capacitance of these membranes with frequency and amplitude differs from that of a simple bilipid membrane that has nearly constant capacitance. The variation appears to be associated with changes in the conformation of the proteins associated with the Na^+ conductance channels. Nonlinearity in conductance and capacitance can be induced into a bilipid membrane by the addition of Alamethicin. The nonlinear inductance or capacitance may also generate both sum and difference frequencies if two signals are applied. For the case of the single signal, a DC term is added to the current density that is proportional to membrane potential and the square of the applied AC signal [80]. The effects due to nonlinear membrane capacitance thus far observed are small. They

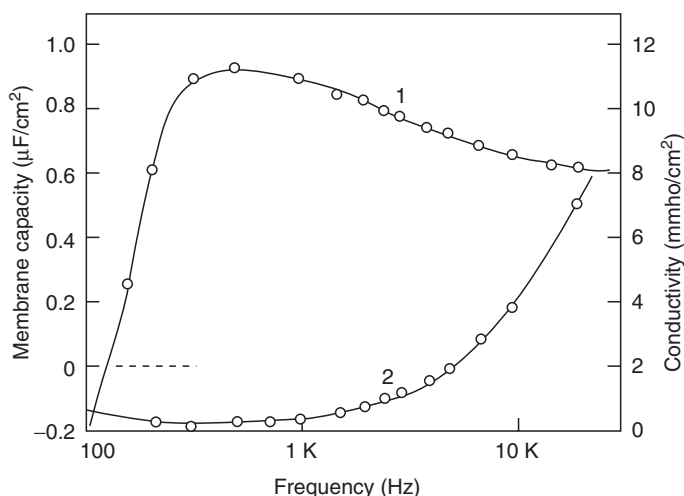


FIGURE 5.10

Membrane capacitance (Curve 1) and conductivity (Curve 2) of squid giant axon at various frequencies. Note the anomalous behavior at low-frequencies. (Note: $1 \mu\text{F}/\text{cm}^2$.) (From Takashima, S., in *Biological Effects of Nonionizing Radiation*, ACS Symposium Series, No. 157, Illinger, K.H., Ed., 133–145, 1981.)

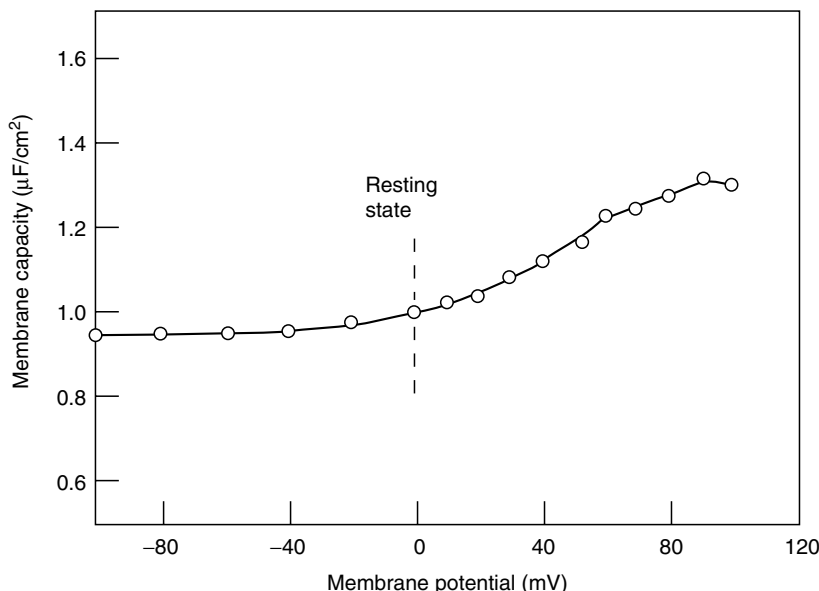


FIGURE 5.11

Membrane capacitance of squid giant axon at various membrane potentials. Membrane potential was shifted by injecting currents. The abscissa shows the actual potential across the membrane in millivolts. (From Takashima, S., in *Biological Effects of Nonionizing Radiation*, ACS Symposium Series, No. 157, Illinger, K.H., Ed., 133–145, 1981.)

appear likely to be more important in providing an understanding of the possible gating mechanism in membranes than as a mechanism for introducing rectification.

Another form of nonlinearity in the electrical response of cells comes about in what is often described as adaptive processes. For example, we found that repetitive exposures of pacemaker cells (taken from the ganglion of an *Aplysia*) to microwave pulses resulted in a decreasing reduction in the firing rate by successive pulses. This kind of change has also been shown to occur in neurons that have been conditioned with repetitive stimulation. Studies of conditioning have shown decreases in potassium ion conductance through membranes, thus raising the internal potential and enhancing the excitability [81,82]. The decrease in resistance between adjacent cells can occur in two ways. First, the resistance of gap junctions may be reduced by repetitive electrical stimulation, which increases the electrical coupling between the cells by up to 62%. Second, repetitive electrical stimulation can modify the chemical excitatory postsynaptic potential by amounts ranging from 31% to 140% [83]. This change is associated with the movement of protein kinase C from the interior of the cell into the membrane. An accompanying change in Ca^{2+} concentrations and the movement of a second messenger, diacylglycerol, into the membrane reduce the potassium ion flow. This enhanced excitability reduces the voltage or the charge required to initiate an action potential. If charge is transferred efficiently between cells, either actively or passively, cell length is effectively multiplied in the linear model by the number of cells in the chain; this, in turn, reduces the external electric field required to generate a given voltage across a terminating membrane (see Chapter 11 in BMA by A. Pilla).

An interesting speculation that is raised by these adaptive processes is whether or not a neural network can be trained to identify a repetitive signal such as 60 Hz in the presence of larger electric fields generated by the surrounding biological material. To test this hypothesis, we programmed a computer to simulate a neural network as shown in Figure 5.12 [65]. Using a backpropagation algorithm to adjust the connecting weights between neurons, a sigmoidal summing junction to model the neurons, and a pseudorandom noise generator,

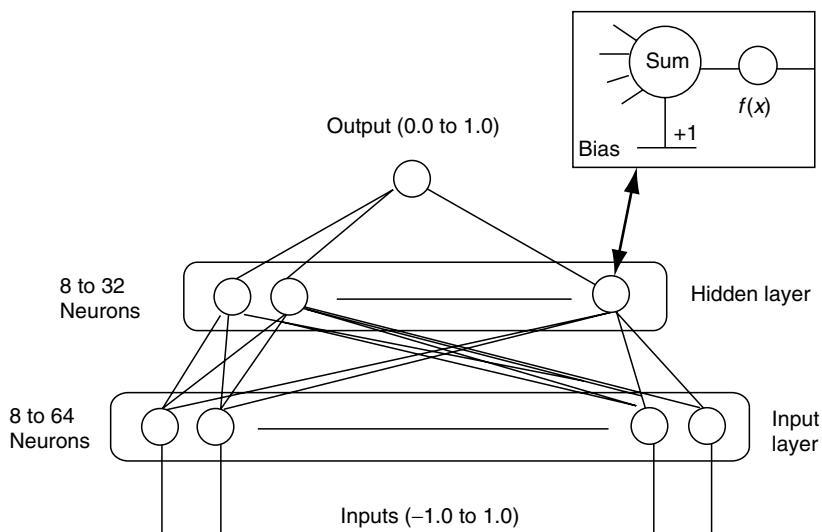


FIGURE 5.12
Backpropagation neural network. (From Barnes, F.S., *Bioelectromagn. Suppl.*, 1, 67–85, 1992. With permission.)

we measured the number of runs required to train the network to recognize a 60 Hz signal with 97% accuracy as a function of the input signal-to-noise ratio. The results in Figure 5.13 show that the training time increased from about 200 runs to about 1400 runs as the signal-to-noise ratio decreased from 1 to 0.001. The way the noise is presented to this network during the training makes a difference. For example, if you want the network to separate 59 Hz from 60 Hz, it helps to tell the network that 59 Hz is noise. This computer network model is clearly too simple to describe a biological nervous

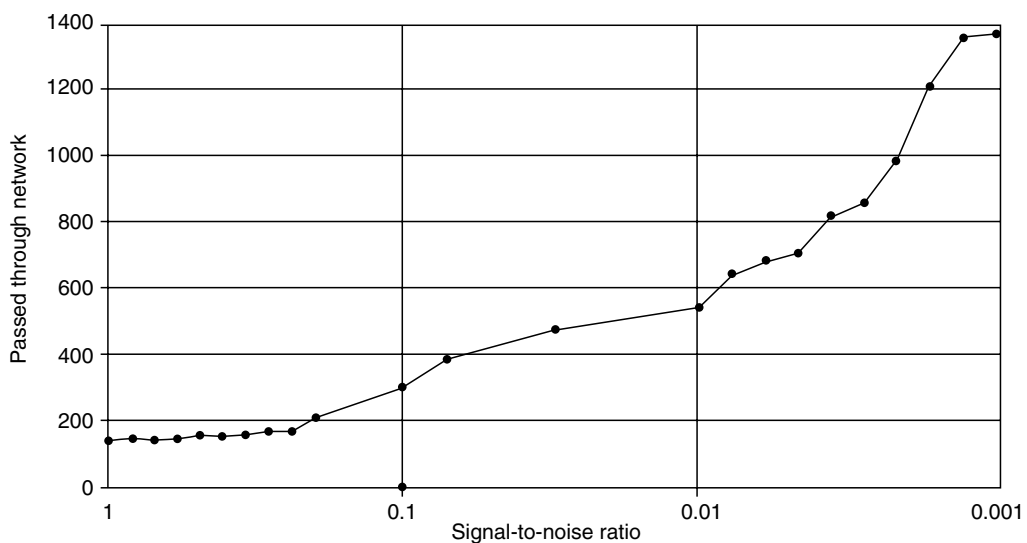


FIGURE 5.13
The learning response of a neural network with 64 input neurons, 8 neurons in the hidden layer, and 1 output neuron to a 60 Hz input signal and a pseudorandom noise signal with a decreasing signal-to-noise ratio. (From Barnes, F.S., *Bioelectromagn. Suppl.*, 1, 67–85, 1992. With permission.)

system, but it may provide a clue to one way in which a collection of cells may be able to respond to weak, externally applied electric fields, but a single cell would not.

5.7 Thermal Effects

One important effect of current flow due to electric fields is heating. The power input to a given volume of material can be expressed by $P' = I^2R$, where I is the total current and R is the resistance of the sample. For many calculations, a more useful expression is given by the power per unit volume or $P = \sigma E^2$, where σ is the conductivity, E is the electric field intensity. (For a more complete treatment of heating, see [Chapter 10](#) and [Chapter 12](#) of *BMA*.) The temperature rise resulting from this heat input is determined by the thermal capacity of the volume and the mechanisms for carrying the heat energy away. Typically, these thermal loss mechanisms include a combination of conduction and convection processes. For short current pulses, the heat dissipation is usually dominated by thermal conduction, and the basic equation for the rate of change of temperature is given by

$$\frac{\partial T}{\partial t} = \frac{P}{\rho' C_p} - \frac{T - T_0}{\tau_c} \quad (5.58)$$

where T is the temperature, T_0 is the initial temperature, t is time, and P is the power supplied per unit volume. ρ' is the density of the material (in kg/m^3), C_p is the specific heat under constant pressure, and τ_c is the thermal relaxation time.

If we consider a homogenous sphere of radius a immersed in an infinite fluid, the thermal conductive relaxation time is approximately given by

$$\tau_c = \frac{a^2}{4\bar{K}} \quad (5.59)$$

where \bar{K} is the thermal diffusivity and is measured in meter square per second [84]. The thermal diffusivity is given by

$$\bar{K} = \frac{K'}{\rho' C_p} \quad (5.60)$$

where K' is the thermal conductivity (in $\text{cal}/(\text{m sec } ^\circ\text{C})$), ρ' is the material density (in kg/m^3), and C_p is the thermal capacity (in $\text{cal}/(^^\circ\text{C kg})$). If an applied current pulse is short compared to τ_c , the maximum temperature change is given by

$$\Delta T_{\max} = \left(\frac{3}{2\pi e} \right)^{3/2} \frac{\bar{H}}{\rho' C_p a^3} \quad (5.61)$$

where \bar{H} is the total input energy in calories and e is the base of natural logarithms [84]. For current inputs that are long compared to the thermal relaxation time τ_c , the peak temperature is determined by a balance between the input power and the dissipation process controlled by conduction and convection. It is interesting to note that if we assume the thermal properties of water as a first approximation to various kinds of tissue, then τ_c for a sphere with a equal to $1\text{ }\mu\text{m}$ is a little less than $2\text{ }\mu\text{s}$. Since a sphere has the

smallest surface to volume ratio, [Equation 5.60](#) gives an upper bound on τ_c , and [Equation 5.61](#) gives an upper bound on the peak temperature excursion for small structures and pulses that are short compared to τ_c . Simply stated, it takes high power densities and large differential absorption coefficients to get significant differential temperature rises in small biological structures.

For situations where the volume involved is a cubic millimeter or larger, the thermal time constant is controlled by the amount of blood flowing through the volume. In these cases, temperatures may be more easily measured than calculated since a complicated thermal and electrical boundary value problem would have to be solved to calculate the temperature rise. This is particularly true since the viscosity η and other thermal and electrical parameters such as ρ , C_p , \bar{K} , etc. are functions of temperature. For example, C_p for an artificial bilipid membrane is shown in [Figure 5.14](#) [85]. Another example of the importance of change in temperature is the conductivity of saline,

$$\sigma \approx C_1[10^{[(1/T)+\alpha](1/b)}] \times 10^{-4} \text{ S/m} \quad (5.62)$$

where C_1 is the concentration of NaCl in milligram equivalents per liter, T is the absolute temperature, $\alpha \simeq 6.23 \times 10^{-3}$ degrees $^{-1}$, and $b \simeq 1.4 \times 10^{-3}$ degrees $^{-1}$ [86]. In the range around 37.5°C, this means that a 5°C change in temperature corresponds to a little less than 9% change in conductivity [86].

Changes in temperature are important, not only because they change transport properties such as viscosity, mobility, and the diffusion coefficient D , but also because they change chemical reaction rates. Typical biochemical reactions can be described by an equation of the form

$$\frac{dS}{dt} = -K'S \quad (5.63)$$

where S is the fraction of the material that has undergone the chemical reaction, t is the time, and K' is the reaction rate [87]. K' is often given by

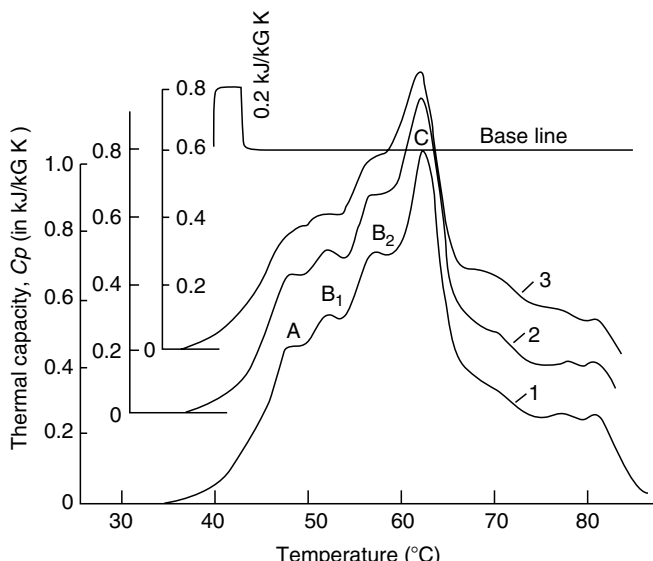


FIGURE 5.14

Differential changes in the heat capacity, C_p , of erythrocyte membranes as a function of temperature in 5 mmol/L sodium phosphate with pH 7.4 and a concentration of 5 mg protein per milliliter. The changes at A, B₁, B₂, and C correspond to changes in the structure of the membrane with temperature and are irreversible. Curve 1: intact membranes. Curve 2: irradiated at 330 mHz for 5 min (SAR 9 W/kg). Curve 3: irradiated at 300 mHz for 30 min (SAR W/kg). (From Shuyrou, V.L., Zhodan, G.G., and Akorv, I.G., Academy of Science, Institute of Biophysics, Pushchino, Moscow Region, Russia, personal communication, 1984. With permission.)

$$K' = \frac{kT}{h} \exp\left(\frac{+\Delta H' - T\Delta S'}{R'T}\right) \quad (5.64)$$

where k is the Boltzmann constant, T is the absolute temperature, H' is the free energy, S' is the entropy, h is Plank's constant, and R' is the gas constant. The significant feature is that the reaction rate K' varies exponentially with temperature, and $\Delta H'$ and $T\Delta S'$ are large numbers. Thus, very small changes in temperature can lead to big changes in chemical reaction rates.

In addition to chemical reaction rate changes, there may be changes in the binding of the proteins to cell membranes that lead to a shedding of proteins with a small increase in temperature. An exponential temperature dependence of the binding to membrane receptors is to be expected just as it is for chemical reactions [88].

A rule of thumb that the author uses to estimate whether or not significant biological changes are likely is to see if ΔT is $>10^\circ\text{C}$ for 10^{-6} sec , 5°C for 1 sec , or 2°C for hours. If the ΔT s are larger, then they can be expected to lead to important changes in the biological system. Typical mammalian temperature regulatory systems will hold the internal body temperature constant to within $+/-0.5^\circ\text{C}$.

In addition to the magnitude of the temperature change, it can be shown that the rate of temperature rise, dT/dt , is important and can induce current to flow across membranes. Changes in the firing rate of pacemaker cells from the ganglion of *Aplysia* have been induced by total temperature changes of as little as $1/10^\circ\text{C}$ when the rates of change are about 1°C/sec [89]. This change of the firing rate corresponds to the injection of approximately 1 nA into the cell. By taking the time derivative of the Nernst equation, which describes the passive equilibrium potential across a membrane for a single ion, it can be shown that a current proportional to the temperature derivative is to be expected, or

$$I = -qV'_1C_1\left(\frac{\phi}{\phi_T}\right)\left(\frac{\dot{\phi}}{\phi} - \frac{\dot{T}}{T}\right) \quad (5.65)$$

where q is the charge of the ion, V'_1 is the volume of the cell, C_1 is the concentration of ions inside the cell, ϕ is the resting potential, ϕ is given by $\phi_T = \frac{kT}{q}$, $\dot{\phi}$ is the derivative of the membrane potential with respect to time, T is the temperature, and \dot{T} is the temperature derivative with respect to time [90].

Bol'shakov and Alekseyev [91] have observed similar changes in the firing rate of pacemaker cells taken from the large parietal ganglion of the central nervous system of *Limnea stagnalis*. In their experiments they observed a slow increase in temperature ($1^\circ\text{C}/\text{min}$ or slower) to increase the firing rate of the pacemaker cell and a rapid increase in temperature (0.1°C/sec or faster) to decrease or stop the firing. They ascribe these changes to changes in the Na^+ pump as the rapid temperature effect was completely blocked by adding ouabain to the solution. In addition to the changes in the Na^+ currents, Ca^+ currents have been shown to be sensitive to rapid changes in temperature [92]. The rate of rise has also been shown to be significant in exciting a brain slice from a mouse with pulses of 10^{-3} sec and peak temperature rises of less than 0.5°C [93].

Temperature rises also lead to thermal expansion, and rapid temperature rises lead to the generation of acoustic waves [94]. These acoustic waves, in turn, can affect stretch receptors in nerve cells and other tissue and thus generate a biological response that may be at a considerable distance from the electrical heating [95].

To get an idea of the magnitudes of both heating (as described in [Equation 5.58](#)) and the effect of the rate of rise (as given by [Equation 5.65](#)), consider the case of liver tissue with $\sigma = 0.14\text{ S/m}$ and a field strength in the tissue of $2 \times 10^3\text{ V/m}$. The rate of

temperature rise is approximately 13°C/sec assuming no conduction or convection heat losses and the thermal capacity of water. For this high field, a significant temperature rise occurs in about $1/2$ sec. However, the rate of rise has been shown to be significant in exciting a brain slice from a mouse with pulses of 10^{-3} sec [96].

5.8 Natural Fields and Man-Made Fields

It is of interest to compare man-made with naturally occurring fields. First, we would like to know the approximate magnitudes of the fields that occur in nature outside man or the biological system of interest. Second, we would like to have values for the internal or physiological fields.

The natural electric fields at the surface of the earth have both DC and AC components [97]. One may think of the earth as a spherical capacitor where the surface is negatively charged with respect to an electrical conducting ionosphere that is about 50 km above the surface. This capacitor is being continuously charged by about 100 lightning strokes per second from thunderstorms worldwide. Since the atmosphere is a finite conductor, it also discharges with an *RC* time constant of about 18 sec. The result is an average electric field of about 130 V/m . This field is not uniform with height and typically falls off to 30 V/m at 1 km above the surface. The local values vary widely with temperature and humidity. In the Sahara during dust storms caused by winds in the dry season, a field of 1500 V/m has been measured with the polarity reversed from the normal. In thunderstorms, fields of up to 3000 V/m have been measured without lightning, and the polarity has been known to reverse in minutes. Storms as far as 50 km away have been shown to affect local fields. [See Chapter 1](#) in this volume by Mild and Greenebaum for more details.

The atmosphere is a relatively poor conductor and as such will suspend a significant number of charged ions, dust particles, etc. This helps to contribute to local field variations of 20% to 50% over the course of the day and is a normal characteristic of our environment. The level of natural AC fields in the atmosphere falls very rapidly from a DC value of about 130 V/m [97]. The average value of the vertical component of the electric field above 1 Hz has a typical value of $10^{-4}\text{ V/m Hz}^{1/2}$. However, this value fluctuates widely with the time of day, the season of the year, and location. Additionally, the Schumann resonances impose multiple-cavity resonances on this spectrum with a periodicity of about 10 Hz. These resonances may be explained in terms of standing waves in a cavity formed by the earth and the atmosphere. These very low levels of the natural fields are one of the reasons why electronic communications in the ELF band are useful for ships at sea and submarines. However, because of the very low level of the natural atmospheric fields at frequencies above a few hertz, there is very little reason for biological organisms to develop natural protection against perturbations at these frequencies. It also means that biological systems could communicate internally at these frequencies using very low signal power levels and still maintain a good signal-to-noise ratio.

The signals generated within the body are the result of nerve firing and other cell activity. A typical nerve cell fires with an action potential of 50 to 100 mV and transmits a current pulse about 0.4 ms long [98]. The rise time for this current spike is approximately 0.1 ms, and the fall time is about 0.5 ms. Each pulse is followed by a refractory period that is typically on the order of 1 to 3 ms. The longitudinal fields along the exterior of a nerve cell membrane are estimated to have a maximum value of about $5 \times 10^{-2}\text{ V/m}$ during an action potential when the cell is surrounded by a relatively high conductivity fluid of 5 S/m .

m [98]. If we look at these signals closely, it will be noted that the interspike interval along any given nerve cell fluctuates in time. Additionally, variations in the beat-to-beat intervals for the ECG are random or chaotic, and the period can vary up to 30%. This is frequently seen, particularly at slow heart rates.

In looking at the natural fields in the body, we have two concerns. The first is how large an external signal takes to perturb the ongoing natural signal that is being used to communicate or control some biological process [99]. The second is how much of the signal field typically leaks away from active nerve fibers or bundles to form a background noise environment for surrounding tissue and processes. Regarding the first of these questions, it is interesting to look on the microscopic level at the electrical noise, i.e., the fluctuations that occur fundamentally as a result of the electrical process itself.

The first of several sources of noise that are always present is blackbody radiation, or Johnson noise, which is given by

$$P_n = kTB \quad (5.66)$$

where P_n is the noise power, k is the Boltzmann constant, T is the absolute temperature, and B is the bandwidth [100–102]. The voltage equivalent of this noise power, which can be delivered to a matched load, or the mean squared voltage fluctuation \bar{V}_n^2 across a resistance R , is given by [101,102]

$$\bar{V}_n^2 = 4kTBR \quad (5.67)$$

or by the mean squared current fluctuations

$$\bar{i}_n^2 = \frac{4kTB}{R} \quad (5.68)$$

Johnson noise applies to systems at thermodynamic equilibrium. Living systems are not at thermodynamic equilibrium. Thus, the foregoing expressions must be applied with caution to only those portions of biological systems where thermodynamic equilibrium is a good approximation. In the case of lasers, the spontaneous emission noise associated with the nonequilibrium population inversion of the energy levels can be obtained from Planck's radiation law by defining a negative temperature that assumes a Boltzmann distribution of atoms with N_2 atoms in the excited energy level E_2 , which is greater than the N_1 atoms in the energy level E_1 , such that

$$\frac{N_1}{N_2} = \exp\left[\frac{E_2 - E_1}{kT}\right] \quad (5.69)$$

In this case, the spontaneous emission noise $P_n = h\nu B$, where h is Planck's constant and ν is the frequency of the radiation corresponding to a transition from E_2 to E_1 [100]. In those situations where the nonequilibrium characteristic may be described by an amplifier that can be modeled by a negative resistor or by energy storage in an inverted population distribution, the concept of a negative temperature may be a useful approach. Note that an equivalent temperature, T , is a convenient way to describe the energy distribution of a large number of particles. A much more complete description of nonequilibrium noise is given in [Chapter 7](#) in this volume.

The second source of noise that is also present is the shot noise, which is given by

$$\bar{i}_n^2 = 2q\bar{I}_{DC}B \quad (5.70)$$

where \bar{i}_n^2 is the mean-squared current fluctuation. This noise comes about because of the discreteness of the electronic charge q and the assumption that the motion of each charge is independent. With negative feedback, this noise may be reduced, as has been shown for space charge-limited diodes. Shot noise results in an AC fluctuation, \bar{i}_n^2 , which is proportional to the average value of the current, \bar{I}_{DC} . A third source of noise is $(1/f)$ noise. This noise may be generated by many processes, some of which are described in [Chapter 7](#) in this volume. $1/f$ noise can be synthesized from Gaussian noise by filtering it with a circuit that requires about one low pass state variable per decade for the period of time over which the model is used to generate noise with a power density spectrum $S(f) = (C/f^\alpha)$, where C is a constant and α is a constant between 1 and 2 [103]. We can expect to find this kind of noise for processes that evolve with time and, or have memory. $1/f$ noise describes the power spectral density of the fluctuations at low-frequencies in such diverse phenomena as transistors, quartz crystal oscillators, the closing Dow Jones Averages for the stock market, and the weather. It is also generated by the flow of ion currents through an orifice and thus is a fundamental part of the transport of current through channels in membranes [102]. Measurements of the noise voltage across a $10 \mu\text{m}$ hole in a $6 \mu\text{m}$ Mylar film showed that for a wide range of ionic concentrations the voltage noise spectral density $S(f)$ is given by

$$\frac{S_\phi(f)}{\phi^2} = \frac{a}{bnr^3 f} \quad (5.71)$$

where b is a numerical geometric factor, n is the density of ions in the solution, r is the radius of the hole, a is a constant, and ϕ is the applied voltage. The data showed that $2.5 < a < 40$ with a mean value of 10 for a wide range of solutions including HCl, KCl, and AgNO₃, with concentrations from 0.05 to 5 mol.

For natural membranes, this noise has been shown to take the form of

$$S_E(f) = \frac{C_E}{f^\alpha} \quad (5.72)$$

where $0.7 < \alpha < 1.2$ with a mean close to $\alpha = 1$. For the frog node of Ranvier, the noise is a function of the membrane voltage as shown in [Figure 5.15](#) [104]. The dominant source of this noise appears to be the K⁺ current, and it has a minimum when the membrane is biased, so that this K⁺ current is biased to zero.

To get an estimate of the size of these noise sources, let us consider a pacemaker cell from the abdominal ganglion of *Aplysia*. This cell fires 20-ms pulses at about 1 Hz/sec. It has a resting voltage of about 50 mV and a resistance R measured with a microelectrode between the inside of the cell and the surrounding solution of approximately $10^6 \Omega$. If we assume a system bandwidth of 100 Hz and $T = 300$ K, the Johnson noise voltage would be $\bar{V}_n \approx 3 \times 10^{-6}$ V. This gives a resting potential-to-noise (\bar{V}_n) ratio of about 4×10^4 . The peak current flow in these cells is estimated to be about 10^{-7} A, and thus the estimated shot noise current is $\bar{i}_n \approx 2 \times 10^{-12}$ A, and the ratio of the peak current to the noise current is about 2×10^4 . We do not have the available value $S(f)$ for the *Aplysia*, $\bar{v}_\phi = \sqrt{S(f)B}$, where B is the bandwidth. If it is assumed that the maximum value of the noise is the same as that of the frog node of Ranvier, then for a bandwidth of 1 Hz we get $\bar{v}_\phi = 1.4 \times 10^{-5}$ V at a center frequency of 1 Hz from the curve for -50 mV in Figure 5.15. This is about a factor of 10^3 greater than the Johnson noise. It is likely that $(1/f)$ noise is the largest source of noise at the cell membranes for frequencies below 160 Hz [105,106].

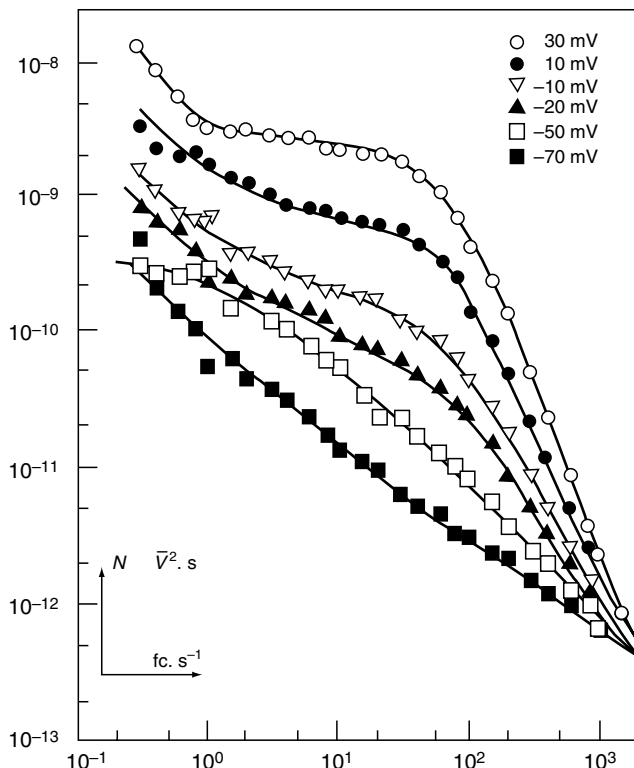


FIGURE 5.15

Voltage noise spectra of a frog node of Ranvier at different levels of membrane potential. (From Sichenga, E. and Verveen, A.A., in *Proceedings of the 1st European Biophysics Congress*, Vol. 5, Verlag Wiener Medizinischen Akademie, Vienna, Austria, 219, 1971. With permission.)

These fundamental sources of noise, which are generated by random fluctuations in the position of ions and their transport through channels, are spatially incoherent [73]. For many processes the important quantity in deciding whether or not an electrical signal is biologically important is the signal-to-noise ratio S/N where S is the power in the signal and N is the noise power. Typically, it is assumed that a signal-to-noise ratio of 1 is required for an externally applied signal to be detectable. In the foregoing discussion for both thermal and shot noise the movement of each charge was assumed to be statistically independent of each other. If for an externally applied signal the openings of the channels in a cell are excited in parallel and coherently and the noise is generated by incoherent random firing, then the signal-to-noise ratio increases with the square root of the number of channels. Similarly, the signal-to-noise ratio for a bundle of nerves would be expected to increase with the square root of the number of nerves for a signal applied externally to the whole bundle. Thus, a collection of cells can be expected to detect smaller signals than a single cell.

In addition to the electrical noise generated by currents and voltages that are part of the single-cell operation, electrical signals propagate through the body as a result of the incomplete confinement of electrical signals propagating in nerve cells. In a sense, these signals may be thought of as noise if they are not pertinent to the activity in that portion of the body through which they are propagating. If, on the other hand, they are used by tissue within the organism at some distance from the source, they must be thought of as signals. In the brain, the fraction of these signals that reach the scalp is called the electroencephalogram (EEG). The EEG is obtained by placing two or more conducting electrodes on the scalp and measuring the voltage between them. For electrodes placed 5 cm apart, the peak-to-peak voltages range up to $30 \mu\text{V}$ [107]. The author views this voltage as the integral of the vector sum of the leakage fields from the firing of the nerve

cells in the brain between the two electrodes. Since there are a very large number of cells firing, most of the 50 mV signals from an isolated nerve are canceled by summing over many like cells firing at different times and by the attenuation caused by propagation through the tissue. Estimates of surface potential gradients along a nerve fiber range from 3×10^{-4} to 5×10^{-2} V/m, and the corresponding current densities external to the nerve cells range from 5×10^{-2} to 4 A/m² [107,108]. The EEG voltage has a strong periodic component (particularly during sleep) near 10 Hz, which is known as the alpha (α) wave. A peak amplitude of this component may be as large as 50 μ V when measured at the surface of the scalp. It is interesting to note that the EEG signal contains significant information on the brain's activity, and a few individuals have been trained to control these signals so as to control a computer in way that allows them write messages.

At the surface of the chest, a signal may be recorded between two electrodes known as the ECG or EKG (electrocardiogram). This signal results from the highly coordinated firing of the cells in the heart and has a definite wave shape that is closely related to the operation of the heart. The peaks of the so-called R wave in this signal may range up to 2.5 mV and are typically 0.5 to 1.5 mV, depending on the placement of the electrodes, the amount of body fat, etc. The pulse repetition rate is usually in the range of 1 to 2 Hz, and the "QRS spike" of the typical cardiogram is 40 ms long. Again, the signal measured at the surface of the skin is the result of leakage from electrically active cells located at a distance. The estimated current density near the firing heart cell ranges up to 1 A/m² [109]. In this case the shape of the signal reaching the skin is so closely related to the activity of the heart that it provides detailed information on heart function.

One result of electric discharges in the atmosphere, as well as natural ionizing radiation, is the creation of small positive and negative ions in the atmosphere. In clean country or mountain air, the typical ion density is about $10^{10}/\text{m}^3$ with an average ion lifetime of a few minutes [110]. When a hot dry wind is blowing, positive ions created by the shearing forces can increase in concentration significantly. It has been shown that increases in the negative ion concentration reduce the amount of serotonin (5-HT) in mice and rabbits, possibly by accelerating the enzymatic oxidation process [111]. A similar result has been demonstrated in the oxidation of cytochrome *c*. Positive ions appear to block monoamine oxidase action, thus raising the concentration of free 5-HT [111]. Changes in 5-HT levels produce significant changes in the central nervous system, with high levels of positive ions raising the anxiety levels under stress. Other effects of increased positive ion concentration include a decrease in the survival rate of mice exposed to a measured dose of influenza virus, while an increase of negative ions reduced the mortality rate [111].

The significance of these results is that it is relatively easy to change the ion concentration in air using high-voltage DC systems where a leakage current of 1 μ A from a burr or other sharp point would correspond to the generation of about 10^{12} ions per second.

Relatively few high-voltage DC transmission lines are in use today for distribution of power. Because the shocks resulting from a short contact across a high DC voltage are so painful and obviously dangerous, these systems are nearly always shielded. Thus, one is rarely exposed to DC electric fields $>10^3$ V/m. An additional feature of this exposure is that air is such a good insulator that the DC currents flowing through the body in a noncontacting situation are very small, as explained in the Introduction. For example, 1000 V across a 1-cm gap would yield a current density of approximately 10^{-7} A/m² flowing across the air gap. Thus, the principal hazards from DC fields occur when parts of the body make contact with a conductor.

5.9 Discussion and Summary

In this review some of the physical mechanisms by which DC and time-varying electric fields affect biological systems are presented. A few typical values of electric field strengths and current densities that are known to affect the biological system are compared with those of natural fields and other forces. Some values of electric fields and their gradients that are shown to modify the currents and shift energy levels are given. These in turn are shown to modify chemical reaction rates, which can lead to changes in the growth cells and other characteristics of biological systems. It is hoped that this information will help the readers to make their own estimates of when a given exposure to electric fields will be significant in modifying biological systems and provide a basis for understanding some of the biological results presented in other chapters of this handbook.

Acknowledgments

The author wishes to express appreciation to Mikhail Zhadin, Howard Wachtel, Maria Stuchly, Ross Adey, Mike Marron, Elliot Postow, Charles Polk, and many students for their many helpful comments and suggestions and to Adam Sadoff for help in the preparation of the text. He also wishes to express his appreciation to the Office of Naval Research under Contract N00014-81-K-0387, the Mobile Manufactures Form, and the University of Colorado for financial support of his work in this area.

References

1. Yariv, A., *Optical Electronics in Modern Communications*, 5th edition, Oxford University Press, Oxford, UK, 1997.
2. Barnes, F.S. and Hu, C.L., Nonlinear interactions of electromagnetic waves with the biological materials, in *Nonlinear Electromagnetics*, Uslenghi, P.L.L., Ed., Academic Press, New York, 391–426, 1980.
3. Singer, S.J. and Nicolson, G.L, The fluid mosaic model of the structure of cell membranes, *Science*, 175, 720–731, 1972.
4. Poo, M., *In situ electrophoresis or membrane components*, in *Annual Review of Biophysics and Bioengineering*, Vol. 10, Mullins, L.J., Ed., Academic Press, New York, 245–276, 1981.
5. Kyriacous, D., *Modern Electroorganic Chemistry*, Springer-Verlag, Berlin, 1994.
6. Pohl, H.A., Dielectrophoresis, the behavior of neutral matter, in *Nonuniform Electric Fields*, Cambridge University Press, Cambridge, MA, 1978.
7. Kwon, Y. and Barnes, F.S., A theoretical study of the effects of RF fields in the vicinity of membranes, *Bioelectromagnetics*, 26, 2, 118–124, 2005.
8. Bier, M., Ed., *Electrophoresis: Theory, Methods, and Applications*, Vol. 2, Academic Press, New York, 1967.
9. Gascoyne, P.R. and Vykoukal, J.V., Dielectrophoresis-based sample handling in general-purpose programmable diagnostic instruments, *Proc. IEEE*, 92, 1, 22–41, 2004.
10. Rand, E.P., Interacting phospholipids bilayers: measured forces and induced structural changes, in *Annual Review of Biophysics and Bioengineering*, Vol. 10, Mullins, L.J., Ed., Academic Press, New York, 277–314, 1981.

11. Pethig, R., *Dielectric and Electronic Properties of Biological Materials*, John Wiley & Sons, New York, 184, 1979.
12. Parsegian, J.L., Long range physical forces in the biological milieu, in *Annual Review of Biophysics and Bioengineering*, Mullins, L.J., Ed., Academic Press, New York, 1973, 221.
13. Lifshitz, F.M., *Zh. Eksp. Teor. Fiz.*, 29, 95, 1955; *Sov. Phys. JETP* 2, 73, 1956.
14. Irailelachvili, J., *Intermolecular and Surface Forces*, 2nd edition, Academic Press, San Diego, CA, 1992.
15. Tasao, Y.T., Evan, D.F., and Wennerstrom, H., Long-range attractive force between hydrophobic surfaces observed by atomic force microscopy, *Science*, 262, 1993.
16. Barnes, F.S., Ginley, H., and Shulls, W., AC electric field effects on bacteria, presented at the Third Annual Conference, Bioelectromagnetics Society (BEMS), Washington, DC, 1981.
17. Zumdahl, S.S., *Chemistry*, 2nd edition, D.C. Health Co., Lexington, MA, 546, 1989.
18. Atkins, P.W., *Physical Chemistry*, 4th edition, W.H. Freeman Co., New York, Chapter 26, 1990.
19. McCaig, C.D., Spinal neurite reabsorption and regrowth *in vitro* depend on the polarity of an applied electric field, *Development*, 100, 31–41, 1987.
20. Nuccitelli, R., Physiological electric fields can influence cell motility, growth, and polarity, *Adv. Cell Biol.*, 2, 213–233, 1988.
21. Erickson, C.A. and Nuccitelli, R., Embryonic fibroblast motility and orientation can be influenced by physiological electric fields, *J. Cell Biol.*, 98, 296–307, 1984.
22. Seto, Y.J. and Hsieh, S.T., Electromagnetic induced kinetic effects on charged substrates in localized enzyme systems, *Biotechnology and Bioengineering*, XVIII, 813–837, 1976.
23. Muraji, M., Nishimura, M., Tatebe, W., and Fujii, T., Effect of alternating magnetic field on the growth of the primary root of corn, *IEEE Trans. Magn.*, 28, 4, 1996–2000, 1992.
24. Towns, C. and Schawlow, A., *Microwave Spectroscopy*, McGraw-Hill, New York, 255–283, 1955.
25. Bublitz, G.U. and Boxer, S.G., Stark spectroscopy: applications in chemistry, biology, and materials science, *Ann. Rev. Phys. Chem.*, 48, 213–242, 1997.
26. Steiner, U. and Ulrich, T., Magnetic field effects in chemical kinetics and related phenomena, *Chem. Rev.*, 89, 47–151, 1989.
27. Guyton, A.C., *Textbook of Medical Physiology*, 8th edition, W.B. Saunders, Philadelphia, PA, 47, 1991.
28. Barnes, F., A model for the detection of weak ELF electric and magnetic fields, *Bioelectrochem. Bioenerg.*, 47, 207–212, 1999.
29. Alkon, D. and Rasmussen, H., A spatial-temporal model of cell activation, *Science*, 26, 998–1004, 1989.
30. Louisell, W., *Coupled Mode and Parametric Electronics*, John Wiley & Sons, New York, 1960.
31. Moss, F., Stochastic resonance, *Ber. Bunsenges. Phys. Chem.*, 95, 3, 302–311, 1991.
32. Gammaitoni, L., Stochastic resonance, *Rev. Mod. Phys.*, 70, 1, 223–287, 1998.
33. McNamara, B. and Wiesenfeld, K., Theory of stochastic resonance, *Phys. Rev. A*, 39, 9, 4854–4869, 1989.
34. MacGregor, R.J. and Lewis, E.R., *Neural Modelling*, Plenum Press, New York, 1977.
35. Cooper, M.S., Miller, J.P., and Fraser, S.E., Electrophoretic repatterning of charged cytoplasmic molecules within tissues coupled by gap junctions by externally applied electric fields, *Dev. Biol.*, 132, 170–188, 1989.
36. Epstein, B.R. and Foster, K.R., Anisotropy in the dielectric properties of skeletal muscle, *Med. Biol. Eng. Comput.*, 21, 51, 1983.
37. Kalmijn, A.J., Electric and magnetic field detection in elasmobranch fishes, *Science*, 281, 916–918, 1982.
38. Kalmijn, A.J., Detection of weak electric fields, in *Sensory Biology of Aquatic Animals*, Atema, E.J. et al., Eds., Springer-Verlag, Berlin, Chapter 6, 1987.
39. McCleave, J.D., Rommel, S., and Cathcart, A.S., Weak electric and magnetic fields in fish orientation, in *Orientation: Sensory Basis*, Vol. 188, Adler, H.E., Ed., New York Academy of Sciences, New York, 270, 1971.
40. Ransom, B.P. and Eyring, H., Membrane permeability and electrical potential, in *Ion Transport across Membranes*, Clarke, H.J. and Nachmansohn, D., Eds., Academic Press, New York, 103, 1954.

41. Tsong, T.Y., Liu, D.S., and Chauvin, R., Electroconformational coupling (ECC): an electric field induced enzyme oscillation for cellular energy and signal transductions, *Bioelectrochem. Bioenerg.*, 21, 319–331, 1989 (a section of *J. Electroanal. Chem.* and constituting Vol. 275, Elsevier Sequoia, S.A., Lausanne, Switzerland, 1985).
42. Liu, D.S., Astumian, R.D., and Tsong, T.Y., Activation of Na^+ and K^+ pumping modes of (Na, K)-ATPase by an oscillating electric field, *J. Biol. Chem.*, 265, 13, 7260–7267, 1990.
43. Horn, L.W., A novel method of the observation of membrane transporter dynamics, *Biophys. J.*, 64, 281–289, 1993.
44. Trifet, T. and Green, H.S., Information and energy flow in a simple nervous system, *J. Theor. Biol.*, 86, 3, 1980.
45. Vaccaro, S.R. and Green, H.S., Ionic processes in excitable membranes, *J. Theor. Biol.*, 81, 771, 1979.
46. Eckert, R. and Ewald, D., Residual calcium ions depress activation of calcium-dependent current, *Science*, 216, 730, 1982.
47. Baumann, G. and Easton, G., Modeling state-dependent sodium conductance data by memory-less random process, *Math. Biosci.*, 60, 265, 1982.
48. Schauf, C.L. and Baumann, G., Experimental evidence consistent with aggregation kinetics in sodium current of myxicola giant axons, *Biophys. J.*, 35, 707, 1981.
49. Baumann, G. and Eastman, G.S., Charge immobilization linked to inactivation in the aggregation model of channel gating, *J. Theor. Biol.*, 99, 249, 1982.
50. Poo, M., Rapid lateral diffusion of functional ACh receptors in embryonic muscle cell membrane, *Nature*, 295, 332, 1982.
51. Poo, M. and Lam, J.W., Lateral electrophoresis and diffusion of concanavalin A receptors in the membrane of embryonic muscle cell, *J. Cell Biol.*, 76, 483, 1978.
52. Lee, K.Y.C., Lingler, J.B., and McConnell, H.M., Electric field-induced concentration gradients in lipid monolayers, *Science*, 263, 655, 1994.
53. Hayashi, H. and Fishman, H., Inward rectifier K^+ channel from analysis of the complex conductance of aplysia neuronal membrane, *Biophys. J.*, 53, 747–757, 1988.
54. Barnes, F.S. and Hu, C.L., Model for some non thermal effects of radio and microwave fields on biological membranes, *IEEE Trans. Microwave Theory Technol.*, 25, 742, 1977.
55. Montaigne, K. and Pickard, W.F., Offset of the vascular potential of characean cells in response to electromagnetic radiation over the range of 250 Hz to 250 kHz, *Bioelectromagnetics*, 5, 31, 1984.
56. Pickard, W.F. and Rosenbaum, F.J., Biological effects of microwaves at membrane level: two possible athermal electrophysiological mechanisms and a proposed experimental test, *Math. Biosci.*, 39, 235, 1978.
57. Pickard, W.F. and Barsoum, Y.H., Radio-frequency bioeffects at the membrane level: separation of thermal and athermal contributions in the Characeae, *J. Membrane Biol.*, 61, 39, 1981.
58. Kalkwarf, D.R., Frasco, D.L., and Brattain, W.H., Current rectification and action potentials across thin lipid membranes, in *Physical Principles of Biological Membranes*, Snell, F., Wolken, J., Iverson, G., and Lam, J., Eds., Gordon & Breach, New York, 1970.
59. Franceschetti, G. and Pinto, I., Cell membrane nonlinear response to applied electromagnetic field, *IEEE Trans. Microwave Theory Technol.*, 32, 7, 1984.
60. Casaleggio, A., Marconi, L., Morgavi, G., Ridella, S., and Rolando, C., Current flow in a cell, with a nonlinear membrane, stimulated by an electric field, personal communication, 1985.
61. Cain, C.A., Biological effects of oscillating electric fields: role of voltage sensitive ion channels, *Bioelectromagnetics*, 2, 23, 1981.
62. Bisceglia and Pinto, I., Volterra series solution of Hodgkin–Huxley equation, personal communication, 1984.
63. Wachtel, H., Firing-pattern changes and transmembrane currents produced by low frequency fields in pacemaker neurons, in *Proceedings of the 18th Annual Hansford Life Science Symposium*, Technical Information Center, U.S. Department of Energy, Richland, WA, 132–147, 1978.
64. Adler, R., A study of locking phenomena in oscillators, *Proc., IEEE* 34, 351, 1946.
65. Barnes, F.S., Smoller, A., and Sheppard, A., Injection locking of pacemaker cells, in *Proceedings of the 9th Annual Conference*, IEEE Engineering in Medicine and Biology Society, 1986.

66. Fohlmeister, J.F., Adelman, W.J., Jr., and Poppele, R.E., Excitation properties of the squid axon membrane and model systems with current stimulation, *Biophys. J.*, 30, 79–98.
67. Barnes, F.S., Some engineering models for interactions of electric and magnetic fields with biological systems, *Bioelectromagn. Suppl.*, 1, 67–85, 1992.
68. Kroupa, V.F., *Frequency Synthesis*, John Wiley & Sons, New York, 1973.
69. Koss, D.A. and Carstensen, E. L, Effects of ELF electric fields on the isolated frog heart, *IEEE Trans. Biomed. Eng.*, 30, 347, 1983.
70. Litovitz, T.A., Krause, D., and Mullins, J.M., Effect of coherence time of the applied magnetic field on ornithine decarboxylase activity, *Biochem. Biophys. Res. Commun.*, 178, 3, 862–865, 1991.
71. Mullins, J.M., Krause, D., and Litovitz, T.A., Simultaneous application of a spatially coherent noise field blocks use response of cell cultures to a 60 Hz electromagnetic field, in *Proceedings of the 1992 World Congress on Bioelectromagnetism*, Bioelectromagnetics Society, Orlando, FL, 1992.
72. Farrell, J.M., Barber, M., Krause, D., and Litovitz, T.A., The superposition of a temporally incoherent magnetic field inhibits 60 Hz-induced changes in the ODC activity of developing chick embryos, *Bioelectromagnetics*, 19, 53–56, 1998.
73. Litovitz, T.A., Montrose, C.J., Doinov, P., Brown, K.M., and Barber, M., Superimposing spatially coherent electromagnetic noise inhibits field induced abnormalities in developing chick embryos, *Bioelectromagnetics*, 15, 2, 105–113, 1994.
74. Walczek, J. and Liburdy, R.P., Nonthermal 60 Hz sinusoidal magnetic-field exposure enhances $^{45}\text{Ca}^{2+}$ uptake in rat lymphocytes: dependence on mitogen activation, *Fed. Eur. Biochem. Soc. Lett.*, 271, 1/2, 157–160, 1990.
75. Liburdy, R.P., Calcium signaling in lymphocytes and ELF fields, *Fed. Eur. Biochem. Soc.*, 301, 1, 53–59, 1992.
76. Liburdy, R.P., Biological interactions of cellular systems with time-varying magnetic fields, *Ann. N.Y. Acad. Sci.*, 649, 74–94, 1992.
77. Yost, M.G. and Liburdy, R.P., Time-varying and static magnetic fields act in combination to alter calcium signal transduction in the lymphocyte. *Fed. Eur. Biochem. Soc.*, 296, 2, 17–122, 1992.
78. McLeod, K. J., Lee, R.C., and Ehrlich, H.P., Frequency dependence of electric field modulation of fibroblast protein synthesis, *Science*, 136, 1465–1469, 1987.
79. Takashima, S., Non-linear properties of nerve membranes, *Biophys. Chem.*, 11, 447, 1980.
80. Berkowitz, G.C. and Barnes, F.S., The effects of nonlinear membrane capacity on the interaction of microwave and radio frequencies with biological materials, *IEEE Trans. Microwave Theory Technol.*, 27, 204, 1979.
81. Alkon, D.L., Memory storage and neural systems, *Sci. Am.*, 261, 42–50, 1989.
82. Alkon, D.L. and Rasmussen, H., A spatial temporal model of cell activation, *Science*, 26, 998–1004, 1988.
83. Yang, X., Korn, H., and Faver, A.S., Long-term potentiation of electronic coupling at mixed synapses, *Nature*, 348, 542–545, 1990.
84. Hu, C.L. and Barnes, F.S., The thermal chemical damage in biological materials under laser irradiation, *IEEE Trans. Biomed. Eng.*, 17, 220, 1970.
85. Shuyrou, V.L., Zhodan, G.G., and Akorv, I.G., Effects of 330 MHz radio frequency, Academy of Science, Institute of Biophysics, Pushchino, Moscow Region, Russia, personal communication, 1984.
86. Trautman, E.D. and Newbower, R.S., A practical analysis of the electrical conductivity of blood, *IEEE Trans. Biomed. Eng.*, 30, 141, 1983.
87. Johnson, F. H., Eyring, H., and Stover, B.J., *The Theory of Rate Processes in Biology and Medicine*, John Wiley & Sons, New York, 1974.
88. Liburdy, R.P. and Penn, A., Microwave bioeffect in erythrocyte are temperature and pO₂ dependent action permeability and protein shedding occur at the membrane phase transition, *Bioelectromagnetics*, 5, 283–291, 1984.
89. Chalker, R., The effect of microwave absorption and associated temperature dynamics on nerve cell activity in Aplysia, M.S. thesis, University of Colorado, Boulder, 1982.
90. Barnes, F.S., Cell membrane temperature rate sensitivity predicted from the Nernst equation, *J. Bioelectromagn.*, 5, 113, 1964.

91. Bol'shakov, M.A. and Alekseyev, S.I., Change in the electrical activity of the pacemaker neurons of *L. stagnalis* with the rate of their heating, *Biophysics*, 31, 569–571, 1986.
92. Alekseyev, S.I., IL'in, V.I., and Tyazhelov, V.V., Effect of electromagnetic radiation in decimeter wavelength range on calcium current of mollusk neurons, *Biophysics*, 31, 2, 290–295, 1986.
93. Philippova, T.M., Novoselov, V.I., Bystrova, M.F., and Alekseev, S.I., Microwave effect on camphor binding to rat olfactory epithelium, *Bioelectromagnetics*, 9, 347–354, 1988.
94. Bushanam, S. and Barnes, F.S., Laser generated thermoelastic shock waves in liquids, *J. Appl. Phys.*, 46, 5, 2074–2082, 1975.
95. Mihran, R.T., Barnes, F.S., and Wachtel, H., Temporally-specific modification of myelinated axon excitability *in vitro* following a single ultrasound pulse, *Ultrasound Med. Biol.*, 16, 3, 297–309, 1990.
96. Ady, G., McNaughton, B.L., and Wachtel, H., A system for recording microwave effects on isolated mammalian brain slices, presented at the 5th Annual Conference, Bioelectromagnetics Society, Boulder, CO, 1983.
97. Polk, C., Sources, propagation amplitude and temporal variations of extremely low frequency (0–100 Hz) electromagnetic fields, in *Biological and Clinical Effects of Low-Frequency Magnetic and Electric Fields*, Llaurodo, J.G., Sances, A., Jr., and Battocletti, J.H., Eds., Charles C Thomas, Springfield, IL, 21, 1974.
98. Plonsey, R., *Bioelectric Phenomena*, McGraw-Hill, New York, 1969.
99. Barnes, F.S. and Seyed-Madani, M., Some possible limits on the minimum electrical signals of biological significance, in *Mechanistic Approaches to Interactions of Electric and Electromagnetic Fields with Living Systems*, Blank, M. and Findl, E., Eds., Plenum Press, New York, 339–349, 1987.
100. Yariv, A., *Introduction to Optical Electronics*, Holt, Reinhart & Winston, New York, 1976.
101. MacDonald, D.K.C., *Noise and Fluctuations: An Introduction*, John Wiley & Sons, New York, 1962.
102. Beck, A.H.W., *Statistical Mechanics, Fluctuations, and Noise*, Edward Arnold, London, 1967.
103. Keshner, M.F., 1/f noise, *Proc. IEEE*, 70, 3, 212–218, 1982.
104. Sichenga, E. and Verveen, A.A., The dependence of the 1/f noise intensity of the diode of Ranvier on membrane potential, in *Proceedings of the 1st European Biophysics Congress*, Vol. 5, Verlag Wiener Medizinischen Akademie, Vienna, Austria, 219, 1971.
105. Dorset, D.L. and Fishman, H.M., Excess electrical noise during current flow through porous membranes separating ionic solutions, *J. Membrane Biol.*, 21, 291–301, 1975.
106. Verveen, A.A. and DeFelice, L.J., Membrane noise, *Prog. Biophys. Mol. Biol.*, 28, 189, 1974.
107. Nuney, P.L. and Katznelson, R. D., *Electric Fields of the Brain—The Neurophysics of EEG*, Oxford University Press, New York, 1981.
108. Bernhardt, J., The direct influence of electromagnetic fields on nerve and muscle cells of man within the frequency range of 1 Hz to 30 MHz, *Radiat. Environ. Biophys.*, 16, 309, 1979.
109. Verveen, A.A. and Derksen, H.E., Fluctuation phenomena in nerve membrane, *Proc. IEEE*, 56, 906, 1968.
110. Beckwith, J.R. and McGuire, L.B., *Basic Electrocardiography and Vector Cardiography*, Raven Press, New York, 1982.
111. Krueger, A. and Reed, E., Biological impact of small air ions, *Science*, 193, 1209, 1976.
112. Weaver, J. C. and Chizmadzhev, Y., Electroporation, *Biological and Medical Aspects*, Barnes, F.S. and Greenebaum, B., Eds., Taylor & Francis, Boca Raton, FL, Chapter 9, 2006.
113. Michaelson, S.M., Elson, E.C., Anderson, L.E., Interaction of non-modulated and pulse modulated radio frequency fields with living fields with living matter: experimental results, *Biological and Medical Aspects*, Barnes, F.S., and Greenebaum, B., Eds., Taylor & Francis, Boca Raton, FL, Chapter 3, 2006.
114. Pilla, A.A., Mechanisms and therapeutic applications of time-varying and static magnetic fields, *Biological and Medical Aspects*, Barnes, F.S., and Greenebaum, B., Eds., Taylor & Francis, Boca Raton, FL, Chapter 11, 2006.

6

Magnetic Field Effects on Free Radical Reactions in Biology

Stefan Engström

CONTENTS

6.1	Introduction	157
6.2	Theoretical Background	158
6.2.1	Hyperfine Interaction-Induced Singlet-to-Triplet Conversion.....	159
6.2.2	High-Field Regime: Spin Rephrasing through the Δg Mechanism.....	159
6.2.3	Low-Field Effect: $B < 1$ mT	160
6.2.4	Free Radicals in Radio Frequency Fields.....	160
6.3	General Characteristics of the Free Radical Mechanism.....	160
6.3.1	Experimental Discrimination of Free Radical Models.....	161
6.4	Free Radicals in Biology	161
6.4.1	Biological Transduction Mechanisms.....	161
6.4.2	Role of Freely Diffusing Radicals.....	162
6.4.3	Animal Navigation Models Based on Free Radicals	163
6.4.4	Coenzyme B ₁₂ -Dependent Reactions.....	163
6.4.5	Other Experimental Observations.....	163
6.5	Conclusion	164
	References	164

6.1 Introduction

The physical chemistry of spin-correlated free radical pairs offers several mechanisms explaining how magnetic fields may influence biochemical processes. The mechanisms are classified on the basis of the dominating contribution to spin interconversion, and they cover a wide range of field strengths. Of particular interest is what is called the low-field mechanism, which has been extensively developed over the last decade and is now capable of explaining biological effects induced by magnetic fields well below 1 mT.

The principal mechanism behind the free radical mechanism was discovered in the physical problem of magnetic field dependence on positronium decay (Deutsch and Brown, 1952; Halpern, 1954). However, the development of the radical pair mechanism in chemistry has its roots in the work of Kaptein and Oosterhoff (1969), Closs (1969), and Brocklehurst (1969).

An ambitious survey of the literature up to its date of publication is the review of Steiner and Ulrich (1989), which lists some 775 references, 58 of which are themselves reviews on magnetokinetic phenomena. Another, now classic, reference on the subject is the book by Salikhov et al. (1984). McLauchlan and Steiner (1991) published a review including the possible mechanisms at lower fields. The review by Grissom (1995) explored the higher-field mechanisms with particular attention to the context of biological systems. A didactic paper geared toward the issues in biological systems is that of Brocklehurst and McLauchlan (1996). There are also some recent reviews on the free radical mechanism in general (Woodward, 2002) and with particular attention to biological systems (Brocklehurst, 2002).

6.2 Theoretical Background

A radical is an atom or a molecule with an unpaired electron. It tends to be highly reactive, a property that defines their best known roles in biology. A spin-correlated (or geminate) radical pair is typically created by hemolytic cleavage of a covalent bond, that is, each molecule retains one of the electrons that formed the chemical bond that was broken. The electron spins may remain correlated for a significant time (microseconds) after the pair's creation. As the radicals separate, the electron interaction term becomes small, and the electron states of the pair will fluctuate between antiparallel (singlet, or "S") and parallel (triplet, or "T") because of coherent spin evolution by hyperfine interactions between the electron spin and the nuclei. There is a chance of reencounter between the spin-correlated radicals. Reforming the bond is only permitted by quantum spin selection rules if the electron spins are oriented in the singlet state.

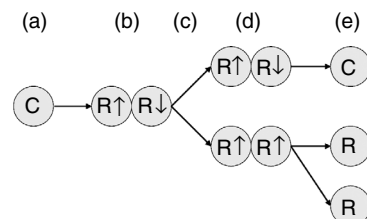
Magnetic fields can affect the electron state in the time before the reencounter; and if singlet and triplet pairs have different chemical fates, we have a basis for magnetic field effects on free radical chemistry (Figure 6.1). In exemplifying the process, we will assume that the radical pair is formed in the singlet state, the normal case for biologically relevant reactions (Eveson et al., 2000).

Many physical transduction mechanisms proposed to explain magnetic field effects in biology are very vulnerable to the randomizing effects of thermal noise at normal temperatures of living systems (Binihi and Savin, 2003). The free radical mechanism is uniquely resistant to this obstacle since it is a nuclear effect and is not strongly coupled to the thermal bath (Adair, 1999).

A quantum mechanical formulation of the free radical mechanism contains many possible contributions to the hamiltonian; Steiner and Ulrich (1989) provide a good categorization of the main components. The stochastic Liouville equation (SLE) is a tool

FIGURE 6.1

A molecule "C" (a) is split into two radicals (b). After diffusion and spin interconversion (c), the radicals may reencounter while still spin correlated (d). If the encounter occurs in the singlet state (e, top), the radicals may recombine. If the encounter occurs in the triplet state (e, bottom), recombination cannot occur, and the radicals will diffuse apart again and eventually lose their spin correlation. A magnetic field can influence this reaction by changing the rate of spin interconversion as long as the singlet and triplet products have different chemical fates.



for addressing the problem of simultaneous spin mixing and diffusion, but simplified models in which these two components are treated separately are often useful for the great reduction in problem complexity (Brocklehurst and McLauchlan, 1996). Recently, analytical results using a backward SLE have been presented (Pedersen and Christensen, 2004).

6.2.1 Hyperfine Interaction-Induced Singlet-to-Triplet Conversion

Hyperfine interactions between the spins of the electron and the nucleus cause the electron spins of the radicals to precess and induce singlet-to-triplet conversion. The triplet state has a net magnetic moment, and in the presence of an external magnetic field the energy levels of the triplet states that have a moment aligned with the magnetic field (T_+ and T_-) will be separated by Zeeman splitting. As the applied field strength is increased, the T_+ and T_- energy levels will be shifted away from the singlet state so much that they are decoupled from the spin interconversion process between singlet and triplet states, and only the remaining triplet state (T_0), which has a magnetic moment that is oriented perpendicular to the field, is capable of participating in the spin conversion process. In this way the magnetic field can reduce the number of triplet states that can be converted into singlet states and subsequently reform the original chemical bond. This is the “normal” magnetic field effect on free radical chemistry. It becomes relevant for external fields larger than the effective field driving the hyperfine interaction mixing, typically 1–10 mT.

A way in which singlet-to-triplet conversion can be facilitated is when an applied field causes the T_- energy level to cross the nonmagnetic singlet level, which occurs when the Zeeman differential matches the electron exchange interaction energy (cf. Figure 6.2). This effect has been observed for fields as low as 6.6 mT (Werner et al., 1993), but it can in principle be observed for much lower fields if the radical pairs are fixed with an appropriate separation.

6.2.2 High-Field Regime: Spin Rephrasing through the Δg Mechanism

The product of the magnetic field and the Landé g -factor determines the precession of the unpaired electron spin, independent of the hyperfine contribution. If the two radicals have slightly different g -factors, this provides an additional source of spin conversion. Differences are usually quite small, so this mechanism typically becomes significant only for quite large fields, $B > 0.1\text{--}1 \text{ T}$.

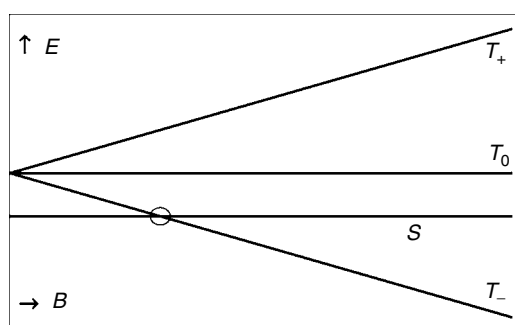


FIGURE 6.2

Energy level diagram for singlet and triplet states of a radical pair. At high fields, T_+ and T_- become completely disconnected from the singlet state, and only the T_0 state is left for singlet–triplet interconversion. At a specific B -field, the Zeeman split causes the T_- state to closely match the singlet state (circled), increasing the likelihood of transitions between the two states.

6.2.3 Low-Field Effect: $B < 1 \text{ mT}$

At fields below the hyperfine interaction energy, it is still possible to see effects of external fields under certain circumstances. It was found by Brocklehurst (1976) that the selection rules of the hyperfine-induced spin mixing are more restrictive in zero field than when a field is applied (McLauchlan and Steiner, 1991). This becomes relevant, even for a very small field, as long as the coherence of the pair's state is maintained for long periods (100 ns to 1 μs). A helpful vector model to visualize this effect, along with some illustrative numerical examples, is given by Till et al. (1998).

The low-field effect (LFE) can theoretically produce a large (40%) drop in the singlet yield if the conditions are optimal (Timmel et al., 1998), but in practice only smaller effects attributed to this mechanism have been reported in the experimental literature.

Since long coherence times are required, it is necessary to understand spin relaxation effects and under what conditions they may be sufficiently long. Anisotropic hyperfine interactions provide noncoherent spin relaxation in solution, and it appears that the relaxation is slower in the low-field situation than has been generally thought (Fedin et al., 2001, 2003). It is becoming clear that understanding the local environment is crucial for evaluating LFEs (Eveson et al., 2000).

An important way to extend free radical magnetic field effects into the low-field region is to extend the lifetime of the spin-correlated pair. Integrating the magnetic field's influence over a longer time increases its ability to influence the spin evolution. Spin relaxation is not the primary problem here; rather, it is the reencounter probability that needs to be enhanced. There are several ways to achieve this:

1. Increased viscosity to restrict diffusion (Krissinel et al., 1999; Christensen and Pedersen, 2003; Kitahama et al., 2004)
2. Oppositely charged radicals that will oppose a tendency to diffuse apart (Adair, 1999)
3. Physically restricted mobility of the radicals through confining them to a surface or having the reaction taking place inside micelles, which are nanometer-scale compartments that form and reform on microsecond timescales and are able to confine the radical pairs and increase the reencounter probability (Eveson et al., 2000).

6.2.4 Free Radicals in Radio Frequency Fields

For higher-frequency fields ($f > 1 \text{ MHz}$) the time modulation of the field starts to correspond to timescales present in the reaction dynamics, and a range of resonant interactions become available (Timmel and Hore, 1996). A detailed treatment of the coenzyme B₁₂ system demonstrated resonant phenomena for relatively low-level radio frequency (RF) fields using a variety of mathematical techniques (Canfield et al., 1994, 1995).

6.3 General Characteristics of the Free Radical Mechanism

Free radical reactions are generally quite fast. There is evidence of picosecond reactions (Gilch et al., 1998; Musewald et al., 1999), but many known reactions occur over nanosecond timescales. If the free radical diffusion is constrained by micelles (Eveson et al.,

2000; Christensen and Pedersen, 2003) or by Coulomb attraction (Horiuchi et al., 2003), it may be possible to extend the radical pair lifetimes to hundreds of nanoseconds or even microseconds.

Since the free radical mechanism is practically instantaneous when compared to the timescale of time-varying magnetic fields in the extremely low-frequency regime (<300 Hz), one would expect that the observable output from a biological detection of the field should depend only on the time-averaged absolute field amplitude (Scaiano et al., 1995). However, if there is a downstream system that is able to decode the low-frequency signal, this statement is not necessarily true (Engstrom, 1997; Engstrom and Fitzsimmons, 1999).

6.3.1 Experimental Discrimination of Free Radical Models

The relative orientation of a static and a much smaller oscillating field will provide a discriminating test for a free radical-based model as long as the timescale of the applied field is long compared to the lifetime of the radical pair. In an isotropic system, such as a liquid suspension, described by this field situation, only the amplitude of the magnetic field is relevant. While the smaller parallel field adds linearly to the larger static field, the perpendicular component is effectively reduced by the calculation of vector length and will cause a much smaller variation in field amplitude (Engstrom, 1997).

For oriented systems in which the free radical chemistry steps have spatial preferences, it is possible to have angular dependence with respect to the angle of the applied field, $f(\theta)$. One can argue that some symmetry properties are very likely to be present in that kind of situation (Ritz et al., 2000). Polarity changes are not expected to be relevant, so $f(\theta + 180^\circ) = f(\theta)$. Furthermore, due to the isotropic distribution of nuclear spins in the initial state of the radical pair, one also expects that $f(180^\circ - \theta) = f(\theta)$.

If the free radical mechanism is active for low-frequency fields, one can also expect a response to RF fields in the same system, a property not expected by any other suggested physical transduction mechanisms for magnetic fields (Henbest et al., 2004). In a comparison between static fields in the range 0–2 mT, it was shown that a 300- μ T, 5-MHz RF field applied perpendicularly or in parallel with the static field induced a response that was dependent on the magnitude of the static field (Henbest et al., 2004). This is qualitatively, if not quantitatively, similar to the observation that the magnetic sense of migratory birds can be disrupted by a 470-nT, 7-MHz field when the field is applied at an angle with the geomagnetic field (Ritz et al., 2004).

Magnetic isotope effects are another possible discriminating character of free radical effects, and it is possible to differentiate this signature from pure mass effects (Brocklehurst, 1997).

6.4 Free Radicals in Biology

6.4.1 Biological Transduction Mechanisms

Direct detection methods for free radicals have been developed in chemistry only relatively recently (Woodward, 2002). In biological systems, almost all experimental evidence for free radical involvement remains indirect. Generating hypotheses based on the signatures of free radical systems as outlined above are necessary to link free radical chemistry

to magnetic field effects, but there is circumstantial evidence that free radical chemistry underlies some effects reported in the bioelectromagnetics literature.

It has been suggested that complex dynamical systems may have special sensitivity to magnetic field influences (Grundler et al., 1992; Waliczek, 1995). This idea has been elaborated in a series of theoretical models of oscillatory systems (Eichwald and Waliczek, 1996a,b; Kaiser, 1996). These models show that enzyme dynamics involving free radical chemistry may be frequency specific, although only for timescales comparable to or slower than the chemical kinetics of the system (Eichwald and Waliczek, 1997). Field amplitude can influence enzyme dynamics in some instances and this can be used to exert some control over enzyme systems (Eichwald and Waliczek, 1998).

The peroxidase–oxidase system has interesting, well-documented dynamical properties (Scheeline et al., 1997). Detailed modeling of this system has shown how a magnetic field-induced perturbation can affect its dynamical behavior (Eichwald and Waliczek, 1998; Moller and Olsen, 1999). The point of interaction in this system is suspected to be electron-transfer enzyme intermediates (Moller and Olsen, 2000; Moller et al., 2000).

Downstream effects from changes in chemistry must be taken into account to evaluate biological significance (Brocklehurst and McLauchlan, 1996). This can both facilitate detection (Waliczek, 1995) as well as introduce interventions that could block the biological significance of a physical detection event.

It may be relevant that other enzyme systems have been studied in detail without the specific intention of addressing free radicals as a possible mechanism. Examples include electric and magnetic field effects in ATPase (Blank and Soo, 2001b). Direct interactions with DNA have been suggested; and electron transfer reactions are proposed interaction targets (Blank and Goodman, 2000; Blank and Soo, 2001a), although not by mechanisms addressed here. Myosin phosphorylation is another enzyme system that has shown sensitivity to time-varying (Markov et al., 1993) and static magnetic fields (Markov and Pilla, 1994), as well as gradient-specific effects (Engstrom et al., 2002).

6.4.2 Role of Freely Diffusing Radicals

Free radicals observed in biology are most commonly oxygen or nitrogen based with an unpaired electron, leading to the terms reactive oxygen species (ROS) and reactive nitrogen species (RNS). A dominant role for these radicals is to act in immunological defense. They are secreted by macrophages and neutrophils and during attempts to kill bacteria, viruses, and tumors (Nathan, 1992). The highly reactive nature of the radicals also means that damage to normal cells is possible, and various defense mechanisms against this have evolved as well (Yu, 1994). This immunological weapon with checks and balances already suggests that there is a signaling system built around free radicals, but it seems that the ROS and RNS also have roles in intracellular cell signaling (Lander, 1997) as well as intercellular communication (Thannickal and Fanburg, 2000).

Consider a biochemical reaction producing a spin-correlated free radical pair in the singlet state. Depending on the specific mechanism at work, the ratio of singlet-to-triplet product at reencounter will be modified. This will increase or decrease the fraction of pairs that tend to recombine because of a reencounter finding the spins in singlet versus the triplet states. For the LFE, the triplet state is favored, and we would see an excess of escape product. The situation is the opposite for the “normal” field effect, in which the T_- and T_+ states are decoupled from the interconversion process, increasing the proportion of singlet reencounters leading to a larger amount of cage product and leaving fewer freely diffusing radicals. The Δg mechanism brings the T_- and T_+ states back into play and therefore again boosts the triplet-reencounter escape products.

Given the wide involvement of free radicals in signaling and biological function, it is clear that there is the potential of both subtle and not-so-subtle effects on biological systems if we are able to alter the production of free radicals and thereby change the dynamics of already ongoing processes. The conventional wisdom regarding the deleterious effects of magnetic field effects on free radical recombination has been that more escape product means more radical-induced damage. This may be an oversimplification since the direct effects on cage or escape products are typically fairly small, certainly not larger than tens of percent, implying that drastic biological effects must involve downstream responses that amplify this relatively slight modulation. The answer may lie in the signaling properties of free radicals.

6.4.3 Animal Navigation Models Based on Free Radicals

The free radical mechanism was the first mechanism suggested as an explanation of avian use of magnetic fields for navigation (Schulten et al., 1978; Schulten, 1982). This model has since undergone several iterations of refinement (Ritz et al., 2000; Cintolesi et al., 2003). One interesting aspect of this work is a connection between photosensitivity and magnetoreception (Ritz et al., 2002). Dependence on light is a well-known feature of the avian magnetoreceptor (Deutschlander et al., 1999; Wiltschko et al., 2004a,b), but it has also appeared in other behavioral studies of animal magnetic field sensitivity (Prato et al., 1997, 1998).

The Ritz-Schulten model (Ritz et al., 2000) has an appealing geometrical application. Being integrated into the bird's retina, the suggested compass would appear as a modulation overlay on the bird's field of view. The mechanism operates through the so-called low field effect (LFE), based on a single nuclear spin, and operates near the limit of the theoretical sensitivity, despite omitting degrading effects such as the presence of multiple nuclear spins, dipolar effects, and various spin relaxation process that will start to become relevant for the long radical pair lifetimes ($>100\text{ ns}$) considered in the model.

Cryptochromes provide one possible source of free radicals in a spatially ordered system (Ritz et al., 2002). A recent theoretical model for avian magnetoreception develops that idea by investigating a flavin–tryptophan radical pair with a high degree of homology to the cryptochromes (Cintolesi et al., 2003). This multinucleus model is realistic in that it still manages to provide sensitivity to fields in the geomagnetic field range. Interestingly, it does not operate through the LFE described above (the multinucleus approach appears to remove most signs of that mechanism), but rather it depends on immobilized radicals and assumes that the free radical pair may have a lifetime up to $5\text{ }\mu\text{s}$.

6.4.4 Coenzyme B₁₂-Dependent Reactions

Magnetic field effects in the coenzyme B₁₂ are well explored experimentally with matching theoretical predictions (Harkins and Grissom, 1994; Grissom and Natarajan, 1997; Taoka et al., 1997). While most work on this model system has been concerned with intermediate and higher-field mechanisms, there are also detailed theoretical investigations suggesting that weak ($<100\text{ }\mu\text{T}$), relatively low-frequency ($<100\text{ kHz}$), might be able to affect this system (Canfield et al., 1994, 1995, 1996).

6.4.5 Other Experimental Observations

The addition of iron ions or exposure to a 7-mT static magnetic field (SMF) did not affect the survival of rat lymphocytes *in vitro* when performed in isolation, but combined

exposure led to a significant increase in cell death (Jajte et al., 2002). One possible explanation of this behavior is that the addition of iron ions enhanced levels of ROS and that the field exposure further promoted the creation of free radicals, leading to cell death by both apoptosis and necrosis. An experiment with a similar rationale used added FeCl₂ to stimulate ROS production, and a 930-MHz, 5-W/m² cell phone-generated field affected a biological marker for ROS production. It should be noted that the vacuum magnetic field associated with this exposure is quite low (approximately 0.14 µT) and the frequency is a relatively unexplored region for this mechanism.

Proliferation of chick fibroblasts was observed to be enhanced by a 100-Hz, 0.7-mT sinusoidal magnetic field (Katsir et al., 1998). In a follow-up study it was found that free radical scavengers (Katsir and Parola, 1998) suppressed this effect, suggesting that free radicals may have a role in mediating the magnetic field effect on proliferation.

Genotoxic effects from intermediate static magnetic fields (250 mT) have been studied in *Escherichia coli* DNA, both *in vivo* and *in vitro* (Potenza et al., 2004). Free radical formation was stimulated, and the genetic damage was mapped as a function of exposure duration. *In vitro* experiments showed detectable genotoxic effects, but the *in vivo* assays did not, indicating that cellular protective responses may prevent damage in the intact system.

A reported effect on the oxidative burst in neutrophils by a 0.1-mT field was attributed to free radicals (Roy et al., 1995). In that study, the connection to free radicals lies in that the fluorescent probe used to study the neutrophil activity reacts specifically with free radical-derived oxidants that create the fluorescing compounds. Work in neutrophils in humans (Heine et al., 1999) using a much larger field (1.5 T) did not find any effects of magnetic fields on the respiratory burst of human neutrophils or on the production of radical species.

Phagocytosis was observed to be affected by 0.5–1.5-mT, 50-Hz sinusoidal magnetic fields (Simko et al., 2001). An attendant increase in superoxide production may be an indication that the field stimulated the system through a free radical process.

6.5 Conclusion

Free radical reactions are ubiquitous in biology, and recent developments of the low-field mechanisms (Timmel et al., 2001) and the consideration of detailed biochemical systems (Cintolesi et al., 2003) make this mechanism a contender for field effects down to geomagnetic field strengths. The physical transduction step is not vulnerable to thermal perturbations, a significant advantage over competing models.

This model does not produce large (factors >2) changes at the initial field detection step. Theoretical models and direct experimental observations in the low-field region typically operate around or below the 10% level, so we should expect the physical detection mechanism to need cooperation from downstream processes for biologically relevant detection of magnetic fields with free radicals as the starting point.

References

- Adair RK (1999): Effects of very weak magnetic fields on radical pair reformation. *Bioelectromagnetics* 20:255–263.
- Binhi VN, Savin AV (2003): Effects of weak magnetic fields on biological systems: physical aspects. *Physics-Uspekhi* 46:259–291.

- Blank M, Goodman R (2000): Stimulation of the stress response by low-frequency electromagnetic fields: possibility of direct interaction with DNA. *IEEE Transactions on Plasma Science* 28:168–172.
- Blank M, Soo L (2001a): Electromagnetic acceleration of electron transfer reactions. *Journal of Cellular Biochemistry* 81:278–283.
- Blank M, Soo L (2001b): Optimal frequencies for magnetic acceleration of cytochrome oxidase and Na,K-ATPase reactions. *Bioelectrochemistry* 53:171–174.
- Brocklehurst B (1969): Formation of excited states by recombining organic ions. *Nature* 221:921.
- Brocklehurst B (1976): Spin correlation in geminate recombination of radical ions in hydrocarbons. 1. Theory of magnetic-field effect. *Journal of the Chemical Society—Faraday Transactions II* 72:1869–1884.
- Brocklehurst B (1997): Magnetic isotope effects in biology: a marker for radical pair reactions and electromagnetic field effects? *International Journal of Radiation Biology* 72:587–596.
- Brocklehurst B (2002): Magnetic fields and radical reactions: recent developments and their role in nature. *Chemical Society Reviews* 31:301–311.
- Brocklehurst B, McLauchlan KA (1996): Free radical mechanism for the effects of environmental electromagnetic fields on biological systems. *International Journal of Radiation Biology* 69:3–24.
- Canfield JM, Belford RL, Debrunner PG, Schulten KJ (1994): A perturbation-theory treatment of oscillating magnetic-fields in the radical pair mechanism. *Chemical Physics* 182:1–18 (see also *Journal of Chemical Physics* 191:347, 1995).
- Canfield JM, Belford RL, Debrunner PG, Schulten KJ (1995): A perturbation treatment of oscillating magnetic-fields in the radical pair mechanism using the Liouville equation. *Chemical Physics* 195:59–69.
- Canfield JM, Belford RL, Debrunner PG (1996): Calculations of Earth-strength steady and oscillating magnetic field effects in coenzyme B-12 radical pair systems. *Molecular Physics* 89:889–930.
- Christensen M, Pedersen JB (2003): On the validity of the one-particle diffusion model of geminate recombination in micelles. *Chemical Physics* 295:235–241.
- Cintolesi F, Ritz T, Kay CWM, Timmel CR, Hore PJ (2003): Anisotropic recombination of an immobilized photoinduced radical pair in a 50-mu T magnetic field: a model avian photomagnetoreceptor. *Chemical Physics* 294:385–399.
- Closs GL (1969): A mechanism explaining nuclear spin polarizations in radical combination reactions. *Journal of the American Chemical Society* 91:4552.
- Deutsch M, Brown SC (1952): Zeeman effect and hyperfine splitting of positronium. *Physical Review* 85:1047–1048.
- Deutschlander ME, Phillips JB, Borland SC (1999): The case for light-dependent magnetic orientation in animals. *Journal of Experimental Biology* 202:891–908.
- Eichwald C, Walleczeck J (1996a): Activation-dependent and biphasic electromagnetic field effects: model based on cooperative enzyme kinetics in cellular signaling. *Bioelectromagnetics* 17:427–435.
- Eichwald C, Walleczeck J (1996b): Model for magnetic field effects on radical pair recombination in enzyme kinetics. *Biophysical Journal* 71:623–631.
- Eichwald C, Walleczeck J (1997): Low-frequency-dependent effects of oscillating magnetic fields on radical pair recombination in enzyme kinetics. *Journal of Chemical Physics* 107:4943–4950.
- Eichwald C, Walleczeck J (1998): Magnetic field perturbations as a tool for controlling enzyme-regulated and oscillatory biochemical reactions. *Biophysical Chemistry* 74:209–224.
- Engstrom S (1997): What is the time scale of magnetic field interaction in biological systems? *Bioelectromagnetics* 18:244–249.
- Engstrom S, Fitzsimmons R (1999): Five hypotheses to examine the nature of magnetic field transduction in biological systems. *Bioelectromagnetics* 20:423–430.
- Engstrom S, Markov MS, McLean MJ, Holcomb RR, Markov JM (2002): Effects of non-uniform static magnetic fields on the rate of myosin phosphorylation. *Bioelectromagnetics* 23:475–479.
- Eveson RW, Timmel CR, Brocklehurst B, Hore PJ, McLauchlan KA (2000): The effects of weak magnetic fields on radical recombination reactions in micelles. *International Journal of Radiation Biology* 76:1509–1522.

- Fedin MV, Purtov PA, Bagryanskaya EG (2001): Anisotropic hyperfine interaction-induced spin relaxation in a low magnetic field. *Chemical Physics Letters* 339:395–404.
- Fedin MV, Purtov PA, Bagryanskaya EG (2003): Spin relaxation of radicals in low and zero magnetic field. *Journal of Chemical Physics* 118:192–201.
- Gilch P, Pollinger-Dammer F, Musewald C, Michel-Beyerle ME, Steiner UE (1998): Magnetic field effect on picosecond electron transfer. *Science* 281:982–984.
- Grissom CB (1995): Magnetic-field effects in biology—a survey of possible mechanisms with emphasis on radical-pair recombination. *Chemical Reviews* 95:3–24.
- Grissom CB, Natarajan E (1997): Use of magnetic field effects to study coenzyme B-12-dependent reactions. *Vitamins and Coenzymes*, Pt K 281:235–247.
- Grundler W, Kaiser F, Keilmann F, Walleczeck J (1992): Mechanisms of electromagnetic-interaction with cellular-systems. *Naturwissenschaften* 79:551–559.
- Halpern O (1954): Mangetic quenching of the positronium decay. *Physical Review* 94:904–907.
- Harkins TT, Grissom CB (1994): Magnetic-field effects on B-12 ethanolamine ammonia-lyase—evidence for a radical mechanism. *Science* 263:958–960.
- Heine J, Scheinichen D, Jaeger K, Herzog T, Sumpelmann R, Leuwer M (1999): Effect of magnetic resonance imaging on human respiratory burst of neutrophils. *FEBS Letters* 446:15–17.
- Henbest KB, Kukura P, Rodgers CT, Hore PJ, Timmel CR (2004): Radio frequency magnetic field effects on a radical recombination reaction: a diagnostic test for the radical pair mechanism. *Journal of the American Chemical Society* 126:8102–8103.
- Horiuchi M, Maeda K, Arai T (2003): Magnetic field effect on electron transfer reactions of flavin derivatives associated with micelles. *Applied Magnetic Resonance* 23:309–318.
- Jajte J, Grzegorczyk J, Zmyslony M, Rajkowska E (2002): Effect of 7 mT static magnetic field and iron ions on rat lymphocytes: apoptosis, necrosis and free radical processes. *Bioelectrochemistry* 57:107–111.
- Kaiser F (1996): External signals and internal oscillation dynamics: biophysical aspects and modelling approaches for interactions of weak electromagnetic fields at the cellular level. *Bioelectrochemistry and Bioenergetics* 41:3–18.
- Kaptein R, Oosterhoff LJ (1969): Chemically induced dynamic nuclear polarization III (anomalous multiplets of radical coupling and disproportionation products). *Chemical Physics Letters* 4:214–216.
- Katsir G, Parola AH (1998): Enhanced proliferation caused by a low frequency weak magnetic field in chick embryo fibroblasts is suppressed by radical scavengers. *Biochemical and Biophysical Research Communications* 252:753–756.
- Katsir G, Baram SC, Parola AH (1998): Effect of sinusoidally varying magnetic fields on cell proliferation and adenosine deaminase specific activity. *Bioelectromagnetics* 19:46–52.
- Kitahama Y, Wakasa M, Sakaguchi Y (2004): Viscosity dependence of the magnetic field effect due to the delta g mechanism. *Journal of Physical Chemistry A* 108:754–757.
- Krissinel EB, Burshtein AI, Lukzen NN, Steiner UE (1999): Magnetic field effect as a probe of distance-dependent electron transfer in systems undergoing free diffusion. *Molecular Physics* 96:1083–1097.
- Lander HM (1997): An essential role for free radicals and derived species in signal transduction. *FASEB Journal* 11:118–124.
- Markov MS, Pilla AA (1994): Static magnetic-field modulation of myosin phosphorylation—calcium-dependence in 2 enzyme preparations. *Bioelectrochemistry and Biohergetics* 35(1–2):57–61.
- Markov MS, Wang S, Pilla AA (1993): Effects of weak low frequency sinusoidal and DC magnetic fields on myosin phosphorylation in a cell-free preparation. *Bioelectrochemistry and Bioenergetics* 30:119–125.
- McLauchlan KA, Steiner UE (1991): The spin-correlated radical pair as a reaction intermediate. *Molecular Physics* 73:241–263.
- Moller AC, Olsen LF (1999): Effect of magnetic fields on an oscillating enzyme reaction. *Journal of the American Chemical Society* 121:6351–6354.
- Moller AC, Olsen LF (2000): Perturbations of simple oscillations and complex dynamics in the peroxidase–oxidase reaction using magnetic fields. *Journal of Physical Chemistry B* 104:140–146.

- Moller AC, Lunding A, Olsen LF (2000): Further studies of the effect of magnetic fields on the oscillating peroxidase–oxidase reaction. *Physical Chemistry Chemical Physics* 2:3443–3446.
- Musewald C, Gilch P, Hartwich G, Pollinger-Dammer F, Scheer H, Michel-Beyerle ME (1999): Magnetic field dependence of ultrafast intersystem-crossing: a triplet mechanism on the picosecond time scale? *Journal of the American Chemical Society* 121:8876–8881.
- Nathan C (1992): Nitric-oxide as a secretory product of mammalian-cells. *FASEB Journal* 6:3051–3064.
- Pedersen JB, Christensen M (2004): The backward stochastic Liouville equation. *Journal of Physical Chemistry B* 108:9516–9523.
- Potenza L, Cuccharini L, Piatti E, Angelini U, Dacha M (2004): Effects of high static magnetic field exposure on different DNAs. *Bioelectromagnetics* 25:352–355.
- Prato FS, Kavaliers M, Cullen AP, Thomas AW (1997): Light-dependent and -independent behavioral effects of extremely low frequency magnetic fields in a land snail are consistent with a parametric resonance mechanism. *Bioelectromagnetics* 18:284–291.
- Prato FS, Kavaliers M, Thomas AW, Ossenkopp KP (1998): Modulatory actions of light on the behavioural responses to magnetic fields by land snails probably occur at the magnetic field detection stage. *Proceedings of the Royal Society of London Series B: Biological Sciences* 265:367–373.
- Ritz T, Adem S, Schulten K (2000): A model for photoreceptor-based magnetoreception in birds. *Biophysical Journal* 78:707–718.
- Ritz T, Dommer DH, Phillips JB (2002): Shedding light on vertebrate magnetoreception. *Neuron* 34:503–506.
- Ritz T, Thalau P, Phillips JB, Wiltschko R, Wiltschko W (2004): Resonance effects indicate a radical-pair mechanism for avian magnetic compass. *Nature* 429:177–180.
- Roy S, Noda Y, Eckert V, Traber MG, Mori A, Liburdy R, Packer L (1995): The phorbol 12-myristate 13-acetate (PMA)-induced oxidative burst in rat peritoneal neutrophils is increased by a 0.1 mT (60 Hz) magnetic-field. *FEBS Letters* 376:164–166.
- Salikhov KM, Molin YuN, Sagdeev RZ, Buchachenko AL (1984): *Spin Polarization and Magnetic Effects in Radical Reactions*. Elsevier, Amsterdam.
- Scaiano JC, Cozens FL, Mohtat N (1995): Influence of combined AC-DC magnetic-fields on free-radicals in organized and biological-systems—development of a model and application of the radical pair mechanism to radicals in micelles. *Photochemistry and Photobiology* 62:818–829.
- Scheeline A, Olson DL, Williksen EP, Horras GA, Klein ML, Larter R (1997): The peroxidase–oxidase oscillator and its constituent chemistries. *Chemical Reviews* 97:739–756.
- Schulten K (1982): Magnetic field effects in chemistry and biology. In Treusch J, ed. *Festkörperprobleme*, Vol. 22. Vieweg, Braunschweig, pp. 61–83.
- Schulten K, Swenberg CE, Weller A (1978): Biomagnetic sensory mechanism based on magnetic-field modulated coherent electron-spin motion. *Zeitschrift für Physikalische Chemie-Frankfurt* 111:1–5.
- Simko M, Droste S, Kriehuber R, Weiss DG (2001): Stimulation of phagocytosis and free radical production in murine macrophages by 50 Hz electromagnetic fields. *European Journal of Cell Biology* 80:562–566.
- Steiner UE, Ulrich T (1989): Magnetic-field effects in chemical-kinetics and related phenomena. *Chemical Reviews* 89:51–147.
- Taoka S, Padmakumar R, Grissom CB, Banerjee R (1997): Magnetic field effects on coenzyme B-12-dependent enzymes: validation of ethanolamine ammonia lyase results and extension to human methylmalonyl CoA mutase. *Bioelectromagnetics* 18:506–513.
- Thannickal VJ, Fanburg BL (2000): Reactive oxygen species in cell signaling. *American Journal of Physiology—Lung Cellular and Molecular Physiology* 279:L1005–L1028.
- Till U, Timmel CR, Brocklehurst B, Hore PJ (1998): The influence of very small magnetic fields on radical recombination reactions in the limit of slow recombination. *Chemical Physics Letters* 298:7–14.
- Timmel CR, Hore PJ (1996): Oscillating magnetic field effects on the yields of radical pair reactions. *Chemical Physics Letters* 257:401–408.
- Timmel CR, Till U, Brocklehurst B, McLauchlan KA, Hore PJ (1998): Effects of weak magnetic fields on free radical recombination reactions. *Molecular Physics* 95:71–89.
- Timmel CR, Cintolesi F, Brocklehurst B, Hore PJ (2001): Model calculations of magnetic field effects on the recombination reactions of radicals with anisotropic hyperfine interactions. *Chemical Physics Letters* 334:387–395.

- Walleczek J (1995): Magnetokinetic effects on radical pairs: a paradigm for magnetic field interactions with biological systems at lower than thermal energy. *Electromagnetic Fields* 250:395–420.
- Werner U, Kuhnle W, Staerk H (1993): Magnetic-field dependent reaction yields from radical-ion pairs linked by a partially rigid aliphatic chain. *Journal of Physical Chemistry* 97:9280–9287.
- Wiltschko W, Gesson M, Stapput K, Wiltschko R (2004a): Light-dependent magnetoreception in birds: interaction of at least two different receptors. *Naturwissenschaften* 91:130–134.
- Wiltschko W, Moller A, Gesson M, Noll C, Wiltschko R (2004b): Light-dependent magnetoreception in birds: analysis of the behaviour under red light after pre-exposure to red light. *Journal of Experimental Biology* 207:1193–1202.
- Woodward JR (2002): Radical pairs in solution. *Progress in Reaction Kinetics and Mechanism* 27:165–207.
- Yu BP (1994): Cellular defenses against damage from reactive oxygen species. *Physiological Reviews* 74:139–162.

7

Signals, Noise, and Thresholds

James C. Weaver and Martin Bier

CONTENTS

7.1 Signals, Detection, and Measurement	169
7.2 Specificity	170
7.3 Signal-to-Noise Ratio.....	171
7.4 Detection Criteria.....	173
7.5 Equilibrium Noise	173
7.6 Nonequilibrium Noise	180
7.7 Chemical Noise	190
7.8 Interpretation of Experiments.....	195
Acknowledgment.....	196
References	196

7.1 Signals, Detection, and Measurement

Measurement is a quantitative observation and well known to be of great importance to science. However, measurements involving biological systems are complicated by the complexity of cells and tissues, particularly if fields are expected to interact weakly and field-induced changes are found to be small. Some key parameters, for example, temperature coefficient of a measured quantity, may be inadequately characterized, and related quantities may be determined incompletely (e.g., measurement or modeling of the time-dependent temperature throughout the volume of the biological system being studied). Detection is a special case of measurement, that is, the measurement is so coarse that an observer can only distinguish between “signal” and “no signal.”

Generally speaking, the smaller the change in an observed quantity (e.g., cell biomass) due to a stimulus (e.g., an applied electromagnetic field), the more difficult the experimental interpretation. There may be multiple candidate causes if small changes in biomass are found, for example, any of many growth-altering biochemical changes, unnoticed and uncharacterized temperature variations, or even changes in ambient light or mechanical vibration. In physical science a model can often be made of the experiment. This allows estimates of the influence of various quantities and parameters on the expected experimental outcome (change in observed quantity in response to a stimulus) and is valuable in the interpretation of experiments. Similar approaches to bioelectromagnetics should also be valuable.

Consider an illustrative measurement on a biological system: a population of microorganisms contained within a glass toroid. Application of an alternating magnetic field to a primary coil wrapped around one part of the toroid induces an alternating current. The induced current can be measured with a coil wound around part of the toroid. The induced current is related to the electrical conductivity of the aqueous electrolyte. The electrical conductivity of the extracellular medium changes when small, charged metabolites are excreted, and measurement of microbial metabolic activity can thus be accomplished electrically. First observed in 1899 by a nulling technique [1], electrical impedance detection of microorganisms has received significant attention as a measurement method [2,3]. A toroidal device has actually been explored as the basis for determining microbial activity [4], with metabolic acid production causing a change in extracellular ion concentration (activity) and therefore creating a change in the electrical conductivity of the extracellular medium. But complications may arise. If cytotoxic chemicals leach from the glass, there can be a time-dependent poisoning of microbial activity. Ambient temperature changes couple through the glass to create internal temperature variations that alter the conductivity. In short, because electrical conductivity change has more than one candidate cause, this measurement system lacks specificity. This also illustrates a basic challenge to measurement of effects of electromagnetic fields on biological systems, namely, demonstrating both a statistically significant change and convincing evidence that it is the field interaction with the biological system, not an associated competing influence, that is responsible for the observation.

7.2 Specificity

Specificity is a hallmark of biological interactions involving biochemicals. A cell contains a large number of coexisting molecules whose interactions are not spontaneous but are instead highly regulated. Enzymes can be highly specific in the reactions they catalyze. Antibodies and receptor-ligand binding are also often specific. However, interactions of electromagnetic fields with a biological system are rather general. Magnetic fields interact indirectly by inducing electric fields and directly through magnetically sensitive reactions [5] and through interactions with magnetic material. Such magnetic materials may be contaminant ferromagnetic particles in the human body [6] or they may be biologically synthesized magnetite granules [7,8]. Electric fields interact nonspecifically with charge and polarizable material. Thus, unlike ligand-receptor biochemical interactions, there are no molecular receptors that are highly specific for electromagnetic fields. Instead, magnetic and electric sensory systems interact broadly and can be regarded as nonspecific. Evolved sensory systems are rather special. To date, it appears that biological, electric and magnetic field reception is indeed accomplished by organized systems.

Lack of electromagnetic field specificity has important implications for interpreting experiments. If an experiment quantifies a change in an observed parameter, the cause of the change is not automatically known. Continuing the example of cell growth determination based on biomass measurement, if an increase in biomass (or cell number) is associated with a field exposure, then additional analysis is needed to determine whether this change is due directly to the field or is instead due to interfering influences such as temperature change or biochemical concentration changes.

The challenge of specificity is not limited to weakly interacting fields. Consider the case of strong, electroporating fields *in vivo*, for which the motivation is local tumor treatment

or gene therapy. Strong fields can generate tissue movement by stimulating muscles and possibly also by bulk tissue polarization forces. Tissue motion can itself create membrane openings, and these can lead to biochemical transport [9–11]. Thus, observation of molecular uptake associated with electrical pulsing does not by itself show that electroporation is responsible. Specificity is an issue.

7.3 Signal-to-Noise Ratio

We adopt a recent discussion of the signal-to-noise ratio (S/N) for experiments with biological systems exposed to weakly interacting electromagnetic fields [12]. The observed quantity is x . For bioelectromagnetics experiments, examples of x include a local or spatially averaged transmembrane voltage change, temperature rise at a particular site, radioactivity of an incorporated unstable isotope, specific enzyme activity, intracellular calcium ion concentration, cell biomass, etc. Typically, experiments obtain data that can be characterized by their means and standard deviations, often presented as a bar chart. One bar of each bar pair represents the control result, and the other bar represents the exposed result. Each bar height represents the mean value, and the error bar is usually the standard deviation. (In some cases the error bars instead represent the standard error, that is, the uncertainty in the mean, rather than the standard deviation, but generally a report states which is being used.) Bar charts present a concise summary of an investigator's knowledge of the underlying natural distributions. The measured mean and standard deviation of the control distribution can be defined to be \bar{x}_{con} and σ_{con} , respectively. Similarly, \bar{x}_{exp} and σ_{exp} are the observed mean and standard deviation of the exposed distribution.

When repeating the same experiment and doing the same measurement many times over, one generally finds a Gaussian distribution of outcomes. This is because in a complex system there are many variables and sources of inaccuracy that are not under the control of the experimentalist. For the cumulative effect of all these imprecisions the central limit theorem becomes applicable. This theorem says that with many independent stochasticities involved, the outcome will be a Gaussian distribution [13]. As an example of this theorem in practice, do 100 coin tosses and record the number N of “heads.” Repeat this experiment many times. The result will converge to a Gaussian distribution of N that is centered around 50.

The threshold for a field exposure effect occurs under conditions of detection, that is, the minimum change of x that is discernable using generally accepted statistical criteria. This is equivalent to determining whether or not the control statistical distribution and the exposed distribution are distinguishable (significantly different by accepted criteria). This requires sufficiently precise knowledge of the statistical distribution parameters. Increasing the number of determinations of the natural distribution generates more precise knowledge of its parameters. For example, if an investigator carries out a number, m_{con} , of determinations of x_{con} and another number, m_{exp} , of determinations of x_{exp} , then the empirically determined values can be reported as

$$x_{\text{con}} = \bar{x}_{\text{con}} \pm \frac{\sigma_{\text{con}}}{\sqrt{m_{\text{con}}}} \quad \text{and} \quad x_{\text{exp}} = \bar{x}_{\text{exp}} \pm \frac{\sigma_{\text{exp}}}{\sqrt{m_{\text{exp}}}} \quad (7.1)$$

The ratio σ/\sqrt{m} actually represents the aforementioned standard error. Increasing the number of determinations reduces the standard error and the ensuing uncertainty in the mean. However, it does not decrease the standard deviation, σ_{exp} , of the underlying distribution, which is assumed unperturbed by the measurement process.

As the means \bar{x}_{con} and \bar{x}_{exp} become better known through more determinations, the potential distinguishability of the two distributions increases. The p -value of the experiment is often reported as a measure of this distinguishability. The p -value is the probability that the two means would be found to be as different as observed (or even more different) purely because of random variability. For example, $p = 0.01$ indicates that there is only a 1% chance that the difference between the control mean and the exposed mean would be due to the (assumed) random variability of the measured quantity, namely, the standard deviation [14]. After an investigator completes an experiment and finds a reasonably small p -value (.01 and .05 are widely used values), it is a common practice for the investigator to report that an effect due to the field exposure has occurred. However this assumes specificity, namely, that the field exposure rather than an associated competing influence is responsible. Indeed, a small p -value supports an effect of some sort but not necessarily one due to the field during the exposure. Additional analysis that considers other competing influences such as temperature variations, vibrations, and chemical concentration variations [15,16] is required for that conclusion.

Bioelectromagnetics experiments with weakly interacting fields typically involve determination of changes with respect to background values of, for instance, transmembrane voltage, fluorescence intensity, enzyme activity, or cell number. Observed changes in “exposed” relative to “control” are generally small. At the other extreme, strongly interacting fields create large changes with respect to background, for example, molecular uptake by electroporation (see Chapter 9 on electroporation in Ref. [127]). For the “weakly interacting” situation the uncertainties (error bars) are about the same for exposed and control. However, there is another figure of merit, distinct from the p -value, namely, an empirically determined signal-to-noise ratio $(S/N)_{\text{obs}}$, which is associated with the observation and which is presumed due to the underlying statistical distributions for the control and exposed cases. Classical detection theory shows that the associated distributions are expected to be Gaussians [17].

In continuation of a recent discussion [12], we consider the observed signal (S_{obs}) to be the difference between the control and the exposed means, and the observed noise (N_{obs}) as the standard deviation of the control distribution [17]. This yields

$$S_{\text{obs}} = \bar{x}_{\text{exp}} - \bar{x}_{\text{con}} \quad \text{and} \quad N_{\text{obs}} = \sigma_{\text{con}} \quad (7.2)$$

so that the empirically determined signal-to-noise ratio is the magnitude of

$$(S/N)_{\text{obs}} = \frac{\bar{x}_{\text{exp}} - \bar{x}_{\text{con}}}{\sigma_{\text{con}}} \quad (7.3)$$

Like the p -value $(S/N)_{\text{obs}}$ is a measure of the distinguishability of the two distributions. However, unlike the p -value, the signal-to-noise ratio is an inherent characteristic of the biological system, its environment, and a particular field exposure and does not depend on the number of determinations. In this view, S_{obs} is the observed change and is assumed to be a measure of the strength of the perturbation to the biological system by the field exposure. N_{obs} is a measure of the natural variability in the system for the conditions of the experiment. In the absence of an exposure, N_{obs} provides the appropriate scale to gauge the strength of S_{obs} .

$(S/N)_{\text{obs}}$ is based only on experimental determinations of x . However, in many cases the field exposure is believed to *indirectly* alter x . According to this general hypothesis, the field exposure affects one or more molecular-level biochemical processes through physical interactions. In this sense, the exposure is creating a “primary” molecular change, which is then amplified through a biochemical cascade that creates a downstream change. It is this downstream change that is eventually measured. The signal-to-noise ratio cannot be increased by the amplification process. Later in this chapter, we will describe how amplification generally adds noise to a signal.

7.4 Detection Criteria

The criterion $(S/N) \leq 0.1$ is a very conservative basis for ruling out a particular class of biophysical mechanism for a given field exposure. Similarly, the criterion $(S/N) \geq 10$ is a conservative basis for ruling in a candidate biophysical mechanism for a given exposure, retaining that biophysical mechanism hypothesis for further evaluation. This approach provides a quantitative basis for rejecting or accepting hypothetical biophysical mechanisms as candidate explanations for an experimental measurement. The traditional choice $(S/N) \approx 1$ is a useful but somewhat arbitrary dividing line, which indicates conditions for which an effect might appear. $(S/N) \leq 0.1$ and $(S/N) \geq 10$ provide criteria for stronger conclusions, allowing rejection or provisional retention of a biophysical mechanism hypothesis.

We should recognize that thresholds are defined by generally accepted statistical criteria. The widely used p -values of .01 and .05 are examples of such generally accepted statistical values. In the case of signal-to-noise ratios, a commonly accepted value is $(S/N) \approx 1$, where the approximately equal symbol denotes the imprecision. Specifically, if (S/N) (empirical or theoretical) exceeds 1, then the threshold is viewed as being exceeded. Similary, if (S/N) is less than 1, the response is interpreted as subthreshold. Clearly, it makes little sense to take a strong position if (S/N) is close to 1. But, as noted above, if the signal-to-noise ratio is significantly greater or less than 1, then some confidence can be attached to the result. In short, a threshold is imprecise but nevertheless a useful guide.

7.5 Equilibrium Noise

In this section we will examine how Brownian noise, the simple random motion of molecules due to thermal agitation, interferes with the coupling of an electromagnetic field to a biochemical system. Some organisms have evolved an ability to sense and effectively “measure” electric and magnetic fields. We will see that the thermal noise that a signal has to compete against sets fundamental limits on detectability. We will also see how evolution has come up with structures to optimize the signal-to-noise ratio in sensory perception.

Fish generally carry a small dipolar field relative to the water that they swim in. Sharks, skates, and rays have developed special organs to detect such fields [18,19] and they use this ability to pinpoint the position of their prey when they get close and the water is too turbulent to rely on smell. To be effective, the shark should be able to sense its prey

instantaneously. So, for the signal not to be mistaken for Brownian noise and for Brownian noise not to be mistaken as a signal, a signal should carry an energy that is significantly larger than kT . kT constitutes the average energy in the thermal noise band [20]. This baseline criterion already works to explain some of the physiology of the electric sensing organs. The electric fields are picked up by the ampullae of Lorenzini. These ampullae terminate at pores in the skin around the fish's head. They are enclosed in a highly resistive material and are filled with a very conductive gel. The eventual setup is equivalent to an electrical wire with no voltage drop inside. These ampullae are, furthermore, well insulated against electrical noise that originates from the fish's own physiology. Two pores that are about 10 cm apart on the surface of the fish's head can, on the inside ends, be separated only by a few nanometers. A field of 500 nV/m can be detected. Two pores that are 10 cm apart on the surface could thus transfer 50 nV into a transmembrane potential.

By having a lot of ion channels that are sensitive to such small voltage variations, the thermal noise can be effectively averaged out. With N ion channels instead of just one, N times as much signal strength is picked up. The thermal noise at each channel is independent of that at any other channel. The noise is zero-average and the noise variances are added up for N channels. So the average noise amplitude will be only \sqrt{N} times as large if N channels are involved instead of one. After detection, the fish has to amplify this signal to the millivolt range that the nervous system operates with. Amplifier noise constitutes a problem that builders of electric circuits have dealt with for decades. Amplifier noise is nonequilibrium noise, and we will discuss it in the next section. Over the past decade, researchers have built up a good and detailed understanding of the physiology [21] and physics [22,23] of the fishes' amplification system.

Many animal species have the ability to detect the geomagnetic field. Two mechanisms have been proposed for magnetosensitivity. The first mechanism involves chemical transitions that are sensitive to external magnetic fields. Upon excitation by light, many polyatomic molecules will start transiting between the singlet ground state, the singlet excited states, and the excited triplet state. The energy difference between a singlet ($\uparrow\downarrow$) state and a triplet ($\uparrow\uparrow$) state is affected by an external magnetic field. This energy difference is generally small for fields of the magnitude of the Earth's magnetic field. But the magnetism that living cells generate is even smaller. A magnetically sensitive reaction of this type is therefore not subject to significant thermal noise. However, a detection limit can be established by considering a model in which reacting product molecules can bind to receptors. There is an innate stochasticity in chemical reactions; rates represent an average behavior, and there is a Gaussian distribution around this average. This is called fundamental chemical noise, and we will come back to it later in this chapter. In this model, the average number of occupied receptors varies with the magnetic field, and the detection limits are set by this fundamental chemical noise [24]. The fact that many bird species actually need light for their magnetic compass to work is a strong indication that singlet-triplet transitions are involved in the navigation. Recently, additional evidence was found when it turned out that robins get disoriented when they are subjected to an RF magnetic field that oscillates at the singlet-triplet resonance frequency [5] (for more details, see [Chapter 6](#) on free radical models).

The second mechanism that has been proposed to explain magnetosensitivity involves the small (<100 nm in diameter) granules of magnetite (Fe_3O_4). This material, also known as lodestone, is biochemically formed and has about 30% of the magnetic strength of pure Fe. In the 1970s, it was discovered that certain microbes use single-domain magnetite granules, also called magnetosomes, as a kind of rudder to help them stay under water right at the interface between the water and the mud at the bottom. There is a force trying to align the magnetic granule(s) with the Earth's magnetic field,

and the microbe thus “finds out” what its own orientation is relative to the inclination of the Earth’s magnetic field [25,26]. For a single-domain magnetite granule of about 100 nm in diameter, the product μB of the magnetic moment μ and the Earth’s magnetic field B amounts to about $5kT$. This $5kT$ alignment is sufficient to exceed the kT thermal agitation in the granule’s rotation. In higher animals it appears that the granules are commonly embedded in biopolymers and lined up to form a rigid linear rod. Such an alignment effectively increases the magnetic moment and thereby the sensitivity to small variations in the magnetic field [27]. Indications are that there can be up to a million magnetite-containing cells in the brain of almost any animal. Even humans, who exhibit no apparent magnetosensitivity, have magnetite in their brain tissue [7,8].

The intensity of the Earth’s magnetic field varies from 25 to 65 μT , and the direction varies from parallel to perpendicular to the Earth’s surface. The magnetic sensitivity of, for instance, homing pigeons has been shown to be such that field variations smaller than 10 nT can be detected. With such a sensitivity the pigeon can use the change of the magnetic field vector to furnish itself a kind of global positioning system (GPS) [29]. Recent data indicate that some birds incorporate both magnetite and singlet-triplet chemistry in their magnetosense [5].

It is tempting to hypothesize that extremely low-frequency (ELF) radiation or microwave radiation could have a physiological effect through the interactions with magnetosomes. Cells produce their own electricity and concurrent electric noise. But there is no significant endogenous magnetic field noise. So the magnetic part of ELF radiation or microwave radiation would not have to compete against such endogenous biological noise. The average 24-h personal 60-Hz magnetic field due to house wiring, distribution lines, electric motors, etc., for individuals in the U.S. population is about 10^{-7} T [30], that is, orders of magnitude smaller than the earth’s stationary magnetic field. Starting from this premise, the magnetosome in the cytoplasm was modeled as a damped harmonic oscillator with an external 60-Hz modulation [31]. The restoring force is the force pushing to align the magnetosome’s moment with the earth’s magnetic field, and the damping is due to the viscosity of the cytoplasm. The associated equation is easily solved. Using reasonable values for the involved parameters, it was found that even with exposure to a 60-Hz field with an amplitude of 5 μT , the alternating field transfers an amount of energy to the magnetosome that is orders of magnitude smaller than kT . In other words, the thermal agitations in the rotation far overwhelm any “signal” from an ambient 60-Hz field. But subsequently, the legitimacy of a simple linear approximation was questioned [32]. It was pointed out that there are intricacies that make the viscosity of the cytoplasm, which determines the damping coefficient in the model, hard to specify. Most importantly, the possibility of many individual magnetosomes in a cell acting in concert should be considered. With N magnetosomes in a cell instead of just one, the signal-to-noise ratio is \sqrt{N} times larger. The explanation for this apparent amplification is the same as with the aforementioned N ion channels in the shark’s electroreception. An alternative model that includes such cooperativity leads to a signal-to-noise ratio that is well over unity with a 2- μT amplitude 60-Hz magnetic field [32]. However, almost nothing is currently known about how forces on magnetosomes are transduced into physiological signals. More solid estimates of detection thresholds can probably be derived only after such bio-physical mechanisms are revealed.

Electric fields are also of interest. Close to a power line, a human can be exposed to an electric field of about 10 kV/m. Two steps have to be taken to get to an assessment of the transmembrane voltage that such an exposure leads to. First of all, living tissue is much more conducting than air. So, charge in the tissue will move and follow the external field until it is compensated. Depending on the amount of movable dipoles, different materials

have different dielectric permittivities. The ratio between the internal field and the field in the air is [33,34]:

$$\frac{E_i}{E_0} \approx \epsilon_0 \omega \rho_t \quad (7.4)$$

Here $\epsilon_0 = 8.8 \times 10^{-12} \text{ C}^2/(\text{N m}^2)$ represents the dielectric permittivity of a vacuum, ω is the angular frequency ($2\pi f$), and ρ_t is the resistivity of the tissue. So for a frequency of about 100 Hz and with a typical tissue resistivity of about $1\text{--}2 \Omega \text{ m}$, the attenuation factor for the field entering the body is found to be in a range of $10^{-8}\text{--}10^{-7}$. Hence, most of the external field goes around the person in the way water in a river flows around a big rock. Once inside the tissue, an amplification at the cell membranes occurs again through the mechanism explained in the previous paragraph. For a spherical cell with a diameter of about $d = 10 \mu\text{m}$ in a field E , the voltage across the diameter will be $\Delta V = Ed$, and the eventual field in the membrane will be of the order of $E_{\text{mem}} \approx E(d/h)$, where h is the thickness of the membrane. With $h \approx 5 \text{ nm}$ we find an amplification factor of about a 1000. We thus find a net conversion factor of $10^{-5}\text{--}10^{-4}$ and an electric field of about 0.1–1.0 V/m across a membrane as a result of the 10-kV/m power line exposure. This leads to an ELF-induced potential difference of at most 10^{-8} V across the membrane. It should, however, be noted that muscle cells or nerve cells are cylindrically shaped and may have lengths in the millimeter or even centimeter range. When the imposed field is along the axis of the cylinder, there may be a conversion factor at the caps of the cylinder that is two to three orders of magnitude higher.

When a living cell is suddenly exposed to an external electric field, ions will start flowing in the conducting interior to compensate for this field. In a typical mammalian cell, it is generally within microseconds that ions have accumulated near the membrane to achieve a zero intracellular electric field. This means that stationary electric fields and ELF (<300 Hz) AC fields distribute over cell membranes. Power lines and high-voltage distribution stations have been the subject of a lot of public anxiety. The power grid operates at 60 Hz in the United States and at 50 Hz in most other countries, that is, well within the ELF regime.

The 10^{-8} V that we derived may appear small relative to, for instance, the transmembrane potential of about 0.1 V that is present in about every living cell. However, when we talk about detectability, this 10^{-8} V should first be compared to the transmembrane voltages due to Brownian motion. The thermal noise voltage across standard resistors was already detected in the 1920s [35]. A formula was subsequently derived by Nyquist [36]:

$$\langle dV^2 \rangle = 4kT R df \quad (7.5)$$

This equation gives the average square voltage in a frequency window of width df . The noise is white, that is, it has the same intensity at all frequencies. Technically, this would lead to an absurdity. It would imply that the noise carries an infinite amount of energy. However, as Nyquist already pointed out, $\langle dV^2 \rangle$ starts vanishing when we get to high frequencies f where $hf \approx kT$. Here, h represents Planck's constant, $h = 6.6 \times 10^{-34} \text{ J sec}$. At these high frequencies, quantum physics takes over and makes $\langle dV^2 \rangle$ go to zero. Such high frequencies are not in our realm of interest.

What Nyquist had in mind for a resistor in his derivation was a Brownian gas of frequently colliding charge carriers. With a 5-nm cell membrane that consists of a lipid bilayer with embedded proteins, the charge carriers are small ions (Na^+ , K^+ , Cl^- , etc.).

The ions do not form a “gas” inside the membrane, and it is not *a priori* obvious that Nyquist’s formalism would apply. The equilibrium noise current through a membrane that separates two ionic solutions is due to two-sided shot noise. Shot noise was first described by Schottky [37] in the context of vacuum amplifier tubes. It is due to the elementary charge being finite and the charge carriers making random “jumps.” It can be shown that two-sided shot noise ultimately leads back again to Nyquist’s [Equation 7.5](#) [38,39]. Ultimately, Equation 7.5 is a manifestation of something much more general than Nyquist may have had in mind. What underlies Equation 7.5 is Einstein’s fluctuation-dissipation theorem. This theorem says that the same random collisions that cause diffusion, thermal noise, or shot noise also cause dissipation, friction, or resistance. The theorem, moreover, makes this connection quantitative:

$$\beta = \frac{kT}{D} \quad (7.6)$$

For the motion of a macromolecule in a liquid, D is the diffusion coefficient and β is the coefficient of friction, that is, the ratio $\beta = F/v$, where F represents the pulling force and v represents the resulting average speed. But in the context of the current through a membrane, β represents the electrical resistance ($R = V/I$). For D we find $D = e^2 P_S c$ in the membrane electrical case. Here, P_S is the membrane permeability to the monovalent ion S that is responsible for the current, c represents the concentration of this ion on both sides of the membrane, and e is the elementary charge.

Electrically, a cell membrane can be modeled as in Figure 7.1a. A lipid bilayer membrane has a capacitance of about $1 \mu\text{F}/\text{cm}^2$. The capacitance of an actual cell membrane is generally not much different. The resistance of a pure lipid bilayer depends on the ionic concentrations of the solutions on either side of the membrane. With these concentrations at biological levels the resistance of a lipid bilayer membrane can be as high as $10^9 \Omega \text{ cm}^2$. Because of the presence of ion channels, ion transporters, and ion pumps [40,41], an actual cell membrane has a resistance that is orders of magnitude smaller (typically about $10^3 \Omega \text{ cm}^2$). The resistance of a patch of membrane is inversely proportional to the area of that patch. So, in order to characterize a membrane, the approach is to measure the resistance through an actual patch and then multiply it with the surface area of that patch. That is why we give the resistance of a membrane in terms of $\Omega \text{ cm}^2$.

The setup in Figure 7.1a is equivalent to the one in Figure 7.1b, that is, an ordinary RC circuit. When calculating the characteristic time, RC , of the circuit, the surface area cancels

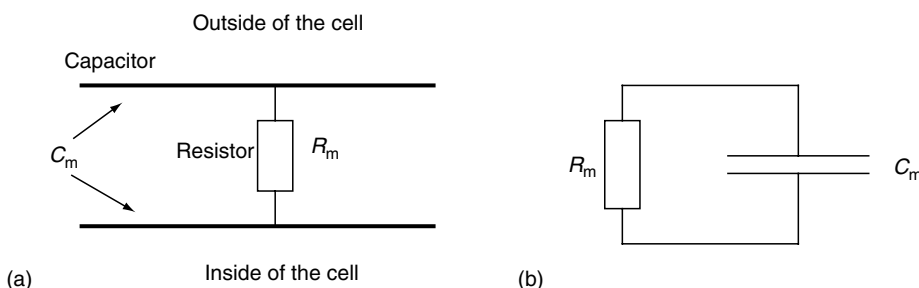


FIGURE 7.1

The electrical structure of the membrane is shown on the left. R_m and C_m are the resistance and capacitance between the inside and outside of the cell, respectively. The resistor also provides a thermal electromotive force. The equivalent circuit is shown on the right.

out. For a pure lipid bilayer the RC time constant can be of the order of minutes. But for a cell membrane it is of the order of milliseconds.

In our context, the resistor in [Figure 7.1](#) is not just a resistor, but, following Nyquist (cf. [Equation 7.5](#)), also a white noise generator. At each frequency the resistor generates a harmonic oscillation. All these harmonic oscillations have the same amplitude. To evaluate the voltage across the capacitor, we thus have to analyze a simple RC circuit with an AC source. It has been argued that the high frequencies, that is, $f > (RC)^{-1}$, that are generated in the resistor do not have enough time to build up across the capacitor [42]. However, for low-frequencies, that is, $f < (RC)^{-1}$, changes are sufficiently slow for the capacitor to keep up and follow the voltage in the resistor. In this view the transmembrane voltage is the voltage across the capacitor, and the equilibrium noise is thus expected to occur mostly at low-frequencies. As mentioned before, the RC time of a cell membrane is of the order of milliseconds, and ELF fields thus operate in the $f < (RC)^{-1}$ regime where the noise is largest. A straightforward quantitative analysis shows that the low-frequency equilibrium noise far overwhelms any reasonable ambient power frequency field [42]. There would be no way to ever instantaneously detect such a field.

It was later put forward that everything that is happening in the cell membrane should, in the model of Figure 7.1, be imagined to happen inside the resistor [43]. Membrane proteins go through their catalytic cycle against a background of intramembrane noise. Inside the membrane means, in the context of Figure 7.1, inside the resistor. In this picture, the thermal noise voltage (cf. [Equation 7.5](#)) derives from a net electric field that results from inhomogeneities in the distribution of the charge carriers. Now at low-frequencies, the capacitor will be able to follow the imposed oscillation and effectively produce a field to counter the field generated inside the resistor ([Figure 7.1a](#)). This model thus leads to a vanishing net potential inside the membrane at low-frequency. At high frequency, the voltage changes in the resistor are too fast for the capacitor to keep up with. The capacitor will remain uncharged, and the thermal AC voltage will not be compensated for.

However, [Figure 7.1](#) is no longer the appropriate model when we try to derive the intramembrane electric fields. For a cell of about $20\text{ }\mu\text{m}$ in diameter, the surface area amounts to about a billion square nanometers. The membrane is only about 5 nm thick, so the resistor resembles a very thin sheet. The lateral conductivity, that is, the conductivity from one place on the sheet to another, is very low. So at different spots on the sheet, different unrelated noise fields are generated. The more sensible model would therefore be one where the resistor in [Figure 7.1](#) is cut up into millions of independent parallel resistors. Each of these resistors creates its own field. The capacitor plate corresponds to the conducting liquid on either side of the membrane, and it can be conceived of as having perfect lateral conductivity. So each resistor generates its own particular field, but they all experience the same field from the capacitor. With this model the noise gets very large. Not only there are more, say N , resistors producing noise. Each of these resistors has a resistance NR (N parallel resistors of resistance NR lead to a net resistance of R) and, according to [Equation 7.5](#), thus produces more noise. Because the N parallel resistors that make up the resistance R are independent, they oscillate out of phase at each frequency f . As a result the parallel resistors end up pushing a lot of current in and out of each other. Most of the generated noise current thus remains intramembrane and never reaches the capacitor. The mathematics associated with this parallel setup is challenging, but an exact solution can be derived [39,44]. The capacitor, and therefore the RC time, plays no role in the intramembrane noise. The intramembrane noise is white and has an intensity that is many orders of magnitude larger than the noise that reaches the capacitor. What matters for biological function is actually the intramembrane noise. This, after all, is the noise that a membrane-embedded protein would “feel.” The protein’s catalytic cycle takes place

against the background of such noise. The parallel setup model leads to a noise intensity that is much larger than that of the earlier models.

At first sight, all this extensive treatment of intramembrane noise may seem to have little to do with the two-sided shot noise that a membrane is subject to. However, when rigorously modeling the membrane as a thin sheet in an ionic solution, something similar to the overwhelming intramembrane noise is found. The ions that constitute the net charge on the membrane in Figure 7.1a move across the membrane–solution interface with an average speed of about 100 m/sec. This is just their thermal motion, and it is easily derived from $(1/2)mv^2 \approx kT$. This effectively causes laterally traveling electric pulses in the membrane. The noise intensity of these traveling electric pulses appears to be many orders of magnitude higher than the noise that is due to the shot noise-like membrane passages by the ions [39].

Current models of membrane noise thus lead to transmembrane voltage noise estimates that far exceed the strength of any reasonable magnitude ELF field-induced “signal.” What the previous paragraphs lead up to is the conclusion that an ELF signal cannot be detected instantaneously.

However, under certain conditions and given enough time, even the smallest signal can get out of the noise band. The following example is meant to illustrate this. Consider the system depicted in Figure 7.2. Let the the resistance R represent a membrane patch. For simplicity, imagine that on either side of the resistor there is an infinite reservoir (i.e., a capacitor with infinite capacitance), so no net voltage can develop across the resistor. The average square charge $\langle q^2(t) \rangle$ that accumulates on either side of the membrane can be easily derived from Equation 7.5 and amounts to

$$\langle q^2(t) \rangle = \frac{2kT}{R} t \quad (7.7)$$

Again, there is an obvious analogy between Equation 7.7 and the well-known diffusion formula $\langle x^2(t) \rangle = 2Dt$, which describes the average square displacement of a particle with a diffusion coefficient D during a time interval of length t . The above formula clearly shows how, in an electrical context, kT/R plays the role of the diffusion coefficient D .

From Equation 7.7 we infer that for the accumulated charge as a function of time we have $|q_{Br}(t)| \approx \sqrt{\langle q^2(t) \rangle} \propto \sqrt{t}$. The thermal noise-driven accumulation of any charged or uncharged molecule on either side of the membrane carries this \sqrt{t} proportionality. The coupling of ELF electromagnetic fields to biochemical activity occurs mostly through

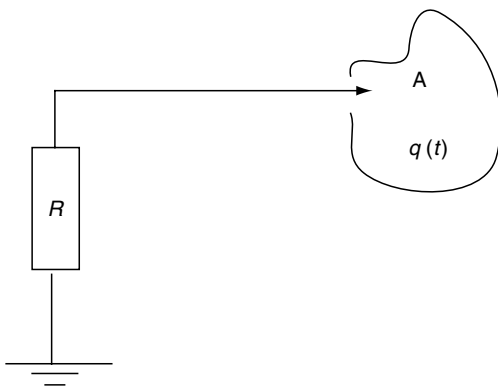


FIGURE 7.2

A resistor is connected to the ground and to an infinite reservoir A. The net voltage between the reservoirs remains zero. The situation is like the one in Figure 7.1 with the capacitor having infinite capacitance. Because of Brownian motion of electrons in the conduction band, there is a zero-average fluctuating current through the resistor. The net charge accumulating in the reservoir A is the result of these fluctuations in the same way that diffusive displacement is the result of random Brownian kicks. We have $\langle q^2(t) \rangle = 2(kT/R)t$ for the average square charge accumulation in time t .

membrane proteins. Membrane proteins whose conformational changes involve significant changes of the dipole moment are particularly sensitive. ELF fields can affect the catalytic rates of such proteins. So, for instance, electrogenic ion pumps [41], and also transporters or pumps that just carry a dipole, may have a slightly altered throughput in the presence of an ELF field. If there is no restoring force for a transported or pumped molecule, the accumulation will continue. The cumulative effect of the altered throughput will be a linear function of time. The excess charge that accumulates because of an ELF field thus follows $q_{\text{ELF}} \propto t$.

Consequently, we see that on a small timescale the Brownian noise ($\propto \sqrt{t}$) will be stronger than the signal ($\propto t$). But there will always come a time $t = t_*$ when $|q_{\text{Br}}(t_*)| = |q_{\text{ELF}}(t_*)|$, and we then achieve $S/N = 1$. It depends on the values of the proportionality constants when t_* occurs. If molecular change is the measurement criterion, then it is only on timescales of the order of t_* that the effect becomes measurable. Estimates for t_* with realistic ELF exposure have been made [45] and have led to a timescale larger than the age of the universe.

7.6 Nonequilibrium Noise

In the previous section, we considered equilibrium noise. A living cell, however, constitutes a system that is far from equilibrium. Between the intracellular and extracellular solutions there is an electric potential difference of about 100 mV. For ions like Na^+ , K^+ , Cl^- , and Ca^{2+} there is a more than tenfold difference between intra- and extracellular concentration. The 100-mV transmembrane voltage over a width of about 5 nm implies a very strong field of tens of megavolts per meter.

The electrochemical potential across the cell membrane is an energy source for many processes [41]. The Na, Ca exchanger, for instance, is a membrane protein that picks up a sodium ion on the outside and then goes through a cycle in the course of which it drops the sodium ion off on the inside. The protein couples the energetically downhill movement of sodium to the uphill transport of calcium. In the course of the cycle a calcium ion is picked up on the inside and pumped, against the electrochemical potential, to the outside. The membrane potential is maintained by ATP-driven ion pumps. The most common of these is Na, K-ATPase. This is a membrane protein that, in the course of its catalytic cycle, hydrolyzes one ATP and uses the released energy to transport three sodium ions out of the cell and bring two potassium ions in.

Each working protein is like a small engine. A living cell contains millions of these engines: they are continuously converting energy from one form to another, and in the process, they are also generating heat, that is, dissipating energy. A living cell constitutes a far from equilibrium system, and the continuous transduction and dissipation of energy generates noise, which adds to the thermal, Brownian noise that was discussed in the previous section.

It would not be against the first law of thermodynamics (i.e., conservation of energy) if ion pumps were to extract heat from the environment and use it to power the maintenance of the transmembrane potential. This would, however, be in gross violation of the second law of thermodynamics. There are many equivalent formulations of the second law. The most common formulation is the proposition that every isolated system strives to increase and maximize its entropy. The teleological form of this formulation is somewhat bewildering. After all, most laws in science are formulated as conservation laws, for

example, conservation of energy, or as causal laws, for instance, Newton's $F = ma$. However, after properly defining entropy, entropy maximization is often the easiest form of the second law to work with when dealing with macroscopic systems.

When going to the molecular realm, the second law can pose some challenging paradoxes. Consider, for instance, an ion channel in a cell membrane. Many ion channels rectify, that is, they pass current more easily in one direction than in the other. So the $I-V$ characteristic is not a straight line through the origin, but it also has a curvature. Any frequency from the white spectrum of equilibrium noise should, in principle, be rectified. It thus might look like a rectifying ion channel could use zero-average equilibrium Nyquist noise to charge a battery. It would not work, of course. As pointed out above, it would be in violation of the second law. Thinking in the context of rectifying p-n junctions, solid-state physicists ran into this paradox long before ion channels were discovered. In 1950, L. Brillouin wrote a paper "Can the Rectifier Become a Thermodynamic Demon?" [46]. In this paper, he presents a short derivation to show that in a circuit with all components at the same temperature, no diode can rectify. He is aware that his case represents a special case of the so-called principle of detailed balance: "No system in thermal equilibrium in an environment at constant temperature spontaneously and of itself arrives in such a condition that any of the processes taking place in the system by which energy may be extracted, run in a preferred direction, without a compensating reverse process." The principle is a consequence of the second law [47,48] and, for our rectifier, basically states that there must, on average, be as much current in one direction as there is in the opposite direction.

In the *Feynman Lectures on Physics* [49] a ratchet and pawl system, originally thought up by Smoluchowski [50], is considered and eloquently discussed. The device operates as a mechanical rectifier (Figure 7.3) and essentially establishes the mechanical equivalent of Brillouin's paradox. The paradox is solved with the realization that the pawl must also be

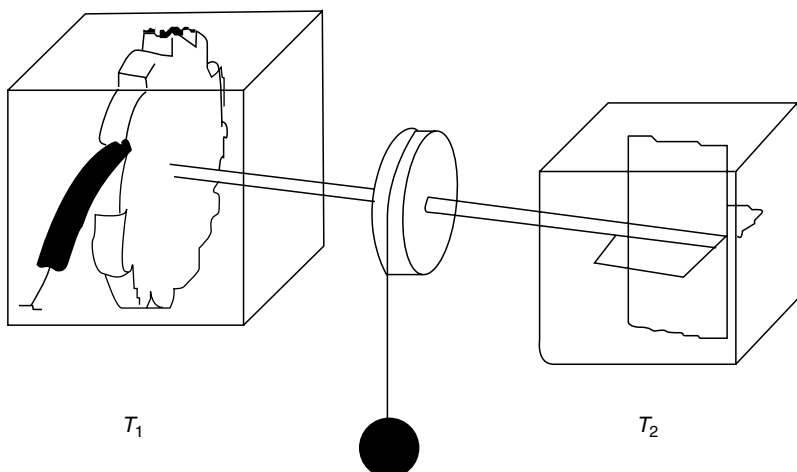


FIGURE 7.3

The mechanical thermal ratchet as it was originally conceived by Smoluchowski [50] and later discussed by Feynman et al. [49]. The device is small, and the paddle wheel in the right reservoir is moved by collisions of the molecules from the surrounding medium against the paddles. Because of the asymmetry of the teeth, the ratchet and pawl in the left reservoir allow motion in one direction and block it in the opposite direction. With the resulting net rotation it should be possible, in principle, to lift a weight. However, it would be in violation of the second law of thermodynamics to extract work from thermal fluctuations in the equilibrium situation, that is, $T_1 = T_2$. The solution of the paradox lies in the realization that the ratchet and pawl are also subject to thermal fluctuations if the system is small.

subject to thermal noise. The pawl involves a spring, and the spring will, at thermal equilibrium, exhibit a Boltzmann distribution over the accessible energy range. Even here the second law is involved, though on a deeper level. Given the macroscopic variables (e.g., temperature, concentration, pressure, etc.) there are still many possible molecular arrangements, that is, microstates, that correspond to that macrostate. For a fixed amount of energy the Boltzmann distribution is the energy distribution that has the most permutations [20]. It is therefore the most likely distribution. On the level of statistical mechanics, the second law can be formulated as the rule that given a macrostate, every microstate that corresponds to that macrostate has equal probability.

Second law issues can be subtle. The connection between statistics, entropy, information, and physical work still poses paradoxes that are hard to fathom. Books and articles still appear in which researchers are attempting to come to a fuller understanding and a better intuition [51,52]. At the scale of ion channels the simple invocation of detailed balance reveals little. An appropriate description is like the one Feynman gave for his mechanical ratchet and pawl: it involves Boltzmann distributions and Brownian motion. So it would simply be wrong to take any frequency from the white spectrum of equilibrium noise and model a rectifying ion channel as subject to this oscillation. The ion channel itself and its Brownian fluctuations have to be included in the description. At equilibrium, no part of a system can be “subject” to any other part. This is what detailed balance can be interpreted to mean.

However, when energy is dissipated, it is possible for one part of the system to impose its fluctuations on another part. When a rectifying ion channel is subject to nonequilibrium fluctuations, it will actually rectify the fluctuations and drive a net current. Consider, for instance, an electrogenic ion pump like Na,K-ATPase. As was mentioned before, this pump utilizes the energy of ATP hydrolysis to pump three sodium ions out and pump two potassium ions in. All this transport is against the electrochemical potential and requires about $15kT$ units of energy per stroke under physiological conditions. The power source is the hydrolysis of ATP, which under physiological conditions, releases about $20kT$ units of energy per cycle. It is the remaining $5kT$ that drives the process forward and that is ultimately released as heat. Na,K-ATPase is binding and releasing ions and thus generates fluctuating electric fields in its direct vicinity. For a nearby ion channel these fields can be conceived of as imposed because the $5kT$ that drives the Na,K-ATPase cycle is enough to overwhelm the small amount of energy ($<1kT$ [53]) necessary for the opening or closing of a channel. There is no feedback from the channel to the pump. The channel will rectify the fluctuations as a result, and a zero-average field can thus lead to net charge transport. In essence, the nonequilibrium fluctuations generated by the pump and imposed on the channel are part of the conversion of chemical energy, that is, the energy in ATP, to an electrochemical potential across the membrane.

So energy-dissipating, nonequilibrium oscillations and fluctuations are able to do work. ELF radiation from outside the organism can impose a varying field on an ion channel in much the same way that the nearby ion pump from the previous paragraph can impose a field on an ion channel. ELF radiation brings energy into the organism. Part of this energy will be dissipated to become heat, and part of it may be converted into chemical or electrical work. There is obviously no feedback from an ion channel back to the ELF source.

The selectivity of ion channels for the different kinds of ions is still hard to understand and model. But the rectification property is much easier to intuit (Figure 7.4). The channel is shaped like an asymmetric double cone, and charges in the lining of the channel are

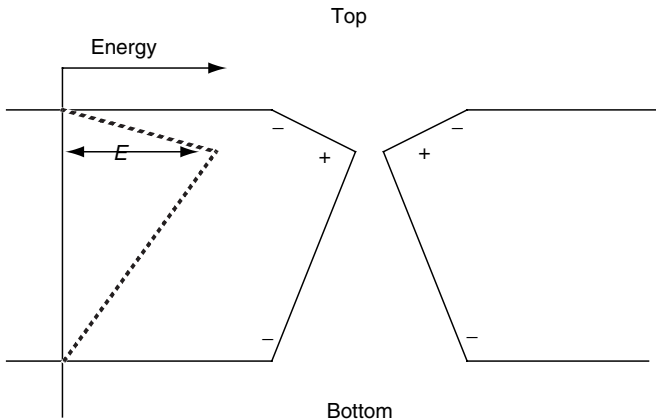


FIGURE 7.4

A simple continuum model of an ion channel imagined to be shaped like an asymmetric double cone. The energy profile on the left depicts the activation barrier that a positive ion going through the channel has to pass. The barrier has an obvious anisotropy.

indicated in the figure. A sodium or potassium ion that is going from the top to the bottom of the channel faces a rapid increase of the potential and then a slow decrease. A sodium or potassium ion that goes through in the opposite direction faces a slow increase and a fast subsequent decrease. A positive ion thus has a larger force to overcome when going from top to bottom than when going from bottom to top. Because of this, an imposed zero-average oscillation will lead to a net current [54]. As a matter of fact, any anisotropic potential shape along the length of the channel will rectify a zero-average harmonic field to lead to a net current [55]. Ion channels are proteins consisting of many amino acids, and anisotropy along the inside lining will be the rule rather than the exception.

The plethora of ratchet research in the late 1990s has made it clear that almost any zero-average oscillation or fluctuation imposed on a ratchet-like structure as in Figure 7.4 leads to a net current. Imagine, for instance, a temperature oscillation. With energy expressed in units of kT , a variation in temperature implies an oscillation of the barrier height E . Because of the difference in relaxation times on the slopes on either side of the barrier, a net current will result [55–58]. Recently, ever more examples have been found of nature exploiting ratchet effects for the purpose of regulation [59].

Researchers have meanwhile also succeeded in making artificial channels. Cone-shaped (and therefore anisotropic) channels form when a heavy ion is shot through an artificial membrane [60,61]. The I - V characteristic for the current of different types of ions has subsequently been recorded. It has even been experimentally shown that net charge transfer results when a zero-average field is imposed on such an artificial channel. The channel is thus made to behave like a kind of pump that converts an AC input into a DC output [62].

Imagine a number of identical anisotropic channels in a vesicle with an otherwise impermeable membrane. Next, put a large number of such vesicles in a beaker with an ionic solution. Any nonequilibrium fluctuation from the environment, or any “signal” for that matter, will now be picked up and converted into an electrochemical potential. The convection caused by a temperature gradient will heat up and cool down the vesicles and lead to their electrically charging up. The electric component of an ELF electromagnetic field will do the same thing. The beaker could thus be a battery that recharges by harnessing any incoming nonequilibrium fluctuation. This mechanism might, moreover, have played a role in the emergence of early prokaryotic life.

The Fourier spectrum of the noise that is associated with processes that dissipate energy is not white. Nonequilibrium noise appears to have higher amplitudes at lower frequencies; in other words, it exhibits an intensity that decreases with frequency. The so-called $1/f$ noise was first studied in the 1920s in the very nonequilibrium context of thermionic vacuum tube amplifiers [37]. In current scientific discourse the term “ $1/f$ noise” actually applies to all noises that have spectral densities behaving like $1/f^\alpha$, where α ranges from about 0.5 to about 1.5. Especially in electrical devices, such noise is very commonly and easily observed. It is also known as “excess noise” or “flicker noise.” In a log–log plot the $1/f^\alpha$ behavior usually extends over several frequency decades.

In the 1930s, it was proposed that the flicker noise originated from a variable number of electrons present in the conduction band. Electrons would shuttle between a free state and a bound state as in a chemical reaction. Let the relaxation time of that reaction be $1/\lambda$. This leads to a simple exponential relaxation $N(t) = N_0 \exp[-\lambda t]$ after any kind of fluctuation that has a magnitude N_0 . The Fourier transform of the exponential decay is easily found:

$$F(\omega) = N_0 \int_{t=0}^{\infty} \exp[-(\lambda + i\omega)t] dt = \frac{N_0}{\lambda + i\omega} \quad (7.8)$$

For the power spectral density, $S(\omega) = \|F(\omega)\|^2$, we find:

$$S(\omega) \propto \frac{1}{\lambda^2 + \omega^2} \quad (7.9)$$

where the proportionality constant involves the magnitudes of the fluctuations as well as the rates at which fluctuations occur. The power spectral density is a useful quantity as it describes how the energy in the noise is distributed over the different frequencies. $S(\omega)d\omega$ is proportional to the amount of power that the noise carries between the frequencies ω and $\omega + d\omega$. Equation 7.8 describes a so-called Lorentzian power spectrum. With a log scale for the frequency, the resulting curve is a sigmoid. At high ω , $S(\omega)$ behaves like $1/\omega^2$. As better data became available, it was found that a better fit was obtained when a distribution of infinitely many relaxation times was assumed [63]. Take, for instance, a uniform distribution of relaxation times between λ_1 and λ_2 . With Equation 7.9 this leads to:

$$S(\omega) \propto \frac{1}{\lambda_2 - \lambda_1} \int_{\lambda_1}^{\lambda_2} \frac{1}{\lambda^2 + \omega^2} d\lambda = \frac{1}{\omega(\lambda_2 - \lambda_1)} \left\{ \arctan \frac{\lambda_2}{\omega} - \arctan \frac{\lambda_1}{\omega} \right\} \quad (7.10)$$

It is easy to check that on $\lambda_1 < \omega < \lambda_2$ this $S(\omega)$ is approximately proportional to $1/(\omega(\lambda_2 - \lambda_1))$. This $S(\omega)$ is, moreover, roughly constant for $\omega < \lambda_1$ and drops off like $1/\omega^2$ when $\omega > \lambda_2$.

If we let, between λ_1 and λ_2 , the relaxation rates contribute proportional to $\lambda^{-\beta}$, we can actually get any $1/f^\alpha$ dependence that we want, since

$$S(\omega) \propto \int_{\lambda_1}^{\lambda_2} \frac{1}{\lambda^\beta (\lambda^2 + \omega^2)} d\lambda \propto \frac{1}{\omega^{1+\beta}} \quad \text{for } \lambda_1 < \omega < \lambda_2 \quad (7.11)$$

At $\omega < \lambda_1$, this spectrum would again flatten out.

In experimental practice with electrical resistors and amplifiers the $1/f^\alpha$ behavior has been observed to extend over more than six frequency decades with no noticeable flattening at low-frequency [64].

$1/f^\alpha$ spectra have been observed in nature in a wide variety of systems: electrocardiac waves [65], the variation of sea levels [66], tardiness at work [67], etc. An essential feature of $1/f^\alpha$ noise is that it exhibits self similarity, that is, if one magnifies both time and space with the appropriate factor, the noise pattern is indistinguishable from the original one. So the noise does not have a characteristic timescale or length scale. $1/f$ noise is often seen as a signature of the fractal character of nature.

In 1987, Bak et al. [68] proposed a model for a universal mechanism behind $1/f$ noise. In their landmark paper they illustrated the concept of “self-organized criticality” with a sandpile model. When a sandpile has an inclination steeper than a critical angle θ , avalanches will occur that bring the pile back to the critical angle. When sand is added to the pile in a random fashion, these avalanches do not exhibit a characteristic size, nor do they appear after regular time intervals. Instead, there are bigger avalanches that are relatively rare and smaller avalanches that occur more frequently. The size distribution follows a power law in the frequency f . For instance, in one day there can be one avalanche involving more than 1000 grains, 10 involving more than 100 grains, 100 avalanches involving more than 10 grains, and so on. The picture that emerges is one of a system that is sitting on the critical edge between two phases and is “organizing” avalanches to stay there [69]. The most commonly cited real-life example of self-organized criticality is the Gutenberg–Richter power law for earthquakes. It appears that every year, on average, there is one earthquake larger than magnitude 8, 10 earthquakes larger than magnitude 7, and 100 earthquakes larger than magnitude 6. Self-organized criticality is an attractive theory. It proposes a simple mechanism and predicts power laws that can be easily verified or falsified. It has been utilized in a wide variety of contexts [69]. It has, for instance, been applied to evolutionary theory [70] and has been used to explain frequency-size distributions of forest fires [71].

How truly universally applicable self-organized criticality is and to what extent its claims may be unwarranted are matters that are still very much under debate. The $1/f$ proportionality for earthquakes applies only between magnitudes 5 and 8. Even for the archetypal sandpile, things turn out to be more involved upon close inspection than self-organized criticality suggests. Accurate measurements [72–74] on real sandpiles showed that in many cases there is no $1/f$ pattern in the avalanches. It turns out that system parameters, like the grain size and the rate of sand addition, determine to a large extent what kind of spectrum eventually emerges. The entire concept of self-organized criticality collapses, of course, if fine tuning by the experimentalist is crucial for the $1/f$ spectrum to materialize. All in all, $1/f$ noise is not as universal as first thought, and the dynamics behind nonequilibrium noise are usually best unraveled with *ad hoc* models.

The node of Ranvier is where the action potential for myelinated nerve cells is generated [75]. There is a high concentration of ion channels in the node of Ranvier, and in the days before patch clamp, it was a good place to record membrane electrical activity. In the mid-1960s, Verveen and Derksen measured 5–10 min of cell membrane voltage noise at a Ranvier node of an unstimulated nerve cell [76,77]. The resulting power spectrum showed two decades, between 10 Hz and 1000 Hz, of $1/f$ noise (see Figure 7.5). This $1/f$ noise, they found, was much larger in magnitude than what Nyquist’s $4kTR$ formula (cf. Equation 7.5) would predict. Following the explanation for $1/f$ noise in ordinary resistors (cf. Equation 7.10 and Equation 7.11), Verveen and Derksen suggested that an ion channel could, from time to time, get “clogged up.” The wide distribution of waiting times (i.e., the λ s in Equation 7.8 through Equation 7.11) before getting unclogged would then give rise to the $1/f$ spectrum [78].

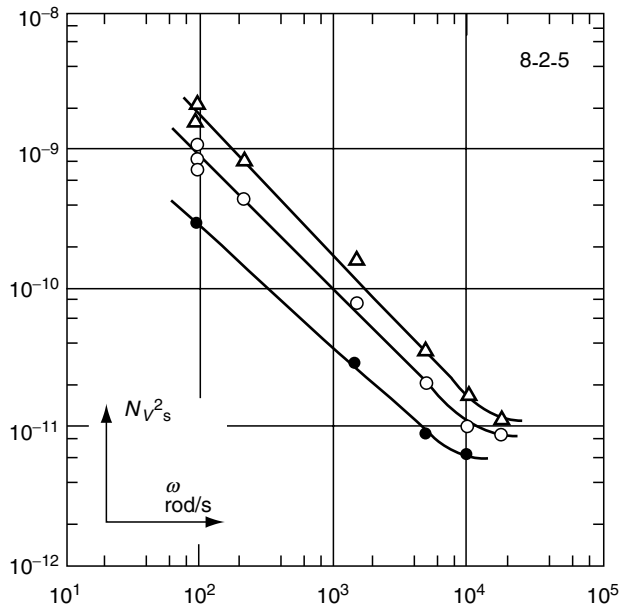


FIGURE 7.5

The voltage noise spectral densities from the frog node of Ranvier at room temperature at rest (open circles), at 10-mV depolarization (open triangles), and at 10-mV hyperpolarization (filled circles) [76,77]. (© Dutch Physiological Society. With permission.)

In the last two decades, single-channel recordings have shown how, even without stimulus, ion channels open and close repeatedly [40,75]. The kinetics behind the openings and closings is still very much a matter of debate. Modeling an ion channel as a two-state molecule with an open and a closed state and chemical steps with constant rates connecting these states appears not to account for the data in many cases. Electrophysiologists have commonly resorted to explaining the nonexponential distributions of open and closed times with a kinetic scheme that contains more than two states. With such an approach any distribution of open and closed times can always be fitted with a kinetic scheme [79–81]. It is just a matter of coming up with sufficiently many parameters (i.e., states and rates) to fit the data. In chemical kinetics the transitions are always assumed to be Markov transitions, that is, the probability of moving from a state 1 to a state 2 is constant and does not depend on the time that the molecule has been in state 1. A channel that is making such Markov transitions between a finite number of states always exhibits a power density spectrum that is a sum of Lorentzians. The number of characteristic times in the spectrum will always be one less than the number of states. If the characteristic times are sufficiently far apart, the power density spectrum will exhibit a number of identifiable plateaus when plotted on the customary logarithmic scale. The inflection points between the plateaus occur at the inverses of the characteristic times.

An alternative approach, foreshadowed by the aforementioned suggestion of Verveen and Derksen, has been to model the open to closed transition rates of an ion channel as time dependent, for instance $k(t) \propto t^{-\mu}$, where $0 < \mu < 1$ [82–85]. The exponent μ is taken to be smaller than unity to make $\int_{\tau}^{\infty} k(t) dt$ diverge for all $\tau > 0$ and thus guarantee the inevitability of an eventual transition. The proportionality $k(t) \propto t^{-\mu}$ leads to a decreasing transition probability, that is, the channel is “stabilizing in its openness,” as more time is spent in the open state. There is ample justification for the use of open-closed transition rates that vary in time. A protein has many degrees of freedom and is subject to many equilibrium and nonequilibrium fluctuations. If an intramolecular rearrangement, like a transition between an open and a closed state, can be modeled as the crossing of an

activation barrier, then that barrier will most likely not be fixed and stationary. A fluctuating barrier implies fluctuating open–closed transition rates. We could thus get the infinitely many relaxation rates that give rise to the $1/f$ power density spectra of [Equation 7.10](#) and [Equation 7.11](#). Under physiological conditions an ion channel is trafficking ions in an electric field of tens of megavolts per meter and comparable chemical gradients. This is a very nonequilibrium setup, and it has been conjectured that the channel operates as a self-organized critical structure. One authoritative textbook [65] states it as follows:

A channel protein may be a self-organizing critical system. The channel protein consists of many pieces that interact with their neighbors. The energy added to the protein from the environment causes local strains that are spread throughout the structure. If these distortions spread faster than the time it takes for the structure to thermally relax, then the channel protein may be a self organizing critical system. If that is the case, then the fluctuations in the channel structure will be due to a global organization of the local interactions between many small interacting pieces of the channel protein. The fractal scaling would then be due to the fact the channel structure is poised at a phase transition between its open and closed conformational shapes.

Over the past few years increasing amounts of data have been gathered with ever more accurate technology. Recently, the $1/f$ power spectral density of a nerve cell that Verveen and Derksen discovered was more accurately rerecorded [86]. But through careful subsequent experimentation and computer simulations, these researchers were also able to show how the apparent $1/f$ result comes about as the sum of a number of Lorentzian contributions. Each type of channel has its own Lorentzian, and because of close characteristic times the sum of the individual sigmoids appears like a smoothly decreasing $1/f$ curve.

For a single channel, things often turn out to be much more intricate than simple $1/f$ versus Markov kinetics. In single-channel recordings of a bacterial ion channel it was found that actual channel openings and closings follow Markov kinetics and lead to Lorentzian contributions to the ultimate net power spectrum [87]. The $1/f$ noise that is present in the power spectrum originates from transitions between open states of a slightly different (about 1–5%) conductance. The rates of these miniconductance transitions appeared to be independent of the transmembrane voltage. The small transitions in conductance have been conjectured to be due to small clusters within the channel's structure moving in and out of the lining of the pore [87]. A cluster can cause a partial flow constriction when it sticks out into the pore. Following this idea, the apparent $1/f$ behavior can be attributed to many different clusters moving in and out with equally many different relaxation times. The voltage independence comes about because these clusters are either uncharged or the external electric field is somehow screened. Noise in synthetic channels has also been studied [88]. There it was found that potassium currents through a one-state, permanently open channel exhibit $1/f^2$ noise. An artificial channel that can open and close, on the other hand, was found to exhibit $1/f$ noise when the externally applied voltage is in the right regime. With this latter artificial channel there is good ground to attribute the open–closed transitions to the movement of “dangling ends” of polymers in the pore's lining. So the result supports the “moving cluster” for the mechanism behind $1/f$ noise in channels.

There appears to be no simple theory that can convincingly bring all manifestations of $1/f$ noise under one common denominator. All the indications are that an *ad hoc* approach to nonequilibrium noise phenomena is still the most fruitful one.

In ordinary resistors the amount of $1/f$ noise grows linearly with the dissipated power W . If we take $S(\omega) d\omega$ to denote the power in energy per unit of time (watts) in an interval $d\omega$, then we have for the power spectral density:

$$S(\omega) = \frac{gW}{f} \quad (7.12)$$

Here, g is a dimensionless constant the value of which depends on the type of resistor.

Nyquist noise is simple in that the net value of the resistance R fully determines the noise amplitude. With $1/f$ noise a more complex situation arises. Experimentally, the constant g (cf. Equation 7.12) turns out to be proportional to the volume-to-power ratio [89]. In Figure 7.6 the four resistors in design (b) are identical to the one resistor in design (a). It is obvious that (a) and (b) will have the same net resistance and therefore the same amount of Nyquist noise. Design (a), however, will exhibit four times as much $1/f$ noise as design (b). Design (b) is quieter because the energy dissipation is distributed over a larger volume. Generally, we have $g \propto 1/V$, where V denotes the resistor's volume. The gW in Equation 7.12 can be expressed as $g_e w$, where g_e is the g -value for a single elementary charge carrier in the resistor and w is the energy dissipated in the volume of such a single, independent charge carrier.

Pumps and carriers move ions one by one. Imagine a single pump or carrier that moves ions across the membrane at a rate ν . During a small time interval dt there is a probability $p = \nu dt$ that an ion is transported. We take dt to be sufficiently small so that the probability of more than one ion being transported during dt is negligible. We also take the duration of the catalytic cycle, that is, the “processing” time for an ion going through the membrane, to be negligible in comparison to the time between catalytic cycles. If we were not to make the latter assumption, we would simply have to multiply by the probability that an average channel is available for transport when we want to express the transport rate. For the average number of ions $\langle n \rangle_{dt}$ transported by the channel in time dt , we now have $\langle n \rangle_{dt} = 1 \cdot p + 0 \cdot (1 - p) = p$. For the variance we have $\sigma_{dt} = \langle n^2 \rangle - \langle n \rangle^2 = 1^2 \cdot p - (1 \cdot p)^2 = p(1 - p)$. For M subsequent timesteps and $M dt = T$, the variances add up, and we have $\langle n \rangle_T = Mp$ and $\sigma_T = Mp(1 - p)$. So the standard deviation, $\sqrt{\sigma_T}$, works out to be proportional to \sqrt{M} . Over time the standard deviation becomes more and more negligible compared to the average. For sufficiently small dt we can take $1 - p$ to be equal to 1, and we then have a variance that equals the average.

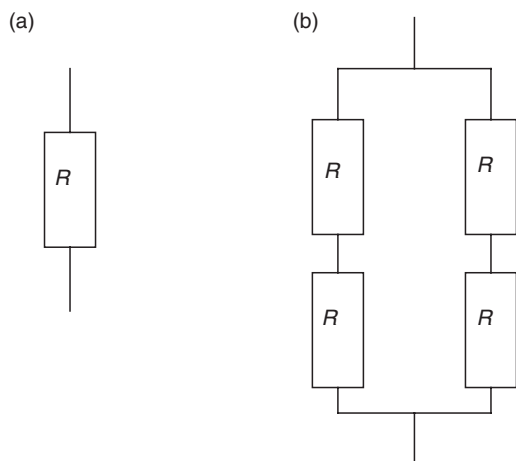


FIGURE 7.6

Design (a) and design (b) both have a net resistance R . They are different in that design (b) actually consists of two parallel resistors of $2R$. Designs (a) and (b) will exhibit the same amount of equilibrium noise, as it is only the net resistance (cf. Equation 7.5) that determines the equilibrium noise amplitude. It appears, however, that design (a) has four times as much power spectral density as design (b). The amount of nonequilibrium noise is proportional to the current density.

In the textbook by DeFelice [89] it is shown how the power spectral density of the process above amounts to $S(f) = 2\sigma_T/T = 2\nu$. The frequency-independent power spectrum can be intuited as follows. If the actual transport time through the membrane is small, then we can conceive of the transmembrane current as delta function-like pulses occurring at a rate ν . The Fourier transform of a Dirac delta function is a flat spectrum. In order to go from particle current to electrical current we must, to obtain the current power spectral density, multiply with the square of the charge of the involved ion. Taking this to be the elementary charge e , we find

$$S_i(f) = 2\nu e^2 = 2e\langle i \rangle \quad (7.13)$$

Here, $\langle i \rangle = ev$ denotes the average current through one pump.

Next, we let $\langle I \rangle$ denote the total transmembrane current due to pumps of a particular ion through the entire cell surface. We then have for the total current power spectral density:

$$S_I^{\text{pu}}(f) = 2e\langle I \rangle \quad (7.14)$$

For a living cell in a steady state, for each kind of ion, there are just as many ions going in as there are going out, that is, there is just as much uphill transport through pumps as there is downhill flow through ion channels. So we have the same current $\langle I \rangle$ uphill as well as downhill. Below, we will first show that the downhill flow through the channels generates much more nonequilibrium noise than the uphill flow through the pumps. We will then show how the channel noise far exceeds the Johnson–Nyquist equilibrium noise.

Ion channels stay open for an average time of about $\tau_{\text{op}} = 10^{-3}$ sec, and during that time there is a current of about 10^7 ions per sec (i.e., about 1 pA). So the equivalent of the elementary charge mentioned in the previous paragraph is now $N = 10^4$ ions.

However, before we blindly substitute Ne for e in Equation 7.14 to obtain the current power spectral density generated by the channel population of a cell, we have to take another source of variance into account. The channel-open time of about a millisecond is an average. If we view opening and closing of a channel as simple chemical steps between an open and a closed state, then the millisecond is the average of an exponential distribution of open times. For an exponential distribution the average open time equals the standard deviation in the open time. So the standard deviation ΔN equals N itself. The associated variance has to be added in. So we have $S_I^{\text{ch}}(f) \approx 2\nu e^2 (N^2 + (\Delta N)^2)$. The rate ν now represents the number of channel openings per unit of time. So we get for the current power spectral density produced by the channels:

$$S_I^{\text{ch}} \approx 4Ne\langle I \rangle \quad (7.15)$$

So the channel contribution to the total nonequilibrium current noise is about 10^4 times as large as the contribution of the pumps. For the total current power spectral density, S_I^{noneq} , due to nonequilibrium currents, we thus neglect the pump contribution.

The above Equation 7.15 constitutes $S_I^{\text{ch}}(0)$. At higher frequencies, when f approaches the average open time τ_{op} of the channel, $S_I^{\text{ch}}(f)$ will decrease. The characteristic inverse time for a channel is $f_* = \tau_{\text{op}}^{-1} + \tau_{\text{cl}}^{-1}$, where τ_{cl} is the average closed time of the channel. With only one type of channel present in a cell, there will be a sigmoidally shaped, Lorentzian noise spectrum with an inflection point at $f = f_*$. With many types of channels for different kinds of ions present it is indeed possible to obtain a $1/f$ spectrum over several decades as the sum of Lorentzians [86].

To obtain the voltage power spectral density, we have to multiply $S_I^{\text{noneq}}(f)$ by R^2 , where R represents the electrical resistance of the entire cell membrane. We let the cell surface area measure A . So we have $S_V^{\text{noneq}}(0) \approx 4Ne\langle I \rangle R^2$. The equilibrium Nyquist voltage noise across the same cell membrane is $S_V^{\text{eq}}(f) \approx 4kTR$. This is white noise and has the same strength at all frequencies. We thus obtain the following formula at $f = 0$ for the ratio $\theta(0)$ of the nonequilibrium noise and the equilibrium noise:

$$\theta(0) \approx \frac{Ne\langle I \rangle R}{kT} \quad (7.16)$$

The transmembrane current $\langle I \rangle$ is proportional to the cell surface A . The resistance R is inversely proportional to A . So eventually, the cell surface area and the cell geometry in general cancel out of the equation.

Data for the steady-state Na^+ flux through several types of cell membranes (e.g., rat soleus, sheep purkinje, squid axon, guinea pig auricles, and frog sartorius) are available [90]. That flux is about $50 \text{ pmol}/(\text{cm}^2 \text{ sec})$. The vast majority of transmembrane ion transport is carried out by $\text{Na},\text{K}-\text{ATPase}$, which transports two K^+ ions for every three Na^+ ions. We assume Na^+ and K^+ transport to therefore be about equal. After multiplying by Faraday's constant (the number of coulombs in a mole, i.e., about 10^5), we get a total current of about $\langle I \rangle \approx 10 \mu\text{A}/\text{cm}^2$. The resistance of a cell membrane varies from $10^3 \Omega \text{ cm}^2$ (squid axon) to $7 \times 10^3 \Omega \text{ cm}^2$ (mammalian cardiac cell). We thus find for $\theta(0)$ a value of about 5000.

Based on experimental data, it has been estimated that at 1 Hz the $1/f$ noise in the frog node of Ranvier is about a thousand times larger than thermal noise [91]. This is consistent with our estimate. Experimentally, it turns out that the power spectral density is constant from $f = 0$ up to about somewhere between 1 and 10 Hz [86,89]. At that point, the power spectral density starts to fall off as $1/f$. This means that we reach $\theta(f) = 1$, that is, the equilibrium and nonequilibrium noise being equal, somewhere near 10^4 Hz . Figure 7.5, in which the horizontal axis is in radians per second, indeed shows flattening between 10^3 and 10^4 Hz . At the 50- and 60-Hz power line frequencies, the nonequilibrium voltage noise is expected to exceed the equilibrium voltage noise by a factor of at least 10^2 .

However, we should pause before taking the value of θ and employ it to incorporate nonequilibrium noise in the evaluation of a signal-to-noise ratio. As we saw earlier in this section, nonequilibrium noise may be a way to transduce energy from one stored form to another. So a signal can come in the form of a piece of nonequilibrium noise. With this gray area between signal and noise, it may no longer be straightforward to calculate a signal-to-noise ratio. There has been a natural selection toward high signal-to-noise ratios for signals whose detection has been important for the survival of the organism for many millennia. But what the signal-to-noise ratios and detection thresholds are for ELF and microwave radiation, which are relatively new phenomena in the environment, and how nonequilibrium noise figures in all of this is still open to conjecture and debate.

7.7 Chemical Noise

Chemical noise consists of both fundamental chemical noise (stochastic variations in net or accumulated amounts of a particular ion or molecule) and nonfundamental changes in chemical amount (molecular number) due to influences other than the applied field. We again adopt a recent discussion [12] in which an arbitrary biological system is considered.

In the discussion, attention focuses on weakly interacting fields that can create small chemical changes, but much of the approach is also relevant to strongly interacting fields, for example, those causing cell membrane electroporation (see Chapter 9 on electroporation in Ref. [127]). To begin, consider a small physical perturbation of the biological system due to the interaction of a local electromagnetic field, $\vec{F}_{\text{local}}(\vec{r}, t)$, that may vary from site to site within the volume of the biological system. In general, F_{local} may have a complicated dependence of its magnitude and direction on time and position, such that a formal prescription for calculating the field-induced molecular change due to an exposure is

$$\bar{n}_S = \int_{t=0}^{t=t_{\text{exp}}} \int_{\text{system volume}} J_0(t') f_{\text{bpm}}(\vec{F}_{\text{local}}(\vec{r}, t')) dV dt' \quad (7.17)$$

We regard \bar{n}_S as a molecular change signal. It is the primary consequence of the field exposure for the case where only one process, or one step in a cascade, is altered. Integration is carried out over the entire biological system volume and over the time comprising the exposure, t_{exp} (or control). This yields the accumulated, total chemical (molecular) change due to the applied field during the exposure. Other changes in the same ionic or molecular species may result from competing influences, for example, temperature variations, during t_{exp} .

The applied field interacts through one or more of a limited class of biophysical mechanisms. Here, *biophysical mechanism* means a class of interactions by which the field alters an ongoing biochemical rate (transport or reaction), with the rate arising from nonequilibrium processes dependent on metabolism. Examples of known biophysical mechanisms involving electric fields are heating (most biochemical processes have a nonzero temperature dependence), voltage-gated channels, electroconformational coupling of membrane enzymes, electroporation, and iontophoresis (mainly electrophoresis, but in some cases also electroosmosis). Examples involving magnetic fields are radical-pair reactions and twisting of magnetic material (magnetite or contaminant magnetic particles). As used here, a biophysical mechanism modulates an ongoing biochemical process, and both the coupling strength and the magnitude of the basal rate are important.

For a particular type of biophysical mechanism (bpm), the function $f_{\text{bpm}}(\vec{F}_{\text{local}}(t))$ describes the instantaneous alteration of the basal rate, J_0 , which itself can vary in time [92]. The local field can be computed numerically at the tissue level (millimeter scale; see Chapter 11 on dosimetry, this volume) [93–99] and at the cellular level [100,101]. The time and position dependence of $\vec{F}_{\text{local}}(\vec{r}, t)$ is often simple, namely, a constant magnitude (steady or DC) field, a constant amplitude periodic (AC) field, or at high frequencies a spatially decaying amplitude field due to power absorption. Environmental and occupational fields can be much more complicated, such that piecewise continuous representations may be needed.

If a weakly coupled physical perturbation alters the basal rate of a biochemical process (transport or reaction), the total chemical (molecular) change, expressed as the number of molecules, is

$$\bar{n} = \bar{n}_0 + \bar{n}_S \quad (7.18)$$

where \bar{n}_0 is the basal change during an exposure (sensing) time t_{exp} , and \bar{n}_S is the (much smaller) molecular change due to the field exposure [22,45,92,102]. As noted above, \bar{n}_S can be regarded as a molecular change signal. The basal process is far from equilibrium,

driven by free-energy differences associated with metabolism. The largest field-induced molecular change occurs for a steady (DC) field exposure [22,102]:

$$\bar{n}_S = K_{\text{bpm,dc}} F_0 J_0 t_{\text{exp}} \quad (7.19)$$

where $K_{\text{bpm,dc}}$ describes the alteration of the basal rate by the steady field, here of magnitude F_0 . Equation 7.19 is the DC version of the case of a weakly coupled periodic perturbation, previously described for the case of an extracellular electric field [45,92], namely,

$$\bar{n}_S = K_{\text{bpm,ac}} F_0^2 J_0 t_{\text{exp}} \quad (7.20)$$

where $K_{\text{bpm,ac}}$ describes the coupling that leads to rectification of the ongoing rate [45]. For basal rates with more complicated time dependence, [Equation 7.17](#) may need to be evaluated numerically, but the same basic ideas apply. Equation 7.20 is valid for long exposures, involving a large number of cycles of the periodic field. Basal rates that can be altered by weakly interacting electromagnetic fields by definition involve small interaction energies, so that thermal fluctuations and chemical free-energy differences result in nonzero basal rates. A zero basal rate with an extremely large activation or interaction energy cannot, therefore, be expected to be changed to a measurable nonzero rate by a weakly interacting field.

A generalized, molecular change-based signal-to-noise ratio can be constructed by estimating the ratio of primary molecular change to the combined competing changes for the same molecular (ionic) species. We consider the simplest case of the field altering the rate at one step in a single pathway but note that in principle the present analysis can be extended to include multiple steps involving more than one biochemical pathway. We further assume that this biochemical has its rate through the pathway altered slightly by a physical perturbation, here an electromagnetic field. But competing influences can also alter the rate. Such influences include temperature variations, normal physiological concentration variations, changes in hormones and other regulating biochemicals, and mechanical perturbations of cells and tissues. Competing molecular changes can also be created by a background electromagnetic field, for example, normal electrical activity within the human body or by movement in the earth's magnetic field, interacting through the same biophysical mechanism. Such competition goes beyond fundamental chemical noise (molecular shot noise). Nonionizing influences can only modulate ongoing processes, and therefore such influences cannot (essentially by definition) introduce foreign molecules. This has the important consequence that competing molecular changes may arise from several sources (Table 7.1).

TABLE 7.1
Quantities Employed in Generalized Chemical Noise

Symbol	Molecular Change	Source
S	\bar{n}_S	Field-induced molecular change signal
N	$\sqrt{\bar{n}} \approx \sqrt{\bar{n}_0}$	Molecular shot noise (fundamental)
V	\bar{n}_V	Molecular change due to temperature variations
C	\bar{n}_C	Molecular change due to concentration variations
I	\bar{n}_M	Molecular change due to mechanical interference
B	\bar{n}_B	Molecular change due to background fields

A generalized signal-to-noise ratio (S/N)_{gen}, can thus be considered. The field-induced molecular change signal, S , is thereby quantitatively compared to the several sources of competing molecular changes for the same biochemical (molecule or ion), yielding

$$(S/N)_{\text{gen}} = \frac{S}{f_{\text{com}}(N,V,C,I,B)} \quad (7.21)$$

The various competing molecular changes, which may or may not be independent, are combined to give the total competing molecular change, f_{com} . Important simplifications can be made if the various competing molecular changes can be approximated as independent and random around their mean values. In this case, f_{com} can be approximated as

$$f_{\text{com}}(N,V,C,I,B) \approx [N^2 + V^2 + C^2 + I^2 + B^2]^{1/2} \quad (7.22)$$

Alternatively, emphasizing the changes in terms of numbers of molecules,

$$f_{\text{com}}(N,V,C,I,B) \approx [\bar{n}_0 + (\Delta n_V)^2 + (\Delta n_C)^2 + (\Delta n_I)^2 + (\Delta n_B)^2]^{1/2} \quad (7.23)$$

All significant sources of competing molecular change are directly relevant.

Consistent with experimental treatment of errors as random, here we consider the special case that all the important competing molecular changes can be approximated as independent and random variations around their mean value, as this allows the competing changes to be added in quadrature (Equation 7.22). This leads to a general molecular change-based signal-to-noise ratio that involves Gaussian distributions, namely,

$$(S/N)_{\text{gen}} \approx \frac{S}{[N^2 + V^2 + C^2 + I^2 + B^2]^{1/2}} \quad (7.24)$$

Each of these competing molecular changes is discussed briefly below, with reference to [Table 7.1](#).

As indicated in [Table 7.1](#), $N = \sqrt{\bar{n}} \approx \sqrt{\bar{n}_0}$ is the competing molecular change due to fundamental stochastic variations in biochemical reaction and transport processes [15,45,92], which provides a fundamental, minimum molecular change noise. Fundamental chemical noise is increasingly recognized as important to understanding other aspects of biological systems, such as the circadian clock [103,104], control of genetic circuits [105,106], and bacterial chemotaxis [107].

Temperature variations within the volume of the biological system are generally expected to result in altered rates. When integrated over the system volume and over the exposure time, a contribution to the end-point molecular change is expected, because most biochemical processes have nonzero temperature dependence. Thus, $V = \bar{n}_v$ is the resulting, competing molecular change due to temperature variations [15]. Human core body temperature has daily variations of more than 1°C [108–113], and there are even larger variations in the extremities. Often *in vitro* electric and magnetic field experiments use feedback control, for instance, in temperature-regulated exposure chambers, but these typically have variations greater than about 0.01°C at one or a few temperature measurement sites. Temperature variations within the biological system itself are often inferred,

preferably by numerical models that can reasonably predict the temperature through the biological system by first predicting the specific absorption rate. During the exposure time, interfering temperature variation can be significant. To allow correction for temperature variations, the biological system should be characterized for its temperature sensitivity, and each particular apparatus should be characterized for its temperature variations for control and exposed conditions. As an example, an investigation first reporting athermal effects [114] was subsequently found to have temperature variation $\sim 0.1^\circ\text{C}$ at temperature measurement sites [115]. Without thermal modeling of the exposure systems and the biological systems, however, larger temperature changes away from the measurement site cannot be ruled out. It is the temperature change and variation over the entire volume containing cells (or other specimens) that need to be quantitatively understood. Temperature measurement at one site, typically somewhere along the perimeter or boundary of a temperature-regulated apparatus, is generally insufficient. The measured biochemical quantity should also be characterized for its temperature sensitivity for the biological system studied, so that the expected V can be determined, to address the basic specificity question of whether an observed change is due to the field or to temperature changes [116].

Changes in concentration of biochemicals involved in a process are well known to alter the rate of a process. Relevant chemical species include substrates, products, inhibitors, etc. The competing molecular change due to one or more interfering concentration changes is $C = \bar{n}_C$. In this case, a significant difference may exist for *in vitro* and *in vivo* experiments. Usually, only small, slow changes of chemical concentrations are expected *in vitro*, occurring, for example, through absorption or release of molecules (ions) from glass- and plasticware, spontaneous chemical decomposition, binding to cellular constituents, or evaporation. Uptake or release of interfering biochemicals from a biological preparation could be the predominant source, particularly if cells grow (taking up molecules) or die (releasing molecules). *In vivo* concentration variations are relatively large, because of normal physiologic variations. For example, Ca^{2+} concentration varies in humans by more than 1% over a day [117,118]. Unless buffered, these normal biochemical variations also compete with the field-induced molecular change.

Movement of tissue *in vivo* and vibration of an experimental apparatus containing a biological system can also create a mechanically induced molecular change, $I = \bar{n}_M$, that competes with a molecular change signal. In this case, the competing molecular change is due to interference of mechanical stress and strain [119,120], often present at high levels in living humans [11,121,122] but at low levels for *in vitro* experiments. *In vitro* apparatus can have quite different mechanical properties and isolation from ambient vibrations. Indeed, it has been found in some experiments that mechanical vibrations create effects larger than the field exposure [123]. Tissues *in vivo* experience significant mechanical deformation, but there is the least strain expected within the bone marrow and the brain [120]. This may be relevant to the “contact current hypothesis,” which suggests that currents in the bone marrow may be important in exposures of children [124–126].

Background fields can, of course, also couple to biochemical processes through the same biophysical mechanisms as the applied field. Background field-induced molecular change competes, and is denoted by $B = \bar{n}_B$. Examples of background electromagnetic fields include the endogenous electrical fields generated within the body by cardiac, muscular, and neural activity and the sampling of different field values (local anomalies) in the ambient magnetic field as mobile humans move about in their environment. *In vitro* background fields will depend on the particular experimental environment, are usually small and constant, and are often measured.

7.8 Interpretation of Experiments

Specificity is fundamentally important to interpret experiments, as one wants to know what agent is responsible for the observed change(s). This is particularly relevant to experiments that find small changes in biological systems that are exposed to small electromagnetic fields. A basic challenge is to show that other influences are not responsible. Because it is well known that most biochemical processes have a significant temperature dependence, the approximate temperature sensitivity of the observed quantity should be determined or known, and some bound should be established for temperature drift or variations in the experiment. However, as already noted, even big changes can have more than one candidate cause. Both tissue electroporation and tissue movement can, for instance, underlie the changes in molecular uptake associated with large field pulses. For this reason, signal-to-noise ratio considerations should be preceded by establishing field specificity, which can be much more difficult than observing a change associated with a field exposure. To establish specificity, a number of issues must be considered, many of which will be discussed next.

Many experiments determine quantities related to biochemical change. Exceptions are experiments that determine physical quantities such as voltages and currents, temperature changes, and magnetic particle rotation. However, electrical measurements are the most frequent physical measurement. These are incredibly important to systems of excitable cells, with experimental preparations ranging from isolated cells to electrophysiologic measurements on humans. Accumulation of charge might be measured, but probably as a voltage on a capacitance. Signal-to-noise ratio issues are still important, of course, but usually there is an important distinction: voltages and currents (rarely charge) are readily measured continuously.

A further distinction is that most experiments involving exposures to small fields use long exposure times (many seconds to hours or even days). Such experiments commonly determine biochemical quantities directly, for example, enzyme activity, or indirectly, for example, fluorescence emission from fluorescent indicators of intracellular calcium concentration. In this broad case, consideration of generalized chemical noise is relevant. Following the discussion in a recent paper [12], both the magnitude of the field perturbation and the nature and magnitude of chemical competition need to be understood. Such analysis should explicitly estimate the coupling to ongoing, far from equilibrium, metabolically driven biochemical processes and should quantitatively determine molecular changes due to competing influences. Only then can the analysis distinguish idealized conditions from *in vitro* conditions and *in vivo* conditions and then determine whether reported effects can be explained by known biophysical mechanisms.

In vivo there are several kinds of noise, and it is important to distinguish between them. Equilibrium noise comes about as a consequence of Brownian motion, that is, the random movement of molecules at finite temperature. At equilibrium, every degree of freedom takes on the same amount of energy, and equilibrium noise is therefore easy to evaluate. For a signal to exceed the equilibrium noise band, the quantitative criteria are often readily derived. Such baseline criteria can be useful when assessing the electroreception and magnetoreception that many organisms exhibit. But the nonequilibrium nature of life brings in nonequilibrium noise. When a primary molecular change is amplified through a biochemical cascade, “amplifier noise” is inevitable. Nonequilibrium noise appears whenever energy is dissipated, that is, when work is done. In many biological contexts the nonequilibrium noise is much more intense than the equilibrium noise. A serious complication is constituted by the fact that nonequilibrium noise, unlike equilibrium noise, is also able to perform work, that is, be a power source for an energetically uphill

process. Many biological processes may rely on the energy transduction that can be accomplished through nonequilibrium noise. The analysis of such situations poses challenges as the noise may be a signal and the signal may be noise. There is no easy general “common denominator” theory for nonequilibrium noise like there is for equilibrium kT -noise.

In a recent discussion [12], it is argued that experimental measurements can be plausibly related quantitatively to an underlying primary molecular change because of a field exposure operating through a biophysical mechanism. It is further argued that only the uncertainty in this change propagates through biochemical amplification and therefore dominates the measurement uncertainty. A more complete approach would involve traditional, independent determination of the instrumental or assay error (quantitative characterization of the experimental measurement system). After removal of the “instrumental noise,” the generalized signal-to-noise ratio $(S/N)_{gen}$, could be revised upward. This would allow interpretation (correction) of experimental error to estimate the uncertainty in the measured quantity itself. Assessment of combinations of biophysical mechanism models and particular exposure can then be carried out, using the most field-sensitive versions of theoretical models for the candidate biophysical mechanisms. The criterion $(S/N)_{gen} \leq 0.1$ is a very conservative basis for ruling out a particular class of biophysical mechanism for a given field exposure. Similarly, the criterion $(S/N)_{gen} \geq 10$ is a conservative basis for ruling in a candidate biophysical mechanism for a given exposure, retaining that biophysical mechanism hypothesis for further evaluation. This approach provides a quantitative basis for rejecting or accepting hypothetical biophysical mechanisms as candidate explanations for an experimental measurement.

The traditional choice $(S/N)_{gen} \approx 1$ is a useful but somewhat arbitrary dividing line, which indicates conditions for which an effect might appear. $(S/N)_{gen} \leq 0.1$ and $(S/N)_{gen} \geq 10$ provide criteria for stronger conclusions, allowing rejection or provisional retention of a biophysical mechanism hypothesis. This approach to interpreting experiments thus provides a general method for carrying out theoretical assessment of reported weak field exposure effects. This approach can distinguish relatively quiet *in vitro* conditions from *in vivo* conditions containing more and larger influences of competing molecular change. This in turn allows quantitative estimates of whether an *in vitro* result is relevant to *in vivo* conditions.

Acknowledgment

This work was supported partially by NIH grant RO1-GM63857.

References

1. G.N. Stewart. The changes produced by the growth of bacteria in the molecular concentration and electrical conductivity of culture media. *J. Exp. Med.*, 4:235–243, 1899.
2. R. Eden and G. Eden. *Impedance Microbiology*. Research Studies Press, Letchworth, Herts, U.K., 1984.
3. M. Wawerla, A. Stolle, B. Schalch, and H. Eisgruber. Impedance microbiology: applications in food hygiene. *J. Food Prot.*, 62:1488–1496, 1999.

4. J. McPhillips and N. Snow. Studies on milk with a new type of conductivity cell. *Aust. J. Dairy Technol.*, 3:192–196, 1958.
5. T. Ritz, P. Thalau, J.B. Phillips, R. Wiltschko, and W. Wiltschko. Resonance effects indicate a radical-pair mechanism for avian magnetic compass. *Nature*, 429:177–180, 2004.
6. D. Cohen. Ferromagnetic contaminants in the lungs and other organs of the body. *Science*, 180:745–748, 1973.
7. J.L. Kirschvink, A.K. Kirschvink, and B.J. Woodford. Magnetite biominerilization in the human brain. *Proc. Natl. Acad. Sci.*, 89:7683–7687, 1992.
8. J.R. Dunn, M. Fuller, J. Zoeger, J. Dobson, F. Heller, J. Ilammann, E. Caine, and B.M. Moskowitz. Magnetic material in the human hippocampus. *Brain Res. Bull.*, 36:149–153, 1994.
9. P.L. McNeil and S. Ito. Molecular traffic through plasma membrane disruptions of cells. *In Vivo J. Cell Sci.*, 96:549–556, 1990.
10. P.L. McNeil and R.A. Steinhardt. Loss, restoration, and maintenance of plasma membrane integrity. *J. Cell Biol.*, 137:1–4, 1997.
11. P.L. McNeil and M. Terasaki. Coping with the inevitable: how cells repair a torn surface membrane. *Nat. Cell Biol.*, 3:124–129, 2001.
12. T.E. Vaughan and J.C. Weaver. Molecular change signal-to-noise criteria for interpreting experiments involving exposure of biological systems to weakly interacting electromagnetic fields. *Bioelectromagnetics*, 26:305–322, 2005.
13. N.G. Van Kampen. *Stochastic Processes in Physics and Chemistry*. Elsevier, Amsterdam, 1992.
14. R.C. Duncan, R.G. Knapp, and M.C. Miller. *Introductory Biostatistics for the Health Sciences*. John Wiley & Sons, New York, 1983.
15. J.C. Weaver, T.E. Vaughan, and G.T. Martin. Biological effects due to weak electric and magnetic fields: the temperature variation threshold. *Biophys. J.*, 76:3026–3030, 1999.
16. J.C. Weaver. Understanding conditions for which biological effects of nonionizing electromagnetic fields can be expected. *Bioelectrochemistry*, 56:207–209, 2002.
17. C.W. Helstrom. *Statistical Theory of Signal Detection*, Second Edition. Pergamon Press, New York, 1968.
18. A.J. Kalmijn. Electro-perception in sharks and rays. *Nature*, 212:1232–1233, 1966.
19. A.J. Kalmijn. Electric and magnetic field detection in elasmobranch fish. *Science*, 218:916–918, 1982.
20. W.J. Moore. *Physical Chemistry*. Longman, London, 1972.
21. A.J. Kalmijn. Graded positive feedback in elasmobranch ampullae of lorenzini. In S.M. Bezrukov, Ed. *Unsolved Problems of Noise and Fluctuations: UPoN 2002: Third International Conference*, volume 665 of *Conference Proceedings*, pp. 133–141, American Institute of Physics, Melville, NY, 2003.
22. R.K. Adair, R.D. Astumian, and J.C. Weaver. Detection of weak electric fields by sharks, rays, and skates. *Chaos*, 8:576–587, 1998.
23. S.M. Bezrukov. Sensing nature's electric fields: ion channels as active elements of linear amplification. In S.M. Bezrukov, Ed. *Unsolved Problems of Noise and Fluctuations: UPoN 2002: Third International Conference*, volume 665 of *Conference Proceedings*, pp. 142–149, American Institute of Physics, Melville, NY, 2003.
24. J.C. Weaver, T.E. Vaughan, and R.D. Astumian. Biological sensing of small field differences by magnetically sensitive chemical reactions. *Nature*, 405:707–709, 2000.
25. R.P. Blakemore. Magnetotactic bacteria. *Science*, 190:377–379, 1975.
26. R. Blakemore. Magnetotactic bacteria. *Annu. Rev. Microbiol.*, 36:217–238, 1982.
27. J.L. Kirschvink, M.M. Walker, and C.E. Diebel. Magnetite-based magnetoreception. *Curr. Opin. Neurobiol.*, 11:462–467, 2001.
28. J.L. Kirschvink. Comment on "Constraints on biological effects of weak extremely-low-frequency electromagnetic fields." *Phys. Rev. A*, 46:2178–2184, 1992.
29. M.M. Walker, T.E. Dennis, and J.L. Kirschvink. The magnetic sense and its use in long-distance navigation by animals. *Curr. Opin. Neurobiol.*, 12:735–744, 2002.
30. National Institute of Environmental Health Sciences (NIEHS). NIEHS Report on Health Effects from Exposure Power-Line Frequency Electric and Magnetic Fields. NIH Publication No. 99–4493, 1999.

31. R.K. Adair. Effects of ELF magnetic fields on biological magnetite. *Bioelectromagnetics*, 14:1–4, 1993.
32. C. Polk. Effects of extremely-low-frequency magnetic fields on biological magnetite. *Bioelectromagnetics*, 15:261–270, 1994.
33. R.K. Adair. Constraints on biological effects of weak extremely-low-frequency electromagnetic fields. *Phys. Rev. A*, 43:1039–1048, 1991.
34. K.R. Foster and H.P. Schwan. Dielectric properties of tissues and biological materials: a critical review. *CRC Crit. Rev. Bioeng.*, 17:25–104, 1989.
35. J.B. Johnson. Thermal agitation of electricity in conductors. *Phys. Rev.*, 32:97–109, 1928.
36. H. Nyquist. Thermal agitation of electric charge in conductors. *Phys. Rev.*, 32:110–113, 1928.
37. W. Schottky. Über spontane stromschwankungen in verschiedenen elektrizitätsleitern. *Ann. Phys. (Leipzig)*, 57:541–568, 1918.
38. R. Sarpeshkar, T. Delbrück, and C.A. Mead. White noise in MOS transistors and resistors. *IEEE Circuits Devices*, Nov.:23–29, 1993.
39. M. Bier. Gauging the strength of power frequency fields against membrane electrical noise. *Bioelectromagnetics*, 26:595–609, 2005.
40. B. Hille. *Ion Channels of Excitable Membranes*. Sinauer, Sunderland, MA, 1992.
41. P. Läuger. *Electrogenic Ion Pumps*. Sinauer, Sunderland, MA, 1991.
42. J.C. Weaver and R.D. Astumian. The response of living cells to very weak electric fields, the thermal noise limit. *Science*, 247:459–462, 1990.
43. W.T. Kaune. Thermal noises limit on the sensitivity of cellular membranes to power frequency electric and magnetic fields. *Bioelectromagnetics*, 23:622–928, 2002.
44. G. Vincze, N. Szasz, and A. Szasz. On the thermal noise limit of cellular membranes. *Bioelectromagnetics*, 26:28–35, 2005.
45. R.D. Astumian, J.C. Weaver, and R.K. Adair. Rectification and signal averaging of weak electric fields by biological cells. *Proc. Natl. Acad. Sci.*, 92:3740–3743, 1995.
46. L. Brillouin. Can the rectifier become a thermodynamical demon? *Phys. Rev.*, 78:627–628, 1950.
47. P.W. Bridgman. Note on the principle of detailed balancing. *Phys. Rev.*, 31:101–102, 1928.
48. R.C. Tolman. The principle of microscopic reversibility. *Proc. Natl. Acad. Sci.*, 11:436–439, 1925.
49. R.P. Feynman, R.B. Leighton, and M. Sands. *The Feynman Lectures on Physics*. Addison-Wesley, Reading, MA, 1966.
50. M. von Smoluchowski. Experimentell nachweisbare, der üblichen thermodynamik widersprechende molekulärphänomene. *Phys. Zeitschr.*, 13:1069–1080, 1912.
51. P.W. Atkins. *The Second Law*. Scientific American Books, New York, 1984.
52. H.S. Leff and A.F. Rex, Eds. *Maxwell's Demon: Entropy, Information, Computing*. Princeton University Press, Princeton, NJ, 1990.
53. J. Howard and A.J. Hudspeth. Compliance of the hair bundle associated with gating of mechanoelectrical transduction channels in the bullfrog's saccular hair cell. *Neuron*, 1:189–199, 1988.
54. M. Magnasco. Forced thermal ratchets. *Phys. Rev. Lett.*, 71:1477–1480, 1993.
55. M. Bier. Brownian ratchets in physics and biology. *Contemp. Phys.*, 38:371–379, 1997.
56. R.D. Astumian and M. Bier. Fluctuation driven ratchets: molecular motors. *Phys. Rev. Lett.*, 72:1766–1769, 1994.
57. R.D. Astumian. Thermodynamics and kinetics of a brownian motor. *Science*, 276:917–922, 1997.
58. M. Bier and R.D. Astumian. Biased Brownian motion as the operating principle for microscopic engines. *Bioelectrochem. Bioenerg.*, 39:67–75, 1996.
59. I. Kosztin and K. Schulten. Fluctuation-driven molecular transport through an asymmetric membrane channel. *Phys. Rev. Lett.*, 93:238102-1–238102-4, 2004.
60. Z. Siwy, I.D. Kosińska, and A. Fuliński. On the validity of continuous modelling of ion transport through nanochannels. *Europhys. Lett.*, 67:683–689, 2004.
61. Z. Siwy, I.D. Kosińska, A. Fuliński, and C.R. Martin. Asymmetric diffusion through synthetic nanopores. *Phys. Rev. Lett.*, 94:048102-1–048102-4, 2005.
62. Z. Siwy and A. Fuliński. Fabrication of a synthetic nanopore ion pump. *Phys. Rev. Lett.*, 89:198103-1–198103-4, 2002.

63. J. Bernamont. Fluctuations in the resistance of thin films. *Proc. Phys. Soc.*, 49:138–139, 1937.
64. B. Pellegrini, R. Saletti, P. Terreni, and M. Prudenziati. $1/f^y$ noise in thick-film resistors as an effect of tunnel and thermally activated emissions, from measures versus frequency and temperature. *Phys. Rev. B*, 27:1233–1243, 1983.
65. J.B. Bassingthwaite, L.S. Liebovitch, and B.J. West. *Fractal Physiology*. Oxford University Press, New York, 1994.
66. C. Wunsch. Bermuda sea level in relation to tides, weather, and baroclinic fluctuations. *Rev. Geophys.*, 10:1–49, 1972.
67. M. Dishon-Berkovits and R. Berkovits. Work-related tardiness: lateness incident distribution and long-range correlations. *Fractals*, 5:321–324, 1997.
68. P. Bak, C. Tang, and K. Wiesenfeld. Self-organized criticality: an explanation of $1/f$ noise. *Phys. Rev. Lett.*, 59:381–384, 1987.
69. P. Bak. *How Nature Works*. Springer-Verlag, New York, 1996.
70. S. Kauffman. *Investigations*. Oxford University Press, New York, 2000.
71. B.D. Malamud, G. Morein, and D.L. Turcotte. Forest fires: an example of self-organized critical behavior. *Science*, 281:1840–1842, 1998.
72. H.M. Jaeger, C. Liu, and S.R. Nagel. Relaxation at the angle of repose. *Phys. Rev. Lett.*, 62:40–43, 1989.
73. S. Nagel. Instabilities in a sandpile. *Rev. Mod. Phys.*, 64:321–325, 1992.
74. M. Bretz, J.B. Cunningham, P.L. Kurczynski, and F. Nori. Imaging of avalanches in granular materials. *Phys. Rev. Lett.*, 69:2431–2434, 1992.
75. J.G. Nicolis, A.R. Martin, and B.G. Wallace, Eds. *From Neuron to Brain*. Sinauer, Sunderland, MA, 1992.
76. H.E. Derksen and A.A. Verveen. Fluctuations of resting neural membrane potential. *Science*, 151:1388–1389, 1966.
77. H.E. Derksen. Axon membrane voltage fluctuations. *Acta Physiol. Pharmacol. Neerl.*, 13:373–466, 1965.
78. H.E. Derksen and A.A. Verveen. Fluctuations in membrane potential of axons and the problem of coding. *Kybernetik* 2:152–160, 1965.
79. D. Colquhoun and A.G. Hawkes. On the stochastic properties of bursts of single ion channel openings and of clusters of bursts. *Philos. Trans. R. Soc. Lond.*, 300:1–59, 1982.
80. S.D. Silberberg and K.L. Magleby. Preventing errors when estimating single channel properties from the analysis of current fluctuations. *Biophys. J.*, 65:1570–1584, 1993.
81. D. Colquhoun, C. Hatton, and A.G. Hawkes. The quality of maximum likelihood estimation of ion channel rate constants. *J. Physiol. (Lond.)*, 547:699–728, 2003.
82. L.S. Liebovitch, J. Fishbarg, and J.P. Koniarek. Ion channel kinetics: a model based on fractal scaling rather than multistate Markov processes. *Math. Biosci.*, 84:37–68, 1987.
83. L.S. Liebovitch. Analysis of fractal ion channel gating kinetics: kinetic rates, energy levels, and activation energies. *Math. Biosci.*, 93:97–115, 1989.
84. L.S. Liebovitch. Testing fractal and Markov models of ion channel kinetics. *Biophys. J.*, 55:373–385, 1989.
85. I. Goychuk and P. Hänggi. Fractional diffusion modeling of ion channel gating. *Phys. Rev. E*, 70:051915-1–051915-9, 2004.
86. K. Diba, H.A. Lester, and C. Koch. Intrinsic noise in cultured hippocampal neurons: experiment and modeling. *J. Neurosci.*, 24:9723–9733, 2004.
87. S.M. Bezrukov and M. Winterhalter. Examining noise sources at the single molecule level: $1/f$ noise of an open maltoporin channel. *Phys. Rev. Lett.*, 85:202–205, 2002.
88. Z. Siwy and A. Fulniński. Origin of $1/f^\alpha$ noise in membrane channel currents. *Phys. Rev. Lett.*, 89:158101-1–158101-4, 2002.
89. L.J. DeFelice. *Introduction to Membrane Noise*. Plenum Press, New York, 1981.
90. O.M. Sejersted. Maintenance of Na,K-homeostasis by Na,K-pumps in striated muscle. *Prog. Clin. Biol. Res.*, 268B:195–206, 1988.
91. F.S. Barnes. Interaction of DC and ELF electric fields with biological materials and systems. In C. Polk and E. Postow, Eds. *Handbook of Biological Effects of Electromagnetic Fields*, pp. 103–147, CRC Press, Boca Raton, FL, 1996.

92. J.C. Weaver, T.E. Vaughan, R.K. Adair, and R.D. Astumian. Theoretical limits on the threshold for the response of long cells to weak ELF electric fields due to ionic and molecular flux rectification. *Biophys. J.*, 75:2251–2254, 1998.
93. M. Stuchly and T. Dawson. Interaction of low-frequency electric and magnetic fields with the human body. *Proc. IEEE*, 88:643–662, 2000.
94. M.A. Stuchly and O.P. Gandhi. Inter-laboratory comparison of numerical dosimetry for human exposure to 60 Hz electric and magnetic fields. *Bioelectromagnetics*, 21:167–174, 2000.
95. P.A. Mason, W.D. Hurt, T.J. Walters, J.A. D'Andrea, P. Gajšek, K.I. Ryan, D.A. Nelson, K.I. Smith, and J.M. Ziriax. Effects of frequency, permittivity and voxel size on predicted specific absorption rate values in biological tissue during electromagnetic-field exposure. *IEEE Trans. Microwave Theory Technol.*, 48:2050–2058, 2000.
96. P. Gajsek, T.J. Walters, W.D. Hurt, D.A. Nelson, and P.A. Mason. Empirical validation of SAR values predicted by FDTD modeling. *Bioelectromagnetics*, 23:37–48, 2002.
97. M. Nadeem, T. Thorlin, O.P. Gandhi, and M. Persson. Computation of electric and magnetic stimulation in human head using the 3-D impedance method. *IEEE Trans. Biomed. Eng.*, 50:900–907, 2003.
98. T.W. Dawson, K. Caputa, M.A. Stuchly, and R. Kavet. Comparison of electric fields induced in humans and rodents by 60-Hz contact currents. *IEEE Trans. Biomed. Eng.*, 50:744–753, 2003.
99. S.J. Allen, E.R. Adair, K.S. Mylacraine, W. Hurt, and J. Ziriax. Empirical and theoretical dosimetry in support of whole body radio frequency (RF) exposure in seated human volunteers at 220 MHz. *Bioelectromagnetics*, 26:440–447, 2005.
100. T.R. Gowrishankar and J.C. Weaver. An approach to electrical modeling of single and multiple cells. *Proc. Natl. Acad. Sci.*, 100:3203–3208, 2003.
101. D.A. Stewart, T.R. Gowrishankar, and J.C. Weaver. Transport lattice approach to describing cell electroporation: use of a local asymptotic model. *IEEE Trans. Plasma Sci.*, 32:1696–1708, 2004.
102. P.C. Gailey. Membrane potential and time required for detection of weak signals by voltage-gated ion channels. *Bioelectromagnetics*, 20:102–109, 1999.
103. N. Barkai and S. Liebler. Circadian clocks limited by noise. *Nature*, 403:267–268, 2000.
104. M.B. Elowitz and S. Leibler. A synthetic oscillatory network. *Nature*, 403:335–338, 2000.
105. T.S. Gardner, C.R. Cantor, and J.J. Collins. Construction of a genetic toggle switch in *Escherichia coli*. *Nature*, 403:339–342, 2000.
106. A. Becskei and L. Serrano. Engineering stability in gene networks by autoregulation. *Nature*, 405:590–593, 2000.
107. T.S. Shimizu, S.V. Aksенov, and D. Bray. A spatially extended stochastic model of the bacterial chemotaxis signalling pathway. *J. Mol. Biol.*, 329:291–309, 2003.
108. H.T. Hammel. Regulation of internal body temperature. *Annu. Rev. Physiol.*, 30:641–710, 1968.
109. S.A. Rubin. Core temperature regulation of heart rate during exercise in humans. *J. Appl. Physiol.*, 62:1997–2002, 1987.
110. W.R. Keatinge, A.C. Mason, C.E. Millard, and C.G. Newstead. Effects of fluctuating skin temperature on thermoregulatory responses in man. *J. Physiol.*, 378:241–252, 1986.
111. K. Shiraki, S. Sagawa, F. Tajima, A. Yokota, M. Hashimoto, and G.L. Brengelmann. Independence of brain and tympanic temperatures in an unanesthetized human. *J. Appl. Physiol.*, 65:482–486, 1988.
112. P. Webb. Temperatures of skin, subcutaneous tissue, muscle and core in resting men in cold, comfortable and hot conditions. *Eur. J. Appl. Physiol.*, 64:471–476, 1992.
113. R.K. Adair. Biophysical limits on athermal effects of RF and microwave radiation. *Bioelectromagnetics*, 24:39–48, 2003.
114. D. de Pomerai, C. Daniells, H. David, J. Allan, I. Duce, M. Mutwakil, D. Thomas, P. Sewell, J. Tattersall, D. Jones, and P. Candido. Non-thermal heat-shock response to microwaves. *Nature*, 405:417–418, 2000.
115. D.I. de Pomerai, B. Smith, A. Dawe, K. North, T. Smith, D.B. Archer, I.R. Duce, D. Jones, and E.P.M. Candido. Microwave radiation can alter protein conformation without bulk heating. *FEBS Lett.*, 543:93–97, 2003.

116. Y.L. Zhao, P.G. Johnson, G.P. Jahreis, and S.W. Hui. Increased DNA synthesis in INIT/10T_{1/2} cells after exposure to a 60 Hz magnetic field: a magnetic-field or a thermal effect? *Radiat. Res.*, 151:201–208, 1999.
117. B. Morrison, A. Shenkin, A. McLelland, D.A. Robertson, M. Barrowman, S. Graham, G. Wuga, and K.J. Cunningham. Intra-individual variation in commonly analyzed serum constituents. *Clin. Chem.*, 25:1799–1805, 1979.
118. M.G. Weyer and H. Lommel. *LONG I: Eine Longitudinal-Studie über individuelle Normbereiche, individuelle Standardbereiche, statistische Normbereiche für Prävention und Früherkennung*. Verlag Kirchheim, Mainz, 1981.
119. T.E. Vaughan and J.C. Weaver. Energetic constraints on the creation of cell membrane pores by magnetic particles. *Biophys. J.*, 71:616–622, 1996.
120. T.E. Vaughan and J.C. Weaver. Molecular change due to biomagnetic stimulation and transient magnetic fields: mechanical interference constraints on possible effects by cell membrane pore creation via magnetic particles. *Bioelectrochem. Bioenerg.*, 46:121–128, 1998.
121. P.L. McNeil. Cell wounding and healing. *Am. Sci.*, 79:222–235, 1991.
122. D. Bansal, K. Miyake, S.S. Vogel, S. Groh, C.C. Chen, R. Williamson, P.L. McNeil, and K.P. Cambell. Defective membrane repair in dysferlin-deficient muscular dystrophy. *Nature*, 423:129–131, 2003.
123. U. Valtersson, K. Hanssson Mild, and M.-O. Mattsson. Uncharacterized physical parameters can contribute more than magnetic field exposure to ODC activity *in vitro*. In F. Bersani, Ed. *Electricity and Magnetism in Biology and Medicine*, pp. 449–452, Plenum Press, New York, 1999.
124. R. Kavet, L. Zaffanella, J. Daigle, and K. Ebi. The possible role of contact current in cancer risk associated with residential magnetic fields. *Bioelectromagnetics*, 21:538–553, 2000.
125. R. Kavet, L.E. Zaffanella, R.L. Pearson, and J. Dallapiazza. Association of residential magnetic fields with contact voltages. *Bioelectromagnetics*, 25:530–536, 2004.
126. R. Kavet. Contact current hypothesis: summary of results to date. *Bioelectromagnetics*, suppl. 7:S75–S85, in press.
127. J.C. Weaver, Y. Chizmadzhev, Electroporation. In F.S. Barnes and B. Greenebaum, *Biological and Medical Aspects*, Eds. Taylor & Francis, Boca Raton, FL, [Chapter 9](#), 2006.

8

Biological Effects of Static Magnetic Fields

Shoogo Ueno and Tsukasa Shigemitsu

CONTENTS

8.1	Introduction	204
8.2	Mechanisms of Biological Effects of Static Magnetic Fields.....	204
8.3	Experimental Studies on Static Magnetic Field Effects	207
8.3.1	<i>In Vivo</i> Studies.....	207
8.3.1.1	Animal Behavior: Recognition and Analgesia	207
8.3.1.2	Reproduction and Development.....	210
8.3.1.3	Circulatory System Effects	212
8.3.1.4	Neuroendocrine, Visual, and Neurophysiological Systems	214
8.3.1.5	Magneto-Mechanical Systems.....	215
8.3.1.6	Musculoskeletal System.....	215
8.3.2	Tissue, Molecular, and Cellular Studies.....	216
8.3.2.1	DNA and Chromatin.....	216
8.3.2.2	Cell Growth, Cell Proliferation, and Cell Cycle	216
8.3.2.3	Cell Membrane and Cell Metabolic Activity.....	220
8.3.2.4	Gene Expression and Signal Transduction.....	221
8.3.2.5	Genotoxicity	222
8.3.2.6	Cell-Free System, Free Radical, Enzyme Activity	223
8.4	Miscellaneous	225
8.4.1	Biological Sensing and Magnetite	225
8.4.2	Plant Growth, Response, and Magnetotropism.....	227
8.4.3	Magnetotaxis.....	229
8.4.4	Others.....	230
8.5	Medical Applications	230
8.5.1	Biomagnetic Phenomena	230
8.5.2	Transcranial Magnetic Stimulation.....	232
8.5.3	Magnetoencephalography	234
8.5.4	Magnetic Resonance Imaging	235
8.5.5	Magnetic Orientation for Tissue Engineering.....	238
8.5.6	Treatments of Pain, Cancer, and Other Diseases	240
8.6	Conclusion	242
	Acknowledgments	243
	References	244

8.1 Introduction

In ancient times, magnetism, especially permanent magnets, were a symbol of mystique because of the magnetic force that remains even after numerous attractions of iron. Although William Gilbert was called the pioneer of modern magnetics, he was surprised by the magnetism associated with living organisms. Magnetism, in contrast to transient static electricity, has been used as an explanation for various invisible effects and is expected to possess miraculous healing powers. Although people have been using magnetism for healing purposes without any scientific evidence, there have not been significant problems concerning the side effects of magnetism. As permanent magnets have improved in quality and achieved higher magnetic strength, magnetism has become more commonly used in modern medicine. For example, magnetism is commonly used in the correction of dentures.

In the society today there are many sources of electromagnetic fields. Humans are exposed daily to man-made and naturally originated fields. During the past decade, questions about whether the exposure to electromagnetic fields may be linked to adverse health effects have been raised. Although the interaction of electromagnetic fields with biological systems has been investigated, there are no biophysical mechanisms that can explain many of the observed biological effects of low-level of magnetic fields. Proposed mechanisms include effects on currents, direct forces on biomagnetic materials, effects on free radicals, ion cyclotron resonance, charge transfer processes, stochastic resonance, etc.

Recent developments in medical instrumentation such as magnetic resonance imaging (MRI) and transcranial magnetic stimulation (TMS) have raised questions as to whether or not strong (in the tesla range) magnetic fields influence human health. Medical applications of weak (1–200 mT) magnetic fields for the purpose of pain reduction and tissue healing have also been studied for many years. Therapeutic applications of permanent magnets and other magnetic devices have recently been expanded to various areas such as treatment of pain and diseases like rheumatoid arthritis and cancer.

The objective of this chapter is to describe some of the more recent information on biological effects and medical applications of static magnetic fields. This chapter consists of four sections. Each section has a comprehensive review of a recent topic of interest. A short summary of the mechanism of static magnetic field action on biological systems is described in the second section, which includes a brief review of well-known mechanisms that are discussed before mentioning the interactions of weak static magnetic fields with biological systems. The third section reviews and summarizes more recent *in vivo* and *in vitro* experimental results of the effects of static magnetic fields, including near-zero magnetic fields, geomagnetic fields, and MRI fields. The fourth section covers special topics including magnetic sensing, magnetite, and plant response to magnetic fields. In parallel with the comprehensive review of biological effects, the development and medical application of the static magnetic field phenomena are introduced in the fifth section and reviewed with emphasis on the applications that are currently under investigation.

8.2 Mechanisms of Biological Effects of Static Magnetic Fields

The biological effects of static magnetic fields are not well understood. Magnetic fields exert a force on moving charged particles at right angles to both the field and the velocity, $\vec{F} = q\vec{v} \times \vec{B}$, where \vec{F} is the force, q is the charge, \vec{v} is the velocity, and \vec{B} is the magnetic flux density. In vacuum, the magnetic flux density is given by $\vec{B} = \mu_0 \vec{H}$, where \vec{H} is the magnetic field strength and μ_0 is the magnetic permeability of a vacuum. (In this section

we will be careful to distinguish between \vec{B} and \vec{H} , although in subsequent sections we will be less careful, using “magnetic field” as a general term that often is used to describe flux density.) Additionally, these fields exert a torque on particles with both fixed and induced magnetic dipole moments. This torque tends to align the dipoles along the magnetic flux density and is given by $\vec{T} = \vec{M} \times \vec{H}$ where \vec{M} is the magnetic dipole moment. For paramagnetic and diamagnetic materials, \vec{M} is proportional to the magnetic flux density. The magnetic susceptibility, χ , is given by the equation, $\vec{M} = \chi \vec{H}$, where \vec{H} is the local value of the magnetic field strength and χ is dimensionless. All materials may be mainly divided into three categories based on their susceptibility values. Materials with negative susceptibility are called diamagnetic. Materials with positive values are referred to as paramagnetic. Materials with large susceptibility include both ferro- and ferrimagnetic materials. Recognition of the role of diamagnetic, paramagnetic, and ferro- or ferrimagnetic materials in the body helps in the understanding the underlying mechanisms of biomagnetic effects.

Table 8.1 shows three types of well-known mechanisms of the biological effects of magnetic fields including time-varying magnetic fields. As shown in Table 8.1, there are two basic mechanisms of static magnetic fields: first, the magnetic torques on objects and second, the mechanical force effects. A radical pair mechanism is also proposed.

When biological materials or systems are exposed to a spatially homogenous magnetic field, they tend to rotate to a stable direction, which is determined by the anisotropy of magnetic susceptibility of the materials and magnetic torque acting on the materials, as described by the following equation:

$$T = -\frac{1}{2\mu_0} B^2 \Delta\chi \sin 2\theta$$

where B is the magnetic flux density, $\Delta\chi$ is the anisotropy of magnetic susceptibility of the materials, θ is the angle between the direction of the magnetic field and the long axis of the materials, and μ_0 is the magnetic permeability of a vacuum. The magnetic orientation of diamagnetic materials such as fibrin and collagen can be observed and explained by this principle (Torbet et al., 1981).

Next, when biological materials or systems are exposed to a spatially inhomogenous magnetic field, the materials or systems tend to move along the direction of the steepest

TABLE 8.1

Well-Known Mechanisms of the Biological Effects of Magnetic Fields

- | | | |
|--|--|--|
| 1. Time-varying magnetic field | | |
| Eddy currents $J = -\sigma \frac{B}{t}$ | Nerve stimulation | |
| Heat SAR = $\sigma \frac{E^2}{\rho}$ | Thermal effects | |
| 2. Static magnetic fields | | |
| a. Homogenous magnetic field | Magnetic orientation of biological cells | |
| Magnetic torque
$T = -\frac{1}{2\mu_0} B^2 \Delta\chi \sin 2\theta$ | | |
| b. Inhomogenous magnetic field | Parting of water by magnetic fields (Moses effect) | |
| Magnetic force
$F = \frac{\chi}{\mu_0} (\text{grad } B) B$ | | |
| 3. Multiplication of magnetic fields and other energy | Yield effect of cage product and escape product | |
| Photochemical reactions with radical pairs | | |
| Singlet-triplet intersystem crossing | | |

gradient of magnetic force. The magnetic force acting on the materials is proportional to the multiplication of the magnetic flux density B , the gradient of the magnetic flux density B (grad B), and the magnetic susceptibility χ of the materials, as described by the following equation:

$$F = \frac{\chi}{\mu_0} (\text{grad}B)B$$

where μ_0 is the magnetic permeability in a vacuum.

Dramatic demonstrations of these forces can be seen when water is parted by magnetic fields using magnetic field exposures of 4–8 T with a gradient of 50 T/m (Ueno and Iwasaka, 1994a,b). Magnetic levitation of diamagnetic materials such as wood and other organic materials, is realized in magnetic fields of more than 20 T (Beaugnon and Tournier, 1991). This phenomenon can also be explained by the principles of magnetic force.

Oxygen is a paramagnetic molecule, and its behavior under magnetic field gradients has an important role both as a gas and when dissolved in solution. The blockage and disturbance of gas flow by magnetic fields have been observed (Ueno and Harada, 1987). This phenomenon, called a magnetic curtain, can be explained by the action of magnetic force on a paramagnetic molecule. The magnetic curtain in this example is a wall of oxygen or air. Experimentation with this principle has demonstrated the quenching of burning candle flames (Ueno, 1989), where the interception of oxygen by the magnetic curtain has a quenching effect on the flames. As a second example, when a human subject is positioned inside a space shielded by the magnetic curtain, one may expect the respiratory function, evaporation of water molecules, body temperature, blood circulation, and other physiological functions to be disturbed or modulated.

The effect of static magnetic fields on water vaporization rate was investigated (Nakagawa et al., 1999). This study demonstrated that the water vaporization rate was found to be significantly influenced when both air and oxygen were in the presence of magnetic fields, and the observed effect was dependent on the field–field gradient product rather than on the B field itself. It should be noted that this magneto-enhancement of vaporization might be the indirect cause of certain physiologic effects on living organisms.

For example, skin temperature decreases in rats exposed to magnetic fields have been observed (Ichioka et al., 2003). This observation can be explained in terms of the effects of the magnetic field on air convection. That is, high magnetic field gradients (135–140 T²/m) push the diamagnetic water molecules toward the magnet bore. This increases the movement of water molecules in the air around the animal body and the vaporization rate. The heat of vaporization leads to a decrease in skin temperature. The decrease in the blood flow of the skin microcirculation is assumed to be a secondary change to the decrease in skin temperature.

Oxygen dissolved in water is also affected by magnetic fields. Changes in dissolved oxygen concentration were observed for magnetic field exposures on the order of 1 T (Ueno and Harada, 1982; Hirota et al., 2000; Kishioka et al., 2000). The changes in oxygen concentration are accelerated or regulated by gas transport of oxygen and water molecules inside and outside the water surface.

The magnetic field effects for large fields can be explained by these well-known mechanisms. With ever-increasing evidence indicating that weak static magnetic fields have profound effects on biological systems, a number of mechanisms for the action of these static magnetic fields, including geomagnetic fields, on biological systems have been proposed.

Possible biomagnetic and chemical effects can be expected when biological systems are exposed to both static magnetic fields and other forms of energy such as light and

radiation (Ueno and Harada, 1986). Photochemical reactions produced by a radical pair intermediate can be expected to show magnetic field effects that arise from an electron Zeeman interaction, electron-nuclear hyperfine interaction, or a hyperfine interaction mechanism including an electron-exchange interaction in a radical pair intermediate (Hata, 1976; Schulten et al., 1976; Tanimoto et al., 1976; Nagakura and Molin, 1992; Natarajan and Grissom, 1996; Hayashi, 2004).

The magnetic field effect observed with radical pair recombination is one of the well-known mechanisms by which magnetic fields interact with biological systems. Throughout the past decades there have been several experimental results describing the effects of magnetic fields on radical pair recombination. Mohtat et al. (1998) examined the behavior of radical pairs derived by hydrogen abstraction of triplet benzophenone and some of its derivatives from bovine serum albumin, human serum albumin, and calf thymus DNA. The magnetic field strength was as high as 150 mT with durations as long as 10 μ s. This result indicated that radical pair behavior is sensitive to magnetic fields, and this effect can be interpreted by using the theory of free radical recombination. Using the triplet state of benzophenone as a convenient source of pairs, Eveson et al. (2000) examined the effects of weak (>1 mT) magnetic fields on radical recombination reactions in micelles. They found that the concentration of free radicals escaping from the micelle was both affected and depended on the conditions surrounding the radical pair.

Timmel and Till discussed the weak magnetic field effects on free radical recombination reactions (Till et al., 1998; Timmel et al., 1998). Vink and Woodward (2004) described the effects of a weak magnetic field, 21 mT, on the recombination reaction of neutral free radicals in isotropic solution.

Ritz et al. (2002) reviewed the physiological basis of animal magnetoreception. They suggested that there was a link between photoreception and magnetoreception, from their findings in behavioral and theoretical studies. Migratory birds have the ability to sense the geomagnetic field and use it as a source of compass information. The candidates for a biophysical mechanism of this magnetoreception are magnetite and magnetically sensitive chemical reactions in animals. Ritz et al. (2000) postulated the possibility that magnetoreception involves radical pair processes as a biophysical mechanism.

8.3 Experimental Studies on Static Magnetic Field Effects

This section focuses on *in vivo* and *in vitro* studies of the effects of static magnetic fields. It covers the field effects observed on behavior, the cardiovascular system, reproductive system, cellular and tissue development, the neuroendocrine system, and the magneto-mechanical system, utilizing molecular, cellular, tissue, and cell-free systems.

8.3.1 *In Vivo* Studies

8.3.1.1 Animal Behavior: Recognition and Analgesia

Scientific interest in behavioral changes has led to the development of a psychology of learning that studies the effects of various external stimuli, and this research has further led to the development of behavioral pharmacology to observe the effects of drugs on the central nervous system. There have been several investigations for studying the effects of magnetic fields on behavior and the central nervous system using techniques developed

specifically in these research fields. Behavioral research directed toward the effects of magnetic exposure of living organisms mainly addresses two questions: whether magnetic fields are sensed and avoided and whether magnetic fields have any influence on the functions of leaning and memory. Magnetic field experiments designed to address both questions have been conducted using several indicators, such as open-field behavior, operant behavior, and spontaneous motor activity, as tools of observation and measurement. (See also Chapter 4 on behavioral effects by Johnston and D'Andrea.)

8.3.1.1.1 *Animal Behavior and Recognition*

Nikolskaya et al. (1996) investigated the influence of inhomogeneity of natural magnetic fields on rat cognition with regard to whether or not magnetic fields could serve as an informational factor for cognition. Under three natural magnetic field conditions, $37 \pm 2 \mu\text{T}$ (condition 1; horizontal component (N–S) is $14 \mu\text{T}$, and vertical $34 \mu\text{T}$), $16\text{--}118 \mu\text{T}$ (condition 2), and $55\text{--}240 \mu\text{T}$ (condition 3), rats were subjected to a food-operant behavior study. All rats in conditions 2 and 3 were unable to form operant behavior, while rats in condition 1 demonstrated the behavior. Using the combination of an original behavioral model and a multiple alternative maze, an impact of Opilong, which is an analog of dermorphine and μ -receptor agonist, on rat sensitivity to $38 \pm 2 \mu\text{T}$, in the static magnetic field has been investigated by the same authors (Nikolskaya et al., 1999). They concluded that chemical modulation of the opioid system in rats induced both an increased magnetic field sensitivity and an allowed perception of magnetic field parameters. In the following study (Nikolskaya and Echenko, 2002), it was reported that cognitive activity in the natural magnetic field of $38 \mu\text{T}$ caused an increase of ethanol intake in 34.8% of rats.

During the 1980s, Liboff (1985) argued favorably for the combined effects of static (DC) with extremely low-frequency (ELF) magnetic fields (see also Chapter 9 resonance phenomena by Liboff on). A surprising effect was observed at the ELF magnetic field frequency close to the cyclotron frequency of a calcium ion. Thomas et al. (1986) reported the disruption of operant behavior in rats after exposure to low-intensity magnetic fields. The protocol developed by them in the report has been reexamined by Stern et al. (1996) in a two-part experiment. In the first part, the vertical component of the static field was reduced to $0.0261 \mu\text{T}$. In the second part, both the horizontal and the vertical components were matched to those used by Thomas et al. The results obtained in these experiments were found to be inconsistent with the results reported by Thomas et al. Effects of the combination of static (DC) and AC magnetic fields at the cyclotron frequency on rat open-field behavior have been investigated (Zhadin et al., 1999). Levels of locomotor and exploratory activities were decreased after exposure to DC and AC magnetic fields at the calcium cyclotron frequency, whereas field exposure at the magnesium cyclotron frequency increased levels of these activities.

Studies have been conducted to determine whether rats could acquire a two-choice discrimination based on a specified discrimination stimulus (Creim et al., 2002). The specified discriminative stimulus used in this study was tested both in ambient illumination as well as in a combination of an oscillatory field of $50 \mu\text{T}$ at 60 Hz and a static field of $26 \mu\text{T}$. The results demonstrated that rats were able to discriminate between two-choice tasks easily during the period of changing illumination and that the presence or absence of the static and oscillatory fields had no observed effect on these findings.

Tsuji et al. (1996) evaluated physiological consummatory behavior by observing intakes of food and water and changes in the body weight using BALB/c mice exposed to magnetic field levels of 5 T for a period of 24 and 48 h . Exposure to a 5-T magnetic field for 48 h suppressed eating and drinking behavior. The decreased body weight, the increased blood urea nitrogen (BUN) level, and the slightly increased BUN–Cr ratio

observed in this experiment might be attributed to the loss of body fluid secondary to decreased food and water intake.

For the purpose of observing changes caused by magnetic field exposure, MRI systems and application of their high-strength static magnetic fields have been useful and widely used to obtain intact images. There have been three reports describing the behavioral effects observed as a result of high-strength static magnetic field exposure of rats and mice. Using a conditioned taste aversion technique, it was shown that rats developed a conditioned taste aversion after exposure to a high magnetic field of 9.4 T for 30 min (Nolte et al., 1998). Following this report, similar experiments were carried out. Restrained rats and both unrestrained and restrained mice were exposed to magnetic fields of 7 and 14 T generated by superconducting magnets (Houpt et al., 2003). In the report, it was found that exposure of rats to high magnetic fields suppressed rearing and locomotor circling and induced conditioned taste aversion and expression of c-Fos in vestibular nuclei. The rat's orientation in magnetic fields is a key factor for the direction of circling. Similar results were obtained with mice (Lockwood et al., 2003). All tested mice showed development of conditioned taste aversion, and a significant number showed tight circling and rearing suppression. Effects were observed more significantly in unrestrained mice than in restrained mice. Snyder et al. (2000) have identified brain stem regions that were activated by exposure to static magnetic field levels of 9.4 T for 30 min, of restrained rats, by using a c-Fos immunohistochemistry detection assay. Increased expression of c-Fos and neural activation in visceral and vestibular nuclei by magnetic field exposure have been reported. It has been suggested that the neural activation response might be a factor in promoting conditioned taste aversion learning.

Superconducting high magnetic field exposures of 7 T have been reported to have reduced the trehalase enzyme activity in honey bees (Kefuss et al., 1999). There were no changes found in the level of fatty acids, triacylycerols, and steroids in this study.

8.3.1.1.2 Analgesia

Effects of a hypogeomagnetic environment with a flux density of 4 μT inside a Mu-metal box on stress-induced analgesia in C57 male mice have been investigated (Del Seppia et al., 2000). This study consisted of three consecutive parts: (1) maintaining the mice under various magnetic exposure conditions: hypogeomagnetic, altered magnetic field, and Earth's geomagnetic field of 46 μT for 90 min; (2) immobilizing the animals in a tube for 30 min under each exposure condition; and (3) recording nociceptive responses of the restraint-stressed mice as the latency of front-paw lifting to hot-plate stimulus. Stress-induced analgesia was significantly reduced in the animal group exposed to the hypogeomagnetic field, and this result was comparable with that in the mice exposed to altered magnetic fields or treated with prototypic opiate antagonist naloxone. It has been suggested that the exposure period in a hypogeomagnetic environment might be responsible for the inhibition of stress-induced analgesia. They also demonstrated that exposure to altered magnetic fields induce more rapid habituation to a novel environment (open field) (Del Seppia et al., 2003). The experiment was carried out to investigate effects of irregularly varying (<1 Hz), 20–70- μT or regular 37-Hz, 80- $\mu\text{T}_{\text{p-p}}$ magnetic fields with a 2-h exposure of mice. The nociceptive response was measured by a hot-plate test and showed that the nociceptive sensitivity was significantly greater in magnetically treated mice than in controls.

Various sensing-transduction mechanisms have been proposed to explain the biological effects of magnetic fields. Prato et al. (1996a) showed inhibitory effects of 60-Hz magnetic fields at levels of $299 \pm 1 \mu\text{T}_{\text{p-p}}$ and static magnetic fields at levels of $78 \pm 1 \mu\text{T}$ on opioid-mediated analgesia in the land snail, *Cepaea nemoralis*. It has been reported that

the effects were dependent on the relative direction of both the weak static and the 60-Hz magnetic field, as well as on the presence of light. In a following study, indirect and direct mechanisms of ELF magnetic fields on an endogenous opioid peptide-mediated analgesic response have been proposed. It was shown that the energy transduction mechanism did not involve induced electric currents or magnetite (Prato et al., 1996b), and the results indicated that a direct magnetic field detection mechanism was consistent with the parametric resonance model. In a later study to reexamine the results obtained and further clarify the role of light, it was found that reduction of the opioid-induced analgesia by magnetic field exposure was enhanced by the presence of light. It was reported that the reduction rate of analgesia was not dependent on ELF frequency; however, the effect of the ELF magnetic field was in fact mediated by direct magnetic field detection.

In order to detect static magnetic field-induced functional changes in brain tissue, Veliks et al. (2004) carried out an investigation to identify the effects of static magnetic fields on rat brain structures using heart rate and heart rhythm as physiologic indicators. Rats put under ketamine-xylazine anesthesia were exposed to magnetic field levels of 100 mT for 15 min. Before and after the exposure, an electrocardiogram was recorded for analysis of heart rate and heart rhythm. Static magnetic fields were found to evoke changes in both heart rate and heart rhythm in 80% of the subject animals.

McLean et al. (2003b) examined the effects of inhomogenous static magnetic fields, alone or in combination with the chemical agent phenytoin (PHT), on audiogenic seizures (AGS) in DBA/2 mice. In experimental studies where the static magnetic fields ranged from 0.26 to 10.5 mT, with a field gradient ranging between 0.012 and 0.48 T/m, seizure severity decreased as the magnetic flux density and exposure duration period increased. It was found that the magnetic field pretreatment enhanced the effect of PHT, and it was also found that a static magnetic field alone had some anticonvulsant effects as well. Further investigation is required to clarify the anticonvulsant effects of magnetic fields in AGS.

8.3.1.2 Reproduction and Development

The effects of static magnetic fields, including MRI fields (static, gradient, and RF), on fertility, the developing embryo, and the fetus have been investigated. There have been a series of reports describing the effects of 10- and 35-day exposures to a magnetic field level of 0.7 T on mice, in terms of sperm motility, maturation, and production and morphological and developmental changes (Tablado et al., 1996, 1998, 2000). In the first report, mice were exposed to a magnetic field level of 0.7 T for time periods between 1 and 24 h/d, over 35 d. It was found that sperm motility, maturation, and production were not affected. Two years later, it was reported that the size of sperm heads was still intact; however, the animals that had undergone continuous exposure demonstrated increased sperm head abnormality. In a study by Tablado et al. of magnetic effects during developmental changes, experiments were carried out to investigate the *in utero* exposure effects from magnetic field levels of 0.5 to 0.7 T on testis and epididymis development in mice. After mating, female mice were exposed from day 7 of gestation until the day of birth. Results showed that there were no significant differences between exposed and sham-exposed animals in terms of body weight gain of dam, litter size, body weight of male pups, and testis–epididymus weight gain of pups up to 35 d of age. In addition, there were no detectable changes found during a histopathological evaluation of the testis and epididymis of pups.

Narra et al. (1996) reported the biological effects of a static magnetic field on spermatogenesis and embryogenesis in Swiss Webster mice. Male and pregnant female mice were exposed to a magnetic field level of 1.5 T for 30 min. There was no increase in sperm head shape abnormality and no reduction in testicular sperm numbers; however, a decreased survival rate of preimplantation embryos was indicated.

It has been reported that there were no harmful effects detected in a static magnetic field of 4.7 T on ICR mice (Okazaki et al., 2001). Pregnant ICR mice were exposed to the field from days 7.5–9.5 of gestation and sacrificed on day 18.5 of gestation. There were no significant differences in the incidence of prenatal death or malformations between the exposed and control groups. The investigation has been conducted for potential adverse effects of a 10-week exposure to a 9.4-T magnetic field on the development of male and female rats as well as their offspring (High et al., 2000). All rats were exposed to 9.4 T for 3 h twice a week with an intermittent duration of 5 week on, 2 week off, and 5 week on. The results demonstrate hematological, biochemical, pathological, and behavioral changes in both adults and their offspring; however, there were no adverse effects observed in either male or female adult rats, as well as in their offspring.

Effects of long duration and high magnetic field exposure on fetal growth and postnatal development in mice have been investigated (Magin et al., 2000). One group of mice was exposed for 9 h on day 9 or on day 12 postcoitus (or both) to MRI conditions (static magnetic field of 4 T with 5-T/s gradient and whole-body SAR of 0.2 W/kg at 170 MHz). A second group was exposed to a combination of ultrasound and MRI fields. There were no significant changes in fetal growth in animals exposed to MRI or ultrasound fields individually. The average fetal weight of animals exposed to combined fields was lower than that of the other group. Carnes et al. (1996) investigated the effects of static magnetic field levels of 4.7 T, which is equivalent to the level used in MRI, on fetus, adult growth, and testicular development in mice. The 8-h exposure was carried out on day 9 or day 12 of gestation (or both). Effects of the combined application of 1 MHz ultrasound on day 9 and MRI on day 12 was also investigated. The average fetal weight of the exposed groups was found to be less than that of the control groups. It was found that the postpartum death rate was higher after the MRI exposure, and sperm production was reduced; however, no changes were detected in embryonic death rate, sex ratio, body weight at day 50, spleen weight, and seminal vesicle weight.

Jove et al. (1999) studied the effects of static magnetic field levels of 18 and 36 mT on the development of chick embryo, including the pineal gland. They found that static magnetic fields affected the development and growth of embryos, and this effect was dependent not only on the intensity but also on the length of exposure time. Ruggiero et al. (2004) reported the effects of a 3-h exposure to a magnetic field level of 0.2 T generated by a clinically used MRI system on the angiogenesis of chick embryo. Angiogenesis was evaluated using a chick embryo chorioallantoic membrane assay. Results indicated that static magnetic field exposure inhibited angiogenesis in chick embryo. Effects of a uniform static magnetic field of 29 mT on cell migration and differentiation in the cerebellum of chick embryo have been studied (Espinar et al., 1997). The cerebella of chick embryos was exposed to the magnetic field on 6 d of incubation and sacrificed at day 13 of incubation. Results showed that static magnetic field exposure could induce irreversible developmental effects on cell migration and differentiation. Clear signs of cell degenerations and delay in the process of neuronal differentiation were indicated.

There have been a series of reports describing the effects of static magnetic field on fish embryos (Formicki and Winnicki, 1996, 1998; Winnicki et al., 1996; Formicki et al. 1997; Formicki and Perkowski, 1998). First, it was reported that during a prolonged transportation of fertilized salmonid eggs and trout (*Salmo trutta* L. and *Oncorhynchus mykiss*), a magnetic field of 4 mT lowered the mortality rate and enhanced the conservation condition (Winnicki et al., 1996). Effects of static magnetic fields ranging from 50 to 70 mT on the cardiac muscle activity of carp (*Cyprinus carpio* L.) embryos and larvae have been investigated (Formicki and Winnicki, 1996). An increase in heart rate was observed after exposure to these fields. Effects from both the strength and the direction of the geomagnetic field and static magnetic fields of 0.5 and 1 mT on the orientation of trout embryo

(*S. trutta*) and rainbow trout (*O. mykiss*) have also been investigated. Results have shown that the embryos were sensitive to the static magnetic fields, with a preference for a certain field direction. Further investigation has been conducted to clarify the response of fish embryos and larvae from the same type of trout to a static magnetic field (Formicki and Winnicki, 1998). Eggs were placed in magnetic fields during the period from fertilization to hatching. The exposure of eggs resulted in slower embryonic development; thus, eggs were incubated for a prolonged period of time. Embryos of rainbow trout (*O. mykiss*) and trout (*S. trutta*) exhibited orientation both in the natural magnetic field and in artificial magnetic fields of 0.5 and 1 mT. In a supplementary paper, Formicki and Perkowski (1998) showed the effects of static magnetic fields of 5 and 10 mT on the gas exchange in rainbow trout (*O. mykiss*) embryos. An increase of oxygen uptake was observed. It was determined that the impact of magnetic field exposure on the respiratory system was significant in the periods of advanced morphogenesis.

It has been reported that the exposure to static magnetic fields of 10–100 mT could alter the early embryonic development in two species of sea urchin embryo, *Lytechinus pictus* and *Strongylocentrotus purpuratus* (Levin and Ernst, 1997). Results suggested that static magnetic fields delayed the onset of mitosis in both species. A static magnetic field of 30 mT caused an eightfold increase in the incidence of exogastrulation in one species. Static magnetic field effects of 4 and 8 mT and effects of exposure to 60-Hz AC magnetic fields of 6 and 8 mT on the first division of two sea urchin embryos, *Sphaerechinus granularis* and *Paracentrotus lividus*, have been studied (Pagnac et al., 1998). No differences were found in the time of the first cleavage in both exposures.

In a static magnetic field of 35 mT, the fruit fly (*Drosophila melanogaster*) was reared through several generations to investigate the width and length variability of both wings (Stamenkovic-Radak et al., 2001). In the second-generation exposure, there was a significant difference between sexes in the context of directional change of wing size variability. In the sixth generation, the differences in wing size between the magnetic field exposure group and control groups showed the same directional pattern in both sexes. Pan and Liu (2004) reported the effects of high static magnetic fields of 9.4 and 14.1 T on the hatching behavior of fresh mosquito eggs. Hatching was delayed, and the delay time depended on the intensity of the magnetic field.

Effects of exposure to high static magnetic field with levels up to 16.7 T on the first three cleavages of *Xenopus laevis* embryos have been investigated (Denegre et al., 1998). Results have indicated that cleavage furrows aligned parallel to the magnetic field. The most significant effects on the second and third cleavages have been observed in homogenous fields, not in the gradient fields. It has been suggested that this phenomenon was caused by interactions between the magnetic fields and the diamagnetic materials in the *Xenopus* embryo. Further studies have shown that after exposure to static magnetic fields of 17–22 T during either or both of the first two cell cycles, the third cell cycle mitotic apparatus at metaphase could be induced, and the third cleavage furrows aligned perpendicular to their nominal orientations (Valles, 2002; Valles et al., 2002). Valles et al. (1997) investigated the magnetic field gradient levitation (MFGL) as a technique for simulating low gravity for biological systems. They levitated living biological specimens, embryos of the frog *X. laevis*, using a large inhomogenous magnetic field. MFGL of embryos reduced the body forces and gravity-induced stress on them.

8.3.1.3 Circulatory System Effects

Recently, effects of static magnetic field applications on the circulatory system have been reviewed in experimental animals (Tenforde, 2005) and in humans (Chakeres and de Vocht, 2005; Crozier and Liu, 2005; van Rongen, 2005). Most of the studies have been

related to MRI systems, and it has been reported that in MRI-related studies using strengths of up to 8 T, there were little or no significant changes in cardiovascular and circulatory parameters. In contrast, it was found that moderate-intensity static magnetic fields ranging from 1 to 350 mT can have significant circulatory system effects, most notably on cutaneous microcirculation and arterial blood pressure.

8.3.1.3.1 Microcirculation

Ohkubo and Xu (1997) studied the acute effects of 1–10-mT static magnetic fields applied for 10 min on the microcirculatory changes in conscious rabbits using a rabbit ear chamber (REC) and microphotovoltaic plethysmography (MPPG). The static magnetic fields induced biphasic changes in vasomotion in a non-dose-dependent manner. Static magnetic fields suppressed vasomotion when the vascular tone was high, while the same level fields enhanced vasomotion when the tone was low. To clarify these effects, the same group, Okano et al. (1999), investigated the effect of a 1-mT static magnetic field for 10 min on microcirculation in conscious rabbits using pharmacological manipulation together with REC and MPPG. The results showed that the static magnetic field enhanced vaso-dilatation and increased vasomotion under norepinephrine, which induced high vascular tone and, in contrast, induced vasoconstriction and decreased vasomotion under acetylcholine, which induced low vascular tone.

These studies are strongly supported by another independent study that examined the effect of a moderate-intensity static magnetic field on microcirculation, suggesting that the static magnetic field could modulate the biphasic responses of relatively smaller-diameter blood vessels (arterioles). Morris and Skalak (2005) studied the acute effect of a 70-mT static magnetic field for 15 min on the diameter of microvessels in rat skeletal muscle placed under pentobarbital anesthesia, using intravital microscopy. This study suggested that the static magnetic field could modulate microvascular tone in a restorative fashion, thereby acting to normalize the tone.

Gmitrov and colleagues reported the acute effects of 250–350 mT static magnetic field exposures for a time period of up to 80 min on microcirculation within cutaneous tissue of the rabbit ear lobe placed under pentobarbital anesthesia using REC and MPPG (Gmitrov and Ohkubo, 1999a,b; Gmitrov et al., 2002). They demonstrated that application of static magnetic fields to the carotid sinus baroreceptor region for a period of 65–80 min increased microcirculation. The static magnetic fields suppressed or recovered a Ca^{2+} channel blocker, verapamil, which reduced microcirculation.

Xu et al. (1998) observed the subchronic effects of a 180-mT static magnetic field, with length of exposure times for up to 4 weeks, on cutaneous microcirculation in conscious rabbits, using REC and MPPG. The static magnetic field significantly increased the long-lasting vasodilatation and enhanced the vasomotion. The same authors found that exposure to static magnetic fields at 1 mT or higher for 10 min enhanced microcirculation and increased peak blood velocity (Xu et al., 2000).

Mayrovitz et al. (2001, 2005) investigated the effects of static magnetic fields with strengths as high as 100 mT and exposure periods of up to 36 min on skin blood flow in humans, using a laser-Doppler flowmeter. They showed that the static magnetic fields have no significant effect on the normal, unstressed circulation or vasoconstrictive response in conjunction with skin temperature. Steyn et al. (2000) also indicated that there are no effects observed on blood flow in horses after exposure to static magnetic fields.

In a series of studies that observed the effects of ultrastrong (>5 T) static magnetic field exposure, Ichioka et al. (1998, 2000) investigated the acute effect of an 8-T static magnetic field exposure for a period of 5 min on blood flow in rat by using a laser-Doppler flowmeter and thermistor-derived measurements. They demonstrated that blood flow

and skin temperature decreased during the field exposure, through the movement of water vapor over the animal and the decreased humidity in the air.

8.3.1.3.2 Blood Pressure

Gmitrov and colleagues studied the influence of both a 350-mT static magnetic field and geomagnetic field activity on mean arterial blood pressure (MAP) in pentobarbital-anesthetized rabbits (Gmitrov and Ohkubo, 2002; Gmitrov et al., 2002). Application of the static magnetic field to the baroreceptor region for 65–80 min decreased MAP. In testing geomagnetic field applications, they found that there was a positive correlation of this field's activity with MAP, and this result implied that magnetic storms could increase the incidence of severe cardiovascular events.

Okano and Ohkubo (2001) examined the acute effect of a 1-mT static magnetic field applied for 30 min on pharmacologically altered blood pressure in conscious rabbits. It was found that (1) the static magnetic field reduced the vasodilatation effect from enhanced vasomotion and antagonized the reduction of blood pressure under a Ca^{2+} channel blocker, nicardipine, which induced low vascular tone, and (2) the static magnetic field attenuated vasoconstriction and suppressed the elevation of blood pressure while under the influence of a nitric oxide (NO) synthase inhibitor, L-NAME, which induced high vascular tone. However, two of their experiments, which were carried out under normal conditions without pharmacological drugs, showed that static magnetic fields did not induce any significant effects on hemodynamics and blood pressure (Okano and Ohkubo, 2001, 2003a). With regard to these undetectable effects, Muehsam and Pilla (1996) speculated that physiologically significant bioresponses to therapeutic signals appear to occur only when the physiologic state of the target system is far from homeostasis.

In contrast to the experiments done without pharmacological manipulation, Okano and Ohkubo (2003a) found that exposure to a 5.5-mT static magnetic field for 30 min caused the suppression of norepinephrine- or L-NAME-induced vasoconstriction and hypertension in rabbits. Furthermore, they tested exposures of 5–10-mT static magnetic fields for a period of several weeks on the development of hypertension in spontaneously hypertensive rats (Okano and Ohkubo, 2003b; Okano et al., 2005a). Experimental results indicated that the static magnetic fields suppressed and retarded the development of hypertension because of the reduction in plasma levels of both angiotensin II and aldosterone together with lower levels of NO metabolites (NO_x).

In addition, the antihypotensive effects of static magnetic fields on reserpine-induced hypotensive rats were investigated (Okano et al., 2005b). The result suggested that exposure to a 25-mT static magnetic field for several weeks suppressed the reserpine-induced hypotension and bradykinesia through the inhibition of norepinephrine depletion.

Saunders (2005) commented that most of these studies were undertaken in the context of the potential therapeutic effects of static magnetic field on various disorders. Further studies with some independent replications are required even if the effects of static magnetic field on both blood flow and blood pressure indicate possible medical applications.

8.3.1.4 Neuroendocrine, Visual, and Neurophysiological Systems

Effects of static magnetic field exposures of 0.05 μT to 80 mT, and 7 T on the level of melatonin in rat have been examined (Kroeker et al., 1996). The first experimental exposure using field strengths of up to 80 mT for 12 h/d and 8 d showed no significant changes in night-time pineal and serum melatonin levels, as did the second experimental exposure using 7 T for 45 min. The visual system of the fruit fly (*D. melanogaster*) was

investigated after an exposure to a zero magnetic field (Creanga et al., 2002). Adults from pupae maintained in a zero magnetic field for 20 h were used for the electroretinogram. A significant increase in sensitivity of neural cells from the first optic ganglion was indicated.

Osuga and Tatsuoka (1999) tested the effects of a 1.5-T static magnetic field by using an MRI system application on neuroconduction in a partially active nerve in the bullfrog (*Rana catesbeiana*). The action potential and nerve impedance measurements indicated that a field strength of 1.5 T had no effect on neuroconduction; therefore, it was determined that neuroconduction in damaged nerves was not affected by the exposure.

8.3.1.5 Magneto-Mechanical Systems

Testorf et al. (2002) studied the influence of homogenous static magnetic fields of 8 and 14 T on melanophore aggregation in black tetra (*Gymnocorymbus ternetzi*). The result showed no significant field effects on the aggregation after exposure to magnetic fields.

Effects of a 0.2-T static magnetic field on a normal human neuronal cell culture, FNC-B4, has been investigated with MCF-7 and WEHI-3 cells as controls (Pacini et al., 1999b). FNC-B4 cells changed their morphology after the exposure. Cells became elongated and formed vortices, while controls did not show any alteration. The morphological changes in MRC-5 fibroblasts were evaluated as well (Pate et al., 2003). The cells were screened for cell mobility, cell distribution, and cellular morphology (size, shape, lysis, and background). These cells were exposed to both a static magnetic field and a pulsating magnetic field for a period of 0, 24, 48, and 72 h. Although the static magnetic field-exposed cells showed cell membrane damage and morphological change, as well as other interesting findings that were included in the report, this report may not be useful because it did not provide essential dosimetric data, such as strength of the field.

Danielyan et al. (1999) examined the effects of a 0.2-T static magnetic field on binding of ouabain-H³, which is a specific inhibitor of Na⁺-K⁺-ATP-ase, in normal glandular breast tissue and in cancerous breast tissue. The static magnetic field-induced decrease of binding was considered as evidence for the dehydration effect of the field. This study has indicated that the static magnetic field tested could influence the cancer cell's metabolism through cell hydration changes. They investigated the effects of a 0.2-T static magnetic field on the hydration of rat tissues (Danielyan and Ayrapetyan, 1999). They assumed that the target for magnetic field action was the structured water of the cell. Decreases in hydration and adaptation of brain, liver, and spleen and an increase in the case of kidney were observed.

8.3.1.6 Musculoskeletal System

Yan et al. (1998) investigated the effects of static magnetic fields on bone formation of rat femurs. They implanted magnetized samarium cobalt rods with a field strength of 180 mT into rat femurs. The bone mineral density (BMD) and bone calcium content were measured 12 weeks after implantation. Results indicated that the femurs adjacent to the magnetized specimens had significantly higher BMD and calcium content. However, BMD and calcium content levels were found to be normal in both magnetized and unmagnetized specimen groups. The same research group further studied the effects of a 180-mT static magnetic field on bone formation, using an ischemic rat femur model (Xu et al., 2001). It was reported that the enhancement of the femoral bone formation was due to the improved blood circulation in the femur.

Satow et al. (2001) observed the effect of a 0.65-T static magnetic field on muscle tension in the neuromuscular preparation of the sartorius muscle of bullfrog (*R. catesbeiana*). The

tension development was obtained by stimulation of the sciatic nerve or of the sartorius muscle itself for a duration of 30 min. A decrease in muscle tension was observed. The results indicated that application of the static magnetic field was responsible for tension development.

8.3.2 Tissue, Molecular, and Cellular Studies

8.3.2.1 DNA and Chromatin

The exposure of isolated rat lymphocytes to a static magnetic field of 7 mT for 3 h did not increase the number of damaged cells (Zmyslony et al., 2000). Although incubation with 10 µg/ml FeCl₂ did not cause DNA damage, the number of damaged cells increased when the FeCl₂-incubated lymphocytes were simultaneously exposed to the field. A hypothesis for these observations was that the number of reactive oxygen species generated by iron ions in cells might increase after the exposure to the magnetic field (Jajte et al., 2002).

Binhi et al. (2001) have reported the effect of a weak static magnetic field on *Escherichia coli* K12 AB1157 cells, by using anomalous viscosity time dependence (AVTD) assay methods. The AVTD changes were found when the cells were exposed to static magnetic field levels up to 110 µT. These results were consistent with the calculations of individual rotations of the ion–protein complexes Ca²⁺, Mg²⁺, and Zn²⁺, provided that all complexes rotated at the same speed. They suggested that the rotation for all ion–protein complexes is on the same carrier, such as DNA.

The effect of a zero magnetic field on the conformation of chromatin in human VH-10 fibroblasts and lymphocytes was investigated by the AVTD method (Belyaev et al., 1997). A decrease in the AVTD peaks was observed within 40–80 min of exposure to fibroblasts, and this decrease was transient, disappearing 120 min after the beginning of exposure. A similar effect of zero field was observed when cells were exposed for 20 min and kept at an ambient field. They concluded that both zero field and γ-rays caused hypercondensation and decondensation of chromatin. Zero field effects were more significant in the beginning of the G₁-phase than in the G₀-phase in human lymphocytes.

Okuda et al. (1998) evaluated the effects of a 6.34-T static magnetic field on the instability of microsatellite repetitive sequences in DNA mismatch repair (MMR)-proficient and MMR-deficient cell lines, HeLa S3, and HCT116, respectively. After exposure to the field, both cell lines exhibited no significant microsatellite sequence changes. This result suggested that the static magnetic field might not induce the genetic changes in microsatellite sequences.

8.3.2.2 Cell Growth, Cell Proliferation, and Cell Cycle

Potenza et al. (2004b) showed that *E. coli* cell growth and gene expression were affected by a static magnetic field exposure level of 300 mT. Cell proliferation at the stationary phase was increased by exposure to those cells growing in a modified medium culture containing glutamic acid; however, cell proliferation was not affected in those cells growing in traditional Luria–Bertani (LB) medium. Gene expression differences were estimated by differential display assays using arbitrary primers, and four genes were found to be responsive to the static magnetic field. One clone, expressed only in the exposed cells, corresponded to a putative transposase. Potenza et al. suggested that the static magnetic field exposure might stimulate transposition activity.

Stansell et al. (2001) reported that antibiotic (piperacillin) resistance of the clinically isolated *E. coli* was increased by the heterogenous static magnetic field exposure level of

8–60 mT for 45 min. They suggested the observation may be unique to the particular strain of *E. coli* or the specific antibiotic used. They did not suggest any mechanistic implication for this observation.

Poia et al. (2003) reported zero magnetic field effect on the antibiotic resistance of *E. coli* strains isolated from human subjects. They used 26 *E. coli* strains and 5 different antibiotics, ampicillin, ceftazidine, tetracycline, ofloxacin, and kanamycin. Approximately one third of the tested strains was sensitive to the zero field treatment. Minimum inhibitory concentrations (MICs) of each antibiotic for some strains were decreased by zero magnetic field exposure, while the MICs for other strains were increased by the exposure. Their mechanistic hypothesis, based on magnetic particles, did not support these observations.

Ruiz-Gomez et al. (2004) showed that growth of the haploid yeast strain *Saccharomyces cerevisiae*, a eukaryotic cell, was not affected by exposure to static magnetic field levels of 0.35 and 2.45 mT.

Effects of a 0.2-T static magnetic field, generated by MRI alone or in combination with vitamin D treatment, on cell damage and proliferation in the human breast cancer cell MCF-7, human neuronal cell FNC-B4, and murine leukemia cell WEHI-3 have been investigated (Pacini et al., 1999a). Three-hour exposures to the 0.2 T field had no effect on the cell colony formation number in all three cell lines. Results demonstrated that [³H] thymidine incorporation level decreased in MCF-7 and FNC-B4 cells, while no changes were observed in WEHI-3. It was also demonstrated that the treatment of cells using vitamin D had a permanent antiproliferative effect.

Long-term effects on proliferation of human fetal lung fibroblast (HFLF) cells of repetitive exposure to a 1.5-T static magnetic field with exposure periods of 1 h/d for 3 weeks have been investigated (Wiskirchen et al., 1999). Results showed no changes in clonogenic activity, DNA synthesis, cell cycle, and proliferation kinetics. In a following paper, effects of static magnetic field levels of 0.2, 1.0, or 1.5 T on the cell cycle in both synchronized and nonsynchronized HFLF cells were evaluated (Wiskirchen et al., 2000). The exposure condition was 1 h/d for 5 consecutive days. Results showed no significant differences in cell cycle events between synchronized and nonsynchronized cells.

A series of research studies on growth enhancement by strong inhomogenous static magnetic fields have been reported. Tsuchiya et al. (1996) showed that the growth of *E. coli* was affected by both a strong homogenous static magnetic field strength of 7 T and inhomogenous field strengths of 5.2–6.1 or 3.2–6.7 T. In the stationary phase, the cell number under a high magnetic field was about two to three times higher than that of a control. The effect of the inhomogenous field was much stronger than that of the homogenous field. They also showed that the transcription activity of *E. coli* was enhanced by the strong inhomogenous static magnetic field levels of 5.2–6.1 T (Tsuchiya et al., 1999). The transcription levels of the *rpoS*, gene which encodes sigma factor of RNA polymerase, was increased in the stationary phase by the static magnetic field exposure. This transcription factor is specifically activated during the stationary phase and plays an important role in the transcription control of other genes in the stationary phase.

Horiuchi et al. (2001) showed that *E. coli* cell death in the stationary phase was suppressed by strong inhomogenous static magnetic field levels of 5.2–6.1 T with a gradient of 24 T/m and that the suppression was dependent on the addition of amino acids to the LB medium. The addition of glutamic acid enhanced cell death as pH increased in the stationary phase, and cell death was dramatically suppressed by the field exposure. At the same time, *rpoS* gene expression was increased 20% by the field exposure. They suggested that the increase of *rpoS* gene expression in the stationary phase by the field exposure might be related to the base resistance because the *rpoS*-disrupted strain showed a lower base resistance than the wild-type strain (Ishizaki et al., 2001). It has

been shown that the medium supernatant, when used after the static magnetic field exposure, could enhance the suppression of cell death (Horiuchi et al., 2002). The pH of the medium after the static magnetic field exposure was only slightly different from that of the control (by a factor of 0.07 pH), and pH-adjusted medium from both exposed and control supernatants still had the suppression effect characteristics from the exposure to static magnetic fields. It has been suggested that other factors also were involved in the full suppression effect of cell death by the field exposure.

The growth advantage in stationary phase (GASP) phenomenon is described as follows. When *E. coli* cells grown for 10 d (aged culture) and *E. coli* cells grown only for 1 d (young culture) were mixed, the cell number of the young culture decreased, and the population of the young culture was taken over by the aged culture, and eventually only aged cells predominantly survived in the system. It has been found that the GASP phenomenon disappeared with the exposure to strong inhomogenous static magnetic field levels of 5.2–6.1 T (Okuno et al., 2001). They suggested that the disruption of the GASP phenomenon might be related to an effect on the *rpoS* gene by the static magnetic field exposure.

Gray et al. (2000) evaluated static electric and magnetic field effects on the action enhancement of the chemotherapeutic agent adriamycin in transplanted mammary adenocarcinoma in female B6C3F1 mice. Treatment consisted of using 10 mg/kg of adriamycin in combination with a 4-h exposure to a 110-mT field. Tumor regression in the groups exposed to a static magnetic field was greater than in the group treated with adriamycin only.

Tanioka et al. (1996) evaluated the effects of a 6.34-T static magnetic field on proliferation and metastatic activity in the B16 melanoma and EL-4 T-lymphoma cell lines. Cell cultures were incubated in the presence of magnetic fields for 12, 24, 36, or 48 h at 37°C. It was found that the proliferative and the metastatic activities of both cell lines were promoted under certain conditions.

Tofani et al. (2003) exposed immunocompetent mice bearing either the murine Lewis lung carcinoma or the B16 melanotic melanomas to static field levels of 3 and 4 mT and treated them with two commonly used anticancer drugs, cisplatin and cyclophosphamide, respectively. The survival time of mice treated with cisplatin and exposure to the magnetic fields was significantly longer than that of mice treated only with cisplatin or only exposed to the magnetic fields, surpassing that of mice treated with 10 mg/kg i.p. of the drug and showing that the magnetic field acts synergically with the pharmacological treatment. When mice treated with cyclophosphamide were exposed to the magnetic field, no synergic effects were observed. No clinical signs or toxicity were seen in any of the mice exposed to the magnetic field alone or along with cisplatin or cyclophosphamide treatment.

Raylman et al. (1996) studied the effects of exposure to a static magnetic field of 7 T for 64 h on cell viability in three malignant human cell lines, melanoma (HTB 63), ovarian carcinoma (HTB 77IP3), and lymphoma (Raji; CCL86). It has been reported that the static field exposure reduced the viable cell count and appeared to inhibit cell growth.

Using two types of mammalian cells, mouse leukemia cells P388 and Chinese hamster fibroblast cells V79, Sakurai et al. (1999) tested the effects on cell growth patterns of exposure to a 7-T static magnetic field for up to 5 d. No significant magnetic field effects on cells were found.

In a series of papers (Kula, 1996; Kula and Drobz, 1996a,b), the magnetic field effects on cultured fibroblasts isolated from the BALB/c mouse have been investigated. The fibroblast cultures were exposed to a static magnetic field of 0.49 T and a 50-Hz AC magnetic field of 0.02 T for a time period of 2–64 min/d over four consecutive days. The following parameters were studied: the dynamics of culture growth; protein content;

thymidine incorporation; Zn, Fe, and Cu ion content; the activity of superoxide dismutase (SOD) and catalase (CT); and glycosaminoglycan metabolism. The static magnetic field exposure had no effect on both the vital functions and glycosaminoglycan metabolism and did not show any changes in the free-radical process in fibroblasts. Kula et al. (2000) further evaluated the activities of SOD, CT, glutathione peroxidase, and malondialdehyde (MDA) in the livers and kidneys of rats exposed to a static magnetic field of 0.49 T and a 50-Hz AC field of 0.018 T. While the 50-Hz magnetic field was found to influence free-radical processes in both liver and kidney tissue, the static magnetic field showed no effects. Magnetic field effects on the lipid peroxidation product, MDA, in mouse subcellular fibroblast have been evaluated by the same protocol in a previous report (Kula et al., 2002). It was found that exposure to a static magnetic field caused no changes in peroxidation of membrane structures.

Effects with a combination of static and alternating magnetic fields on cell attachment and induction of apoptosis in rat tendon fibroblast and rat bone marrow (RBM) osteoprogenitor cells have been reported (Blumenthal et al., 1997). Experiments utilized 60-and 1000-Hz AC magnetic fields of up to $0.25\text{ mT}_{\text{p-p}}$ and static magnetic fields of up to 0.25 mT. It was found that AC fields and static magnetic fields tested with various combinations of field strengths and frequencies resulted in extensive detachment of preattached cells and prevented the normal attachment of cells not previously attached to substrates. Results suggested significant alterations in cell metabolism and cytoskeleton structure after the exposure.

Blanchard and Blackman (1994) proposed the ion parametric resonance (IPR) model for the prediction of the interaction between magnetic fields and biological systems ([see also Chapter 9](#) on resonance phenomena by Liboff). According to the IPR model, the relationships among the strength of a static magnetic field, the AC magnetic field frequency, and the charge-to-mass ratio of ions of biological relevance were important key factors. Blackman et al. (1996) tested the influence of magnetic fields on neurite outgrowth in PC-12 cells and showed that the PC-12 cell response to perpendicular AC and static magnetic fields was distinct and predictably different from that found for parallel AC and static magnetic fields. It has been reported that the response to perpendicular fields was dominant in an intensity-dependent nonlinear manner.

The effects of the combination of AC and static magnetic fields on the behavior of Friend erythroleukemia cells have been studied (Eremenko et al., 1996). The combined fields were a geomagnetic field of 45 μT , together with a 70- μT field at 50 Hz which was produced in a solenoid coil, and 20-nT DC and 2.5-pT AC fields in a magnetically shielded room. It was found that the culture growth cycle of cells was slightly accelerated inside the solenoid, and the degree of acceleration appeared to depend on sensitivity of the cell cycle to the magnetic field. On the other hand, it was found that the culture growth cycle of cells inside the magnetically shielded room was slightly decreased.

Effects of a static magnetic field exposure of 10 T for up to 4 d on the rate of cell growth or cell cycle distribution in Chinese hamster ovary (CHO-K1) cells have been investigated (Nakahara et al., 2002). The exposure to the static magnetic field alone did not affect micronucleus formation. In x-ray irradiated cells, exposure to the 10-T static magnetic field resulted in a significant increase in micronucleus formation. Buemi et al. (2001) examined the effects of a 0.5-mT static magnetic field on the cell proliferation and cell death balance in monkey renal cells (VERO) and in rat cortical astrocyte cells. After 6 d of exposure to the magnetic field, they observed the effects on cell proliferation and cell death balance and suggested that the effects might vary depending on the cell type. Magnetic fields may also have a nephropathogenic effect.

Tofani et al. (2001) investigated the role of magnetic field characteristics on the growth of WiDr human colon adenocarcinoma, MCF-7 human breast adenocarcinoma,

and MRC-5 embryonal lung fibroblast. Cell death induction was observed with a magnetic field exposure of greater than 1 mT when the combined static magnetic field and 50-Hz magnetic field was applied. The report showed that significant tumor growth inhibition appeared when the total field strength was greater than 3.59 mT.

Schiffer et al. (2003) studied the effects of four different types of magnetic field applications on the cell cycle progression in two different tumor cell lines, the human acute myeloid leukemia cell HL-60 and the mouse lymphoma cell EA2. The four types of magnetic field applications used were (1) the static magnetic field of 1.5 and 7.05 T, (2) the magnetic gradient field with ± 10 and ± 100 mT/m at 100 Hz; (3) the pulsed high frequency magnetic field (5.8 μ T at 63.6 MHz); and (4) the combination of (1)–(3). The exposure duration ranged from 1 to 24 h. Cell cycle fractions at G₀/G₁, S, and G₂/M phases were analyzed by flow cytometry. Cell cycle analysis did not show differences between the exposed and control cells. In conclusion, during MRI, no influence of magnetic field on cell cycle progression was observed in these cell lines.

8.3.2.3 Cell Membrane and Cell Metabolic Activity

Chignell et al. (1998) studied the effects of static magnetic fields of 25–150 mT on the photohemolysis of human erythrocytes by ketoprofen. An application of a static magnetic field during UV (>300 nm) irradiation of ketoprofen and erythrocytes significantly decreased the time required for photohemolysis. It has been suggested that the magnetic field increases the concentration and lifetime of free radicals that escape from the radical pair.

Chionna et al. (2005) investigated the effects of a 6-mT static magnetic field, applied for 24 h, on cell shape, cell surface sugar residue, cytoskeleton, and apoptosis in the hepatic transformed cell line Hep G2. Significant modifications of cell shape and surface by the field exposure have been observed. The exposed cells were found to be elongated, with many irregular microvilli randomly distributed on the cell surface. The shape of the cells was found to be less flat at the end of the exposure, although the morphology of the organelles remained unmodified throughout the exposure period. It has been reported that cell proliferation was partially affected. Results suggested that the static magnetic field caused a time-dependent biological effect on Hep G2 cells.

Sonnier et al. (2000) found that there were no effects from the exposure of static magnetic field levels of 0.1, 0.5, 5, or 7.5 mT, applied for 5 sec, on resting potential in cultured neuroblastoma cells. They also used the patch-clamp technique to measure transmembrane Na⁺, K⁺ currents in neuroblastoma cells SH-Sy5Y exposed to static magnetic fields of up to 7.5 mT (Sonnier et al., 2003). The magnetic field exposure did not result in detectable changes in any of the action potential parameters.

Trabulsi et al. (1996) measured the excitatory postsynaptic potential (EPSP) after the exposure of a mouse hippocampal slice to static magnetic field levels of 2–3 mT and 8–10 mT for a period of 20 min. They observed biphasic effects at 2–3 mT and depression of EPSP at 8–10 mT. It has been suggested that changes in intracellular Ca²⁺ concentration were responsible for these effects. Isolated *Helix aspersa* neurons were exposed to static magnetic field levels of 0.07–0.7 T, and their action potential was measured (Azanza and del Moral, 1996). A decrease in the spike depolarization voltage has been observed, and it has been attributed to desensitization of the membrane Na⁺-K⁺-ATP-ase pumps through an anisotropic diamagnetism reorientation.

Wieraszko (2000) studied the effect of 2–3-mT static magnetic fields applied for 20 min on the evoked potential response in B57/J56 mice hippocampal slices. Results, which were based on measurements of hippocampal function, showed both an alteration of the evoked potential and an effect on the influence of dantrolene, an inhibitor of intracellular Ca²⁺ channels.

The voltage-activated calcium channel function in cultured GH3 cells has been investigated (Rosen, 1996). A static magnetic field of 120 mT was applied for 150 sec. Reversible changes in calcium channel function were observed and were found to be temperature dependent. Results indicated that these changes were a result of alterations in the membrane proper because of the magnetically induced deformation.

Using the whole-cell patch-clamp technique, voltage-activated Na^+ channels in GH3 cells were examined (Rosen, 2003). The effects of exposure to a static magnetic field of 125 mT for 150 sec on voltage-gated Na^+ channel kinetics included a slight shift in the current–voltage relationship, a 5% reduction in peak current, and an increase in the activation time constant, τ_m , during and at least 100 sec after the exposure to the field. Significant changes were only observed at 35°C and 37°C. It was suggested that the temperature dependence factor that affected this process was probably due to the greater ease with which the liquid crystal membrane was deformed. Results suggested that the changes might be due to the reorientation of diamagnetic anisotropic molecules in the membrane. Hinch et al. (2005) showed the effects of static magnetic fields on action potential propagation and excitation recovery in nerve. At a field level of 125 mT, which was the same condition previously used by Rosen, they did not observe major changes in the electrical functioning of neurons.

Aldinucci et al. (2003a,b) investigated the effects of a 4.75-T static magnetic field exposure applied for 1 h, and also a 1-h exposure using combined fields of 4.75 T with a pulsed field of 0.7 mT, on proinflammatory cytokines, in human peripheral blood mono-nuclear cells (PBMCs) and Jurkat cells. They measured Ca^{2+} , proliferation, and the eventual production of proinflammatory cytokines. The static magnetic field exposure alone did not show any effects on the physiologic behavior of normal lymphocytes; however, the combined static and alternating magnetic field exposure contributed synergistically to the increase of $[\text{Ca}^{2+}]_i$. The exposure of PBMCs was carried out in a static magnetic field of 10 T (Onodera et al., 2003). It was reported that the magnetic field exposure reduced the viability of phytohemagglutinin (PHA)-activated T cells in both CD4+ and CD8+ subclasses. Sabo et al. (2002) observed a decrease in the metabolic activity of human promyelocytic leukemic cells HL-60 when exposed to a field of 1 T for 72 h. The decrease was also observed in the presence of antineoplastic drugs, which included 5-fluorouracil, cisplatin, doxorubicin, and vincristine.

Miyamoto et al. (1996) studied the effects of strong 6-T homogenous magnetic fields on both active and passive Rb^+ influx into HeLa cells. Using field exposures of 1.6 T and lower, and of 2.0 T, at various temperatures did not cause any changes in active or passive Rb^+ influxes.

Mouse islet of Langerhans cells have a very regular oscillation of calcium concentration. Madec et al. (2003) showed no effects of combined AC and static magnetic fields on these calcium oscillations in mouse islet of Langerhans.

8.3.2.4 Gene Expression and Signal Transduction

Fanelli et al. (1999) found a decrease of apoptosis in the human cell lines U937 and CEM, following exposure to a static magnetic field of 600 μT . It was suggested that the protective antiapoptotic effect was due to cellular modifications from the static field exposure, which affected the ability of the cell to enhance Ca^{2+} influx from the extracellular medium. Cohly et al. (2003) examined the effects of a 0.618-mT static magnetic field on a human osteoblast cell line (MG-63) culture, in terms of proliferation, proline uptake, and gene expression. Results showed that the exposure might be detrimental to bone formation.

Mnaimneh et al. (1996) investigated the effects of static magnetic field levels from 1 to 100 mT and also an AC field of 1.6 mT delivered at 1 Hz on NO production by murine

BCG-activated macrophages. No significant differences were observed in NO levels after a 14-h exposure.

Brief exposure effects from a static magnetic field of 100 mT for 15 min on protein expression in cultured rat primary hippocampal cells have been reported (Hirai et al., 2002). Expression of DNA binding activator protein-1 (AP-1), neural marker protein (MAP2), and neural differentiation marker protein (GAP-43, c-Fos, Fos-B, Fra-2, c-Jun, Jun-B, and Jun-D) were examined. Cytoplasmic Ca²⁺ and lactate dehydrogenase activities were also analyzed. It was found that exposure to the static field increased AP-1 DNA binding through expression of Fra-2, c-Jun, and Jun-D in immature cultured hippocampal neurons.

Flipo et al. (1998) examined *in vitro* effects of the static magnetic field levels of 2.5–150 mT applied for 24 h on the mitogen response to concanavalin A, phagocytosis, apoptosis, and Ca²⁺ influx in C57Bl/6 murine macrophages, spleen lymphocytes, and thymic cells. The exposure resulted in a decrease of phagocytosis, an inhibition of mitogenic response in lymphocytes, and a marked increase of apoptosis in thymic cells.

Salerno et al. (1999) measured *in vitro* expressions of activation markers and interleukin release in human PBMCs after exposure to a static magnetic field of 0.5 T for 24 h. They observed that the expression of CD69 at 0.5 T was reduced after PHA stimulation. Increases in interferon-γ and interleukin 4L (IL-4L) releases were observed; however, no changes in tumor necrosis factor α (TNF-α), IL-6, and IL-10 releases were observed.

Effects of a static magnetic field of 1.5 T applied for 240 min on human L-132 cells have been investigated (Guisasola et al., 2002). Heat shock proteins hsp70, hsp27, and their corresponding messenger RNAs (mRNAs), along with cyclic AMP and Ca²⁺ ions were analyzed. No field exposure effects were observed.

Effects of the exposure of HL-60 cells to a 6-T spatially inhomogenous magnetic field with a strong gradient of 41.7 T/m and to a spatially homogenous magnetic field of 10 T have been studied (Hirose et al., 2003b). The expression of c-Jun protein increased in HL-60 cells after exposure to the 6-T static magnetic field for 24, 36, 48, and 72 h.

Using budding yeast (*S. cerevisiae*) as a model for an *in vitro* biological test system, Ikehata et al. (2003) examined the genome-wide gene expression profile of yeast cells after exposure to 5- and 10-T fields for periods of 2 and 24 h. Exposure to static magnetic fields did not affect gene expression. Slight changes in the expression of several genes were observed after exposure to 14 T for 24 h.

8.3.2.5 Genotoxicity

Previous studies have shown that static magnetic fields alone did not have a lethal effect on cell growth and survival under normal culture conditions, regardless of the strength of the magnetic field applied. Effects of 5-h exposures of HL-60 cells to 6-mT static magnetic fields, with or without camptothecin, which is a DNA topoisomerase I inhibitor, have been investigated (Teodori et al., 2002). Results indicated that the field exposure did not cause apoptogenic or necrogenic effects. It was reported that exposure to the static magnetic field alone or with camptothecin did not affect cell viability.

Potenza et al. (2004a) showed that the conformation of plasmid DNA was altered by exposure to static magnetic fields of 250 mT. Various DNA point mutations were found, while no DNA degradation was observed. It was shown that the DNA degradation from H₂O₂ was accelerated by simultaneous field exposure; however, the plasmid DNA in *E. coli* cells exposed to the same static magnetic field did not show any alteration. They suggested that the magnetic field could change DNA stability directly or by activating the reactivity of oxidant radicals. It has also been suggested that the genotoxic effect could be minimized in living organisms by the presence of protective cellular responses, such as the DNA repair system and the buffering action of heat shock proteins.

In order to reveal the genetic effects of a 0.6-T static magnetic field, mutagen-sensitive mutants of the fruit fly (*D. melanogaster*) were used for the somatic cell test (Koana et al., 1995). It was shown that the exposure resulted in damaging effects in larval cellular DNA, and somatic cells without normal DNA repair functions failed to continue cell division, which resulted in developmental lethality of mutant larvae. The genotoxic activity of the field exposure was estimated to be the same as that of UV irradiation with 0.14 mJ/m²/sec. Further study has been conducted with *D. melanogaster* using a wing spot test to estimate possible mutagenic or carcinogenic activity of the static magnetic field (Koana et al., 1997). A DNA repair defective mutation *mei-41^{D5}* was introduced into the conventional *mwh/flr* test system to enhance mutant spot frequency. Third-instar larvae were exposed to a field of 5 T for 24 h. It was shown that the exposure significantly enhanced the somatic recombination, and the recombination was found to be suppressed by supplementation of vitamin E. Results indicated that the magnetic field enhanced the genotoxic effects of spontaneously produced free radicals (Takashima et al., 2004).

In a report describing the investigations of whether static magnetic fields have cytogenetic effects in BALB/c AnNCrj male mouse bone marrow cells, Suzuki et al. (2001) indicated that the frequency of micronuclei was significantly increased by exposure to a 3-T field for 48 and 72 or a 4.7-T field for 24, 48, and 72 h. The increase in micronucleus frequency was shown to be dose dependent.

Micronuclei in cells have been used as an indicator of DNA damage. A study for *in vitro* assessment of the effects of a 4.7-T static magnetic field on the frequency of micronucleated cells in the Chinese hamster CHL/IU cell line with preexisting damage induced by exposure to mitomycin C (MMC) has been carried out (Okonogi et al., 1996). Results indicated a decrease in the frequency of micronuclei formation after 6 h of exposure and also the influence of the static magnetic field on the DNA damage stage produced by MMC.

An *E. coli* mutation assay has been carried out to assess the mutagenic effects of strong static magnetic fields (Zhang et al., 2003). Results obtained with a wild-type *E. coli* strain GC4468 and several derivatives, which were defective in DNA repair enzymes or redox-regulating enzymes, showed no effects of the exposure in terms of the survival rate of cells. On the other hand, the mutation frequency was significantly increased by exposure to the 9-T static magnetic field for 24 h in *soxR* and *sodAsodB* mutants, which were defective in their defense mechanism against oxidative stress. Results indicated that static magnetic fields induced mutations by increasing the production of intracellular superoxide radicals.

Ikehata et al. (1999) reported that 2- and 5-T static magnetic fields did not have mutagenic potential in a bacterial mutation test using *Salmonella typhimurium* (TA98, TA100, TA1535, and TA1537) and *E. coli* (WP2 *uvrA*) strains. They also reported that the exposure resulted in an increased mutation rate of the WP2 *uvrA* strain when induced by the agents N-ethyl-N'-nitro-N-nitrosoguanidine (ENNG), N-methyl-N'-nitro-N-nitrosoguanidine (MNNG), ethylmethanesulfonate (EMS), 4-nitroquinoline-N-oxide (4NQO), 2-amino-3-methyl-3H-imidazo-[4,5-f]-quinoline (IQ), and 2-(2-furyl)-3-(5-nitro-2-furyl) acrylamide (AF-2). The mutagenicities of 2-aminoanthracene (2-AA), 9-aminoacridine (9-AA), N-4-aminocytidine, and 2-acetoamidofluorene (2-AAF) were not affected by the exposure. The bacterial growth did not change after the exposure. They suggested that the mechanism of these effects might be related to *in vitro* interactions between the chemicals and DNA and to repair systems in the test strains.

8.3.2.6 Cell-Free System, Free Radical, Enzyme Activity

Markov and Pilla (1994, 1997) studied the Ca²⁺/calmodulin-dependent myosin phosphorylation and observed magnetic field effects of 44-μT, ambient, and 200-μT vertical fields for 5 min on the Ca²⁺ binding property. Phosphorylation increased up to at 200 μT

depending on the $[Ca^{2+}]$ concentration. The magnetic field effect disappeared as $[Ca^{2+}]$ approached saturation for calmodulin. They emphasized that very small alterations in ambient level static magnetic fields are sufficient to have a profound effect on a cell-free enzyme system. In an attempt to replicate the results of Markov and Pilla, Coulton et al. (2000) saw no effects on myosin phosphorylation in a cell-free system in vertical static magnetic fields up to 400 μ T. As a result, in this experiment, no effects of static magnetic fields on the calcium/calmodulin binding property were observed. Engstrom et al. (2002) investigated the effects of nonuniform static magnetic fields of 0.7–87 mT with a gradient of 0.4–20 T/m for a period of 5 min on myosin phosphorylation and reported that the magnetic field exerted an influence on the rate of myosin phosphorylation. Increased phosphorylation was observed. It can be seen that the magnetic field gradients played a specific role in this experiment. Liboff et al. (2003) investigated the effect of a 30-min exposure to a static magnetic field of 20 μ T on calmodulin-dependent cyclic nucleotide phosphodiesterase activity in cell-free systems and reported that the activity was altered in comparison to zero magnetic field exposures.

After studying the theoretical background of a cell-free system— Ca^{2+} /calmodulin-dependent myosin light chain phosphorylation reaction—Markov (2004a,b) designed experiments to test the effects of a pulsed radio frequency (RF) field, pulsating magnetic fields, gradient magnetic fields, and homogenous static magnetic fields on this cell-free system. He suggested that the magnetic fields affect the cell-free enzyme system by modulating ion–protein interactions.

Watanabe et al. (1997) measured and evaluated lipid peroxidation in the liver, kidneys, heart, lung, and brain of 8-week-old male BALB/c mice. The mice were exposed to 3.0- and 4.7-T fields for 3–48 h. The lipid peroxidation level in the liver was increased after exposure to the 4.7-T field. In kidney, heart, lung, and brain, no changes in the level of lipid peroxidation were observed compared to the control. The exposure to the 3.0-T field showed no alteration of the lipid peroxide level in all the tissues. The combination of CCl_4 administration and 4.7-T field exposure increased the lipid peroxidation level in the liver. It was concluded that the exposure to high static magnetic fields could induce the increase of lipid peroxidation levels in the liver of mice and could enhance the hepatotoxicity caused by CCl_4 injection.

Using fireflies, *Hotaria parvula* and *Luciola cruciata*, as bioluminescence systems, Iwasaka and Ueno (1998a) studied the effects of 8- and 14-T static magnetic fields on the emission of light. They showed that changes in the emission intensities under a magnetic field were related to the change in certain biochemical systems of the firefly, systems such as the enzymatic process of luciferase and the excited singlet state responsible for subsequent light emission.

Zhadin et al. (1998) have undertaken experiments that investigated the combined action of static and AC magnetic fields on ionic current in aqueous glutamic acid solution. Results showed that the combined parallel static and AC magnetic field causes a rapid change in the ionic current flow when the AC frequency is equal to the cyclotron frequency.

During the last few years, Brocklehurst and McLauchlan (1996) discussed the free radical mechanism involved in the observed effects of environmental electromagnetic fields on biological systems. Grissom and Natarajan (1997) summarized the theory of magnetic field effects on chemical and enzymatic reactions. Magnetic field effects have been used as a powerful technique to study enzymatic and chemical reactions with radical pair intermediates. They suggested that the coenzyme B₁₂-dependent enzymes with radical pair intermediates are well suited for the study of this effect. Taoka et al. (1997) tested the magnetic field effects on coenzyme B₁₂-dependent enzymes. The end point was that ethanolamine ammonia lyase and human enzyme

methylmalonyl-coenzyme A mutase catalyze coenzyme B₁₂-dependent rearrangement reactions. While the end point was affected, the authors speculate that the change would have little physiological significance.

Eichwald and Wallczek (1996) showed a model for magnetic field effects on radical pair recombination in enzyme kinetics. The magnetic field effects in radical pair chemistry have been reviewed (Grissom, 1995; Brocklehurst, 2002; [see also Chapter 6 on free radicals by Engström](#)).

8.4 Miscellaneous

8.4.1 Biological Sensing and Magnetite

Many studies have suggested that the magnetic field is an important marker for animal navigation and spatial discrimination (Wiltschko and Wiltschko, 1995). The blind mole-rat (*Spalax ehrenbergi*) was used as a model to examine the possibility of the perception and use of magnetic fields in their orientation in space (Kimchi and Terkel, 2001). Experiments were performed in an eight-arm maze under Earth's natural and artificial magnetic fields. Results showed that the blind mole-rat was able to perceive and use Earth's magnetic field to orient in space. Kimchi and Terkel showed that blind mole-rats spontaneously preferred to place their nests toward the south of the magnetic North. Deutchlander et al. (2003) showed that Siberian hamsters (*Phodopus sungorus*) used directional information from the magnetic field to set a position for their nests. In contrast to blind mole-rats, the directional preference for nest position demonstrated by Siberian hamsters appeared to be a learned response.

Since the neural substrate subserving magnetic orientation is not known, the combination of two techniques, a behavioral test for magnetic compass orientation and an immunocytochemical visualization of the transcription factor c-Fos as a neuronal activity marker, has been used to investigate magnetoreception in the mole rat (*Crytomys anselli*) (Nemec et al., 2001). Nemec et al. found that the superior colliculus of the hypothalamus contained neurons that would respond to magnetic stimuli, and thus determined the involvement of a specific mammalian brain structure in magnetoreception.

Edmond (1996) showed that a very sensitive magnetic compass is formed by the incorporation of a small quantity of ferromagnetic, single-domain crystals, such as magnetite, within a nematic liquid crystal. Winklhofer et al. (2001) localized high concentrations of Fe³⁺ in the upper-beak skin of homing pigeons (*Columba livia*), and identified the materials of magnetite nanocrystals as the core of a magnetic field receptor.

Lohman et al. (2001) found that hatchling loggerhead sea turtles (*Caretta caretta*), when they were exposed to magnetic fields found in three widely separated oceanic regions, swam in the direction that would help to keep them within the currents of the North Atlantic gyre and facilitate their migratory pathway. It was found that young loggerheads used a guidance system of magnetic fields to assist in their navigation.

Although the mechanism of magnetoreception has not been clearly identified, geomagnetic orientation has been well recognized. A biophysical model has shown that changes in the wavelength of light can influence magnetic field orientation through the interaction between the geomagnetic field and photoreceptors. Deutschlander et al. (1999a) found that light-dependent orientation in the newt (*Notophthalmus viridescens*), was mediated by extraocular photoreceptors located in the pineal complex or deeper in the brain. Using newts, Phillips et al. (2001, 2002b) showed the role of photoreceptors in magnetic compass

orientation and the magnetic inclination for deriving map information. They investigated the possibility that the fixed-axis response of the newts was mediated by a magnetoreception mechanism involving single-domain particles of magnetite (Phillips et al., 2002a).

There are several explanations for the magnetic sensitivity in fish. The aquatic animal might perceive an electric voltage induced by the water current or by its own movement in the geomagnetic fields. Elasmobranch fish such as sharks, skates, and rays are known to possess a sensitivity to the induced electric field through the sensory organs called the ampullae of Lorenzini.

Yano et al. (1997) studied the migrating behavior of the chum salmon (*Oncorhynchus keta*) fitted with a magnet to investigate the role of magnetic compass orientation in the North Pacific off the coast of Kushiro, Hokkaido. The magnetic field strength was about 0.6 mT around the head area, with polarity changes every 11.25 min. There were no effects observed on the movement of salmon.

Effects of electric and magnetic fields have been observed in the behavior of marine animals and freshwater and terrestrial species. In addition, there are a growing number of questions concerning the effect on aquatic ecosystems of the growing spread of artificial techniques such as underwater sea DC cables. There are many underwater DC cables under various seas all over the world, which carry electrical currents (see also Chapter 1 on fields in the environment by Mild and Greenebaum). These electric currents induce static magnetic fields with intensities up to 3.5 mT around cables on the sea bottom, where there are many invertebrate and vertebrate species. Research has been carried out to examine whether the exposure to magnetic fields of 3.7 mT for several weeks could influence the survival rate and fitness of common benthic animals of the Baltic Sea (Bochert and Zettler, 2004). The investigation was carried out on the crustacean (*Crangon crangon*, *Rhithropanopeus harrisii*, and *Saduria entomon*); the mussel (*Mytilus edulis*); and the flounder (*Platichthys flesus*). Results showed no differences between experimental and control animals. Since this is the first study for investigating the effects of static magnetic fields generated by sea-positioned DC cables, on aquatic organisms and marine benthic animals, further studies are required.

In a study to confirm the magnetite-based detection mechanism in rainbow trout (*O. mykiss*), magnetic crystals in the area of olfactory lamellae were found, and the arrangement of several magnetic crystals in a chain of about 1 μm has been confirmed (Diebel et al., 2000).

It was shown that magnetizable material abolishes the behavior of bobolink (*Dolichonyx oryzivorus*) by blocking the ophthalmic branch of the trigeminal nerve (Beason and Semm, 1996). The result was consistent with the hypothesis that magnetite is a constituent of the magnetoreceptors associated with the ophthalmic nerve.

It is suggested that migratory birds, amphibians, and reptiles may have the ability to sense the geomagnetic field and use it as a source of compass information. Phillips (1996) presented a graphical model that predicts qualitatively the changes in the direction of homing orientation. Munro et al. (1997) investigated the effect of pulse remagnetization on the orientation of inexperienced, juvenile migrant birds, such as the Australian silver-eye (*Zosterops l. lateralis*). The ability of juvenile birds to maintain their normal magnetic orientation after pulse application indicated that the pulse does not impair the magnetic compass. On the other hand, the deflection observed in adult birds after pulse treatment appeared to reflect "false" map information, which leads to a change in course. This is consistent with evidence that the magnetic compass involves light-dependent magnetoreception mechanisms.

Wiltschko and Wiltschko (2001) studied the behavior of European robins (*Erithacus rubecula*), under monochromatic light of various wavelengths and intensities to investigate magnetoreception. At a quantal flux of 7×10^{15} quanta/sec/m², the birds were well

oriented in their migratory direction under 424 nm blue, 510 nm turquoise, and 565 nm green, whereas they were disoriented under 590 nm yellow. Changes in behavior depended on increasing the light intensity. This finding suggested that light-dependent magnetoreception may involve receptors and a neuronal pathway of its own.

Ritz et al. (2000) postulated the possibility that magnetoreception involves radical pair processes as a biophysical mechanism. They first considered a system of radical pairs as a model for the magnetic sensory organ and evaluated the influence of the geomagnetic field on radical pair systems. European robins (*E. rubecula*), were used in this study, and the results showed the disruption of magnetic orientation behavior of robins when exposed to a vertically aligned broadband field of 0.1–10 MHz and 0.085 µT or the single frequency of 7 MHz and 0.47 µT, together with the geomagnetic field (Ritz et al., 2004). The disorientation observed was found to depend on the angle between the 7-MHz oscillating field and the geomagnetic field. The robins oriented in the migratory direction when the oscillating field was parallel to the geomagnetic field. The author suggested a magnetic compass based on a radical pair mechanism, due to the resonance effect on singlet-triplet transitions in the oscillating fields.

Fuller suggested the significance of the time constants of magnetic field sensitivity in animals (Fuller and Dobson, 2005). Conditioning experiments have had great success in the analysis of animal sensory physiology. Wiltschko and Wiltschko (1996) commented that the conditioning technique did not appear to be suitable for testing magnetic sensitivity.

Some insects are able to respond to magnetic fields, especially the geomagnetic field. Mosquitoes were tested for the presence of remanent ferromagnetic material and their behavioral response to magnetic fields. Most mosquitoes, when placed in a uniform static magnetic field of 0.1 mT, moved around until they were oriented parallel to the field. It was reported that a significant remanence found on the surface of both living and dead mosquitoes might be due to attraction of ferromagnetic dust onto the body (Strickman et al., 2000). It is well-known that magnetic fields influence honey bee behavior, moth navigation, beetle larvae, the behavior of hatchling loggerhead sea turtles, migration of birds, etc. Slowik et al. (1997b) speculated that the red imported fire ant (*Solenopsis invicta*) might use magnetic field information in their nesting activities and in orientation, since their first observation suggested that fire ant workers moved as a colony toward the magnetic field. In a second paper, Slowik et al. (1997a) suggested the presence of small amounts of ferromagnetic material in fire ants.

Many review papers have been published during the last few years. Deuslander et al. (1999b) and Wiltschko and Wiltschko (2002) reviewed the light-dependent magnetoreception in animals. Lohmann and Johnsen (2000) described the difference between a magnetic directional sense and a magnetic map sense and reviewed the three hypotheses of vertebrate magnetoreception.

8.4.2 Plant Growth, Response, and Magnetotropism

The enhancement of plant growth using various magnetic field applications has been reported by many researchers (Phirke et al., 1996). Effects of magnetic fields on seed germination, crop growth, physiological response, sporulation, water uptake, and rate of seed have been studied; however, there has been no consistency in results among the various reports.

Studies directed toward investigating the effects of magnetic field treatment on seeds and water in terms of the rate and percentage of germination of rice (*Oryza sativa* L.) and on the length and weight of germinating barley (*Hordeum vulgare* L.) and wheat (*Triticum aestivum* L.) have been carried out (Carbonell et al., 2000; Martinez et al., 2000, 2002). The

field strength ranged from 125 to 250 mT depending on the research strategies. Results by Carbonell et al. showed that the rate and percentage of germination increased after chronic exposure to 150-mT fields. Magnetically treated water was found to improve the germination of rice seeds. Martinez et al. (2000) showed that the magnetic field increased the length and weight of barley seed, and the degree of this effect depended on the duration of exposure. Effects of magnetic biostimulation on the initial growth stages of wheat, with an exposure duration of 0, 1, 10, 20 min, 1 h, 24 h, and chronic exposure were investigated (Martinez et al., 2002). In the report, they defined the magnetic doses in terms of magnetic field energy density (J/m^3). An increase in plant height had been observed as the magnetic dose increased; thus, it was suggested that the stimulatory effects might be related to the amount of magnetic field energy. Florez et al. (2004) investigated the effects of 125- and 250-mT static magnetic fields on the germination and the initial growth stages of rice seeds (*O. sativa* L.). The seeds were exposed to the magnetic fields for various time durations, and the germination time was found to be shortened when the seeds were exposed to these fields. The seeds' maximum length and weight were obtained for the chronic exposure. It was shown that magnetic treatments, when applied under specific conditions, affected germination and the first stage of growth.

Piatti et al. (2002) investigated the effects of inhomogenous static magnetic fields ranging between 6 and 10 mT on the growth and viability of the plant-growing bacteria *Serratia marcescens*, barley callus cells (*Hordeum vulgare*), and blackberry (*Rubus fructiosus*). While there was no field effect observed on blackberry cells, it was found that the exposure reduced the number of bacterial cells and lowered both the number and the viability of barley cells. Diamagnetic susceptibility and root growth response to magnetic field exposure on three plant species, *Lens culinaris*, *Glycine soja*, and *T. aestivum* were investigated (Penuelas et al., 2004). Magnetic fields of 17.6 mT reduced root growth in all three plants. The field strength of 2.1 mT had no significant effect on reduction in the cereal *T. aestivum*.

Among the many studies that examined gradient magnetic field effects on various engineering, biological, and physicochemical phenomena, a study of effects of gradient magnetic fields of up to 10 T on the germination and growing process of cucumber (*Cucumis sativus* L.) was carried out (Hirota et al., 1999). It was found that the shoot germinated toward the field center, whereas the root grew in the opposite direction of the shoot. This observation seemed to be a result of the magnetic force influencing the geotaxis of the cucumber.

After calculating the magnetic field dependence of the ionic current density across the cellular membrane, Reina and colleagues examined the effects of 0–10 mT static magnetic fields on the amount and rate of water absorption in the lettuce seed cell membrane (*Lactuca sativa*) in order to compare the calculated and experimental results (Reina and Pascual, 2001; Reina et al., 2001). Theoretical calculations showed that the static magnetic field induced changes in the ionic concentration and in the osmotic pressure, which regulates the entrance of water into the seeds. The magnetic field exposure was 10 min in a Helmholtz coil, and this was carried out immediately before placing the seeds in water inside a climatized room. The investigators demonstrated a close correlation between their theoretical calculations and the actual experimental results. It was shown that exposure to the static magnetic fields altered the water absorption in seeds, which may possibly explain the change of germination rate. Adair (2002) discussed and questioned these results. Amyan and Ayrapetyan (2004) investigated changes in the wet and dry weight of barley seed after treatment by static magnetic field levels of 1.25, 2.50, and 3.75 mT. Seed treatment was carried out in cold (4°C) and warm (20°C) distilled water. After pretreatment by the fields, the seeds were incubated for 72 h. Results suggested that effects depend on not only the field strength but also the incubation time period.

Growth and sporulation of phytopathogenic microscopic fungi have been investigated under exposure to a static magnetic field that ranged from 0.1 to 1 mT (Nagy, 2004). It was

shown that the growth was decreased by the magnetic field exposures. Increases in the number of developed conidia of *Alternaria alternata* and *Curvularia inaequalis* and a decrease in the number of *Fusarium oxysporum* conidia have been observed as well.

Effects of combined AC and DC magnetic fields on the germination of hornwort seed (*Cryptotaenia japonica* Hassk) have been reported by Kobayashi et al. (2004). They tested three directions of the AC magnetic field, which were vertical, parallel, and perpendicular to the direction of total geomagnetic field (DC). The frequency and strength of the AC magnetic fields ranged between 3.5 and 14 Hz and 500 and 750 μT . The total geomagnetic field was 50 μT . The seeds were exposed to the fields for 16 d at 24 h/d. The vertical AC magnetic field applied simultaneously with the DC field was found to promote the germination of seeds. Field level applications of 7 Hz, 750 μT and 14 Hz, 500 μT showed the maximum effects.

Effects of static magnetic fields ranging from 0 to 350 μT on gravitropic bending in the apical stem segments of flax seedlings (*Linum bienne*) have been investigated (Belova and Lednev, 2001). In comparison with the control group kept in a geomagnetic field of 46.5 μT , stimulation of the gravitropic bending was observed at $0 \leq B_{\text{DC}} \leq 2 \mu\text{T}$ and $200 \leq B_{\text{DC}} \leq 350 \mu\text{T}$, and inhibition was observed at $100 \leq B_{\text{DC}} \leq 170 \mu\text{T}$.

Investigations of static magnetic field effects on the curvature of primary roots of radish seedling (*Raphanus sativus* L.) have been carried out (Yano et al., 2001). When radish roots were exposed to an inhomogenous static magnetic field, they responded to the south pole of the magnet. Trophic response was found at a field level of 13–68 mT with a gradient of 1.8–14.7 T/m. A small response to the north pole of the magnet was found as well.

Jovanic and Sarvan (2004) studied the effects of static magnetic fields on fluorescence spectra and leaf temperature in intact plant bean (*Phaseolus vulgaris* L.). The field strengths were as high as 160 mT, and the plant was grown for 3 weeks. It was reported that significant changes in fluorescence spectra and leaf temperature were induced after the field exposure. An increase of fluorescence intensity ratio and changes in leaf temperature ΔT were observed in parallel with increase in field intensity.

8.4.3 Magnetotaxis

There have been many studies reporting that magnetic fields affect the swimming behavior of *Paramecium*. A decrease in swimming velocity and an increase in the frequency of directional changes were observed after exposure to a magnetic field of 0.126 T during a motility study of *Paramecium* (Rosen and Rosen, 1990). Nakaoka et al. (2002) found that a typical ciliated protozoan, *Paramecium*, swam perpendicular to a static magnetic field of 0.68 T. It was suggested that the diamagnetic anisotropy of cellular components cilia and trichocysts was important for the magnetic orientation of their swimming.

Effects of horizontal magnetic fields on the movement of *Euglena gracilis* (ca. 50 μm in length) have been reported (Tanimoto et al., 2001). When the horizontal magnetic field with a gradient of ca. 400 T^2/m was applied, living *E. gracilis* moved to the higher field (positive magnetotaxis), whereas dead *E. gracilis* moved to the opposite, lower field. *E. gracilis* was found to be oriented perpendicularly to the magnetic field regardless of whether they were alive or dead. Thus, magnetotaxis of living *E. gracilis* may be explained by taking into account both the environmental inhomogenous magnetic forces and the magnetic orientation of *E. gracilis*. In contrast, magnetotaxis was not observed in a uniform magnetic field of 8 T. Effects of strong magnetic field gradient (max. 8 T, ca. 400 T^2/m) on the movement of *E. coli* have been investigated (Tanimoto et al., 2005). *E. coli* cells were placed in a 5 mm (diameter) \times 150 mm (length) glass tube containing viscous media that flowed in the tube. The speed at zero field was 0.65 cm/h. The observed velocities of the movement from a high field (8 T) to a low field (1.5 T) and the movement in the opposite direction around

were 1.35 and 0.49 cm/h, respectively. Diamagnetic *E. coli* experienced a repulsive behavior to magnetic forces of increased magnetic gradient. Therefore, it has been speculated that the velocity of *E. coli* would be accelerated toward the direction of the lower-strength field, while it would be decelerated in the direction of the stronger fields. Results suggested the magnetic force specifically, could be an important mechanism of magnetic field effects when a low-frequency high magnetic field was applied, since the microorganism might respond to mechanical stress due to alternating magnetic forces.

8.4.4 Others

As an initial study for investigating the relationship between magnetic fields and amoebae, Berk et al. (1997) examined the inhibitory effects of static magnetic fields on the population growth of amoebae. They tested three species, *Acanthamoeba hatcheii*, *Acanthamoeba castellanii*, and *Acanthamoeba polyphaga*. Amoebae were exposed to magnetic field strengths of 71 and 106.5 mT with an exposure duration up to 72 h. Results showed that magnetic fields decreased the growth of all three potentially pathogenic ameba populations significantly within 72 h. It was reported that the inhibitory effect did not depend on the field strength, and it was shown that this research would be important and advantageous in the development of disinfection strategies for surface material, such as the surface of contact lenses.

Rai et al. (1997) investigated the effects of a 0.1-T static magnetic field on the electrical parameters of goat eye lens. Under magnetic field application, the complex impedance between real and imaginary parts was obtained in the form of a Cole–Cole plot. It was reported that the static magnetic field altered the current flow in the tissue.

Iwasaka and Ueno (1998b) investigated the effects of a static magnetic field of up to 14 T on the near-infrared spectrum of water molecules and glucose solutions. They demonstrated the possibility that the static magnetic field affected the formation of hydrogen bonds of water molecules and the hydration of glucose molecules.

Morariu et al. (2000) exposed human blood samples to zero magnetic fields for 72 h in order to observe the aging process of erythrocytes. The control samples were kept in a normal geomagnetic field. In a zero magnetic field, increases in the rate of Na^+ and Ca^{2+} influx, in the rate of K^+ outflow, and in homolysis were observed. Reduction in Na^+-K^+ -ATPase and Ca^{2+} -ATPase activities has been observed in a zero magnetic field; thus, zero fields significantly accelerated the aging of erythrocytes. Effects of zero magnetic fields were further investigated on Zn and Cu concentrations in the human blood serum during *in vitro* aging of blood with a 48-h exposure (Ciortea et al., 2001). Blood samples were collected from both healthy donors and chronic bronchial asthma (BA) patients. While the Zn concentration was not found to be affected by the zero magnetic field exposure, Cu concentration was found to be sensitive to this field. It was also reported that the aging effect appeared to be decelerated for most BA types.

8.5 Medical Applications

8.5.1 Biomagnetic Phenomena

Biomagnetic phenomena for different intensities of magnetic fields and their frequency are shown in [Figure 8.1](#). It is important to know the intensities and frequencies of magnetic fields involved in biomagnetic phenomena while discussing the relationship

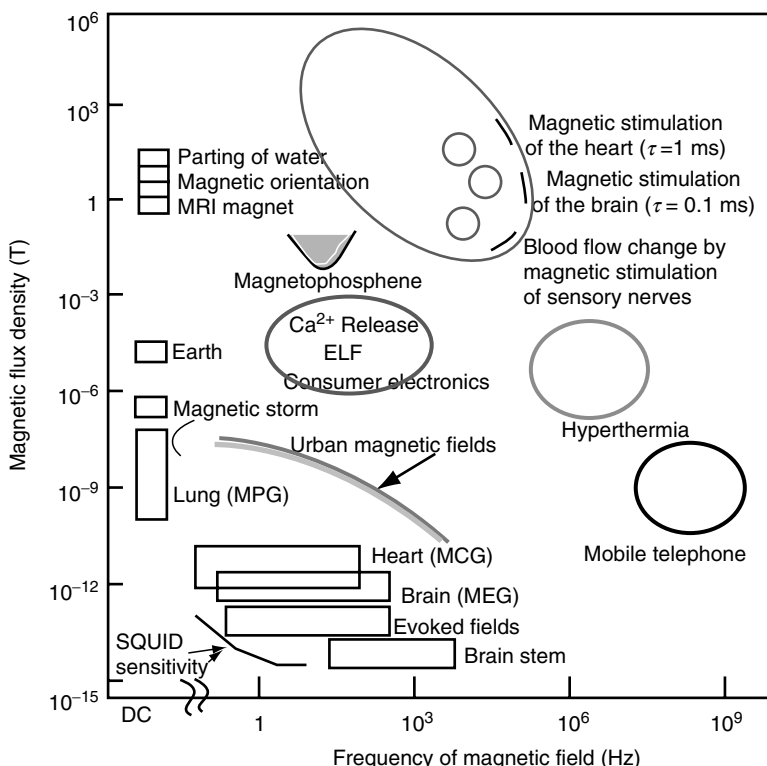


FIGURE 8.1
Biomagnetic phenomena for medical and therapeutic application.

between magnetism and living organisms. Regarding the effects of magnetism on living organisms, it should be realized that the actions of static and variable magnetic fields differ from each other in terms of the fundamental mechanism.

Studies on the biological effects of electromagnetic fields have resulted in significant developments in medical applications for electromagnetic fields, after the development of high-strength superconducting magnets. TMS, measurement of biomagnetic fields with the superconducting quantum interference device (SQUID), and MRI are the three mainstays of these medical applications. These techniques have also been leading the amazing progress in the understanding of the brain function. TMS locally stimulates the human cerebral cortex with millimeter-order spatial resolution from a figure-eight coil placed on the skull. A three-dimensional imaging of the brain neuron function has been enabled by utilization of SQUID in magnetoencephalography (MEG), functional magnetic resonance imaging (fMRI), and current-distribution MRI. Results from TMS and imaging studies indicate potential applications of biomagnetics in brain science and clinical neuropsychiatry.

In TMS, when a strong electric current is applied to a figure-eight coil positioned over the head for 0.1–0.2 ms, a pulsed magnetic field of 1 T is produced. This pulsed magnetic field generates eddy currents in the brain, which excite the targeted area of the nervous system.

Incidentally, unconscious and uncontrolled exposure of the brain to high-frequency electromagnetic waves has been increasing with the recent, rapid widespread use of cellular phones by the general public. Cellular phones in Japan are designed for operation with a frequency of 800 MHz and a microwave of 1.5 GHz ([see Chapter 1](#) on environmental exposures by Mild and Greenebaum).

In biomagnetic measurements, MEG associated with auditory brain stem response is of the order of 10^{-15} T (1 fT), and it can be measured on the extremum of the sensitivity limitation of the SQUID gradiometer (Erne et al., 1988; Iramina and Ueno, 1995). In 10^{-12} T (1 pT)-order measurements, while α -wave spontaneous MEG can be detected without a signal-averaging technique, the technique is required to increase a signal-to-noise ratio (SNR) in order to detect various evoked responses and brain stem responses.

The recent development of noninvasive brain function measurement technologies, such as MEG and fMRI, has been contributing to the rapid progress in brain science research. Scientific discussions of mental problems such as thinking and psychomotor activities (e.g., joy, anger, sadness, and happiness) in terms of brain function became possible with the development of these new technologies.

In static magnetic fields of a few tesla, fibrin polymers, which are involved in blood coagulation, orient parallel to the magnetic fields in the course of polymerization (Yamagishi et al., 1989; Ueno et al., 1993). Furthermore, magnetic alteration of blood coagulation and dissolution processes by magnetic fields and magnetic orientation of biopolymers, such as fibrin and collagen, have been observed. These findings introduce a new aspect of biomagnetic applications in the regulation of living systems and biological materials.

8.5.2 Transcranial Magnetic Stimulation

TMS is the technique of locally applying magnetic stimulation by a strong pulsed magnetic field on the order of 1 T transcranially to the brain. When a strong electric current is applied to a figure-eight coil placed over the head for 150 μ s, a pulsed magnetic field on the order of 1 T is produced that generates eddy currents in the brain, which excite the nervous system. The first study of magnetic stimulation in a human brain by Barker et al. (1985) utilized single coils; thus, localized magnetic stimulation of a targeted portion of the human brain was impossible. The localized vectorial magnetic stimulation of a human cortex using a figure-eight coil was developed by Ueno et al. (1978, 1986b, 1988, 1989, 1990a,b, 1991), which enabled stimulation of the motor cortex of a human brain at 5-mm resolution. Localized magnetic stimulation contributed to the creation of functional maps of the motor cortex related to hand and foot areas. An optimal direction of probe placement for the targeting of stimulating currents, which induce neural excitation in each functional area of the cortex, based on functional maps was observed, the so-called vectorial feature. Variations in the functional maps of the cortex with changes in orientation of the stimulating current were observed as well. It is proven that the vectorial feature allows for studies that reflect both functional and anatomical organizations of neural fibers in the brain. Localized magnetic nerve stimulation of the brain is suitable for investigations of brain function and construction without damaging any tissues.

Applications of TMS temporarily disturb brain function, which results in a virtual lesion in the brain. Zangaladze et al. (1999) showed that the disruption of the function of the occipital cortex with the use of focal TMS interferes with the tactile discrimination of grating orientation. Epstein et al. (2002) used TMS to investigate memory encoding and retrieval, particularly the role of the dorsolateral prefrontal cortex in associative memory for visual patterns. TMS disrupted associative learning of abstract patterns over the right frontal area, which suggests that the participating cortical networks may be lateralized in accordance with classic concepts of hemispheric specialization.

Traditionally, stimuli are applied at various scalp positions using a latitude- and longitude-based coordinate system referenced to Cz in the 10–20 international system at the vertex, while simultaneously, the amplitude of the motor evoked potentials generated in contralateral muscles is also measured (Ueno et al., 1989, 1990a). This gives a “map” of sites on the scalp from which responses can be obtained by each reference muscle.

Rothwell et al. (1987) revealed the enormous clinical importance of TMS, namely, for motor functional evaluation.

Recent developments in the navigated brain stimulation (NBS) stereotactic TMS devices allow noninvasive mapping of the spatial and temporal representation of any brain activity that reacts to magnetic stimuli (Krings et al., 2001), such as sensory, motor, language, and cognitive functions. Stereotactic TMS coil positioning and real-time visualization of the stimulating electromagnetic field effect using MRI allow precise replicability of stimulation parameters as well as accurate dose definition. Frameless NBS allows precise localization of a stimulation target in combination with other imaging modalities or by the use of anatomical landmarks. In a case where a brain tumor was resting adjacent to the precentral gyrus, the motor strip identified by TMS compared preoperative MRI and fMRI and revealed fine functional differences between results that were integrated on the navigation system. Distribution of the tumor margin and the motor cortex (both fMRI and TMS assisted) can be drawn on the patient's scalp using the navigation system. Skin incision, craniotomy, and operative approaches were considered from these results so as to avoid motor deterioration.

There has been no verification of which nerve cells are actually stimulated by TMS. There is one subject under discussion: whether a target neuron cell is directly stimulated by TMS (direct stimulation) or whether an interneuron is first stimulated and then a target neuron cell is stimulated indirectly (indirect stimulation). It is possible that alteration of eddy currents by heterogeneity of conductivity in the brain may affect the path of these currents and result in both neuronal excitation and excitatory directional changes at sites other than those targeted by the original intended direction of stimulation. Further investigation and analysis of TMS and construction of models using magnetic nerve stimulation are required to clarify how the relationship between a position of a coil and a site of stimulation can be affected by strength of stimulation, arrangement of neurons, heterogeneity of conductivity, and interneuronal participation. While a figure-eight coil is suitable for local stimulations at the surface of the cortex along the surface of the head, tridimensional localized stimulations are not possible with the coil at present.

Despite the problems described above related to TMS, there are high expectations for magnetic stimulation to contribute to a new era of brain science. A major and possibly very important future field of study is the application of TMS for obtaining therapeutic effects in neurological disorders. A number of animal studies testing the basic mechanisms of TMS-induced alterations of neurotrophic factors, gene expression, and changes in plasticity have been conducted (Fujiki and Stewart, 1997; Keck et al., 2000; Fujiki et al., 2003; Ogiue-Ikeda et al., 2003a).

There is strong evidence that the expression of certain genes such as the immediate early gene, astrocyte-specific glial fibrillary acidic protein mRNA (Fujiki and Stewart, 1997), and brain-derived neurotrophic factor is altered in response to repetitive TMS (rTMS). This indicates that the measurable effects of TMS reach the molecular and signaling levels. The most promising hypothesis is that magnetic field-induced neuroprotective or trophic factors may protect neurons from hypoxic insult (Fujiki et al., 2003). Long-duration rTMS modulates the monoamine neurotransmitter system in content and turnover and may also induce sprouting of mossy fibers in the hippocampus (Keck et al., 2000). Increased dopaminergic neurotransmission may contribute to the beneficial effects of rTMS in the treatment of affective disorders and Parkinson's disease.

The results of these studies provide strong evidence that noninvasive TMS can strongly modulate gene expression in neurons and astrocytes. Thus, TMS, originally used simply as a way to assess the function of descending motor tracts noninvasively, may in the end be used as a means to modulate gene expression and to induce restorative plasticity or tolerance against injury in the brain.

TMS does not cause any pain and requires no physical invasion of the body; therefore, it should become more important in functional, diagnostic, and therapeutic research of the brain. In brain functional research, application of magnetic stimulation for the temporary blockage or modification of the facultative information process and cognitive process of various sensory systems may be used to identify localization and connecting pathways of brain function. If a magnetic stimulation can effectively block and modify various sensory systems, it should be advantageous for pain treatment. Elucidation of the effects of magnetic stimulation on synaptic functions may lead to further research associated with brain plasticity. Further research for investigation of magnetic compensation and reconstruction of neuronal functions around damaged neurons may lead to the development of various magnetic field-based stimulation applications, including the treatment of depression, the prevention of dementia, and a safer and more effective magnetic pulse treatment, which may replace the current electroconvulsive therapy (ECT).

8.5.3 Magnetoencephalography

MEG measures the very weak magnetic fields of the order or 10^{-13} T (100 fT) generated by neuronal current flow, by the detection of magnetic signals measured by SQUID arrays. MEG can detect brain functions with high millisecond-order temporal resolution and high millimeter-order spatial resolution noninvasively; thus, it is useful for investigation of brain functions in humans, including higher brain functions such as memory and cognition. Since Cohen obtained a magnetoencephalogram for human α -waves with the use of a SQUID, a prototype developed by Zimmerman and Colleagues (1972), it was only until recently that the use of a whole-head MEG system that is able to carry out spontaneous measurement at multiple points has become practical (Squires, 1991; Ahonen et al., 1993; Vrva et al., 1993). In recent years, the whole-head MEG system has been incorporated into brain functional research all over the world and has accelerated progress in research.

Application of forward and inverse problems in MEG analysis is critical to estimate a localization of brain function. Ueno and Iramina (1991) measured MEG associated with short memory, cognition, and mental rotation in humans, constructed current-dipole and distributed intracerebral electrical source models, and carried out estimations for the localization of various brain functions during the processing of information. The electrical source of a visually evoked reaction with approximately 150 ms at latency localized in the primary visual cortex was described in a current-dipole model relatively well, while a distributed intracerebral electrical source model was more useful in estimation of the electrical source incident to a mental rotation with approximately 180 ms or higher at latency. In the distributed electrical source model, a chronological transition of electrical source groups from the occipital lobe area to the posterior temporal lobe area was captured. MEG is not only a tool for basic brain functional research, but is also applicable to medical research. Clinical applications of MEG include detection of epileptic spikes, measurements of slow waves associated with brain tumors and cerebrovascular diseases, and cerebroelectric activity of ELF induced by event-related potentials.

It is necessary to construct experimental paradigms that are able to perform more precise extraction of a specific brain function, allow understanding of brain function dynamics, and provide measuring techniques to assess the acquired information (Yoshida et al., 1995; Iwaki et al., 1999). It is also important to develop signal processing techniques for source determination of signals with very small SNRs and with distributed electrical sources, improve inverse problem approach methods, and construct suitable current source models (Ueno and Iramina, 1991; Iramina et al., 1994, 1995b). There are several factors to be taken into account in MEG inverse problem analysis: the shape of the head, heterogeneity of conductivity, alignment of neuron cells, interneurons, and

thalamocortical specific projection system. An ideal electrical source model possesses electrophysiological features of complex cranial nerve systems with consideration of these factors.

In a study on language-related brain activities, Kuriki et al. (1995, 1998) used MEG imaging to examine the temporal and topographical characteristics of neural activities in the comprehension of Japanese complex sentences with a clause structure. The Korean language was also used as an experimental language (Kwon et al., 2005). The Korean language has a subject-object-verb order structure, ending with a verb. Semantic and syntactic violations, that is, errors introduced in a sentence, can be made by altering a single word, that is, a verb, in an inappropriate manner. Neural activities in response to such a violation are measured as the response elicited by the final verb in the verb-ending sentence. This study is aimed to identify neural activities in the cerebral cortex that occur during a latency course, processing syntactic and semantic aspects of spoken sentences.

In another MEG study on music, Kuriki and colleagues used melodies to measure the responses that are elicited by an out-of-key tone in musical phrases (Hirata et al., 1999; Kuriki et al., 2005). The musical context is established by the sense of a key and melodic pitch sequence. The responses would reflect the perception of these restricted aspects of melody. The results of the present study should provide an understanding of the spatio-temporal characteristics of cortical activities involved in melody perception. MEG measurements were also performed for musical tones and chord stimuli for well-experienced musicians and nonmusicians. The principal purpose of this study was to explore how the brain activity reflected in late auditory evoked responses would behave when exposed to the successively presented tones and chords stimuli and also how the activity would vary according to experience of musical training.

Although there is still ambiguity in the analytical technique, MEG still attracts medical researchers because it can reflect the chronological change of source signals to that of magnetic fields. It is obvious that MEG will become an essential technique in human brain function research, since there is only one technique that is noninvasive with millisecond-order high temporal resolution, electroencephalography, available at this time for estimation of brain function localization,. Development of MEG with higher sensitivity and operativity, construction of an intracerebral electric source model, and improvement of inverse problem analysis may become more important.

8.5.4 Magnetic Resonance Imaging

Since Lauterber suggested a linear magnetic field gradient in 1973, MRI has been rapidly developed (Lauterbur, 1973). MRI utilizes fusion techniques of spatially uniform direct current magnetic fields, spatially gradient direct current magnetic fields, and RF electromagnetic fields. A guideline of static magnetic field exposure to a human body by the International Commission on Non-Ionizing Radiation Protection (ICNIRP) suggests 2 T as the ceiling value for body parts, except for arms and legs, in occupational exposure. In the application of clinical MRI, although the exposure is carried out under supervision of doctors, the current exposure level is confirmed to be 2 T or less. It is not feasible to obtain resonance images, except from hydrogen atoms, in static magnetic fields at this strength.

The use of MRI conducted at high static magnetic field levels is fast growing (Robitaille et al., 1998). With the advent of the 8-T/80-cm MRI scanner (Schenck et al., 1992; Kangarlu et al., 1999) the safety of the static magnetic field became a paramount issue for MRI researchers. While the primary concern in high magnetic field MRI has been excessive RF deposition in human subjects (Kangarlu et al., 2003, 2005), the static magnetic field could equally cause alarm for its potential for interaction with biological cells and molecules. One concern regarding human exposure to a high static magnetic field is the

orientation of the molecules. Magnetohydrodynamics, which describes the interaction of moving charged particles with the magnetic field, has also raised concern with high magnetic field applications. Investigation of this effect with its possible consequences on human cognition has not received enough attention. As such, Chakeres et al. (2003) have recently conducted a series of studies on the effect of high static magnetic fields on human cognitive function. In spite of the availability and use of high magnetic field instrumentation for three decades, high magnetic field exposures of human subjects for extended periods of time have not been conducted. Such exposures did not pose a significant biological hazard at field strengths of up to 8 T as measured within the capability of their experimental design. In addition, human neuropsychological performance as a measure of any possible static magnetic field modification of cognition was not detected (Chakeres et al., 2003). To our knowledge, such a study has not been performed in the past at a field strength of 8 T for such an extended period of exposure time (Schenck et al., 1992; Kangarlu et al., 1999). In spite of the complex nature of an investigation of such effects, our present lack of observation of any detectable change in human cognition as related to high magnetic field exposure is an important reason for further research. In this regard, studies such as this could serve as a good starting point for *in vivo* characterization of static field effects in humans, in light of the rapidly expanding applications of high magnetic field MRI.

A time-varying magnetic field with sufficient intensity may be excitatory to peripheral nerve stimulation (PNS) (Ueno et al., 1986a; Barker, 1991; Sandrey et al., 2002; So et al., 2004). The physiologic mechanism is presumably due to interaction of neuronal structures with the induced electric field, rather than a direct physiologic effect of the magnetic field (Reilly, 1989).

Relatively early in the development of MRI, it was recognized that the pulsed gradient magnetic fields might induce PNS or cardiac stimulation (Reilly, 1991; Ueno et al., 1992). The pulsed gradients are of audio frequency, and they modulate the frequency and phase of the signal from the precessing magnetization as part of the MRI image reconstruction process. Reilly (1989) projected that a long-duration (>1 ms) pulse of induced electric field of 6.2 V would be sufficient to stimulate a 20- μm -diameter nerve fiber. The same amplitude of electric field was estimated to be the 1-percentile rank for stimulation of the human heart. Because of the much longer chronaxie for cardiac muscle, about 3 vs. 0.38 ms, the gradient field intensity, expressed in terms of the time derivative dB/dt of the magnetic field, required to achieve cardiac stimulation is far greater than that for PNS. The large projected values of dB/dt required for cardiac stimulation were confirmed in measurements in dogs by Mouchawar et al. (1992) and by Bourland et al. (1999), who reported that cardiac stimulation by pulsed gradient fields requires a dB/dt amplitude in excess of 2000 T/s for a 530- μs period. These values compare with representative dB/dt intensities of less than 100 T/s in an MRI system. For healthy patients, cardiac stimulation in MRI is avoided by a wide margin.

Mild PNS in MRI is not thought to be harmful, but painful stimulation should be avoided. To determine the population distribution for physiologic response to the time-varying gradient fields, the MRI safety group at Purdue University undertook a study with 84 human volunteers (Bourland et al., 1999; Nyenhuis et al., 2001). The volunteers were exposed to magnetic field patterns similar to those that would be experienced in a cylindrical bore MRI system. (Nyenhuis et al., 1997). The volunteers were asked to rate their responses to a gradient pulse sequence on a scale covering the range of 1 = onset of PNS, 5 = uncomfortable but acceptable for the duration of a scan, and 10 = intolerable. The duration of the dB/dt pulses ranged from 50 to 1000 μs , in order to determine parameters for the strength duration given by:

$$\frac{dB}{dt} = b \left(1 + \frac{c}{d}\right)$$

where b is rheobase for a long-duration pulse, c is chronaxie, and d is the pulse duration. The measured responses were well fit by a chronaxie of 380 μ s. For onset of PNS (score = 1), the median rheobase b was found to be 18.8 T/s for the y -coil and 28.8 T/s for the z -coil. Median dB/dt intensities for scores of 5 and 10 were approximately 50% and 100% greater than the score = 1 values, respectively. From the population distribution, the lowest 1-percentile value for PNS (score = 1) was about half the median value, and the lowest 1-percentile for uncomfortable (score = 5) was approximately equal to the median of the PNS threshold.

den Boer et al. (2002) found good agreement among the Purdue and other studies for the PNS thresholds by the switched gradients. Accordingly, the results of these studies were used for determination of the allowable gradient field intensities in MRI, which were set to be 80% of the mean PNS threshold (IEC, 2002).

The values of chronaxie and rheobase in the Purdue study were determined for rectangular waveforms. Models based on the physiologic response to rectangular pulses can be used to predict the threshold intensities for nonrectangular waveforms (Havel et al., 1997; den Boer et al., 2002).

So et al. (2004) recently reported results of calculations incorporating a realistic human model of the rheobase electric field intensity for PNS in the Purdue study. The rheobase electric field intensities in subcutaneous fat ranged from 3.3 to 4.4 V/m for the different body models and coil configurations. These values are in reasonable agreement with a rheobase electric field of 5.36 V/m for PNS with a solenoidal coil enclosing the arm (Havel et al., 1997).

MRI of electrical phenomena in living bodies is potentially useful for quantitative evaluations of the biological effects of electromagnetic fields and for direct detection of neuronal electrical activities in the brain. Magnetic fields in an object cause a shift in the resonant frequency (Manassen et al., 1988; Sekino et al., 2004b) and a change in the phase of magnetic resonance signals (Joy et al., 1989). Spatial distributions of an externally applied magnetic field and electrical current can be estimated from these changes in magnetic resonance signals. These methods have use in certain medical applications, such as the imaging of current distributions in electrical defibrillation (Yoon et al., 2003).

The fMRI developed by Ogawa et al. (1992) utilizes a technology that reflects various magnetic features of hemoglobin in blood on magnetic resonance signal patterns. Tomograms of brain function can be obtained from information on localized blood flow in the brain. fMRI utilizes a blood oxygenation level dependent (BOLD) effect of localized blood flow on brain activation for indirect imaging of brain activities. However, no information on electrical conditions *in vivo* can be obtained with current MRI and fMRI systems.

Detection of electrical currents associated with neuronal or muscular electrical activities requires extremely high measurement sensitivity. The sensitivity for detecting weak magnetic fields in the human brain was estimated using numerical simulations (Hatada et al., 2005). The theoretical limit of sensitivity was approximately 10^{-8} T. The effect of neuronal electrical activities on magnetic resonance signals was investigated in several experimental studies (Kamei et al., 1999; Xiong et al., 2003). These studies potentially lead to a new method for visualizing brain function with a spatial resolution of millimeters and a temporal resolution of milliseconds.

Impedance-weighted magnetic resonance images were obtained during applications of external oscillating magnetic fields, which induce impedance-dependent eddy currents in a sample (Ueno and Iriuchi, 1998). In another study, spatial distribution of electrical impedance was obtained from the electrical current distributions by using an iterative algorithm (Khang et al., 2002). The apparent diffusion coefficient reflects electrical conductivity of a tissue, which enables an estimation of anisotropic conductivity of that tissue (Tuch et al., 2001; Sekino et al., 2004a). This method was applied to imaging of electrical

conductivity in the human brain. Several regions in the white matter, such as the corpus callosum and the internal capsule, exhibited high anisotropy in conductivity. The magnitude and phase of magnetic resonance signals are affected by permittivity (Sekino et al., 2005). A distinctive signal inhomogeneity arises in images of objects whose dimension is comparable to the wavelength of the electromagnetic fields at the resonant frequency. This phenomenon, dielectric resonance, particularly appears in scanners with high static fields.

Once high-quality current distribution MRI of the detailed distribution of electric source incident to brain neural activities becomes available, comparison of results of MRI and fMRI will show the relationship between brain neural activities associated with BOLD effects and neural current distributions, which may lead to various new observations of dynamics in brain function localizations.

Impedance MRI may not be applied widely in brain function research; however, high-quality impedance MRI for impedance and admittance *in vivo* may lead to development of a new research field of impedance physiology. It is obvious that the information of impedance distributions is important for studying magnetic stimulation and MEG inverse problems.

8.5.5 Magnetic Orientation for Tissue Engineering

In the last decade, it has become possible to create static magnetic fields of 10 T and higher. With this development, studies regarding magnetic effects on macromolecules have increased. These studies include investigations into the magnetic effects on fibrin, collagen, erythrocytes, and platelets (Higashi et al., 1993a,b; Iwasaka and Ueno, 1994; Iwasaka et al., 1998; Iino and Okuda, 2001). Recent research on effects of strong static magnetic fields includes their impact on morphogenesis, cell adhesion, and apoptosis (Tofani et al., 2001).

When technology for generation of stronger magnetic fields becomes available in the future, magnetic orientation research will be subdivided into several areas. Effects of magnetic orientation on cell functions such as morphogenesis, adhesion, motility, proliferation, differentiation, and apoptosis may become one of the important areas of research.

Macromolecules such as fibrin and collagen are oriented by static magnetic fields of several tesla. Fibrin polymers are diamagnetic materials that are oriented in a magnetic field. Collagen fibers orient perpendicular to the magnetic field orientation (Torbet and Ronziere, 1984). Polymerization and dissolution of fibrin in homogenous magnetic fields of up to 14 T have been investigated (Iwasaka et al., 1998). It was shown that the magnetic orientation of fibrin fibers accelerated both the polymerization and the dissolution of fibrin fibers.

Magnetic orientation of cells is associated with magnetic anisotropy of proteins and lipids. Erythrocytes orient the disk surface parallel to magnetic fields because of magnetic anisotropy of the biomembrane lipid bilayer. However, halophilic bacteria orient their membrane plane vertical to magnetic fields even though the purple membrane has a similar membrane structure as the erythrocyte membrane (Neugebauer et al., 1977). The purple membrane contains a membrane-bound protein (bacteriorhodopsin) that contributes 75% to the membrane weight. Since the magnetic anisotropy of bacteriorhodopsin is larger than that of the lipid bilayer, halophilic bacteria posses a different magnetic orientation from erythrocytes. Therefore, magnetic orientation is determined by the quantity and the alignment of cell components that possess magnetic anisotropy.

Higashi et al. (1996) found that an orientation of glutaraldehyde-fixed erythrocytes in strong static magnetic fields up to 8 T was perpendicular to the field. The effect was attributed to the paramagnetism of membrane-bound hemoglobin. The rates of

sedimentation and aggregation of human erythrocytes in a homogenous magnetic field of 6.3 T have been studied (Iino, 1997; Iino and Okuda, 2001). It was reported that the cell aggregation accelerated the sedimentation rate. Results have suggested that the enhancement was especially significant in anisotropic erythrocytes, and the increase in an intermembrane adhesive area might be due to the magnetic orientation of anisotropic erythrocytes.

DNA, which occupies most of the head portion in bovine sperm, may be involved in magnetic anisotropy and orientation determination of sperm. Cricket sperm with an acicular head part show the same magnetic orientation (vertical) as bovine sperm in magnetic fields of 0.09 T (Suzuki et al., 1995); this is because DNA, which is folded lengthwise, possesses large diamagnetic anisotropy. If DNA in the head part of bovine sperm is orderly aligned as in cricket sperm, the magnetic anisotropy may contribute to the magnetic orientation of sperm.

A significant feature of magnetic orientation of bovine sperm is the direction of orientation. Platelets orient parallel to magnetic fields because of the microtubules inside, which have a magnetic orientation parallel to the magnetic fields. Thus, bovine sperm without motility are assumed to orient parallel to magnetic fields as platelets do, since the tail (flagellum) consists of microtubules. On the contrary, the whole body of bovine sperm shows magnetic orientation vertical to magnetic fields, and the flat surface of the head also orients vertically to magnetic fields. A sperm with the tail removed shows the same orientation. Since it is impossible to obtain a tail without damaging flagellum, the magnetic orientation of a tail alone cannot be observed. In two separate experiments, Emura et al. (2001, 2003) studied the orientation of bull sperm cells and *Paramecium* cilia in static magnetic fields and measured their anisotropic diamagnetic susceptibility ($\Delta\chi$). Bovine sperm consists of a very flat head part (5 μm) and a long tail part (flagellum, 50 μm), which consists of microtubules. Compared to sperm of other species, the head, which contains DNA, is notably larger. The sperm showed an orientation perpendicular to the field of 1 T or lower. The diamagnetic cell components, such as cell membrane, DNA in the head, and microtubule in the tail, were thought to contribute to this orientation. It was observed that *Paramecium* cilia became oriented in parallel to the magnetic field at the strength of 8 T. The author suggested that $\Delta\chi$ for each was the quantitative index of the effect.

Iwasaka et al. (2003a) reported the effects of 14-T fields on assemblies of A7r5 smooth muscle cells. It was shown that the field affected the morphology of smooth muscle cell assemblies and the shapes of the cell colonies extended along the direction of the magnetic flux. They speculated that the mechanism was a diamagnetic torque force acting on cytoskeleton fibers, which are dynamically polymerizing and depolymerizing during cell division and cell migration. They also investigated the effects of the static magnetic field on the convection flow in a cell culture medium and on cell adhesion patterns (Iwasaka et al., 2003b). The mouse osteoblast cell line MC3T3-E1 and HeLa cell line were used in this study. The magnetic field of 6 T with a gradient of 60 T/m affected the convection of floating cell aggregations in a cell culture flask and reversibly changed the direction of convectional flow. After the exposure of MC3T3-E1 cells to the magnetic field of 8 T for 1 d, the thermal convectional flow in the medium was found to promote the cell orientation.

Iwasaka and Ueno (2003) examined the displacement of intracellular macromolecules under a static magnetic field of 14 T using linearly polarized light. The changes in polarized light intensity through the lamellar cell assembly under magnetic fields corresponded to the behavioral changes in cell components. They speculated that intracellular macromolecules rotated and showed a displacement due to diamagnetic torque forces during the exposure to the 14-T magnetic field for 2–3 h.

Matrix proteins provide a permissive environment for the orientation of cells, as demonstrated, for example, with the testing of smooth muscle cells and endothelial cells in collagen fibers under strong magnetic fields (Stefano and Tranquillo, 1993; Tranquillo et al., 1996).

Eguchi et al. (2003) observed the effect of a static magnetic field on orientation of Schwann cells. After a 60-h exposure, cultured Schwann cells from dissected sciatic nerves of neonatal rats oriented parallel to the field of 8 T, whereas Schwann cells suspended in a medium with collagen oriented perpendicular to the field after a 2-h exposure. It was suggested that magnetic field-oriented collagen fibers were the key factor in the orientation of Schwann cells.

Kotani et al. (2000) studied the effect of an 8-T magnetic field generated by a superconducting magnet on the orientation of osteoblasts alone and a mixture of osteoblasts and collagen. It was found that osteoblast cells oriented parallel to the magnetic field, but a mixture oriented perpendicular to the field.

Hirose et al. (2003a) investigated the preferred orientation of human glioblastoma cells A172 after exposure to a 10-T static magnetic field, in the presence or absence of collagen. It was found that A172 cells embedded in collagen gel oriented perpendicular to the direction of the static magnetic field.

By placing dorsal root ganglia (DRG) explants onto one end of magnetically aligned collagen gel formed into 4-mm-diameter rods, Dubey et al. (1999) developed an *in vitro* assay to study neurite elongation. The depth of neurite elongation from chick embryo DRG neurons into these aligned rods was found to be substantially greater than that under the control condition. The depth increased as the magnetic field strength increased, as did the collagen gel rod birefringence; collagen fibril aligned along the rod axis. These results may translate into an improved method of entubulation repair of transected peripheral nerves by directing and stimulating axonal growth through a tube filled with magnetically aligned collagen gel. The same research group later reported the improvement of peripheral nerve regeneration in mice after the treatment of magnetically aligned collagen gel filling of a collagen nerve guide (Ceballos et al., 1999). The hypothesis of this study was that contact guidance of regenerating axons or invading nonneuronal cells to the longitudinally aligned collagen fibrils would improve nerve regeneration. It was reported that mice exhibited regeneration with magnetically aligned collagen gel, including the appearance of nerve fascicle formation.

Application of magnetic orientation in the production of biologically functional materials and artificial organs has been started. By attaching aligned vascular smooth muscle cells and endothelial cells to artificial vascular walls in an orderly fashion, rheologically rational biological functions can be obtained. As techniques in bionics and biomaterials improve, application of magnetic orientation should expand.

8.5.6 Treatments of Pain, Cancer, and Other Diseases

Static magnetic fields or ELF-modulated static magnetic fields potentially have therapeutic effects on several diseases (see also Chapter 11 on medical applications of pulsed fields by Pilla). A static magnetic field in the 10-mT range blocks sensory neuron action potentials, which suggests that the magnetic field alleviates pain (Cavopol et al., 1995; McLean et al., 1995). To characterize the inhibitory effect of a static magnetic field, action potentials were elicited by intracellular application of 1-ms pulses of depolarizing current to the somata of mouse DRG neurons. During the control period, less than 5% of stimuli failed to elicit action potentials. During exposure to an approximate 11-mT static magnetic field produced by an array of four permanent center-charged magnets of alternating polarity, 66% of stimuli failed to elicit action potentials.

The efficacy of a nonpharmacologic, noninvasive static magnetic device was assessed for knee pain in patients with rheumatoid arthritis (Segal et al., 2001). Magnetic devices with four steep field gradients or one steep field gradient were taped to the knee of each subject for 1 week. Both devices demonstrated statistically significant pain reduction in comparison to baseline. Comparison between the two groups demonstrated a statistically insignificant difference.

Prato et al. (2005) reported effect of a magnetically shielded environment on opioid-induced analgesia. Mice were placed in a Mu-metal-lined box or an opaque Plexiglas box (sham condition) for 1 h/d for 10 consecutive days. Nociception was measured as the latency time to a foot lift/lick in response to an aversive thermal stimulus before and immediately after exposure. It was shown that mice can detect and will respond to the repeated absence of the ambient magnetic field, with the maximum analgesic response occurring over days 4–6 of exposure and returning to baseline thereafter. The effect was robust, independent of pre-exposure and intermittent testing, and seems to be opioid related, since the results obtained on day 5 were similar to those from a 5-mg/kg dose of morphine and were abolished with the opioid antagonist, naloxone.

Exposure to pulsed magnetic fields has been shown to have a therapeutic benefit in both animals (e.g., mice and snails) and humans. Shupak et al. (2004b) investigated the potential analgesic benefit of magnetic field exposure on sensory and pain thresholds following experimentally induced warm and hot sensations. Subjects were assigned to 30 min of magnetic field or sham exposure, between two sets of tests of sensory and pain thresholds and latencies at 1°C above and 2°C above pain thresholds. Results indicated that magnetic field exposure does not affect sensory thresholds. Pain thresholds were significantly increased following magnetic field exposure but not following sham exposure. A significant condition by gender interaction existed for postexposure pain thresholds. Taken together, these results indicate that magnetic field exposure does not affect basic human perception, but can increase pain thresholds in a manner indicative of an analgesic response.

Shupak et al. (2004a) showed an induction of analgesia in mice equivalent to a moderate dose of morphine (5 mg/kg) and the effect of both pulsed magnetic field (complex neuroelectromagnetic pulse, Cnp) exposure and morphine injection on some open-field activity. Cnp exposure was found to prolong the response latency to a nociceptive thermal stimulus (hot plate). Cnp plus morphine offset the increased movement activity found with morphine alone. These results suggest that pulsed magnetic fields can induce analgesic behavior in mice without the side effects often associated with opiates like morphine.

The effects of static and sinusoidal (AC) magnetic fields on myosin light chain phosphorylation were studied (Markov et al., 1993). In a cell-free preparation, exposure to DC (0–200 µT, vertically or horizontally controlled) or AC (16 Hz, 20.9 µT) magnetic fields significantly influenced myosin phosphorylation. Variations of the DC magnetic field (in the absence of AC components) were not only sufficient to alter the rate of phosphorylation but also gave the maximum effect.

The possibilities that magnetic fields cause antitumor activities *in vitro* (Tofani et al., 2001), *in vivo* (Tofani et al., 2002), and in human subjects (Ronchetto et al., 2004) have been investigated. *In vitro* experiments were carried out to study the role of magnetic field characteristics (intensity, frequency, and modulation) on two transformed cell lines (WiDr human colon adenocarcinoma and MCF-7 human breast adenocarcinoma) and one non-transformed cell line (MRC-5 embryonal lung fibroblast). Increase in cell death morphologically consistent with apoptosis was reported exclusively in the two transformed cell lines. Cell-death induction was observed with magnetic fields of more than 1 mT. Two different *in vivo* experiments were carried out on nude mice bearing a subcutaneous

human colon adenocarcinoma (WiDr). In the first experiment, a significant increase in survival time (31%) was obtained in mice exposed daily to 70 min of modulated magnetic fields (static with a superimposition of 50 Hz) having a time average total intensity of 5.5 mT. In the second independent experiment, when mice bearing tumors were exposed to the same treatment for four consecutive weeks, significant inhibition of tumor growth (40%) was reported, together with a decrement in tumor cell mitotic index and proliferative activity. Human patients with heavily pretreated advanced cancer were enrolled in a pilot study, in which they were exposed to static magnetic fields that were amplitude modulated by ELF. Toxicity was assessed according to WHO criteria. ECG, chest x-ray, physical examination, blood cell count, and complete blood chemistry were performed before and at the end of the treatment. The results indicated that magnetic fields can be safely administrated according to the magnetic field exposure schedules.

Recently, several studies tested the application of pulsed magnetic stimulation as a form of cancer therapy. In one case, use of magnetizable beads and pulsed magnetic stimulation enabled targeted-cell destruction *in vitro* (Ogiiue-Ikeda et al., 2003b). The cells were combined with the beads by an antigen–antibody reaction (cell–bead–antibody complex), aggregated by a magnet, and stimulated by a magnetic stimulator. The viability of the aggregated and stimulated cell–bead–antibody complexes was significantly decreased, and the cells were destroyed by the penetration of the beads into the cells or by rupturing of the cells by the beads. In another study, exposure to a pulsed magnetic stimulation caused a decrease of tumor weight in mice B16-BL6 melanoma models and induced the increase of cytokine (TNF- α and IL-2) production (Yamaguchi et al., 2006). These studies show the potential therapeutic possibilities of pulsed magnetic stimulation in cancer treatment.

Basic studies for magnetic stimulation treatment of depression, which has the potential to replace ECT, and also, magnetic treatment for a wide range of clinical problems, such as Parkinson's disease and various kinds of pain, are in progress. It is important to recognize the safety of magnetic stimulation and the limitations of its usefulness.

8.6 Conclusion

Over the last two decades, various studies have been carried out to examine the effects of static magnetic fields, including MRI fields, on biological systems. This chapter consisted of two parts. The first part focused on recent experiments covering behavior, cardiovascular system responses, reproduction and development, genotoxicity, molecular and cellular systems, cell-free systems, free radical and enzyme activity, etc. The second part concentrated on the recent development of medical and therapeutic applications of static magnetic fields.

There are many studies that have been mentioned in this chapter. With exposure to about 1 T and above, there are no adverse effects on reproduction and development, genotoxicity, and molecular and cellular systems, and no consistent evidence on behavioral effects. However, several studies suggest that static magnetic fields in millitesla ranges may affect microcirculation and blood pressure, and furthermore, higher-strength static magnetic fields at levels up to 10 T may reduce skin blood flow and lead to change in skin temperature. These findings need to be confirmed in further studies.

Although there are so many experiments to test the effects of static magnetic fields on the biology of living systems, using *in vivo* and *in vitro* techniques, the International Agency for Research on Cancer (IARC) has stated that static magnetic fields are *not*

classifiable as to their carcinogenicity to humans by inconclusive carcinogenic evidence (IARC, 2002).

There are many experimental findings that suggest that animals use the static magnetic field, that is, the geomagnetic field for orientation, navigation, and migration. In order to establish the existence of a magnetoreception system in animals, Phillips argued that there are several key points that require further investigation: (1) establishing the lower limits of sensitivity to static magnetic, ELF, and RF fields in biological systems; (2) localizing specialized receptors responsible for sensing the geomagnetic field; (3) characterizing the underlying molecular and biophysical mechanisms; (4) identifying the regions of the brain involved in processing magnetic stimuli; and (5) understanding how the animal's perception of the magnetic field is physiologically processed for determining compass direction and spatial positioning (Phillips, 2005).

With the increasing exposure of humans to environmentally higher static magnetic fields generated from magnetic field equipment of higher capacity, it is necessary to investigate the possibilities of high static field effects on human biological and physiological processes.

There are an abundance of review papers and books published in recent years describing the possible physical and biological interactions of electromagnetic fields (Polk and Postow, 1986, 1997; Ueno, 1996; Andra and Nowak, 1998; Jin, 1999; Takebe et al., 1999; Lin, 2000; Shellock, 2001; Binhi, 2002; McLean et al., 2003a; Stavroulakis, 2003; Rosch and Markov, 2004). In addition, there have been many short reviews on the biological effects of static magnetic fields (Holden, 2005; Miyakoshi, 2005), since the physical interactions of static magnetic fields with living tissues were described (Schenck, 2005). In a report on the biological effects of exposure to MRI, an overview of the safety concerns regarding exposure to static magnetic fields, RF fields, and time-varying magnetic field gradients has been discussed (Formica and Silverstri, 2004). Application of novel high-throughput screening techniques for transcriptomics, proteomics, and metabolomics to determine *in vitro* effects of static magnetic fields have been suggested (Leszczynski, 2005). This report emphasized the research beyond screening that is required for the assessment of any possible health consequences. Possible physical mechanisms underlying the biological effects and interactions of zero-frequency (DC) and oscillating (AC) magnetic fields with biological matter have been reviewed (Binhi, 2001; Volpe, 2003). Effects of static and ELF electric and magnetic fields on human health have also been discussed (Repacholi and Greenebaum, 1999; McKinlay and Repacholi, 2005). Zhadin (2001) has introduced the Russian literature on the biological effects of DC and LF AC magnetic fields. These articles offer multidisciplinary information and knowledge for the understanding of magnetic field effects within living systems.

Acknowledgments

The authors wish to thank Drs. Ben Greenebaum and Frank Barnes for their suggestions and comments for organizing this chapter. The authors also wish to thank Drs. Minoru Fujiki, Yngve Hamnerius, Masateru Ikehata, Masakazu Iwasaka, Saeko Kanagawa, Alayar Kangarlu, Yohsuke Kinouchi, Shinya Kuriki, Tatsuki Matsumoto, Junji Miyakoshi, John Nyenhuis, Chiyoji Ohkubo, Hideyuki Okano, Frank Prato, Masaki Sekino, Masao Taki, Yoshifumi Tanimoto, Sotoshi Yamada, and Sachiko Yamaguchi for their valuable discussions.

References

- Adair, R.K., Comments: influence of stationary magnetic fields on water relations in lettuce seeds, *Bioelectromagnetics*, 23, 550, 2002.
- Ahonen, A.I., Hämäläinen, M.S., Knuttila, J.E.T., Kajola, M.J., Laine, P.P., Lounasmaa, O.V., Parkkonen, L.T., Simola, J.T., and Tesch, C.D., 122-Channel SQUID instrument for investigating the magnetic signals from the human brain, *Phys Scripta*, T49, 198, 1993.
- Aldinucci, C., Garcia, J.B., Palmi, M., Sgaragli, G., Benocci, A., Meini, A., Pessina, F., Rossi, C., Bonechi, C., and Pessina, G.P., The effect of exposure to high flux density static and pulsed magnetic fields on lymphocyte function, *Bioelectromagnetics*, 24, 373, 2003a.
- Aldinucci, C., Garcia, J.B., Palmi, M., Sgaragli, G., Benocci, A., Meini, A., Pessina, F., Rossi, C., Bonechi, C., and Pessina, G.P., The effect of strong static magnetic field on lymphocytes, *Bioelectromagnetics*, 24, 109, 2003b.
- Amyan, A. and Ayrapetyan, S., On the modulation effect of pulsing and static magnetic field and mechanical vibrations on barley seed hydration, *Physiol Chem Phys Med NMR*, 36, 69, 2004.
- Andra, W. and Nowak, H. (Eds.), *Magnetism in Medicine*, Wiley, New York, 1998.
- Azanza, M.J. and del Moral, A., Isolated neuron amplitude spike decrease under static magnetic fields, *J Magn Magn Mater*, 157/158, 593, 1996.
- Barker, A.T., An introduction to the basic principles of magnetic nerve stimulation, *J Clin Neurophysiol*, 8, 26, 1991.
- Barker, A.T., Jalilov, R., and Freeston, I.L., Noninvasive magnetic stimulation of the human motor cortex, *Lancet*, 1, 1106, 1985.
- Beason, R.C. and Semm, P., Does the avain ophthalmic nerve carry magnetic navigational information? *J Exp Biol*, 199, 1241, 1996.
- Beaugnon, E. and Tournier, R., Levitation of organic materials, *Nature*, 349, 470, 1991.
- Belova, N.A. and Lendnev, V.V., Activation and inhibition of gravitropic response in segments of flax stems exposed to static magnetic field with flux density ranging from 0 to 350 microtesla, *Biophysics*, 46, 117, 2001.
- Belyaev, I.Y., Alipov, Y.D., and Harms-Ringdahl, M., Effects of zero magnetic field on the conformation of chromatin in human cells, *Biochim Biophys Acta*, 1336, 465, 1997.
- Berk, S.G., Srikanth, S., Mahajan, S.M., and Ventrice, C.A., Static uniform magnetic fields and amoebae, *Bioelectromagnetics*, 18, 81, 1997.
- Binhi, V.N., Theoretical concepts in magnetobiology, *Electr. Magnetobiol*, 20, 43, 2001.
- Binhi, V.N., *Magnetobiology—Underlying Physical Problems*, Academic Press, New York, 2002.
- Binhi, V.N., Alipov, Y.D., and Belyaev, I.Y., Effect of static field on *E. coli* cells and individual rotations of ion–protein complexes, *Bioelectromagnetics*, 22, 79, 2001.
- Blackman, C.F., Blanchard, J.P., Benane, S.G., and House, D.E., Effect of AC and DC magnetic field orientation on nerve cells, *Biochem Biophys Res Commun*, 220, 807, 1996.
- Blanchard, J.P. and Blackman, C.F., Clarification and application of an ion parametric resonance model for magnetic field interactions with biological systems, *Bioelectromagnetics*, 15, 217, 1994.
- Blumenthal, N.C., Ricci, J., Breger, L., Zychlinsky, A., Solomon, H., Chen, G.G., Kuznetsov, D., and Dorfman, R., Effects of low-intensity AC and/or DC electromagnetic fields on cell attachment and induction of apoptosis, *Bioelectromagnetics*, 18, 264, 1997.
- Bochert, R. and Zettler, M.L., Long-term exposure of several marine benthic animals to static magnetic fields, *Bioelectromagnetics*, 25, 498, 2004.
- Bourland, J.D., Nyenhuis, J.A., and Schaefer, D.J., Physiologic effects of intense MRI gradient fields, *Neuroimaging Clin North Am* 9, 363, 1999.
- Brocklehurst, B., Magnetic fields and radical reactions: recent development and their role in nature, *Chem Soc Rev*, 31, 301, 2002.
- Brocklehurst, B. and McLauchlan, K.A., Free radical mechanism for the effects of environmental electromagnetic fields on biological systems, *Int J Radiat Biol*, 69(1), 3, 1996.
- Buemi, M., Marino, D., Di Pasquale, G., Floccari, F., Senatore, M., Aloisi, C., Grasso, F., Mondio, G., Perillo, P., Frisina, N., and Corica, F., Cell proliferation/cell death balance in renal cell cultures after exposure to a static magnetic field, *Nephron*, 87, 269, 2001.

- Carbonell, M.V., Martinez, E., and Amaya, J.M., Stimulation of germination in rice (*Oryza sativa* L.) by a static magnetic field, *Electr Magnetobiol*, 19, 121, 2000.
- Carnes, K.I. and Magin, R.L., Effects of in utero exposure to 4.7 T MR imaging conditions on fetal growth and testicular development in the mouse, *Magn Reson Imaging*, 14, 263, 1996.
- Cavopol, A.V., Wamil, A.W., Holcomb, R.R., and McLean, M.J., Measurement and analysis of static magnetic fields that block action potentials in cultured neurons, *Bioelectromagnetics*, 16, 197, 1995.
- Ceballos, D., Navarro, X., Dubey, N., Wendelschafer-Crabb, G., Kennedy, W.R., and Tranquillo, R.T., Magnetically aligned collagen gel filling a collagen nerve guide improves peripheral nerve regeneration, *Exp Neurol*, 158, 290, 1999.
- Chakeres, D.W. and de Vocht, F., Static magnetic field effects on human subjects related to magnetic resonance imaging systems, *Prog Biophys Mol Biol*, 87, 255, 2005.
- Chakeres, D.W., Kangarlu, A., Boudoulas, H., and Young, D.C., Effect of static magnetic field exposure of up to 8 tesla on sequential human vital sign measurements, *J Magn Reson Imaging*, 18(3), 346, 2003.
- Chignell, C.F. and Sik, R.H., The effect of static magnetic fields on the photohemolysis of human erythrocytes by ketoprofen, *Photochem Photobiol*, 67, 591, 1998.
- Chionna, A., Tenuzzo, B., Panzarini, E., Dwikat, M.B., Abbro, L., and Dini, L., Time dependent modifications of Hep G2 cells during exposure to static magnetic fields, *Bioelectromagnetics*, 26, 275, 2005.
- Ciortea, L.I., Morariu, V.V., Todoran, A., and Popescu, S., Life in zero magnetic field. 3. Effect on zinc and copper in human blood serum during *in vitro* aging, *Electr Magnetobiol*, 20, 127, 2001.
- Cohen, D., Edelsack, E.A., and Zimmerman, J.E., Magnetocardiograms taken inside a shielded room with a superconducting point contact magnetometer, *Appl Phys Lett*, 16, 278, 1972.
- Cohly, H.H.P., Abraham, G.E. III, Ndebele, K., Jenkins, J.J., Thompson, J., and Angel, M.F., Effects of static electromagnetic fields on characteristics of MG-63 osteoblasts grown in culture, *Biomed Sci Instrum*, 39, 454, 2003.
- Coulton, L.A., Barker, A.T., Van Lierop, J.E., and Walsh, M.P., The effect of static magnetic fields on the rate of calcium/calmodulin-dependent phosphorylation of myosin light chain, *Bioelectromagnetics*, 21, 189, 2000.
- Creanga, D.E., Morariu, V.V., and Isac, R.M., Life in zero magnetic field. IV. Investigation of developmental effects on fruit fly vision, *Electromagn Biol Med*, 21, 31, 2002.
- Creim, J.A., Lovely, R.H., Miller, D.L., and Anderson, L.E., Rats can discriminate illuminance, but not magnetic fields, as a stimulus for learning a two-choice discrimination, *Bioelectromagnetics*, 23, 545, 2002.
- Crozier, S. and Liu, F., Numerical evaluation of the fields induced by body motion in or near high-field MRI scanners, *Prog Biophys Mol Biol*, 87, 267, 2005.
- Danielyan, A.A. and Ayrapetyan, S.N., Changes of hydration of rats' tissues after *in vivo* exposure to 0.2 tesla steady magnetic field, *Bioelectromagnetics*, 20, 123, 1999.
- Danielyan, A.A., Mirakyan, M.M., Grigoryan, G.Y., and Ayrapetyan, S.N., The static magnetic field effects on quabain H3 binding by cancer tissue, *Physiol Chem Phys Med NMR*, 31, 139, 1999.
- Del Seppia, C., Luschi, P., Ghione, S., Crosio, E., Choleris, E., and Papi, E., Exposure to hypogeomagnetic field or to oscillating magnetic fields similarly reduce stress-induced analgesia in C57 male mice, *Life Sci*, 66, 1299, 2000.
- Del Seppia, C., Mezzasalma, L., Choleris, E., Luschi, P., and Ghione, S., Effects of magnetic field exposure on open field behaviour and nociceptive responses in mice, *Behav Brain Res*, 144, 1, 2003.
- den Boer, J.A., Bourland, J.D., Nyenhuis, J.A., Ham, C.L.G., Engels, J.M.L., Hebrank, F.X., Frese, G., and Schaefer, D.J., Comparison of the threshold for peripheral nerve stimulation during gradient switching in whole body MR systems, *J Magn Reson Imaging*, 15, 520, 2002.
- Denegre, J.M., Valles, J.M., Lin, K., Jordan, W.B., and Mowry, K.L., Cleavage planes in frog eggs are altered by strong magnetic fields, *Proc Natl Acad Sci USA*, 95, 14729, 1998.
- Deutschlander, M.E., Borland, S.C., and Phillips, J.B., Extraocular magnetic compass in newts, *Nature*, 400, 324, 1999a.

- Deutschlander, M.E., Phillips, J.B., and Borland, S.C., The case for light-dependent magnetic orientation in animals, *J Exp Biol*, 202, 891, 1999b.
- Deutschlander, M.E., Freake, M.J., Borland, S.C., Phillips, J.B., Madden, R.C., Anderson, L.E., and Wilson, B.W., Learned magnetic compass orientation by the Siberian hamster, *Phodopus sungorus*, *Anim Behav*, 65, 779, 2003.
- Diebel, C.E., Proksch, R., Green, C.R., Neilson, P., and Walker, M.M., Magnetite defines a vertebrate magnetoreceptor, *Nature*, 406, 299, 2000.
- Dubey, N., Letourneau, P.C., and Tranquillo, R.T., Guided neurite elongation and Schwann cell invasion into magnetically aligned collagen in simulated peripheral nerve regeneration, *Exp Neurol*, 158, 338, 1999.
- Edmond, D.T., A sensitive optically detected magnetic compass for animals, *Proc R Soc Lond B*, 263, 295, 1996.
- Eguchi, Y., Ogiue-Ikeda, M., and Ueno, S., Control of orientation of rat Schwann cells using an 8-T static magnetic field, *Neurosci Lett*, 351, 130, 2003.
- Eichwald, C. and Walleczeck, J., Model for magnetic field effects on radical pair recombination in enzyme kinetics, *Biophys J*, 71, 623, 1996.
- Emura, R., Ashida, N., Higashi, T., and Takeuchi, T., Orientation of bull sperms in static magnetic fields, *Bioelectromagnetics*, 22, 60, 2001.
- Emura, R., Takeuchi, T., Nakaoka, Y., and Higashi, T., Analysis of anisotropic diamagnetic susceptibility of a bull sperm, *Bioelectromagnetics*, 24, 347, 2003.
- Engstrom, S., Markov, M.S., McLean, M.J., Holcomb, R.R., and Markov, J.M., Effects of non-uniform static magnetic fields on the rate of myosin phosphorylation, *Bioelectromagnetics* 23, 475, 2002.
- Epstein, C.M., Sekino, M., Yamaguchi, K., Kamiya, S., and Ueno, S., Asymmetries of prefrontal cortex in human episodic memory: effects of transcranial magnetic stimulation on learning abstract patterns, *Neurosci Lett*, 320, 5, 2002.
- Eremenko, T., Esposito, C., Pasquarelli, A., Pasquali, E., and Volpe, P., Cell-cycle kinetics of friend erythroleukemia cells in a magnetically shielded room and in a low-frequency/low-intensity magnetic field, *Bioelectromagnetics*, 18, 58, 1996.
- Erne, S.N., Hoke, M., Lutkenhoner, B., Pantev, C., and Scheer, H.J., Brainstem auditory evoked magnetic fields, in *Biomagnetism '87* (Atsumi, K., Kotani, M., Ueno, S., Katila, T., and Williamson, S.J., Eds.), Tokyo Denki University Press, Tokyo, 158–161, 1988.
- Espinar, A., Piera, V., Carmona, A., and Guerrero, J.M., Histophysiological changes during development of the cerebellum in the chick embryo exposed a static magnetic field, *Bioelectromagnetics*, 18, 36, 1997.
- Eveson, R.W., Timmel, C.R., Brocklehurst, B., Hore, P.J., and McLauchlan, K.A., The effects of weak magnetic fields on radical recombination reactions in micelles, *Int J Radiat Biol*, 76, 1509, 2000.
- Fanelli, C., Coppola, S., Barone, R., Colussi, C., Gualandi, G., Volpe, P., and Ghibelli, L., Magnetic fields increase cell survival by inhibiting apoptosis via modulation of Ca²⁺ influx, *FASEB J*, 13, 95, 1999.
- Flipo, D., Fournier, M., Benquet, C., Roux, P., Le Boulaire, C., Pinsky, C., Labella, F.S., and Krzystyniak, K., Increased apoptosis, changes in intracellular Ca²⁺, and functional alterations in lymphocytes and macrophages after *in vitro* exposure to static magnetic field, *J Toxicol Environ Health A*, 54, 63, 1998.
- Florez, M., Carbonell, M.V., and Martinez, E., Early sprouting and first stages of growth of rice seeds exposed to a magnetic field, *Electromagn Biol Med*, 23, 157, 2004.
- Formica, D. and Silvestri, S., Biological effects of exposure to magnetic resonance imaging: an overview, *Biomed Eng Online*, 3, 11, 2004.
- Formicki, K. and Perkowski, T., The effect of a magnetic field on the gas exchange in rainbow trout *Oncorhynchus mykiss* embryos (Salmonidae), *Ital J Zool*, 65 Suppl, 475, 1998.
- Formicki, K., and Winnicki, A., Effects of constant magnetic field on cardiac muscle activity in fish, *Publ Espec Inst Esp Oceanogr*, 21, 287, 1996.
- Formicki, K. and Winnicki, A., Reactions of fish embryos and larvae to constant magnetic fields, *Ital J Zool*, 65 Suppl, 479, 1998.
- Formicki, K., Bonislawska, M., and Jasinski, M., Spatial orientation of trout (*Salmo trutta* L.) and rainbow trout (*Oncorhynchus mykiss* Walb.) embryos in natural and artificial magnetic fields, *Acta Ichtyol Piscat*, 27, 29, 1997.

- Fujiki, M. and Steward, O., High frequency transcranial magnetic stimulation mimics the effects of ECS in upregulating astroglial gene expression in the murine CNS, *Brain Res Mol Brain Res*, 44, 301, 1997.
- Fujiki, M., Kobayashi, H., Abe, T., and Kamida, T., Repetitive transcranial magnetic stimulation for protection against delayed neuronal death induced by transient ischemia, *J Neurosurg*, 99, 1063, 2003.
- Fuller, M. and Dobson, J., On the significance of the time constants of magnetic field sensitivity in animals, *Bioelectromagnetics*, 26, 234, 2005.
- Gmitrov, J. and Ohkubo, C., Geomagnetic field decreases cardiovascular variability, *Electr Magnetoiol*, 18, 291, 1999a.
- Gmitrov, J. and Ohkubo, C., Static magnetic field and calcium channel blocking agent combined effect on baroreflex sensitivity in rabbits, *Electr Magnetoiol*, 18, 43, 1999b.
- Gmitrov, J. and Ohkubo, C., Artificial static and geomagnetic field interrelated impact on cardiovascular regulation, *Bioelectromagnetics*, 23, 329, 2002.
- Gmitrov, J., Ohkubo, C., and Okano, H., Effect of 0.25 static magnetic field on microcirculation in rabbits, *Bioelectromagnetics*, 23, 224, 2002.
- Gray, J.R., Frith, C.H., and Parker, J.D., *In vivo* enhancement of chemotherapy with static electric or magnetic fields, *Bioelectromagnetics*, 21, 575, 2000.
- Grissom, C.B., Magnetic field effects in biology: a survey of possible mechanisms with emphasis on radical-pair recombination, *Chem Rev*, 95, 3, 1995.
- Grissom, C.B. and Natarajan, E., Use of magnetic field effects on study coenzyme B₁₂-dependent reactions, *Methods Enzymol*, 281, 235, 1997.
- Guisasola, C., Desco, M., Millano, O., Villanueva, F.J., and Garcia-Barreno, P., Biological dosimetry of magnetic resonance imaging, *J Magn Reson Imaging*, 15, 584, 2002.
- Hata, N., The effect of external magnetic field on the photochemical reaction of isoquinoline N-oxide, *Chem Lett*, 5, 547, 1976.
- Hatada, T., Sekino, M., and Ueno, S., Finite element method-based calculation of the theoretical limit of sensitivity for detecting weak magnetic fields in the human brain using magnetic-resonance imaging, *J Appl Phys*, 97, 10E109, 2005.
- Havel, W.J., Nyenhuis, J.A., Bourland, J.D., Foster, K.S., Geddes, L.A., Gruber, G.P., Waninger, M.S., and Schaefer, D.J., Comparison of rectangular and damped sinusoidal dB/dt waveforms in magnetic stimulation, *IEEE Trans Magn*, 33, 4269, 1997.
- Hayashi, H., *Introduction to Dynamic Spin Chemistry*, World Scientific Publishing Co, Singapore, 2004.
- Higashi, T., Sagawa, S., Kawaguchi, N., and Yamagishi, A., Effects of a strong static magnetic field on blood platelets. *Platelet*, 4, 341, 1993a.
- Higashi, T., Yamagishi, A., Takeuchi, T., Kawaguchi, N., Sagawa, S., Onishi, S., and Date, M., Orientation of erythrocytes in a strong static magnetic field, *Blood*, 82, 1328, 1993b.
- Higashi, T., Sagawa, S., Ashida, N., and Takeuchi, T., Orientation of glutaraldehyde-fixed erythrocytes in strong static magnetic fields, *Bioelectromagnetics*, 17, 335, 1996.
- High, W.B., Sikora, J., Ugurbil, K., and Garwood, M., Subchronic *in vivo* effects of a high static magnetic field (9.4 T) in rats, *J Magn Reson Imaging*, 12, 122, 2000.
- Hinch, R., Lindsay, K.A., Noble, D., and Rosenberg, J.R., The effects of static magnetic field on action potential propagation and excitation recovery in nerve, *Prog Biophys Mol Biol*, 87, 321, 2005.
- Hirai, T., Nakamichi, N., and Yoneda, Y., Activator protein-1 complex expressed by magnetism in cultured rat hippocampal neuron, *Biochem Biophys Res Commun*, 292, 200, 2002.
- Hirata, Y., Kuriki, S., and Pantev, C., Musicians with absolute pitch show distinct neural activities in the auditory cortex, *NeuroReport*, 10, 999, 1999.
- Hirose, H., Nakahara, T., and Miyakoshi, J., Orientation of human glioblastoma cells embedded in type I collagen, caused by exposure to a 10 T static magnetic field, *Neurosci Lett*, 338, 88, 2003a.
- Hirose, H., Nakahara, T., Zhang, Q.-M., Yonei, S., and Miyakoshi, J., Static magnetic field with a strong magnetic field gradient (41.7 T/m) induces C-jun expression in HL-60 cells, *In Vitro Cell Dev Biol Anim*, 39, 348, 2003b.
- Hirota, N., Nakagawa, J., and Kitazawa, K., Effects of magnetic field on the germination of plants, *J Appl Phys*, 85, 5717, 1999.

- Hirota, N., Ikezoe, Y., Uetake, H., Nakagawa, J., and Kitazawa, K., Magnetic field effect on the kinetics of oxygen dissolution into water, materials transaction, *JIM*, 41, 976, 2000.
- Holden, A.V., The sensitivity of the heart to static magnetic fields, *Prog Biophys Mol Biol*, 87, 289, 2005.
- Horiuchi, S., Ishizaki, Y., Okuno, K., Ano, T., and Shoda, M., Drastic high magnetic field effect on suppression of *Escherichia coli* death, *Bioelectrochemistry*, 53, 149, 2001.
- Horiuchi, S., Ishizaki, Y., Okuno, K., Ano, T., and Shoda, M., Change in broth culture is associated with significant suppression of *Escherichia coli* death under high magnetic field, *Bioelectrochemistry*, 57, 139, 2002.
- Houpt, T.A., Pittman, D.W., Barranco, J.M., Brooks, E.H., and Smith, J.C., Behavioral effects of high-strength static magnetic fields on rats, *J Neurosci*, 23, 1498, 2003.
- Ichioka, S., Iwasaka, M., Shibata, M., Harii, K., Kamiya, A., and Ueno, S., Biological effects of static magnetic fields on the microcirculatory blood flow *in vivo*: a preliminary report, *Med Biol Eng Comput*, 36, 91, 1998.
- Ichioka, S., Minegishi, M., Iwasaka, M., Shibata, M., Nakatsuka, T., Harii, K., Kamiya, A., and Ueno, S., High-intensity static magnetic fields modulate skin microcirculation and temperature *in vivo*, *Bioelectromagnetics*, 21, 183, 2000.
- Ichioka, S., Minegishi, M., Iwasawa, M., Shibata, M., Nakatsuka, T., Ando, J., and Ueno, S., Skin temperature changes induced static magnetic field exposure, *Bioelectromagnetics*, 24, 380, 2003.
- Iino, M., Effects of a homogeneous field on erythrocyte sedimentation and aggregation, *Bioelectromagnetics*, 18, 215, 1997.
- Iino, M. and Okuda, Y., Osmolality dependence of erythrocyte sedimentation and aggregation in a strong magnetic field, *Bioelectromagnetics*, 22, 46, 2001.
- Ikehata, M., Koana, T., Suzuki, Y., Shimizu, H., and Nakagawa, M., Mutagenicity and co-mutagenicity of static fields detected by bacterial mutation assay, *Mutat Res*, 427, 147, 1999.
- Ikehata, M., Iwasaka, M., Miyakoshi, J., Ueno, S., and Koana, T., Effects of intense magnetic fields on sedimentation pattern and gene expression profile in budding yeast, *J Appl Phys*, 93, 6724, 2003.
- International Agency for Research on Cancer (IARC), *IARC Monographs on the Evaluation of Carcinogenic Risks to Humans, Non-Ionising Radiation. Part I: Static and Extremely Low Frequency (ELF) Electric and Magnetic Fields*, vol. 80, IARC, Lyon, France, 2002.
- International Electrotechnology Commission (IEC), *Particular Requirements for the Safety of Magnetic Resonance Equipment for Medical Diagnosis*, Standard 60601-2-33, 2nd ed., Geneva, Switzerland, 2002.
- Iramina, K. and Ueno, S., Measurement of brainstem auditory evoked magnetic fields using a highly sensitive SQUID magnetometer with a variable base line, *IEEE Trans Magn*, 31, 4271, 1995.
- Iramina, K., Ueno, K., and Ueno, S., Influence of spreading neuronal electric sources on spatio-temporal neuromagnetic fields, *J Appl Phys*, 75, 7168, 1994.
- Iramina, K., Ueno, K., and Ueno, S., Spatio-temporal MEG pattern produced by spreading multiple dipoles, *IEEE Trans Magn*, 31, 4265, 1995.
- Ishizaki, Y., Horiuchi, S., Okuno, K., Ano, T., and Shoda, M., Twelve hours exposure to inhomogeneous high magnetic field after logarithmic growth is sufficient for drastic suppression of *Escherichia coli* death, *Bioelectrochemistry*, 54, 101, 2001.
- Iwaki, S., Ueno, S., Imada, T., and Tonoike, M., Dynamic cortical activation in mental image processing revealed by biomagnetic measurement, *Neuroreport*, 10, 1793, 1999.
- Iwasaka, M. and Ueno, S., Effects of magnetic fields on fibrinolysis, *J Appl Phys*, 75, 7162, 1994.
- Iwasaka, M. and Ueno, S., Bioluminescence under static magnetic fields, *J Appl Phys*, 83, 6456, 1998a.
- Iwasaka, M. and Ueno, S., Structure of water molecules under 14 T magnetic field, *J Appl Phys*, 83, 6459, 1998b.
- Iwasaka, M. and Ueno, S., Detection of intracellular macromolecule behavior under strong magnetic fields by linearly polarized light, *Bioelectromagnetics*, 24, 564, 2003.
- Iwasaka, M., Takeuchi, M., Ueno, S., and Tsuda, H., Polymerization and dissolution of fibrin under homogeneous magnetic fields, *J Appl Phys*, 83, 6453, 1998.
- Iwasaka, M., Miyakoshi, J., and Ueno, S., Magnetic field effects on assembly pattern of smooth muscle cells, *In Vitro Cell Biol Anim*, 39, 2003a.
- Iwasaka, M., Yamamoto, K., Ando, J., and Ueno, S., Verification of magnetic field gradient effects on medium convection and cell adhesion, *J Appl Phys*, 93, 6715, 2003b.

- Jajte, J., Grzegorczyk, J., Zmyslony, M., and Rajkowska, E., Effect of 7 mT static magnetic field and iron ions on rat lymphocytes: apoptosis, necrosis and free radical processes, *Bioelectrochemistry*, 57, 107, 2002.
- Jin, J., *Electromagnetic Analysis and Design in Magnetic Resonance Imaging*, CRC Press, Boca Raton, FL, 1999.
- Johnston, S.A., D'Andrea, J.A., Behavioral and cognitive effects of electromagnetic field exposures, in *Biological and Medical Aspects* (Barnes, F.S. and Greenebaum, B., Eds.), Taylor & Francis, Boca Raton, FL, 2006, Chapter 4.
- Jovanic, B.R. and Sarvan, M.Z., Permanent magnetic field and plant leaf temperature, *Electromagn Biol Med*, 23, 1, 2004.
- Jove, M., Torrente, M., Gilabert, R., Espinar, A., Cobos, P., and Piera, V., Effects of static electromagnetic fields on chick embryo pineal gland development, *Cell Tissues Organs*, 165, 74, 1999.
- Joy, M., Scott, G., and Henkelman, M., *In vivo* detection of applied electric currents by magnetic resonance imaging, *Magn Reson Imaging*, 7, 89, 1989.
- Kamei, H., Iramina, K., Yoshikawa, K., and Ueno, S., Neuronal current distribution imaging using magnetic resonance, *IEEE Trans Magn*, 35, 4109, 1999.
- Kangarlu, A., Burgess, R.E., Zhu, H., Nakayama, T., Hamlin, R.L., Schenck, J.F., Abduljalil, A.M., and Robitaille, P.M.L., Cognitive, cardiac and physiological safety studies in ultra high field magnetic resonance imaging, *J Magn Reson Imaging*, 17, 1407, 1999.
- Kangarlu, A., Shellock, F.G., and Chakeres, D.W., 8.0-Tesla human MR system: temperature changes associated with radiofrequency-induced heating of a head phantom, *J Magn Reson Imaging*, 17(2), 220, 2003.
- Kangarlu, A., Ibrahim, T.S., and Shellock, F.G., Effects of coil dimensions and field polarization on RF heating inside a head phantom, *Magn Reson Imaging*, 23(1), 53, 2005.
- Keck, M.E., Sillaber, I., Ebner, K., Welt, T., Toschi, N., Kaehler, S.T., Singewald, N., Philippu, A., Elbel, G.K., Wotjak, C.T., Holsboer, F., Landgraf, R., and Engelmann, M., Acute transcranial magnetic stimulation of frontal brain regions selectively modulates the release of vasopressin, biogenic amines and amino acids in the rat brain, *Eur J Neurosci*, 12, 3713, 2000.
- Kefuss, J., M'Diaye, K., Bounias, M., Vanpoucke, J., and Ecochard, J., Biochemical effects of high intensity constant magnetic fields on worker honey bees, *Bioelectromagnetics*, 20, 117, 1999.
- Khang, H.S., Lee, B.I., Oh, S.H., Woo, E.J., Lee, S.Y., Cho, M.H., Kwon, O., Yoon, J.R., and Seo, J.K., J-substitution algorithm in magnetic resonance electrical impedance tomography (MREIT): phantom experiments for static resistivity images, *IEEE Trans Med Imaging*, 21, 695, 2002.
- Kimchi, T. and Terkel, J., Magnetic compass orientation in the blind mole rat *Spalax ehrenbergi*, *J Exp Biol*, 204, 751, 2001.
- Kishioka, S., Yamada, A., and Aogaki, R., Analysis of gas dissociation rate into liquid phase under magnetic-field gradient, *Phys Chem Chem Phys*, 2, 4179, 2000.
- Koana, T., Ikehata, M., and Nakagawa, M., Estimation of genetics effects of a static magnetic field by a somatic cell test using mutagen-sensitive mutants of *Drosophila melanogaster*, *Bioelectrochem Bioenerg*, 36, 95, 1995.
- Koana, T., Okada, M.O., Ikehata, M., and Nakagawa, M., Increase in the mitotic recombination frequency in *Drosophila melanogaster* by magnetic field exposure and its suppression by vitamin E supplement, *Mutat Res*, 373, 55, 1997.
- Kobayashi, M., Soda, N., Miyo, T., and Ueda, Y., Effects of combined DC and AC magnetic fields on germination of hornwort seeds, *Bioelectromagnetics*, 25, 552, 2004.
- Kotani, H., Iwasaka, M., and Ueno, S., Magnetic orientation of collagen and bone mixture, *J Appl Phys*, 87, 6191, 2000.
- Krings, T., Chiappa, K.H., Foltys, H., Reinges, M.H., Cosgrove, G.R., and Thron, A., Introducing navigated transcranial magnetic stimulation as a refined brain mapping methodology, *Neuro-surg Rev*, 24, 171, 2001.
- Kroeker, G., Parkinson, D., Vriend, J., and Peeling, J., Neurochemical effects of static magnetic field exposure, *Surg Neurol*, 45, 62, 1996.
- Kula, B., A study of magnetic field effects on fibroblast cultures Part 3. The evaluation of the effects of static and extremely low frequency (ELF) magnetic fields on glycosaminoglycan metabolism in fibroblasts, cell coats and culture medium, *Bioelectrochem Bioenerg*, 39, 31, 1996.

- Kula, B. and Drozbz, M., A study of magnetic field effects on fibroblast cultures Part 1. The evaluation of the effects of static and extremely low frequency (ELF) magnetic fields on vital functions of fibroblasts, *Bioelectrochem Bioenerg*, 39, 21, 1996a.
- Kula, B. and Drozbz, M., A study on magnetic field on fibroblast cultures. Part 2. The evaluation of the effects of static and extremely low frequency (ELF) magnetic fields on free-radical processes in fibroblast cultures, *Bioelectrochem Bioenerg*, 39, 27, 1996b.
- Kula, B., Sobczak, A., and Kuska, R., Effects of static and ELF magnetic fields on free-radical processes in rat liver and kidney, *Electr. Magnetobiol*, 19, 99, 2000.
- Kula, B., Sobczak, A., and Kuska, R., A study of the effects of static and extremely low frequency magnetic fields on lipid peroxidant products in subcellular fibroblast fractions, *Electromagn Biol Med*, 21, 161, 2002.
- Kuriki, S., Okita, Y., and Hirata, Y., Source analysis of magnetic field responses from the human auditory cortex elicited by short speech sounds, *Exp Brain Res*, 104, 144, 1995.
- Kuriki, S., Takeuchi, F., and Hirata, Y., Neural processing of words in the human extrastriate visual cortex, *Cogn Brain Res*, 6, 193, 1998.
- Kuriki, S., Isahai, N., and Otsuka, A., Spatiotemporal characteristics of the neural activities processing consonant/dissonant tones in melody, *Exp Brain Res*, 162, 46, 2005.
- Kwon, H., Kuriki, S., Kim, J., Lee, Y., Kim, K., Park, Y., and Nam, K., MEG study on neural activities associated with syntactic and semantic violations in spoken Korean sentences, *Neurosci Res*, 51, 349, 2005.
- Lauterbur, P.C., Image formation by induced local interactions: examples employing nuclear magnetic resonance, *Nature*, 242, 190, 1973.
- Leszczynski, D., Rapporteur report: cellular, animal and epidemiological studies of the effects of static magnetic fields relevant to human health, *Prog Biophys Mol Biol*, 87, 247, 2005.
- Levin, M. and Ernst, S.G., Applied DC magnetic fields cause alterations in the time of cell divisions and developmental abnormalities in early sea urchin embryos, *Bioelectromagnetics*, 18, 255, 1997.
- Liboff, A.R., Geomagnetic cyclotron resonance in living cells, *J Biol Phys*, 13, 99, 1985.
- Liboff, A.R., Cherng, S., Jenrow, K.A., and Bull, A., Calmodulin-dependent cyclic nucleotide phosphodiesterase activity is altered by 20 μ T magnetostatic fields, *Bioelectromagnetics*, 24, 32, 2003.
- Lin, J.C. (Ed.), *Advances in Electromagnetics Fields in Living Systems*, vol. 3, Kluwer Academic/Plenum Publishers, Hingham, MA, 2000.
- Lockwood, D.R., Kwon, B., Smith, J.C., and Houpt, T.A., Behavioral effects of static high magnetic fields on unrestrained and restrained mice, *Physiol Behav*, 78, 635, 2003.
- Lohmann, K.J. and Johnsen, S., The neurobiology of magnetoreception in vertebrate animals, *Trends Neurosci*, 23, 153, 2000.
- Lohmann, K.J., Cain, S.D., Dodge, S.A., and Lohmann, C.M.F., Regional magnetic fields as navigational markers for sea turtles, *Science*, 294, 364, 2001.
- Madec, F., Billaudel, B., Charlet de Sauvage, R., Sartor, P., and Veyret, B., Effects of ELF and static magnetic fields on calcium oscillations in islets of Langerhans, *Bioelectrochemistry*, 60, 73, 2003.
- Magin, R.L., Lee, J.K., Klintsova, A., Carnes, K.I., and Dunn, F., Biological effects of long-duration, high-field (4 T) MRI on growth and development in the mouse, *J Magn Reson Imaging*, 12, 140, 2000.
- Manassen, Y., Shalev, E., and Navon, G., Mapping of electrical circuits using chemical-shift imaging, *J Magn Reson*, 76, 371, 1988.
- Markov, M.S., Myosin light chain modification depending on magnetic fields. II. Experimental, *Electromagn Biol Med*, 23, 125, 2004a.
- Markov, M.S., Myosin light chain phosphorylation modification depending on magnetic fields. I. Theoretical, *Electromagn Biol Med*, 23, 55, 2004b.
- Markov, M.S. and Pilla, A.A., Static field modulation of myosin phosphorylation: calcium dependence in two enzyme preparations, *Bioelectrochem Bioenerg*, 35, 57, 1994.
- Markov, M.S. and Pilla, A.A., Weak static magnetic field modulation of myosin phosphorylation in a cell-free preparation: calcium dependence, *Bioelectrochem Bioenerg*, 43, 233, 1997.
- Markov, M.S., Wang, S., and Pilla, A.A., Effects of weak low-frequency sinusoidal and DC magnetic fields on myosin phosphorylation in a cell-free preparation, *Bioelectrochem Bioenerg*, 30, 119, 1993.

- Martinez, E., Carbonell, M.V., and Amaya, J.M., A static magnetic field of 125 mT stimulates the initial growth stages of barley (*Hordeum vulgare* L.), *Electr. Magnetobiol.*, 19, 271, 2000.
- Martinez, E., Carbonell, M.V., and Florez, M., Magnetic biostimulation of initial growth stages of wheat, *Electromagn Biol Med*, 21, 43, 2002.
- Mayrovitz, H.N., Groseclose, E.E., Markov, M., and Pilla, A.A., Effect of permanent magnets on resting skin blood perfusion in healthy persons assessed by laser Doppler flowmetry and imaging, *Bioelectromagnetics*, 22, 494, 2001.
- Mayrovitz, H.N., Groseclose, E.E., and King, D., No effect of 85 mT permanent magnets on laser-Doppler measured blood flow response to inspiratory gasps, *Bioelectromagnetics*, 26, 331, 2005.
- McKinlay, A.F. and Repacholi, M.H., More research is needed to determine the safety of static magnetic fields, *Prog Biophys Mol Biol*, 87, 173, 2005.
- McLean, M.J., Holcomb, R.R., Wamil, A.W., Pickett, J.D., and Cavopol, A.V., Blockade of sensory neuron action potentials by a static magnetic field in the 10 mT range, *Bioelectromagnetics*, 16, 20, 1995.
- McLean, M.J., Engstrom, S., and Holcomb, R.R., *Magnetotherapy: Potential Therapeutic Benefits and Adverse Effects*, TFG Press, New York, 2003a.
- McLean, M.J., Engstrom, S., Holcomb, R.R., and Sanchez, D., A static magnetic field modulates severity of audiogenic seizures and anticonvulsant effects of phenytoin in DBA/2 mice, *Epilepsy Res*, 55, 105, 2003b.
- Miyakoshi, J., Effects of static magnetic fields at the cellular level, *Prog Biophys Mol Biol*, 87, 213, 2005.
- Miyamoto, H., Yamaguchi, H., Ikehara, T., and Kinouchi, Y., Effects of electromagnetic fields on K⁺ (Rb⁺) uptake by HeLa cell, in *Biological Effects of Magnetic and Electromagnetic Fields* (Ueno, S., Ed.), Plenum Press, New York, 101, 1996.
- Mnaimneh, S., Bizri, M., and Veyret, B., No effect of exposure to static and sinusoidal magnetic fields on nitric oxide production by macrophages, *Bioelectromagnetics*, 17, 519, 1996.
- Mohtat, N., Cozens, F.L., Hancock-Chen, T., Scaiano, J.C., McLean, J., and Kim, J., Magnetic field effects on the behavior of radicals in protein and DNA environments, *Photochem Photobiol*, 67, 111, 1998.
- Morariu, V.V., Ciorba, D., and Neamtu, S., Life in zero magnetic field. I. *In vitro* human blood aging, *Electr. Magnetobiol.*, 19, 289, 2000.
- Morris, C. and Skalak, T., Static magnetic fields alter arteriolar tone *in vivo*, *Bioelectromagnetics*, 26, 1, 2005.
- Mouchawar, G.A., Bourland, J.D., Nyenhuis, J.A., Geddes, L.A., Foster, K.S., Jones, J.T., and Graver, G.P., Closed-chest cardiac stimulation with a pulsed magnetic field, *Med Biol Eng Comput*, 30, 162, 1992.
- Muehsam, D.J. and Pilla, A.A., Lorentz approach to static magnetic field effects on bound-ion dynamics and binding kinetics: thermal noise considerations, *Bioelectromagnetics*, 17, 89, 1996.
- Munro, U., Munro, J.A., Phillips, J.B., Wiitschko, R., and Wiltschko, W., Evidence for a magnetite-based navigational "map" in birds, *Naturwissenschaften*, 84, 26, 1997.
- Nagakura, S. and Molin, Y. (guest eds.), Magnetic field effects upon photophysical and photochemical phenomena, *Chem Phys*, 162(1), 1, 1992 (special issue).
- Nagy, P. and Fischl, G., Effect of static magnetic field on growth and sporulation of some plant pathogenic fungi, *Bioelectromagnetics*, 25, 316, 2004.
- Nakagawa, J., Hirota, N., Kitazawa, K., and Shoda, M., Magnetic field enhancement of water vaporization, *J Appl Phys*, 86, 2923, 1999.
- Nakahara, T., Yaguchi, H., Yoshida, M., and Miyakoshi, J., Effects of exposure to CHO-K1 cells to a 10-T static magnetic field, *Radiology*, 224, 817, 2002.
- Nakaoka, Y., Takeda, R., and Shimizu, K., Orientation of *Paramecium* swimming in a DC magnetic field, *Bioelectromagnetics*, 23, 607, 2002.
- Narra, V.R., Howell, R.W., Goddu, S.M., and Rao, D.V., Effects of a 1.5-tesla static magnetic field on spermatogenesis and embryogenesis in mice, *Investig Radiol*, 31, 586, 1996.
- Natarajan, E. and Grissom, C.B., The origin of magnetic field dependent recombination in alkylcobalamin radical pairs, *Photochem Photobiol*, 64, 286, 1996.
- Nemec, P., Altmann, J., Marhold, S., Burda, H., and Oelschlaeger, H.H.A., Neuroanatomy of magnetoreception: the superior colliculus involved in magnetic orientation in a mammal, *Science*, 294, 366, 2001.

- Neugebauer, D.C., Blauruck, A., and Worcester, D.L., Magnetic orientation of purple membranes demonstrated by optical measurements and neutron scattering, *FEBS Lett*, 78, 31, 1977.
- Nikolskaya, K. and Echenko, O., Alcohol addiction as the result of cognitive activity in altered natural magnetic field, *Electromagn Biol Med*, 21, 1, 2002.
- Nikolskaya, K., Shtemler, V., Yeschenko, O., Savonenko, A., Osipov, A., and Nickolsky, S., The sensitivity of cognitive processes to the inhomogeneity of natural magnetic fields, *Electr Magnetobiol*, 15, 163, 1996.
- Nikolskaya, K.A., Yeshchenko, O.V., and Pratusevich, V., The opioid system and magnetic field perception, *Electr. Magnetobiol*, 18, 277, 1999.
- Nolte, C.M., Pittman, D.W., Kalevitch, B., Henderson, R., and Smith, J.C., Magnetic field conditioned taste aversion in rats, *Physiol Behav*, 63, 683, 1998.
- Nyenhuis, J.A., Bourland, J.D., and Schaefer, D.J., Analysis from a stimulation perspective of the field patterns of magnetic resonance imaging coils, *J Appl Phys*, 81, 4314, 1997.
- Nyenhuis, J.A., Bourland, J.D., Kildishev, A.V.D.J., and Schaefer, D.J., Health effects and safety of intense MRI gradient fields, in *Magnetic Resonance Procedures: Health Effects and Safety* (Shellock, F.G., Ed.), CRC Press, Boca Raton, FL, 31–54, 2001.
- Ogawa, S., Tank, D.W., and Menon, R., Intrinsic signal changes accompanying stimulation: functional brain mapping with magnetic resonance imaging, *Proc Natl Acad Sci USA*, 89, 5951, 1992.
- Ogiue-Ikeda, M., Kawato, S., and Ueno, S., The effect of repetitive transcranial magnetic stimulation on long-term potentiation in rat hippocampus depends on stimulus intensity, *Brain Res*, 993, 222, 2003a.
- Ogiue-Ikeda, M., Sato, Y., and Ueno, S., A method to destruct targeted cells using magnetizable beads and pulsed magnetic force, *IEEE Trans Magn* 39, 3390, 2003b.
- Ohkubo, C. and Xu, S., Acute effects of static magnetic fields on cutaneous microcirculation in rabbits, *In Vivo*, 11, 221, 1997.
- Okano, H. and Ohkubo, C., Modulatory effects of static magnetic fields on blood pressure in rabbits, *Bioelectromagnetics*, 22, 408, 2001.
- Okano, H. and Ohkubo, C., Anti-pressor effects of whole body exposure to static magnetic field on pharmacologically induced hypertension in conscious rabbit, *Bioelectromagnetics*, 24, 139, 2003a.
- Okano, H. and Ohkubo, C., Effects of static magnetic fields on plasma levels of angiotensin II and aldosterone associated with arterial blood pressure in genetically hypertensive rats, *Bioelectromagnetics*, 24, 403, 2003b.
- Okano, H., Gmitrov, J., and Ohkubo, C., Biphasic effects of static magnetic field on cutaneous microcirculation in rabbits, *Bioelectromagnetics*, 20, 161, 1999.
- Okano, H., Masuda, H., and Ohkubo, C., Decreased plasma levels of nitric oxide metabolites, angiotensin II and aldosterone in spontaneously hypertensive rats exposed to 5 mT static magnetic field, *Bioelectromagnetics*, 26, 161, 2005a.
- Okano, H., Masuda, H., and Ohkubo, C., Effects of 25 mT static magnetic field on blood pressure in reserpine-induced hypotensive Wistar-Kyoto rats, *Bioelectromagnetics*, 26, 36, 2005b.
- Okazaki, R., Ootsuyama, A., Uchida, S., and Norimura, T., Effects of a 4.7 T static magnetic field on fetal development in ICR mice, *J Radiat Res*, 42, 273, 2001.
- Okonogi, H., Nakagawa, M., and Tsuji, Y., The effects of a 4.7 tesla static magnetic field on the frequency of micronucleated cells induced by mitomycin C, *Tohoku J Exp Med*, 180, 209, 1996.
- Okuda, T., Nishizawa, K., Ejima, Y., Nakatsugawa, S., Ishigaki, T., and Ishigaki, K., The effects of static magnetic fields and x-rays on instability of microsatellite repetitive sequences, *J Radiat Res*, 39, 279, 1998.
- Okuno, K., Fujinami, R., Ano, T., and Shoda, M., Disappearance of growth advantage in stationary phase (GASP) phenomenon under a high magnetic field, *Bioelectromagnetics*, 53, 165, 2001.
- Onodera, H., Jin, Z., Chida, S., Suzuki, Y., Tago, H., and Itoyama, Y., Effects of 10-T static magnetic field on human peripheral blood immune cells, *Radiat Res*, 159, 775, 2003.
- Osuga, T. and Tatsuoka, H., Effect of 1.5 T steady magnetic field on neuroconduction of a bullfrog sciatic nerve in a partially active state within several hours after extraction, *Magn Reson Imaging*, 17, 791, 1999.

- Pacini, S., Aterini, S., Pacini, P., Ruggiero, C., Gulisano, M., and Ruggiero, M., Influence of static magnetic field on the antiproliferative effects of vitamin D on human breast cancer cells, *Oncol Res*, 11, 265, 1999a.
- Pacini, S., Vannelli, G.B., Barni, T., Ruggiero, M., Sardi, I., Pacini, P., and Gulisano, M., Effect of 0.2 T static magnetic field on human neurons: remodeling and inhibition of signal transduction without genome instability, *Neurosci Lett*, 267, 185, 1999b.
- Pagnac, C., Geneviere, A.-M., Moreau, J.-M., Picard, A., Joussot-Dubien, J., and Veyret, B., No effects of DC and 60-Hz AC magnetic fields on the first mitosis of two species of sea urchin embryos, *Bioelectromagnetics*, 19, 494, 1998.
- Pan, H. and Liu, X., Apparent biological effect of strong magnetic field on mosquito egg hatching, *Bioelectromagnetics*, 25, 84, 2004.
- Pate, K., Benghuzzi, H., Tucci, M., Puckett, A., and Cason, Z., Morphological evaluation of MRC-5 fibroblasts after stimulation with static magnetic field and pulsating electromagnetic field, *Biomed Sci Instrum*, 39, 460, 2003.
- Penuelas, J., Llusia, J., Martinez, B., and Fontcuberta, J., Diamagnetic susceptibility and root growth responses to magnetic fields in *Les culinaris*, *Glycine soja*, and *Triticum aestivum*, *Electromagn Biol Med*, 23, 97, 2004.
- Phillips, J.B., Magnetic navigation, *J Theor Biol*, 180, 309, 1996.
- Phillips, J.B., Animal magnetoreception: future directions, *BioEM* 2005, 160, 2005.
- Phillips, J.B., Deutschlander, M.E., Freake, M.J., and Borland, S.C., The role of extraocular photoreceptors in newt magnetic compass orientation: parallels between light-dependent magnetoreception and polarized light detection in vertebrates, *J Exp Biol*, 204, 2543, 2001.
- Phillips, J.B., Borland, S.C., Freake, M.J., Brassart, J., and Kirschvink, J.L., 'Fixed-axis' magnetic orientation by an amphibian: non-shoreward-directed compass orientation, misdirected homing or positioning a magnetite-based map detector in a consistent alignment relative to the magnetic field, *J Exp Biol*, 205, 3903, 2002a.
- Phillips, J.B., Freake, M.J., Fischer, J.H., and Vorland, S.C., Behavioral titration of a magnetic map coordinate, *J Comp Physiol A*, 188, 157, 2002b.
- Phirke, P.S., Kubde, A.B., and Umbarkar, S.P., The influence of magnetic field on plant growth, *Seed Sci Technol*, 24, 375, 1996.
- Piatti, E., Cristina, A.M., Baffone, W., Fraternale, D., Citterio, B., Piera, P.M., Dacha, M., Vetrano, F., and Accorsi, A., Antibacterial effect of a magnetic field on *Serratia marcescens* and related virulence to *Hordeum vulgare* and *Rubus fruticosus* callus cells, *Comp Biochem Physiol B Biochem Mol Biol*, 132, 359, 2002.
- Pilla, A.A., Mechanisms and therapeutic applications of time-varying and static magnetic fields, in *Biological and Medical Aspects* (Barnes, F.S., and Greenebaum, B., Eds.), Taylor & Francis, Boca Raton, FL, 2006, [Chapter 11](#).
- Poiata, A., Creanga, D.E., and Morariu, V.V., Life in zero magnetic field. V. *E. coli* resistance to antibiotics, *Electromagn Biol Med*, 22, 171, 2003.
- Polk, C. and Postow, E. (Eds.), *Handbook of Biological Effects of Electromagnetic Fields*, CRC Press, Boca Raton, FL, 1986.
- Polk, C. and Postow, E. (Eds.), *Handbook of Biological Effects of Electromagnetic Fields*, 2nd ed., CRC Press, Boca Raton, FL, 1997.
- Potenza, L., Cuccharini, L., Piatti, E., Angelini, U., and Dacha, M., Effects of high static magnetic field exposure on different DNAs, *Bioelectromagnetics*, 25, 352, 2004a.
- Potenza, L., Ubaldi, L., De Sanctis, R., De Bellis, R., Cuccharini, L., and Dacha, M., Effects of a static magnetic field on cell growth and gene expression in *Escherichia coli*, *Mutat Res*, 561, 53, 2004b.
- Prato, F.S., Kavaliers, M., and Carson, J.J.L., Behavioural evidence that magnetic field effects in the land snail, *Cepaea nemoralis*, might not depend on magnetite or induced electric currents, *Bioelectromagnetics*, 17, 123, 1996a.
- Prato, F.S., Kavaliers, M., and Carson, J.J.L., Behavioural responses to magnetic fields by land snails are dependent on both magnetic field direction and light, *Proc R Soc Lond B*, 263, 1437, 1996b.
- Prato, F.S., Robertson, J.A., Desjardins, D., Hensel, J., and Thomas, A.W., Daily repeated magnetic field shielding induces analgesia in CD-1 mice, *Bioelectromagnetics*, 26, 109, 2005.

- Rai, D.V., Kohli, K.S., Goyal, N., and Jindal, V.K., The effect of static magnetic field on electrical properties of lens, *Electr. Magnetobiol.*, 16, 293, 1997.
- Raylman, R.R., Clavo, A.C., and Wahl, R.L., Exposure to strong static magnetic field slows the growth of human cancer cell *in vitro*, *Bioelectromagnetics*, 17, 358, 1996.
- Reilly, J.P., Peripheral nerve stimulation in induced electric currents: exposure to time-varying magnetic fields, *Med Biol Eng Comput*, 27, 101, 1989.
- Reilly, J.P., Magnetic field excitation of peripheral nerves and the heart: a comparison of thresholds, *Med Biol Eng Comp*, 29, 571, 1991.
- Reina, F.G. and Pascual, L.A., Influence of a stationary magnetic field on water relations in lettuce seeds. Part 1: theoretical considerations, *Bioelectromagnetics*, 22, 589, 2001.
- Reina, F.G., Pascual, L.A., and Fundora, I.A., Influence of a stationary magnetic field on water relations in lettuce seeds. Part 2: experimental results, *Bioelectromagnetics*, 22, 596, 2001.
- Repacholi, M.H. and Greenebaum, B., Interaction of static and extremely low frequency electric and magnetic fields with living systems: health effects and research needs, *Bioelectromagnetics*, 20, 133, 1999.
- Ritz, T., Adem, S., and Schulten, K., A model for photoreceptor-based magnetoreception in birds, *Biophys J*, 78, 707, 2000.
- Ritz, T., Dommer, D.H., and Phillips, J.B., Shedding light on vertebrate magnetoreception, *Neuron*, 34, 503, 2002.
- Ritz, T., Thalau, P., Phillips, J.B., Wiltschko, R., and Wiltschko, W., Resonance effects indicate a radical-pair mechanism for avian magnetic compass, *Nature*, 429, 177, 2004.
- Robitaille, P.M.L., Abduljalil, A.M., Kangarlu, A., Zhang, X., Yu, Y., Burgess, R., Bair, E., Noa, P., Yang, L., Zhu, H., Palmer, B., Jiang, Z., Chakeres, D.W., and Spigos, D., Human magnetic resonance imaging at eight tesla, *NMR Biomed*, 11, 263, 1998.
- Ronchetto, F., Barone, D., Cintorino, M., Berardelli, M., Lissola, S., Orlassino, R., Ossala, P., and Tofani, S., Extremely low frequency-modulated static magnetic fields to treat cancer: a pilot study on patients with advanced neoplasm to assess safety and acute toxicity, *Bioelectromagnetics*, 25, 563, 2004.
- Rosch, P.J. and Markov, M.S., *Bioelectromagnetic Medicine*, Marcel Dekker, New York, 2004.
- Rosen, A.D., Inhibition of calcium channel activation in GH3 cells by static magnetic fields, *Biochim Biophys Acta*, 1282, 149, 1996.
- Rosen, A.D., Effect of a 125 mT static magnetic field on kinetics of voltage activated Na^+ channels in GH3 cells, *Bioelectromagnetics*, 24, 517, 2003.
- Rosen, M. and Rosen, A., Magnetic influence on *Paramecium* motility, *Life Sci*, 46, 1509, 1990.
- Rothwell, J.C., Day, B.L., Thompson, P.D., Dick, J.P.R., and Marsden, C.D., Some experiences of techniques for stimulation of the human cerebral motor cortex through the scalp, *Neurosurgery*, 20(1), 156, 1987.
- Ruggiero, M., Bottaro, D.P., Liguri, G., Gulisano, M., Peruzzi, B., and Pacini, S., 0.2 T magnetic field inhibits angiogenesis in chick embryo chorioallantoic membrane, *Bioelectromagnetics*, 25, 390, 2004.
- Ruiz-Gomez, M.J., Prieto-Barcia, M.I., Ristori-Bogajo, E., and Martinz-Morillo, M., Static and 50 Hz magnetic field of 0.35 and 2.45 mT have no effect on the growth of *Saccharomyces cerevisiae*, *Bioelectromagnetics*, 64, 151, 2004.
- Sabo, J., Mirossay, L., Horovcak, L., Sarissky, M., Mirossay, A., and Mojzis, J., Effect of magnetic field on human leukemic cell line HL-60, *Bioelectrochemistry*, 56, 227, 2002.
- Sakurai, H., Okuno, K., Kubo, A., Nakamura, K., and Shoda, M., Effect of 7-tesla homogeneous magnetic field on mammalian cells, *Bioelectrochem Bioenerg*, 49, 57, 1999.
- Salerno, S., Lo Casto, A., Caccamo, N., D'Anna, C., de Maria, M., Lagalla, R., Scola, L., and Cardinale, A.E., Static magnetic fields generated by a 0.5 T MRI unit affects *in vitro* expression of activation markers and interleukin release in human peripheral blood mononuclear cells (PBMC), *Int J Radiat Biol*, 75, 457, 1999.
- Sandrey, M.A., Vesper, D.N., Johnson, M.T., Nindl, G., Swez, J.A., and Chamberlain, J., Effect of short duration electromagnetic field exposure on rat mass, *Bioelectromagnetics*, 23, 37658, 2002.
- Satow, Y., Matsunami, K., Kawashima, T., Satake, H., and Huda, K., A strong constant magnetic field affects muscle tension development in bullfrog neuromuscular preparations, *Bioelectromagnetics*, 22, 53, 2001.

- Saunders, R., Static magnetic fields: animal studies, *Prog Biophys Mol Biol*, 87, 225, 2005.
- Schenck, J.F., Physical interactions of static magnetic fields with living tissues, *Prog Biophys Mol Biol*, 87, 185, 2005.
- Schenck, J.F., Dumoulin, C.L., Redington, R.W., Kressel, H.Y., Elliott, R.T., and McDougall, I.L., Human exposure to 4.0-tesla magnetic fields in a whole-body scanner, *Med Phys*, 19, 1089, 1992.
- Schiffer, I.B., Schreiber, W.G., Graf, R., Schreiber, E.M., Jung, D., Rose, D.M., Hehn, M., Ebhard, S., Sagmuller, J., Spiess, H.W., Oesch, F., Thelen, M., and Hengstler, J.G., No influence of magnetic fields on cell cycle progression using conditions relevant for patients during MRI, *Bioelectromagnetics*, 24, 241, 2003.
- Schlutten, K., Staerk, H., Weller, A., Werner, H.J., and Nickel, B., Magnetic field dependence of the geminate recombination of radical ion pairs in polar solvents, *Z Phys Chem NF*, 101, 371, 1976.
- Segal, N.A., Toda, Y., Huston, J., Saeki, Y., Shimizu, M., Fuchs, H., Shimaoka, Y., Holcomb, R., and McLean, M.J., Two configurations of static magnetic fields for treating rheumatoid arthritis of the knee: a double-blind clinical trial, *Arch Phys Med Rehabil*, 82, 1453, 2001.
- Sekino, M., Inoue, Y., and Ueno, S., Magnetic resonance imaging of mean values and anisotropy of electrical conductivity in the human brain, *Neurol Clin Neurophysiol*, 55, 1, 2004a.
- Sekino, M., Matsumoto, T., Yamaguchi, K., Iriguchi, N., and Ueno, S., A method for NMR imaging of a magnetic field generated by electric current, *IEEE Trans Magn*, 40, 2188, 2004b.
- Sekino, M., Mihara, H., Iriguchi, N., and Ueno, S., Dielectric resonance in magnetic resonance imaging: signal inhomogeneities in samples of high permittivity, *J Appl Phys*, 97, 10R303, 2005.
- Shellock, F.G. (Ed.), *Magnetic Resonance Procedures: Health Effects and Safety*, CRC Press, Boca Raton, FL, 2001.
- Shupak, N.M., Hensel, J.M., Cross-Mellor, S.K., Kavaliers, M., Prato, F.S., and Thomas, A.W., Analgesic and behavioral effects of a 100 microT specific pulsed extremely low frequency magnetic field on control and morphine treated CF-1 mice, *Neurosci Lett*, 354(1), 30, 2004a.
- Shupak, N.M., Prato, F.S., and Thomas, A.W., Human exposure to a specific pulsed magnetic field: effects on thermal sensory and pain thresholds, *Neurosci Lett*, 363(2), 157, 2004b.
- Slowik, T.J., Green, B.L., and Thorvilson, H.G., Detection of magnetism in the red imported fire ant (*Solenopsis invicta*) using magnetic resonance imaging, *Bioelectromagnetics*, 18, 396, 1997a.
- Slowik, T.J., Green, B.L., and Thorvilson, H.G., Response of red imported fire ant to magnetic field in the nest environment, *South Entomol*, 22, 301, 1997b.
- Snyder, D.J., Jahng, J.W., Smith, J.C., and Houpt, T.A., c-Fos induction in visceral and vestibular nuclei of the rat brain stem by a 9.4 T magnetic field, *Neuro Report*, 11, 2681, 2000.
- So, P., Stuchly, M.A., and Nyenhuis, J.A., Peripheral nerve stimulation by gradient switching fields in MRI, *IEEE Trans BioMed Eng*, 51, 1907, 2004.
- Sonnier, H., Kolomytkin, O., and Marino, A., Resting potential of excitable neuroblastoma cell in weak magnetic fields, *Cell Mol Life Sci*, 57, 514, 2000.
- Sonnier, H., Kolomytkin, O., and Marino, A., Action potentials from human neuroblastoma cells in magnetic fields, *Neurosci Lett*, 337, 163, 2003.
- Squires, K.C., Development of a 37-channel SQUID-based magnetometer for study of the brain and heart, *Med Biol Eng Comput*, 29(Suppl), 761, 1991.
- Stamenkovic-Radak, M., Kitanovic, I., Prolic, Z., Tomisic, I., Stojkovic, B., and Andjelkovic, M., Effect of permanent magnetic field on wing size parameters in *Drosophila melanogaster*, *Bioelectromagnetics*, 22, 365, 2001.
- Stansell, M.J., Winters, W.D., Doe, R.H., and Dart, B.K., Increased antibiotic resistance of *E. coli* exposed static magnetic fields, *Bioelectromagnetics*, 22, 129, 2001.
- Stavroulakis, P. (ed.), *Biological Effects of Electromagnetic Fields*, Springer-Verlag, Berlin, 2003.
- Stefano, G. and Tranquillo, R.T., A methodology for the systematic and quantitative study of cell contact guidance in orientated collagen gels, *J Cell Sci*, 105, 317, 1993.
- Stern, S., Laties, V.G., Nguyen, Q.A., and Cox, C., Exposure to combined static and 60 Hz magnetic fields: failure to replicate a reported behavioral effect, *Bioelectromagnetics*, 17, 279, 1996.
- Steyn, P.F., Ramey, D.W., Kirschvink, J., and Uhring, J., Effect of a static magnetic field on blood flow to the metacarpus in horses, *J Am Vet Med Assoc*, 217, 874, 2000.
- Strickman, D., Timberlake, B., Estrada-Franco, J., Weissman, M., Fenimore, P.W., and Novak, R.J., Effects of magnetic fields on mosquitoes, *J Am Mosq Control Assoc*, 16, 131, 2000.

- Suzuki, M., and Nakamura, H., Orientation of sperm DNA under a magnetic field, *Proc Jpn Acad*, 71(Ser B), 36, 1995.
- Suzuki, Y., Ikehata, M., Nakamura, K., Nishioka, M., Asanuma, K., Koana, T., and Shimizu, H., Induction of micronuclei in mice exposed to static magnetic fields, *Mutagenesis*, 16, 499, 2001.
- Tablado, L., Perez-Sanchez, F., and Soler, C., Is sperm motility maturation affected by static magnetic field? *Environ Health Perspect*, 104, 1212, 1996.
- Tablado, L., Perez-Sanchez, F., Nunez, J., Nunez, M., and Soler, C., Effects of exposure to static magnetic fields on the morphology and morphometry of mouse epididymal sperm, *Bioelectromagnetics*, 19, 377, 1998.
- Tablado, L., Soler, C., Nunez, M., Nunez, J., and Perez-Sanchez, F., Development of mouse testis and epididymis following intrauterine exposure to a static magnetic field, *Bioelectromagnetics*, 21, 19, 2000.
- Takashima, Y., Miyakoshi, M., Ikehara, M., Iwasaka, M., Ueno, S., and Koana, T., Genotoxic effects of strong static magnetic fields in DNA-repair defective mutants of *Drosophila melanogaster*, *J Radiat Res*, 45, 393, 2004.
- Takebe, H., Shiga, T., Kato, M., and Masada, E., *Biological and Health Effects from Exposure to Power-Line Frequency Electromagnetic Fields—Confirmation of Absence of Any Effects at Environmental Field Strengths*, IOS Press, Amsterdam, 1999.
- Tanimoto, Y., Hayashi, H., Nagakura, S., Sakurai, H., and Tokumaru, K., The external magnetic field effect on the singlet sensitized photolysis of dibenzoyl peroxide, *Chem Phys Lett*, 41, 267, 1976.
- Tanimoto, Y., Izumi, S., Furuta, K., Suzuki, T., Fujiwara, Y., Fujiwara, M., Hirata, T., and Yamada, S., Effects of high magnetic field on *Euglena gracilis*, *Int J Appl Electromagn Mech*, 14, 311, 2001.
- Tanimoto, Y., Ogawa, S., Fujitani, K., Fujiwara, Y., Izumi, S., and Hirata, T., Effects of a high magnetic field on *E. coli* movement, *Environ Sci*, 18, 53, 2005.
- Tanioka, N., Sawada, S., and Hosokawa, T., Proliferative and metastatic activities of mouse tumor cells exposed to a strong static magnetic field, *Bioelectrochem Bioenerg*, 40, 29, 1996.
- Taoka, S., Padmakumar, R., Grissom, C.B., and Banerjee, R., Magnetic field effects on coenzyme B12-dependent enzymes: validation of ethanolamine ammonia lyase results and extension to human methylmalonyl CoA mutase, *Bioelectromagnetics*, 18, 506, 1997.
- Tenforde, T.S., Magnetically induced electric fields and currents in the circulatory systems, *Prog Biophys Mol Biol*, 87, 279, 2005.
- Teodori, L., Grabarek, J., Smolewski, P., Ghibelli, L., Bergamaschi, A., De Nocla, M., and Darzynkiewicz, Z., Exposure of cells to static magnetic field accelerated loss integrity of plasma membrane during apoptosis, *Cytometry*, 49, 113, 2002.
- Testorf, M.F., Oberg, P.A., Iwasaka, M., and Ueno, S., Melanophore aggregation in strong static magnetic fields, *Bioelectromagnetics*, 23, 444, 2002.
- Thomas, J.R., Schrot, J., and Liboff, A.R., Low-intensity magnetic fields alter operant behavior in rats, *Bioelectromagnetics*, 7, 349, 1986.
- Till, U., Timmel, C.R., Brocklehurst, B., and Hore, P.J., The influence of very small magnetic field on radical recombination reactions in the limit of slow recombination, *Chem Phys Lett*, 298, 87, 1998.
- Timmel, C.R., Till, U., Brocklehurst, B., McLauchlan, K.A., and Hore, P.J., Effects of weak magnetic fields on free radical recombination reactions, *Mol Phys*, 95, 71, 1998.
- Tofani, S., Barone, D., Cintorino, M., de Santi, M.M., Ferrara, A., Orlassino, R., Ossola, P., Peroglio, F., Rolfo, K., and Ronchetto, F., Static and ELF magnetic fields induce tumor growth inhibition and apoptosis, *Bioelectromagnetics*, 22, 419, 2001.
- Tofani, S., Cintorino, M. et al., Increased mouse survival, tumor growth inhibition and decreased immunoreactive p53 after exposure to magnetic fields, *Bioelectromagnetics*, 23, 230, 2002.
- Tofani, S., Barone, D., Berardelli, M., Berno, E., Cintorino, M., Foglia, L., Ossola, P., Ronchetto, F., Toso, E., and Eandi, M., Static and ELF magnetic fields enhance the *in vivo* anti-tumor efficacy of cis-platin against Lewis lung carcinoma, but not of cyclophosphamide against B16 melanotic melanoma, *Pharmacol Res*, 48, 83, 2003.
- Torbet, J. and Ronziere, M.C., Magnetic alignment of collagen during self-assembly, *Biochem J*, 219, 1057, 1984.
- Torbet, J., Fryssinet, M., and Hudry-Clergeon, G., Oriented fibrin gels formed by polymerization in strong magnetic fields, *Nature*, 289, 91, 1981.

- Trabulsi, R., Pawlowski, B., and Wierszko, A., The influence of steady magnetic fields on the mouse hippocampal evoked potentials *in vitro*, *Brain Res*, 728, 135, 1996.
- Tranquillo, R.T., Girton, T.S., Bromberek, B.A., Triebes, T.G., and Mooradian, D.L., Magnetically oriented tissue-equivalent tubes: application to a circumferentially oriented media-equivalent, *Biomaterials*, 17, 349, 1996.
- Tsuchiya, K., Nakamura, K., Okuno, K., Ano, T., and Shoda, M., Effect of homogeneous and inhomogeneous high magnetic fields on the growth of *Escherichia coli*, *J Ferment Bioeng*, 81, 343, 1996.
- Tsuchiya, K., Okuno, K., Ano, T., Tanaka, K., Takahashi, H., and Shoda, M., High magnetic field enhances stationary phase-specific transcription activity of *Escherichia coli*, *Bioelectrochem Bioenerg*, 48, 383, 1999.
- Tsuji, Y., Nakagawa, M., and Suzuki, Y., Five-tesla static magnetic fields suppress food and water consumption and weight gain in mice, *Ind Health*, 34, 347, 1996.
- Tuch, D.S., Wedeen, V.J., Dale, A.M., George, J.S., and Belliveau, J.W., Conductivity tensor mapping of the human brain using diffusion tensor MRI, *Proc Natl Acad Sci USA*, 98, 11697, 2001.
- Ueno, S., Quenching of flames by magnetic fields, *J Appl Phys*, 65(3), 1243, 1989.
- Ueno, S., *Biological Effects of Magnetic and Electromagnetic Fields*, Plenum Press, New York, 1996.
- Ueno, S. and Harada, K., Redistribution of the dissolved oxygen concentration under strong DC magnetic field, *IEEE Trans Magn*, MAG-18, 1704, 1982.
- Ueno, S. and Harada, K., Experimental difficulties in observing the effects of magnetic fields on biological and chemical processes, *IEEE Magn*, 22, 868, 1986.
- Ueno, S. and Harada, K., Effects of magnetic fields on flames and gas flow, *IEEE Trans Magn*, MAG-23, 5, 2752, 1987.
- Ueno, S. and Iramina, K., Modeling and source localization of MEG activities, *Brain Topogr*, 3, 151, 1991.
- Ueno, S. and Iriguchi, N., Impedance magnetic resonance imaging: a method for imaging of impedance distributions based on magnetic resonance imaging, *J Appl Phys*, 83, 6450, 1998.
- Ueno, S. and Iwasaka, M., Parting of water by magnetic fields, *IEEE Trans Magn*, 30, 4698, 1994a.
- Ueno, S. and Iwasaka, M., Properties of diamagnetic fluid in high gradient magnetic fields, *J Appl Phys*, 75, 7177, 1994b.
- Ueno, S., Matsumoto, S., Harada, K., and Oomura, Y., Capacitative stimulatory effect in magnetic stimulation of nerve tissue, *IEEE Trans Magn*, MAG-14, 958, 1978.
- Ueno, S., Lovsund, P., and Oberg, P.A., Effects of alternating magnetic fields and low-frequency electric currents on human skin blood flow, *Med Biol Eng Comput*, 24, 57, 1986a.
- Ueno, S., Lovsund, P., and Oberg, P.A., Effects of time-varying magnetic fields on action potential in lobster giant axon, *Med Biol Eng Comput*, 24, 521, 1986b.
- Ueno, S., Tashiro, T., and Harada, K., Localized stimulation of neural tissues in the brain by means of a paired configuration of time-varying magnetic fields, *J Appl Phys*, 64, 5862, 1988.
- Ueno, S., Matsuda, T., and Fujiki, M., Localized stimulation of the human cortex by opposing magnetic fields, in *Advances in Biomagnetism* (Williamson, S.J., Hoke, M., Stroink, G., and Kotani, M., Eds.), Plenum Press, New York, 529, 1989.
- Ueno, S., Matsuda, T., and Fujiki, M., Functional mapping of the human motor cortex obtained by focal and vectorial magnetic stimulation of the brain, *IEEE Trans Magn*, 26, 1539, 1990a.
- Ueno, S., Matsuda, T., and Hiwaki, O., Estimation of structures of neural fibers in the human brain by vectorial magnetic stimulation, *IEEE Trans Magn*, 27, 5387, 1990b.
- Ueno, S., Matsuda, T., and Hiwaki, O., Localized stimulation of the human brain and spinal cord by a pair of opposing pulsed magnetic fields, *J Appl Phys*, 66, 5838, 1991.
- Ueno, S., Hiwaki, O., Matsuda, T. et al., Safety problems of dB/dt associated with echo planar imaging, *Ann NY Acad Sci*, 369, 96, 1992.
- Ueno, S., Iwasaka, M., and Tsuda, H., Effects of magnetic fields on fibrin polymerization and fibrinolysis, *IEEE Trans Magn*, 29, 3352, 1993.
- Valles, J.M. Jr., Model of magnetic field-induced mitotic apparatus reorientation in frog eggs, *Biophys J*, 82, 1260, 2002.
- Valles, J.M. Jr., Lin, K., Denegre, J.M., and Mowry, K.L., Stable magnetic field gradient levitation of *Xenopus laevis*: toward low-gravity simulation, *Biophys J*, 73, 1130, 1997.

- Valles, J.M. Jr., Wasserman, S.R.R.M., Schweidenback, C., Edwardson, J., Denegre, J.M., and Mowry, K.L., Processes that occur before second cleavage determine third cleavage orientation in *Xenopus*, *Exp Cell Res*, 274, 112, 2002.
- van Rongen, E., International workshop "effects of static magnetic fields relevant to human health" Reporteurs report: dosimetry and volunteer studies, *Prog Biophys Mol Biol*, 87, 329, 2005.
- Veliks, V., Ceihnere, E., Svikis, I., and Aivars, J., Static magnetic field influence on rat brain function detected by heart rate monitoring, *Bioelectromagnetics*, 25, 211, 2004.
- Vink, C.B. and Woodward, J.R., Effect of a weak magnetic field on the reaction between neural free radicals in isotropic solution, *J Am Chem Soc*, 126, 16730, 2004.
- Volpe, P., Interactions of zero-frequency and oscillating magnetic fields with biostructures and biosystems, *Photochem Photobiol Sci*, 2, 637, 2003.
- Vrva, J., Bette, K., and Burband, M., Whole cortex 64 channel SQUID biomagnetometer system, *IEEE Trans, AS* 3, 1878, 1993.
- Watanabe, Y., Nakagawa, M., and Miyakoshi, Y., Enhancement of lipid peroxidation in liver of mice exposed to magnetic fields, *Ind Health*, 35, 285, 1997.
- Wieraszko, A., Dantrolene modulates the influence of steady magnetic fields on hippocampal evoked potentials *in vivo*, *Bioelectromagnetics*, 21, 175, 2000.
- Wiltschko, R. and Wiltschko, W., *Magnetic Orientation in Animals, Zoophysiology*, vol. 33, Springer-Verlag, Berlin, 1995.
- Wiltschko, R. and Wiltschko, W., Magnetoreception: why is conditioning so seldom successful? *Naturewissenschaften*, 83, 241, 1996.
- Wiltschko, W. and Wiltschko, R., Light-dependent magnetoreception in birds: the behaviour of European robins, *Eriothacus rubecula*, under monochromatic light of various wavelengths and intensities, *J Exp Biol*, 204, 3295, 2001.
- Wiltschko, W. and Wiltschko, R., Magnetic compass orientation in birds and its physiological basis, *Naturwissenschaften*, 89, 445, 2002.
- Winklhofer, M., Holtkamp-Roetzler, E., Hanzlik, M., Fleissner, G., and Petersen, N., Clusters of superparamagnetic magnetite particles in the upper-beak skin of homing pigeons: evidence of a magnetoreceptor? *Eur J Miner*, 13, 659, 2001.
- Winnicki, A., Formicki, K., and Sobocinski, A., Application of constant magnetic field in transportation of gametes and fertilized eggs of salmonid fish, *Publ Espec Inst Esp Oceanogr*, 21, 301, 1996.
- Wiskirchen, J., Groenwaeller, E.F., Kehlbach, R., Heinzelmann, F., Wittau, M., Rodemann, H.P., Claussen, C.D., and Duda, S.H., Long-term effects of repetitive exposure to a static magnetic field (1.5 T) on proliferation of human fetal lung fibroblasts, *Magn Reson Med*, 41, 464, 1999.
- Wiskirchen, J., Groenwaller, E.F., Heinzelmann, F., Kehlbach, R., Rodegerdts, E., Wittau, M., Rodemann, H.P., Claussen, C.D., and Duda, S.H., Human fetal lung fibroblasts, *in vitro* study of repetitive magnetic field exposure at 0.2, 1.0, and 1.5 T, *Radiology*, 215, 858, 2000.
- Xiong, J., Fox, P.T., and Gao, J.H., Directly mapping magnetic field effects of neuronal activity by magnetic resonance imaging, *Hum Brain Mapp*, 20, 41, 2003.
- Xu, S., Okano, H., and Ohkubo, C., Subchronic effects of static magnetic fields on cutaneous microcirculation in rabbits, *In Vivo*, 12, 383, 1998.
- Xu, S., Okano, H., and Ohkubo, C., Acute effects of whole-body exposure to static magnetic fields and 50-Hz electromagnetic fields on muscle microcirculation in anesthetized mice, *Bioelectromagnetics*, 53, 127, 2000.
- Xu, S., Tomita, N., Ohata, R., Yan, Q., and Ikada, Y., Static magnetic field effects on bone formation of rats with an ischemic bone model, *BioMed Mater Eng*, 11, 257, 2001.
- Yamagishi, A., Takeuchi, T., Higashi, T., and Date, M., Diamagnetic orientation of polymerized molecules under high magnetic field, *J Phys Soc Jpn*, 58, 2280, 1989.
- Yamaguchi, S., Ogiue-Ikeda, M., Sekino, M., and Ueno, S., The effect of repetitive magnetic stimulation on the tumor development, *IEEE Trans Magn*, 40, 3021, 2004.
- Yamaguchi, S., Ogiue-Ikeda, M., Sekino, M., and Ueno, S., Effects of pulsed magnetic stimulation on tumor development and immune functions in mice, *Bioelectromagnetics*, 27, 64, 2006.
- Yan, Q.C., Tomita, N., and Ikada, Y., Effects of static magnetic field on bone formation of rat femurs, *Med Eng Phys*, 20, 397, 1998.

- Yano, A., Ogura, M., Sato, A., Sakaki, Y., Shimizu, Y., Baba, N., and Nagasawa, K., Effect of modified magnetic field on the ocean migration of maturing chum salmon, *Oncorhynchus keta*, *Mar Biol*, 129, 523, 1997.
- Yano, A., Hidaka, E., Fujiwara, K., and Iimoto, M., Induction of primary root curvature in radish seedlings in a static magnetic field, *Bioelectromagnetics*, 22, 194, 2001.
- Yoon, R.S., DeMonte, T.P., Hasanov, K.F., Jorgenson, D.B., and Joy, M.L.G., Measurement of thoracic current flow in pigs for the study of defibrillation and cardioversion, *IEEE Trans Biomed Eng*, 50, 1167, 2003.
- Yoshida, H., Ueno, S., Cheyne, D., and Weinberg, H., Measurements of low frequency brain magnetic fields associated with four-tone memory processes, *IEEE Trans Magn*, 31, 4268, 1995.
- Zangaladze, A., Epstein, C.M., Grafton, S.T., and Sathian, K., Involvement of visual cortex in tactile discrimination of orientation, *Nature*, 401, 587, 1999.
- Zhadin, M.N., Review of Russian literature on biological action of DC and low-frequency AC magnetic fields, *Bioelectromagnetics*, 22, 27, 2001.
- Zhadin, M.N., Novikov, V.V., Barnes, F.S., and Pergola, N.F., Combined action of static and alternating magnetic fields on ionic current in aqueous glutamic acid solution, *Bioelectromagnetics*, 19, 41, 1998.
- Zhadin, M.N., Deryugina, O.N., and Pisachenko, T.M., Influence of combined DC and AC magnetic fields on rat behavior, *Bioelectromagnetics*, 20, 378, 1999.
- Zhang, Q.-M., Tokiwa, M., Doi, T., Nakahara, T., Chang, P.-Q., Nakamura, N., Hori, M., Miyakoshi, J., and Yonei, S., Strong static magnetic field and the induction of mutations through elevated production of reactive oxygen species in *Escherichia coli* soxR, *Int J Radiat Biol*, 79, 281, 2003.
- Zmyslony, M., Palus, J., Jajte, J., Dziubaltowska, E., and Rajkowska, E., DNA damage in rat lymphocytes treated *in vivo* with iron cations and exposed to 7 mT magnetic fields (static or 50 Hz), *Mutat Res*, 453, 89, 2000.

9

The Ion Cyclotron Resonance Hypothesis

A.R. Liboff

CONTENTS

9.1	Introduction	261
9.1.1	General Remarks.....	261
9.1.2	Background History	264
9.2	Experimental Evidence	266
9.2.1	Rat Behavior	269
9.2.2	Plants.....	270
9.2.3	Bone.....	274
9.2.4	Harmonics	276
9.2.5	Physiological Reversals.....	278
9.2.6	Water.....	278
9.3	Theoretical Approaches	280
9.3.1	Physical Constraints	280
9.3.2	Ion Channels.....	281
9.3.3	Dependence on AC Magnetic Field.....	283
9.3.4	Precessional Effects.....	285
9.3.5	Coherence Domains.....	285
9.4	Discussion	286
	References	287

9.1 Introduction

9.1.1 General Remarks

Ion cyclotron resonance (ICR) is one among a number of possible mechanisms that have been advanced to explain observed interactions between weak low-frequency electromagnetic fields and biological systems. Despite the failure to find a reasonable physical explanation, there remains an impressive body of experimental evidence that can be taken as an empirical basis for this hypothesis. The ICR suggestion has proven fruitful in framing both experimental and theoretical work, despite the biophysical situation being far from the literal cyclotron resonance model of an isolated classical charged particle moving in a vacuum under the influence of a magnetic field.

The properties of the applied fields that are used in ICR experiments include linear or circular polarization, the presence of a finite magnetostatic field, frequencies ranging from a few to several hundred hertz, magnetic intensities ranging from about 1 μT to 1 mT, and,

most important, a directional constraint on the relative orientation of the time-varying electromagnetic field to the magnetostatic (DC) field. This orientation requires that time-varying magnetic fields be parallel to the DC field or, equivalently, that time-varying electric fields are perpendicular to the DC field.

The ICR hypothesis holds that the physiological activity of those ions implicated in cell signaling processes, including, among others, Ca^{2+} , Mg^{2+} , and K^+ , can be altered when the ratio of applied signal frequency to the static magnetic field is equal to the ionic charge-to-mass ratio. This is expressed as

$$\omega/B = q/m \quad (9.1)$$

where the radial frequency $\omega = 2\pi f$, as measured in radians per second, is used instead of f , the frequency measured in hertz. In SI units, B is the DC field intensity measured in tesla, and q/m is the ratio of the ionic charge to mass, in coulombs per kilogram. For any given ionic species, the specific frequency that equals the product of B and q/m is called the cyclotronic frequency, ω_c .

The resonance concept is attractive for a number of reasons. There is a potential connection to interactions involving the Earth's magnetic field (geomagnetic field [GMF]). Further, the ICR mechanism may help provide the basis for at least some of the reports of low-frequency electromagnetic interactions that otherwise lack explanation. Finally, given the wide variety of biological systems in which ICR effects are observed, it is reasonable to ask if there are fundamental scientific questions connected to this phenomenon.

The ICR hypothesis has especial significance attached to magnetostatic fields whose intensity is of the order of the GMF (20–60 μT). This becomes apparent when the charge-to-mass ratios of key biological ions are substituted into Equation 9.1. These ratios range from about 2 to $8 \times 10^6 \text{ C/kg}$, implying that a static magnetic field of 50 μT corresponds to resonance frequencies of the order of 10–100 Hz (Figure 9.1). Such frequencies could

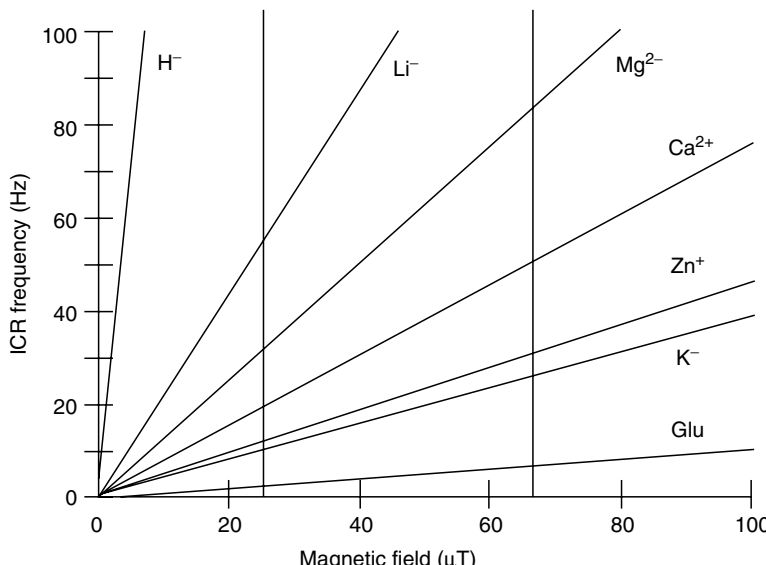


FIGURE 9.1

Ion cyclotron resonance frequencies for many biologically important ions in the Earth's magnetic field are in the ELF range.

TABLE 9.1
ICR Cation Possibilities

Ion	q/m (C/kg) $\times 10^{-6}$	f/B (Hz/ μ T)
H ⁺	95.76	15.241
Li ⁺	13.90	2.212
Mg ²⁺	7.937	1.263
H ₃ O ⁺	5.066	0.807
Ca ²⁺	4.814	0.766
Zn ²⁺	2.951	0.470
K ⁺	2.467	0.393
Arg ²⁺	1.235	0.197
Asn ⁺	0.838	0.133
Glu ⁺	0.747	0.119
Tyr ⁺	0.591	0.094

conceivably have physiological significance since they correspond approximately to the frequency range generated in the central nervous system [1]. This, coupled to the focus on the potential hazards attached to 50/60-Hz electromagnetic power delivery sources [2], has sparked study of the ICR hypothesis, in terms of both experiments specifically designed to test this hypothesis as well as theoretical models seeking an explanatory basis at the molecular level.

Some specific ions that have been implicated are listed in Table 9.1. Note that four polar amino acids and the hydronium ion are included. The ratios of frequency to DC magnetic field, as calculated from [Equation 9.1](#), are shown in the right-hand column. This ratio can be regarded as an invariant characteristic for any given ion.

Although experimental evidence provides support for the ICR hypothesis [3], there is no widely accepted theoretical explanation. Indeed, because of constraints mainly arising from unfavorable damping conditions, there are strong arguments [4] against the occurrence in living tissue of any classical ICR mechanism [5], as occurs, say, for energetic charged particles moving in a vacuum under the influence of parallel static and AC magnetic fields. The circular and helical paths associated with such undamped motion are invariably the result of the Lorentz force, which imparts an acceleration \mathbf{a} to a charged particle of mass m moving at velocity \mathbf{v} in a magnetic field \mathbf{B} :

$$\mathbf{a} = (q/m)(\mathbf{v} \times \mathbf{B}) \quad (9.2)$$

Nevertheless, arguments have been raised [6–11] that although the biological response may not correspond to the effects resulting from ICR-specific helical pathways of charged particles [4], the coupling is nevertheless a function of the ICR frequency as predicted by [Equation 9.1](#). Although there has been no consistent experimental verification for any of these models, there is little question concerning the observed dependence on the cyclotron resonance frequency. Because the cyclotronic frequency is the common denominator in all these models, it is preferable to subsume all of them under the umbrella term ICR hypothesis.

The great variety of biosystems in which ICR effects have been observed implies a ubiquitous response that may have fundamental physiological significance. One can generalize this response R in terms of its functional dependence. From [Equation 9.1](#), we can write

$$R = R(\omega, B, q/m) \quad (9.3)$$

Lednev [7] added a fourth variable, namely the intensity of the AC magnetic field, B_{AC} . Thus, the expanded expression for the response $R = R(\omega, B, B_{AC}, q/m)$, or, in terms of the two key variables,

$$R = R(\omega_c, B_{AC}) \quad (9.4)$$

There is no question as to the relevance of B_{AC} in studying the interactions between ICR field combinations and biological systems. However, it is not clear if the experimentally observed dependences on B_{AC} are a direct result of the underlying resonance mechanism, as has been suggested [7,9], or if there are other separate physiological factors that limit the levels of the AC field under which an ICR mechanism may be operative.

9.1.2 Background History

ICR was originally invoked [4] to explain an extraordinary set of observations by Blackman's group [12] indicating a strong dependence on the orientation of the magnetostatic field when studying the Ca-efflux model system [13]. The original discovery of the Ca-efflux effect [13] and subsequent studies [14–17] showed conclusively that the level of $^{45}\text{Ca}^{2+}$ efflux from preloaded chick brain was a nonlinear function of low-frequency (ca. 15 Hz) modulation signals when these brains were exposed to high-frequency carrier electric fields. Typically, this nonlinear signature (Figure 9.2), at first referred to as a "window," has the appearance of a resonance curve. The Blackman experiment [12] discovered that this resonance signature appeared only when certain specific values of the vertical DC magnetic field were superposed on the system. In [Table 9.2](#), "Yes" indicates the appearance of a resonance signature for a given combination of f and B .

In addition to Blackman's original set of results, a fourth column has been added in [Table 9.2](#) to show the putative charge-to-mass ratio as determined from [Equation 9.1](#). One sees that the sign of the magnetic field direction, either pointing up or down, does not affect the outcome. The specific combination of 15 Hz and 38 μT is positive, as is the combination of 30 Hz and 76 μT , suggesting that the ratio of frequency to field is involved as a key factor.

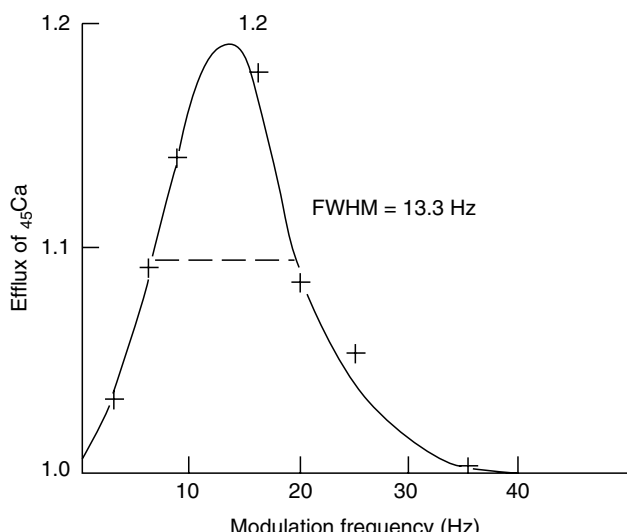


FIGURE 9.2

Comparison of shape of "window" data for Ca-efflux results [13] (seven points) with predicted resonance curve [18] (smooth curve). The best fit is for the charge-to-mass ratio for K^+ , a magnetostatic field of 35.0 μT , and a collision time of 0.026 sec.

TABLE 9.2

Analysis of Blackman [12] Data

<i>f</i> (Hz)	<i>B</i> (μ T)	Outcome	<i>q/m</i> (C/kg)
15	38	Yes	2.48×10^6
15	19	No	4.96×10^6
30	38	No	4.96×10^6
30	76	Yes	2.48×10^6
30	-76	Yes	2.48×10^6
30	50	No	3.77×10^6
30	25	Yes	7.54×10^6
30	-25	Yes	7.54×10^6
30	-83	No	2.27×10^6

Despite the fact that calcium was explicitly measured in this and the earlier Ca-efflux experiments, the data in Table 9.2 give reason to believe that the potassium ion was the primary target for the electromagnetic interactions. First, note that the charge-to-mass ratio of 2.48×10^6 C/kg is associated with positive outcomes. This ratio is less than 0.5% different from the *q/m* ratio for the potassium ion as shown in Table 9.1. The evidence linking K^+ to a positive outcome is further strengthened by examining the results obtained for the combination of 30 Hz and 25 μ T. The positive outcome in this case suggests a *q/m* value of 7.54×10^6 C/kg, three times larger than the *q/m* ratio for K^+ . In cyclotron resonance, one typically observes a set of resonance frequencies ω_n , where the fundamental at $n = 1$ is given in Equation 9.1, and the higher harmonic frequencies are restricted to the odd [19–21] harmonics $n = 3, 5, 7, \dots$. The *f/B* ratio of 30/25 Hz/ μ T is nearly three times larger than the ratio 15/38 Hz/ μ T, again implying that the K^+ ion is interacting with the magnetic field, this time as a result of an excitation at the third harmonic.

There is further evidence that the K^+ ion is an important interactive factor in the nonlinear effects observed in the Ca-efflux experiments. McLeod and Liboff [18,22] derived the resonance signature for a charged particle as a function of frequency, showing that the relative conductivity, with and without the presence of an ion resonance field combination, is

$$\frac{\sigma_x}{\sigma_0} = \frac{(1 + (\omega_c + \omega)^2 \tau^2)}{(1 + [(\omega_c^2 - \omega^2) \tau^2]^2 + 4\omega^2 \tau^2)} \quad (9.5)$$

This is a typical resonance expression that includes the effects of damping, expressed in terms of the collision time τ . By varying the choices of *q/m* ratios and collision times this expression can be directly compared to the results of Bawin and Adey [13], as shown in Figure 9.2. The smooth curve that best fits Equation 9.5 to the experimental points is also shown in Figure 9.2. This fitting procedure reveals that the most likely explanation for the data involves charged particles in cyclotron resonance with a *q/m* ratio equal to that of the potassium ion.

Thus, two independent sets of Ca-efflux data, one with DC magnetic fields applied as part of the experiment [12] and the other with the ambient magnetic field in the laboratory playing an unsuspected role [14], yield the same conclusion, that ICR stimulation of the K^+ ion results in the nonlinear resonance response.

9.2 Experimental Evidence

There is a surprisingly wide variety of biological systems in which ICR effects are observed. This suggests a heretofore unknown electromagnetic biological interaction. The model systems that have been examined in the literature can be conveniently divided into the categories of bone, cell culture, rat behavior, neural cell culture, diatom motility, complex biological systems, plants, and cell-free systems. These eight separate broad categories are listed respectively in Table 9.3 through Table 9.10. There is some

TABLE 9.3

ICR Effects in Skeletal Tissues

Frequency (Hz)	B_0 (μT)	Tuning	Ratio B/B_0	Comments	Reference
100	130	Ca^{2+}	1.0	Enhanced cell (fibroblast) proliferation; B varied between 50 and 500 μT	23
75	98	Ca^{2+}	1.0	Enhanced proliferation	23
16	42	Ca^{2+}	1.0	Enhanced proliferation	23
16	20.9	Ca^{2+}	1.0	Increases in rudiment length and midshaft diameter in embryonic chick femur	24
16	12.7	Mg^{2+}	1.0	Similar results to Ca^{2+} tuning	24
16	40.9	K^+	1.0	Results opposite to Ca^{2+} and Mg^{2+} cases: bone growth inhibited	24
80	20	$\text{Ca}^{2+}/\text{Mg}^{2+}$	1.0	Both fifth Ca^{2+} to third Mg^{2+} harmonics; enhanced collar thickness and length	24
72.6–80.6	20	Ca^{2+}	1.0	Resonance in IGF-II concentration at 76.6 Hz in osteosarcoma cell line	25
76.6	20	Ca^{2+}	1.0	Fifth harmonic: enhanced proliferation in osteosarcoma and human bone cells	25
15.3	20	Ca^{2+}	1.0	Reduction in tissue growth factor (TGF) β -1 inhibition in chondrocyte culture	26
25.4	20	Mg^{2+}	1.0	Reduction of TGF β -1 inhibition in chondrocyte culture	26
76.6	20	$\text{Ca}^{2+}/\text{Mg}^{2+}$	1.0	Reduction of TGF β -1 inhibition in chondrocyte culture	26
15.3	20	Ca^{2+}	1.0	Enhanced proteoglycans synthesis in bovine cartilage	26
76.6	20	$\text{Ca}^{2+}/\text{Mg}^{2+}$	1.0	Mixed third and fifth harmonics reduce bone loss related to castration in rats	27
14.3–18.3	20		1.0	Increase in ^{45}Ca maximized at 16.3 Hz in osteosarcoma cell line	28
14.3–18.3	20		1.0	Increase in ^{45}Ca maximized at 15.3 Hz in a different osteosarcoma cell line	28
15.3	20	Ca^{2+}	1.0	370% increase in stiffness in ovariectomized rabbit fibula after 24 h/28 d exposure	29
25.4	20	Mg^{2+}	1.0	137% increase in stiffness in ovariectomized rabbit fibula after 24 h/28 d exposure	29
15.3	20	Ca^{2+}	1.0	Enhanced DNA synthesis and IGF-II levels in osteosarcoma cell line	30
13.3–17.3	20		1.0	Resonance maximum in IGF-II receptor number and affinity at 15.3 Hz	31
16	20.9	Ca^{2+}	1.0	Enhanced chick femoral diameter and glycosaminoglycans (GAGS) content	32
16	12.7	Mg^{2+}	1.0	Large (90%) GAGS enhancement	32
16	40.7	K^+	1.0	Opposite effects for Ca^{2+} and Mg^{2+} tuning, replicating Smith et al. [24]	32

TABLE 9.4
ICR Effects in Cell Culture

Frequency (Hz)	B_0 (μ T)	Tuning	Ratio B/B_0	Comments	Reference
14.3	21	$^{45}\text{Ca}^{2+}$	1.0	Isotopic shift in q/m resonance confirmed, ^{40}Ca to ^{45}Ca	33
14.3	21	$^{45}\text{Ca}^{2+}$	1.0	Threefold incorporation of ^{45}Ca into human lymphocytes	33
14.3	21	$^{45}\text{Ca}^{2+}$		Effect on human lymphocytes disappears at larger AC intensity	33
14.3	20.9	$^{45}\text{Ca}^{2+}$	1.0	2.3-fold uptake in ^{45}Ca disappears with addition of calcium blocker nifedipine	34
38.15	50	Ca^{2+}	1.0	No effect on Ca^{2+} in four different cell lines as observed using calcium fluorochrome fura-2	35
16	20.9	Ca^{2+}	1.0	Enhanced proliferation (46%) for fibroblast culture at Ca^{2+} ICR tuning	36
?	20.9	K^+	1.0	Reduced proliferation (18%) for Raji cells exposed to K^+ ICR; frequency not provided	36
13.6	16.5	$^{45}\text{Ca}^{2+}$	1.2	ICR frequency off by 3.5 Hz; enhanced $^{45}\text{Ca}^{2+}$ levels (75–126%) in three cell lines	37
60	20	$^{45}\text{Ca}^{2+}$	1.0	Fifth harmonic for $^{45}\text{Ca}^{2+}$ uptake is enhanced by 37%	37
16	23.4	$^{45}\text{Ca}^{2+}$	1.8	Decreased Ca^{2+} influx in mitogen-activated lymphocytes but no effect on resting cells	38
16	51.1	K^+	1.0	Third harmonic: enhanced proliferation of lymphoma cells; very narrow FWHM ^a	39
16	40.9	K^+	1.0	Enhanced proliferation of human lymphoma cells	39
16	23.4	Ca^{2+}	3.8, 5.3	No change in Ca^{2+} influx at AC/DC ratio of 3.8 but enhanced influx at ratio of 5.3	40
16	20.9	Ca^{2+}	1.4	No effect on mouse lymphocytes as observed using Ca fluorochrome Quin-2	41
50	65.3	Ca^{2+}	1.4	No effect on mouse lymphocytes with and without mitogenic stimulation	41
5–100	50–60	? Ca^{2+}	2.3–3.0	Enhanced calcium oscillations over broad frequency range, maximized at 50 Hz	42
32	42	Ca^{2+}	2.5, 5.0	Increased micronuclei formation in human lymphocytes at Ca^{2+} ICR tuning	43
32.50	0			No change in micronuclei formation when DC field is zero	43
15.3	20	Ca^{2+}	1.0	ICR effect on fura-2 calcium activity only found for added serum in cell medium	44
76.6	20	Ca^{2+}	1.0	Fifth harmonic is also successful	44
100	130	Ca^{2+}	1.9	Another ICR fundamental successful	44
100	130	Ca^{2+}	2.8	Repeating ICR application to primary bone cell culture at higher AC intensity	44

^aFWHM, full width at half maximum.

unavoidable overlap among these, particularly in Table 9.3 (skeletal systems), where references to bone research in cell cultures and animals are grouped together.

Although most of the reports summarized in Table 9.3 through Table 9.10 lend considerable weight to the hypothesis that ICR magnetic stimulation can affect biological systems, the effects on diatom motility (Table 9.7) are not as clear-cut, in that a number of observers [62–65] failed to find any effects whatsoever. The explanation for the poor reproducibility in this case may rest with difficulties in handling the diatom model system, one that is especially sensitive to sample preparation.

TABLE 9.5

ICR Effects on Rat Behavior

Frequency (Hz)	B_0 (μT)	Tuning	Ratio B/B_0	Comments	Reference
60	26	Ca^{2+}	1.9	Third harmonic: loss of short-term (temporal) memory in rats	45
60	26	Ca^{2+}	1.9	Third harmonic: AC threshold observed ($27 \mu\text{T}$) for above results	46
60	27	Ca^{2+}	1.9	Third harmonic: learning inhibited relative to controls	47
60	48	Mg^{2+}	1.0	Learning enhanced relative to controls	47
60	26	Ca^{2+}	1.9	Third harmonic: no effect	48
50	65	Ca^{2+}		Reduced short-term memory and aggressiveness	49
630	500	Mg^{2+}	0.5	Enhanced exploratory activity	50
380	500	Ca^{2+}	0.5	Reduced exploratory activity	50
63	50	Mg^{2+}	0.7	Enhanced locomotor and exploratory activity	51
38	50	Ca^{2+}	0.7	Reduced locomotor and exploratory activity	51
630	500	Mg^{2+}	0.7	Enhanced locomotor and exploratory activity	51
380	500	Ca^{2+}	0.7	Reduced locomotor and exploratory activity	51

TABLE 9.6

ICR Effects on Neural Cell Culture

Frequency (Hz)	B_0 (μT)	Tuning	Ratio B/B_0	Comments	Reference
16	15–40.8	? Co^{2+} or Fe^{2+} ?	0.5–1.3	Enhanced proliferation over controls (60%) in neuroblastoma cell culture	52
16	15–40.8		0.5–1.3	Decreased neurite outgrowth for ? $\text{Co}^{2+}/\text{Fe}^{2+}$ ICR stimulation; possible Na^+ ICR effect?	52
15.3	20	Ca^{2+}	1.0	Ca^{2+} tuning increases rate of neuronal differentiation in PC-12 cells	53
45	36.6	Mg^{2+}	0.03–1.81	Changes in neurite outgrowth for Mg^{2+} ICR at different AC intensities in PC-12 cells	54
25	20.3	Mg^{2+}	0.54–1.26	Similar Mg^{2+} ICR effect on PC-12 neurite outgrowth at another frequency	54
45	2.96	H^+	0.14–2.0	H^+ ICR alters PC-12 neurite outgrowth	55
30	1.97	H^+	0.57–1.4	Similar effects at different ICR combinations	55
45	59	Ca^{2+}	0.26–1.49	PC-12 cells at Ca^{2+} ICR exhibit changes in neurite outgrowth at different AC intensities	56
42.5–47.5	2.97	H^+	0.56–1.5	Bandwidth for PC-12 neurite outgrowth due to H^+ ICR is $\pm 10\%$	57
40, 50	2.97		0.56–1.5	No effect	57

TABLE 9.7

ICR Effects on Diatom Motility

Frequency (Hz)	B_0 (μT)	Tuning	Ratio B/B_0	Comments	Reference
5–32	20.9		1.0	Maximum motility occurs at 16 Hz when Ca^{2+} concentration is 0.25 nM; no effect when fields are at 90°	58
16	20.9	Ca^{2+}	0.0–3.0	Motility maximized when B/B_0 ratio is 1	58
16	20.9	Ca^{2+}	0.7	Enhanced motility	59
32	20.9	Ca^{2+}	0.7	Even harmonic: no effect	59
48	20.9	Ca^{2+}	0.7	Third harmonic: enhanced motility	59
64	20.9	Ca^{2+}	0.7	Even harmonic: no effect	59
8	10.45	Ca^{2+}	1.4	Enhanced motility	60
12–64	15.7–83.6	Ca^{2+}		Additional ICR frequencies at 12, 16, 23, 31, 32, 46, 64 Hz also enhance motility	60
24, 40, 120	10.45	Ca^{2+}	1.4	Three ICR harmonics for 10.45 μT ($n = 3, 5, 15$) enhance motility	60
16–136	10.45	Ca^{2+}	1.40–73	Thirteen other frequencies ($n = 2, 4, 6, 7, 8, 9, 10, 11, 12, 13, 14, 16, 17$) fail to show effect	60
8	20.45	K^+	0.73	Motility inhibited	60
16	41	K^+	0.37	Motility inhibited	60
24, 40, 120	20.45	K^+	0.37	Three ICR harmonic frequencies for $B_0 = 20.45 \mu\text{T}$ ($n = 3, 5, 15$) also inhibit motility	60
16–136	20.45	K^+	0.37	Thirteen other frequencies ($n = 2, 4, 6, 7, 8, 9, 10, 11, 12, 13, 14, 16, 17$) fail to show effect	60
16	21	Ca^{2+}	1.0	Enhanced motility	61
16	20.9	Ca^{2+}	1.0	No effect on motility	62
30	39.2	Ca^{2+}	1.0	No effect on motility	62
60	78.4	Ca^{2+}	1.0	No effect on motility	62
16	20.9	Ca^{2+}	1.0	No effect on motility	63
16	21	Ca^{2+}	1.0	No effect on motility	64
16	20.9	Ca^{2+}	1.0	No effect on motility as viewed with real-time video system	65

9.2.1 Rat Behavior

On the other hand, some of the experimental evidence merits special emphasis because of the way the results have been positively replicated and reinforced. This is particularly true of the work on rat behavior (Table 9.5), in which four independent groups [45,47,49,51] observed significant changes in behavior for ICR exposures that were tuned to either the calcium or the magnesium ion. The end points of these experiments included changes in short-term memory [45,51], learning capacity [47], and aggressiveness [49], behavioral factors that are conceivably interconnected. Most important, these were undoubtedly resonance effects, since changes were not observed when separate runs were made for exposures to either the AC magnetic field alone or the DC magnetic field alone. Only when the AC and DC magnetic fields were jointly applied and parallel and, moreover, when the combined field characteristics conformed to Equation 9.1 were the altered behavioral responses observed.

An interesting possible explanation for the neural interaction site in these experiments has been proposed by Lovely et al. [47,92]. Using a Y-maze setup this group observed precisely opposite learning abilities for Ca^{2+} tuning and for Mg^{2+} tuning. Since the ICR combined field affects learning capacity oppositely for Ca^{2+} tuning and Mg^{2+} tuning, it may be reasonable to assume that the glutamate receptor *N*-methyl D-aspartate (NMDA) is

TABLE 9.8

ICR Effects on Complex Biological Systems

Frequency (Hz)	B_0 (μT)	Tuning	Ratio B/B_0	Comments	Reference
3–770	10–220		0.064–2.8	No effect on turtle colon transepithelial current as measured in Ussing chamber	66
33.7	44	Ca^{2+}	1.41	Synthesis and release of rat pineal melatonin is reduced by Ca^{2+} ICR tuning	67
15	21	Ca^{2+}	6.7	Fluctuations in heart rate in Daphnia are maximized at Ca^{2+} ICR frequency	68
60	78.4	Ca^{2+}	0.13	Cephalic regeneration in planaria is delayed by 48 h	69
60	51.1	K^+	1.0	Regeneration rate unchanged when K^+ tuning is used instead of Ca^{2+} tuning	69
60	78.4	Ca^{2+}	0.51	Regeneration anomalies occur at Ca^{2+} tuning when larger AC intensity is used	70
16	20.9	Ca^{2+}	1.8	Enhanced rate of blastema growth during cephalic regeneration in planaria	71
16	20.9	Ca^{2+}	0.24–9.6	Evidence that ICR effect on planaria regeneration has an intensity window	71
30	39.1	Ca^{2+}	1.8	Evidence corroborating Lednev [7] prediction: ICR effects are maximized at AC/DC ratio of 1.8	72
60	78.1	Ca^{2+}	1.8	Effect of light on ICR modulation of snail opioid analgesia is independent of frequency	72
120	156.2	Ca^{2+}	3.6	Effect due to light appears to scale with DC intensity	72
60	78	Ca^{2+}	0–5.3	Ca^{2+} ICR variations with AC intensity support Lednev [7] model	73
30	76	K^+	0–2.8	K^+ ICR effects on snail opioid analgesia are reversed with K^+ channel blocker	73
35	45	Ca^{2+}	1.8	Maximum influence on bioluminescence of dinoflagellate, agreement with PRM model	74
35	45	Ca^{2+}	5.3	Influence reversed, again in agreement with PRM model	74
35	45	Ca^{2+}	3.8	No effect at ratio of 3.8, again in agreement with PRM model	74

involved. NMDA receptors act as a graded switch for memory formation, to enhance learning and memory [93], and it is well established that NMDA activity is differently sensitive to calcium and magnesium concentrations [94,95]. Similar reversals of behavioral outcome depending on which ions are tuned have been observed by Zhadin et al. [51].

This explanation also serves to reinforce the original suggestion [4] concerning the molecular explanation for ICR stimulation, namely, in terms of enhanced ionic permeability within ion channels. Further support for locating the ion channel as the site of magnetic interaction is the fact that the changes in Ca^{2+} concentration within the cell that result from ICR stimulation tuned to the Ca^{2+} ion are not observed with the addition of nifedipine [34], a well-known calcium ion channel blocker (Figure 9.3).

9.2.2 Plants

Highly consistent results have also been independently obtained in studying the effects of ICR stimulation on plant growth [75–77,96] and seed germination [20,78] (Table 9.9,

TABLE 9.9
ICR Effects on Plants

Frequency (Hz)	$B_0(\mu\text{T})$	Tuning	Ratio B/B_0	Comments	Reference
60	78.3	Ca^{2+}	0.26	Ca^{2+} ICR field combination stimulates radish growth after delaying germination	75
60	153.3	K^+	0.13	K^+ ICR field enhances germination while reducing growth	75
60	0			No effect	75
60	78.4	Ca^{2+}	0.26	Ca^{2+} fundamental stimulates growth but slows down germination	20
60	39.2	Ca^{2+}	0.51	Ca^{2+} second harmonic: no effect	20
60	26.1	Ca^{2+}	0.77	Ca^{2+} third harmonic: same result as Ca^{2+} fundamental	20
60	153.3	K^+	0.13	K^+ fundamental results opposite to those of Ca^{2+} : growth inhibited, germination enhanced	20
60	76.6	K^+	0.26	K^+ second harmonic results weakly opposite to fundamental and third harmonics	20
60	51.1	K^+	0.39	K^+ third harmonic: effect same as K^+ fundamental	20
60	47.5	Mg^{2+}	0.42	Mg^{2+} fundamental stimulates growth	20
60	9.5	Mg^{2+}	2.11	Mg^{2+} fifth harmonic stimulates growth	20
60	0			AC only: no effect	20
60	78.3	Ca^{2+}	0.26	Replication of Smith et al.'s [75] work	76
60	78.3	Ca^{2+}	0.26	No effect on mustard plant; possible effect on barley plant	76
50	65.3	Ca^{2+}	0.61	Replication of Smith et al.'s [75] work on radish, for the 50-Hz Ca^{2+} ICR condition	77
50	39.6	Mg^{2+}	0.60	Replication of Smith et al. [75] for 50-Hz Mg^{2+} condition	77
60	76.3	Ca^{2+}	0.26	Germination weakly enhanced following Ca^{2+} ICR exposure of dry radish seeds	78
60	153.5	Mg^{2+}	0.13	No effect on germination	78
60	47.6	K^+	0.42	Significantly greater (earlier) germination of dry seeds following K^+ ICR exposure	78
35.8	46.5	Ca^{2+}	1.84	Gravitropic response in millet, flax, and clover seedlings enhanced by Ca^{2+} ICR	79
58.7	46.5	Mg^{2+}	1.84	Gravitropic response unaffected by Mg^{2+} tuning	79
54.7	46.5	K^+	1.84	Gravitropic response inhibited by K^+ ICR	79
33.8–37.8	46.5	Ca^{2+}	1.84	Frequency-dependent gravitropic response exhibits Ca^{2+} peak: FWHM ^a = 1.6 Hz	80
60	48	Mg^{2+}	1.48	CO_2 uptake significantly below control in radish, replication of Smith et al. [75]	81

^aFWHM, full width at half maximum.

Figure 9.4). The approach in the earlier reports [75] involved direct observations of aspects of plants that are readily measurable: plant height, aboveground height, root mass, stem diameter, leaf length, and width. Remarkably, all aspects related to growth are significantly affected, suggesting that magnetic fields play some unknown role in plant physiology. As observed in other systems (see Table 9.3), Ca^{2+} and Mg^{2+} tuning tends to enhance growth while tuning to the potassium ion acts as an inhibitor. Radish (*Raphanus sativus*) was used because of its rapid growth cycle (21 d), ease of handling, and seed availability. Davies [76] observed positive results when stimulating radish with ICR

TABLE 9.10

ICR Effects in Cell-Free Systems

Frequency (Hz)	B_0 (μT)	Tuning	Ratio B/B_0	Comments	Reference
8–20	20.9		1.0	Three frequencies (13.0, 14.0, and 16.0) affect calmodulin-dependent phosphorylation	82
100	0–260		>0.45	No Ca^{2+} ICR effect on conductance in pure bilipid layer	83
50–120	0–299		>0.31	Binding of Ca^{2+} to calmodulin is not enhanced using Ca^{2+} ICR fields	84
20	50	K^+	1.4	No changes from ICR tuning in gram A channel conductance in lipid bilayer	85
760	50	H^+	15.2	No changes from ICR tuning in gram A channel conductance in lipid bilayer	85
0.1–40	25	Asn^+	0.002	Enhanced aqueous conductivity in asparagine solution at 2.9 Hz; ICR prediction 2.9 Hz	86
0.1–40	25	Arg^{2+}	0.002	Enhanced aqueous conductivity in arginine solution at 4.4 Hz; ICR prediction 4.4 Hz	86
0.1–40	25	Glu^+	0.002	Enhanced aqueous conductivity in glutamic acid solution at 2.5 Hz; ICR prediction 2.6 Hz	86
0.1–40	25	Tyr^+	0.002	Enhanced aqueous conductivity in glutamic acid solution at 1.9 Hz; ICR prediction 2.1 Hz	86
0.1–40	25		0.2	ICR effect disappears at higher ratio of AC to DC intensities	86
0.1–40	0		0.002	ICR effect disappears for very small DC fields	86
0.1–40	25		0.002	ICR effects disappear when AC magnetic field is at 90° to DC field	86
12–60	20.9		1.0	No change in Ca^{2+} transport through patch-clamped cell membrane	87
10–22	20.9		1.0	No change in Ca^{2+} transport through patch-clamped system, measured over longer times	87
1–10	20–40	Glu^+	625–1.25 ($\times .001$)	Changes in glutamic acid conductivity in solution; good agreement with Glu^+ ICR q/m prediction	88
1–10	40		0.25–2.0 ($\times .001$)	Confirmation of earlier work; amino acid response at AC levels of 0.02–0.04 μT	88
0–10	40	Arg^{2+}	0.001	Sharp change in conductivity observed at 7.1 Hz, the ICR tuning point for Arg^{2+}	11
20.6	48	$\text{H}_3\text{O}^+(\text{H}_2\text{O})$	0.02	ICR fields trigger long-term increases in electrical conductivity in pure water	89
40.1	48	H_3O^+	0.02	Data in agreement with ICR effect in hydronium ion	89
530	35	H^+	0.03	Data in agreement with ICR effect in proton	89

TABLE 9.10 (continued)
ICR Effects in Cell-Free Systems

Frequency (Hz)	B_0 (μT)	Tuning	Ratio B/B_0	Comments	Reference
16	20.9	Ca^{2+}	1.0	Binding of Ca^{2+} to calmodulin is not enhanced using Ca^{2+} ICR fields	90
25.4	37	$^{45}\text{Ca}^{2+}$	0.70	$^{45}\text{Ca}^{2+}$ efflux in plasma membrane vesicles: ICR peak observed	91
24	37		0–3.2	Agreement with Blanchard and Blackman's [9] IPR model	91

magnetic fields but reported observing no similar effect in mustard plants, implying that the influence on growth may be species specific. ICR effects on radish metabolism were also reported by Yano et al. [81] using a distinctly different assay, the rate of uptake of CO_2 as a surrogate for photosynthesis activity. Still another assay [97] that responds to ICR magnetic stimulation in radish is the optical transmittivity in leaf.

The work in radish was extended [96] to four species of orchid (*Brassavola*, *Encyclium*, *Phalaenopsis*, and *Bulbophyllum*) (Figure 9.4 and Figure 9.5), with the magnetic exposures tuned to Ca^{2+} ICR lasting months instead of days. In all treated cases, plant heights were significantly higher compared to controls.

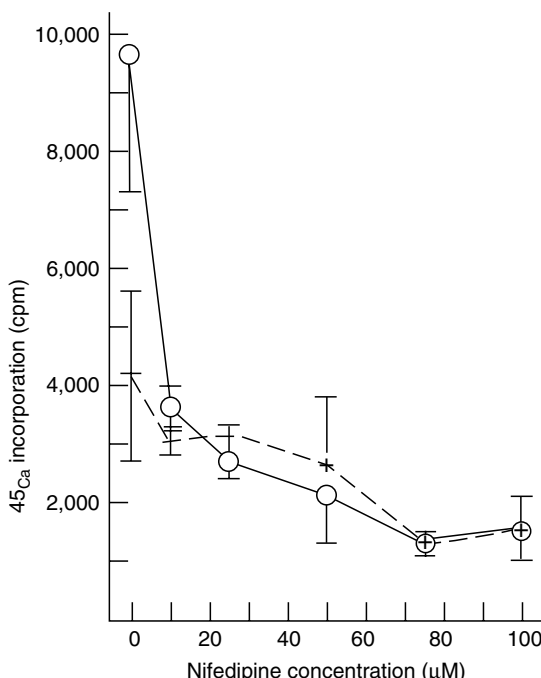


FIGURE 9.3
Incorporation of ^{45}Ca in human lymphocytes for unexposed cells (dashed line) and for ICR exposure tuned to the isotopic mass of ^{45}Ca (solid line) after 1 h. In the absence of calcium blocker nifedipine, there is a greater than twofold increase in calcium concentration over controls. The addition of nifedipine completely blocks the calcium uptake resulting from ICR stimulation, providing evidence that the ICR mechanism is related to ion channel transport. (From Rozek, R.J., Sherman, M.L., Liboff, A.R., McLeod, B.R., and Smith, S.D., Nifedipene is an antagonist to cyclotron resonance enhancement of ^{45}Ca incorporation in human lymphocytes, *Cell Calcium*, 8, 413, 1987.)

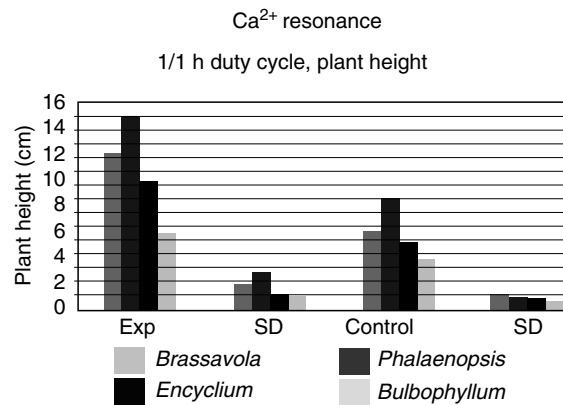


FIGURE 9.4

Comparisons of mean plant heights for four orchid varieties between unexposed controls and plants subjected to Ca^{2+} ICR stimulation. SD, standard deviation. (From Smith, S.D., Liboff, A.R., and McLeod, B.R., Calcium ICR and seedling growth in orchids (abstract), 20th Annual Meeting, Bioelectromagnetics Society, St. Petersburg Beach, FL, 1998.)

A distinctly different type of plant experiment has examined the rate of seed germination [21,78] instead of growth. In this case the assay simply involves a comparison of the time it takes for the seedling to be observed after the exposed seed is planted to the time it takes for a nonexposed seed to emerge. Unlike what is observed when examining growth rates, germination rates are significantly enhanced under K^+ stimulation and inhibited for Ca^{2+} tuning.

9.2.3 Bone

Elaborating on earlier work that used high-intensity pulsed magnetic fields [98] to treat bone disorders, ICR stimulation, operating at a much lower intensity, has proven very useful in repairing bone nonunions [29,99] and as an adjunct in enhancing spinal fusion following surgery [99]. Both these medical applications are approved by the U.S. Food and Drug Administration (FDA) and have been used to treat more than 100,000 patients in the United States [99]. There are two great advantages in these applications compared

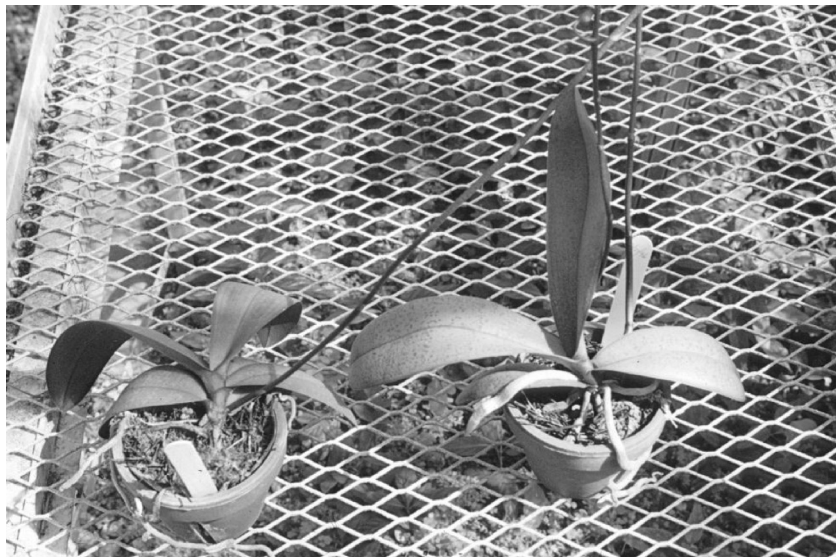


FIGURE 9.5

Typical example of difference between treated (right) and unexposed (left) orchid (*Phalaenopsis*) plants. (From Smith, S.D., Liboff, A.R., and McLeod, B.R., Calcium ICR and seedling growth in orchids (abstract), 20th Annual Meeting, Bioelectromagnetics Society, St. Petersburg Beach, FL, 1998.)

to pulsed magnetic fields therapy. Much weaker AC magnetic field intensities, less than 0.1 mT in amplitude, are employed, requiring very small power and providing the patient with greater portability. The treatment is also more efficient, requiring only 30 min/d during the therapeutic regimen.

This FDA-approved ICR device (Figure 9.6) also makes use of harmonic frequencies. The orientation of the local GMF relative to the plane of the AC coil is sensed, and the frequency of the applied sinusoidal magnetic signal generated by the coil is automatically adjusted to be in cyclotron resonance with the GMF following the relation $\omega_n = nqB/m$, where n is an integer representing either the third or the fifth ICR harmonic. [Table 9.11](#) lists the ICR harmonics for a number of ions. In the case of bone, tuning to either Ca²⁺ or Mg²⁺ tends to stimulate bone growth [24] ([Figure 9.7](#) and [Figure 9.8](#)). The FDA-approved device makes use of this fact by employing one resonance condition (3.80 Hz/μT) that fits both types of stimulation, namely the third harmonic for Mg²⁺ and the fifth for Ca²⁺.

It is likely that the level of efficacy of ICR magnetic treatment in repairing bony nonunions is far from optimal. There is good evidence [9,73,82] that the ICR response may depend on the ratio of the AC to DC magnetic fields that are used in combination. As such, one can expect the search for improvements in therapeutic signals for bone repair to continue.



FIGURE 9.6

Device used to assist repair of bony nonunions. The two rectangular parallel coils are clamped over the defect, and the GMF component normal to the plane of these coils is automatically determined regardless of limb orientation. An AC magnetic field is applied parallel to the GMF field that is in ion resonance tuned to harmonics of calcium and magnesium. (Courtesy of OrthoLogic Corp., Tempe, AZ.)

TABLE 9.11

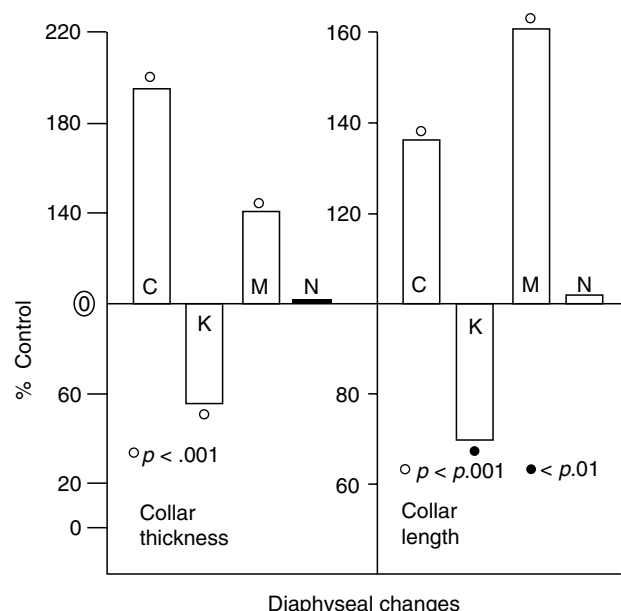
ICR Harmonics for Selected Ions

Ion	Fundamental (Hz/ μ T) f/B	Higher Harmonics (Hz/ μ T)		Subharmonics (Hz/ μ T)	
		$3f/B$	$5f/B$	$f/3B$	$f/5B$
Mg ²⁺	1.26	3.79	6.31	0.421	0.253
Ca ²⁺	0.77	2.30	3.83	0.255	0.153
Zn ²⁺	0.47	1.41	2.35	0.157	0.094
K ⁺	0.39	1.18	1.97	0.131	0.026

In attempting to further probe the response of skeletal tissues to resonant magnetic fields, Ryaby and colleagues [25–28,30,31] reported a number of associated metabolic changes in bone cells, most notably an increase in insulin-like growth factor-II (IGF-II) expression (Figure 9.9 and Figure 9.10) under ICR tuning for Ca²⁺. This body of work was rather complete in that separate experiments were carried out to justify Equation 9.1. With the magnetostatic field held at one value the frequency was varied as shown in Figure 9.10. In addition, separate runs were made with a fixed frequency and different values of the DC magnetic field. Resonance peaks were observed for both arrangements in accordance with Equation 9.1.

9.2.4 Harmonics

In general, the question of which harmonics are observed in the experimental data remains unresolved. McLeod et al. [59], studying diatom motility, showed that when the DC field is kept constant, odd multiples of the ICR fundamental frequency also result in enhanced motility. The same type of frequency harmonic dependence was found for ICR stimulation of plant growth [21]. Similar experimental results were obtained by Blackman et al. [100] in determining the degree of radioactive calcium flux from chick

**FIGURE 9.7**

Ca²⁺ and Mg²⁺ ICR exposures aid bone growth. Changes in diaphysis of embryonic chick femur due to ICR stimulation are shown as percentage of controls. C and M correspond to Ca²⁺ and Mg²⁺ tuning, and K represents the effects of tuning to the q/m ratio for K⁺. Note the reversal of effect following exposure to potassium-tuned magnetic fields. (From Smith, S.D., Liboff, A.R., and McLeod, B.R., Effects of resonant magnetic fields on chick femoral development *in vitro*, *J. Bioelectr.*, 10, 81, 1991.)

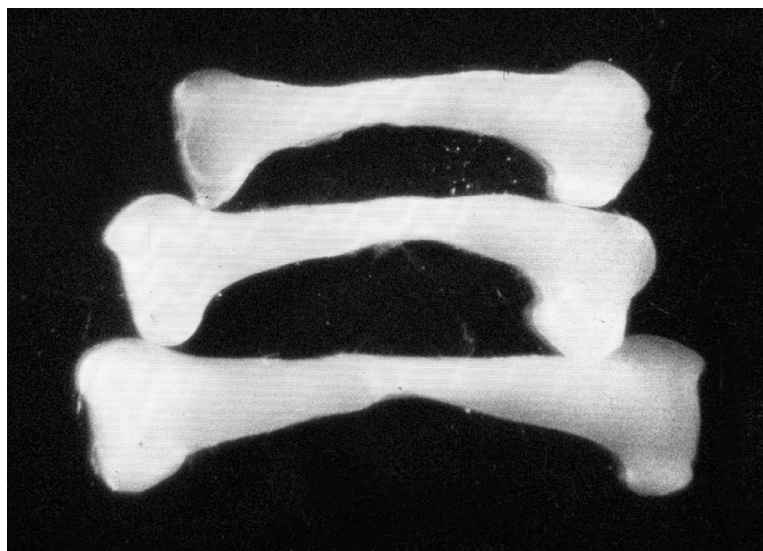


FIGURE 9.8

Typical examples of changes in embryonic chick femora with different ICR exposures. The longest femur corresponds to calcium ion stimulation, the shortest femur to potassium tuning, and the in-between size is the control. (From Smith, S.D., Liboff, A.R., and McLeod, B.R., Effects of resonant magnetic fields on chick femoral development *in vitro*, *J. Bioelectr.*, 10, 81, 1991.)

brain as a function of electric-field modulation frequency. These various findings are in reasonable agreement with the predicted higher harmonic ICR signatures listed in Table 9.11.

Because subharmonics are predicted [7,101] in several theoretical models, the first two predicted odd subharmonic characteristics are also listed for convenience in Table 9.11. It

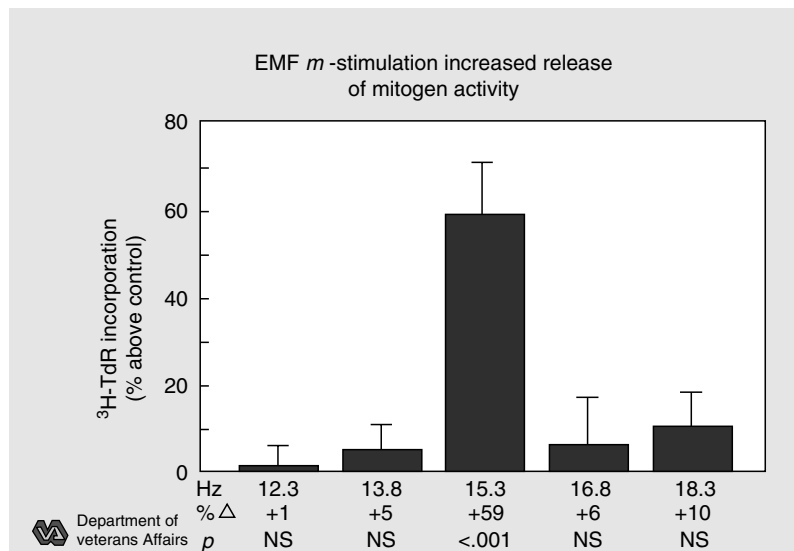


FIGURE 9.9

A sharp increase in mitogen expression in osteosarcoma cells exposed to a 20- μ T DC magnetic field occurs when the AC magnetic field frequency is 15.3 Hz, corresponding to Ca^{2+} resonance. (Courtesy of Veterans Administration Hospital, Phoenix, AZ.)

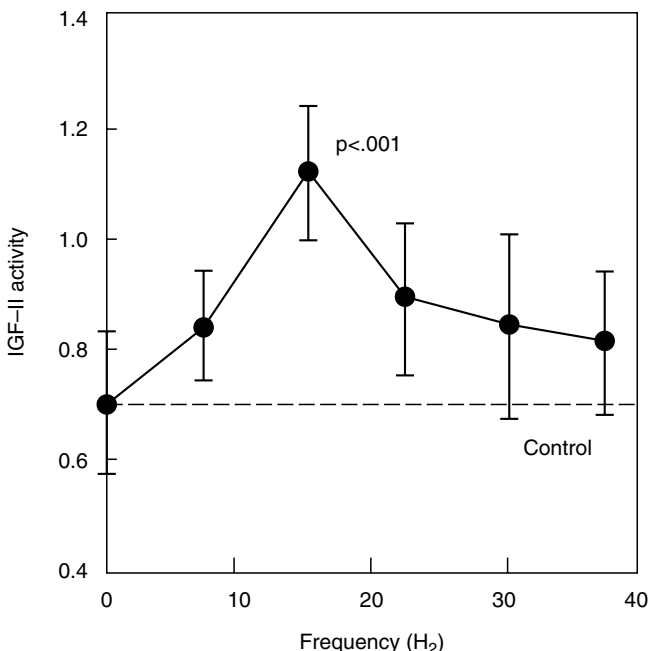


FIGURE 9.10

Peak in IGF-II expression at the fifth harmonic for Ca^{2+} . (Courtesy of J. Ryaby.) Fitzsimmons, R.J., Ryaby, J.T., Magee, F.P., and Baylink, D.J., Combined magnetic fields increase insulin-like growth factor-II in TE-85 human osteosarcoma bone cell cultures, *Endocrinology*, 136, 3100, 1995.

is clear that a better fit between the theoretical predictions of harmonics and the nature of their experimental observations could be an important factor in further understanding of ICR phenomena in living things.

9.2.5 Physiological Reversals

There is substantial evidence [102] that changing the ICR tuning from one ionic species to another has the capacity to completely reverse physiological outcomes (Figure 9.8 and Figure 9.11). This has been reported in a number of separate fascinating observations in widely different ICR experiments. The effect is manifested by applying, at the same frequency, relatively small shifts in the local magnetic field or, equivalently, applying a changed frequency with the local magnetic field kept the same, both variations made according to Equation 9.1. Eight such sets of results are given in Table 9.12.

This type of opposite response in the data may provide an important clue in trying to understand the ICR effect at the molecular level. Such a response might be expected when looking at the effects of competitive ion concentrations on cell metabolism and signaling. One such example, mentioned above [47], is the difference in the effects of binding Ca^{2+} and Mg^{2+} to NMDA. The concentration of Ca^{2+} in the cytoplasm, itself an implicit function of other ionic concentrations, is carefully regulated through the use of calcium pumps. The production of key enzymes such as cyclic AMP is enhanced or inhibited depending on the cytoplasmic calcium ion concentration. Because of this it is reasonable to think that the action of ICR fields has its origin in membrane-bound ion channels or in those proteins involved in the cell-signaling process.

9.2.6 Water

There have been numerous puzzling reports [103–105] claiming that the physical properties of water (e.g., conductivity) can be sufficiently altered by exposure to magnetic

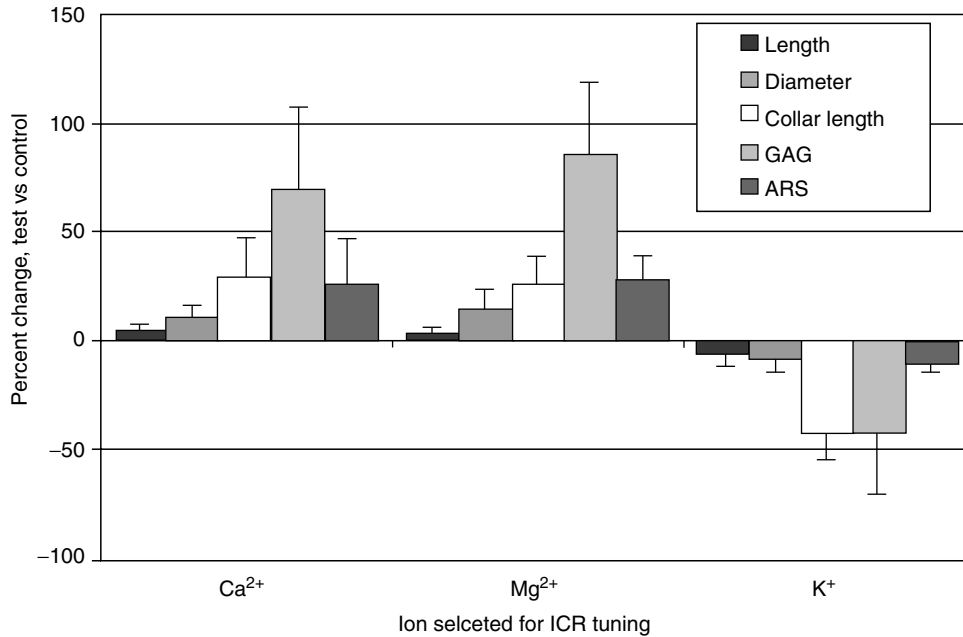


FIGURE 9.11

Independent confirmation of the results shown in Figure 9.8 for embryonic chick femur [32]. The additional assay for glycosaminoglycans (GAGS) reveals a greatly increased production of cartilage with Ca²⁺ or Mg²⁺ ICR stimulation and reduced cartilage production with K⁺ tuning.

fields to alter biological properties. Zhadin [86,88] explored this question using combined AC and DC magnetic fields, to see if there might be an ICR response. The conductivity of polar amino acids in solution (Table 9.1 and Table 9.10) was chosen as an assay. The frequency of the magnetic field was swept slowly, and a single sharp current peak was observed at the cyclotron frequency, determined from Equation 9.1 using the naked (unhydrated) molecular mass. Originally made in glutamic acid solutions [86], these observations were subsequently extended to additional amino acids, even to the case

TABLE 9.12

Opposite Responses Resulting from Shifts in Frequency or Field

Model System	Frequency (Hz)	B ₀ (μT)	Ion	Response	Reference
Diatom motility	16	20.9	Ca ²⁺	Motility ↑	58
	16	41.0	K ⁺	Motility ↓	
Embryonic bone	16	20.9	Ca ²⁺	Growth ↑	24
	16	40.7	K ⁺	Growth ↓	32
Plant growth	60	78.3	Ca ²⁺	Growth ↑	75
	60	153.3	K ⁺	Growth ↓	
Rat behavior	60	48	Mg ²⁺	Learning ↑	47
	60	27	Ca ²⁺	Learning ↓	
Rat behavior	63	50	Mg ²⁺	Activity ↑	51
	38	50	Ca ²⁺	Activity ↓	
Gravitropic response	35.8	46.5	Ca ²⁺	Response ↑	79
	54.7	46.5	K ⁺	Response ↓	
Glycosaminoglycans (GAGs) concentration	16	20.9	Ca ²⁺	GAGs ↑	32
	16	40.7	K ⁺	GAGs ↓	

where it was possible to shift the ICR peak by changing the pH of the solution, and therefore the valence of the ion. This work has been independently confirmed in two other laboratories [11,105]. One interesting aspect of these observations is the remarkably small AC magnetic field intensity required to see this effect, on the order of 0.05 μT .

It has also been shown [89] that very short (minutes) applications of ICR-tuned magnetic fields act to trigger large (days) continuing increases in conductivity in highly purified water. The required AC intensities (1 μT) are greater than that was found necessary in the Zhadin experiments, but they are still far less than reported elsewhere as interactive. The ions that are presumably affected are hydronium (H_3O^+) and its water clusters. One intriguing aspect of this work are the long-term changes in conductivity that are observed, even after removal of the magnetic field, a phenomenon somewhat akin to that of water “memory” [106,107].

9.3 Theoretical Approaches

9.3.1 Physical Constraints

The conditions in living things are such that charged particles are not free but subject to damping forces. If a particle such as an ion carries charge q and mass m and is moving with velocity \mathbf{v} , damping is manifested in the form of a retarding force, above and beyond the Lorentz force $q(\mathbf{v} \times \mathbf{B})$ and the Coulomb force $q\mathbf{E}$:

$$\mathbf{F} = q(\mathbf{v} \times \mathbf{B} + \mathbf{E}) - mv/\tau \quad (9.6)$$

The last term in Equation 9.6 is the mean damping force acting on the particle expressed in terms of the collision rate τ^{-1} .

The possibility of ICR occurring in living systems is counterintuitive, mainly because of damping. Cyclotron resonance, whether involving ions [108] or electrons [109], is usually associated with motion in a vacuum, or at least a low-pressure gas. In sharp contrast, the biological milieu is generally approximated as a liquid. Electron cyclotron resonance is observed in metals [109], but only at extremely high frequencies ranging from megahertz to gigahertz, many orders of magnitude greater than the typically observed frequencies listed in [Table 9.3](#) through [Table 9.10](#). At very high frequencies, the periodic motion of charged particles in cyclotron resonance can take place because the periods are shorter than the collision times. At 15 Hz, however, one loop is executed in 70 ms, a time over which one might expect as many as 10^{12} collisions because of thermal scattering [110]. The problem of explaining ICR effects in living systems is indeed challenging.

A second argument against the ICR hypothesis is that ions in solution are never totally free but are surrounded by layers of water. Therefore, one would think that the values of the q/m ratio indicated in [Equation 9.1](#) would have to be lowered to reflect the extra mass that is part of the overall ionic package.

One further criticism lies in estimates of the path radius for (free) charged particles in cyclotron resonance. This is based on equating the kinetic energy $mv^2/2$ of the charged particle to the thermal energy kT , and then arguing that the radius of the particle path must necessarily reflect the resulting velocity, because this radius is given as $\rho = v(m/qB)$. At a temperature of 37°C this results in radii that are of the order of meters, much larger than the extent of the system itself. However, it is hardly clear that one can use classical kinetics to discuss low energy charged particle interactions with

molecular structures. Further, it must be noted that the cyclotronic frequency ω_c , as given in [Equation 9.1](#) under the condition of vanishing damping, is entirely independent of particle radius and energy.

ICR tends to somewhat mute one of the strongest arguments against the likelihood of weak extremely low-frequency (ELF) magnetic interactions with biosystems. For an electric signal to initiate a biological effect, this signal must be greater than the electric potential generated by thermal noise [111]. The mean square thermal noise voltage $(\delta V)^2$ generated is proportional to Boltzmann's constant k , the temperature T , the tissue resistance R , and the bandwidth $\Delta\nu$ as follows:

$$(\delta V)^2 = 4RKT\Delta\nu \quad (9.7)$$

The original interaction site suggested by Weaver and Astumian [111] was the plasma membrane of the cell. The lipid membrane, however, is a highly electrically insulating material, with physical properties that are not conducive to any low-frequency interaction mechanism [112] except at high voltages. When more conductive substances such as proteins are considered as weak-field interaction sites, the effective resistance R can be many orders of magnitude lower than that found in lipids. Further, experimental evidence indicates that much narrower bandwidths, $\Delta\nu$, are encountered in ICR applications [39,106] than was previously [111,113] assumed. If the product $R\Delta\nu$ is reduced in [Equation 9.7](#) by a factor of 10^{-4} , this lowers δV by a factor of 10^{-2} below the original estimates. The "kT" question becomes even less of a problem if one considers electric-field ICR [114], where the frequency of oscillation in [Equation 9.1](#) is derived from endogenous sources within the living system.

9.3.2 Ion Channels

Placing the site of the ICR interaction within the lumen of membrane-bound ion channels deals with the problems of damping and hydration layers but leaves other questions unresolved. It is clear that damping within channels is quite different from that in liquids. The very function of ion channels helps define their intrinsically small effective resistivity, often less than $0.1 \Omega\text{m}$ [115], and therefore their vanishing damping. Channels function as shunts across the insulating cell membrane, allowing ions to percolate through, often in single file [116]. The passage of ions is determined less by collision rate, as in the solution-like regions external to channels, but is more dependent on the molecular architecture [117] of the channel proteins: the gating mechanisms that permit entry into the channel lumen and the electrical potential of the atoms lining the lumen walls.

Further, this passage of ions is unencumbered by the layers of hydration that surround all ions in solution. These waters are replaced upon entry into the channel by an equivalent fixed cage lining the lumen ([Figure 9.12](#)). Although the energetics of this water replacement is still puzzling [118], there is little question that ions can pass through ion channels in a naked fashion, with no attached waters [119]. The path of ions in a channel is clearly determined in a manner that does not permit one to apply kT arguments in trivial ways.

Although one can readily deal with the two problems associated with first, damping and second, ionic hydration layers, it is not as easy to dismiss the disparity in relaxation times when one compares the very rapid passage of ions through channels to the far slower movements associated with resonance frequencies. The ratio of these times can be well in excess of 10^{10} . To illustrate the problems raised by this disparity, consider the argument that the helicity of ionic paths occurring under ICR might be such as to match the helicity of the electric potential in the lumen [120].

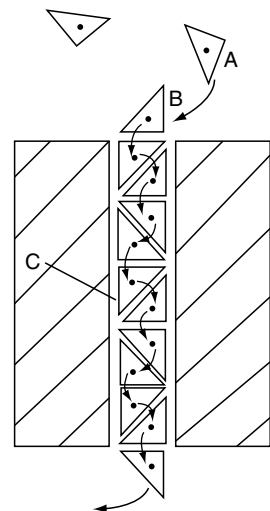


FIGURE 9.12

Hydrated ions near the mouth of an ion channel exchange their layers of water for an equivalent potential distribution within the lumen of the channel.

The electric field in [Equation 9.6](#) can have a number of distinctly different origins. In living tissue, the electric field can be the result of endogenous sources independent of \mathbf{B} . If \mathbf{B} is time varying, and of sufficiently large intensity or frequency, an electric field will in addition be induced by Faraday's law. There are also experimental situations in which an electric field may be applied independently of the first two sources. When an electric field \mathbf{E} is present, whatever the source, and it is at right angles to both \mathbf{v} and \mathbf{B} , then the circular motion becomes helical (Figure 9.13). It is then convenient to treat the velocity of the particle as composed of two components: v_{\parallel} , directed parallel to the direction of \mathbf{E} , and

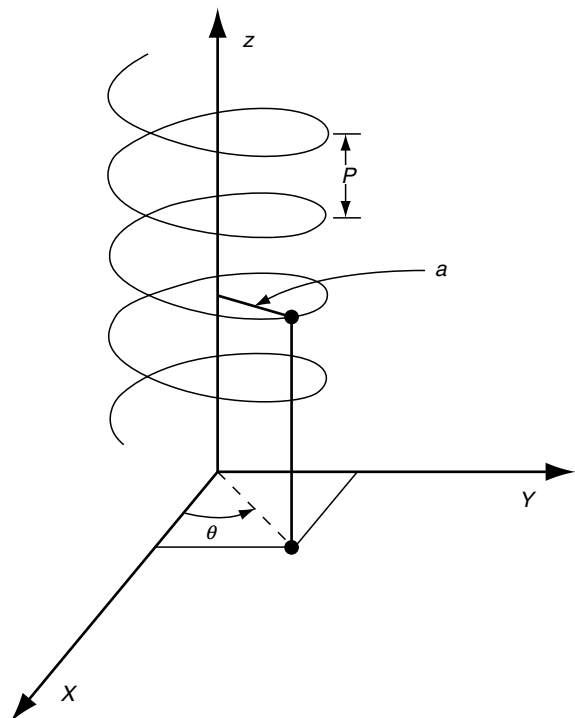


FIGURE 9.13

The Lorentz force acting on a charged particle often results in helical motion.

v_{\perp} , directed within the plane perpendicular to \mathbf{E} . Then the radius of the helix is $a = mv_{\perp}/qB$, and its pitch is $p = 2\pi mv_{\parallel}/qB$. It is not difficult to show that the total velocity v is

$$v = f_c(4\pi^2 a^2 + p^2)^{1/2} \quad (9.8)$$

The ICR frequency f_c is often only 15 Hz, and for ion channels the dimensions a and p are of the order of ångstroms (10^{-10} m). This implies a velocity of about 10^{-9} m/sec, a value that is totally inconsistent with the much greater experimentally observed speeds with which ions are transported across membranes.

Even though transit times directly through the channel lumen are very rapid, much longer relaxation times are found in other compartments of the larger channel structure. Times as long as, if not longer than, 10 ms are associated with voltage gating [121], making it conceivable that ICR could play an interactive role in channel-gating mechanisms.

9.3.3 Dependence on AC Magnetic Field

Borrowing from the theory of atomic spectroscopy [122], Lednev [7] hypothesized a functional relationship between the strength of the ICR signature and B_{AC} . When the calcium ion is bound to a calcium-binding protein such as calmodulin, the energy levels for the ion protein complex will be split, Zeeman-like, by the application of a magneto-static field B , such that the difference in frequency between the two new levels is equal to the cyclotron resonance frequency ω_c .

Application of an AC magnetic field at this frequency then leads to a resonant condition that can alter the transition to the ground state. The ICR response itself then becomes a function of the peak value of B_{AC} expressed in terms of the probability $p(B_{AC})$ for Ca^{2+} transitions to the ground state. The field-dependent part of this probability is

$$p(B_{AC}) = (-1)^n K J_n \left(n \frac{B_{AC}}{B_0} \right) \quad (9.9)$$

where K is a constant, B_0 is the DC magnetic intensity parallel to B_{AC} , and J_n is the n th-order Bessel function having the argument nB_{AC}/B_0 .

One great advantage of this expression for the probability is that one can readily design experiments that can test the predicted dependence on the AC magnetic field. Thus, the first extremum of $J_1(B_{AC}/B_0)$ occurs when the ratio B_{AC}/B_0 is equal to 1.84 (Figure 9.14). By varying this ratio while maintaining the same ICR condition, Prato et al. [72] obtained data tending to confirm this prediction. The effectiveness of this numerical ratio was also reported [74] in connection with studies on changes in calcium concentrations under ICR stimulation.

An alternative formulation to Equation 9.9 has been proposed by Blanchard and Blackman [9]. Termed ion parametric resonance (IPR) this approach considers a wider range of potential ELF interactions with metallic ions, beyond merely those processes associated with the activation of calcium-binding proteins. In the IPR formulation the probability $p(B_{AC})$ has the dependence $J_n(2nB_{AC}/B_0)$. The factor of 2 in the argument of the Bessel function has the effect of altering where the first extremum occurs, in this case at the B_{AC}/B_0 ratio of 0.92 (Figure 9.14). This ratio is close to the value of 1.0 successfully used by Smith [21,24,58,75] in all his experiments. However it is not clear in Smith's body of work whether further manipulation of the AC magnetic intensity away from this ratio of unity might have enhanced the responses that were observed. Koch et al. [91] were also able to obtain good agreement with the IPR predictions. One set of experimental results in sharp

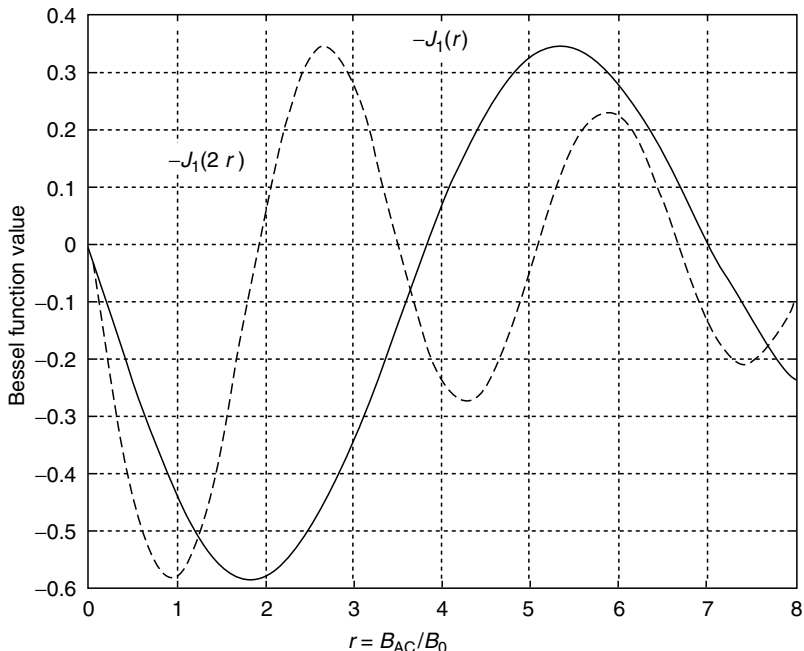


FIGURE 9.14

Comparing first-order Bessel functions with arguments B_{AC}/B_0 (solid line) and $2B_{AC}/B_0$ (dotted line). The first extremum is of experimental interest. By doubling the argument, the ratio where this extremum occurs is shifted from 1.84 to 0.92. In principle, one holds B_0 and the ICR frequency fixed and varies B_{AC} to determine where the maximum biological response occurs.

contrast with the predictions of parametric resonance are the consistent reports by Zhadin's group [86,88] and others [11], in which ICR exposures of polar amino acids in solution lead to narrow resonances, but only for B_{AC}/B_0 ratios of approximately 0.002.

The question of the dependence of the ICR interactive response on AC magnetic intensity is clouded by two additional possibilities. First, there is the problem of experimentally sorting out effects due to Faraday induction with larger AC fields [70]. Second, it is conceivable that biological responses to different AC fields may have little to do with the ICR response but rather with poorly understood physiological and energetic constraints. In any event, there is a clear record in the literature (e.g., Figure 9.15) of ICR threshold effects that do not appear to be related to functional variations such as Equation 9.9.

Adair [123,124] has criticized the parametric resonance approaches. Similar to earlier arguments [111,113] related to energetic constraints imposed by thermal noise, it was pointed out that the transition energy is only 10^{-11} of the thermal energy, kT , which would greatly suppress any meaningful effects due to Zeeman splitting. For this and other reasons [123], he concludes that application of the cyclotronic frequency ω_c cannot affect the transition rate of Ca^{2+} .

A very different approach to the problem of whether resonant magnetic fields can influence the binding of calcium has been suggested by Binhi [101]. Using Schrodinger's equation, it has been shown that ICR magnetic field combinations may redistribute the ionic probability density when one takes into account interference effects between quantum states. However, there is some question as to how much the wave function must shrink to allow ions as large as Ca^{2+} to escape.

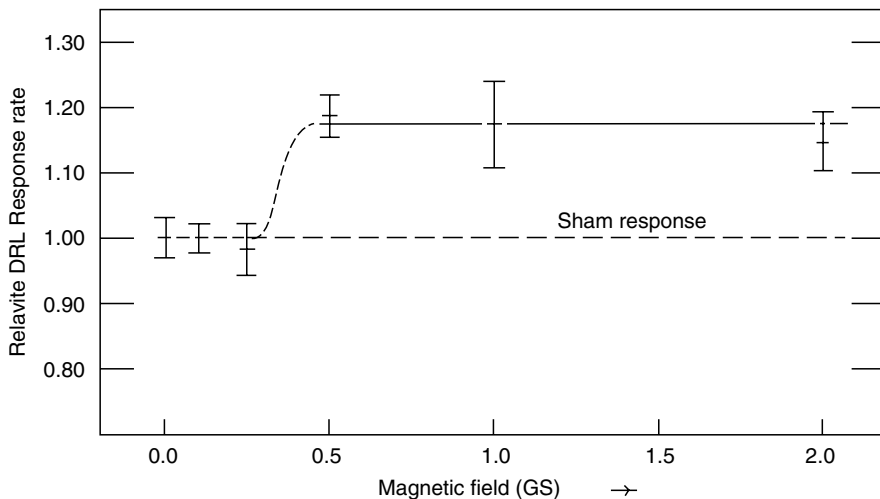


FIGURE 9.15

ICR-induced changes in rat behavior as a function of the AC magnetic field intensity. A clear threshold is evident, below which there is no effect on rat behavior. (From Liboff, A.R., Thomas, J.R., and Schrot, J., Intensity threshold for 60-Hz magnetically induced behavioral changes in rats, *Bioelectromagnetics*, 10, 111, 1989.)

9.3.4 Precessional Effects

It has been shown [8,10] that Larmor precessional effects can result from the application of weak ICR magnetic field combinations. In principle, these effects might carry physiological consequences, although no evidence along these lines has been reported. One interesting aspect of this approach [10] suggests the possibility of magnetically induced changes in the thermal energy distribution. The altered biological response in this model would not be the result of dissociative processes between ion and protein but would rather follow transfers of energy to the protein by the ion, resulting in appropriate conformational changes.

9.3.5 Coherence Domains

Del Giudice [11] has employed the principles of quantum electrodynamics (QED) in attempting to explain biological ICR, especially those results obtained in connection with the "Zhadin Experiment" [11,86,88]. The great advantage in this approach is that it fineses the limitations caused by Maxwell-Boltzmann statistics predictions [111,113], which require kT as a minimal threshold informational energy for electromagnetic interactions. In the QED model it is argued that in the case of electromagnetic interactions with water, coherent, highly ordered spherical domains are formed, with diameters close to 100 nm and embedded in a surrounding noncoherent water phase. An applied ICR frequency in this case couples to ions on the perimeter of the coherent spheres stimulating circulatory motion, allowing ions to escape into the noncoherent phase, where they act to enhance the measured conductivity.

One interesting aspect of this model is that because phase transitions are involved, temperature is expected to play a prominent role in the experimental outcome. The changes in amino acid conductivity under ICR conditions first reported by Novikoff and Zhadin [86] were temperature sensitive. Similar observations regarding the experimental relevance of temperature were reported in earlier [125,126] Ca-efflux studies.

9.4 Discussion

Accepting the abundant evidence that biological systems are sensitive to ICR-tuned field combinations, the question remains as to the molecular explanation. There is also the more subtle question dealing with the implications of this effect. From the physical standpoint, the seeming inability of theorists to come to grips with this phenomenon may not mean that a new physics is called for. But there is certainly good reason to believe that something is missing in the way we categorize biological function.

The fact that a low-frequency ion resonance interaction is found in an extraordinarily wide variety of organisms argues against the commonly held notion that this phenomenon merely represents one fortuitous example of the Lorentz force acting on materials that happen to occur within a biological context.

Indeed, the reports listed in [Table 9.10](#) lend strength to another notion, that the weak-field ICR phenomenon is not limited to biological systems, but is actually a subtle physical effect that has not heretofore been recognized. For example, one can argue that this effect is particularly evident in water, which in turn results in the biological effects that are observed. In other words, because of the ubiquity of water in biological systems, any ELF-induced change in the properties of water might help explain the variety of biological effects that have been reported.

Whatever its molecular origin, it is likely that the ICR-related biophenomenon is an evolutionarily well-conserved property of the physiological armory, one that is enabled by the interaction of the ubiquitous Earth's magnetic field with the equally ubiquitous electric fields that are found throughout living things. This concept is embodied in the reasonable likelihood [114] that electric-field ICR processes were incorporated into living things over evolutionary times. Unlike the laboratory experiments involving the applications of parallel combined AC and DC magnetic fields, *E*-field resonance occurs maximally for time-varying electric and magnetostatic fields at right angles. This naturally occurring interaction therefore relates the GMF and the AC electric fields found within the biosystem. It has been hypothesized [127], for example, that this putative interaction mechanism can be used to explain the problem of bird navigation.

One can speculate that this ICR phenomenon conserved very early in living things has evolved into a number of separate biological expressions, where the physics is always the same but the physiological pathway leads to different end points. For example, two sharply different possible end points, both apparently relying on ICR, are the magnetic compasses in animals [124] and growth and repair mechanisms [24,37,75]. A third intriguing possibility is found in the ICR interactive changes in the central nervous system [45,47,49,51], an area where there are obvious effects but where the end points are still unresolved.

It is also tempting to speculate on the larger implications of the work that is detailed in [Table 9.3](#) and [Table 9.9](#), on bone and plants, respectively. In both cases there is evidence that ICR signals affect growth and repair responses more than they affect stasis. Drawing on possible endogenous mechanisms related to *E*-field ICR, it is conceivable that the interactive relation of the GMF to living systems is especially important as regards growth and repair during development.

Whatever be the explanation for the ICR effect, it is clear that while nothing new may be required in our understanding of physical law, new approaches are necessary in comprehending how physics has been incorporated in biology, particularly with regard to cell signaling and regulation. This is strongly implied by the remarkable data indicating reversed physiological outcomes with minor changes in electromagnetic field conditions. There are protein systems in physiology that are switch-like in their function. Two such

examples are the calcium-binding proteins and NMDA. Another example is found in synaptic transmission. The electromagnetic reversal effects observed in ICR experiments are evocative of the way such switch-like proteins function.

This begs the fascinating question as to whether the ICR stimulus merely serves as an adjunct to an existing biochemical process, perhaps acting to sharpen enhancement or inhibition, or whether it acts in a totally different manner, as a separate and distinct class of interactions, one that is completely electromagnetic in its operation. In this regard, note that the GMF preceded by far the first appearance of living things on Earth and would therefore have been part of the original physical template that determined the course of early evolution.

References

1. Jenrow, K.A. and Liboff, A.R., Electromagnetic techniques in neural therapy, in *Bioelectromagnetic Medicine*, Rosch, P.J. and Markov, M.S., Eds., Marcel Dekker, New York, 2004, Chapter 14.
2. Wertheimer, N. and Leeper, E., Electrical wiring configurations and childhood cancer, *Am. J. Epidemiol.*, 109, 273–284, 1979.
3. Liboff, A.R., The charge-to-mass ICR signature in weak ELF bioelectromagnetic effects, in *Advances Electromagnetic Fields in Living Systems*, Vol. 4, Lin, J., Ed. Kluwer/Plenum, New York (in press).
4. Liboff, A.R., Geomagnetic cyclotron resonance in living cells, *J. Biol. Phys.*, 13, 99–102, 1985.
5. Tipler, P., *Physics*, 2nd ed., Vol. 2, Worth Publishers, New York, 1982, 729.
6. Zhadin, M.N. and Fesenko, E.E., Ionic cyclotron resonance in biomolecules, *Biomed. Sci.*, 1, 245–250, 1990.
7. Lednev, V.V., Possible mechanism for the influence of weak magnetic fields on biological systems, *Bioelectromagnetics*, 12, 71–75, 1991.
8. Edmonds, D.T., Larmor precession as a mechanism for the detection of static and alternating magnetic fields, *Bioelectrochem. Bioenerg.*, 30, 3–12, 1993.
9. Blanchard, J.P. and Blackman, C.F., Clarification and amplification of an ion parametric resonance model for magnetic field interactions with biological systems, *Bioelectromagnetics*, 15, 217–238, 1994.
10. Zhadin, M.N., Combined action of static and alternating magnetic fields on ion motion in a macromolecule: theoretical aspects, *Bioelectromagnetics*, 19, 279–292, 1998.
11. Del Giudice, E., Fleischmann, M., Preperata, G., and Talpo, G., On the “unreasonable” effects of ELF magnetic fields upon a system of ions *Bioelectromagnetics*, 23, 522–530, 2002.
12. Blackman, C.F., Benane, S.G., Rabinowitz, J.R., House, D.E., and Joines, W.T., A role for the magnetic field in the radiation-induced efflux of calcium ions from brain tissue *in vitro*, *Bioelectromagnetics*, 6, 327–337, 1985.
13. Bawin, S.M., Kazmarek, K.L., and Adey, W.R., Effects of modulated VHF fields on the central nervous system, *Ann. NY Acad. Sci.*, 247, 74–81, 1975.
14. Blackman, C.F., Elder, J.A., Weil, C.M., Benane, S.G., Eichinger, D.C., and House, D.E., Induction of calcium-ion efflux from brain tissue by radiofrequency radiation and field strength, *Radio Sci.*, 14, 93–98, 1979.
15. Blackman, C.F., Benane, S.G., Kinney, L.S., Joines, W.T., and House, D.E., Effects of ELF fields on calcium-ion efflux from brain tissue *in vivo*, *Rad. Res.*, 92, 510–520, 1982.
16. Dutta, S.K., Subramaniam, A., Ghosh, B., and Parshad, R., Microwave radiation-induced calcium ion efflux from human neuroblastoma cells in culture, *Bioelectromagnetics*, 5, 71–78, 1984.
17. Blackman, C.F., Benane, S.G., House, D.E., and Joines, W.T., Effects of ELF (1–120 Hz) and modulated (50 Hz) RF fields on the efflux of calcium ions from brain tissue, *in vitro*, *Bioelectromagnetics*, 6, 1–11, 1985.

18. McLeod, B.R. and Liboff, A.R., Dynamic characteristics of membrane ions in multifield configurations of low-frequency electromagnetic radiation, *Bioelectromagnetics*, 7, 177–189, 1986.
19. McLeod, B.R. and Liboff, A.R., Cyclotron resonance in cell membranes: the theory of the mechanism, in *Mechanistic Approaches to Interactions of Electric and Electromagnetic Fields with Living Systems*, Blank, M. and Findl, E., Eds., Plenum Press, New York, 1987, 97–108.
20. McLeod, B.R., Smith, S.D., and Liboff, A.R., Calcium and potassium cyclotron resonance curves and harmonics in diatoms, *J. Bioelectr.*, 6, 153–168, 1987.
21. Smith, S.D., McLeod, B.R., and Liboff, A.R., Testing the ion cyclotron resonance theory of electromagnetic field interaction with odd and even harmonic tuning for cations, *Bioelectrochem. Boenerg.*, 38, 161–167, 1995.
22. Liboff, A.R. and McLeod, B.R., Kinetics of channelized membrane ions in magnetic fields, *Bioelectromagnetics*, 9, 39–51, 1988.
23. Ross, S.M., Combined DC and ELF magnetic fields can alter cell proliferation, *Bioelectromagnetics*, 11, 27–36, 1990.
24. Smith, S.D., Liboff, A.R., and McLeod, B.R., Effects of resonant McLeod fields on chick femoral development *in vitro*, *J. Bioelectr.*, 10, 81–99, 1991.
25. Fitzsimmons, R.J., Baylink, D.J., Ryaby, J.T., and Magee, F., EMF-stimulated bone-cell proliferation, in *Electricity and Magnetism in Biology and Medicine*, Blank, M., Ed., San Francisco Press, San Francisco, 1993, 899–901.
26. Ryaby, J.T., Grande, D.A., Magee, F.P., and Weinstein, A.M., The effects of combined AC/DC magnetic fields on resting articular cartilage metabolism, in *Electricity and Magnetism in Biology and Medicine*, Blank, M., Ed., San Francisco Press, San Francisco, 1993, 371–374.
27. Ryaby, J.T., Magee, F.P., Weinstein, A.M., Fitzsimmons, R.J., and Baylink, D.J., Prevention of experimental osteopenia by use of combined magnetic fields, in *Electricity and Magnetism in Biology and Medicine*, Blank, M., Ed., San Francisco Press, San Francisco, 1993, 807–810.
28. Fitzsimmons, R.J., Ryaby, J.T., Magee, F.P., and Baylink, D.J., Combined magnetic fields increased net calcium flux in bone cells. *Calcif. Tissue Int.*, 55, 376–380, 1994.
29. Diebert, M.C., McLeod, B.R., Smith, S.D., and Liboff, A.R., Ion resonance electromagnetic field stimulation of fracture healing in rabbits with a fibular ostectomy, *J. Orthop. Res.*, 12, 878–885, 1994.
30. Fitzsimmons, R.J., Ryaby, J.T., Magee, F.P., and Baylink, D.J., Combined magnetic fields increase insulin-like growth factor-II in TE-85 human osteosarcoma bone cell cultures, *Endocrinology*, 136, 3100–3106, 1995.
31. Fitzsimmons, R.J., Ryaby, J.T., Magee, F.P., and Baylink, D.J., IGF-II receptor number is increased in TE-85 human osteosarcoma cells by combined magnetic fields, *J. Bone Miner. Res.*, 10, 812–819, 1995.
32. Regling, C., Brueckner, C., Liboff, A.R., and Kimura, J.H., Evidence for ICR magnetic field effects on cartilage and bone development in embryonic chick bone explants (abstract), 48th Annual Meeting, Orthopedic Research Society, Dallas, 2002.
33. Liboff, A.R., Rozek, R.J., Sherman, M.L., McLeod, B.R., and Smith, S.D., $^{45}\text{Ca}^{2+}$ resonance in human lymphocytes. *J. Bioelectr.*, 6, 99–102, 1987.
34. Rozek, R.J., Sherman, M.L., Liboff, A.R., McLeod, B.R., and Smith, S.D., Nifedipine is an antagonist to cyclotron resonance enhancement of ^{45}Ca incorporation in human lymphocytes, *Cell Calcium*, 8, 413–427, 1987.
35. Parkinson, W.C. and Hanks, C.T., Search for cyclotron resonance in cells *in vitro*, *Bioelectromagnetics*, 10, 129–145, 1989.
36. Rochev, Y.A., Narimanov, A.A., Sosunov, E.A., Kozlov, A.N., and Lednev, V.V., Effects of weak magnetic field on the rate of cell proliferation in cell culture, *Stud. Biophys.*, 135, 93–98, 1990.
37. Lyle, D.B., Wang, X., Ayotte, R.D., Sheppard, A.R., and Adey, W.R., Calcium uptake by leukemic and normal T-lymphocytes exposed to low frequency magnetic fields, *Bioelectromagnetics*, 12, 145–156, 1991.
38. Yost, M.G. and Liburdy, R.P., Time-varying and static magnetic fields act in combination to alter calcium signal transduction in the lymphocyte, *FEBS Lett.*, 296, 117–122, 1992.
39. Liboff, A.R., Jenrow, K.A., and McLeod, B.R., ELF-induced proliferation at 511 mG in HSB-2 cell culture as a function of 60 Hz field intensity, in *Electricity and Magnetism in Biology and Medicine*, Blank, M., Ed., San Francisco Press, San Francisco, 1993.

40. Liburdy, R.P. and Yost, M.G., Time-varying and static magnetic fields act in combination to alter calcium signal transduction in the lymphocyte, in *Electricity and Magnetism in Biology and Medicine*, Blank, M., Ed., San Francisco Press, San Francisco, 1993.
41. Coulton, L.A. and Barker, A.T., Magnetic fields and intracellular calcium: effects on lymphocytes exposed to conditions for "cyclotron resonance", *Phys. Med. Biol.*, 38, 347–360, 1993.
42. Lindstrom, E., Lindstrom, P., Berglund, A., Lundgren, E., and Mild, K.H., Intracellular calcium oscillations in a T-cell line after exposure to extremely-low-frequency magnetic fields with variable frequencies and flux densities, *Bioelectromagnetics*, 16, 41–47, 1995.
43. Tofani, S., Ferrara, A., Anglesio, L., and Gilli, G., Evidence for genotoxic effects of resonant ELF magnetic fields, *Bioelectrochem. Bioenerg.*, 36, 9–13, 1995.
44. Reinbold, K.A. and Pollack, S.R., Serum plays a critical role in modulating $[Ca^{2+}]_c$ of primary cell culture bone cells exposed to weak ion-resonance magnetic fields, *Bioelectromagnetics*, 18, 203–214, 1997.
45. Thomas, J.R., Schrot, J., and Liboff, A.R., Low-intensity magnetic fields alter operant behavior in rats, *Bioelectromagnetics*, 7, 349–357, 1986.
46. Liboff, A.R., Thomas, J.R., and Schrot, J., Intensity threshold for 60-Hz magnetically induced behavioral changes in rats, *Bioelectromagnetics*, 10, 111–113, 1989.
47. Lovely, R.H., Creim, J.A., Miller, D.L., and Anderson, L.E., Behavior of rats in a radial arm maze during exposure to magnetic fields: evidence for effects of magnesium ion resonance (abstract), 15th Annual Meeting, Bioelectromagnetics Society, Los Angeles, 1993.
48. Stern, S., Laties, V.G., Nguyen, Q.A., and Cox, C., Exposure to combined static and 60Hz magnetic fields: failure to replicate a reported behavioral effect, *Bioelectromagnetics*, 17, 279–292, 1996.
49. Lyskov, Y.B., Chernysev, M.V., Michailov, V.O., Kozlov, A.P., Makarova, T.M., Vasilyeva, Y.V., Druzin, M.Y., Sokolov, G.V., and Vishnevski, A.M., The effect of a magnetic field with the frequency of 50 Hz on behavior in rats depends on the value of the constant magnetic field, *Biophysics*, 41, 881–886, 1996.
50. Derjugina, O.N., Pisachenko, T.M., and Zhadin, M.N., Combined action of alternating and static magnetic fields on behavior of rats in the "Open-field" test, *Biophysics*, 41, 762–764, 1996.
51. Zhadin, M.N., Deryugina, O.N., and Pisachenko, T.M., Influence of combined DC and AC magnetic fields on rat behavior, *Bioelectromagnetics*, 20, 378–386, 1999.
52. Smith, S.D., Liboff, A.R., McLeod, B.R., and Barr, E.J., Effects of ion resonance tuned magnetic fields on N-18 neuroblastoma cells, in *Charge and Field Effects in Biosystems-3*, Allen, M.J., Cleary, A.F., Sowers, A.E., and Shillady, D.D., Eds., Birkhauser, Boston, 1992, 263–271.
53. Horton, P., Ryaby, J.T., Magee, F.P., and Weinstein, A.M., Stimulation of specific neuronal differentiation proteins in PC-12 cells by combined AC/DC magnetic fields, in *Electricity and Magnetism in Biology and Medicine*, Blank, M., Ed., San Francisco Press, San Francisco, 1993, 619–622.
54. Blackman, C.F., Blanchard, J.P., Benane, S.G., and House, D.E., Empirical test of an ion parametric resonance model for magnetic field interactions with PC-12 cells, *Bioelectromagnetics*, 15, 239–250, 1994.
55. Trillo, M.A., Ubeda, A., Blanchard, J.P., House, D.E., and Blackman, C.F., Magnetic fields at resonant conditions for the hydrogen atom can affect neurite outgrowth in PC-12 cells, *Bioelectromagnetics*, 17, 10–20, 1996.
56. Blanchard, J.P., Blackman, C.F., Benane, S.G., and House, D.E., IPR response of PC-12 cells exposed to magnetic fields tuned for calcium ions, The Annual Review of Research on Biological Effects of Electric and Magnetic Fields from the Generation, Delivery and Use of Electricity, San Diego, CA, W/L Associates, Ltd, Frederick, MD, 1997, 4.
57. Blackman, C.F., Blanchard, J.P., Benane, S.G., and House, D.E., Experimental determination of hydrogen bandwidth for the Ion Parametric Resonance model, *Bioelectromagnetics*, 20, 5–12, 1999.
58. Smith, S.D., McLeod, B.R., Liboff, A.R., and Cooksey, K., Calcium cyclotron resonance and diatom motility, *Bioelectromagnetics*, 8, 215–227, 1987.
59. McLeod, B.R., Smith, S.D., Cooksey, K.E., and Liboff, A.R., Ion cyclotron resonance frequencies enhance Ca^{2+} -dependent motility in diatoms, *J. Bioelectr.*, 6, 1–12, 1987.
60. McLeod, B.R., Smith, S.D., and Liboff, A.R., Calcium and potassium cyclotron resonance curves and harmonics in diatoms, *J. Bioelectr.*, 6, 153–168, 1987.

61. Reese, J.A., Frazier, M.E., Morris, J.E., Buschbom, R.L., and Miller, D.L., Evaluation of changes in diatom motility after exposure to 16-Hz electromagnetic fields, *Bioelectromagnetics*, 12, 21–25, 1991.
62. Parkinson, W.C. and Sulik, G.L., Diatom response to extremely low frequency magnetic fields, *Rad. Res.*, 130, 319–330, 1992.
63. Saalman, E., Galt, S., Hamnerius, Y., and Norden, B., Diatom motility: replication study in search of cyclotron resonance effects, in *Interaction Mechanisms of Low-Level Electromagnetic Fields in Living Systems*, Norden, B. and Ramel, C., Eds., Oxford University Press, Oxford, 1992, 280–292.
64. Prasad, A.V., Miller, M.W., Cox, C., Carstensen, E.L., Hops, H., and Brayman, A.A., A test of the influence of cyclotron resonance exposures on diatom motility, *Health Phys.*, 66, 305–312, 1994.
65. Clarkson, H., Davies, M.S., and Dixey, R., Diatom motility: the search for independent replication of biological effects of extremely low-frequency electromagnetic fields, *Int. J. Rad. Biol.*, 75, 387–392, 1999.
66. Liboff, A.R. and Parkinson, W.C., Search for ion-cyclotron resonance in an Na^+ transport system, *Bioelectromagnetics*, 12, 77–83, 1991.
67. Lerchl, A., Reiter, R.J., Nonaka, K.O., and Stokken, K.-A., Evidence that extremely low frequency Ca^{2+} -cyclotron resonance depresses pineal melatonin synthesis *in vitro*, *Neurosci. Lett.*, 124, 213–215, 1991.
68. Chemeris, N.K. and Safranova, V.G., Weak low-frequency magnetic field initiates frequency-dependent fluctuations of period of *Daphnia magna*'s heart beatings, *Biophysics*, 38, 511–519, 1993.
69. Jenrow, K.A., Smith, C.H., and Liboff, A.R., Weak extremely-low-frequency magnetic fields and regeneration in the planarian *Dugesia tigrina*, *Bioelectromagnetics*, 16, 106–112, 1995.
70. Jenrow, K.A., Smith, C.H., and Liboff, A.R., Weak, extremely-low-frequency magnetic field-induced regeneration anomalies in the planarian *Dugesia tigrina*, *Bioelectromagnetics*, 17, 467–474, 1996.
71. Tiras, K.P., Srebnitskaya, L.K., Il'jasova, A.A., and Lednev, V.V., The influence of weak combined magnetic fields on the rate of regeneration in planarian *Dugesia tigrina*, *Biophysics*, 42, 826–831, 1996.
72. Prato, F.S., Kavaliers, M., Cullen, A.P., and Thomas, A.W., Light-dependent and -independent behavioral effects of extremely low frequency magnetic fields, *Bioelectromagnetics*, 18, 284–291, 1997.
73. Prato, F.S., Kavaliers, M., and Thomas, A.W., Extremely low frequency magnetic fields can either increase or decrease analgesia in the land snail depending on field and light conditions, *Bioelectromagnetics*, 21, 287–301, 2000.
74. Berden, M., Zrimec, A., and Jerman, I., New biological detection system for weak ELF magnetic fields and testing of the parametric resonance model, *Electro. Magnetobiol.*, 20, 27–41, 2001.
75. Smith, S.D., McLeod, B.R., and Liboff, A.R., Effects of CR-tuned 60 Hz magnetic fields on sprouting and early development of *Raphanus sativus*, *Bioelectr. Bioenerg.*, 32, 67–76, 1993.
76. Davies, M.S., Effects of 60 Hz electromagnetic fields on early growth in three plant species and a replication of previous results, *Bioelectromagnetics*, 17, 154–161, 1996.
77. Tohtz, S.W., The Influence of Ultra Weak Magnetic Fields on Growth and Differentiation Using the ICR Hypothesis: An Experimental Study on Radish Seedlings and a Theoretical Discussion on Relevant Aspects of Cartilage, Bone, and Other Connective Tissues, Ph.D. Dissertation, Medical Faculty of Humboldt University, Berlin, 1996 (in German).
78. Smith, S.D., Liboff, A.R., and McLeod, B.R., Potassium ion cyclotron resonance magnetic fields stimulate germination, Proceedings of Millennium International Workshop on Biological Effects of Electromagnetic Fields, Heraclion, Crete, Greece, 2000, 347–351.
79. Belova, N.A. and Lednev, V.V., Activation and inhibition of gravitropic response in plants by weak combined magnetic fields, *Biophysics*, 45, 1069–1074, 2000.
80. Belova, N.A. and Lednev, V.V., Dependence of gravitropic response in the segments of flax stems on the frequency and amplitude of weak combined magnetic fields, *Biophysics*, 45, 1075–1078, 2000.
81. Yano, A., Ohashi, Y., Hirasaki, T., and Fujiwara, K., Effects of a 60 Hz magnetic field on photosynthetic CO_2 uptake and early growth of radish seedlings, *Bioelectromagnetics*, 25, 572–581, 2004.

82. Shuvalova, L.A., Ostrovskaja, M.V., Sosunov, E.A., and Lednev, V.V., Effect of weak magnetic field in the parametric resonance mode on the rate of calmodulin-dependent phosphorylation of myosin in the solution, *Doklady Akademii Nauk SSSR* (Reports of the Academy of Science of the USSR), Vol. 317, 1991, 227–230 (in Russian).
83. Durney, C.H., Kaminski, M., Anderson, A.A., Bruckner-Lea, C., and Rappaport, C., Investigation of AC–DC magnetic field effects in planar phospholipid layers, *Bioelectromagnetics*, 13, 19–33, 1992.
84. Bruckner-Lea, C., Durney, C.H., Janata, J., Rappaport, C., and Kaminski, M., Calcium binding to metallochromic dyes and calmodulin in the presence of combined AC–DC magnetic fields, *Bioelectromagnetics*, 13, 147–162, 1992.
85. Galt, S., Sandblom, A., Hamnerius, Y., Hojevic, P., Saalman, E., and Norden, B., Experimental search for combined AC and DC magnetic field effects on ion channels, *Bioelectromagnetics*, 14, 315–327, 1993.
86. Novikoff, V.V. and Zhadin, M.N., Combined action of weak constant and variable low-frequency magnetic fields on ionic currents in aqueous solutions of amino acids, *Biophysics*, 39, 41–45, 1994.
87. Hojevic, P., Sandblom, J., Galt, S., and Hamnerius, Y., Ca^{2+} ion transport through patch-clamped cells exposed to magnetic fields, *Bioelectromagnetics*, 16, 33–40, 1995.
88. Zhadin, M.N., Novikoff, V.V., Barnes, F.S., and Pergola, M.F., Combined action of static and alternating magnetic fields on ionic current in aqueous glutamic acid solution, *Bioelectromagnetics*, 19, 41–45, 1998.
89. Mohri, K., and Fukushima, M., Gradual decreasing characteristics and temperature stability of electric resistivity in water triggered with milligauss AC field, *IEEE Trans. Magn.*, 38, 3353–3355, 2002.
90. Liboff, A.R., Cherng, S., Jenrow, K.A., and Bull, A., Calmodulin dependent cyclic nucleotide phosphodiesterase activity is altered by $20\text{ }\mu\text{T}$ magnetostatic fields, *Bioelectromagnetics*, 24, 32–38, 2002.
91. Koch, C.L.M.B., Sommarin, M., Perrson, B.R.R., Salford, L.G., and Eberhardt, J.L., Interaction between weak low frequency magnetic fields and cell membranes, *Bioelectromagnetics*, 24, 395–402, 2003.
92. Creim, J.A., Lovely, R.H., Miller, D.L., and Anderson, L.E., Rats can discriminate illuminance, but not magnetic fields, as a stimulus for learning a two-choice discrimination, *Bioelectromagnetics*, 23, 545–549, 2002.
93. Tang, Y-P., Shimizu, E., Dube, G.R., Rampon, C., Kerchner, G.A., Zhuo, M., Liu, G., and Tsien, J.Z., Genetic enhancement of learning and memory in mice, *Nature*, 401, 63–69, 1999.
94. Muller, D., and Lynch, G., Synaptic modulation of N-methyl D-aspartate receptor mediated responses in hippocampus, *Synapse*, 5, 94–103, 1990.
95. Shiekhattar, R. and Aston-Jones, G., NMDA-receptor-mediated sensory responses of brain noradrenergic neurons are suppressed by *in-vivo* concentrations of extracellular magnesium, *Synapse*, 10, 103–109, 1992.
96. Smith, S.D., Liboff, A.R., and McLeod, B.R., Calcium ICR and seedling growth in orchids (abstract), 20th Annual Meeting, Bioelectromagnetics Society, St. Petersburg Beach, FL, 1998.
97. Poggi, C., private communication, 2004.
98. Bassett, C.A.L., Pawluk, R.J., and Pilla, A.A., Acceleration of fracture repair by electromagnetic fields: a surgically non-invasive method, in *Electrically Mediated Growth Mechanisms in Living Systems*, Liboff, A.R. and Rinaldi, R.A., Eds., *Ann. NY Acad. Sci.*, 238, 242–262, 1974.
99. Liboff, A.R., Electrical treatment of ununited bone fracture and spinal fusion, in *Encyclopedia of Medical Devices*, 2nd ed., Webster, Ed., John Wiley, New York, 2005.
100. Blackman, C.F., Benane, S.G., Elliott, D.J., House, D.E., and Pollock, M.M., Influence of electromagnetic fields on the efflux of calcium ions from brain tissue *in vitro*: a three-model analysis consistent with the frequency response up to 510 Hz, *Bioelectromagnetics*, 9, 215–227, 1988.
101. Binhi, V.N., Amplitude and frequency dissociation spectra of ion-protein complexes rotating in magnetic fields, *Bioelectromagnetics*, 21, 34–45, 2000.
102. Liboff, A.R., Comment on “Extremely low frequency magnetic fields can either increase or decrease analgesia in the Land Snail depending on field and light conditions”, *Bioelectromagnetics*, 23, 406–407, 2002.

103. Ayrapetyan, S., Grigorian, K., Avanesyan, A., and Stambolsian, K., Magnetic fields alter electrical properties of solutions and their physiological effects, *Bioelectromagnetics*, 15, 133–142, 1994.
104. Rai, S., Singh, U., Singh, K., and Singh, A., Germination responses of fungal spores to magnetically restructured water, *Electro. Magnetobiol.*, 13, 237–246, 1994.
105. Ruzic, R. and Jerman, I., Influence of Ca^{2+} in biological effects of direct and indirect ELF magnetic field stimulation, *Electro. Magnetobiol.*, 17, 205–216, 1998.
106. Pazur, A., Characterization of weak magnetic field effects in an aqueous glutamic acid solution by nonlinear dielectric spectroscopy and voltammetry, *Biomagn. Res. Technol.*, 2, 1–18, 2004.
107. Binhi, V.N., *Magnetobiology*, Academic Press, London, 2002, 333–343.
108. Beauchamp, J.L., Ion cyclotron resonance spectroscopy, *Ann. Rev. Phys. Chem.*, 22, 527–561, 1971.
109. Azbel, M.Ya. and Kaner, E.A., Cyclotron resonance in metals, *J. Phys. Chem. Solids*, 6, 113–135, 1958.
110. Hobbie, R.K., *Intermediate Physics for Medicine and Biology*, 3rd ed., Springer, New York, 1997, 83–84.
111. Weaver, J.C. and Astumian, R.D., The response of living cells to very weak magnetic fields: the thermal noise limit, *Science*, 247, 459–462, 1990.
112. Liboff, A.R. and Jenrow, K.A., Cell sensitivity to magnetic fields, *Electro. Magnetobiol.*, 19, 223–236, 2000.
113. Adair, R.K., Constraints on biological effects of weak extremely-low-frequency electromagnetic fields, *Phys. Rev. A*, 43, 1039–1048, 1991.
114. Liboff, A.R., Electric-field ion cyclotron resonance, *Bioelectromagnetics*, 18, 85–87, 1997.
115. Aidley, D.J. and Stanfield, P.B., *Ion Channels*, Cambridge University Press, Cambridge, 1996, 146.
116. Nelson, P.H., A permeation theory for single-file ion channels: concerted-association/dissociation, *J. Chem. Phys.*, 119, 6981–6982, 2003.
117. Yellen, G., Permeation in potassium channels: implications for channel structure, *Ann. Rev. Biophys. Biophys. Chem.*, 16, 227–246, 1987.
118. Liboff, A.R., Ion cyclotron resonance in biological systems: experimental evidence, in *Biological Effect of Electromagnetic Fields*, Stavroulakis, P., Ed., Springer, Berlin, 2003, 76–113.
119. Hille, B., *Ionic Channels of Excitable Membranes*, Sinauer Associates, Sunderland, MA, 183, 1984.
120. Li-Smerin, Y., Hackos, D.H., and Swartz, K.J., α -Helical structural elements within the voltage-sensing domain of a K^+ channel, *J. Gen. Physiol.*, 115, 33–49, 2000.
121. Kuyucak, S., Andersen, O.S., and Chung, S.-H., Models of permeation in ion channels, *Rep. Prog. Phys.*, 64, 1427–1472, 2001.
122. Lednev, V., Interference with the vibrational energy sublevels of ions bound in calcium-binding proteins as the basis for the interaction of weak magnetic fields with biological systems, in *On the Nature of Weak Magnetic Fields with Biological Systems*, Frey, A.H., Ed., Landes, Austin, TX, 1994, Chapter 5.
123. Adair, R.K., Criticism of Lednev's mechanism for the influence of weak magnetic field on biological systems, *Bioelectromagnetics*, 13, 231–235, 1992.
124. Adair, R.K., A physical analysis of the ion parametric resonance mode, *Bioelectromagnetics*, 19, 181–191, 1998.
125. Lee, Q.P., Guy, A.W., Lai, H., and Horita, A., The effects of modulated radiofrequency radiation on calcium efflux from chick brains *in vitro* (abstract), 9th Annual Meeting, Bioelectromagnetics Society, Portland, OR, 1987.
126. Blackman, C.F., Benane, S.G., and House, D.G., The influence of temperature during electric- and magnetic-field induced alteration of calcium-ion release from *in vitro* brain tissue, *Bioelectromagnetics*, 12, 173–182, 1991.
127. Liboff, A.R. and Jenrow, K.A., New model for the avian magnetic compass, *Bioelectromagnetics*, 21, 555–565, 2000.

10

Computational Methods for Predicting Field Intensity and Temperature Change

James C. Lin and Paolo Bernardi

CONTENTS

10.1	Introduction	294
10.1.1	Induced Field Intensity and Dosimetric Quantities.....	295
10.1.2	Characterizing EMFs.....	296
10.2	Planar Tissue Models	297
10.2.1	Thick or Semi-Infinite Layers	297
10.2.2	Multiple Layers	301
10.3	Bodies of Revolution	304
10.3.1	Spherical Models.....	304
10.3.2	Prolate Spheroidal Models	308
10.4	Anatomically Based Models	311
10.4.1	Brief Survey of Numerical Methods.....	311
10.4.1.1	Quasi-Static Impedance Method	311
10.4.1.2	Volume Integral Equation MoM	312
10.4.1.3	SMoM.....	313
10.4.1.4	FEM	314
10.4.1.5	FDTD Method.....	314
10.4.2	Human Bodies Exposed to EMFs	318
10.4.2.1	Realistic Models of the Human Body.....	318
10.4.2.2	Currents Induced in the Human Body by Low-Frequency EMFs.....	319
10.4.2.3	Absorption in Human Bodies Exposed to Far Field of RF Sources	327
10.4.2.4	Human Exposure to the Field Radiated by Transceiver Base-Station Antennas	335
10.4.2.5	Coupling of Transient EM Pulses into the Human Body	340
10.4.2.6	Absorption in the Head of Cellular Phone Users	343
10.5	Temperature Elevations Induced in Biological Tissues by EM Power Absorption.....	348
10.5.1	Introduction	348
10.5.2	Bio-Heat Equation.....	348
10.5.2.1	Initial Conditions	350
10.5.2.2	Boundary Conditions	350
10.5.3	Thermoregulatory Responses	351
10.5.4	Numerical Methods for Solving the Thermal Problem.....	353
10.5.4.1	Explicit Finite Difference Formulation.....	353
10.5.4.2	ADI Formulation.....	355

10.5.5	Temperature Elevations in Subjects Exposed to EM Fields	357
10.5.5.1	Temperature Increments in the Human Body Exposed to the Far Field of Radiating RF Sources	357
10.5.5.2	Temperature Increments in the Head of a Cellular Telephone User	359
10.6	Thermal Therapeutic Applications of Microwave Energy	361
10.6.1	Ablation for Cardiac Arrhythmias.....	362
10.6.2	Ablation for Endometrial Disorders.....	363
10.6.3	Microwave Interstitial Hyperthermia for Cancer Treatment	364
10.7	Concluding Remarks.....	366
	Acknowledgment.....	368
	References	368

10.1 Introduction

Electromagnetic energy at both high and low-frequencies can be transmitted into biological materials through the use of antennas or applicators. Antennas launch the electromagnetic energy into the medium. They serve to couple the generating source of electromagnetic energy into the medium, which surrounds it. The spatial distribution of electromagnetic energy from an antenna is directional and varies with distance from the antenna. At distances sufficiently far from an antenna, so that local field distribution changes predictably and varies mostly with distance, the region is called a far field or radiation zone. In the near field or near zone close to the antenna, the electromagnetic energy distribution varies as a function of both angle and distance. Moreover, the behavior of electromagnetic fields (EMFs) and their coupling and interaction with biological systems are very different, depending on whether they are in the near or far zone. In fact, these differences constitute the major variances between radio frequency (RF) and low-frequency energy deposition into biological systems. As shown in subsequent sections, the induction of electric and magnetic fields, deposition of electromagnetic power, absorption of electromagnetic energy, and their penetration into tissue, all are functions of the source and its frequency or wavelength. In general, when considering the interaction of EMFs with biological systems, it is necessary to account for the frequency or wavelength and its relationship to the physical dimensions of the body.

In addition, the interaction of EMFs with biological systems is characterized by the electromagnetic properties of tissue media, specifically, dielectric permittivity. Biological materials have magnetic permeability values close to that of free space and are independent of frequency. In a medium such as biological tissue with a finite electrical conductivity σ , a conduction current, $\mathbf{J} = \sigma\mathbf{E}$, can be induced to flow, giving rise to energy loss by joule heating. Clearly, fields must be coupled into tissues, and energy must be deposited or absorbed in the biological systems, regardless of the mechanism that is accountable for an effect, for the system to respond in some manner. Thus, to achieve any biological response, the electric field, magnetic field, or EMF that is exerting its influence must be quantified and correlated with the observed phenomenon.

The purpose of this chapter is to present an account of electromagnetic interactions in biological media, with special emphasis on the energy coupling and distribution characteristics in models of biological structures. Such information is essential for analyzing the interrelationships among various observed biological effects, for separating known and substantiated effects from those that are speculative and unsubstantiated, for assessing

the therapeutic effectiveness of electromagnetic waves, and for extracting diagnostic information from field effects.

There exist a wide variety of methods for quantifying fields in biological bodies. The extent of computer usage varies, depending on the specific information sought and the complexity of tissue geometry. This chapter outlines a number of techniques that have been successfully employed to analyze the propagation and absorption characteristics of electromagnetic energy in tissue structures. There are two general approaches: one involves extensive use of analytical development and the other relies more heavily on numerical formulation. Analytical computations are most suited for calculation of the distribution of absorbed energy in simplified tissue geometries such as plane slabs, cylinders, and spheroids, whereas numerical methods offer the opportunity of analyzing the coupling of electromagnetic energy to animal and human bodies, which is difficult, if not impossible, to approach analytically. The advantages and limitations of various methods for field computations, along with representative results, are provided in this chapter. In some cases, for additional details, the reader is referred to previous editions of this handbook [1,2]. This chapter will begin with a brief introduction to the concepts of induced field and power deposition and the characteristics of field intensities and dosimetric quantities.

10.1.1 Induced Field Intensity and Dosimetric Quantities

The quantities of import to characterize coupling of electromagnetic energy into biological systems include the incident field, induced field, power deposition, and absorbed energy. The metrics of specific absorption rate (SAR) and specific absorption (SA) in biological systems or tissue models have been adopted as the dosimetric quantities, especially at RF frequencies. The metric SAR (in W/kg) is defined as the time derivative of the incremental energy absorbed by (or dissipated in) an incremental mass contained in a volume of a given density. SA (in J/kg) is the total amount of energy deposited or absorbed and is given by the integral of SAR over a finite interval of time. Information on SA and SAR is of interest because it may serve as an index for comparison and extrapolation of experimental results from tissue to tissue, from animal to animal, from animal to human, and from human to human exposures. It is also useful in analyzing the relationships among various observed biological effects in different experimental models and subjects. This is in clear contrast to incident field or any other external measures of exposure, which often do not provide the same field inside biological systems of different sizes, species, or constitutions.

Moreover, determination of the induced field would be preferred because it (1) relates the field to specific responses of the body, (2) facilitates understanding of biological phenomena, and (3) is independent of mechanisms of interaction. Once the induced field is known, quantities such as SAR (in W/kg) can be derived from it by a simple conversion formula. For example, from an induced electric field E (in V/m), the SAR can be derived as

$$\text{SAR} = \frac{\sigma E^2}{\rho_m} \quad (10.1)$$

where σ is the bulk electrical conductivity (S/m) and ρ_m is the mass density (kg/m^3) of tissue. However, at present, a small, isotropic, implantable electric field probe has yet to be developed with sufficient sensitivity for practical use. Consequently, a common practice in experimental dosimetry relies on the use of temperature elevation produced under a short-duration (<30 sec), high-intensity exposure condition. The short duration is not enough for

significant convective or conductive heat contribution to tissue temperature rises. In this case, the time rate of initial rises in temperature (slope of transient temperature response curve) can be related to SAR through a secondary procedure, that is,

$$\text{SAR} = \frac{c\Delta T}{\Delta t} \quad (10.2)$$

where ΔT is the temperature increment ($^{\circ}\text{C}$), c is the specific heat capacity of tissue ($\text{J/kg } ^{\circ}\text{C}$), and Δt is the duration (sec) over which ΔT is measured. Thus, the rise in tissue temperature during the initial or a transient period of RF energy absorption is linearly proportional to the value of SAR. It is important to distinguish the use of SAR and its derivation from temperature measurement. The quantity of SAR is merely a metric for energy deposition or absorption, and it should not be construed to imply any mechanism of interaction, thermal or otherwise. However, it is a quantity that pertains to a macroscopic phenomenon by virtue of the use of bulk electrical conductivity in its derivation (Equation 10.1).

It is of particular significance to emphasize the use of bulk electrical conductivity, the specific heat capacity, and the mass density (kg/m^3) of tissue in the derivation of SAR from electric field strength or temperature elevation. Their use in the definition means that a volume of tissue mass must be selected over which SAR is determined. It is self-evident that the numerical value of SAR would be the same, regardless of what volume is chosen, if the induced field or power deposition is uniform in a tissue medium. A difficulty arises when the absorption is not uniform or when tissues with differing properties and conductivities are within the same volume. Thus, in general, a smaller averaging mass or volume would allow SAR—as a metric—to provide a closer representation of its variation inside the body or tissue medium.

10.1.2 Characterizing EMFs

The space surrounding a source antenna can be divided into near and far zones as a function of distance from the antenna [3]. The demarcating boundary occurs at a conservative distance of $R = 2D^2/\lambda$, where D is the largest dimension of the antenna. Furthermore, the near zone can be divided into two subregions: the radiative region and the reactive region. In *the radiative region*, the region closer than $2D^2/\lambda$, the radiated power varies with distance from the antenna. The vicinity of the antenna where the reactive components predominate is known as *the reactive region*. The precise extent of these regions varies for different antennas. For most antennas, the transition point between reactive and radiative regions occurs from 0.2 to $0.4D^2/\lambda$. For a short dipole antenna, the reactive component predominates to a distance of approximately $\lambda/2\pi$, where the radiative and reactive components are equal to each other. However, the outer limit is on the order of a few wavelengths or less in most cases.

A typical wavelength in free space at extremely low-frequencies (ELF between 3 Hz and 3 kHz) is ~ 5000 km. The $\lambda/2\pi$ distance is about 800 km for the induction and radiation fields to have equal amplitudes. Therefore, for most purposes, ELF transmission line fields are not radiative but are inductive and quasi-static in nature. This fact governs the coupling and induced field characteristics of ELF and other low-frequency electric and magnetic fields in biological tissue. In particular, (1) the electric field is enhanced at the surface of the biological body and is nearly perpendicular to the surface of the body, (2) electric and magnetic fields are decoupled inside a biological body, (3) the electric field applied through air is weakened by a large dielectric permittivity (by about 10^{-6}) upon penetration into biological tissues, (4) the magnetically induced electric field encircles the

magnetic field and produces an eddy current whose magnitude increases with distance from the center of the body, and (5) an eddy current appears in each region inside the body with a different conductivity and behaves as a unit with its own body center and radius or an equivalent radius. These observations apply to all frequencies where the wavelength is high or the largest dimension of the body is small compared with the wavelength [2].

In contrast, the $2D^2/\lambda$ distance is approximately 6 cm for a 10-cm RF antenna operating at 900 MHz in free space. Clearly, both near-zone reactive and far-zone radiative interactions are encountered in the vicinity of wireless RF telecommunication systems. In the near zone, the coupling of RF energy into the human head is substantial. As much as 40% to 50% of the radiated RF power is transferred back and forth between the radiating antenna and the head. SAR will vary with specific antenna configuration and its placement next to the head. The bulk of power deposition is on the side of the head nearest to the radiating structure of the cellular mobile telephone and follows an exponential trend away from the antenna side. The anatomy of the head and tissue inhomogeneity can influence the maximum value and distribution of SAR in the head of a mobile telephone user. However, the integrated SAR in the head is similar for a homogenous or inhomogenous model. Some of the major features of near-zone field are that (1) RF electric and magnetic fields are decoupled and are not uniform, (2) wave impedance varies from point to point, (3) beam width from the antenna is divergent and is small compared with the head or human body, (4) electric field effect is weaker since dielectric permittivity of tissue is relatively high, and (5) inductive coupling of antenna-current-generated magnetic field dominates power deposition.

In the far field, coupling is characterized by plane wave RF field interaction and is independent of source configurations. Electric and magnetic fields are uniquely defined through the intrinsic impedance of the medium. Thus, determination of the electric field behavior is sufficient to characterize the interaction. The coupling of RF power from air into planar tissue ranges from 20% to 60% at wireless communication frequencies. However, enhanced coupling can occur at a greater depth in bodies with curved surfaces. In fact, RF energy is resonantly absorbed by the head at 400 to 1500 MHz, and SAR peaks or hot spots may occur near the center of the head. The interaction of RF energy with biological systems depends on electric field polarization for elongated bodies whose height-to-width ratio is large. It is significant to observe that the integrated SAR or total absorption in the biological body is similar for a homogenous and inhomogenous model.

10.2 Planar Tissue Models

When the radius of curvature of the body surface is large compared to the wavelength and beam width of the impinging radiation, planar tissue models may be used to estimate the absorbed energy and its distribution inside the body. As a first-order approximation, the plane wave configuration is often used for its simplicity to assess EMF interaction with planar biological tissues. This section presents a summary of specific results that have been obtained, using analytical approaches, for thick or semi-infinite layers and for multilayered planar models of biological tissue structures.

10.2.1 Thick or Semi-Infinite Layers

The reflection and transmission of a plane wave at a planar tissue interface depend on the frequency, polarization, and angle of incidence of the wave and on the dielectric constant and conductivity of the tissue. For a linearly polarized plane wave impinging normally on

a boundary separating two semi-infinite media, the reflection and transmission coefficients are given by

$$\Gamma = \frac{\eta_2 - \eta_1}{\eta_2 + \eta_1} \quad (10.3)$$

and

$$T = \frac{2\eta_2}{\eta_2 + \eta_1} \quad (10.4)$$

respectively, where η_1 and η_2 are the intrinsic impedances ($= \sqrt{(\mu/\epsilon)}$) of media 1 and 2. If intrinsic impedances of the two media are approximately equal or if the dielectric permittivities are comparable, most of the energy is transmitted into the second medium, and the reflected field is relatively small. Conversely, if intrinsic impedances differ greatly, or if the dielectric permittivities are very different, the transmitted field is small, and the quantity of reflected energy is large.

Table 10.1 summarizes the magnitude of the reflection coefficient at the boundary separating various tissues. The fraction of normally incident power reflected by the

TABLE 10.1

Reflection Coefficient (Magnitude in %) between Biological Tissues at 37°C

	Frequency (MHz)	Air	Fat (Bone)	Lung	Muscle (Skin)	Blood	Saline
Air	433	0	46	76	82	81	83
	915	0	43	73	78	79	80
	2,450	0	41	71	76	77	79
	5,800	0	39	70	75	76	78
	10,000	0	37	70	74	76	78
Fat (bone)	433	0	46	56	56	56	60
	915	0	43	52	54	54	57
	2,450	0	42	50	53	53	57
	5,800	0	42	50	53	53	56
	10,000	0	45	52	54	54	58
Lung	433	0	14	13	13	19	19
	915	0	12	14	14	18	18
	2,450	0	10	15	15	19	19
	5,800	0	10	14	14	19	19
	10,000	0	10	13	13	18	18
Muscle (skin)	433	0	0	4	4	6	6
	915	0	0	4	4	7	7
	2,450	0	0	5	5	10	10
	5,800	0	0	4	4	9	9
	10,000	0	0	3	3	9	9
Blood	433	0	0	0	0	6	6
	915	0	0	0	0	4	4
	2,450	0	0	0	0	5	5
	5,800	0	0	0	0	5	5
	10,000	0	0	0	0	6	6
Saline	433	0	0	0	0	0	0
	915	0	0	0	0	0	0
	2,450	0	0	0	0	0	0
	5,800	0	0	0	0	0	0
	10,000	0	0	0	0	0	0

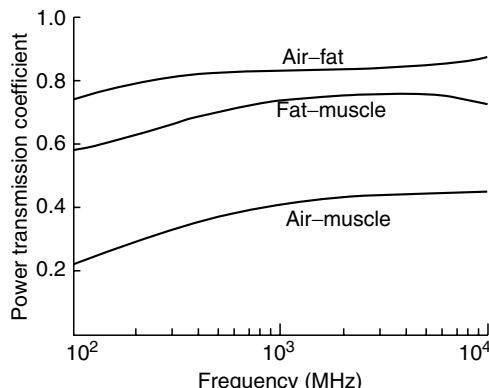


FIGURE 10.1
Power transmission coefficients at three tissue interfaces as functions of frequency.

discontinuity is given by Γ^2 . Clearly, about one half of the incident power is reflected at these boundaries. Further, the reflection coefficient for tissue–tissue interfaces generally is smaller than for air–tissue interfaces. The percent reflected power for tissue–tissue interfaces ranges from a low of 5 for muscle–blood to a high of 50 for bone–biological fluid interfaces. This suggests that the closer are the dielectric properties on both sides of the interface, the smaller is the power reflection.

The fraction of power transmitted is related to the power transmission coefficient, T^2 . It is readily apparent from [Table 10.1](#) that the power transmitted at air–tissue interfaces is quite substantial at RF and microwave frequencies. Moreover, Figure 10.1 shows that the power transmission coefficient is highly frequency dependent, especially at lower frequencies.

As the transmitted wave propagates in the tissue medium, energy is extracted from the wave and absorbed by the medium. This absorption will result in a progressive reduction of the power density of the wave as it advances in the tissue. This reduction is quantified by the depth of penetration, which is the distance in which the power density decreases by a factor of e^{-2} . [Table 10.2](#) presents the calculated depth of penetration in selected tissues using typical dielectric constants and conductivities. A graphical representation of penetration depth vs. frequency for blood, muscle, and fat is given in [Figure 10.2](#). It is seen that the penetration depth is frequency dependent and takes on different values for different tissues. In particular, the penetration depth for fat and bone is nearly five times greater than for higher-water-content tissues.

TABLE 10.2

Depth of Penetration of an EMF in Biological Tissues as a Function of Frequency

Frequency (MHz)	Tissue				
	Saline	Blood	Muscle (Skin)	Lung	Fat (Bone)
<i>Depth of Penetration (cm)</i>					
433	2.8	3.7	3.0	4.7	16.3
915	2.5	3.0	2.5	4.5	12.8
2,450	1.3	1.9	1.7	2.3	7.9
5,800	0.7	0.7	0.8	0.7	4.7
10,000	0.2	0.3	0.3	0.3	2.5

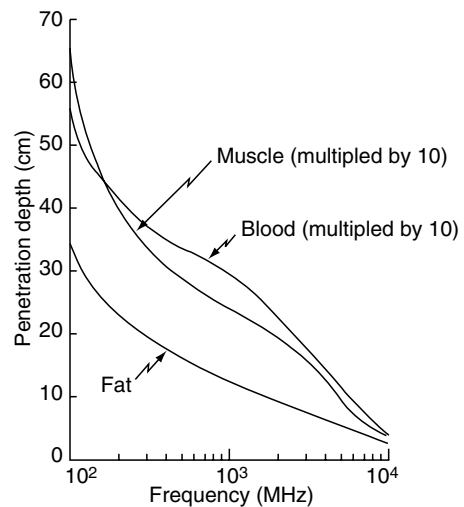


FIGURE 10.2
Depth of penetration for blood, muscle, and fat as functions of frequency.

A wave of general polarization usually is decomposed into its orthogonal linearly polarized components whose electric or magnetic field parallels the interface. These components can be treated separately and combined afterward. Figure 10.3 and Figure 10.4 illustrate the magnitude and phase of the reflection coefficients of representative tissue interfaces at a temperature of 37°C for irradiation at 2450 MHz. The figures clearly show the difference between E and H polarization. E polarization, also called perpendicular polarization, and H polarization, also referred to as parallel polarization, are defined in Chapter 1. For E polarization, there is only a slight variation in magnitude and phase of the reflection coefficient with incidence angle. For H polarization, however, there is a

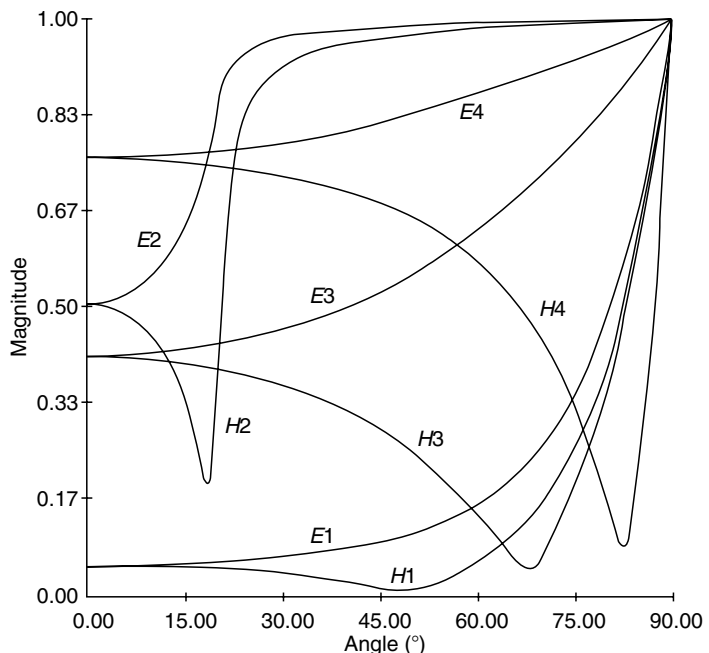


FIGURE 10.3
Magnitudes of reflection coefficients for E - and H -polarized plane waves at 2450 MHz.

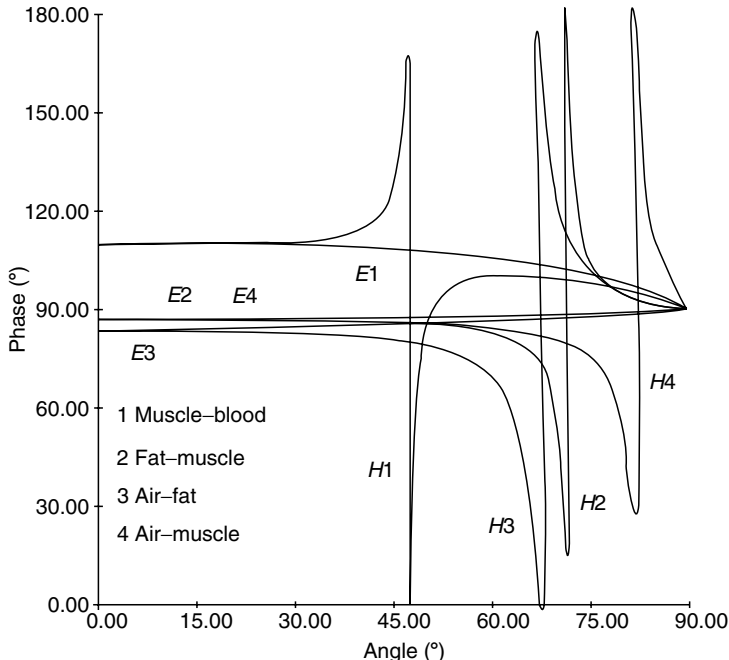


FIGURE 10.4

Phase of reflection coefficients for E - and H -polarized 2450 MHz plane waves.

pronounced dependence on incidence angle. The reflection coefficient reaches a minimum magnitude and has a phase angle of 90° at Brewster's angle. Thus, the H polarized wave is totally transmitted into the muscle medium at Brewster's angle.

10.2.2 Multiple Layers

When there are several layers of different tissues, the reflection and transmission characteristics become more complicated. Multiple reflections can occur between the skin and subcutaneous tissue boundaries, with a resulting modification of the reflection and transmission coefficients [4–7]. In general, the transmitted wave will combine with the reflected wave to form standing waves in each layer. This phenomenon becomes especially pronounced if the thickness of each layer is less than the penetration depth for that tissue. Plane waves impinging on the human body, considered as consisting of parallel layers of subcutaneous fat and more deeply lying muscle, have been studied in detail by Schwan and Li [5,6].

For the tissue model depicted in Figure 10.5, the electric field strength in the fat layer is given by

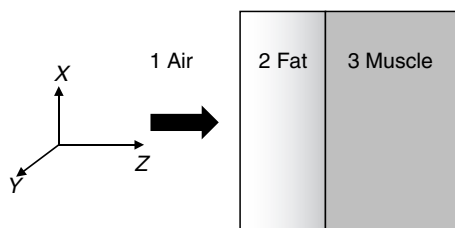


FIGURE 10.5

Plane wave impinging on a composite fat–muscle layer.

$$E_f = F_1 E_0 [e^{-(\alpha_2+j\beta_2)z} + \Gamma_{32} e^{(\alpha_2+j\beta_2)z}] \quad (10.5)$$

and the electric field in the underlying muscular tissue is given by

$$E_m = F_t E_0 e^{-(\alpha_3+j\beta_3)z} \quad (10.6)$$

where α_2, β_2 and α_3, β_3 are the attenuation and propagation coefficients in fat and muscle, respectively. The layer function F_1 and the transmission function F_t are given by

$$F_1 = \frac{T_{12}}{e^{(\alpha_2+j\beta_2)l} + \Gamma_{21}\Gamma_{32} e^{-(\alpha_2+j\beta_2)l}} \quad (10.7)$$

$$F_t = \frac{T_{12}T_{23}}{e^{(\alpha_2+j\beta_2)l} + \Gamma_{21}\Gamma_{32} e^{-(\alpha_2+j\beta_2)l}} \quad (10.8)$$

where T_{12} and T_{23} are the transmission coefficients at the air-fat and fat-muscle boundaries, respectively. Γ_{21} and Γ_{32} denote the reflection coefficients at these boundaries, respectively; l is the thickness of the fat layer. The power deposition in a given layer can be obtained from [Equation 10.1](#).

Figure 10.6 shows the results of SAR distribution obtained using the dielectric data given in part 1. The values are normalized to the SAR in muscle at the fat-muscle boundary. Note that the absorbed energy is much lower in fat than in muscle. The standing-wave maximum becomes bigger in fat, and the penetration into muscle becomes less as the frequency increases.

The electromagnetic energy absorbed in models composed of planar layers of skin, fat, and muscle can be analyzed in a similar manner [5–8], except that the distribution of

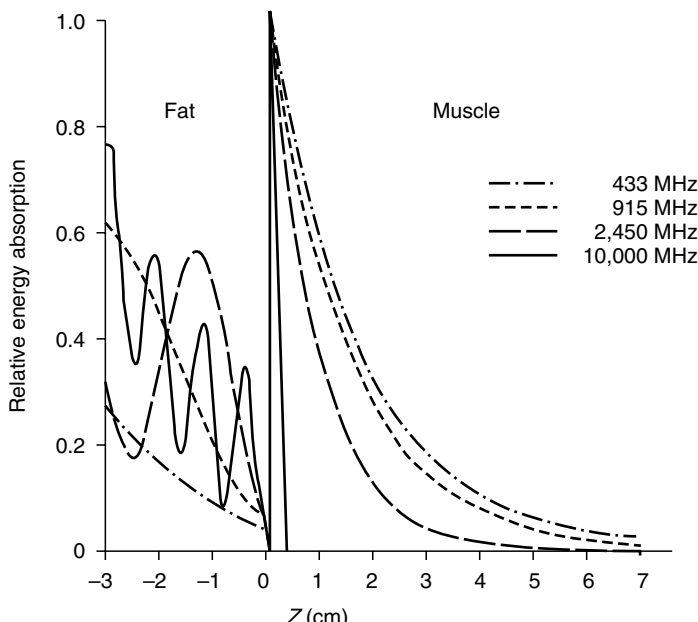


FIGURE 10.6
SAR (absorbed power density) in plane fat–muscle layers.

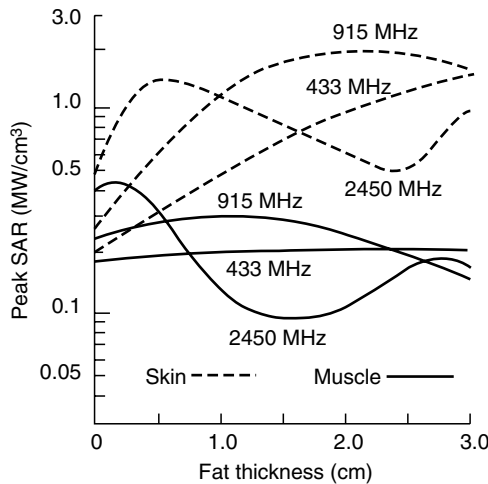


FIGURE 10.7

Peak SAR (absorbed power density) in models composed of fat-skin-muscle layers.

absorbed energy becomes more complex. Figure 10.7 shows that in addition to frequency dependence, the peak SAR exhibits considerable fluctuation with thickness of the subcutaneous fatty layer. The incident power density is, in this case, 10 W/m^2 , and the skin layer is 0.2 cm thick. Note that the peak SAR is always higher in the skin layer for planar models at microwave frequencies. The depth of penetration for 10 GHz radiation in skin is less than 0.5 mm—the transmitted energy is almost completely absorbed in the skin, and the SAR is rather unaffected by changing fatty layer thickness. The fact that SAR is highest in the skin is significant, since skin is populated with thermosensitive free nerve endings, which may be excited along with cutaneous pain receptors when the absorbed energy exceeds the normal range that can be handled by thermoregulation.

Figure 10.8 shows the distribution of induced electric field strength in a layer of muscle beneath layers of fat, muscle, and bone for two frequencies [5–8]. It is seen that in addition

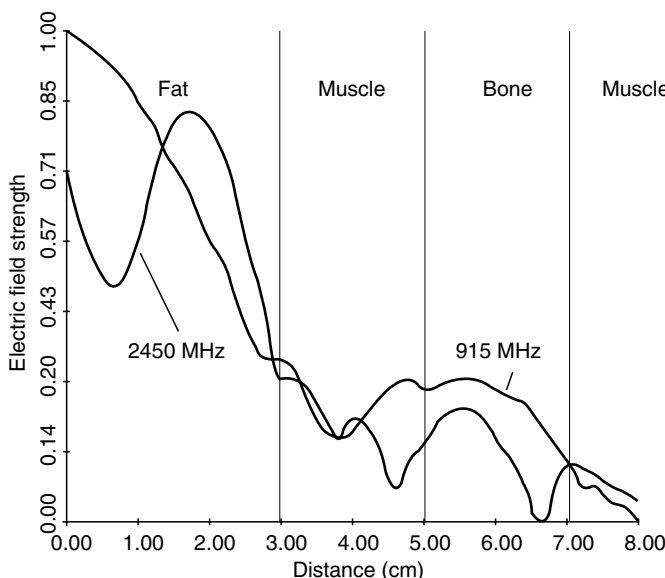


FIGURE 10.8

Distribution of electric field strength in planar layer of fat-muscle-bone-muscle tissue model.

to frequency dependence, the electric fields exhibit considerable fluctuation within each tissue layer. While the standing-wave oscillations are larger at 2450 than at 915 MHz, microwave energy at both frequencies penetrates to deeper tissues. This result, together with [Figure 10.6](#) and [Figure 10.7](#), implies that at frequencies between 300 and 3000 MHz, sufficient energy may be transmitted and reflected to allow examination of organs within the body. Furthermore, at these frequencies, electromagnetic energy can penetrate into more deeply situated tissues, making it especially desirable for therapeutic applications. They also call for special attention for safety considerations since electromagnetic energy in this frequency range can produce higher SAR at greater depth compared to superficial tissues.

10.3 Bodies of Revolution

Although depth of penetration and reflection and transmission characteristics in planar tissue provide considerable physical insight into the coupling and distribution of electromagnetic energy, biological structures generally are more complex in form and exhibit substantial curvature that can modify electromagnetic energy transmission and reflection. For bodies with complex shapes, the propagation characteristics depend critically on polarization and on orientation of the incident wave with respect to the body, as well as on the ratio of body size to wavelength. These complications place severe limitations on calculations of reflected and transmitted energy for bodies of arbitrary shape and complex permittivity. This section presents a summary of results for homogenous and multilayered models based on bodies of revolution that approximate certain mammalian tissue structures.

10.3.1 Spherical Models

Some representative calculations of the SAR are shown in [Figure 10.9](#) for four different-sized models at 918 and 2450 MHz [7,8]. The 6-cm diameter sphere approximates a cat or rhesus monkey brain, and the 10-cm diameter sphere approximates the head of a child, while the 14- and 18-cm diameter spheres are more typical of human adult heads. The figures illustrate the SAR distributions along the three perpendicular axes whose origin coincides with the center of the sphere. An incident plane wave power density of 10 W/m^2 is assumed. The plane wave is propagating in the positive z direction and is polarized along the x axis. It is seen that for 918 MHz, maximum absorption occurs near the center or inside of all the brain spheres. When the frequency is increased to 2450 MHz, the location of peak SAR for the cat-size brain sphere remains near the center, whereas that for a human-size brain sphere is moved to an anterior location.

In general, standing-wave patterns with many oscillations are observed. Note that while peak and average SARs in the cat brain are larger by a factor of 2 than in the human brain at 918 MHz, at 2450 MHz the peak absorption is four times and the average absorption is three times greater in the cat brain than in the human brain. Other studies [9–12] indicate that the peak absorption may be as much as five times greater than the average, and the enhanced absorptions near the center of these brain models may be two to three orders of magnitude greater than that expected from the planar tissue models. The increased absorptions are due to a combination of high dielectric constant and curvature of the model, which produces a strong focusing of energy toward the interior of the sphere that more than compensates for the transmission losses through the tissue.

The peak absorption per unit volume, average absorption per unit volume, and average absorption per unit surface area as functions of frequency and radius of the spherical brain model are illustrated in Figure 10.10. It can be seen that the absorbed energy varies widely with sphere size and frequency. In general, the absorption increases rapidly with increasing radius and is then followed by some resonant behavior. The peaks of these resonant oscillations are related to the maxima, or hot spots, in the distribution of absorbed energy inside the head model, as shown in Figure 10.9. Therefore, for $(2\pi a/\lambda_0) < 0.4$, where a is the sphere radius and λ_0 is the wavelength in vacuum, hot spots do not occur inside the sphere. However, for some combinations of irradiation frequency and radius, hot spots will occur, for example, in spheres with radii between 2 and 8 cm at 918 MHz and between 0.9 and 5 cm at 2450 MHz. For spheres whose radii exceed the size ranges mentioned above, the maximum absorption appears at the anterior portion (exposed surface) of the sphere, and the penetration depth at the surface becomes a dominating factor for exposures at frequencies in this range. The planar model discussed previously may be applied to obtain a theoretical estimation of the absorbed energy in this case.

The frequency dependence of energy absorption is illustrated in the upper graphs in Figure 10.10 for the head of a small animal, such as a cat or rhesus monkey, and a sphere the

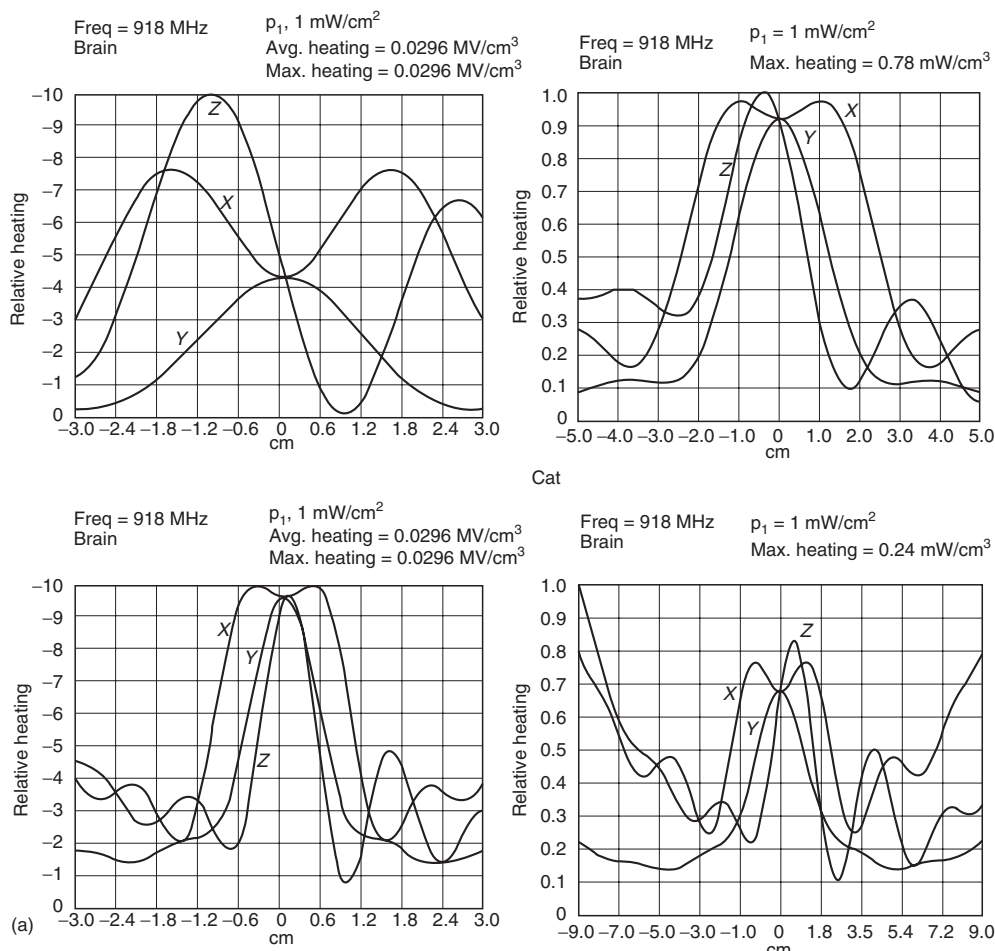


FIGURE 10.9

(a) Predicted SAR distribution (heating pattern) along the three rectangular axes of spherical models of brain exposed to 918-MHz uniform plane waves.

continued

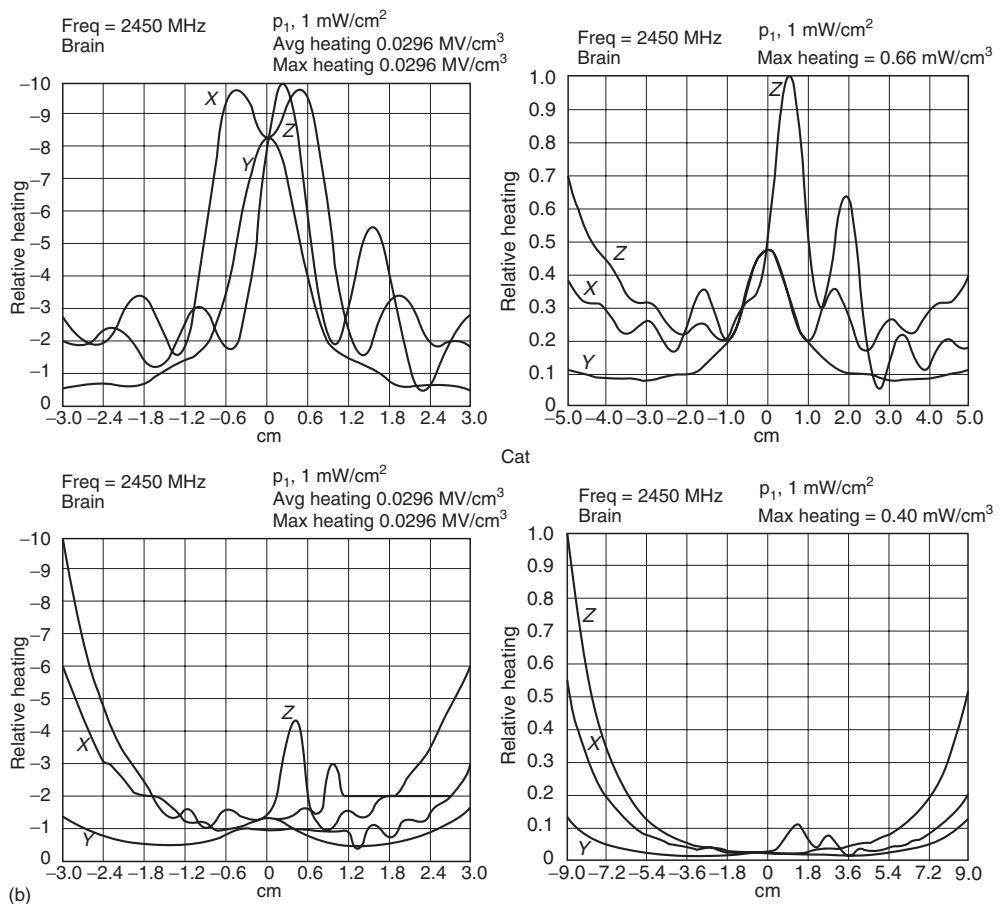


FIGURE 10.9 (continued)

(b) Predicted SAR distribution (heating pattern) along the three rectangular axes of spherical models of brain exposed to 2450-MHz uniform plane waves.

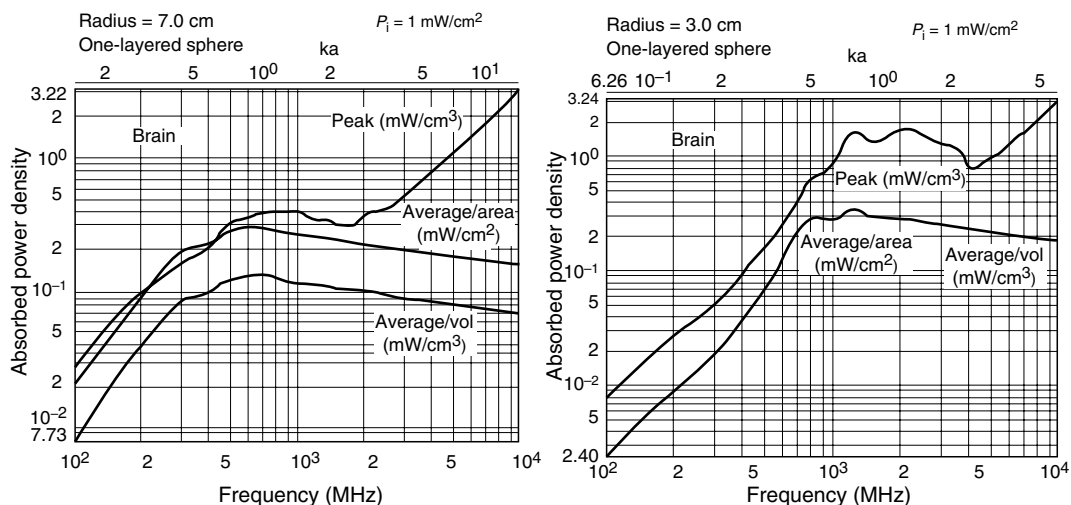


FIGURE 10.10

Electromagnetic energy absorption characteristics for spherical models of brain.

size of a human head. Besides the occurrence of resonant peaks, with increasing frequency, energy is absorbed in a decreasing volume as a result of shortened penetration depth.

The effects of skin, fat, bone, dura, and cerebrospinal fluid on the absorption of RF radiation by the brain have been investigated in several laboratories [9,13–15], using more complex spherical structures where the spherical core of brain is surrounded by five concentric shells of tissues. It is interesting to note that if brain sizes remain unchanged, but the overall sphere diameter is increased to account for the outer tissue layers, absorption in brain tissues may be increased by 25% for human- and cat-size heads at 918 MHz or decreased by 70% or more in the case of 2450 MHz. Moreover, surface absorption is greatly increased in the case of layered models, while fat and bone always absorb the least amount of energy.

If the outer diameter of the sphere remains the same, while the tissue layers are allowed to be either layered or homogenous, the peak and average SARs show very little change except when the radius of the spherical head is between 0.1 and 1.0 times the wavelength in air. The peak and average SARs for layered models may be several times greater than for homogenous models. Enhancement is apparently the result of resonant coupling of energy into the sphere by the outer tissue layers.

A study also has been made of the interaction of circularly polarized plane electromagnetic waves with six-layered spherical models of the mammalian head [15]. The approach is a classic one; Mie equations were modified to account for the two polarizations that are orthogonal in space. For example, calculations at 918 and 2450 MHz for a 7-cm diameter sphere representing a cat or monkey head and a 20-cm diameter sphere typical of a human adult head indicated that the maximum absorption for 918 MHz occurs near the center of a cat-size head, whereas the maximum absorption for a human-size head is at the surface, as in the case of linearly polarized plane waves. However, at 2450 MHz the location of maximum absorption for both the smaller and the larger spheres shifts to the leading surface. The distribution of absorbed energy for circularly polarized waves is more uniform compared with the linearly polarized case. In fact, the absorbed energy distribution in the planes transverse to the direction of propagation is rotationally symmetric, that is, it is independent of angular variation. Note also that the maximum energy absorbed in the spherical head models varies only slightly between these two frequencies. However, a greater quantity of energy is deposited in the inner sphere (representing the brain of a human head) for 918- than for 2450-MHz radiation.

Spherical models of muscle [16,17] have been used as a first-order approximation for the extrapolation to human beings of results obtained from laboratory animals and as an index of whole-body absorption of electromagnetic energy as a function of frequency. The spherical model is attractive since exact solutions for absorbed energy can be obtained for all frequencies and body sizes. While in this case the peak absorption is of very limited utility, the average absorption per unit surface area is related to the time and power required to overload the thermoregulatory capacity of an exposed subject. The absorptions for homogenous muscle spheres, whose volumes correspond to small animals, such as a rat, and standard man, computed as functions of frequency, showed that the average absorption for the rat model is at least ten times higher than for a muscle sphere representing a human body at frequencies greater than 500 MHz. The absorption increases rapidly with frequency until the free space wavelength of the impinging radiation approaches the diameter of the sphere. A number of resonant oscillations appear that tend to increase the amount and nonuniformity of absorbed energy. Above this range the absorption falls off slowly, indicating that details of body surface curvature are of little significance.

We have, thus far, dealt mainly with situations where the diameter of the sphere is comparable to or larger than the wavelength in air. It is interesting to note that when the sphere is small compared with the wavelength, the absorbed energy distribution varies

almost as the square of the radius or distance from the axis parallel to the direction of the magnetic field vector. If the sphere is extremely small compared with the wavelength, the absorbed energy distribution becomes nearly uniform in the transverse directions but decreases continuously with distance from the exposed surface. This behavior can be explained by a quasi-static field theory [16]. The electric component of the incident field couples to the object in the same fashion as an electrostatic field. This gives rise to a constant induced electric field inside the sphere that has the same direction but is reduced by $3/\epsilon$ from the applied electric field for biological materials and is independent of sphere size. Similarly, the magnetically induced electric field inside the body is identical to the quasi-static solution whose magnitude is given by $E = \pi f \mu r H$, where f is the frequency, μ is the permeability, r is the radius, and H is the magnetic field component. Thus, the magnetic component of the incident field produces an internal electric field that varies directly with distance from the axis and in proportion to the frequency. This magnetically induced electric field encircles the magnetic axis and gives rise to an eddy current whose magnitude increases with distance from the y axis. It indicates that while the H -induced energy absorption in a mouse or larger animal is much greater than the E -induced component, electrically and magnetically induced absorption may be equally significant in smaller animals at lower frequencies (below 30 to 40 MHz). Moreover, for a small insect or pupae the electric field will be the predominant factor.

The variation of average and maximum energy absorption with frequency for a human-size sphere is illustrated in [Figure 10.11](#). In the frequency range from 1 to 20 MHz, the maximum absorption rate is only 10^{-6} to 10^{-3} (W/kg)/(W/m²) of incident power. Inspection of the maximum absorption rate induced by a plane wave, a quasi-static electric field, and a quasi-static magnetic field shows that absorption at frequencies below 20 MHz is primarily due to the magnetically induced eddy current and is characterized by a square-of-frequency dependence. The approximate frequency dependence of average or total energy absorption throughout the frequency range from 1 MHz to 10 GHz is indicated by the dashed line. For frequencies below 20 MHz the average absorption varies as the square of the frequency. In the frequency range of 20 to 200 MHz, the average absorption increases directly in proportion to frequency and attains a maximum of about 2×10^{-3} (W/kg)/(W/m²) of incident power at 200 MHz. The average absorption rate remains fairly constant with increasing frequency. (Its slow variation is inversely proportional to frequency for higher frequencies.) There is thus little doubt that electromagnetic energy absorption varies both with frequency and with body size, and in a predictable manner.

10.3.2 Prolate Spheroidal Models

Since the bodies of humans and experimental animals are seldom spherical in shape, a better geometric model is needed to analytically and numerically describe the induced fields and absorbed energy inside experimental subjects. A prolate spheroid emulates more closely the shape of mammalian bodies, but most analyses have been restricted to homogenous models for humans and experimental animals [18–22]. As in the case of spherical models, for frequencies below resonance, long-wavelength formulations [19,20] and quasi-static approximations [22] have been used to obtain absorption information. Geometric optics approximations also have been developed for computation of absorption characteristics of prolate spheroidal models of humans at frequencies whose wavelengths are short compared with body size [21].

Three orientations of the impinging plane wave with respect to the body must be distinguished: E -polarization, in which the electric field is parallel to the major axis of

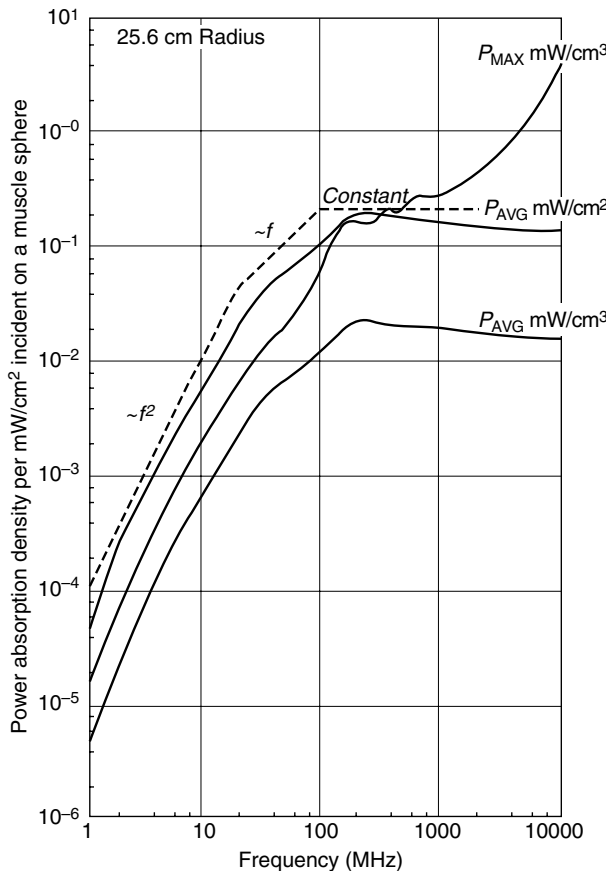


FIGURE 10.11
Frequency dependence of absorption in a spherical model of the human body.

the spheroid; *H*-polarization, in which the magnetic field vector is parallel to the major axis; and *K*-polarization, in which both electric and magnetic field vectors are perpendicular to the major axis of the spheroid. In general, *E*-polarization produces the highest energy absorption for frequencies up to and slightly beyond the resonance region.

For a plane wave with long wavelength, that is, $\lambda > a$, where a is the semimajor axis of the prolate spheroid, the induced fields within the spheroid are uniform and independent of size when the external field is uniform. For $\epsilon_r > 1$, the field inside the spheroid is weaker than the applied field. Moreover, the whole-body energy absorption depends not only on the strength of impressed fields but also on the orientation of the field with respect to the major axis of the body. As in the case of spherical models, the absorption is produced by an electrically induced current in the direction of the applied *E*-field vector, combined with a circulating eddy current induced by the incident magnetic field [16]. One would therefore expect the electrically induced absorption to be uniform, whereas the absorption due to the circulating eddy current would be zero at the center of the body and increase as the square of the distance from the center.

Note that for a given incident field orientation, the average SAR for humans may be either higher or lower than for rats, depending on the frequency. For example, at 70 MHz, the average SAR is the highest for humans, having a value of 0.25 W/kg for an incident power density of 10 W/m²; the average SAR for a rat is only 0.0125 W/kg. In contrast, the average SAR of 0.8 W/kg at 700 MHz is the highest for rats; the corresponding value for humans is less than 1/25. It is thus extremely important to take into account the body size

and operating frequency to draw any relationship between the biological effects that arise in the laboratory and the corresponding effects that might occur in humans at a given incident power density [1,2].

The frequency for maximal absorption (resonance frequency) depends on the subject and its orientation with respect to the incident field. In general, the shorter the subject, the higher the resonance frequency and vice versa. Further, the frequency dependence of whole-body or average absorption may be partitioned into three regions. This may be illustrated using the orientation that is most efficient in energy coupling, *E*-polarization. For frequencies well below resonance such that the ratio of the longest body dimension (*L*) to free space wavelength (λ) is less than 0.2, the average SAR is characterized by an f^2 dependence. The average absorption goes through a resonance in the region where $0.2 < L/\lambda < 1.0$. In this case, the average SAR rapidly increases to a maximum near $L/\lambda = 0.4$ and then falls off as $1/f$. At frequencies for which $L/\lambda > 1.0$, the whole-body absorption decreases slightly but approaches asymptotically the geometrical optics limit of about one half of the incident power (1 – power reflection coefficient).

It should be noted that the resonant absorption length of 0.4λ is in good agreement with results from antenna analysis. In addition, whole-body absorptions for *H*- and *K*-polarizations are totally different. The resonances are not nearly as well-defined as for *E*-polarization. In fact, the whole-body absorption curve for *H*-polarization gradually reaches a plateau and stays at that plateau for higher frequencies.

At 10 MHz, the size of the spheroidal model approximating an average human body—height equals 1.75 m with a major-to-minor axis ratio of 6.34 and a 70-kg mass—is small compared with the wavelength. The distribution of absorbed energy in the spheroidal model is qualitatively similar to that for spherical models. But quantitatively, the difference could be as much as one order of magnitude. As expected, the absorbed energy is highest for *E*-polarization. There is a strong coupling of the applied electric field into the interior of the prolate spheroid, and a relatively weak eddy current contribution due to a smaller cross section for intercepting the magnetic flux. The current distribution along the direction of incident field indicates that the electrically and magnetically induced field components are nearly equal. The electric polarization field and the circulating eddy current add at the front side and subtract on the back side of the spheroid to render an absorption pattern that peaks at the front surface and is reduced to almost zero deeper inside the spheroid.

For *H*-polarization, the electrically induced current flows along the *x* axial direction of incident *E* field, and the eddy current field encircles the *z* axial direction of incident *H* field. The relatively low power on the *z* axis comes solely from the incident electric field. The combination of *E*- and *H*-induced components generates a displaced parabolic energy absorption pattern along both the *x* and the *y* axes. Clearly, the magnetically induced eddy current predominates in this case, and the absorption is highest along the transverse circumference at the middle of the prolate spheroid. For *K*-polarization, both the electric and the magnetic components of the incident field are along the minor axes of the spheroid: the electrically induced current flows along one axis, and the incident magnetic field induces an eddy current electric field that encircles another axis. The absorption is lowest at the center. Whereas in both *E*- and *H*-polarization cases, the peak absorption occurs at the front surface of the spheroid irradiated by the incident field, this is not the case for *K*-polarization. Maximum absorption appears at the surface of the narrow cross section, and the absorbed energy varies parabolically. This is the result of the large quantity of magnetic flux intercepted by the broad cross section (and the resulting concentration of eddy current). It should be noted that the results match very well with experimental measurements [23]. Moreover, the peak absorptions may be two orders of magnitude higher than those for dielectric spheres of equal mass.

10.4 Anatomically Based Models

We have summarized above some of the computational approaches to quantify the absorbed energy in simple models of biological objects. It should be recognized that while spheres and spheroids are good models of some animal bodies and certain body parts, they may not always be adequate for humans and experimental animals under a variety of exposure situations. More realistic models, such as models of human bodies formed from small-sized, computational-cell volumes have been developed to account for the irregular shapes [24–28]. These models, based on numerical techniques have been a great asset in efforts to accurately predict energy absorption and its distribution in biological objects exposed to EMFs and RF radiation. In what follows we shall summarize a number of computer techniques that have been applied with some success in solving electromagnetic energy absorption and SAR distribution problems. We shall also describe some results obtained using these methods.

10.4.1 Brief Survey of Numerical Methods

The numerical methods used to predict induced fields in biological bodies of realistic shape and composition include the quasi-static impedance method, the method of moments (MoM), the finite element method (FEM), and the finite difference time domain (FDTD) method. Note that the quasi-static impedance method is restricted to lower frequencies (<30 to 40 MHz for the human body), but the MoM, the FEM, and the FDTD method may be used for any frequency of interest. In addition, both the finite element and the FDTD methods involve solving Maxwell's equations in the differential form for the computation of induced fields.

10.4.1.1 Quasi-Static Impedance Method

For low-frequency situations, where the dimensions of the biological body are small compared to the wavelength, the impedance method has been found to be highly efficient as a numerical procedure for calculating internal current densities and induced electric fields [29–33]. In this method, the biological body or the exposed part thereof is represented by a three-dimensional (3-D) network of impedances whose individual values are obtained from the complex conductivities $\sigma + j\omega\epsilon$ for the various locations of the body. The impedances for various directions for the 3-D network can be written as

$$Z_m^{i,j,k} = \frac{\delta_m}{\delta_n \delta_p (\sigma_m^{i,j,k} + j\omega\epsilon_m^{i,j,k})} \quad (10.9)$$

where i, j, k indicate the cell index; m is the direction in x, y , or z for which the impedance is calculated; and σ_m and $j\omega\epsilon_m$ are the conductivities and the dielectric permittivities for the cell (i,j,k) . δ_m is the thickness of the cell in the m th direction, and δ_n and δ_p are the widths of the cell in directions at right angles to the m th direction.

In the impedance method formulation, it can be seen that the cells need not be identical so that fairly thin features of the body can be modeled as well as the interfaces between the various tissues and organs. Also, the conductivity for a given cell can be directionally dependent. This feature will be useful in allowing for the highly anisotropic conductivities of the tissues that have been reported for low-frequencies including the power-line frequencies [34,35].

Employing anatomically based models of the human body, the impedance method has been used for the following applications:

1. Calculation of SAR distributions for operator exposure to spatially variable fields of induction heaters [31]
2. SAR distributions for linearly or circularly polarized RF magnetic fields representative of magnetic resonance imagers [32]
3. SAR distributions due to capacitive-type electrodes used for hyperthermia [33]
4. SAR distributions for interstitial RF needle applicators for hyperthermia [36]

Some calculations using the impedance method are listed below:

1. Internal electric fields and current densities induced in the human body by exposure to magnetic fields of high-voltage power transmission lines [37]
2. Electric fields and current densities induced in the human head by magnetic fields of a hair dryer [38]
3. Current densities induced in the arm and the body by magnetic fields of an electric hand drill [39]
4. Currents induced in the anatomically based model of the human body by the electric and magnetic fields of electric blankets [40].

In the section that follows, the use of the impedance method is described for calculating currents in models of the human body exposed to electric and magnetic fields of both the conventional (pre-1990) electric blanket and the new low-magnetic-field electric blanket.

10.4.1.2 Volume Integral Equation MoM

The MoM [41] is used in conjunction with either the volume integral equation method or the surface integral equation method for finding solutions to the unknown fields inside the body. The approaches differ, however, in specifics, in that the surface integral equation MoM (SMoM) finds the unknown currents on the body surface and calculates the interior fields from the surface currents, the reciprocity theorem, and a “measurement matrix.” In contrast, the volume integral equation MoM (VMoM) requires determination of unknown fields throughout the volume of the body using the volume equivalence principle and the MoM.

The numerical technique that has been adopted for most of the early field intensity computations is the VMoM, employing the volume equivalence principle [26,27,42,43]. The MoM is used to transform the integral equation into a matrix equation by subdividing the body into N simply shaped cells. This is accomplished with the aid of an appropriate set of expansion functions, chosen to satisfy the boundary conditions, and a set of weighting (testing) functions to reduce the matrix fill-in time. The total electric field in each of the N cells is given by matrix inversion. A more detailed description of the volume integral equation method is included in the next section.

However, it should be noted that a fundamental limitation of this method is the use of full or nearly full matrices and, therefore, the requirement of extensive computer storage and long running time. Even with the availability of larger and faster computers, this difficulty is not completely resolved. The need for excessively large numbers of mathematical cells to render a more accurate representation of the body will give rise to an equally large and full matrix. The inversion of large, full matrices often leads to numerical instabilities in the solution. Nevertheless, the method does allow the use of inhomogenous models

with up to 1000 cells. In fact, this method has been employed, successfully, to calculate whole-body averaged absorption and to obtain regional distribution of absorbed RF energy using inhomogenous block models composed of rectangular cells [29–28,44]. This method also has been used to study the interaction of the near-zone field of an antenna with biological bodies [45,46].

10.4.1.3 SMoM

Another approach for predicting the distribution of absorbed electromagnetic energy is the SMoM [47–50]. This method makes use of two coupled integral equations, that is, the electric field and magnetic field integral equations for the tangential components of the field on the surface separating the biological body from air. The unknown surface currents are found by Fourier decomposition and the moment method. The fields inside the biological body are calculated using the previously computed surface currents, the reciprocity theorem, and the concept of measurement matrix [48,51–53].

The method begins with the matrix representation of the coupled integral equations. If the body is assumed to be rotationally symmetric, the incident wave and the induced current could then be expanded in a Fourier series expansion in the angle of rotation. This reduces the problem to that of solving a system of orthogonal modes. The method further expands the surface components in terms of triangular expansion or basis functions and allows the testing functions to be the complex conjugate of the basis functions taking advantage of the orthogonality property. Thus, the major advantage of introducing the Fourier series is to enable each mode to be treated completely independently of all other modes. This results in a much smaller-size, manageable matrix equation to be evaluated for the unknown expansion coefficients that determine the surface currents. It should be noted that for biological bodies, triangular expansion and testing functions are preferred over flat pulse expansion functions [47,48]. In fact, an expansion function with a continuous first derivation may constitute an even better choice for the expansion basis function. In any event, once the surface currents are obtained, the fields everywhere, or SAR at each point inside the body, can be calculated using the reciprocity theorem [52,53]. The total absorption can be found by integrating the surface Poynting vector.

The validity of SMoM has been substantiated by using a dielectric sphere [47]. Calculations for a human torso modeled by a homogenous muscle body of revolution with a height of 1.78 m at 30, 80, and 300 MHz showed enhanced absorption in the neck region for all three frequencies and both vertical and horizontal polarizations [48]. Note that the vertical direction is aligned with the long dimension of the torso and serves as the axis of symmetry. The strongest absorption in the torso model was found to occur with vertical polarization and near the first resonance frequency of the torso (80 MHz). In general, the surface integral equation method is applicable to any arbitrarily shaped homogenous body of revolution. The method can be used not only with incident plane waves but also with a wide variety of other field exposure conditions, including direct contact situations and near-zone sources.

Since both the surface and volume integral equation methods for field intensity prediction rely on the MoM for implementation, it is instructive to compare the relative advantages of these two techniques. For simplicity, consider a homogenous cube with N samples on each side: the computer storage requirements are N^2 and N^3 for the surface and volume integral methods, respectively [48]. For sufficient sampling to ensure accurate description of field variations, N is usually a large number. Thus, the surface integral equation method requires significantly fewer unknowns for homogenous models. Moreover, in cases where permittivity and conductivity values are large, such as in biological bodies, the wavelength becomes contracted inside the body, and a much larger number of cells than that indicated above may actually be needed. If the model is inhomogenous,

then the volume integral equation would prove to be more suitable. It is possible, however, to generalize the surface integral equation technique to account for inhomogeneities by employing the invariant imbedding procedure [54].

10.4.1.4 FEM

The FEM has been a preferred numerical algorithm in many fields of application. However, its use and popularity in predicting field intensities in biological systems have been modest until recent progress in mesh generation, boundary conditioning, and large matrix solvers. The FEM method is a near-neighbor, volume method for solving Maxwell's differential equations and is associated with a sparse system of equations [55,56]. Aside from the low memory requirement (on the order of N), an inherent attraction of FEM is its adaptability in modeling inhomogeneities and complex geometries. The feature of conforming and the variable-sized cell elements of the computational volume are extremely important in bioelectromagnetics.

The basic approach of the FEM method for predicting EMF distributions inside biological bodies starts by subdividing the physical space and biological body of interest into meshes of small volumes or cells of tetrahedral elements. This step is very important since the manner in which the volume is subdivided will dictate the computational resources required and the speed of the computation and accuracy of the results. Each cell element and node location will have to be systematically numbered and described. Once the volume has been subdivided, labeled, and the appropriate property values ascribed, the unknown field within each element is then approximated using linear extrapolation. A major step in FEM is the formulation of the system of linear equations using either the Ritz or the Galerkin algorithm with proper boundary conditions. There are two approaches to solve the system of linear algebraic equations: the direct method of Gaussian elimination or the iterative method that starts with an initial guess. In practice, either method can produce an approximate solution to the unknown field intensity with a prescribed accuracy.

It should be noted that a large region exterior to the biological body is often encountered in bioelectromagnetic situations, where the biological body, or portion of it, is part of a region into which electromagnetic energy is radiated and scattered. The region of space exterior to the biological body and applicator must be truncated with an artificial boundary to limit the volume elements and the number of unknowns. Consequently, an appropriate boundary condition needs to be established at this artificial boundary for a unique finite element determination of the induced fields inside the body. The most common boundary conditions selected for this purpose are the absorbing boundary conditions that minimize the nonphysical reflections from the artificial boundaries by making boundaries transparent to the scattered field.

Fairly large-scale calculations, on the order of 200,000 elements, have been conducted effectively in the workstation-computing environment. Specifically, detailed power deposition patterns have been simulated in full and partial models of the human body undergoing electromagnetic hyperthermia treatment for cancer [57]. In this case, the cell elements were generated from computerized tomographic data obtained on human patients.

10.4.1.5 FDTD Method

The FDTD approach is an attempt to solve Maxwell's curl equations by directly modeling propagation of waves into a volume of space containing the biological body. By repeatedly implementing a finite difference representation of the curl equations at each cell of

the corresponding space lattice, the incident wave is tracked as it first propagates to the body and then interacts with it through surface current excitation, transmission, and diffraction. This wave tracking process is completed when the steady-state behavior is observed at each lattice cell. Considerable simplification is achieved by analyzing the interaction of the wavefront with a part of the body surface at a time, rather than attempting a simultaneous solution of the entire problem.

The FDTD method has become one of the most successful methods for SAR calculations. The method was first proposed by Yee [58] and later developed by Taflove [59–61], Holland [62], and Kunz and Lee [63]. Several books [64–66] are devoted to the FDTD method and some of its applications. For bioelectromagnetic applications the FDTD method has been found to be extremely versatile and has been used for whole-body or partial-body exposures due to spatially uniform or nonuniform fields (far or near fields), sinusoidally varying EMFs, and transient fields such as ultra-wide-band (UWB) and electromagnetic pulses (EMPs) [67–71]. Accordingly, some details of FDTD are included in this section.

10.4.1.5.1 The Traditional FDTD Method

In this method, the time-dependent Maxwell's curl equations

$$\nabla \times \mathbf{E} = -\mu \frac{\partial \mathbf{H}}{\partial t} \quad (10.10)$$

and

$$\nabla \times \mathbf{H} = \sigma \mathbf{E} + \epsilon \frac{\partial \mathbf{E}}{\partial t} \quad (10.11)$$

are implemented for a lattice of subvolumes or Yee "cells" that may be cubical or parallelepiped with different dimensions, δ_x , δ_y , and δ_z in the x -, y -, or z -directions, respectively. The components of \mathbf{E} and \mathbf{H} are positioned about each of the cells as shown in Figure 10.12 and calculated alternately with half-time steps where the time

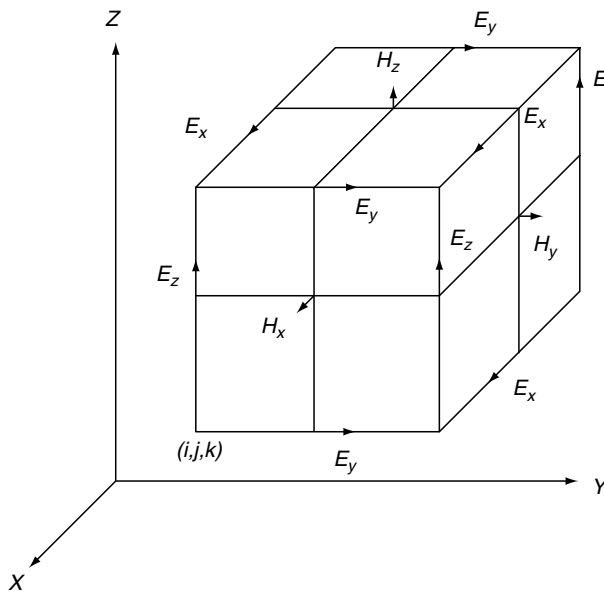


FIGURE 10.12

Unit cell of Yee lattice indicating positions for various field components.

step $\delta t = \delta/2c$. Here δ is the smallest of the dimensions used for any of the cells, and c is the maximum phase velocity of the fields in the modeled space. Since some of the modeled volume is air, c corresponds to the velocity of EM waves in air.

In the FDTD method, it is necessary to represent not only the scatterer or absorber, such as the human body or a part thereof, but also the EM sources, including their shapes, excitations, etc., if these sources are in the near-field region [70,71]. The far-field sources, on the other hand, are described by means of incident plane wave fields prescribed for a “source” plane [68,69], typically six to ten cells away from the exposed body. The source–body interaction volume is subdivided into Yee cells of the type shown in [Figure 10.12](#). The interaction space consisting of several hundred thousand to a few million cells is truncated by means of absorbing boundaries. The prescribed incident fields are tracked in time for all cells of the interaction space. The solution is considered completed when either the fields have died off or, for sinusoidal excitation, when a sinusoidal steady-state behavior for \mathbf{E} and \mathbf{H} is observed for the interaction space.

The body of interest is mapped into the lattice space by first choosing the lattice increment and then assigning values of permittivity and conductivity to each cell. The boundary conditions at media interfaces are naturally generated by the curl equations. Thus, once a computer program is developed, the basic routines need not be changed for different model geometries. In fact, inhomogeneities and fine structural details could be modeled with a maximum resolution of one unit cell.

Time stepping for the FDTD method is accomplished by an explicit finite difference procedure [58,64]. For a cubic-cell lattice space, this procedure involves positioning the electric and magnetic field components about a unit cell of the lattice and then evaluating the components at alternate half-time steps. In this manner, centered difference expression can be used for both the space and the time increments without solving simultaneous equations to compute the fields at the latest time step.

The explicit formulation of the FDTD method is particularly suited for execution with minimum computer storage and run time using current array-processing computers. The required computer storage and run time increase only linearly with N , the number of cells. In fact, it has been shown that the FDTD method is capable of solving for more than 1 million unknown field components within a few minutes on an array-processing computer. Field intensities have been predicted to within 2.5% accuracy relative to known analytical and experimental bench marks. Recently, this FDTD technique has been improved to allow solutions for field penetration and absorption in large, complex, inhomogenous, and irregularly shaped biological bodies in three dimensions, with millimeter range spatial resolution. With the exception of a few early attempts with lossy biological objects [59,67], a majority of early efforts have been directed toward application of the FDTD method to electromagnetic interaction in time-varying inhomogenous media [60], and with metallic bodies of revolution [61]. However, during the last decade, the FDTD method has become the most extensively used numerical procedure for bioelectromagnetic computations.

10.4.1.5.2 Frequency-Dependent FDTD Formulation

For short pulses where wider bandwidths are generally involved, a frequency-dependent FDTD or $(FD)^2TD$ method is needed. Two general approaches have been used for the $(FD)^2TD$ method. One approach is to convert the complex permittivity from the frequency domain to the time domain and convolve this with the time domain electric fields to obtain time domain fields for the dispersive material. This discrete time domain method may be updated recursively for some rational forms of complex permittivity, which removes the need to store the time history of the fields and makes the method feasible. This method has

been applied to materials such as water, for which the permittivity may be described by a first-order Debye relaxation equation [72–74] or more complex materials with dielectric properties given by a second-order Lorentz equation with multiple poles [75].

A second approach is to add a differential equation relating the electric flux density \mathbf{D} to the electric field \mathbf{E} and solve this new equation simultaneously with the standard FDTD equations. This method has been applied to 1-D and 2-D examples with materials described by a first-order Debye equation or second-order single-pole Lorentz equation [76], and to a 3-D sphere and homogenous two-thirds muscle-equivalent man model with properties described by a second-order Debye equation [77,78]. In the following we describe this differential equation approach, which has now been used for induced current and SAR calculations for a heterogenous model of the human body [79].

The time-dependent Maxwell's curl equations used for the FDTD method have already been given as [Equation 10.10](#) and [Equation 10.11](#). The curl \mathbf{H} can also be written as follows:

$$\nabla \times \mathbf{H} = \frac{\partial \mathbf{D}}{\partial t} \quad (10.12)$$

where the flux density vector \mathbf{D} is related to the electric field through the complex permittivity $\varepsilon^*(\omega)$ of the local tissue by the following equation:

$$\mathbf{D} = \varepsilon^*(\omega) \mathbf{E} \quad (10.13)$$

Since Equation 10.10 and Equation 10.12 are to be solved iteratively in the time domain, Equation 10.13 must also be expressed in the time domain. This may be done by choosing a rational function for $\varepsilon^*(\omega)$, such as the Debye equation with two relaxation constants ([see Chapter 1](#)):

$$\varepsilon^*(\omega) = \varepsilon_0 \left[\varepsilon_\infty + \frac{\varepsilon_{s1} - \varepsilon_\infty}{1 + j\omega\tau_1} + \frac{\varepsilon_{s2} - \varepsilon_\infty}{1 + j\omega\tau_2} \right] \quad (10.14)$$

Rearranging Equation 10.14 and substituting in Equation 10.13 gives

$$\mathbf{D}(\omega) = \varepsilon^*(\omega) \mathbf{E}(\omega) = \varepsilon_0 \frac{\varepsilon_s + j\omega(\varepsilon_{s1}\tau_2 + \varepsilon_{s2}\tau_1) - \omega^2\tau_1\tau_2\varepsilon_\infty}{1 + j\omega(\tau_1 + \tau_2) - \omega^2\tau_1\tau_2} \mathbf{E}(\omega) \quad (10.15)$$

where the static (zero frequency) dielectric constant is given by

$$\varepsilon_s = \varepsilon_{s1} + \varepsilon_{s2} - \varepsilon_\infty \quad (10.16)$$

Assuming $e^{j\omega t}$ time dependence, Equation 10.15 can be written as a differential equation in the time domain:

$$\tau_1\tau_2 \frac{\partial^2 \mathbf{D}}{\partial t^2} + (\tau_1 + \tau_2) \frac{\partial \mathbf{D}}{\partial t} + \mathbf{D} = \varepsilon_0 \left[\varepsilon_s \mathbf{E} + (\varepsilon_{s1}\tau_2 + \varepsilon_{s2}\tau_1) \frac{\partial \mathbf{E}}{\partial t} + \varepsilon_\infty \tau_1\tau_2 \frac{\partial^2 \mathbf{E}}{\partial t^2} \right] \quad (10.17)$$

For the (FD)²TD method, Equation 10.10 and Equation 10.12 need to be solved subject to Equation 10.17. These equations can be written in the difference form [77,78] and solved to find \mathbf{E} , \mathbf{H} , and \mathbf{D} at each cell location. The $\mathbf{E} \rightarrow \mathbf{H} \rightarrow \mathbf{D}$ loop is then repeated until the pulse has died off.

10.4.2 Human Bodies Exposed to EMFs

Computational algorithms based on numerical techniques described in the previous section have been applied to predict field intensities and SAR distributions in anatomically realistic models of human bodies. However, the use of a given numerical method and the number of computational cells involved in the models typically dictate the applicability of the techniques, how real the model is, the degree of accuracy attainable, and its domain of applicability. In the following sections, a few of the models will be described, and they will be followed by some representative results obtained using the models.

10.4.2.1 Realistic Models of the Human Body

Models proposed as better representations of the complex geometry and composition of the human body include constructions using small-volume cubic cells or cell meshes and anatomically based models generated from computerized tomographic and magnetic resonance image data.

10.4.2.1.1 Cubic-Cell Models

Models of the human body consisting of 200 to 1000 cubic cells that account more realistically for the gross anatomic and biometric characteristics of human bodies have been used by several investigators [24–28]. The models are 1.75 m tall and can be made either homogenous or inhomogenous by choosing an equivalent or a volume-weighted complex permittivity for each cell. The cubic-cell model has been employed successfully to calculate whole-body averaged absorption. It is important to note that for subdivision with less than three cells per wavelength, the magnitude and phase resolutions would be such that even with convergence the reliability of the MoM-computed SAR would be questionable. Therefore, if the interest is primarily in whole-body SAR, this model may provide quite adequate results for frequencies lower than 30 MHz. To achieve more accurate structural representation of the human body, anatomically based models have been offered in recent years.

10.4.2.1.2 Millimeter-Resolution Model Based on Magnetic Resonance Imaging Scans of the Human Body

A new millimeter-resolution model of the human body has been developed from the magnetic resonance imaging (MRI) scans of a male volunteer of 176.4-cm height and 64-kg weight [80,81]. The MRI scans were taken with a resolution of 3 mm along the height of the body and 1.875 mm for the orthogonal axes in the cross-sectional planes. Even though the height of the volunteer was quite appropriate for an average adult male, the weight was somewhat lower than an average of 71 kg, which is generally assumed for an average male. This problem can, to some extent, be ameliorated by assuming that the cell dimensions for the cross sections are larger than 1.875 mm by the ratio of $(71/64)^{1/2} = 1.053$. By taking the larger cell dimensions of $1.053 \times 1.875 = 1.974$ mm for the cross-sectional axes, the volume of the model can be increased by $(1.053)^2 = 1.109$, that is, by about 10.9%, which results in an increase of its weight by approximately the same percentage, that is, to a new weight of approximately 71 kg. The MRI sections were converted into images involving 29 tissue types whose electrical properties can then be prescribed at the exposure frequency. The tissue types are fat, muscle, bone, cartilage, skin, brain, nerve, cerebrospinal fluid (CSF), intestine, spleen, pancreas, heart, blood, eye, eye humor, eye sclera, eye lens, ear, liver, kidney, lung, bladder, stomach, ligament, compact bone, testicle, spermatic cord, prostate gland, and erectile tissue. As described above, this

model has been used to calculate the electromagnetic absorption in the human head, neck, and shoulders for cellular telephones operating at frequencies of 800 to 900 MHz. Because of the localized nature of EMFs, it was possible to use the model corresponding to the top 42 cm of the body for SAR calculations.

10.4.2.1.3 *The “Visible Human” Model*

The Visible Human (VH) Project, developed by the National Library of Medicine, is a 3-D digital image library representing an adult human male and female [82]. The dataset for both male and female includes photographic images obtained through cryosectioning of human cadavers and digital images obtained by computer tomography and MRI of the same cadavers. In particular, the photographic images represent a highly accurate and realistic counterpart of the anatomical cross sections contained in human anatomy atlases. The male dataset, the first to be constructed, consists of 1871 digital axial images obtained at 1.0-mm intervals, with a pixel resolution of 1 mm, while the female one contains 5189 digital axial images, obtained with a finer spatial step of 0.33 mm. While these digital datasets represent a unique tool to explore human anatomy, their direct use for computational electromagnetic dosimetry is limited by the fact that images cannot be directly used as an input for a numerical electromagnetic tool but must be converted to a so-called “segmented” version. A segmented model is a model where every pixel, usually called in such models “voxel,” does not contain information about the color (like in digital images) but rather a label that is uniquely associated to a given tissue. In such a way, it is possible to know which tissue fills each of the model voxels and hence assign the correct complex permittivity values to be used in numerical simulations.

Segmentation of the original image sets is a complex and time-consuming activity, which is difficult to carry out making exclusive use of automatic procedures, such as contour recognition algorithms, but inevitably requires intervention by experts in human anatomy. The segmentation procedure has been carried out for the male model by researchers at the Air Force Research Laboratory, Brooks Air Force Base, TX [83]. The final segmented model, made freely available to the scientific community, comprises $586 \times 340 \times 1878$ voxels with a resolution of $1 \times 1 \times 1$ mm, and is segmented in about 40 different tissue types [84]. The model has been widely used to study both whole-body and localized human exposure to EMFs radiated by different types of sources and is now being included in many commercially available electromagnetic simulation tools with capabilities for dosimetric evaluation.

10.4.2.2 *Currents Induced in the Human Body by Low-Frequency EMFs*

This section reports the results obtained for low-frequency EMF. Specifically, it includes the use of the impedance method to calculate currents induced in the human body by the EMFs of electric blankets. It also includes the use of the FDTD method for calculations of internal **E** and **H** fields and induced current densities for exposure to electric, magnetic, or combined electric and magnetic fields at power-line frequencies. The results given below were obtained using a 1.31-cm resolution, anatomically based model of the human body. Since the term $j\omega\epsilon$ can be neglected as compared to σ for the various tissues at ELF including electric power frequencies (50/60 Hz), the impedances for the various cells of the model given by [Equation 10.9](#) can be replaced by resistances. It is recognized that the conductivities of various tissues, for example, skeletal muscle, heart, and bone, are anisotropic for power-line frequencies [34,35,85]. This has been neglected in this case, however, and average values of conductivities given in [Table 10.3](#) have been taken for the various tissues for the calculations.

TABLE 10.3

Tissue Conductivities Used for Calculations
at the Power-Line Frequency of 60 Hz

Tissue Type	σ (S/m)
Air	0
Muscle	0.52 or 0.11
Fat, bone	0.04
Blood	0.6
Intestine	0.11
Cartilage	0.04
Liver	0.13
Kidney	0.16
Pancreas	0.11
Spleen	0.18
Lung ^a	0.04
Heart	0.11
Nerve, brain	0.12
Skin	0.11
Eye	0.11

^aThe dielectric properties of the lung consist of 33% lung tissue and 67% air.

10.4.2.2.1 Electric Blankets

To illustrate the use of the impedance method, currents induced in the human body by the EMFs of two types of electric blankets have been calculated [1,2]. The two models used for the blanket are (a) a low-magnetic-field blanket and (b) a conventional (pre-1990) electric blanket. The low-magnetic-field blanket uses two parallel leads carrying equal and opposite currents to reduce the net magnetic field around the conductors. The two leads are separated typically by 1.5 mm and are embedded in a positive temperature coefficient (PTC) conductive polymer and insulated by polyvinyl chloride (PVC). The PTC conductive polymer surrounding the two leads may be represented by a set of distributed resistors, which would result in linearly decreasing equal but opposite currents flowing through the two leads over the length of the wiring used for the blanket. By comparison, the conventional electric blanket uses a resistive alloy wire wrapped on a nylon cord and insulated with PVC. Because of the distributed resistance of the wire, this blanket would therefore have a linearly diminishing voltage and identical magnitude of current over the length of the wiring used for the blanket.

The validity of the calculated results has been established by comparing the results obtained using the impedance algorithm and those reported by others. The calculated fields are in excellent agreement with the data given by Florig et al. [86] and Hayashi et al. [87].

Currents are induced in the body by the following sources:

1. Time- and spatially varying magnetic fields of the blanket induced voltages in the various resistance loops of the body.
2. Currents launched into different subareas at the body surface by means of the capacitively coupled currents from the various conductors of the blanket.

The spatial variations of the magnetic fields were calculated from Biot-Savart's law for a short current-carrying conductor [2]. By integrating it over the entire length of the

current-carrying conductors, one can obtain the vector magnetic fields at the centers of the cells representing the model of the human body or any of the other points in space. From the vector magnetic fields thus calculated for each of the cell centers for the impedance model of the human body, the induced voltages for each of the faces of the cells can be written [32]. This information is then used to calculate the induced currents for the various impedances, that is, resistances. The average current densities J_x , J_y , and J_z for each of the cell centers can be obtained by taking the average of the currents through the resistances representing each of the four edges of the cell in the respective directions and dividing the same by the cross-sectional area δ^2 ($= 1.31 \times 1.31 \text{ cm}$).

To calculate the electric field distribution in air, a 3-D impedance model consisting of capacitors representing the space between the various faces of the cells was used. For cubic cells of dimension $\delta = 1.31 \text{ cm}$, the capacitances used are $\epsilon_0 \delta^2/\delta = 0.116 \text{ pF}$.

For currents induced in the human body due to electric fields, it should be recognized that the energized conductors of the blanket are capacitively coupled to the body. The capacitance between a given conductor and the highly conducting human body can be obtained by using an expression similar to that for a conductor at a distance S from the ground plane. Capacitance per unit length C of a wire of diameter d parallel to but separated at a distance S from the ground plane is given by

$$C = (2.73\epsilon_{\text{eff}})/[\log_{10}(4S/d)], \text{ pF/m} \quad (10.18)$$

For a spacing $S = 5 \text{ mm}$ and a wire diameter $d = 0.8 \text{ mm}$, and for $\epsilon_{\text{eff}} = 2.5\epsilon_0$, which is a value intermediate between the permittivity ϵ_0 for air and $4\epsilon_0$ for the material of the blanket, we can calculate $C = 43.1 \text{ pF/m}$. For a cell length $d = 1.31 \times 10^{-2} \text{ m}$, the coupling capacitance C_c between the wire and the cell can be calculated to be 0.565 pF . Since the interconductor spacing of 1.5 mm for a PTC blanket is fairly small as compared to the cell size, a proportionately smaller resistance is taken for the tissue-equivalent cells immediately underneath the conductors for the direction parallel to the interconductor spacing. Capacitances of 0.565 pF are taken from each of the conductors of the PTC blanket to the appropriate points on the impedance model of the human body. In the presence of an electrical grounding surface, the space underneath the model is represented by a 3-D network of capacitors, each of value 0.116 pF , representing the air space between the various faces of the cubic cells of dimension $d = 1.31 \text{ cm}$ for each of the sides.

For the PTC low-magnetic-field blanket, a constant voltage of 110 V AC is taken between the conductors of the twin-lead wiring for calculation of currents induced or injected into the human body as a result of electric fields. For calculating the magnetic fields, an input current of 1 A is taken. On account of the conductive polymer surrounding the parallel wires, this current diminishes linearly to zero at the end of the PTC wiring. This assumes a blanket input power of 110 W under normal operating conditions. If magnetic fields or induced current densities due to higher input powers are desired, the numbers calculated for 1 A input current may then be multiplied by the appropriate factor.

The conventional blanket, on the other hand, uses a resistive conductor for which the voltage diminishes linearly from 110 to 0 V over the length of the wiring. For this blanket the current throughout the length of the wiring is the same as at the input, that is, 1 A , which is assumed for the calculation of magnetic fields.

The magnetically induced, section-averaged magnitudes of the total current densities from head to feet for the two types of blankets are shown in Figure 10.13a and b, respectively. For these calculations, the wiring of the blanket was taken to be 0.5 cm from the surface of the body. Nearly identical current densities were also obtained for a grounding plate underneath the body at distances of 0.25 , 0.5 , and 1.0 m . It is interesting to

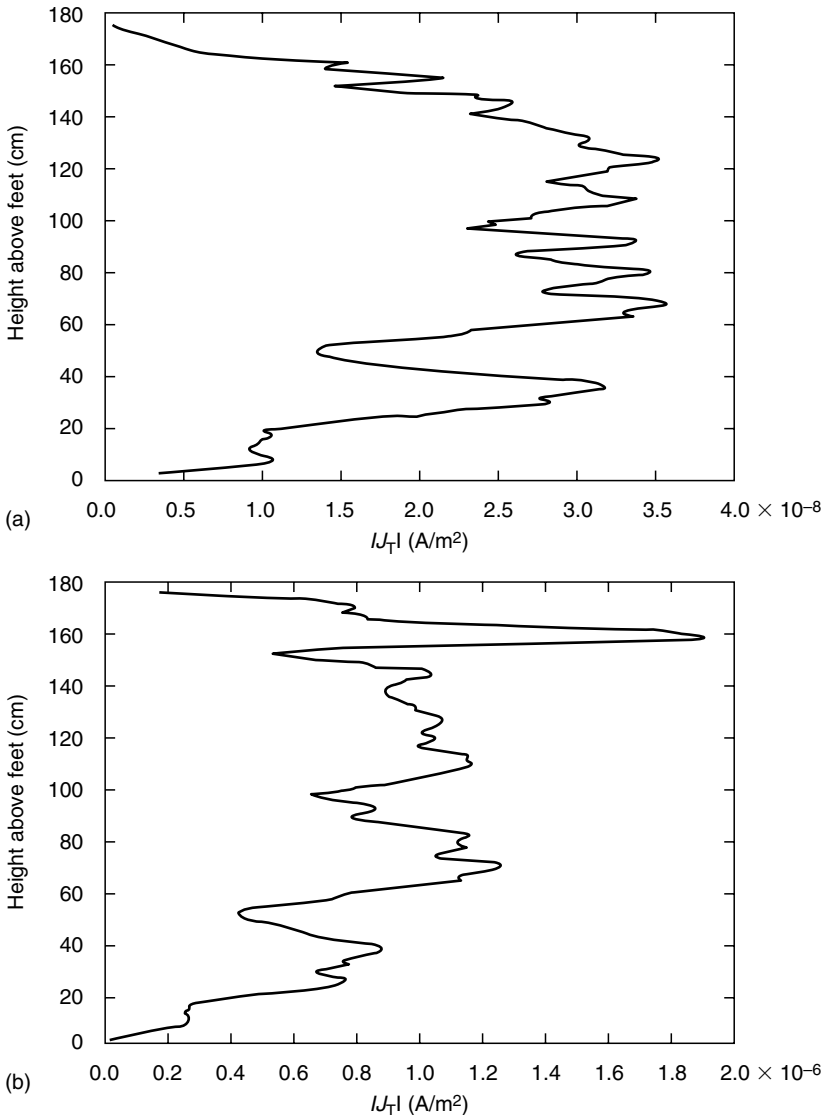


FIGURE 10.13

Section-averaged magnitudes of total current densities for the various sections of the body for magnetic fields of the blankets. Nearly identical current densities were obtained also for a grounding plate at distances of 0.25, 0.5, and 1.0 m underneath the body. Input current = 1 A.

note that the induced current densities are larger by a factor of about 500 for the conventional blanket vis-a-vis those for the low-magnetic-field blanket.

The calculated section-averaged magnitudes of the total current densities due to electric fields of both the blankets in the absence of a grounded plane are shown in Figure 10.14a and b, respectively. It should be noted that while the current densities induced by the electric fields of a low-magnetic-field blanket (Figure 10.14a) are considerably higher than those due to magnetic fields (Figure 10.25a), the converse is true for a conventional blanket. For this blanket, the current densities induced by the magnetic fields (Figure 10.13b) are higher than those due to electric fields (Figure 10.14b). In fact, while the current densities due to magnetic fields are fairly small for a low-magnetic-field blanket

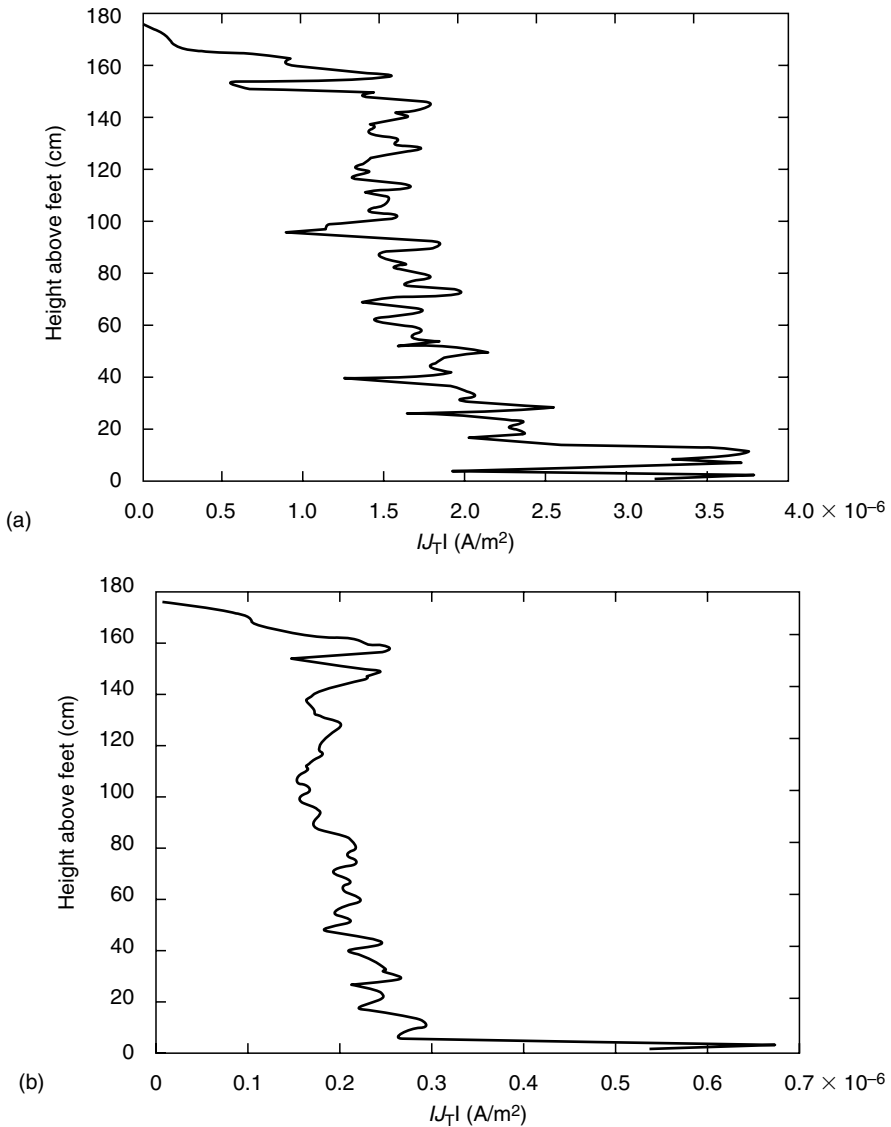


FIGURE 10.14

Section-averaged magnitudes of total current densities for the various sections of the body for electric fields of the blankets. No ground plane underneath the body.

as compared to those for a conventional blanket, the current densities due to electric fields of a low-magnetic-field blanket are even higher than those for a conventional blanket (see Figure 10.14a and b). The reasons for these observations can be seen from the values of magnetic and electric fields given in Table 10.4 for the two types of blankets, respectively. While fairly small magnetic fields are calculated for the low-magnetic-field blanket as compared to those for the conventional blanket, the converse is true for the electric fields created by these blankets. As seen in Table 10.5, somewhat higher electric fields are created by the low-magnetic-field blanket as compared to those for the conventional blanket. This is likely due to the higher potential difference between the twin-lead conductors that are used for the low-magnetic-field blankets.

TABLE 10.4

Comparison of the Calculated and Measured Magnetic Field (μT) and Electric Field (V/m) Close to a Flat Blanket [2]

	Grid Size (cm)	Calculated	Measured
<i>Low-magnetic-field blanket^a</i>			
<i>Magnetic field</i>			
Average	1.31×1.31 10.5×10.5	0.056 0.072	— 0.09
Peak	—	0.20	0.26
<i>Electric field</i>			
Average	1.31×1.31 10.5×10.5	103.7 144.6	— 111.2
Peak	—	159.7	176.0
<i>Conventional electric blanket^b</i>			
<i>Magnetic field</i>			
Average	1.31×1.31 10.5×10.5	2.16 2.45	— 2.18
Peak	—	3.52	3.94
<i>Electric field</i>			
Average	1.31×1.31 10.5×10.5	57.3 70.1	— 95.4
Peak	—	176.1	167.2

^aFor this blanket, the magnetic-field results are normalized for a blanket input current of 1.227 A, that is, a power input of 135 W.

^bFor this blanket, an input current of 1 A is assumed.

10.4.2.2.2 Power Transmission Lines

The FDTD method has been used for calculations of internal \mathbf{E} and \mathbf{H} fields and induced current densities for exposure to electric, magnetic, or combined electric and magnetic fields at power-line frequencies [37]. While recognizing that the conductivities of many biological tissues (skeletal muscle, bone, etc.) are highly anisotropic for power-line frequencies, however, the effect of anisotropy is neglected for the sake of simplicity. They could be included in more complex models by separately identifying these tissues.

Both sinusoidal and prescribed time-varying incident fields can be used with the FDTD procedure—hence the method is well suited also for transient exposures that are often of interest at power-line-related frequencies. For sinusoidally varying fields, the solution is completed when a sinusoidal steady-state behavior for \mathbf{E} and \mathbf{H} fields is observed for each of the cells. For lossy biological bodies this typically takes a time step on the order of three to four time periods of oscillation. Since Δt is fixed for a given cell size, a larger number of iterations are therefore needed at lower frequencies. Because of the large number of iterations, the FDTD procedure would be clearly inapplicable for calculations at power-line frequencies were it not for the quasi-static nature of the coupling at low-frequencies [16,88,89]. Thus, the field outside the body does not depend on the internal tissue properties, but it depends only on the shape of the body so long as the quasi-static approximation holds, that is, the size of the body is a factor of 10 or more smaller than the wavelength, and $|\sigma + j\omega\epsilon| \gg \epsilon_0$, where σ and ϵ are the conductivity and the permittivity of the tissues, respectively; $\omega = 2\pi f$ is the radian frequency; and ϵ_0 is the permittivity of the free space outside the body. Under these conditions, the electric fields in air are normal to the body surface, and the internal tissue electric fields can be obtained from the boundary conditions in terms of fields outside:

TABLE 10.5Reported SAR Values, Averaged over the Whole Body (SAR_{WB}), for Plane Wave Exposures

Frequency (MHz)	SAR (W/kg)					
	Grounded		Isolated [102]	Isolated (resolution 3 mm) [103]		Isolated (resolution 5 mm) [103]
	Shoes [98]	Grounded [102]		[103]	[103]	
10	0.027	0.045				
20	0.102	0.182	0.021			
30	0.180	0.313	0.054			
40	0.291	0.348	0.114			
50	0.230	0.293	0.199			
60	0.177	0.231	0.288			
70	0.152	0.188	0.302	0.270	0.290	
80	0.130	0.162	0.251			
90	0.107		0.195			
100	0.092	0.118	0.155			0.123 ^a
200	0.062	0.081	0.080	0.048	0.051	0.078 ^b
300	0.054					
400	0.060	0.063	0.063	0.064	0.060	
500	0.058					0.060
600	0.057		0.063	0.067	0.066	
700	0.059					
800	0.061			0.064	0.063	
900	0.061	0.062	0.064			
1000				0.063	0.061	0.057
1400			0.063			
1800		0.057	0.058	0.056	0.060	
2000				0.055	0.060	

^aThe frequency considered is 120 MHz.^bThe frequency considered is 210 MHz.

$$j\omega\epsilon_0E_0 = (\sigma + j\omega\epsilon)E_{\text{tissue}} \quad (10.19)$$

A higher quasi-static frequency f' , at 5 to 20 MHz, may therefore be used for irradiation of the E model, and the internal fields E thus calculated may be scaled back to frequency f of interest, for example, 60 Hz. Since in the FDTD method, one needs to calculate in the time domain until convergence is obtained, this frequency scaling to 5 to 20 MHz for f reduces the required number of iterations by over five orders of magnitude. From Equation 10.19 we can write

$$\omega'(\sigma + j\omega\epsilon)E_{\text{tissue}}(f) = \omega(\sigma' + j\omega\epsilon')E'_{\text{tissue}}(f') \quad (10.20)$$

or

$$E_{\text{tissue}}(f) = (f\sigma'/f'\sigma)E'_{\text{tissue}}(f') \quad (10.21)$$

assuming that $\sigma + j\omega\epsilon \sim \sigma'$ at both f' and f [2,90]. To validate the use of a higher frequency f to obtain induced E fields at ELF frequencies, test cases involving homogenous and layered spheres have been used. Excellent agreement between the numerical and analytical results lends support to the validity of the FDTD method for calculating internal E fields and current densities at power-line-related frequencies. It should be noted that incident E and H fields of any orientation and relative magnitudes can be prescribed in the FDTD method, allowing the possibility of calculations for realistic

exposure conditions. Also, the choice of a considerably higher frequency such as 5 to 20 MHz reduces the number of iterations needed to obtain converged results by five to six orders of magnitude as compared to those that would be needed at ELF frequencies of 10 Hz to 1 kHz.

Some calculated results using a 16-tissue, 1.31-cm resolution, anatomically based model of the human body are given in Figure 10.15. A frequency f' of 5 to 10 MHz was used to reduce the computation time. At the higher irradiation frequency f' , $\sigma' = \sigma$ was assumed, that is, conductivities of the various tissues at 60 Hz. Furthermore, the incident E field, $E_i(f') = 60E_i(f)/f'$, was used to obtain $E_{\text{tissue}}(f)$ at, say, $E_i(f) = 10 \text{ kV/m}$. The incident magnetic field $H_i(f')$ has similarly been taken to be considerably lower ($= 60H_i(f)/f'$) to account for the fact that the induced current densities and internal electric fields are proportional to the frequency of the incident fields and would therefore be higher at the assumed frequency f' . Recognizing the anisotropy in the conductivity of skeletal muscles, two different values of muscle conductivities are taken for curves (1) and (2). For these curves a higher conductivity of 0.52 S/m is taken for the skeletal muscle, and an average value of 0.11 S/m is taken for the muscle in the interior of the body. For curves (3) and (4), however, a lower conductivity of 0.11 S/m is taken for all of the muscle, interior or skeletal. The results shown in Figure 10.15, curves (1), (3), and (4) are for $E_{\text{inc}} = 10 \text{ kV/m}$ (vertical) and $H_{\text{inc}} = 26.5 \text{ A/m}$ ($B_{\text{inc}} = 33.3 \mu\text{T}$) from side to side of the model. To point out the preponderance of the induced currents due to incident electric field, $H_{\text{inc}} = 0$ is assumed for the calculations shown in curve (2). It is interesting to note that the layer currents due to E -field exposure alone are almost 98% to 99% of the currents calculated for the combined electric and magnetic fields. It is also interesting to note that the calculated foot currents of 155 to 160 μA are in excellent agreement with 165 μA that would be projected from the measurements of Deno [91] for the human body. The variations of the induced currents calculated along the height of the body have been checked against the results by DiPlacido et al. [92]. The agreement with the results of these two authors who had

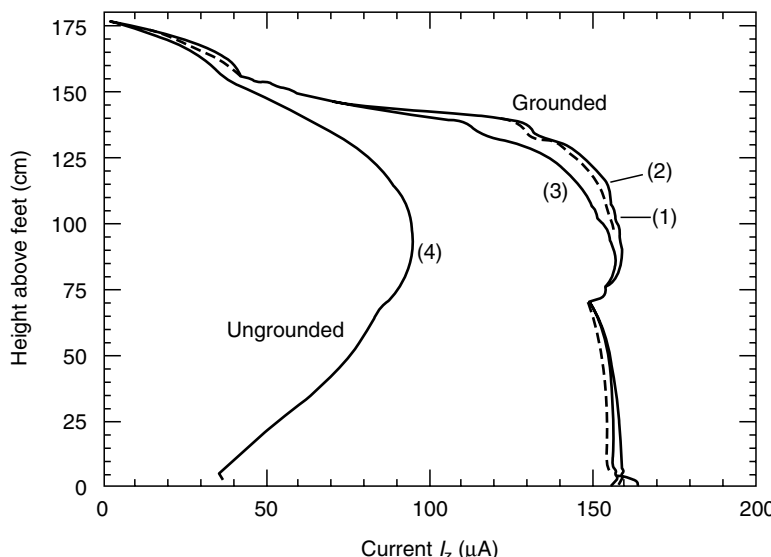


FIGURE 10.15

Calculated layer currents for anatomically based grounded and ungrounded models exposed to EMFs at 60 Hz. For curves (1) and (2), $s = 0.52 \text{ S/m}$ for skeletal muscle, and $s = 0.11 \text{ S/m}$ for the interior muscle. For curves (3) and (4), $s = 0.11 \text{ S/m}$ for all of the muscle. $E = 10 \text{ kV/m}$ (vertical), $H = 26.5 \text{ A/m}$ from side to side for all of the curves except for curve (2), for which only E -field exposure is assumed.

used a vertical electric field such as that under a high-voltage power line was found to be very good [37].

10.4.2.3 Absorption in Human Bodies Exposed to Far Field of RF Sources

As noted, the configuration and frequency of the electromagnetic source and the geometry and composition of the biological body will influence the induced field and power absorption and distribution inside the body. Moreover, the field emitted from a source is dictated by the frequency, size, and configuration of the source. Near an antenna, the radiated energy is in the form of a spherical wave in which the wave fronts are concentric shells. The spheroidal wave front expands as the wave propagates outward from the source. At distances far from the source, the radius of curvature of the spherical shells becomes so large that the wave front would essentially appear as a plane. They are therefore referred to as plane waves. Plane waves are important since their behavior is well quantified; the fields are uniform in planes normal to the direction of propagation, and the power density varies only in the direction of propagation. In this case, both electric and magnetic fields of the propagating wave are orthogonal in space and lie in the plane of the wave front, and are related through the intrinsic impedance of the medium. In other words, in the far or radiation zone, the electric and magnetic fields have only transverse components.

In this section, we shall briefly summarize some of the efforts devoted to field computation using various models of the human body, which consists of large quantities of numerical cells, and present some results obtained for plane wave exposures. Note that some, especially the simpler, models are of interest primarily for whole-body SAR and can provide quite adequate results for frequencies lower than 30 MHz. To achieve more accurate structural representation of the human body, anatomically based models are needed.

10.4.2.3.1 SAR Induced in Cubic-Cell Models

The VMoM for field computation has been used for models of the human body consisting of 200 to 1000 cubic cells. These models account for the gross anatomic and biometric characteristics of human bodies and have been used by several investigators [24–28]. The models are 1.75 m tall and can be made either homogenous or inhomogenous by choosing an equivalent or a volume-weighted complex permittivity for each cell. The cubic-cell model has been employed, successfully, to calculate whole-body averaged absorption. It is important to note that for subdivision with less than three cells per wavelength, the magnitude and phase resolutions would be such that even with convergence the reliability of the MoM computed SAR would be questionable.

According to the MoM, the body may be partitioned into N cubic subvolumes or cells that are sufficiently small for the electric field and dielectric permittivity to be constant within each cell. The integral equation is then transformed into a system of $3N$ simultaneous linear equations for the three orthogonal components of the electric field at the center of each cell. The simultaneous equations may be written in matrix form as

$$[G][E] = -[E^i] \quad (10.22)$$

where $[G]$ is a $3N \times 3N$ matrix and $[E^i]$ and $[E]$ are column matrices representing incident and induced electric fields at the center of each cell. The elements of $[G]$ can be evaluated as shown in Liversy and Chen [24]. In particular, the diagonal elements of the $[G]$ matrix may be evaluated exactly by approximating each subvolume with a sphere of equal volume centered at the position of an interior point. If the actual shape of the cell differs

appreciably from that of a sphere, this approximation may lead to unsatisfactory numerical results [36]. In such cases, a small cylindrical volume may be created around an interior point. It may also be necessary to evaluate these terms by numerical integration throughout the cubic subvolume for increased accuracy. The evaluation of off-diagonal elements of the $[G]$ matrix is considerably simplified since it does not involve principal value operations. Therefore, for a given applied field configuration, the induced electric fields inside the body are obtained by matrix inversion. That is,

$$[E] - [G]^{-1}[E^i] \quad (10.23)$$

Factors that influence the computational accuracy include frequency, body size, cell dimensions, and computer memory. It has been found that reliable numerical results can be obtained if the linear dimensions of the cell do not exceed a quarter free-space wavelength [24]. For a computer with sufficient capacity to invert a 120×120 matrix, the maximum number of cells is limited to 40. If we assume, for simplicity, symmetries between the right and the left half and the front and the back of a 1.7-m-tall adult human body, this computer would handle approximately a cell size around 10^{-5} m^3 . Once the 10^{-5} m^3 cell size is adopted, 750 MHz would be the highest frequency that can be considered for field intensity calculation without violating the criterion that the linear dimension of the cell not exceed a quarter free-space wavelength.

The computational resources necessary to obtain even a regional SAR using this MoM approach are quite extensive. A relatively full complex matrix, $3N \times 3N$ in dimensions, is required for a model with N cells. The computation time required for a noniterative solution of the matrix equation is therefore proportional to a value between N^2 and N^3 , which increases rapidly as N increases. The faithfulness with which a cubic-cell model approximates the detailed structure of a biological body and the maximum usable frequency increases with the number of cells. In fact, substantial errors will occur if

$$N \leq (2\pi L)/(\lambda' 6^{1/2}) \quad (10.24)$$

where L/λ' is the ratio between the linear dimension of the body and the wavelength in the body.

The accuracy of the numerical method can be verified by comparison with known results from exact analytic solutions based on well-characterized geometric bodies, such as spheres. It should be noted that perfect agreement between the exact solution, based on Mie theory, and the numerical method, based on the volume integral equation, is not expected unless a large number of cubic cells are used to simulate the sphere. [Figure 10.16](#) shows one eighth of a sphere approximated by one eighth of a “cubic model of a sphere,” which is constructed from 73 cubic cells. Clearly, a better approximation can be achieved by a larger number of smaller cubic cells. Nevertheless, for a brain sphere constructed from 40 cubic cells at a frequency of 918 MHz, the computed maximum field intensity deviated from the exact solution by less than 9% [93].

A model of a human body consisting of 180 cubic cells that accounts for the anatomic and biometric characteristics of human beings is shown in [Figure 10.17](#). The model is 1.75 m tall and can be made either homogenous or inhomogenous by using an equivalent or a volume-weighted complex permittivity for each cell [94]. The average absorption or whole-body SAR for the model of the human body shown in Figure 10.17 as a function of frequency is illustrated in [Figure 10.18](#). The electric field vector is along the height of the body, and the plane wave propagates from front to back of the model with an incident power density of 10 W/m^2 . A homogenous complex permittivity approximately two thirds of that for muscle is used in the calculations. Note that the whole-body SAR

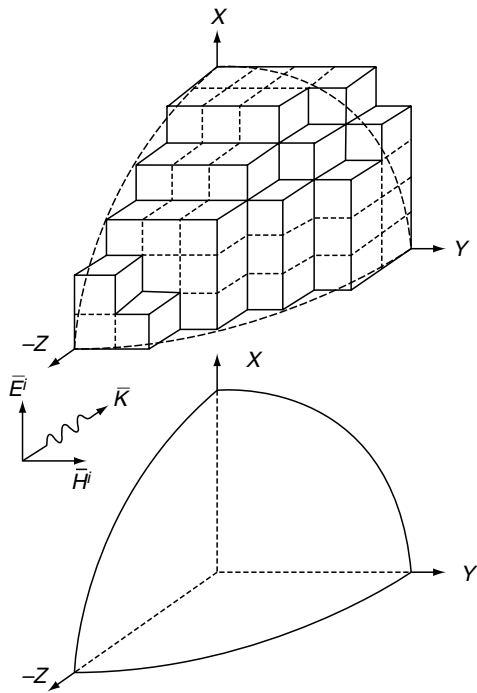


FIGURE 10.16
Approximation of one eighth of a sphere by an equivalent cubic-cell-formed structure.

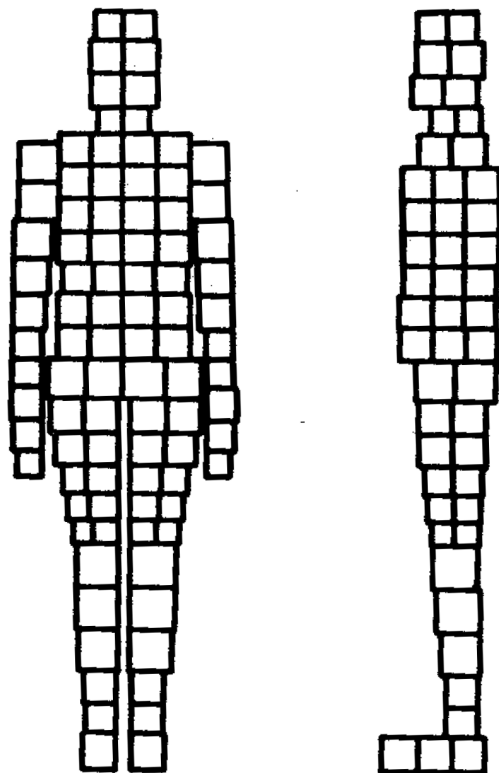


FIGURE 10.17
A cubic-cell representation of the human body.

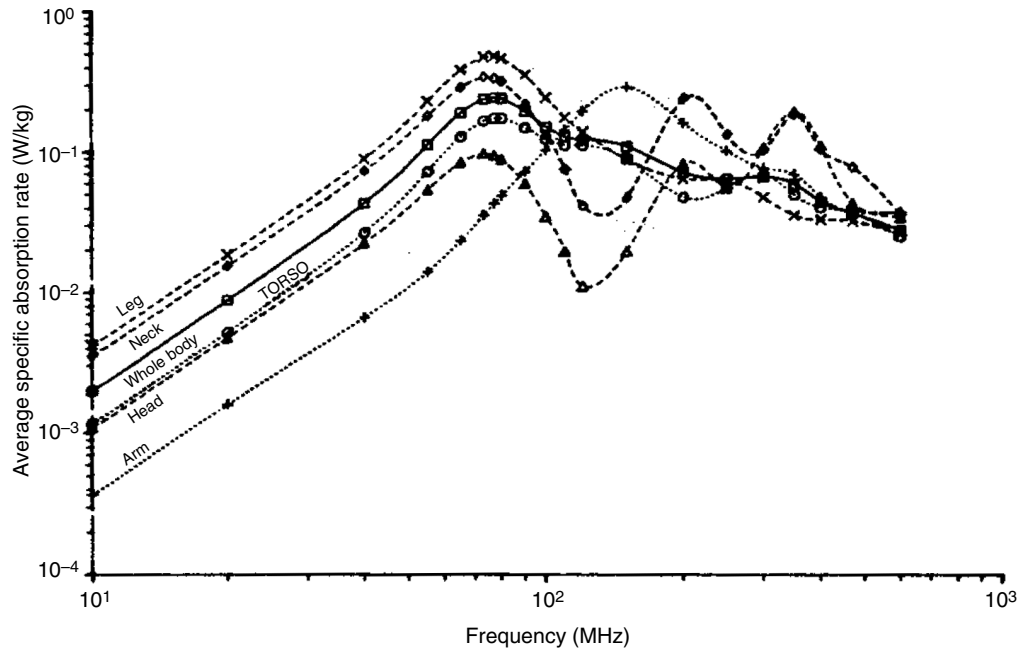


FIGURE 10.18

Average SARs for a homogenous 180-cell model of the human body exposed to a vertically polarized, 80-MHz plane wave. The incident power density is 10 W/m^2 .

increases with frequency until it reaches a maximum of about 0.23 W/kg at 77 MHz (resonance frequency), and it then decreases as $1/\text{frequency}$. The experimental data shown in Figure 10.19 are obtained from a saline-filled scale model of the human body. It can be seen that the calculated absorption is in good agreement with that found experimentally [27,95], except for the resonant frequency, which is somewhat lower (70 MHz) in the experimental case. It should be mentioned that whole-body SAR, given in Figure 10.18, is typically within 10% of that estimated from prolate spheroidal models of the same height and dielectric property. Further, when inhomogenous complex permittivities are used with the model, the whole-body SAR changes less than 2% from that depicted in Figure 10.18. Thus, if one is primarily concerned with average absorption over the body, a homogenous prolate spheroidal model may be quite adequate.

While the MoM based on the volume integral equation has been a useful numerical procedure for computation of average SAR and SAR distribution in complex tissue geometries, the requirement of a full $3N \times 3N$ matrix presents severe limitations. The computation times required to provide even regional SAR distribution of sufficient resolution to delineate the resonant frequency for the head region are enormous. A minimum of 340 cells was needed, increasing the computation time by a factor of 4 over the 180-cell models [95,96].

Matrix inversion operations consume the largest block of time in moment method solutions for the cubic-cell models. The computer time required is proportional to the cube of the number of cells. However, the matrix generated is usually diagonally dominant and well-conditioned. For a human-size body, iterative procedures for matrix inversion are practical at frequencies below about 60 MHz . The convergence rate decreases with increasing frequency and fails above 90 MHz . This is most likely caused by the decrease in the degree of diagonal dominance with increasing frequency. A number of approaches have been investigated to alleviate this difficulty. A semi-iterative procedure

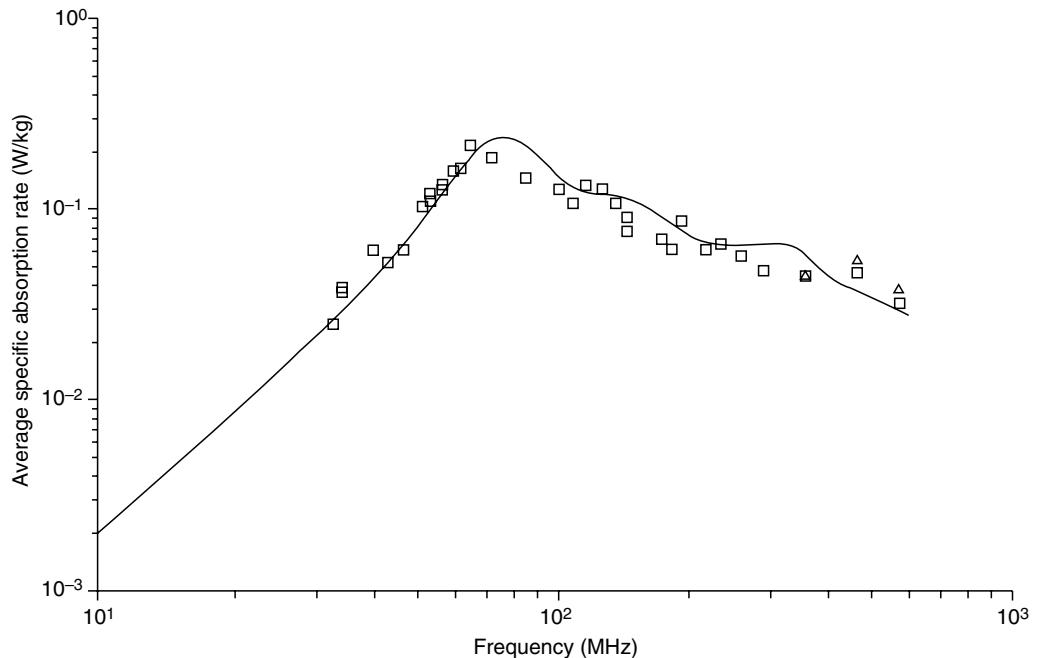


FIGURE 10.19

Whole-body averaged absorption for a homogenous cubic-cell model of humans exposed to vertically polarized plane in free space. The incident power density is 10 W/m^2 .

called band approximation method appears to be an efficient algorithm that can be profitably used to invert large matrices generated by the number of cells for human models at arbitrarily high frequencies, and converges significantly faster than standard iterative algorithms [96].

10.4.2.3.2 SAR Induced in Fine Resolution Anatomical Models

To accurately evaluate the SAR induced in the human body, the FDTD method was introduced during the late 1980s, when the limitations of the MoM due to its memory requirements were reached. The capability of FDTD to take into account heterogeneities in models of the human body was first demonstrated using a model of the isolated human torso [69]. Later, a complete model of the human body was considered [97], and results for an isolated homogenous man model standing in free space were compared with results for an inhomogenous man model, under both isolated and grounded conditions [97]. The incident field was a plane wave propagating parallel to the ground plane and with the electric field vertically polarized (parallel to the long axis of the human body), at frequencies of 100 and 350 MHz. The human body model was obtained from cross-sectional diagrams and had a resolution of 2.62 cm at 100 MHz. The total occupied volume was $23 \times 12 \times 68$ cubic cells. At 350 MHz, the resolution was 1.31 cm for a total volume of $45 \times 24 \times 135$ cubic cells. The result, depicted as layer-averaged SAR or organ-averaged SAR, demonstrated the importance of considering inhomogenous models of the human body. For example, the homogenous model was not able to predict the peak SAR obtained in the eyes at 350 MHz, or the difference in absorption among the different organs.

Since these first works on power absorption, several papers have been published using anatomical models of the human body with finer resolutions.

The VH body model has been used to evaluate power absorption and temperature increase as a function of frequency of the incident plane wave, by considering a grounded male, either barefoot or with shoes [98]. The model had a resolution of 5 mm, a total height of 180 cm, and weight of about 103 kg. The large mass was due to the use of the VH model, which is far from the so-called “reference man,” as defined by International Commission on Radiological Protection (ICRP). The reference man weighs 73 kg and has a height of 176 cm [99]. In the referenced paper [98], for the frequency range between 10 and 900 MHz, SARs averaged over the whole body (SAR_{WB}) and locally, that is, averaged over 1.0 g (SAR_{1g}) and 10 g (SAR_{10g}), were evaluated. In particular, it has been found [98] that when the incident power density is equal to the reference levels set in the exposure standards, the basic restrictions on SAR_{WB} and on local SARs are never exceeded. Moreover, it has been shown [98] that the ratio, SAR_{10g}/SAR_{WB} was about the same (either 25 or 50 according to the body part considered) as the value used in the safety guidelines to convert basic restrictions on SAR_{WB} to basic restriction on local peak SAR [100]. On the other hand, the SAR_{1g}/SAR_{WB} ratio was found to be always higher than the value of 20 adopted in the safety guideline [101].

Figure 10.20 gives the SAR_{WB} as a function of frequency in a grounded male for an incident plane wave with a power density of 10 W/m^2 for two different human body models [98,102]. The SARs are slightly different because the two body models were different in height, weight, and tissue composition. The influence of the human body model on electromagnetic power absorption is further illustrated in Figure 10.21, where a comparison among the SAR_{WB} values obtained with the heterogenous VH model and a homogenous VH model consisting either of muscle or fat is reported. The frequencies considered are from 10 to 200 MHz to highlight the differences in power absorption at resonance.

It can be seen from the figures that a higher peak appeared at resonance in the homogenous muscle model, and lower absorptions were obtained in the homogenous fat model. Moreover, data from a lighter model (65.8 kg) obtained by reducing the cell dimension on the horizontal plane suggested that the lighter body absorbed more elec-

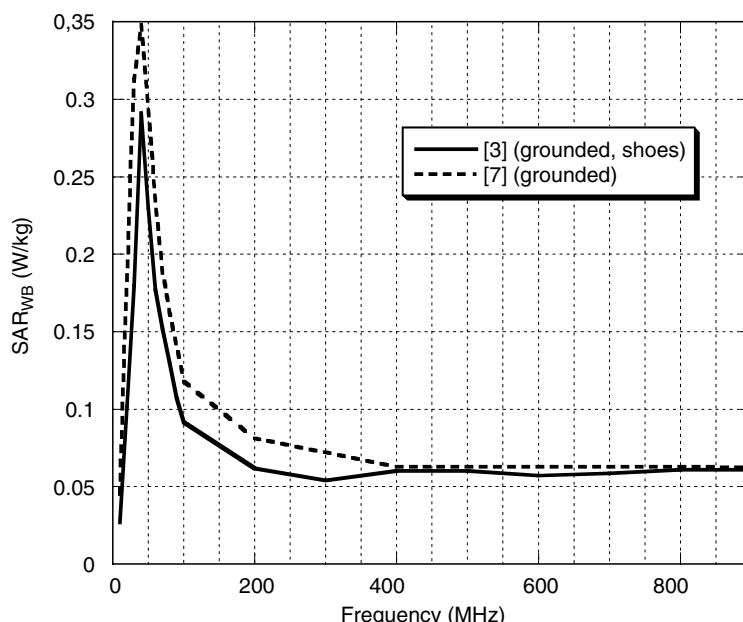


FIGURE 10.20

SAR as averaged over the whole body as a function of the frequency.

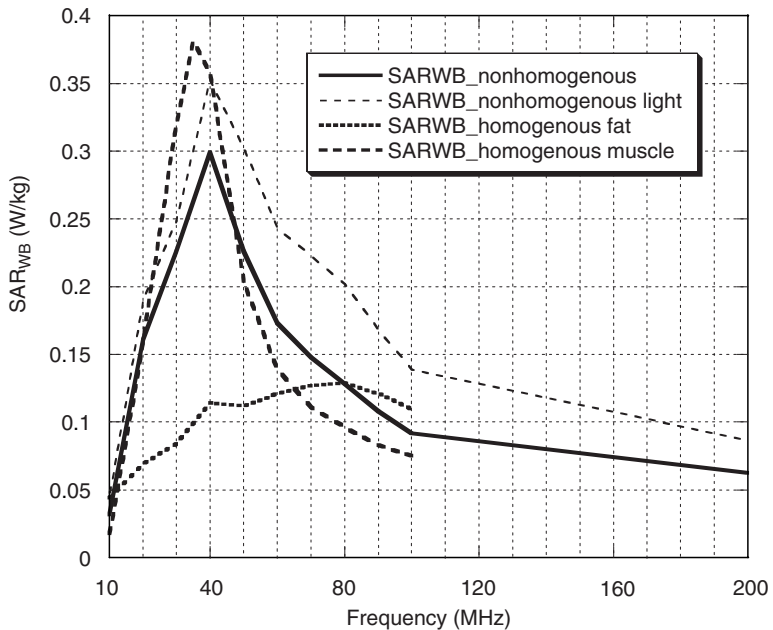


FIGURE 10.21

SAR as averaged over the whole body as a function of the frequency for different VH body models: nonhomogenous, nonhomogenous with a lighter weight (65.8 vs. 103 kg), homogenous fat, and homogenous muscle.

tromagnetic power than the heavier one. The frequency dependence of power absorption is clearly evidenced by Figure 10.20 and Figure 10.21. Indeed, this frequency dependence was the basis of the different limits imposed on the reference levels for different frequencies in the safety guidelines [100,101].

In Table 10.5 some literature data are summarized for the SAR_{WB} as a function of frequency (10 MHz to 2 GHz) for a grounded and isolated man model exposed to an incident power density of 1.0 mW/cm^2 .

The first two columns refer to data in Figure 10.20, while the successive columns report data from published literature. Note the resonant frequencies of 40 vs. 70 MHz for grounded or isolated bodies. Moreover, the data in Table 10.5 show nonsignificant differences in SAR averaged over the whole body by changing the model resolution from 3 to 5 mm [103]. For the same reason the cubic-cell model described in the previous section had been employed, successfully, to calculate whole-body averaged absorption. The SAR_{WB} has a weak dependence on model resolution.

Likewise, a study on the SAR dependence on permittivity values [104] showed that uncertainty in permittivity values does not substantially affect the SAR as averaged over the whole body, while the same uncertainties have a greater effect on local SAR. In particular, considerations of different frequencies and orientations of the incident plane wave, or higher or lower permittivity values, showed that the maximum difference in SAR_{WB} was within $\pm 20\%$ [103]. Larger differences were found in local SAR, particularly when the permittivity of muscle, representing about 42% of the whole-body mass, was changed [103].

The data in the last column of Table 10.5 were obtained from a human body model [105] that was developed by using a new, semiautomatic procedure to construct numerically a frequency-dependent, dielectric anatomy model, starting from MRI images. The main difference between this human body model and the models usually considered in FDTD calculations is that in this model permittivity and conductivity can vary, even for the

same tissue, thus reflecting the realistic spatial inhomogeneity of such parameters. The semiautomatic procedure requires a short time to construct the model; thus, it could be used for dosimetry studies based on the model of specific persons.

A high-resolution human body model ($1.974 \times 1.974 \times 3.0$ mm) and a coarser one ($5.922 \times 5.922 \times 6.0$ mm), both for isolated and grounded conditions, were employed to determine the power absorption in the head and neck region and to evaluate the frequencies at which the absorption may be maximized [106]. It was observed that under isolated conditions two resonant frequencies occurred for the head and neck, one associated with the whole-body resonance and the other with a local resonance of the head and neck. Under grounded conditions, three resonances were observed; the additional resonance was attributed to a torso resonance.

Some studies were conducted to evaluate power absorption in models of women and children. Specifically, a 10-year-old child and a 5-year-old child were considered by scaling the adult human body model [106]. It should be noted that simply scaling the adult human body model to the children's dimensions does not produce an accurate model since the different organs scale differently; however, the general features in terms of height and weight are fulfilled, thus allowing for the determination of general properties of electromagnetic power absorption. In this way, resonant frequencies of 104 MHz for the isolated model and 65 MHz for the grounded 10-year-old child were obtained, while for the 5-year-old model, they were 126 and 73 MHz, respectively.

In a different study, power absorption in scaled versions of the adult human body model representing 10-, 5-, and 1-year-old children was evaluated for both grounded and isolated conditions [102]. Figure 10.22 gives the SAR_{WB} obtained for the three child models under isolated conditions and an incident power density of 1 mW/cm^2 . A shift in the resonant frequency with the height of the model—the taller the model, the lower

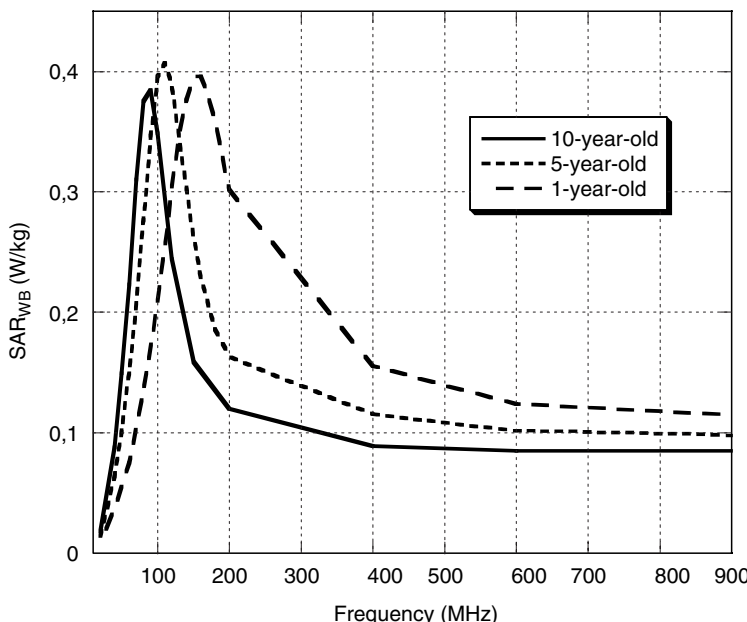


FIGURE 10.22

SAR as averaged over the whole body as a function of the frequency for different child body models: 10, 5, and 1 year old. Incident power: 1 mW/cm^2 . (Data from Dimbylow, P.J., *Phys. Med. Biol.*, 47, 2835, 2002.)

the resonance frequency—can be observed from the figure; note also the higher absorption in the smaller child body model [102].

The potential differences between SAR induced in man and woman have been explored using slightly different models [107,108]. In one study, 2-mm resolution models were developed for evaluating power absorption in Japanese males and females. Note that the use of the 2-mm resolution body models had led to an overestimation of the skin weight by 50% or more than the average value for the Japanese reference body [107]. The computed results showed that the difference in SAR_{WB} between male and female models was small, within 1.1 dB. The authors concluded that gender does not affect SAR_{WB} . Similarly, they obtained no significant differences between the male and female models with regard to local SARs. However, the overestimation of skin weight, and perhaps other tissues, in the 2-mm resolution body models could have influenced their results and conclusions.

In contrast, a clear difference in power absorption was reported [108] between Caucasian male and female models. The two Caucasian body models were developed using the semiautomated procedure previously cited [105]. In particular, considerably greater SAR_{WB} was obtained in the female model than in the male one (about 40% higher in the frequency range between 500 MHz and 2.0 GHz and 25% higher in the frequency range between 2.0 and 4.0 GHz). The difference in local SARs (both SAR_{1g} and SAR_{10g}) were insignificant between genders for up to 3.0 GHz, while above this frequency, say up to 4 GHz, the SAR_{1g} and SAR_{10g} in the female model became larger than those in the male model. The authors observed that this result could be explained by the difference in subcutaneous fat between man and woman. It was noted that a better identification and modeling of the skin layer could influence the results. Clearly, further studies are needed to assess the similarities and differences in power absorption between male and female body models exposed to EMFs of radiating sources.

In summary, available data on electromagnetic power absorption in human body models exposed to plane wave fields show that the choice of the human body model affects the results obtained. The observed differences among the published data are usually more pronounced in local SARs than in SARs averaged over the whole body. The body height, mass, tissue distribution and composition, including fat and muscle, are important factors in power absorption and can explain some differences among the published data. Another fundamental aspect is the value assigned to the dielectric properties of different tissues or organs identified in the body model. In the case of children, the variation in tissue dielectric properties with age also may influence the computed results. It is noteworthy that the above publications have used dielectric properties from the same sources [109,110].

10.4.2.4 Human Exposure to the Field Radiated by Transceiver Base-Station Antennas

The enormous growth in the number of subscribers of mobile telecommunication systems during the past few years has pushed upward the system's capacity. As a result, more and more base stations have been installed on the rooftop of existing buildings in densely populated areas, and many more are expected to be set up as the next-generation mobile networks (UMTS, IMT2000, etc.) are deployed. These installations are giving rise to widespread concerns among the population about possible deleterious effects on human health from exposure to the EMFs radiated by the base-station antennas. Recently, increasing attention has been paid to the topic of numerical exposure and compliance assessment for base-station installations.

A great deal of work has been done in the area of field intensity prediction in the vicinity of base-station antennas to determine the so-called free-space compliance boundary. The studies were aimed toward a direct comparison with reference levels suggested

by international exposure guidelines [100,101]. They generally have neglected both the influence of the environment in which the antennas operate and the dosimetric problem of SAR evaluation inside an exposed subject. In particular, considerable efforts have been spent on determining simplified and efficient analytical [111,112] and numerical [113,114] models to evaluate field levels near base-station antennas. Starting from the theory of collinear dipole arrays, typically employed in base transceiver station (BTS) antennas, practical analytical formulas have been derived to predict average power density falloff as a function of distance from the antenna. The space surrounding the antenna is often divided into a cylindrical-wave region, closest to the antenna, and a spherical-wave region, further away [111]. A complementary formulation also has been proposed, on the basis of an exact asymptotic solution for the radiated field, to derive approximate analytical formulas that allow a conservative prediction of equivalent peak power density as a function of the distance from the antenna [112].

Besides the aforementioned practical analytical formulations, simplified numerical models are often used, by subdividing the antenna into elementary radiators [113,114]. Under the hypothesis of weak coupling between the subelements, the near field can be quickly computed through a superposition of the fields independently radiated by the different elements. Once the radiation pattern of the subelements is known, the field is derived using the antenna gain-based formula [113,114]. For better accuracies in the vicinity of the antenna, an MoM simulation of the subelement can be invoked [114]. These simplified approaches represent extremely fast tools for field intensity prediction, but they are limited by a minimum distance from the antenna where they can be applied in order to maintain an acceptable computational accuracy. On the other hand, when field computations within a distance of a few wavelengths from the antenna have to be done, full-wave numerical techniques, such as FDTD, must be adopted. The accuracy of FDTD models for evaluating the near field of base-station antennas has been investigated and validated through a comparison with measurements carried out in a fully anechoic chamber [115].

Full-wave approaches require knowledge of the internal structure of the antenna, which is not always available. Cylindrical- and spherical-wave expansion techniques have been proposed to evaluate the near field, starting from measurements performed on a surface enclosing the antenna [116–118]. The basic approach consists of performing field measurements on a spherical surface surrounding the antenna and describing the measured field as a superposition of spherical modes [115]. Once the spherical-wave expansion coefficients have been determined, the near field can be extrapolated for all points lying outside the minimum sphere enclosing the antenna. This technique also has been improved to allow extrapolation of the field inside the minimum sphere [117]. To this end, the spherical-wave expansion coefficients are derived for each of the antenna subelements. This approach extends the range of applicability of the formulation to all points outside the minimum sphere of a single subelement, which is much closer to the antenna than the minimum sphere of the overall array. Recently, an alternative solution to extend field extrapolation close to the antenna was proposed, which consists of spherical-wave expansion outside the minimum sphere of the antenna and cylindrical-wave expansion for the region close to the antenna, with an appropriate matching of the two expansions [118].

The effect of the surrounding environment must be taken into account to some extent in dealing with the problem of evaluating induced SAR in a subject exposed to the field radiated by BTS antennas, since the antenna is not operating in a free-space condition. A very interesting approach, applicable to on-site evaluations, consists of using mixed experimental and numerical procedures [119–121]. One procedure is based on on-site measurement of the amplitude and phase of the exposure field distribution over a surface

surrounding the antenna. The measurement is then used to numerically evaluate induced SAR distributions inside a phantom. The measured fields are used to excite the FDTD domain via the equivalence principle [119]. A much faster and efficient procedure uses previously stored FDTD-computed E-field distributions inside a phantom exposed to spatially impulsive electric fields, the equivalent spatial impulsive responses of the phantom or Green's functions. The on-site measurement of amplitude and phase of the exposure field is made over an equally spaced grid of points placed on an appropriately chosen surface [120]. The procedure has recently been enhanced and made faster by substituting the spatial impulse response with responses to spatial harmonic components [121]. In this way, good accuracy is achieved using only six to ten spatial harmonic components, as opposed to the 54 spatial impulse responses needed previously.

The aforementioned hybrid experimental-numerical procedures have the great advantage of allowing easy characterization of environmental perturbations to the exposure field by directly including them in the measured field. On the other hand, they require the antenna to be already installed and operating at the time of measurement. The last point makes such procedures not suitable for *a priori* compliance assessment evaluations during the planning stage of a cellular network. For such evaluations, a thorough numerical dosimetric analysis is required. Once again, a possible approach, when the environment can be neglected and the antenna can be supposed to operate under free-space conditions, consists of performing full-wave FDTD simulations and modeling both the BTS antenna and a numerical phantom of the exposed subject. The applicability of such an approach has also been demonstrated, through a comparison with SAR measurements, for exposure locations in close proximity to the antenna [122]. The main drawback of full-wave FDTD analysis is the large amount of memory required to discretize the simulation space for phantom locations not in the close proximity of the antenna. This problem can be faced by exploiting parallel computer architectures with parallelized versions of the FDTD code [123]. Parallel FDTD also has the potential to allow SAR computations for large antenna-phantom distances.

More efficient techniques have been developed that combine two different techniques, one to model BTS antenna and propagation in free space and the other, SAR inside the phantom [124,125]. In particular, if the antenna-phantom distance is such that mutual coupling can be neglected, a hybrid ray-tracing (RT)-FDTD approach can be used [124]. RT is used to model field propagation from the BTS antenna to an equivalent surface surrounding the phantom, and FDTD is employed to study absorption inside the phantom, using RT-derived exposure fields for excitation. For closer antenna-phantom distances, where the mutual coupling cannot be neglected, a hybrid FEM-MoM technique has been proposed [125]. In this case, MoM is used to model the BTS antenna, while FEM is used to study absorption inside the phantom. The MoM and FEM formulations are coupled together and are solved iteratively. These hybrid approaches allow very efficient SAR computation for different antenna-phantom distances and are well suited for evaluating free-space compliance distances, on the basis of SAR restrictions. They do not require the use of derived exposure field reference levels. For example, the RT-FDTD technique has been applied to a common 14-dBi-gain GSM900 antenna using the VH phantom. It was shown that for a total radiated power of 30 W, typical for urban area installations, SAR basic restrictions for the general population may be exceeded at distances of 2 m or less. Note that, at these distances, only occupational personnel are allowed [124].

The RT-FDTD hybrid technique also has been successfully employed to study human exposure to the field radiated by a BTS antenna in an urban scenario, including the effect of environmental perturbations to the exposure field [126]. In this case, image sources have been introduced to represent corner-reflector-like urban scenarios. Three different exposure conditions have been considered for a rooftop-mounted 14-dBi-gain BTS

TABLE 10.6

Spatial Maximum ($E_{i\text{MAX}}$) and Spatial Average ($E_{i\text{AVE}}$) of the Incident Field (rms Value); Maximum SAR Values Averaged over 1 g (SAR_{1g}) and over 10 g (SAR_{10g}), and SAR Value Averaged over the Whole Body (SAR_{WB}) for Three Exposure Conditions

	$E_{i\text{MAX}}$ (V/m)	$E_{i\text{AVE}}$ (V/m)	SAR _{1g} (mW/kg)	SAR _{10g} (mW/kg)	SAR _{WB} (mW/kg)
Rooftop	4.2	2.8	5.3	3.0	0.12
Balcony	8.1	5.5	13.2	8.5	0.46
Street	1.3	1.1	0.26	0.17	0.01

antenna, radiating 30 W in the GSM900 frequency band: (1) a subject standing on the rooftop, near the antenna mast; (2) a subject standing on a balcony of a building facing the antenna at a distance of 30 m, within the antenna main beam; and (3) a subject standing in the street below the 30-m tall building on which the BTS antenna was mounted. The computed results for the incident electric field and SARs, under these exposure conditions, are given in Table 10.6.

From Table 10.6, because of the high directivity over the vertical plane of base-station antennas, it appears that the highest field levels are not obtained on the rooftop of the building where the antenna is located. Instead, they are on the nearby building, in the direction of the maximum antenna radiation. As expected, the lowest field levels are experienced by a subject standing in the street, as a result of the large distance from the antenna and the off-axis position with respect to the antenna pointing direction. In all cases, the computed SARs are at least two orders of magnitude lower than the basic restrictions, confirming the expected low exposure levels for people living near a BTS installation in urban areas.

More recently, some hybrid techniques have been developed, with enhanced capabilities in modeling complex urban environments, by taking into account diffraction phenomena [127–129]. One such technique uses FEM to model the BTS antenna, the uniform theory of diffraction (UTD) to model the effects of the environment on field propagation, and FDTD to study power absorption in the exposed subject [127]. The technique has been employed to study exposure of a subject standing inside a room with a microcell BTS antenna mounted on the external wall. Another possible hybrid solution exploits time domain physical optics, instead of UTD, to model field scattering from the environment and FDTD to study absorption inside the exposed subject [128].

Finally, a hybrid UTD–FDTD technique has been developed to highlight some key points related to compliance assessment procedures for cellular base-station antennas, in a realistic urban environment [129]. The scenario analyzed consists of a room in one building where the field, radiated by a GSM900 or a UMTS BTS antenna installed on a facing building, penetrates through the room's external wall and window. The relation between SAR in an exposed subject and ambient field in the absence of the subject has been investigated for the complex scenario. As expected, the ambient field showed a highly nonuniform distribution resulting from the many reflections and diffractions that took place. The results showed that whole-body averaged SARs (SAR_{WB}) are closely correlated with the exposure field value averaged over the volume that would be occupied by the exposed subject. In particular, it has been estimated that assessing SAR_{WB} on the basis of volume-averaged field values yields an average error of approximately 6%. Peak 1-g and 10-g averaged SARs, instead, show a rather complex and difficult-to-predict relation with reference to the exposure field. Analysis of the results has revealed that the use of the volume-averaged exposure field value, in the absence of the subject, can lead to

an underestimation of the peak local SARs, up to 36%. On the contrary, using the maximum volumetric value yields an overestimation of peak local SAR (up to approximately four times). The conclusion was that peak local SAR showed a good correlation (15% average error) with the maximum average exposure field value obtained by varying the position of a vertical averaging plane, having a surface equivalent to the projected human body area, inside the volume occupied by the subject.

10.4.2.4.1 Human Exposure to the Fields Produced by Coexisting Wireless Communication Systems

The discussions thus far have dealt with the problem of human exposure to fields radiated by a single base-station antenna from the cellular mobile communication systems (i.e., GSM, UMTS, etc.). However, as the development of communication systems making use of wireless technology expands, new exposure scenarios are encountered in everyday life. Following the enormous growth in the number of base stations in densely populated areas, one of the most promising systems in the near future may be the so-called Wi-Fi system, namely, wireless LAN adopting the IEEE 802.11b communication standard. Wi-Fi is characterized by completely different coverage ranges. Unlike base-station antennas of cellular systems, which are installed almost entirely in outdoor locations, access points (APs) of Wi-Fi systems would operate essentially inside buildings. Nonetheless, the EMFs radiated by the two systems will coexist in indoor environments, particularly if buildings located in front of a rooftop-mounted base-station antenna are considered. This poses new questions about human exposure in such environments. It becomes important to assess typical exposure levels attributable to each system.

The problem has been recently addressed by considering exposure of a subject standing inside a room with a Wi-Fi AP and facing a dual-band GSM900/GSM1800 BTS antenna mounted on the rooftop of a nearby building [130]. The AP radiates a power of 100 mW at 2.44 GHz, while the GSM BTS employs an antenna with a 18-dBi gain, radiating a total power of 30 and 20 W in the GSM900 and GSM1800 frequency bands, respectively. The computed results for exposure field values and SAR levels are summarized in Table 10.7 and [Table 10.8](#). Specifically, the first two columns of Table 10.7 show the peak ($E_{vol\ peak}$) and average ($E_{vol\ ave}$) root mean square (rms) exposure field values over the entire parallelepiped volume where the subject will be placed, while the third column reports the average ($E_{sup\ ave}$) rms exposure field values over vertical sections of the parallelepiped volume. In particular, the minimum and maximum field values are given because the averages depend on where exactly the surface is placed. Table 10.8 presents whole-body, peak 1-g and 10-g averaged SARs inside the exposed subject.

It can be seen from Table 10.7 that the highest contribution to the total field level inside the room is not due to the indoor source but to the outdoor one. In particular, the average E-field

TABLE 10.7

Exposure Field (rms Values) for the Indoor Scenario (Coexisting Outdoor GSM BTS and Indoor Wi-Fi AP)

	$E_{vol\ peak}$ (V/m)	$E_{vol\ ave}$ (V/m)	$E_{sup\ ave}$, min.–max. (V/m)
GSM900	5.57	3.13	2.73–3.44
GSM1800	3.61	1.70	1.62–1.91
Total GSM	6.18	3.56	3.19–3.93
Wi-Fi	2.51	1.13	1.05–1.19
Total	6.30	3.74	3.40–4.09

TABLE 10.8

SAR Values for the Indoor Scenario (Coexisting Outdoor GSM BTS and Indoor Wi-Fi AP)

	SAR _{WB} (mW/kg)	SAR _{1g} (mW/kg)	SAR _{10g} (mW/kg)
GSM900	0.109	2.41	1.08
GSM1800	0.027	1.31	0.58
Total GSM	0.136	3.07	1.46
Wi-Fi	0.014	0.79	0.35
Total	0.150	3.66	1.60

value attributable to the Wi-Fi system is as low as 1 V/m. The computed data also demonstrate that coexistence of the two systems (GSM and Wi-Fi) is possible without exceeding the reference levels for the exposure field, as averaged over the volume occupied by the body or over an equivalent surface, even if the particularly stringent limits issued by some national regulations (e.g., 6 V/m) are considered. Finally, the SARs presented in Table 10.8 suggest that a typical exposure scenario results in RF absorption that is two orders of magnitude below the basic restrictions, both for whole-body and for locally averaged SAR.

10.4.2.5 Coupling of Transient EM Pulses into the Human Body

Electromagnetic transient radiations are widely used for studying the susceptibility of test objects to broadband EMPs, and increasingly, pulsed fields are being explored for telecommunication purposes. The main characteristics of these pulse fields are waveforms that include high peak powers, fast rise times, and a narrow pulse width. Earlier investigations on their interaction with biological systems relied on mathematical analyses of canonical shapes of dielectric equivalent bodies, such models as planar tissue layers and bodies of revolution [131–134]. The well-known effect of microwave heating from pulse-induced thermoelastic pressure in the human head have been investigated both analytically [135–140] and numerically [141–143]. More recently, major strides have been made in the development of UWB systems for wireless telecommunications [144,145]. It promises a powerful combination of low power, high throughput, greater range, and better inherent security, using nanosecond pulses. This section presents predictions of fields and power depositions, which have been obtained from the frequency-dependent FDTD formulations described in [Section 10.4.1.5](#), for models of the biological body.

10.4.2.5.1 Modeling of Tissue Properties with the Debye Equation

For UWB calculations using the (FD)²TD method, the measured properties for the various tissues may be fitted to the Debye equation ([Equation 10.14](#)) with two relaxation constants [77–79]. For the results shown here, the measured properties of biological tissues (muscle, fat, bone, blood, intestine, cartilage, lung, kidney, pancreas, spleen, lung, heart, brain/nerve, skin, and eye) were obtained from the literature. Optimized values for ϵ_{s1} , ϵ_{s2} , ϵ_∞ , τ_1 , and τ_2 in Equation 10.14 were obtained by nonlinear least squares matching to the measured data for fat and muscle ([Table 10.9](#)), with τ_1 and τ_2 being the average of the optimized values for fat and muscle. All other tissues have properties falling roughly between these two types of tissues. This was done to facilitate volume averaging of the tissue properties in cells of the heterogenous human model. Having τ_1 and τ_2 constant for all tissues, allowed linear (volume) averaging of the ϵ values for each tissue in a given cell to calculate ϵ values for that cell.

TABLE 10.9

Debye Constants for Tissues, $\tau_1 = 46.2 \times 10^{-9}$ s and $\tau_2 = 0.91 \times 10^{-10}$ s (Average of Optimum for Fat And Muscle)

Tissue	ϵ_∞	ϵ_{s1}	ϵ_{s2}
Muscle	40.0	3948	59.09
Bone/cartilage	3.4	312.8	7.11
Blood	35.0	3563	66.43
Intestine	39.0	4724	66.09
Liver	36.3	2864	57.12
Kidney	35.0	3332	67.12
Pancreas/spleen	10.0	3793	73.91
One-third lung	10.0	1224	13.06
Heart	38.5	4309	54.58
Brain/nerve	32.5	2064	56.86
Skin	23.0	3399	55.59
Eye	40.0	2191	56.99

10.4.2.5.2 Induced Currents and SAs

The (FD)²TD formulation has been used to calculate coupling of an ultrashort pulse to the heterogenous model of the human body. From the calculated internal fields, the vertical currents passing through the various layers of the body are calculated by using the following equation:

$$I_z(t) = \delta^2 \sum_{i,j} \frac{\partial D_z}{\partial t} \quad (10.25)$$

where δ is the cell size ($= 1.31$ cm), and the summation is carried out for all cells in a given layer. The layer-averaged absorbed energy density or SA and the total energy W absorbed by the whole body can be calculated using the following relationships:

$$SA|_{\text{layer } k} = \frac{\delta t}{N_k} \sum_{i,j,t} \frac{E(i,j,k,t)}{\rho(i,j,k)} \frac{\partial D(i,j,k,t)}{\partial t} \quad (10.26)$$

$$W = \delta t \delta^3 \sum_{i,j,k,t} E(i,j,k,t) \frac{\partial D(i,j,k,t)}{\partial t} \quad (10.27)$$

In Equation 10.26 and Equation 10.27, δt is the time step ($= \delta/2c = 0.02813$ nsec) used for the time domain calculations, N_k is the number of cells in layer k of the body, and $\rho(i,j,k)$ is the mass density (in kg/m³) for each of the cells in the corresponding layers.

A typical time domain, UWB pulse with a peak amplitude of 1.1 V/m is shown in Figure 10.23. It is interesting to note that the pulse has a rise time of about 0.2 nsec and a total time duration of about 7 to 8 nsec. The Fourier spectrum of the pulse is shown in Figure 10.24. Most of the energy in the pulse is concentrated in the 200- to 900-MHz band with the peak of the energy being at about 500 MHz.

For purposes of illustration, the results that follow assume the incident fields to be vertically polarized, since this polarization is known to result in the strongest coupling for standing individuals [146]. Also, a uniform plane wave illumination of the whole body is assumed by the incident fields. The (FD)²TD procedure is used to calculate the temporal

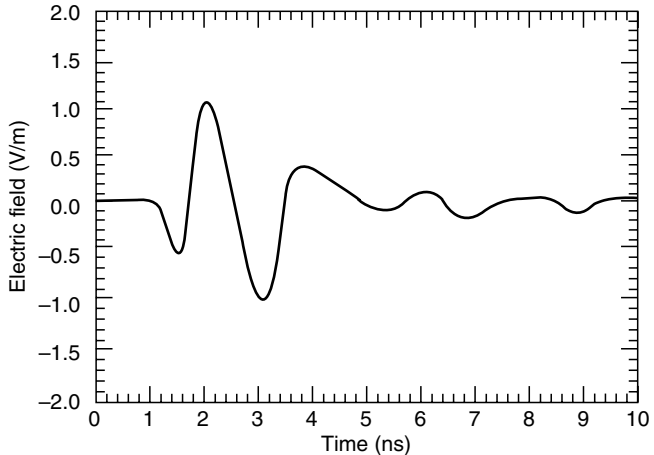


FIGURE 10.23

A representative UWB EMP. Peak incident field = 1.1 V/m.

varyations of total vertical currents for the various sections of the body for both the shoe-wearing grounded and ungrounded exposure conditions of the model. The current variations for a couple of representative sections such as those through the eyes and the bladder are given in [Figure 10.25a](#) and b, respectively. The calculated peak currents for the various sections are on the order of 1.1 to 3.2 mA/(V/m). It is interesting to note that there is very little difference in the induced currents, whether the model is grounded or not. This is due to the fact that most of the energy in the pulse is at frequencies in excess of 300 MHz, where the effect of the ground plane on the induced currents or the SARs is minimal.

In [Figure 10.26](#), the peak current for each section of the body is plotted with a section resolution of 1.31 cm. The maximum peak sectional current of 3.5 mA, which is equal to 3.2 mA/(V/m), occurs at a height of 96.3 cm above the bottom of the feet. A very similar result also had been observed for calculations using isolated and grounded models of the human body for plane wave exposures at frequencies of 350 to 700 MHz, where the highest induced currents on the order of 3.0 to 3.2 mA/(V/m) were calculated for sections of the body that are at heights of 85 to 100 cm relative to the feet.

The SA and the total absorbed energy for exposure to the UWB pulse can be calculated using [Equation 10.26](#) and [Equation 10.27](#). The total energy absorbed by the body exposed

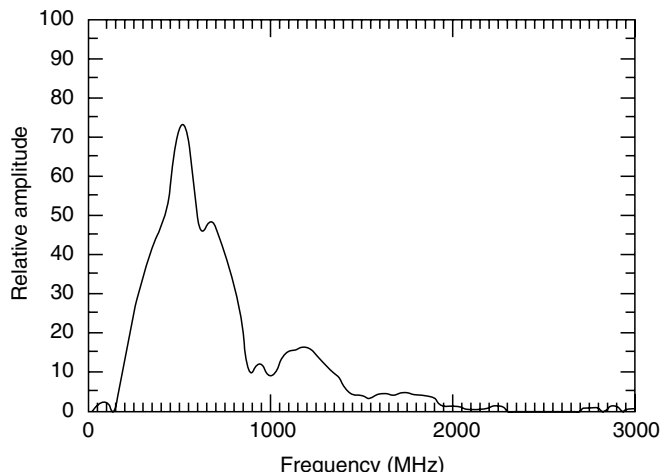


FIGURE 10.24

Fourier spectrum of the EMP of Figure 10.23.

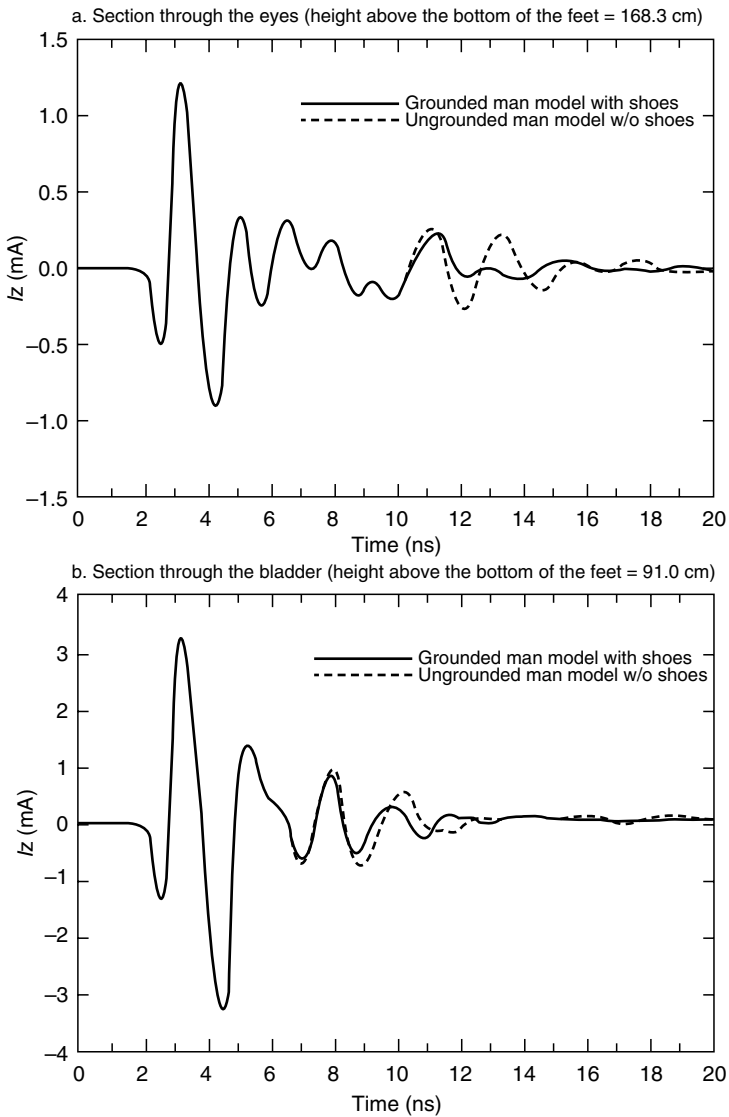


FIGURE 10.25

Currents induced for the various sections of the body for shoe-wearing grounded and ungrounded conditions of exposure. $E_{\text{peak}} = 1.1 \text{ V/m}$.

to a single pulse of the type shown in Figure 10.23 is 2.0 and 1.91 pJ for isolated and shoe-wearing grounded conditions, respectively.

10.4.2.6 Absorption in the Head of Cellular Phone Users

The widespread use of cellular mobile telephone systems has brought about an increased concern for possible adverse health effects from the RF field emitted by the handset. Indeed, exposure standards have been mandated by various national bodies to limit human exposure to cell phone radiations. These RF exposure standards provide specifications in terms of power deposition per unit mass, that is, SAR induced in the user's head, with which cell phones must comply [100,101].

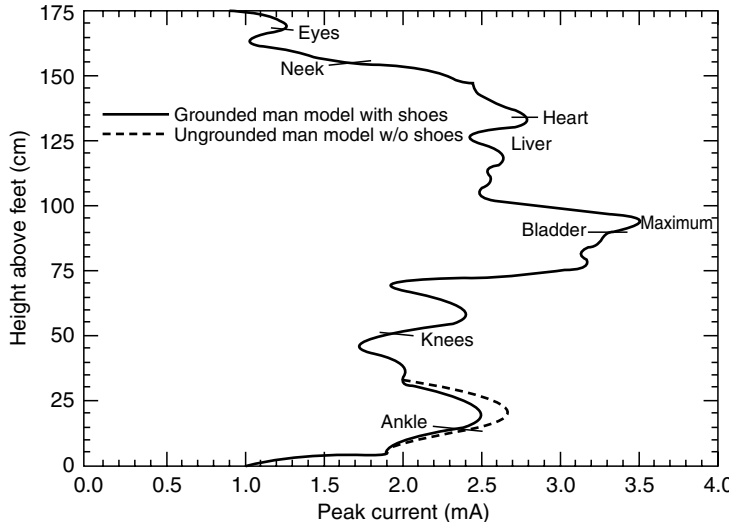


FIGURE 10.26

Peak currents induced for the various sections of the body for shoe-wearing grounded and ungrounded conditions of the model. $E_{\text{peak}} = 1.1 \text{ V/m}$.

Laboratory procedures for compliance testing of mobile phones are based on experimental measurements, performed according to published protocols [147,148]. In these tests, real phones and phantom head models, shells filled with a material with dielectric properties equivalent to those of the brain tissue at the frequencies of interest, are used. Clearly, the phantom is a simplified model of the human head and is specifically designed for compliance testing. Consequently, it is not suited for an accurate analysis of the SAR distribution in various tissues and organs of the head. A detailed analysis of the distribution of the power absorption would be required to obtain a better understanding of SARs inside the head. Such information is needed for the necessary extrapolation of results from *in vivo* and *in vitro* experimental studies devoted to investigating the effects of RF radiation on humans. They would provide the exposure data needed in epidemiological studies aimed at evaluating any possible dose–effect relations.

Increasingly, advances in computational bioelectromagnetics have made detailed evaluation of SAR distribution inside the human head possible through the use of accurate and realistic models of the human head and the source, that is, the mobile phone, and the use of suitable numerical methods such as the FDTD technique.

The first numerical studies were performed by simulating the phone radiating element as a half-wavelength dipole or a quarter-wavelength monopole mounted on a box [149–154]. These antenna models, and the last in particular, can only be used as a rough model of the retractable antenna, which at the beginning was in nearly all cell phone handsets. However, at present, the need for more and more compact terminals and for dual-band operation has given rise to new antenna types. In particular, two types of antennas have been developed: planar integrated antennas and helical antennas. While half-wavelength dipoles and monopoles can be easily implemented inside an FDTD code, modeling of helix or planar antennas can become a rather difficult task.

The difficulties in modeling helical structures with the FDTD method were revealed in some recent studies. For example, only rather large structures have been studied employing a pure FDTD scheme [155,156]. For smaller structures, published reports had either employed equivalent sources [157] or a hybrid MoM–FDTD technique [158,159]. While these reports show some problems and drawbacks, investigations using FDTD, properly

modified through the use of a graded mesh, have obtained good agreement with MoM and experimental results [160,161]. In these studies, both near-field and radiation patterns of dual-band cell phones equipped with a helical antenna have been reproduced. Moreover, the SAR distributions inside the VH model of the head have been computed, showing a higher penetration depth at 900 MHz and higher superficial SARs at 1800 MHz. Moreover, approximately 80% and 50% of the radiated power was absorbed inside the head at 900 and 1800 MHz, respectively. For a phone in contact with the ear and tilted to bring its axis along the ear-mouth direction (the so-called cheek position), radiating an average power of 250 mW at 900 MHz and 125 mW at 1800 MHz, peak 1-g SARs of 1.65 and 1.08 W/kg were obtained in the head at 900 and 1800 MHz, respectively. In the same examples, the peak 1-g SARs in the brain were 0.13 and 0.06 W/kg at the two considered frequencies, respectively.

Planar antennas can be mounted on the top, lateral, or back sides of the phone [162–165]. Shorted patch antennas typically have a 10-dB bandwidth between 5% and 10% that can be increased to about 12% by parasitically coupling another printed radiator in the vertical direction (stacked patch). For comparison, the bandwidth is about 30% for the monopole antenna [163]. In this case, an important consideration is the influence of the hand wrapped around the handset. For a cell phone equipped with a planar antenna, the hand has a detuning effect on the antenna resonant frequency and causes a reduction of the bandwidth; both are evident where the hand masks the antenna. About 30% of the radiated power was absorbed by the hand, while for the monopole the hand absorption was only 15% [162]. For a radiated power of 250 mW at the frequency of 900 MHz and a head–handset separation of 2 cm, the computed peak 1-g SAR was 0.95 W/kg for a laterally mounted planar inverted F antenna (PIFA), and the result was 0.49 W/kg for a monopole antenna [162]. When a phone equipped with a side-mounted PIFA was kept in contact with the ear, the peak 1-g SAR increased to 1.4 W/kg [164]. Note that the back-mounting configuration gave rise to a substantial (up to three times) reduction in the peak SAR [162].

Another important task for an accurate evaluation of the power absorption in the head is the model adopted for the phone case. The typical approach, followed in the literature, consists of representing the case as a box, that is, a plastic-coated metal parallelepiped [149–165]. In order to model the correct shape of cell phones, both CAD files [166] and topometric sensors [167] have been used. However, in most previous studies, the internal structures of the phone have been modeled simply as a homogenous perfect conductor. Recently, CAD files have been used also to model the internal structures (printed circuit board, battery, keypad and buttons, etc.) of the phone [168]. An alternate approach to a suitable numerical model of the mobile phone was proposed by Pisa et al. [169]. It starts with a simplified model, which includes only the main phone parts (antenna, keyboard, internal box, plastic coating, etc.) having “realistic” dimensions and electric properties. The realistic parameters are then tuned by using an optimization procedure, which minimizes a functional that depends on the differences between the measured and simulated electric and magnetic fields in front of the phone and on the SAR inside a cubic phantom. As an example for the applicability of the proposed optimization method, a numerical model of a commercial phone, operating at 900 MHz, was implemented, and the power deposition in the VH model of the human head was computed for various phone–head distances. The results in terms of peak SAR in various head organs and tissues and for various phone–head distances are presented in Table 10.10. The SAR_{1g} and SAR_{10g} show a monotonic decrease when the phone–head distance increases, while the peak SARs inside the head tissues reach their maxima when the phone is kept at specific distances from the head. This behavior is due to the fact that with the telephone pressed against the head, the power absorption is confined to a limited region in front of the

TABLE 10.10

Peak SAR Averaged over 1 g (SAR_{1g}) and 10 g (SAR_{10g}) and Peak SAR as Averaged over 1 g in Various Organs and Tissues, for Different Distances between the Phone and the Visible Human Phantom for a Radiated Power of 250 mW at 900 MHz

	SAR _{1g} (W/kg)	SAR _{10g} (W/kg)	SAR ₁ brain (W/kg)	SAR ₁ eye (W/kg)	SAR ₁ skin (W/kg)	SAR ₁ muscle (W/kg)	SAR ₁ fat (W/kg)	SAR ₁ gland (W/kg)
$d = 0 \text{ mm}$	1.450	0.600	0.125	0.0102	0.504	0.223	0.142	0.448
$d = 2 \text{ mm}$	0.740	0.500	0.123	0.0101	0.504	0.244	0.162	0.493
$d = 6 \text{ mm}$	0.670	0.470	0.174	0.0100	0.482	0.278	0.165	0.471
$d = 8 \text{ mm}$	0.630	0.450	0.109	0.0103	0.460	0.280	0.160	0.445
Cheek position ($d = 0 \text{ mm}$) optimized	0.810	0.410	0.088	0.0360	0.171	0.447	0.301	0.420
Cheek position ($d = 0 \text{ mm}$) nonoptimized	2.568	0.888	0.177	0.0578	0.315	0.721	0.400	0.664

antenna feed point, whereas by moving the handset away from the head, a greater portion of the head is exposed. When the distance was further increased, the SAR decreased monotonically as a result of the decay in field intensity. This study also showed that the use of inaccurate phone models (last row in Table 10.10) could give rise to SARs, averaged over 1 g, up to three times higher than those computed for the optimized model [169].

Faced with a rapid saturation of the cellular phone market, many cell phone manufacturers and service providers are turning their attention toward youths in promoting handsets that are cheap, with inexpensive service plans, or both [170]. An issue of particular interest is the possible difference in power absorption between children and adults. To answer this question, the first problem to be addressed is the realization of an accurate numerical model of a child's head. Because of ethical concerns, the availability of anatomical models of children has been limited. The common approach for obtaining a model of the child has been the reduction of the dimensions of the voxel size of adult models. Sometimes, this reduction was performed by employing different scaling factors for the different parts of the head. It appears that dielectric constants for children may be considerably higher than adults [171]. However, since the detailed data for the dielectric properties of tissues in children are scarce, they are usually assumed to be equal to those of adults or generically increased by a constant factor in most models. Nevertheless, using these models, some papers have reported increases of up to 50% in the peak 1-g SARs in the child head, compared to an adult head, for exposure to cell phones operating at frequencies around 835 and 1900 MHz [151,172]. A similar increase has been observed in the peak 1-g SARs obtained in the brain. A possible explanation of these results is the larger depth of penetration of power in the child models as compared to the adult one [151,172]. Other papers devoted to the investigation of differences between child and adult exposure to cellular phones have shown no significant difference in peak 1-g SAR between adults and children [173,174]. There are several possible explanations for the discrepancy. It has been suggested that the contradictory results may be due to the different phone excitation schemes used by different authors [175]. The disparity in distances of separation between the antenna and the head also was suggested as a pivotal factor in determining the reported discrepancies [170].

In an effort to help resolve the discrepancies, the SAR distributions induced in two child's head models, an isotropic scaling of the VH head (child size, CS) and an

TABLE 10.11

Peak SAR Averaged over 10 g (SAR_{10g}) and Peak SAR as Averaged over 1 g in Various Organs and Tissues, for Radiated Powers of 250 mW at 900 MHz and 125 mW at 1800 MHz in Children and Adults

		SAR_{10g} (W/kg)	SAR_1 skin (W/kg)	SAR_1 muscle (W/kg)	SAR_1 bone (W/kg)	SAR_1 csf (W/kg)	SAR_1 brain (W/kg)
900 MHz	VH	0.67	2.00	0.67	0.20	0.34	0.16
	CS	1.18	4.02	1.03	0.31	0.45	0.25
	CL	1.03	1.15	0.41	0.14	0.23	0.20
1800 MHz	VH	0.39	0.99	0.30	0.08	0.12	0.08
	CS	0.29	0.87	0.30	0.08	0.13	0.09
	CL	0.27	0.91	0.30	0.06	0.15	0.10

anisotropic scaling of the VH head (childlike, CL), have been computed and compared with SAR distributions induced in the VH by a mobile phone equipped with a back-mounted dual-band patch antenna [176]. Some of the results are presented in Table 10.11. It can be seen that the peak SAR_{10g} showed an increase of about 50% and a reduction of about 25% for the child models compared to the adult model at 900 and 1800 MHz, respectively. Moreover, as the brain is closer to the mobile phone in the case of CS and CL heads, the SAR_{1g} in the brain of children is slightly more significant than that for the adult.

Other exposure scenarios also have been investigated, including head exposure inside a car and cell phones not placed in contact with the ear. In some studies, the influence of the metallic and dielectric structures of a car on SAR induced by a cellular phone inside an adult head was analyzed [155,177–179]. Studies performed by modeling the whole car have shown that the main influence on SAR distribution was due to structures that were very close to the head [178,179]. In particular, the presence of a vertical glass wall in parallel with the antenna axis did not significantly influence the SAR distribution, while a metallic wall can cause up to an 80% increase in the peak 1-g SAR [155,177]. The presence of a reflecting wall placed horizontally over the head, simulating the roof of a car, rendered the SAR distribution more uniform, increasing the lower values and reducing the higher ones [155].

Cellular phones commonly are used in contact with the ear. However, when they are used with a headset, they can be positioned at different body locations. Moreover, unintentional exposures also might occur for a subject standing close to someone using a cellular phone, for example, in a crowded environment. The peak SAR produced by a phone placed slightly above the navel of the VH model has been calculated by using the FDTD method, and the results have been compared to those of a flat phantom—modeled as a multilayered transmission line—whose thickness was varied statistically [180]. The exposure of a human subject to a half-wavelength dipole placed at various positions at a distance of 9 mm from the body surface also has been investigated [181]. In particular, 11 different locations have been considered, that is, in front of the right ear and left ear, the nose, eye, heart, lung, shoulder, stomach, hip, lower back, and the groin. The computed results showed that the maximum values of SAR_{1g} and SAR_{10g} occurred, in all cases, when the phone is close to the ear. For all other positions, corresponding to possible locations of the phone when used in conjunction with a headset, peak 1-g SAR values were at least 30% lower than those obtained in the common ear position.

10.5 Temperature Elevations Induced in Biological Tissues by EM Power Absorption

10.5.1 Introduction

EM energy impinging on the human body induces currents and fields inside the body. A major biological response from absorption of EM energy in the RF and microwave frequency range is the elevation of tissue temperature. Consequently, most internationally recognized guidelines for limiting human exposure to EMFs in the RF and microwave range use SAR as the basic dosimetric metric [100,101]. Likewise, the vast majority of studies available in the literature, addressing the topic of human exposure to EMFs, focus their attention on the dosimetric problem of quantifying induced power absorption inside the exposed subject. A central premise of these exposure guidelines is to protect exposed subjects against temperature increases exceeding the threshold for induction of adverse thermal effects. Therefore, an increasing number of investigators are beginning to address the problem of human exposure to EMFs with a thermal analysis to estimate the temperature increment induced inside the exposed subject.

Another domain in which a thermal analysis can be very useful, or even essential, is that of therapeutic applications where EMFs are deliberately used to cause predefined temperature increases in specific target tissues in the body. Some of the applications include hyperthermia cancer treatment and microwave tissue ablation. In such cases, performing a numerical electromagnetic and thermal study of the applicator in its intended operating environment, inside the body, can be a valuable aid in designing the applicator, in establishing the clinical protocol (i.e., power to be delivered, time of application, etc.), and for treatment planning purposes.

In the following, an overview of the available analytical formulations to characterize heating induced by EMFs is presented. Some numerical implementations, suitable to study the thermal problem in realistic situations, are summarized with specific examples.

10.5.2 Bio-Heat Equation

The bio-heat equation (BHE) was originally proposed by Pennes in 1948 to analyze temperature distributions in a resting forearm [182]. Subsequently, it has been modified to study phenomena of heat transport and exchange for the whole body [183,184]. It is an analytical model that describes the temperature distribution $T = T(\mathbf{r},t)$ inside the body. One of the more general formulations of the BHE is given here for temperature rises associated with exposures to EMFs:

$$\nabla \cdot (K(\mathbf{r})\nabla T) + A(\mathbf{r},T) + Q_v(\mathbf{r}) - R_L(\mathbf{r}) - B(\mathbf{r},T)(T - T_B) = C(\mathbf{r})\rho(\mathbf{r})\frac{\partial T}{\partial t} (\text{W/m}^3) \quad (10.28)$$

The five terms on the left side of Equation 10.28 represent heat accumulation (or loss) per unit time and per unit volume at a point inside the body. Specifically, the various ways through which heat is transferred, produced, or removed from the tissue are:

- Heat transfer through internal conduction, where K ($\text{W}/(\text{m}^\circ\text{C})$) is the tissue thermal conductivity
- Metabolic heat production (A [W/m^3])
- Electromagnetic power deposition (Q_v [W/m^3])

- Respiratory heat losses in the lungs (R_L [W/m³])
- Heat exchange due to capillary blood perfusion, which is proportional to blood flow and is represented by the parameter B (W/(°C m³)), and the difference between blood and tissue temperature ($T_B - T$); note that T_B is a function of time (i.e., $T_B = T_B(t)$)

The right side of [Equation 10.28](#) denotes the temperature increase (or decrease) per unit time. The thermal capacitance per unit volume is given by the product between the tissue specific heat, C (J/(kg °C)) and density, ρ (kg/m³).

It should be mentioned that the BHE assumes that heat exchange with blood takes place exclusively via capillary perfusion. In reality, heat exchange also occurs with large blood vessels. This mechanism does not take the form of a distributed exchange throughout the tissue volume, like the $B(T - T_B)$ term in the BHE, but instead, the form of a localized exchange at the blood vessel walls. To account for it would require the introduction of an additional term in the BHE [185,186]. Moreover, it would require precise knowledge of the structure of the vasculature inside the biological body, which is not always available. However, this mechanism only alters temperature distribution near large blood vessels and does not significantly affect the overall temperature distribution, especially the maximum temperature increases elsewhere in an exposed body [187]. Therefore, this mechanism can generally be neglected without significant loss of accuracy, if the principal purpose is to assess safety compliance of a given exposure situation, from the thermal point of view. On the other hand, proper inclusion of large blood vessels may be important when planning hyperthermia or ablation treatments. The presence of a large blood vessel in the target region may cause temperature elevations to remain below the minimum threshold required for effective treatment.

A first step in using the BHE to compute the temperature increases induced by exposure to EMFs is the evaluation of SAR or local power deposition. In fact, $Q_v = \rho$ SAR is the exogenous heat source responsible for the alteration in temperature profiles inside the exposed subject. Once the Q_v term is determined, the BHE would provide the time evolution of temperature, provided that appropriate initial and boundary conditions are imposed, as discussed later. In this manner, the BHE allows assessment of both the transient response and steady-state temperature increases.

An implicit assumption in the above discussion is that the electromagnetic and thermal problems are independent and can be investigated sequentially. This is equivalent to assuming that electromagnetic transients are irrelevant and therefore the steady-state SAR distributions can be used as the input for the thermal analysis, and that changes in tissue temperature do not alter the field distribution inside the tissue. Concerning the first assumption, the time constants of the electromagnetic and thermal processes are of orders of magnitude different, with the EMF reaching steady state at most after a few microseconds, while thermal constants inside living biological tissues are of the order of a few minutes under usual circumstances. This means that electromagnetic transients can indeed be neglected for the thermal analysis. The second assumption, instead, deserves some more attention. In fact, dielectric constants of biological tissues are temperature dependent, and therefore, the EMF distribution could change as heating proceeds and temperature increases. However, this effect may be neglected so long as the temperature elevation is small, that is, on the order of a few degree Celsius, as is expected for common EMF exposures. If temperature increase is large and the induced variation in dielectric constants is no longer negligible, for example, when heating food in a microwave oven, the electromagnetic and thermal problems must be solved in a coupled manner, iteratively updating the electromagnetic solution as heating progresses [188–190].

10.5.2.1 Initial Conditions

The BHE is a partial differential equation in time and space; its solution requires the specification of both initial and boundary conditions. For studies involving RF- and microwave-induced heating inside the human body, the initial temperature distribution typically is set to the physiological norm, computed as the steady-state solution of [Equation 10.28](#) in the absence of external power deposition ($Q_v = 0$). Thus, the resulting equation is

$$\nabla \cdot (K(\mathbf{r})\nabla T) + A_0(\mathbf{r}) - R_L(\mathbf{r}) - B_0(\mathbf{r})(T - T_{B0}) = 0 \text{ (W/m}^3\text{)} \quad (10.29)$$

In this case, thermal parameters do not depend on temperature and are set to their physiological values at approximately 37°C. Similarly, the physiological value at rest is used for blood temperature. Note that Equation 10.29 does not contain time derivatives and, therefore, does not require any initial condition to be solved.

10.5.2.2 Boundary Conditions

Boundary conditions are needed to account for the heat exchange between the body surface, namely, the skin, and the external environment, in both the general and the steady-state formulations of the BHE as represented by [Equation 10.28](#) and [Equation 10.29](#), respectively. The simplest boundary conditions that can be applied are the adiabatic condition, that is, a thermally insulated surface, or the Dirichelet boundary condition, that is, an enforced surface temperature. Adiabatic conditions can be used to model tissue surfaces in close contact with highly insulating materials, such as the catheters used to insert antennas employed in hyperthermia or ablation treatment. In contrast, Dirichelet boundary conditions can be used for surfaces in close contact with a circulating fluid kept at a constant temperature (forced convection).

Adiabatic and Dirichelet boundary conditions are rather simple but they are not suitable for representing the general heat exchanges that take place at the skin. A general boundary condition, obtained by imposing the continuity of the heat flow perpendicular to the surface of the body, can be expressed as [191]:

$$-K(\mathbf{r})(\nabla T \cdot \mathbf{n}_0)_S = H(T_s - T_A) + SW(T)(\text{W/m}^2) \quad (10.30)$$

where S is the skin surface and \mathbf{n}_0 is the outward unit vector normal to S . The terms on the right side of [Equation 10.30](#) represent the two ways in which heat is exchanged with the environment. In particular, the first term describes heat loss due to convection, and it is proportional to the difference between skin temperature (T_s) and ambient air temperature (T_A) through the convection coefficient H (W/(m²°C)). The last term represents heat loss due to sweating (SW).

A few words are needed about radiative heat exchange. If one assumes the body surface is surrounded by objects that are all at the same ambient temperature T_A , the expression for heat exchange through radiation from the body surface to the environment, per unit area, is given by [192,193]:

$$Q_r = e\sigma(T_s^4 - T_A^4)(\text{W/m}^2) \quad (10.31)$$

where e is the surface emissivity, σ is Stefan–Boltzmann’s constant, and the temperatures are expressed in degrees Kelvin (K). Under normal conditions, T_s and T_A do not differ significantly from about 300 K, and [Equation 10.31](#) can be approximated as [193]:

$$Q_r = H_r(T_s - T_A)(W/m^2) \quad (10.32)$$

where H_r is an equivalent convection coefficient. Therefore, the convective term in Equation 10.32 can effectively model both convective and radiative heat exchanges, by using an overall convection coefficient that also takes into account the equivalent convection parameter H_r in Equation 10.32. There are cases, however, in which the surrounding objects are at different temperatures. In such circumstances, the problem becomes very complex and a possible solution, based on the use of an RT method to connect mutually visible surfaces and consider radiant heat transfer between them, has been proposed [194]. However, the simple approach of an equivalent convection is generally sufficient for an accurate analysis of the thermal problem.

It is worthy of mention that the convective boundary condition also can be used to represent an adiabatic condition by simply setting the convective coefficient to zero. It can also represent an approximate Dirichelet boundary condition, by using a very high convective coefficient and setting T_A equal to the imposed surface temperature.

10.5.3 Thermoregulatory Responses

The temperature of the human body is regulated to within a narrow range of about 37°C , in its core. Under normal circumstances, this is accomplished through an exquisite thermoregulatory mechanism involving sweating and vasodilatation (see Chapter 5 by Black for more details on thermoregulation [285]). The thermoregulatory mechanism is activated whenever the temperature $T(r)$ in specific parts of the body, where thermal sensors are placed, shifts from its basal value $T_0(r)$. In particular, the basal temperature distribution $T_0(r)$, which corresponds to a state of “thermal comfort,” is the one obtained in a naked subject when the external air temperature T_A is about 30°C (in a dry environment) [184,195].

Since a part or all of the absorbed electromagnetic energy is converted into heat inside the human body, computations of tissue temperature must take into account the thermoregulatory mechanisms in response to the heat input from RF and microwave absorption, starting from a state of thermal comfort [195]. Specifically, the presence of thermoregulatory mechanisms causes some of the terms in Equation 10.28 and Equation 10.30 to vary with body temperature. The first term that shows a dependence on temperature in Equation 10.28 is metabolic heat production, which may be characterized by the following equation [196]:

$$A(\mathbf{r}, T(\mathbf{r})) = A_0(\mathbf{r})(1.1)^{(T(\mathbf{r}) - T_0(\mathbf{r}))} \quad (10.33)$$

where A_0 is the basal metabolic rate in the tissue. Equation 10.33 shows that metabolic heat production depends only on local tissue temperature. It must be noted that this dependence is not related to thermoregulation but rather to the fact that metabolic processes are slightly accelerated when the temperature increases.

With regard to the variation of blood flow, there are two different, but essential, phenomena: one for internal tissue perfusion and the other for peripheral (skin) perfusion. For blood perfusion to the internal tissues, the regulation depends only on local tissue temperature [196,197]. Thus, in a simple model, blood perfusion could be assumed to be at its basal value B_0 until the local temperature reaches 39°C . When the local temperature exceeds 39°C , the blood perfusion starts to increase linearly with temperature in order to enhance the local heat removal process, until the local temperature rises to above a value of about 44°C . At this point, the increasing rate of blood perfusion arrives at a maximum. Accordingly, the internal blood perfusions are modeled by the following expressions:

$$B(\mathbf{r}, T(\mathbf{r})) = B_0(\mathbf{r}) \quad T(\mathbf{r}) \leq 39^\circ\text{C} \quad (10.34)$$

$$B(\mathbf{r}, T(\mathbf{r})) = B_0(\mathbf{r})[1 + S_B(T(\mathbf{r}) - 39)] \quad 39^\circ\text{C} < T(\mathbf{r}) < 44^\circ\text{C} \quad (10.35)$$

$$B(\mathbf{r}, T(\mathbf{r})) = B_0(\mathbf{r})(1 + 5S_B) \quad T(\mathbf{r}) \geq 44^\circ\text{C} \quad (10.36)$$

The above model of the internal temperature regulation mechanism is rather simple. A more complex temperature control model, instead, would include regulation of blood perfusion in the skin through vasodilatation. In particular, two different signals are used as feedback to regulate vasodilatation: one is the hypothalamic temperature increase ($T_H - T_{H0}$), used as an indicator of the elevation of the body core temperature, and the other is the average skin temperature increase $\overline{\Delta T}_s$, defined as follows:

$$\overline{\Delta T}_s = \frac{\int (T(\mathbf{r}) - T_0(\mathbf{r})) dS}{S} \quad (10.37)$$

where S is the skin surface of the body. The two feedback signals are assigned different weights, with a greater importance given to the hypothalamic temperature, and then used, together with local skin temperature, to regulate skin blood flow according to [183,184]:

$$B(\mathbf{r}, T(\mathbf{r})) = [B_0(\mathbf{r}) + F_{HB}(T_H - T_{H0}) + F_{SB}\overline{\Delta T}_s] 2^{(T(\mathbf{r}) - T_0(\mathbf{r}))/6} \quad (10.38)$$

where F_{HB} and F_{SB} are the weights of the hypothalamic and skin temperature signals, respectively.

From the above discussion, it can be noted that blood acts as a heat transfer agent, taking heat away from the inner body parts, whose temperature is higher than that of the blood, and bringing this heat to the body periphery. There, heat is passed to the skin layers, whose temperature is lower than that of the blood, and dissipated through sweating and evaporation. During microwave irradiation, the net heat exchange, between blood and the various body tissues, is different from zero, and consequently the blood temperature T_B varies according to the following equation:

$$Q_{BTOT} = C_B \rho_B V_B \frac{\partial T_B}{\partial t} (W) \quad (10.39)$$

where Q_{BTOT} is the net rate of heat acquisition of the blood from the body tissues, C_B and ρ_B are the blood specific heat and mass density, respectively, and V_B is the total blood volume, assumed equal to about 5 L [198]. When the thermal equilibrium is reached, the net heat exchange is null, and therefore blood temperature stays at a constant value, slightly higher than the basal one.

The feedback mechanism that regulates sweating (SW in [Equation 10.30](#)) is very similar to that regulating peripheral blood flow and can be described as follows [183,184]:

$$SW(\mathbf{r}, T(\mathbf{r})) = [PI + F_{HS}(T_H - T_{H0}) + F_{SS}\overline{\Delta T}_s] 2^{(T(\mathbf{r}) - T_0(\mathbf{r}))/10} \quad (10.40)$$

where PI represents *perspiratio insensibilis* (insensible perspiration), that is the basal evaporative heat loss from the skin.

In fact, this model still represents a simplification of the thermoregulatory system of the human body, which is very complex. For example, the skin from different parts of the body does not have the same sweating behavior, as implied by [Equation 10.40](#), and there exist other internal temperature sensors, besides the hypothalamus. Notwithstanding these limitations and the great variability in thermoregulatory behavior among different subjects, the model can be considered a good starting point to assess thermal responses in a human subject exposed to an EMF. It must also be observed that in most practical situations, induced thermal elevations are very small and thermoregulatory responses may not be invoked, so that basal physiological values for thermal parameters may be assumed for the BHE.

10.5.4 Numerical Methods for Solving the Thermal Problem

The combination of the BHE and the thermal boundary condition represent a complicated problem, which can become nonlinear if thermoregulatory mechanisms are considered. Analytical solutions of this problem, neglecting thermoregulation, can be obtained only for simplified body geometries and exposure conditions, which allow an analytical determination of the SAR distribution. For example, an analytical solution in stratified media may be obtained as an expansion in eigenfunctions, which are applicable to planar, cylindrical, and spherical multilayer geometries [199,200]. Also, an analytical solution for the case of a multilayer slab has been investigated in terms of Green's functions [201]. More complicated solutions, able to take into account thermoregulatory mechanisms, have also been developed, based on a simplified cylindrical segment approximation of the human body [183,184,202,203]. In particular, the thermal behavior of the human body is simulated by means of two systems: a controlling system and a controlled one. The controlled system, modeled by the BHE, determines the temperature distribution inside the body, while the controlling system provides feedback signals able to modify the thermal parameters of the controlled one in order to maintain a constant body core temperature (thermoregulation). The principal limitation of this approach stems from modeling the body as a few homogenous cylindrical segments, each having a uniform SAR and temperature distribution.

When studying more realistic and detailed geometries, like an anatomically based body model, analytical or cylindrical segment solutions are no longer feasible, and a numerical approach becomes necessary. One possibility is the development of a finite element solution of the BHE [204,205]. However, the most common approach is to use a finite difference scheme, which will be discussed in some detail in the following. One of the main reasons for preferring a finite difference solution, besides its computational efficiency, is that it allows a very simple link with the FDTD method, which is the most popular numerical method for SAR computations. Earlier finite difference solutions of the BHE, used in conjunction with cubic-cell models of the human body, comprised only a few hundred voxels. They used an implicit formulation to avoid the restrictions on the size of the time step. Since these solutions required matrix inversions, they were computationally intensive [16]. As more detailed body models, comprising thousands of voxels, became available, new finite difference solutions were developed. These techniques, based either on explicit or on alternate direction implicit (ADI) formulations, are discussed in the following.

10.5.4.1 Explicit Finite Difference Formulation

One approach to obtain a finite difference explicit formulation of the BHE is based on the thermal balance approach [98]. The body under consideration is divided into cubic cells of

side δ , and the temperature is evaluated at the center of each cell. Temperatures are computed at equal-time steps, δt . In the following, the expression $T^n(i,j,k)$ represents temperature computed at time $n\delta t$ in the (i,j,k) cell. The finite difference formulation is derived by imposing the thermal balance to each cell [192], such that

$$Q_{\text{tot}}^{n,n+1}(i,j,k) = \Gamma(T^{n+1}(i,j,k) - T^n(i,j,k))(\delta t) \quad (10.41)$$

where $Q_{\text{tot}}^{n,n+1}$ is the total heat accumulated (positive) or lost (negative) in the cell during the time interval $[n\delta t - (n+1)\delta t]$, $(T^{n+1} - T^n)$ is the variation of the cell temperature in the same time interval, and $\Gamma = C\rho\delta^3$ is the thermal capacitance of the cell. The heat $Q_{\text{tot}}^{n,n+1}$ is accumulated (or lost) in the cell through the five mechanisms present in the BHE, and, for boundary cells, also through convection to external air and sweating (Equation 10.30).

Heat transfer through internal conduction is governed by Fourier's law. For the (i,j,k) cell, the heat $Q_K^{n,n+1}$ entering the cell through conduction from the $(i-1,j,k)$ cell in the time interval $[n\delta t - (n+1)\delta t]$ can be derived by exploiting the well-known analogy between heat conduction and electrical current conduction [185,192]. In particular, if K_1 and K_2 are the thermal conductivities of the two cells under examination, heat flows through the series connection of two thermal conductances, equaling $K_1\delta^2/(\delta/2)$ and $K_2\delta^2/(\delta/2)$, respectively. Therefore, heat flowing from the center of the $(i-1,j,k)$ cell to the center of the (i,j,k) cell, through the boundary face, experiences an overall thermal conductance equal to $2K_1K_2\delta^2/((K_1 + K_2)\delta)$. As a result, we obtain:

$$Q_K^{n,n+1}(i,j,k) = \frac{2K_1K_2}{K_1 + K_2} \delta^2 \frac{T^n(i-1,j,k) - T^n(i,j,k)}{\delta} \delta t \quad (10.42)$$

An expression similar to Equation 10.42 holds for heat exchanged with the other neighboring cells.

The contributions of metabolic heat production and electromagnetic power deposition are volumetric heat sources, and therefore the contribution they give to $Q_{\text{tot}}^{n,n+1}$ can be immediately derived and is expressed by Equation 10.43 and Equation 10.44, respectively:

$$Q_A^{n,n+1}(i,j,k) = A(i,j,k)\delta^3\delta t \quad (10.43)$$

$$Q_{Q_v}^{n,n+1}(i,j,k) = Q_v(i,j,k)\delta^3\delta t \quad (10.44)$$

Respiratory losses in the lungs are taken into account by subtracting the volumetric loss R_L from the metabolic heat production A in the corresponding cells for the lung.

Finally, the contribution to $Q_{\text{tot}}^{n,n+1}$ due to capillary blood perfusion takes the form of a volumetric term and can be represented, as in metabolic heat production and exogenous heat deposition, as:

$$Q_B^{n,n+1}(i,j,k) = B(i,j,k)((T_B - T^n(i,j,k))\delta^3\delta t) \quad (10.45)$$

For boundary cells in contact with air, heat flow through the face is governed by convection rather than conduction. For a generic cell (i,j,k) , considering a face in direct contact with air, the heat $Q_H^{n,n+1}$ entering the cell through convection in the time interval $[n\delta t - (n+1)\delta t]$ is:

$$Q_H^{n,n+1}(i,j,k) = H(T_A - T^n(i,j,k))\delta^2\delta t \quad (10.46)$$

Heat losses due to sweating at the skin surface (SW) are converted to a volumetric heat loss term and are directly subtracted from the metabolic heat production term A in the skin cells.

Note that in [Equation 10.42](#), [Equation 10.45](#), and [Equation 10.46](#), the temperature has been referred to the time instant $n\delta t$ in order to obtain, at the end, an explicit formulation. Starting from the equations given above, general explicit formulations that hold for each cell can be derived. (See the paper by Bernardi et al. [98] for additional details)

10.5.4.1.1 Stability Criterion

Explicit finite difference formulations are straightforward to implement and are computationally efficient, but they have a limitation on the maximum time step δt that can be used without incurring numerical instability.

The stability criterion for the previously mentioned finite difference scheme can be obtained through Fourier's analysis, which yields the following restriction on δt , derived for internal cells (no convective contributions) [206]:

$$\delta t \leq \frac{1}{6(K/C\rho\delta^2) + (B_0/2C\rho)} \quad (10.47)$$

Because of the typical values of thermal parameters and convection coefficients for the human body, the stability criterion for the peripheral voxels, where some of the faces exchange heat through convection rather than conduction, is less stringent than that of [Equation 10.47](#). Consequently, [Equation 10.47](#) may be safely assumed as the stability criterion for the overall scheme.

10.5.4.2 ADI Formulation

While the explicit finite difference formulation of the BHE has been applied to many simulations, it becomes computationally unaffordable when very small cell sizes are used or when high thermal conductivity materials are present in the domain under study. This stems from the extremely small time steps δt that would be required according to [Equation 10.47](#). In such cases, the ADI formulations can be used [207]. ADI is a general method, developed for numerical solution of parabolic equations. It combines unconditional stability, typical of implicit methods, with the computational efficiency due to the tri-diagonal nature of the resulting matrices [208–210]. Note that the Fourier heat conduction equation is a typical parabolic equation. While the BHE is no longer parabolic, because of the presence of the term related to blood flow, ADI can still be applied, but it loses its unconditional stability. In any case, for time steps on the order of a few seconds, the scheme has proved to be stable in typical applications. It can yield reductions on the order of tenfold or more [207] in execution time, over the classical explicit formulation.

The basic idea behind the ADI technique is to extend to the 3-D case the 1-D Crank–Nicolson's scheme, which averages the outcome from the explicit and the implicit formulations to obtain second-order accuracy both in space and in time variables [192]. In particular, Crank–Nicolson's scheme can be extended to the full 3-D case, by using a sequence of approximate Crank–Nicolson solutions along the three axes, indicated as $T^*(i,j,k)$, $T^{**}(i,j,k)$, and $T^{***}(i,j,k)$, the last one being used as the final estimate for $T^{n+1}(i,j,k)$.

The first approximate solution is obtained using Crank–Nicolson's scheme along the x axis only, while backward differencing is used along y and z :

$$\begin{aligned}
& \frac{K}{\rho C} \frac{1}{2} \left(\frac{T^*(i-1, j, k) - 2T^*(i, j, k) + T^*(i+1, j, k)}{(\delta x)^2} + \frac{T^n(i-1, j, k) - 2T^n(i, j, k) + T^n(i+1, j, k)}{(\delta x)^2} \right) \\
& + \frac{K}{\rho C} \frac{T^n(i, j-1, k) - 2T^n(i, j, k) + T^n(i, j+1, k)}{(\delta y)^2} \\
& + \frac{K}{\rho C} \frac{T^n(i, j, k-1) - 2T^n(i, j, k) + T^n(i, j, k+1)}{(\delta z)^2} \\
= & \frac{T^*(i, j, k) - T^n(i, j, k)}{\delta t} - \frac{A_0 + Q_v + B_0 T_B}{\rho C} \\
& + \frac{B_0}{\rho C} \frac{T^*(i, j, k) + T^n(i, j, k)}{2}
\end{aligned} \tag{10.48}$$

Extending subsequently Crank–Nicolson’s solution along the y axis and the z axis, the following expressions are obtained for the second and third estimates:

$$\begin{aligned}
& \frac{K}{\rho C} \frac{1}{2} \left(\frac{T^*(i-1, j, k) - 2T^*(i, j, k) + T^*(i+1, j, k)}{(\delta x)^2} + \frac{T^n(i-1, j, k) - 2T^n(i, j, k) + T^n(i+1, j, k)}{(\delta x)^2} \right) \\
& + \frac{K}{\rho C} \frac{1}{2} \left(\frac{T^{**}(i, j-1, k) - 2T^{**}(i, j, k) + T^{**}(i, j+1, k)}{(\delta y)^2} + \frac{T^n(i, j-1, k) - 2T^n(i, j, k) + T^n(i, j+1, k)}{(\delta y)^2} \right) \\
& + \frac{K}{\rho C} \frac{T^n(i, j, k-1) - 2T^n(i, j, k) + T^n(i, j, k+1)}{(\delta z)^2} \\
= & \frac{T^{**}(i, j, k) - T^n(i, j, k)}{\delta t} - \frac{A_0 + Q_v + B_0 T_B}{\rho C} \\
& + \frac{B}{\rho C} \frac{T^{**}(i, j, k) + T^n(i, j, k)}{2}
\end{aligned} \tag{10.49}$$

$$\begin{aligned}
& \frac{K}{\rho C} \frac{1}{2} \left(\frac{T^*(i-1, j, k) - 2T^*(i, j, k) + T^*(i+1, j, k)}{(\delta x)^2} + \frac{T^n(i-1, j, k) - 2T^n(i, j, k) + T^n(i+1, j, k)}{(\delta x)^2} \right) \\
& + \frac{K}{\rho C} \frac{1}{2} \left(\frac{T^{**}(i, j-1, k) - 2T^{**}(i, j, k) + T^{**}(i, j+1, k)}{(\delta y)^2} + \frac{T^n(i, j-1, k) - 2T^n(i, j, k) + T^n(i, j+1, k)}{(\delta y)^2} \right) \\
& + \frac{K}{\rho C} \frac{1}{2} \left(\frac{T^{n+1}(i, j, k-1) - 2T^{n+1}(i, j, k) + T^{n+1}(i, j, k+1)}{(\delta z)^2} + \frac{T^n(i, j, k-1) - 2T^n(i, j, k) + T^n(i, j, k+1)}{(\delta z)^2} \right) \\
= & \frac{T^{n+1}(i, j, k) - T^n(i, j, k)}{\delta t} - \frac{A_0 + Q_v + B_0 T_B}{\rho C} \\
& + \frac{B_0}{\rho C} \frac{T^{n+1}(i, j, k) + T^n(i, j, k)}{2}
\end{aligned} \tag{10.50}$$

Starting from the above expressions, it is possible to derive the general ADI formulation that holds for each internal cell. (See the paper by Pisa et al. [207] for additional details.) The formulation can also be adapted to boundary cells, where convective heat exchange must be considered, by introducing a fictitious external node.

10.5.5 Temperature Elevations in Subjects Exposed to EM Fields

When an EM field impinges on the biological body, a fraction of the incident power is absorbed by the body and is converted into heat in the body tissue. Thus, the absorbed energy can cause temperature increases in various body organs and tissues. If the temperature increase is small, it has little effect and is controlled by the thermoregulatory mechanisms of the body. However, if the temperature increment is large, it can produce irreversible biological damage. For example, a temperature increase of about 4.5°C for more than 30 min would produce neuronal damage [211]. Experiments performed on the rabbit eye indicated that a threshold increase of 3°C to 5°C in the lens can induce cataract formation [212,213]. The temperature increase necessary to induce thermal damage to the skin is about 10°C [214,215], while it is 8°C for muscle tissues [216]. Also, experiments performed using laboratory animals have shown various physiological and behavioral effects when the body core temperature rises more than 1°C to 2°C [100]. ([See also Chapter 5](#) by Black [285].)

Moreover, most RF protection standards have adopted basic restrictions in order to keep the thermal increments below some agreed upon level. In particular, the value of 4 W/kg averaged over the whole body (SAR_{WB}) had been adopted by exposure guidelines as the threshold for the induction of adverse thermal effects associated with an increase of the body core temperature of about 1°C in animal experiments. Restrictions on local SAR were introduced in order to limit local temperature increments, since the ratio of the local peak to whole-body averaged SAR can be as high as 20:1 for exposure to a uniform plane wave [217]. However, it is important to note that tissue heating during EM exposure is strongly influenced not only by the power dissipated in the local tissue volume, but also by the way in which absorption is distributed in the surrounding area, by the thermal characteristics of the tissue and its neighbors, and, finally, by the heat exchange with the external environment. The correlation between local SAR values and temperature increases and between SAR and temperature distributions is not straightforward. There have been many studies dealing with thermal increments due to exposures both to the far field of radiating sources and to the near field of cellular phones. In the following some of these studies will be summarized and discussed.

10.5.5.1 Temperature Increments in the Human Body Exposed to the Far Field of Radiating RF Sources

In the past, temperature elevations due to EM power absorption in the human body have been evaluated using several models. The earlier studies were based on a simplified cylindrical segment approximation of the human body [183,184,202,203]. In these studies, the thermal behavior of the human body was simulated by means of two systems: a controlling system and a controlled one. The controlled system, modeled by the BHE, determines the temperature distribution inside the body, while the controlling system provides feedback signals able to modify the thermal parameters of the controlled one in order to maintain a constant body core temperature (thermoregulation). These studies are limited to modeling the body as few homogenous cylindrical segments, each one having a uniform SAR and temperature distribution. A subsequent study [197] used a cubic-cell model with tissue inhomogeneity and took into account the thermoregulatory mechanisms in the BHE. In this case, the BHE was solved using an implicit formulation, which

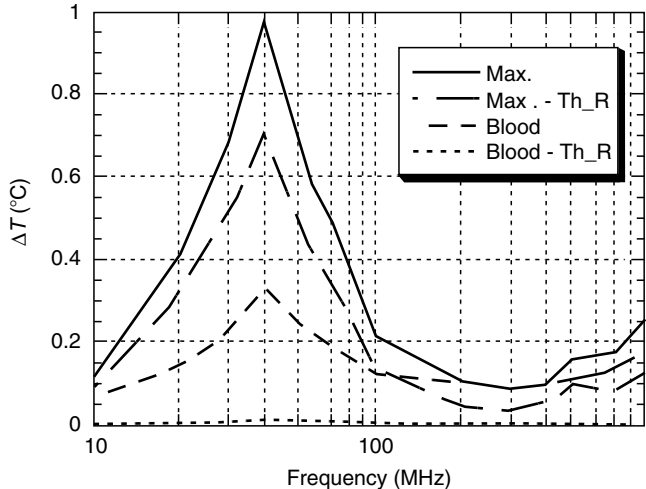


FIGURE 10.27

Maximum temperature increases (ΔT) in the body and blood of a subject wearing shoes, as a function of frequency, with or without thermoregulation (Th_R) for a P_{inc} equal to the limits set by ICNIRP [101].

avoided the restriction in the size of the time step. The explicit formulation requires a computationally intensive matrix inversion. Lately, explicit formulations of the BHE have been developed to study thermal responses in anatomically accurate body models [196,218,219]. In most of these studies, only limited body regions were considered, and thermoregulation mechanisms were neglected.

More recently, the electromagnetic and thermal problems have been combined in a detailed anatomical model of the human body (5-mm resolution) [98]. The FDTD method was used to compute the EMF distribution inside the exposed body, while an explicit finite difference formulation of the BHE, together with an accurate model of the human thermoregulatory system, were developed to compute the corresponding temperature increase.

For an incident power density equal to the maximum permissible value in the International Commission on Non-Ionizing Radiation Protection (ICNIRP) exposure guidelines for the general public [101], Figure 10.27 shows the maximum temperature increase ΔT_{max} obtained inside the body and in the blood as a function of frequency for a subject wearing shoes, both with and without thermoregulation [98]. It can be seen that the highest ΔT values are obtained at 40 MHz. It is also interesting to note that when thermoregulation is considered, the increase in blood temperature is practically zero, while the maximum temperature rise in the body can reach 0.72°C . This happens since blood temperature is very close to the body core temperature, which thermoregulation tends to keep as constant, while the maximum temperature increments are usually found in the superficial tissue layers.

It is worth noting that at 40 MHz, the maximum temperature increase (i.e., 0.72°C in the presence of thermoregulation) is found in the muscle tissues of the ankle. The threshold for the induction of thermal damage in muscle is about 45°C [216], which corresponds to a temperature increase of about 8°C . This temperature differential coincides with the safety factor of 10 promulgated by ICNIRP [100] for occupational exposure in limiting the power density from inducing a thermal effect. Moreover, a safety factor of 50 can be deduced from the temperature increase obtained at 10 MHz and in the frequency range between 100 and 900 MHz, where the maximum temperature increases are less than 0.16°C .

Figure 10.28 shows the distribution of the maximum temperature increase for each horizontal layer of the body at 40 MHz (a) and 900 MHz (b), for an incident power density of 1 mW/cm^2 . At 40 MHz, the maximum temperature increases are obtained at the level

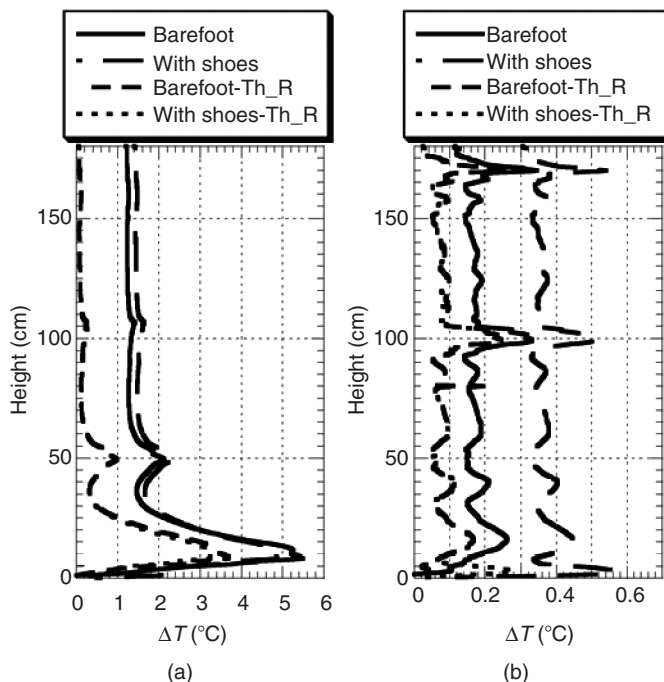


FIGURE 10.28

Layer peak temperature increase (ΔT) in the absence or presence of thermoregulation (Th_R) for a grounded subject barefoot or with shoes ($P_{\text{inc}} = 1 \text{ mW/cm}^2$). (a) $f = 40 \text{ MHz}$ and (b) $f = 900 \text{ MHz}$.

of the ankles, where the maximum local SARs also are located. The result showed that the presence of the shoes could influence temperature change. Since shoes are isolators from the thermal point of view, they prevent heat flow from going to the ground through them and provoking higher heating within the body. The only exception is in the ankle section, where heating was higher in the barefoot model because of the higher SAR values, at 40 MHz.

Also, the presence of the thermoregulatory mechanisms reduced the temperature increase almost uniformly along the body. Figure 10.28 illustrates clearly the role of blood convection in heat exchanges. In fact, even without active thermoregulation, heat could be spread from the point where its deposition is relatively high (e.g., the ankle at 40 MHz) to the rest of the body, by an increase in the temperature of the circulating blood. Therefore, even if power absorption is limited to one body region, temperature elevations may occur throughout the body. This is clearly visible at 40 MHz, where, although power absorption is mainly confined to the ankle region, in the absence of thermoregulation significant temperature elevations (about 1.4°C , $P_{\text{inc}} = 1.0 \text{ mW/cm}^2$ —see Figure 10.28a) can be observed in the brain. The corresponding elevation in blood temperature elevation is about 1.46°C . It is interesting to note that at 900 MHz, in the absence of active thermoregulation, the brain temperature elevation (0.5°C , $P_{\text{inc}} = 1.0 \text{ mW/cm}^2$ —see Figure 10.28b) is higher than blood temperature elevation (0.35°C), as a result of power deposition inside the brain.

10.5.5.2 Temperature Increments in the Head of a Cellular Telephone User

One consequence of RF power absorption in the human head exposed to the field emitted by a cellular phone is temperature increase in the head. In practical situations, in addition to RF power deposition, there are two other causes for temperature increase. The first one is the contact between the phone case and the user's head (ear and cheek, in particular), which blocks the convective heat exchange between the skin layers and the air. It causes

the temperature to rise in tissues around the contact zone. Obviously, this heating is independent of the radiated power, and indeed it was observed also for a wired phone. The second cause for temperature increase is the heating of the phone itself, because of the power dissipated in the internal circuitry, especially the power amplifier. This heating is transferred to the head tissues via thermal conduction.

Studies on temperature rises in the human head, associated with the field emitted by the cell phone, are usually conducted by using anatomically based head models, a numerical solution of the electromagnetic problem, and finite difference formulations of the BHE [161,164,172,187,220–223]. For example, the dissipation in the power amplifier was simulated by adding a power deposition of 250 mW at 900 MHz and 125 mW at 1800 MHz, uniformly distributed inside the upper part of the phone with a 50% efficiency [161]. The heating effects due to SAR, phone contact, and power dissipation in the amplifier were considered separately and were subsequently added together in order to obtain the temperature elevation. The maximum temperature elevations obtained in the ear and in the brain of a user's head are given in Table 10.12 for 900 and 1800 MHz. The ambient air temperature was assumed to be 24°C and a time interval of 15 min, approximating the duration of a long phone call. Although a steady state would not have been reached, the temperature elevation after 15 min is expected to be very close to the steady-state value [164].

The data shown in Table 10.12 reveal some interesting aspects. First, the temperature elevation induced inside the brain by SAR alone was less than 0.1°C, especially when the phone was kept in the "cheek" position. This configuration resulted in a marked reduction in power deposition inside the brain. Table 10.12 also shows that the mere contact of the cellular phone with the ear and cheek, even in a standby mode, in which no RF power is radiated, can cause a temperature elevation in the ear reaching as high as 1.5°C. This is due to the highly insulating properties assumed for the phone plastic shell. A negligible maximum temperature elevation of about 0.01°C, instead, is obtained in the external brain region. If the contribution from power dissipation in the amplifier is included, the induced temperature elevations are not significantly altered. It must be noted, however, that this result arises from consideration of power dissipation in the power amplifier alone. In the real situation, additional power dissipation is present in the internal circuitry of the handset, besides the power amplifier, and hence slightly higher temperature elevations may be observed [221].

Note: Results are for visible human (VH) adult, isotropically reduced child size (CS), and anisotropically reduced child-like (CL) numerical phantoms.

TABLE 10.12

Temperature Elevations Induced in the User's Head, after 15 min, by a Phone Equipped with a Dual-Band Monopole-Helix Antenna (Average Radiated Power: 250 mW at 900 MHz and 125 mW at 1800 MHz)

Frequency (MHz)	Position	Heating Cause	ΔT_{\max} (°C)	$\Delta T_{\max\text{brain}}$ (°C)
900	Vertical	SAR	0.221	0.061
		SAR	0.136	0.023 ^a
		Contact	1.543	0.012 ^b
	Cheek	Contact + power dissipation	1.544	0.012 ^b
		Contact + power dissipation + SAR	1.581	0.023 ^a
		SAR	0.155	0.036
1800	Vertical	SAR	0.085	0.011 ^a
		Contact	1.543	0.012 ^b
		Contact + power dissipation	1.543	0.012 ^b
	Cheek	Contact + power dissipation	1.549	0.012 ^b
		SAR		
		Contact		

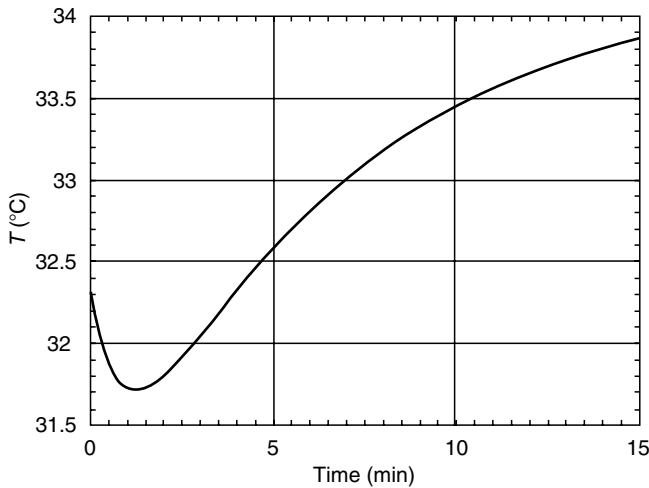


FIGURE 10.29

Time evolution of the temperature at a point on the ear in direct contact with a nonradiating phone.

The effect of the phone contact on the temperature evolution in the ear region is shown in Figure 10.29. It can be seen that when the phone was put in contact with the ear, the ear temperature experienced a quick decrease. This is because the phone was initially at ambient temperature (24°C), which was lower than the ear temperature. However, soon afterward, the heat supplied by the blood and conducted from the neighboring tissues stopped the decrease. Indeed, the temperature started to elevate, going beyond the initial value, because of the suppressed convective exchange with air.

When all heating sources are considered simultaneously, the results indicate that the maximum temperature elevation in the ear was almost entirely due to the contact effect, with only a very slight contribution due to SAR deposition in the ear region. However, the situation was completely different in the brain region. In fact, the heating effects due to SAR and phone contact tend to heat different parts of the brain. The contact-effect heating occurred in the lower external brain region, and the SAR-induced heating appeared mostly in the upper external brain region. Therefore, these two heating effects are not additive in the brain, and when they are simultaneously present, as opposed to the case when only one is considered, the result is that the portion of the brain affected by heating becomes larger. The peak temperature increase in the brain is therefore governed by the more significant of the two heating causes. At 900 MHz, SAR is more dominant, while at 1800 MHz, because of the lower radiated power, the two heating effects are comparable. Note that the ANSI/IEEE safety guidelines, which restrict the 1-g averaged spatial peak SAR to 1.6 W/kg , are associated with maximum temperature rises in the brain between 0.03°C and 0.09°C . These values are about 50 times lower than the threshold for thermal damage. The ICNIRP safety guideline of a 10-g averaged spatial peak SAR equal to 2 W/kg , results in maximum temperature rises in the brain between 0.1°C and 0.2°C , which is about 25 times lower than the threshold value.

10.6 Thermal Therapeutic Applications of Microwave Energy

Recent advances in technological development and in the understanding of EMF interaction with biological materials and systems have launched a broad range of biomedical applications. The following is a brief overview of computational techniques involved in

the development of ablative and hyperthermia therapies, including microwave cardiac ablation, endometrial ablation, and hyperthermia treatment of cancer. All of these therapeutic applications involve the use of microwave technologies to produce localized depositions of electromagnetic energy and, as a result, a rise of the local temperature in biological tissues. The target tissue temperature for the ablative treatments is about 65°C [224,225], whereas for the hyperthermia treatments, it is about 43°C [226]. The ablation treatments include the treatment for cardiac arrhythmias and for endometrial disorders such as menorrhagia. In all cases, the distribution of temperature increase must be carefully controlled in order to avoid excessive temperature increase in the surrounding healthy tissue. (See also Chapter 12 by Chou [284].)

10.6.1 Ablation for Cardiac Arrhythmias

Cardiac arrhythmias are mainly due to the presence of abnormal electrical sources or current paths in the cardiac tissues and are usually treated by destroying the tissue substrate where the electrical anomaly is localized [227–230]. This was performed by surgical resection initially, and later on by delivering a high-intensity DC shock with a defibrillator [227,230]. However, the high voltages and currents associated with the DC shock resulted in uncontrollable cardiac damages and severe complications. Subsequently, the use of RF EMFs to heat and destroy the arrhythmic tissue was proposed [230], and the advantages of microwave technology were demonstrated [228,229].

The RF ablation of cardiac tissue is usually performed using a unipolar arrangement, in which a catheter electrode placed into the heart delivers RF current to a large dispersive ground electrode on the skin surface of the patient. The RF current that flows from the catheter to the ground electrode following radial paths generates heat. While flowing from the catheter, the RF current density decreases as the second power of distance; consequently, the heat generation decreases according to the fourth-power law with the distance from the electrode. With this arrangement, the lesion (ablated tissue) is restricted to a small region (usually about 2 to 3 mm in diameter) contiguous to the catheter electrode, and the lesion dimensions cannot be extended by increasing the delivered power [225,227,229–231]. In microwave ablation, a catheter antenna is inserted into the cardiac chamber and is used to deliver MW power [225,228]. Since MW power deposition inside tissue decays with distance by following a second-power law, deeper lesions can be obtained compared to RF ablation [229,232–234].

In cardiac ablation treatments the lesion is usually defined as the region where temperature exceeds 65°C, which represents the threshold for irreversible damage of this tissue. This region must be large enough to ablate all the abnormal tissue responsible for the arrhythmia. Catheter antennas used for MW ablation have included monopoles [235,236], dipoles [229,237,238], and helices [232,239]. The design of a MW catheter antenna is a crucial point in MW ablation treatments and requires a complete study of the performance of the antenna imbedded in blood and in contact with the cardiac tissue. Performance parameters usually analyzed include the radiation pattern in the tissue; antenna impedance, which governs the bandwidth of the antenna; surface current suppression, in order to prevent heating of tissue along the catheter feeding cable; and dimensions of the induced lesion [240,241].

The design and performance evaluation of the microwave ablation antennas can be conducted by using computational tools and tested through *in vitro* or *in vivo* experimental studies [229,233,238,242]. Numerical tools allow the analysis of antenna performances under different operating conditions, and the evaluation of both electromagnetic power deposition and temperature increase in the tissue. In particular, the numerical evaluation of temperature increase induced inside the cardiac tissue allows the evaluation of blood flow influence on the induced lesion. This evaluation is of fundamental importance since the

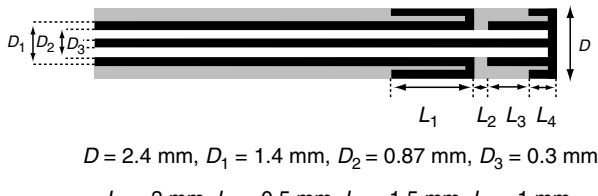


FIGURE 10.30
The cap-choke microwave catheter antenna.

presence of high blood flow rates inside the heart chambers provides a very effective heat removal process at the heart tissue surface so that the blood flow strongly limits the efficiency of both RF and MW ablation systems. Several numerical studies of SAR and temperature increase have been performed with the FEM [236,243–245] as well as the FDTD [246].

Figure 10.30 shows a cap-choke antenna mounted on an RG/178BU flexible coaxial cable operating at 2450 MHz [238]. The structure was realized by connecting an annular cap to the inner conductor of the cable, and a cylindrical coaxial choke to the outer conductor. A junction, filled with high-temperature epoxy resin, was used to separate the cap from the choke. Figure 10.31 shows the same antenna inserted in a two-layer cylindrical model of the heart. The heart model was used to study the influence of antenna position (touching or pressed into the cardiac muscle) and of blood flow (high or low) on the induced lesion. As an example, some computed results are presented in Table 10.13 for the amount of power to be delivered to the cardiac tissue to obtain lesions of different depths, under four operating conditions for an exposure duration of 60 sec [246].

10.6.2 Ablation for Endometrial Disorders

While still in the beginning stage, microwave and RF thermal ablation of the endometrium have been suggested recently as efficient and cost-effective alternatives to surgical resection as a treatment for dysfunctional uterine bleeding [247–251]. Techniques presently in

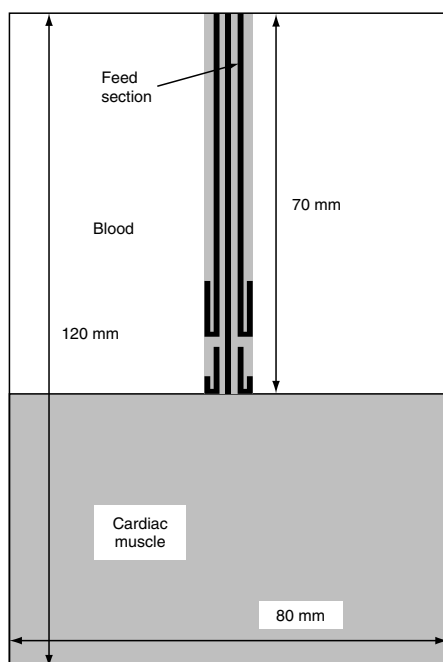


FIGURE 10.31
Cross section of the two-layer numerical model. The antenna's radial dimensions are not in scale.

^a $\Delta T_{\text{maxbrain}}$ located in the upper external brain region.

^b $\Delta T_{\text{maxBRAIN}}$ located in the lower external brain region.

TABLE 10.13

Microwave Power Required to Produce a Given Lesion Depth for Different Operating Conditions (Exposure Duration: 60 sec)

Lesion Depth (mm)	Power (W)			
	Touch Low Perfusion	Touch High Perfusion	Pressed Low Perfusion	Pressed High Perfusion
1	2.5	4.0	2.0	2.5
3	6.2	10	5.0	6.2

use include electrosurgery resection and Nd:YAG laser coagulation under direct hysteroscopic visualization [247,248,252–256]. The reported rates of complete amenorrhea are between 25% and 70% [253,256]. The variability arises principally from the unpredictable nature of induced thermal injury and perforation of the uterine wall [253]. Quantitative measures and patients' subjective reports of microwave endometrial ablation suggest a higher rate of satisfaction, acceptability, and life quality improvement [257,258].

In endometrial ablation, as in cardiac ablation, the design of the catheter antenna should be carefully tested to ensure the desired temperature increase (up to an increase of about 40°C in this case) in the tissue of interest. A sleeved-slot antenna designed for endometrial ablation operation at 915 MHz is depicted in Figure 10.32. The antenna configuration is similar to that of the catheter antenna for cardiac ablation, and is mounted on an RG8U coaxial cable. Figure 10.33 shows a comparison of the axial SAR distribution obtained from an FDTD analysis and from temperature measurements made in a cylindrical phantom filled with a muscle-equivalent material [259]. Two radial distances from the antenna axis, 2.5 and 7.5 mm, are shown. The SAR data obtained experimentally were normalized to the ones obtained from the FDTD simulation with 1.0 W of radiated power.

Figure 10.34 presents the lesion depth, defined as the region around the antenna where the temperature increase was greater or equal to 38°C (final temperature 75°C), as a function of the time of the exposure at different radiated powers. The curves were obtained by considering an antenna inserted in a cylindrical phantom filled with muscle-equivalent material. They simulate an antenna touching the endometrial tissue to be ablated. The lesion dimensions were evaluated as the depth from the antenna outer conductor. These curves can serve as guides in clinical trials where the antenna feeding power and time of exposure are key parameters to be chosen for a desired lesion dimension.

10.6.3 Microwave Interstitial Hyperthermia for Cancer Treatment

Hyperthermia cancer therapy is a treatment procedure in which tumor temperatures are elevated to above 43°C [226]. Investigations performed on cell cultures, tumor-bearing animals, and human patients have clearly shown that hyperthermia affords preferential

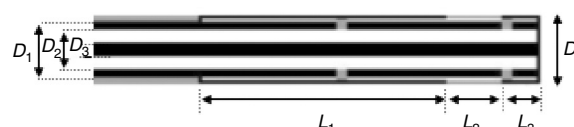


FIGURE 10.32

A microwave catheter antenna for endometrial ablation.

$$D = 12 \text{ mm}, D_1 = 9.8 \text{ mm}, D_2 = 7 \text{ mm}, D_3 = 2.6 \text{ mm}$$
$$L_1 = 45 \text{ mm}, L_2 = 10 \text{ mm}, L_3 = 7 \text{ mm}$$

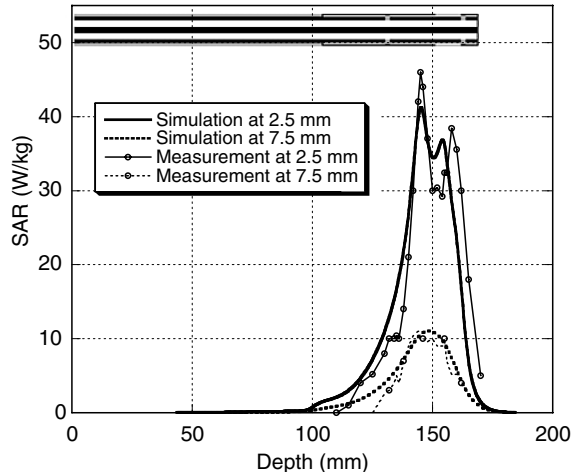


FIGURE 10.33

Comparison of axial SAR distributions obtained from FDTD and from temperature measurements made in tissue phantoms for the endometrial sleeved-slot antenna. The data are shown for radial distances of 2.5 and 7.5 mm.

killing of malignant cells, enhances the cytotoxic effects of many anticancer drugs, and potentiates the cell-killing ability of ionizing irradiation [260–266].

An important aspect of the development of applicators for microwave hyperthermia is the production of required temperature distributions in superficial and deep-seated tumors, that is, to produce temperatures in excess of 43°C in the tumor tissue, in order to guarantee the destruction of the malignant cells, while maintaining the temperature in the healthy tissue below 42°C to avoid thermal damage. In microwave hyperthermia, the antenna must provide efficient power delivery, good impedance matching at the frequency of operation, and a uniform SAR distribution in the tumor region. However, if the region to be treated is large compared to the field penetration depth, the required SAR uniformity cannot be achieved with a single microwave antenna, and the use of antenna

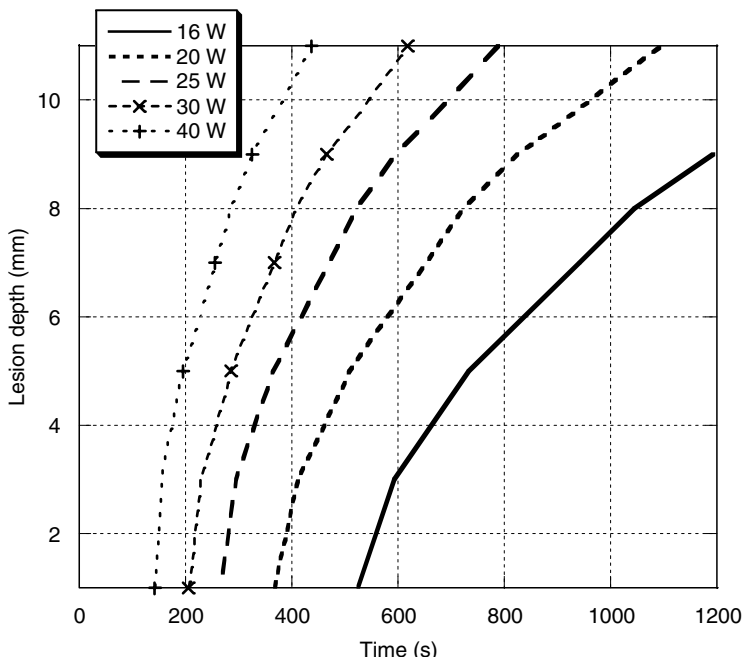


FIGURE 10.34

Endometrial lesion depth as a function of exposure duration for different radiated powers.

arrays becomes necessary. The following paragraphs present some computational results for thin catheter antennas designed for interstitial hyperthermia treatment of brain tumors.

Many investigations have been conducted on electromagnetic power deposition with regard to hyperthermia treatment for cancer. Most earlier studies were conducted analytically, modeling the catheter dipole antenna and surrounding tissue with a lossy transmission line [267–270]. Later, numerical and experimental studies were conducted on several antenna types, with the aim of optimizing antenna performances [270–274]. Considerable attention was devoted to arrays of antennas that have been studied both experimentally [275–277], by measuring the rate of temperature change caused by the radiated power, and theoretically, using antenna theory approaches [275,276,278] or approximate numerical procedures [277,279]. Indeed, antenna arrays have proved to be more suitable for increasing the region of uniform SAR deposition. More recent studies calculated, besides the electromagnetic power deposition, also the corresponding temperature increase. In fact, thermal analysis is a fundamental step in evaluating the effectiveness of the microwave applicator since it allows the assessment of the region where the temperature is above the threshold, and estimation of the required input power. Temperature distributions produced by interstitial antennas in tumor tissues have been experimentally evaluated by using microwave radiometry [277] and computed by using finite difference explicit solutions of the BHE [280,281]. A numerical solution of the BHE allows the analysis of the influence of different parameters such as blood flow on the temperature increase [280] and the development of clinical protocols [281].

Recently, an ADI solution of the BHE has been developed to study a 3-D array of catheter antennas inserted into a brain-equivalent phantom [282]. The antenna considered ([Figure 10.35](#)) was a sleeved-slot antenna mounted on a UT-34 coaxial cable [259,283]. An equilateral triangular array of the sleeved-slot antennas was studied in a phantom of brain-equivalent tissue in order to assess its capability in heating tumor regions of various dimensions [282]. [Figure 10.36a](#) shows the SAR distribution for 15-mm spacing among the antennas in the array; while in Figure 10.36b, contour plots at $\Delta T = 6^\circ\text{C}$ for various radiated powers and for a 15-mm spacing are presented. The graphs shown in Figure 10.36a and b are for a horizontal plane passing through the antenna slot [282].

Results such as those in Figure 10.36 can provide guidance to clinical protocols regarding the input power and optimal geometry (array spacing) for achieving an efficient tumor heating. For example, there is a minimum input power below which three separated regions around the three interstitial antennas constitute the region with temperatures above 43°C . Once this power is exceeded, a simply connected domain is obtained.

It is interesting to note that blood flow is remarkably low in the necrotic core of tumor tissues compared to normal tissue. Moreover, the rate of blood flow in normal tissue increases during hyperthermia. These phenomena may be investigated by varying the blood perfusion parameter in the BHE. Computer simulations, performed by varying the blood perfusion parameter from 5% to 200% of the nominal value, showed that the heat removal mechanism becomes less efficient as the blood flow is decreased, and the effective region of hyperthermia therapy is enlarged [282]. Consequently, the reduced blood flow in the necrotic tumor core and the increase in blood flow in normal tissue can serve to facilitate hyperthermia therapy.

10.7 Concluding Remarks

Knowledge of internal electric and magnetic fields, induced current densities, and SARs is fundamental in the study of biological responses, health effects, and medical applications

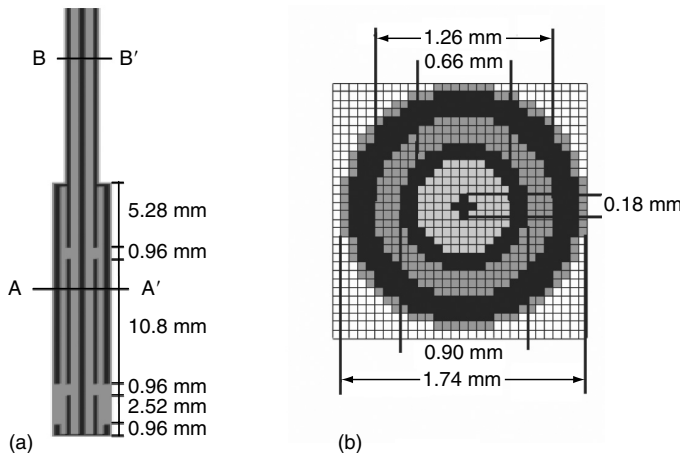


FIGURE 10.35
Longitudinal (a) and horizontal AA' (b) sections of the sleeved-slot antenna.

of EMFs. Complexities of biological tissues and of the incident fields make closed-form analytical solutions impractical, and computer methods are needed to predict the internal fields and their distributions. Great strides have been made during the past decade in the area of numerical dosimetry using anatomically based models of the human body. Among the most valuable of the numerical methods for predicting field intensities and SAR calculations are the impedance method for use at lower frequencies, where quasi-static approximations may be made ($<\sim 40$ MHz for the human body), and the FEM and FDTD methods, which may be used at any frequency of interest. For numerical calculations, the FDTD method requires a computer memory and computation time that is proportional to N . This is a considerable advantage over the computing methods, such as MoM or MoM-FFT. This chapter described the salient features of these methods and the many bioelectromagnetic exposure conditions for which they have been applied. Because of the limitations on the length of the chapter, only a few of the important recent applications of some of these methods were presented in some detail.

Note that numerical methods have matured to a level that they are being increasingly used by researchers in many laboratories for dosimetric calculations for important and

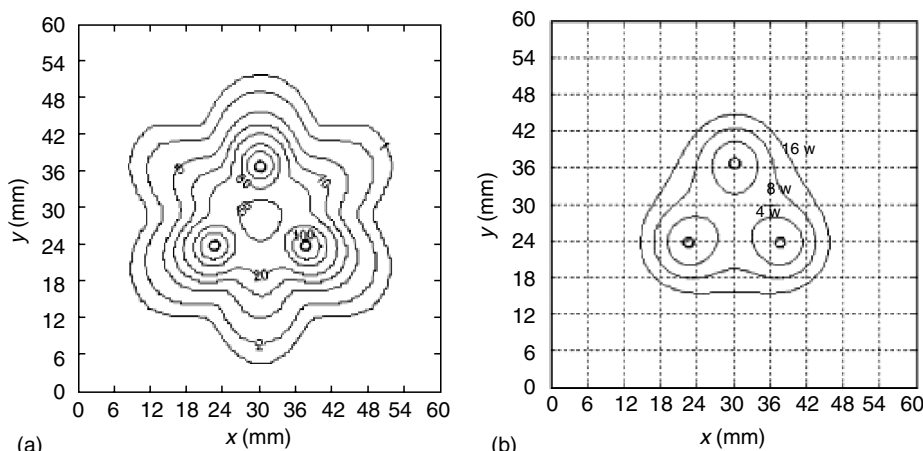


FIGURE 10.36
SAR distribution (a) and contour plots at $\Delta T = 6^\circ\text{C}$ for various radiated powers (b), on a horizontal plane passing through the antenna slot, for 15-mm spacing among the antennas in the array.

meaningful bioelectromagnetic problems. Some of the future developments will involve improving the efficiencies of the various codes by techniques such as use of the expanding grid rather than the regular grid, elimination of the relatively shielded interior regions of the modeled space at higher frequencies, and use of truncated models of the body at microwave frequencies where there is a lack of coupling between the various regions of the body. Because of accurate modeling of the tissue heterogeneities and shapes, these models have and will continue to play an important role in emerging technologies with bioelectromagnetic concerns. Some of the likely applications are personal wireless and mobile communications systems, automotive devices such as electric automobiles and collision avoidance systems, medical devices such as MRIs, implantable pacemakers and defibrillators, applicators for hyperthermia, and other minimally invasive therapeutic and surgical procedures.

Acknowledgment

We wish to thank Stefano Pisa, Marta Cavagnaro, Emanuele Piuzzi, and Zhangwei Wang for their valuable assistance in preparing the manuscript.

References

1. Lin, J.C., Computer methods for field intensity predictions, in *CRC Handbook of Biological Effects of Electromagnetic Fields*, Polk, C., and Postow, E., Eds., CRC Press, Boca Raton, FL, 1986, 273–313.
2. Lin, J.C. and Gandhi, O.P., Computer methods for predicting field intensity, in *Handbook of Biological Effects of Electromagnetic Fields*, Polk, C., and Postow, E., Eds., CRC Press, Boca Raton, FL, 1996, 337–402.
3. Lin, J.C., Mechanisms of field coupling into biological systems at ELF and RF frequencies, in *Advances in Electromagnetic Fields in Living Systems*, vol. 3, Kluwer/Plenum, New York, 2000, 1–38.
4. Schwan, H.P. and Piersol, G.M., Absorption of electromagnetic energy in body tissues, *Am. J. Phys. Med.*, 33, 371, 1954.
5. Schwan, H.P. and Li, K., Hazards due to total body irradiation by radar, *Proc. IRE*, 44, 1572, 1956.
6. Schwan, H.P. and Li, K., The mechanism of absorption of ultrahigh frequency electromagnetic energy in tissue as related to the problem of tolerance dosage, *IRE Trans. Med. Electron.*, 4, 45, 1956.
7. Johnson, C.C. and Guy, A.W., Nonionizing electromagnetic wave effects in biological materials and systems, *Proc. IEEE*, 60, 692, 1972.
8. Michaelson, S.M. and Lin, J.C., *Biological Effects and Health Implications of Radiofrequency Radiation*, Plenum Press, New York, 1987.
9. Shapiro, A.R., Lutomirski, R.F., and Yura, H.T., Induced fields and heating within a cranial structure irradiated by an electromagnetic plane wave, *IEEE Trans. Microwave Theory Technol.*, 19, 187, 1971.
10. Kritikos, H.N. and Schwan, H.P., Hot spot generated in conduction spheres by EM waves and biological implications, *IEEE Trans. Biomed. Eng.*, 19, 53, 1972.
11. Lin, J.C., Guy, A.W., and Kraft, G.H., Microwave selective brain heating, *J. Microwave Power*, 8, 275, 1973.
12. Ho, H.S. and Guy, A.W., Development of dosimetry for RF and microwave radiation, *Health Phys.*, 29, 317, 1975.

13. Weil, C.M., Absorption characteristics of multi-layered sphere models exposed to UHF/micro-wave radiation, *IEEE Trans. Biomed. Eng.*, 22, 468, 1975.
14. Joines, W.T. and Spiegel, R.J., Resonance absorption of microwaves by the human skull, *IEEE Trans. Biomed. Eng.*, 21, 46, 1975.
15. Lin, J.C., Interaction of two cross-polarized electromagnetic waves with mammalian cranial structures, *IEEE Trans. Biomed. Eng.*, 23, 371, 1976.
16. Lin, J.C., Guy, A.W., and Johnson, C.C., Power deposition in a spherical model of man exposed to 1–20 MHz electromagnetic fields, *IEEE Trans. Microwave Theory Technol.*, 21, 791, 1973 (see also corrections *IEEE MTT*, 23, 265, 1975).
17. Kritikos, H.N. and Schwan, H.P., The distribution of heating potential inside lossy spheres, *IEEE Trans. Biomed. Eng.*, 22, 457, 1975.
18. Johnson, C.C., Durney, C.H., and Massoudi, H., Long-wavelength electromagnetic power absorption in prolate spheroidal models of man and animals, *IEEE Trans. Microwave Theory Technol.*, 23, 739, 1975.
19. Durney, C.H., Johnson, C.C., and Massaud, A., Long wave-length analysis of plane wave irradiation of a prolate spheroidal model of man, *IEEE Trans. Microwave Theory Technol.*, 23, 246, 1975.
20. Massoudi, H., Durney, C.H., and Johnson, C.C., Long wavelength electromagnetic power absorption in ellipsoidal models of man and animals, *IEEE Trans. Microwave Theory Technol.*, 24, 41, 1977.
21. Rowlandson, G.I. and Barber, P.W., Absorption of high frequency RF energy by biological models: calculations based on geometrical optics, *Radio Sci.*, 14, 43S, 1979.
22. Lin, J.C., Whole-body exposure in the near zone of HF electromagnetic fields, *URSI International Electromagnetic Waves and Biology Symposium*, Jouy en Josas, France, 1980.
23. Guy, A.W., Webb, M.D., and Sorenson, C.C., Determination of power absorption in man exposed to HF electromagnetic fields by thermographic measurements on scale models, *IEEE Trans. Biomed. Eng.*, 23, 361, 1976.
24. Liversy, D.E. and Chen, K.M., Electromagnetic fields induced inside arbitrary shaped biological bodies, *IEEE Trans. Microwave Theory Technol.*, 22, 1273, 1974.
25. Guru, B.S. and Chen, K.M., Experimental and theoretical studies in electromagnetic field induced inside finite biological bodies, *IEEE Trans. Microwave Theory Technol.*, 24, 433, 1976.
26. Chen, K.M. and Guru, B.S., Internal EM field and absorbed power density in human torsos induced by 1–500 MHz EM waves, *IEEE Trans. Microwave Theory Technol.*, 25, 746, 1977.
27. Hagman, M.J., Gandhi, O.P., and Durney, C.H., Numerical calculation of electromagnetic energy deposition for a realistic model of man, *IEEE Trans. Microwave Theory Technol.*, 27, 804, 1979.
28. Gandhi, O.P., Electromagnetic absorption in inhomogeneous model of man for realistic exposure conditions, *Bioelectromagnetics*, 3, 81, 1982.
29. Armitage, D.W., Leveen, H.H., and Pethig, R., Radio-frequency induced hyperthermia: computer simulation of specific absorption rate distributions using realistic anatomical models, *Phys. Med. Biol.*, 28, 31, 1983.
30. Gandhi, O.P., DeFord, J.F., and Kanai, H., Impedance method for calculation of power deposition patterns in magnetically induced hyperthermia, *IEEE Trans. Biomed. Eng.*, 31, 644, 1984.
31. Gandhi, O.P. and DeFord, J.F., Calculation of EM power deposition for operator exposure to RF induction heaters, *IEEE Trans. Electromagn. Compat.*, 30, 63, 1988.
32. Orcutt, N. and Gandhi, O.P., A 3-D impedance method to calculate power deposition in biological bodies subjected to time-varying magnetic fields, *IEEE Trans. Biomed. Eng.*, 35, 577, 1988.
33. Orcutt, N. and Gandhi, O.P., Use of the impedance method to calculate 3-D power deposition patterns for hyperthermia with capacitive plate electrodes, *IEEE Trans. Biomed. Eng.*, 37, 36, 1990.
34. Epstein, B.R. and Foster, K.R., Anisotropy in dielectric properties of skeletal muscle, *Med. Biol. Eng. Comput.*, 21, 51, 1983.
35. Zheng, E., Shao, S., and Webster, J.G., Impedance of skeletal muscle from 1 Hz to 1 MHz, *IEEE Trans. Biomed. Eng.*, 31, 477, 1984.

36. Zhu, X.L. and Gandhi, O.P., Design of RF needle applicators for optimum SAR distributions in irregularly-shaped tumors, *IEEE Trans. Biomed. Eng.*, 35, 382, 1988.
37. Gandhi, O.P. and Chen, J.Y., Numerical dosimetry at power-line frequencies using anatomically based models, *Bioelectromagnetics*, Supplement 1, 43, 1992.
38. Tofani, S., Ossola, P., d'Amore, G., and Gandhi, O.P., Electric fields and current density distributions induced in an anatomically based model of the human head by magnetic fields from a hair dryer, *Health Phys.*, 68, 71–79, 1995.
39. Wu, D., Ren, J., and Gandhi, O.P., Currents induced in the arm and the body by the magnetic fields of an electric hand drill, *Abstracts of the Fifteenth Annual Meeting of the Bioelectromagnetics Society*, Los Angeles, CA, 1993, 31.
40. Ren, J., Gandhi, O.P., Casamento, J.P., and Bassen, H.I., Currents induced in the human body by electric blankets, *Abstracts of the 15th Annual Meeting of the Bioelectromagnetics Society*, Los Angeles, CA, 1993, 32.
41. Harrington, R.F., *Field Computation by Moment Methods*, McGraw-Hill, New York, 1968.
42. Schelkunoff, S.A., Field equivalence theorems, *Comm. Pure Appl. Math.*, 4, 43, 1951.
43. Lin, J.C. and Wu, C.L., Scattering of microwaves by dielectric materials used in laboratory animal restrainers, *IEEE Trans. Microwave Theory Technol.*, 24, 219, 1976.
44. Gandhi, O.P., Hagman, M.J., and D'Andrea, J.A., Part-body and multi-body effects on absorption of radio frequency electromagnetic energy by animals and by models of man, *Radio Sci.*, 14, 155, 1979.
45. Karimullah, K., Chen, K.M., and Nyquist, D.P., Electromagnetic coupling between a thin-wire antenna and a neighboring biological body, *IEEE Trans. Microwave Theory Technol.*, 28, 1218, 1980.
46. Chatterjee, I., Hagman, M.J., and Gandhi, O.P., Electromagnetic energy deposition in an inhomogeneous block model for near-field irradiation conditions, *IEEE Trans. Microwave Theory Technol.*, 28, 1452, 1980.
47. Wu, T.K. and Tsai, L.L., Electromagnetic fields induced inside arbitrary cylinders of biological tissue, *IEEE Trans. Microwave Theory Technol.*, 25, 61, 1977.
48. Wu, T.K. and Tsai, L.L., Scattering from arbitrary-shaped lossy dielectric bodies of revolution, *Radio Sci.*, 12, 709, 1977.
49. Poggio, A.J. and Miller, E.K., Integral equation solutions of three-dimensional scattering problems, in *Computer Techniques for Electromagnetics*, Mittra, R., Ed., Pergamon Press, Elmsford, New York, 1973, 159.
50. Massoudi, H., Durney, C.H., Barber, P.W., and Iskander, M.F., Post resonance EM absorption by man and animals, *Bioelectromagnetics*, 3, 333, 1982.
51. Wu, T.K., Electromagnetic fields and power deposition in body of revolution models of man, *IEEE Trans. Microwave Theory Technol.*, 27, 279, 1979.
52. Mautz, J.R. and Harrington, R.F., Radiation and scattering from bodies of revolution, *Appl. Sci. Res.*, 20, 405, 1969.
53. Harrington, R.F. and Mautz, J.R., Green's functions for surfaces of revolution, *Radio Sci.*, 7, 603, 1972.
54. Pogorzelski, R.J. and Wu, T.K., Computations of scattering from inhomogeneous penetrable elliptic cylinders by means of invariant imbedding, in *URSI Symposium of Electromagnetic Wave Theory*, Stanford, CA, 1977, 323.
55. Jin, J., *The Finite Element Method in Electromagnetics*, Wiley, New York, 1993.
56. Boyes, W.E., Lynch, D.R., Paulsen, K.D., and Minerbo, G.N., Nodal-based finite element modelling of Maxwell's equations in three dimensions, *IEEE Trans. Antennas Propagat.*, 40, 642, 1992.
57. Paulsen, K.D., Jia, X., and Sullivan, J.M., Jr., Finite element computations of specific absorption rates in anatomically conforming full-body models for hyperthermia treatment analysis, *IEEE Trans. Biomed. Eng.*, 40, 933, 1993.
58. Yee, K.S., Numerical solutions of initial boundary value problems involving Maxwell's equations in isotropic media, *IEEE Trans. Antennas Propagat.*, 14, 303, 1966.
59. Taflove, A. and Brodwin, M.E., Computation of the electromagnetic fields and induced temperatures within a model of the microwave-irradiated human eye, *IEEE Trans. Microwave Theory Technol.*, 23, 888, 1975.

60. Taflove, A. and Brodwin, M.E., Numerical solution of steady-state EM scattering problems using the time dependent Maxwell's equation, *IEEE Trans. Microwave Theory Technol.*, 23, 623, 1975.
61. Taflove, A., Application of the finite-difference time domain method to sinusoidal steady-state electromagnetic-penetration problems, *IEEE Trans. Electromagn. Compat.*, 22, 191, 1980.
62. Holland, R., THREDE: a free field EMP coupling and scattering code, *IEEE Trans. Nuclear Sci.*, 24, 2416, 1977.
63. Kunz, K.S. and Lee, K.M., A three-dimensional finite-difference solution of the external response of an aircraft to a complex transient EM environment: part 1—the method and its implementation, *IEEE Trans. Electromagn. Compat.*, 20, 328, 1978.
64. Kunz, K.S. and Luebbers, R.J., *The Finite-Difference Time-Domain Method for Electromagnetics*, CRC Press, Boca Raton, FL, 1993.
65. Taflove, A., *Computational Electrodynamics: The Finite-Difference Time-Domain Method*, Artech House, London, 1995.
66. Taflove, A. and Hagness, S.C., Eds., *Computational Electrodynamics: The Finite-Difference Time-Domain Method*, Artech House, London, 2000.
67. Spiegel, R.J., Fatmi, M.B.A., Stuchly, S.S., and Stuchly, M.A., Comparison of finite-difference time-domain SAR calculations with measurements, in a heterogeneous model of man, *IEEE Trans. Biomed. Eng.*, 36, 849, 1989.
68. Chen, J.Y. and Gandhi, O.P., Currents induced in an anatomically based model of a human for exposure to vertically polarized electromagnetic pulses, *IEEE Trans. Microwave Theory Technol.*, 39, 31, 1991.
69. Sullivan, D.M., Borup, D.T., and Gandhi, O.P., Use of the finite-difference time-domain method in calculating EM absorption in human tissues, *IEEE Trans. Biomed. Eng.*, 34, 148, 1987.
70. Chen, J.Y. and Gandhi, O.P., Numerical simulation of annular-phased arrays of dipoles for hyperthermia of deep-seated tumors, *IEEE Trans. Biomed. Eng.*, 39, 209, 1992.
71. Chen, J.Y., Gandhi, O.P., and Conover, D.L., SAR and induced current distributions for operator exposure to RF dielectric sealers, *IEEE Trans. Electromagn. Compat.*, 33, 252, 1991.
72. Luebbers, R., Hunsberger, F.P., Kunz, K.S., Standler, R.B., and Schneider, M., A frequency-dependent finite-difference time-domain formulation for dispersive materials, *IEEE Trans. Electromagn. Compat.*, 32, 222, 1990.
73. Bui, M.D., Stuchly, S.S., and Costache, G.I., Propagation of transients in dispersive dielectric media, *IEEE Trans. Microwave Theory Technol.*, 39, 1165, 1991.
74. Sullivan, D.M., A frequency-dependent FDTD method for biological applications, *IEEE Trans. Microwave Theory Technol.*, 40, 532, 1992.
75. Luebbers, R.J., Hunsberger, F., and Kunz, K.S., FDTD for nth order dispersive media, *IEEE Trans. Antennas Propagat.*, 40, 1297, 1992.
76. Joseph, R.M., Hagness, S.C., and Taflove, A., Direct time integration of Maxwell's equations in linear dispersive media with absorption for scattering and propagation of femtosecond electromagnetic impulses, *Optics Lett.*, 16, 1412, 1991.
77. Gandhi, O.P., Gao, B.Q., and Chen, J.Y., A frequency-dependent finite-difference time-domain formulation for induced current calculations in human beings, *Bioelectromagnetics*, 13, 543, 1992.
78. Gandhi, O.P., Gao, B.Q., and Chen, J.Y., A frequency-dependent finite-difference time-domain formulation for general dispersive media, *IEEE Trans. Microwave Theory Technol.*, 41, 658, 1993.
79. Furse, C.M., Chen, J.Y., and Gandhi, O.P., A frequency-dependent finite-difference time-domain method for induced current and SAR calculations for a heterogeneous model of the human body, *IEEE Trans. Electromagn. Compat.*, 36, 128, 1994.
80. Gandhi, O.P. and Chen, J.Y., Electromagnetic absorption in the human head for a proposed 6 GHz mobile communication system, *IEEE Trans. Electromagn. Compat.*, 37, 547, 1995.
81. Gandhi, O.P., Some numerical methods for dosimetry: ELF to microwave frequencies, *Radio Sci.*, 30, 161–177, 1995.
82. Ackerman, M.J., The visible human project, *Proc. IEEE*, 86, 504, 1998.

83. Mason, P.A., Ziriax, J.M., Hurt, W.D., Walters, T.J., Ryan, K.L., Nelson, D.A., Smith, K.I., and D'Andrea, J.A., Recent advancements in dosimetry measurements and modeling, in *Radio Frequency Radiation Dosimetry*, Klauenberg, B.J. and Miklavcic, D., Eds., Kluwer, Newyork, 2000, 141.
84. http://starview.brooks.af.mil/EMF/dosimetry_models/
85. Rush, S., Abildskov, J.A., and McFee, R., Resistivity of body tissues at low frequencies, *Circ. Res.*, 12, 40, 1963.
86. Florig, H.K., Hoburg, J.F., and Morgan, M.G., Electric-field exposure from electric blankets, *IEEE Trans. Power Deliv.*, 2, 527, 1987.
87. Hayashi, N., Isaka, K., and Yokoi, Y., Analysis of magnetic-field profiles in electric blanket users, *IEEE Trans. Power Deliv.*, 4, 1897, 1989.
88. Kaune, W.T. and Gillis, M.F., General properties of the interaction between animals and ELF electric fields, *Bioelectromagnetics*, 2, 1, 1981.
89. Guy, A.W., Davidow, S., Yang, G.Y., and Chou, C.K., Determination of electric current distributions in animals and humans exposed to a uniform 60-Hz high-intensity electric field, *Bioelectromagnetics*, 3, 47, 1982.
90. Stratton, J.A., *Electromagnetic Theory*, McGraw-Hill, New York, 1941.
91. Deno, D.W., Currents induced in the human body by high voltage transmission line electric field—measurement and calculation of distribution and dose, *IEEE Trans. Power Apparatus Syst.*, 96, 1517, 1977.
92. DiPlacido, J., Shih, C.H., and Ware, B.J., Analysis of the proximity effects in electric field measurements, *IEEE Trans. Power Apparatus Syst.*, 97, 2167, 1978.
93. Ruksopollmuang, S. and Chen, K.M., Heating of spherical vs. realistic models of human and infrahuman heads by electromagnetic waves, *Radio Sci.*, 14, 51, 1979.
94. Hagman, M.J., Gandhi, O.P., D'Andrea, J.A., and Chatterjee, I., Head resonance: numerical solutions and experimental results, *IEEE Trans. Microwave Theory Technol.*, 27, 809, 1979.
95. Gandhi, O.P., Hunt, E.L., and D'Andrea, J.A., Deposition of EM energy in animals and in models of man with and without grounding and reflector effects, *Radio Sci.*, 12, 39S, 1977.
96. Deford, J.F., Gandhi, O.P., and Hagman, M.J., Moment-method solutions and SAR calculations for inhomogeneous models of man with large number of cells, *IEEE Trans. Microwave Theory Technol.*, 31, 848, 1983.
97. Sullivan, D.M., Gandhi Om, P., and Taflove, A., Use of the finite-difference time-domain method for calculating EM absorption in man models, *IEEE Trans. Biomed. Eng.*, 35, 179, 1988.
98. Bernardi, P., Cavagnaro, M., Pisa, S., and Piuzzi, E., Specific absorption rate and temperature elevation in a subject exposed in the far-field of radio-frequency sources operating in the 10–900-MHz range, *IEEE Trans. Biomed. Eng.*, 50, 295, 2003.
99. Dimbylow, P.J., FDTD calculations of the whole-body averaged SAR in an anatomically realistic voxel model of the human body from 1 MHz to 1 GHz, *Phys. Med. Biol.*, 42, 479, 1997.
100. ICNIRP, Guidelines for limiting exposure to time-varying electric, magnetic, and electromagnetic fields (up to 300 GHz), *Health Phys.*, 74, 494, 1998.
101. IEEE, IEEE standard for safety levels with respect to human exposure to radio frequency electromagnetic fields, 3 kHz to 300 GHz, in *IEEE Standard C95.1*, 1999.
102. Dimbylow, P.J., Fine resolution calculations of SAR in the human body for frequencies up to 3 GHz, *Phys. Med. Biol.*, 47, 2835, 2002.
103. Mason, A.P., Hurt, W.D., Walters, T.J., D'Andrea, J.A., Gajšek, P., Ryan, K.L., Nelson, D.A., Smith, K.I., and Ziriax, J.M., Effects of frequency, permittivity, and voxel size on predicted specific absorption rate values in biological tissue during electromagnetic-field exposure, *IEEE Trans. Microwave Theory Technol.*, 48, 2050, 2000.
104. Gajšek, P., Hurt, W.D., Ziriax, J.M., and Mason, A.P., Parametric dependence of SAR on permittivity values in a man model, *IEEE Trans. Biomed. Eng.*, 48, 1169, 2001.
105. Mazzurana, M., Sandrini, L., Vaccari, A., Malacarne, C., Cristoforetti, L., and Pontalti, R., A semi-automatic method for developing an anthropomorphic numerical model of dielectric anatomy by MRI, *Phys. Med. Biol.*, 48, 3157, 2003.
106. Tinniswood, A.D., Furse, C.M., and Gandhi Om, P., Power deposition in the head and neck of an anatomically based human body model for plane wave exposures, *Phys. Med. Biol.*, 43, 2361, 1998.

107. Nagaoka, T., Watanabe, S., Sakurai, K., Kunieda, E., Watanabe, S., Taki, M., and Yamanaka, Y., Development of realistic high-resolution whole-body voxel models of Japanese adult males and females of average height and weight, and application of models to radio-frequency electromagnetic-field dosimetry, *Phys. Med. Biol.*, 49, 1, 2004.
108. Sandrini, L., Vaccari, A., Malacarne, C., Cristoforetti, L., and Pontalti, R., RF dosimetry: a comparison between power absorption of female and male numerical models from 0.1 to 4 GHz, *Phys. Med. Biol.*, 49, 5185, 2004.
109. Gabriel, S., Lau, R.W., and Gabriel, C., The dielectric properties of biological tissues: III. Parametric models for the dielectric spectrum of tissues, *Phys. Med. Biol.*, 41, 2271, 1996.
110. Gabriel, C., Compilation of the Dielectric Properties of Body Tissues at RF and Microwave Frequencies, Technical Report, AL/OE-TR-1996-0037, Brooks Air Force, Brooks AFB, TX, 1996.
111. Faraone, A., Tay, R.Y.-S., Joyner, K.H., and Balzano, Q., Estimation of the average power density in the vicinity of cellular base-station collinear array antennas, *IEEE Trans. Veh. Technol.*, 49, 984, 2000.
112. Cicchetti, R. and Faraone, A., Estimation of the peak power density in the vicinity of cellular and radio base station antennas, *IEEE Trans. Electromagn. Compat.*, 46, 275, 2004.
113. Buzzi, M. and Gianola, P., Electromagnetic fields radiated by GSM antennas, *Electron. Lett.*, 35, 855, 1999.
114. Altman, Z., Begasse, B., Dale, C., Karwowski, A., Wiart, J., Wong, M.F., and Gattoufi, L., Efficient models for base station antennas for human exposure assessment, *IEEE Trans. Electromagn. Compat.*, 44, 588, 2002.
115. Bernardi, P., Cavagnaro, M., Cristoforetti, L., Malacarne, C., Pisa, S., Piuzzi, E., Pontalti, R., and Vaccari, A., Modelling of BTS antennas: Dependence of the accuracy on FDTD mesh size and implementation criteria, in *Proceedings of the 2nd International Workshop on Biological Effects of Electromagnetic Fields*, Rhodes, Greece, Kostarakis, P., Ed., 2002, 74.
116. Blanch, S., Romeu, J., and Cardama, A., Near field in the vicinity of wireless base-station antennas: an exposure compliance approach, *IEEE Trans. Antennas Propagat.*, 50, 685, 2002.
117. Adane, Y., Gati, A., Wong, M.-F., Dale, C., Wiart, J., and Hanna V.F., Optimal modeling of real radio base station antennas for human exposure assessment using spherical-mode decomposition, *Antennas Wireless Propagat. Lett.*, 1, 215, 2002.
118. Fridén, J., RF exposure compliance boundary analysis of base station antennas using combined spherical-cylindrical near-field transformations, *Electron. Lett.*, 39, 1783, 2003.
119. Nicolas, E., Lautru, D., Jacquin, F., Wong, M.F., and Wiart, J., Specific absorption rate assessments based on a selective isotropic measuring system for electromagnetic fields, *IEEE Trans. Instrum. Meas.*, 50, 397, 2001.
120. Lazzi, G. and Gandhi, O.P., A mixed FDTD-integral equation approach for on-site safety assessment in complex electromagnetic environments, *IEEE Trans. Antennas Propagat.*, 48, 1830, 2000.
121. Gandhi, O.P. and Lam, M.S., An on-site dosimetry system for safety assessment of wireless base stations using spatial harmonic components, *IEEE Trans. Antennas Propagat.*, 51, 840, 2003.
122. Cooper, J., Marx, B., Buhl, J., and Hombach, V., Determination of safety distance limits for a human near a cellular base station antenna, adopting the IEEE standard or ICNIRP guidelines, *Bioelectromagnetics*, 23, 429, 2002.
123. Catarinucci, L., Palazzari, P., and Tarricone, L., Human exposure to the near field of radiobase antennas—a full-wave solution using parallel FDTD, *IEEE Trans. Microwave Theory Technol.*, 51, 935, 2003.
124. Bernardi, P., Cavagnaro, M., Pisa, S., and Piuzzi, E., Human exposure in the vicinity of radio base station antennas, in *Proceedings of EMC Europe 2000 (4th European Symposium on Electromagnetic Compatibility)*, Brugge, Belgium, 2000, 187.
125. Meyer, F.J.C., Davidson, D.B., Jakobus, U., and Stuchly M.A., Human exposure assessment in the near field of GSM base-station antennas using a hybrid finite element/method of moments technique, *IEEE Trans. Biomed. Eng.*, 50, 224, 2003.
126. Bernardi, P., Cavagnaro, M., Pisa, S., and Piuzzi, E., Human exposure to cellular base station antennas in urban environment, *IEEE Trans. Microwave Theory Technol.*, 48, 1996, 2000.

127. Alaydrus, M., Bitz, A., Streckert, J., and Hansen, V., Combination of the hybrid⁽²⁾-method and the FDTD for safety assessment of human for base station antennas mounted in real environments, in XXVIIth General Assembly of International Union of Radio Science, Maastricht, The Netherlands, 2002.
128. Martinez-Burdalo, M., Nonidez, L., Martin, A., and Villar, R., Near-field time-domain physical-optics and FDTD method for safety assessment near a base-station antenna, *Microwave Opt. Technol. Lett.*, 39, 393, 2003.
129. Bernardi, P., Cavagnaro, M., Cicchetti, R., Pisa, S., Piuzzi, E., and Testa, O., A UTD/FDTD investigation on procedures to assess compliance of cellular base-station antennas with human-exposure limits in a realistic urban environment, *IEEE Trans. Microwave Theory Technol.*, 51, 2409, 2003.
130. Bernardi, P., Cavagnaro, M., Cicchetti, R., Pisa, S., Piuzzi, E., and Testa, O., Human exposure to the electromagnetic fields produced by coexisting wireless communication systems in a complex indoor environment, in *Proceedings of EMC Europe 2004 (International Symposium of Electromagnetic Compatibility)*, Eindhoven, The Netherlands, 2004, 79.
131. Lin, J.C., Interaction of electromagnetic transient radiation with biological materials, *IEEE Trans. Electromagn. Compat.*, 17, 93, 1975.
132. Lin, J.C., Wu, C.L., and Lam, C.K., Transmission of electromagnetic pulse into the head, *Proc. IEEE*, 63, 1726, 1975.
133. Lin, J.C., Electromagnetic pulse interaction with mammalian cranial structures, *IEEE Trans. Biomed. Eng.*, 23, 61, 1976.
134. Lin, J.C. and Lam, C.K., Coupling of Gaussian electromagnetic pulse into muscle-bone model of biological structure, *J. Microwave Power*, 11, 67, 1976.
135. Lin, J.C., The microwave auditory phenomenon, *Proc. IEEE*, 68, 67, 1980.
136. Lin, J.C., Microwave-induced hearing sensation: some preliminary theoretical observations, *J. Microwave Power*, 11, 295, 1976.
137. Lin, J.C., On Microwave-induced hearing sensation, *IEEE Trans. Microwave Theory Technol.*, 25, 605, 1977.
138. Lin, J.C., Further studies on the microwave auditory effects, *IEEE Trans. Microwave Theory Technol.*, 25, 936, 1977.
139. Lin, J.C., Calculations of frequencies and threshold of microwave-induced auditory signals, *Radio Sci.*, 12, SS-1, 237, 1977.
140. Lin, J.C., *Microwave Auditory Effects and Applications*, Charles C. Thomas, Publisher, Springfield, IL, 1978.
141. Watanabe, Y., Tanaka, T., Taki, M., and Watanabe, S., FDTD analysis of microwave hearing effect, *IEEE MTT*, 48, 2126, 2000.
142. Lin, J.C. and Wang, Z.W., RF thermoelastic pressures induced in a human head model in high-pass MRI birdcage coils, in ISMRM, Miami, 2005.
143. Wang, Z.W. and Lin, J.C., RF induced thermoelastic pressure waves in different size human head models in MRI birdcage coils, in 27th Annual Meeting of Bioelectromagnetics Society, Dublin, Ireland, June 2005.
144. Yang, L.Q. and Giannakis, G.B., Ultra-wideband communications, *IEEE Signal Process. Mag.*, 21, 26, 2004.
145. Qiu, R.C., Liu, H.P., and Shen, X.M., Ultra-wideband for multiple access communications, *IEEE Commun. Mag.*, 43, 80, 2005.
146. Gandhi, O.P., Gu, Y.G., Chen, J.Y., and Bassen, H.I., Specific absorption rates and induced current distributions in an anatomically based human model for plane-wave exposures, *Health Phys.*, 63, 281, 1992.
147. FCC, Evaluating compliance with FCC guidelines for human exposure to radiofrequency electromagnetic fields, in *OET Bulletin 65*, FCC, Washington, DC, Aug. 1997.
148. IEC, human exposure to radio frequency fields from hand-held and body-mounted wireless communication devices—human models, instrumentation, and procedures—part 1: procedure to determine the specific absorption rate (SAR) for hand-held devices used in close proximity to the ear (frequency range of 300 MHz to 3 GHz), in *IEC Standard*, 62209-1, 2005.

149. Toftgard, J., Hornsleth, S.N., and Andersen, J.B., Effects on portable antennas of the presence of a person, *IEEE Trans. Antennas Propagat.*, 41, 739, 1993.
150. Dimbylow, P.J. and Mann, S.M., SAR calculations in an anatomically realistic model of the head for mobile communication transceivers at 900 MHz and 1.8 GHz, *Phys. Med. Biol.*, 39, 1537, 1994.
151. Gandhi, O.P., Lazzi, G., and Furse, C.M., Electromagnetic absorption in the human head and neck for mobile telephones at 835 and 1900 MHz, *IEEE Trans. Microwave Theory Technol.*, 44, 1884, 1996.
152. Okoniewski, M., and Stuchly, M.A., A study of the handset antenna and human body interaction, *IEEE Trans. Microwave Theory Technol.*, 44, 1855, 1996.
153. Hombach, V., Meier, K., Burkhardt, M., Kuhn, E., and Kuster, N., The dependence of EM energy absorption upon human head modeling at 900 MHz, *IEEE Trans. Microwave Theory Technol.*, 44, 1865, 1996.
154. Watanabe, S., Taki, M., Nojima, T., and Fujiwara, O., Characteristics of the SAR distributions in a head exposed to electromagnetic fields radiated by a hand-held portable radio, *IEEE Trans. Microwave Theory Technol.*, 44, 1874, 1996.
155. Bernardi, P., Cavagnaro, M., and Pisa, S., Evaluation of the SAR distribution in the human head for cellular phones used in a partially closed environment, *IEEE Trans. Electromagn. Compat.*, 38, 357, 1996.
156. Colburn, J.S., and Rahmat-Samii, Y., Human proximity effects on circular polarized handset antennas in personal satellite communications, *IEEE Trans. Antennas Propagat.*, 46, 813, 1998.
157. Lazzi, G., and Gandhi, O.P., On modeling and personal dosimetry of cellular telephone helical antennas with the FDTD code, *IEEE Trans. Antennas Propagat.*, 46, 525, 1998.
158. Mangoud, M.A., Abd-Alhameed, R.A., and Excell, P.S., Simulation of human interaction with mobile telephones using hybrid techniques over coupled domains, *IEEE Trans. Microwave Theory Technol.*, 48, 2014, 2000.
159. Cerri, G., Russo, P., Schiavoni, A., Tribellini, G., and Bielli, P., A new MoM-FDTD hybrid technique for the analysis of scattering problems, *Electron. Lett.*, 34, 438, 1998.
160. Bernardi, P., Cavagnaro, M., Pisa, S., and Piuzzi, E., A graded-mesh FDTD code for the study of human exposure to cellular phones equipped with helical antennas, *Appl. Comput. Electromagn. Soc. J.*, 16, 90, 2001.
161. Bernardi, P., Cavagnaro, M., Pisa, S., and Piuzzi, E., Power absorption and temperature elevations induced in the human head by a dual-band monopole-helix antenna phone, *IEEE Trans. Microwave Theory Technol.*, 49, 2539, 2001.
162. Jensen, M.A. and Rahmat-Samii, Y., EM interaction of handset antennas and a human in personal communications, *Proc. IEEE*, 83, 7, 1995.
163. Rowley, J.T. and Waterhouse, R.B., Performance of shorted patch antennas for mobile communication handsets at 1800 MHz, *IEEE Trans. Microwave Theory Technol.*, 47, 815, 1999.
164. Bernardi, P., Cavagnaro, M., Pisa, S., and Piuzzi, E., Specific absorption rate and temperature increases in the head of a cellular-phone user, *IEEE Trans. Microwave Theory Technol.*, 48, 1118, 2000.
165. de Salles, A.A., Fernandez, C.R., and Bonadiman, M., FDTD simulations and measurements on planar antennas for mobile phones, *Proc. SBMO/IEEE MTT-S IMOC*, 1043, 2003.
166. Tinniswood, A.D., Furse, C.M., and Gandhi, O.P., Computations of SAR distributions for two anatomically based models of the human head using CAD files of commercial telephones and the parallelized FDTD code, *IEEE Trans. Antennas Propagat.*, 46, 829, 1998.
167. Schiavoni, A., Bertotto, P., Richiardi, G., and Bielli, P., SAR generated by commercial cellular phones—phone modeling, head modeling, and measurements, *IEEE Trans. Microwave Theory Technol.*, 48, 2064, 2000.
168. Chavannes, N., Tay, R., Nikoloski, N., and Kuster, N., Suitability of FDTD-based TCAD tools for RF design of mobile phones, *IEEE Antennas Propagat. Mag.*, 45, 52, 2003.
169. Pisa, S., Cavagnaro, M., Lopresto, V., Piuzzi, E., Lovisolo, G.A., and Bernardi, P., A procedure to develop realistic numerical models of cellular phones for an accurate evaluation of SAR distribution in the human head, *IEEE Trans. Microwave Theory Technol.*, 53, 2005.
170. Lin, J.C., Cellular mobile telephones and children, *IEEE Antennas Propagat. Mag.*, 44, 142, 2002.
171. Peyman, A., Rezazadeh, A.A., and Gabriel, C., Changes in the dielectric properties of rat tissue as a function of age at microwave frequencies, *Phys. Med. Biol.*, 46, 1617, 2001.

172. Gandhi, O.M. and Kang, G., Some present problems and a proposed experimental phantom for SAR compliance testing of cellular telephone at 835 and 1900 MHz, *Phys. Med. Biol.*, 47, 1501, 2002.
173. Schoenborn, F., Burkhardt, M., and Kuster, N., Differences in energy absorption between heads of adults and children in the near field of sources, *Health Phys.*, 74, 160, 1998.
174. Guy, A.W., Chou, C.K., and Bit-Babik, G., FDTD derived SAR distributions in various size human head models exposed to simulated cellular telephone handset transmitting 600 mW at 835 MHz, in *24th Bioelectromagnetics Society Annual Meeting*, Quebec, Canada, 7, 2002.
175. Wang, J. and Fujiwara, O., Comparison and evaluation of electromagnetic absorption characteristic in realistic human head models of adult and children for 900-MHz mobile telephones, *IEEE Trans. Microwave Theory Technol.*, 51, 966, 2003.
176. Hadjem, A., Lautru, D., Dale, C., Wong, M.F., Hanna, V.H., and Wiart, J., Study of specific absorption rate (SAR) induced in two child head models and in adult heads using mobile phones, *IEEE Trans. Microwave Theory Technol.*, 53, 4, 2005.
177. Dominguez, H., Raizer, A., and Carpes, W.P., Jr., Electromagnetic fields radiated by cellular phone in close proximity to metallic walls, *IEEE Trans. Magn.*, 38, 793, 2002.
178. Anzaldi, G., Delgado, E.C., Riu, P.J., and Silva, F., FDTD analysis of SAR from a cell phone inside a vehicle, in *Proceedings of the 16th International Symposium on Electromagnetic Compatibility*, Zurich, Switzerland, 2005, 155.
179. Ruddle, A.R., Modelling electromagnetic field exposure and SAR in vehicles due to on-board transmitters, in *Proceedings of the 16th International Symposium on Electromagnetic Compatibility*, Zurich, Switzerland, 2005, 145.
180. Onishi, T., Iyama, T., and Uebayashi, S., The estimation of the maximum SAR with respect to various types of wireless device usage, in *Proceedings of 16th International Symposium on Electromagnetic Compatibility*, Zurich, Switzerland, 2005, 151.
181. Bernardi, P., Cavagnaro, M., Pisa, S., Piuzzi, E., and Lin, J., SAR distribution produced by cellular phones radiating close to the human body, in *BioEM-2005 Meeting*, Dublin, Ireland, 2005.
182. Pennes, H.H., Analysis of tissue and arterial blood temperatures in resting forearm, *J. Appl. Physiol.*, 1, 93, 1948.
183. Stolwijk, J.A.J. and Hardy, J.D., Control of body temperature, in *Handbook of Physiology—Reaction to Environmental Agents*, Lee, D.H.K., Ed., Am. Physiol. Soc. Bethesda, MD, 1977, 45.
184. Spiegel, R.J., A review of numerical models for predicting the energy deposition and resultant thermal responses of humans exposed to electromagnetic fields, *IEEE Trans. Microwave Theory Technol.*, 32, 730, 1984.
185. Mooibroek, J. and Lagendijk, J.J.W., A fast and simple algorithm for the calculation of convective heat transfer by large vessels in three-dimensional inhomogeneous tissues, *IEEE Trans. Biomed. Eng.*, 38, 490, 1991.
186. Kolios, M.C., Sherar, M.D., and Hunt, J.W., Large blood vessel cooling in heated tissues: a numerical study, *Phys. Med. Biol.*, 40, 477, 1995.
187. Van Leeuwen, G.M.J., Lagendijk, J.J.W., Van Leersum, B.J.A.M., Zwamborn, A.P.M., Hornsleth, S.N., and Kotte, A.N.T.J., Calculation of change in brain temperatures due to exposure to a mobile phone, *Phys. Med. Biol.*, 44, 2367, 1999.
188. Ma, L., Paul, D.-L., Pothecary, N., Railton, C., Bows, J., Barratt, L., Mullin, J., and Simons, D., Experimental validation of a combined electromagnetic and thermal FDTD model of a microwave heating process, *IEEE Trans. Microwave Theory Technol.*, 43, 2565, 1995.
189. Torres, F. and Jecko, B., Complete FDTD analysis of microwave heating process in frequency-dependent and temperature-dependent media, *IEEE Trans. Microwave Theory Technol.*, 45, 108, 1997.
190. Lu, C.-C., Li, H.-Z., and Gao, D., Combined electromagnetic and heat-conduction analysis of rapid rewarming of cryopreserved tissues, *IEEE Trans. Microwave Theory Technol.*, 48, 2185, 2000.
191. Gordon, R.G., Roemer, R.B., and Horvath, S.M., A mathematical model of the human temperature regulatory system—transient cold exposure response, *IEEE Trans. Biomed. Eng.*, 23, 434, 1976.

192. Ozisik, N., *Heat Transfer: A Basic Approach*, McGraw-Hill, New York, 1985.
193. Gagge, A.P. and Nishi, Y., Heat exchange between human skin surface and thermal environment, in *Handbook of Physiology—Reaction to Environmental Agents*, Lee, D.H.K., Ed., Am. Physiol. Soc. Bethesda, MD, 1977, 69.
194. Haala, J. and Wiesbeck, W., Modeling microwave and hybrid heating processes including heat radiation effects, *IEEE Trans. Microwave Theory Technol.*, 50, 1346, 2002.
195. Adair, E.R., Thermal physiology of radiofrequency radiation (RFR) interactions in animals and humans, in *Radiofrequency Radiation Standards*, Klanenberg, B.J., Grandolfo, M., and Erwin, D.N., Eds., Plenum Press, New York, 1994, 245.
196. Hoque, M. and Gandhi, O.P., Temperature distributions in the human leg for VLF-VHF exposures at the ANSI recommended safety levels, *IEEE Trans. Biomed. Eng.*, 35, 442, 1988.
197. Chatterjee, I. and Gandhi, O.P., An inhomogeneous thermal block model of man for the electromagnetic environment, *IEEE Trans. Biomed. Eng.*, 30, 707, 1983.
198. Guyton, A.C., *Textbook of Medical Physiology*, W.B. Saunders Company, Philadelphia, PA, 1991.
199. Bardati, F., Gerosa, G., and Lampariello, P., Temperature distribution in simulated living tissues irradiated electromagnetically, *Alta Freq.*, XLIX, 61, 1980.
200. Durkee, J.W., Antich, P.P., and Lee, C.E., Exact solutions to the multiregion time-dependent bioheat equation. I: solution development, *Phys. Med. Biol.*, 35, 847, 1990.
201. Vyas, R. and Rustgi, M.L., Green's function solution to the tissue bioheat equation, *Med. Phys.*, 19, 1319, 1992.
202. Way, W.I., Kritikos, H., and Schwan, H., Thermoregulatory physiological responses in the human body exposed to microwave radiation, *Bioelectromagnetics*, 2, 341, 1981.
203. Charny, C.K., Hagmann, M.J., and Levin, R.L., A whole body thermal model of man during hyperthermia, *IEEE Trans. Biomed. Eng.*, 34, 375, 1987.
204. Scott, J.A., A finite element model of heat transport in the human eye, *Phys. Med. Biol.*, 33, 227, 1988.
205. Labonté, S., Blais, A., Legault, S.R., Ali, H.O., and Roy, L., Monopole antennas for microwave catheter ablation, *IEEE Trans. Microwave Theory Technol.*, 44, 1832, 1996.
206. Wang, J. and Fujiwara, O., FDTD computation of temperature rise in the human head for portable telephones, *IEEE Trans. Microwave Theory Technol.*, 47, 1528, 1999.
207. Pisa, S., Cavagnaro, M., Piuzzi, E., Bernardi, P., and Lin, J.C., Power density and temperature distributions produced by interstitial arrays of sleeved-slot antennas for hyperthermic cancer therapy, *IEEE Trans. Microwave Theory Technol.*, 51, 2418, 2003.
208. Peaceman, D.W. and Rachford, H., The numerical solution of parabolic and elliptic differential equations, *J. Soc. Ind. Appl. Math.*, 3, 28, 1955.
209. Douglas, J., On the numerical integration of $u_{xx} + u_{yy} = u_t$ by implicit methods, *J. Soc. Ind. Appl. Math.*, 3, 42, 1955.
210. Douglas, J., Alternating direction methods for three space variables, *Numer. Math.*, 4, 41, 1962.
211. Guyton, A.C., *Textbook of Medical Physiology*, W.B. Saunders Company, Philadelphia, PA, 1991.
212. Guy, A.W., Lin, J.C., Kramar, P.O., and Emery, A.F., Effect of 2450 MHz radiation on the rabbit eye, *IEEE Trans. Microwave Theory Technol.*, 23, 492, 1975.
213. Appleton, B., Hirsch, S.E., and Brown, P.V.K., Investigation of single-exposure microwave ocular effects at 3000 MHz, *Ann. NY Acad. Sci.*, 247, 125, 1975.
214. Sliney, D.H. and Stuck, B.E. Microwave exposure limits for the eye: applying infrared laser threshold data, in *Radiofrequency Radiation Standards*, Klanenberg, B.J., Grandolfo, M., and Erwin, D.N., Eds., Plenum Press, New York, 1994, 79.
215. Hardy, J.D., Wolff, H.G., and Goodell, H., *Pain Sensations and Reactions*, Williams and Wilkins, Baltimore, MD, 1952.
216. Foster, K.R., and Erdreich, L.S., Thermal models for microwave hazards and their role in standards development, *Bioelectromagnetics*, 20, 52, 1999.
217. Riu, P.J. and Foster, K.R., Heating of tissue by near-field exposure to a dipole: a model analysis, *IEEE Trans. Biomed. Eng.*, 46, 911, 1999.
218. Cherry, P.C. and Iskander, M.F., Calculations of heating patterns of an array of microwave interstitial antennas, *IEEE Trans. Biomed. Eng.*, 40, 771, 1993.

219. Bernardi, P., Cavagnaro, M., Pisa, S., and Piuzzi, E., SAR distribution and temperature increase in an anatomical model of the human eye exposed to the field radiated by the user antenna in a wireless LAN, *IEEE Trans. Microwave Theory Technol.*, 46, 2074, 1998.
220. Wainwright, P., Thermal effects of radiation from cellular telephones, *Phys. Med. Biol.*, 45, 2363, 2000.
221. Gandhi, O.M., Li, Q.X., and Kang, G., Temperature rise for the human head for cellular telephones and for peak SARs prescribed in safety guidelines, *IEEE Trans. Microwave Theory Technol.*, 49, 1607, 2001.
222. Hirata, A., Morita, M., and Shiozawa, T., Temperature increase in the human head due to a dipole antenna at microwave frequencies, *IEEE Trans. Electromagn. Compat.*, 45, 109, 2003.
223. Hirata, A. and Shiozawa, T., Correlation of maximum temperature increase and peak SAR in the human head due to handset antennas, *IEEE Trans. Microwave Theory Technol.*, 51, 1834, 2003.
224. Beckman, K.J., Lin, J.C., Wang, Y., Illes, R.W., Papp, M.A., and Hariman, R.J., Production of reversible and irreversible atrio-ventricular block by microwave energy, in *The 60th Scientific Sessions, American Heart Association, Anaheim, CA*, 1987; also in *Circulation* 76, 1612, 1987.
225. Lin, J.C., Beckman, K.J., Hariman, R.J., Bharati, S., Lev, M., and Wang, Y.J., Microwave ablation of the atrioventricular junction in open heart dogs, *Bioelectromagnetics*, 16, 97, 1995.
226. Lin, J.C., Hyperthermia therapy, in *Encyclopedia of Electrical and Electronics Engineering*, vol. 9, Webster, J.G., Ed., Wiley, New York, 1999, 450–460.
227. McRury, I.D. and Haines, D.E., Ablation for the treatment of arrhythmias, *Proc. IEEE*, 84, 404, 1996.
228. Lin, J.C., Hariman, R.J., Wang, Y.G., and Wang, Y.J., Microwave catheter ablation of the atrioventricular junction in closed-chest dogs, *Med. Biol. Eng. Comput.*, 34, 295, 1996.
229. Lin, J.C., Catheter microwave ablation therapy for cardiac arrhythmias, *Bioelectromagnetics*, 20, S4, 120, 1999.
230. Huang, S.K.S. and Wilber, D.J., Eds., *Radiofrequency Catheter Ablation of Cardiac Arrhythmias: Basic Concepts and Clinical Applications*, 2nd ed., Futura, Armonk, New York, 2000.
231. Lin, J.C., Biophysics of radiofrequency ablation, in *Radiofrequency Catheter Ablation of Cardiac Arrhythmias: Basic Concepts and Clinical Applications*, 2nd ed., Huang, S.K.S. and Wilber, D.J., Eds., Futura, Armonk, New York, 2000, 13–24.
232. Wonnell, T.L., Stauffer, P.R., and Langberg, J.J., Evaluation of microwave and radio-frequency catheter ablation in a myocardium-equivalent phantom model, *IEEE Trans. Biomed. Eng.*, 39, 10, 1086, 1992.
233. Lin, J.C., Wang, Y.L., and Heriman, R.J., Comparison of power deposition patterns produced by microwave and radio frequency cardiac ablation catheters, *Electron. Lett.*, 30, 12, 922, 1994.
234. Lin, J.C., Studies on microwaves in medicine and biology: from snails to humans, *Bioelectromagnetics*, 25, 146, 2004.
235. Labonté, S., Blais, A., Legault, S.R., Ali, H.Q., and Roy, L., Monopole antennas for microwave catheter ablation, *IEEE Trans. Microwave Theory Technol.*, 44, 1832, 1996.
236. Kaouk, Z., Khebir, A., and Savard, P., A finite element model of a microwave catheter for cardiac ablation, *IEEE Trans. Microwave Theory Technol.*, 44, 1848, 1996.
237. Lin, J.C. and Wang, Y.J., The cap-slot catheter antenna for microwave ablation therapy, *IEEE Trans. Biomed. Eng.*, 43, 657, 1996.
238. Lin, J.C. and Wang, Y.J., A catheter antenna for percutaneous microwave therapy, *Microwave Opt. Technol. Lett.*, 8, 70, 1995.
239. Gu, Z., Rappaport, C.M., Wang, P.J., and VanderBrink, B.A., Development and experimental verification of the wide-aperture catheter-based microwave cardiac ablation antenna, *IEEE Trans. Microwave Theory Technol.*, 48, 1892, 2000.
240. Nevels, R.D., Arndt, G.D., Raffoul, G.W., Carl, J.R., and Pacifico, A., Microwave catheter design, *IEEE Trans. Biomed. Eng.*, 45, 885, 1998.
241. Rosenbaum, R.M., Greenspon, A.J., Hsu, W.L., Walinsky, S.P., and Rosen, A., RF and microwave ablation for the treatment of ventricular tachycardia, *IEEE MTT-S Int. Microwave Symp. Digest*, 1993, 1155.
242. Greenspon, A.J., Advances in catheter ablation for the treatment of cardiac arrhythmias, *IEEE Trans. Microwave Theory Technol.*, 48, 2670, 2000.

243. Panescu, D., Whayne, J.G., Fleischman, S.D., Mirotznik, M.S., Swanson, D.K., and Webster, J.G., Three-dimensional finite element analysis of current density and temperature distributions during radio-frequency ablation, *IEEE Trans. Biomed. Eng.*, 42, 879, 1995.
244. Cao, H., Vorperian, V.R., Tungjikitkusolmun, S., Tsai, J.Z., Haemmerich, D., Choy, Y.B., and Webster, J.G., Flow effect on lesion formation in RF cardiac catheter ablation, *IEEE Trans. Biomed. Eng.*, 48, 425, 2001.
245. Tungjikitkusolmun, S., Vorperian, V.R., Bhavaraju, N., Cao, H., Tsai, J.Z., and Webster, J.G., Guidelines for predicting lesion size at common endocardial locations during radio-frequency ablation, *IEEE Trans. Biomed. Eng.*, 48, 194, 2001.
246. Bernardi, P., Cavagnaro, M., Lin, J.C., Pisa, S., and Piuzzi, E., Distribution of SAR and temperature elevation induced in a phantom by a microwave cardiac ablation catheter, *IEEE Trans. Microwave Theory Technol.*, 52, 1978, 2004 (special issue on medical applications and biological effects of RF/microwaves).
247. McLucas, B., Management of uncontrolled menorrhagia with the resectoscope, *Minim. Invasive Ther.*, 1, 131, 1992.
248. Brooks, P.G., Clouse, J., and Morris, L.S., Hysterectomy vs resectoscopic endometrial ablation for the control of abnormal uterine bleeding—a cost-comparative study, *J. Reprod. Med.*, 39, 755, 1994.
249. Pinion, S.B., Parkin, D.E., Abramovich, D.R., Naji, A., Alexander, D.A., Russel, I.T., and Kitchener, H.C., Randomized trial of hysterectomy, endometrial laser ablation, and transcervical endometrial resection for dysfunctional uterine bleeding, *Br. Med.J.*, 309, 979, 1994.
250. Seymour, J., Wallage, S., Graham, W., Parkin, D., and Cooper, K., The cost of microwave endometrial ablation under different anaesthetic and clinical settings, *BJOG: Int. J. Obstet. Gynaecol.*, 110, 922, 2003.
251. Wallage, S., Cooper, K.G., Graham, W.J., and Parkin, D.E., A randomised trial comparing local versus general anaesthesia for microwave endometrial ablation, *BJOG: Int. J. Obstet. Gynaecol.*, 110, 799, 2003.
252. Lalonde, A., Evaluation of surgical options in menorrhagia, *Br.J. Obstet. Gynaecol.*, 101, 8, 1994.
253. Erian, J., Endometrial ablation in the treatment of menorrhagia, *Br.J. Obstet. Gynaecol.*, 104, 19, 1994.
254. Daniell, J.F., Kurtz, B.R., and Ke, R.W., Hysteroscopic endometrial ablation using the rollball electrode, *Obstet. Gynecol.*, 80, 329, 1992.
255. Reid, P.C., Turrell, W., Smith, J.H.F., Kenndy, A., and Sharp, F., Nd-YAG laser endometrial ablation—histological aspects of uterine healing, *Int. J. Gynecol. Pathol.*, 11, 174, 1992.
256. Phillips, D.R., A comparison of endometrial ablation using the Nd:YAG laser or electrosurgical techniques, *J. Am. Assoc. Gynecol. Laparosc.*, 1, 235–239, 1993.
257. Sharp, N.C., Cronin, N., Feldberg, I., Evans, M., Hodgson, D., and Ellis, S., Microwaves for menorrhagia: a new fast technique for endometrial ablation, *Lancet*, 346, 1003, 1995.
258. Cooper, K.G., Bain, C., and Parkin, D.E., Comparison of microwave endometrial ablation and transcervical resection of the endometrium for treatment of heavy menstrual loss: a randomised trial, *Lancet*, 354, 1859, 1999.
259. Pisa, S., Cavagnaro, M., Bernardi, P., and Lin, J.C., A 915-MHz antenna for microwave thermal ablation treatment: physical design, computer modeling and experimental measurement, *IEEE Trans. Biomed. Eng.*, 48, 599, 2001.
260. Stea, B., Kittleson, J., and Cassady, J.R., Treatment of malignant glioma with interstitial irradiation and hyperthermia, *Int. J. Radiat. Oncol. Biol. Phys.*, 24, 657, 1992.
261. Overgaard, J., Gonzalez, D.G., Hulshof, M., Arcangeli, G., Dahl, O., Mella, O., and Bentzen, S.M., Randomised trial of hyperthermia as adjuvant to radiotherapy for recurrent or metastatic malignant melanoma, *Lancet*, 345, 540, 1995.
262. Kuwano, H., Sumiyoshi, K., Watanabe, M., Sadanaga, N., Nozoe, T., Yasuda, M., and Sugimachi, K., Preoperative hyperthermia combined with chemotherapy and irradiation for the treatment of patients with esophageal carcinoma, *Tumorigenesis*, 81, 18, 1995.
263. Nakajima, T., Roberts, D.W., Ryan, T.P., Hoopes, P.J., Coughlin, C.T., Trembly, B.S., and Strohbehn, J.W., Pattern of response to interstitial hyperthermia and brachytherapy for malignant intracranial tumour: a CT analysis, *Int. J. Hyperthermia*, 9, 491, 1993.
264. Snead, P.K., Stauffer, P.R., McDermott, M.W., Diederich, C.J., Lamborn, K.R., Prados, M.D., Chang, S., Weaver, K.A., Spry, L., Malec, M.K., Lamb, S.A., Voss, B., Davis, R.L., Wara, W.M.,

- Larson, D.A., Phillips, T.L., and Gutin, P.H., Survival benefit of hyperthermia in a prospective randomized trial of brachytherapy boost +/- hyperthermia for glioblastoma multiforme, *Int. J. Radiat. Oncol. Biol. Phys.*, 40, 287, 1998.
265. Coughlin, C.T., Douple, E.B., Strohbehn, J.W., Eaton, J.W., Jr., Trembly, B.S., and Wong, T.Z., Interstitial hyperthermia in combination with brachytherapy, *Radiobiology*, 148, 285, 1983.
 266. Hiraoka, M., Mitsumori, M., Hiroi, N., Ohno, S., Tanaka, Y., Kotsuka, Y., and Sugimachi, K., Development of RF and microwave heating equipment and clinical applications to cancer treatment in Japan, *IEEE Trans. Microwave Theory Technol.*, 48, 1789, 2000.
 267. King, R.W.P., Trembly, B.S., and Strohbehn, J.W., The electromagnetic field of an insulated antenna in a conducting or dielectric medium, *IEEE Trans. Microwave Theory Technol.*, 31, 574, 1983.
 268. Jones, K.M., Mechling, J.A., Trembly, B.S., and Strohbehn, J.W., SAR distribution for 915 MHz interstitial microwave antennas used in hyperthermia for cancer therapy, *IEEE Trans. Biomed. Eng.*, 35, 851, 1988.
 269. Iskander, M.F. and Tume, A.M., Design optimization of interstitial antennas, *IEEE Trans. Biomed. Eng.*, 36, 238, 1989.
 270. Su, D.W.-F. and Wu, L.-K., Input impedance characteristics of coaxial slot antennas for interstitial microwave hyperthermia, *IEEE Trans. Microwave Theory Technol.*, 47, 302, 1999.
 271. Camart, J.C., Despretz, D., Chive, M., and Pribetich, J., Modeling of various kinds of applicators used for microwave hyperthermia based on the FDTD method, *IEEE Trans. Microwave Theory Technol.*, 44, 1811, 1996.
 272. Ahn, H.R. and Lee, K., Interstitial antennas tipped with reactive load, *IEEE Microwave Wireless Comp. Lett.*, 15, 83, 2005.
 273. Longo, L., Gentili, G.B., Cerretelli, M., and Tosoratti, N., A coaxial antenna with miniaturized choke for minimally invasive interstitial heating *IEEE Trans. Biomed. Eng.*, 50, 82, 2003.
 274. Brace, C.L., Laeseke, P.F., van der Weide, D.W., and Lee, F.T., Jr., Microwave ablation with a triaxial antenna: results in *ex vivo* bovine liver, *IEEE Trans. Microwave Theory Technol.*, 53, 215, 2005.
 275. Jones, K.M., Mechling, J.A., Strohbehn, J.W., and Trembly, B.S., Theoretical and experimental SAR distributions for interstitial dipole antenna arrays used in hyperthermia, *IEEE Trans. Microwave Theory Technol.*, 37, 1200, 1989.
 276. Lin, J.C., Hirai, S., Chiang, C.L., Hsu, W.L., and Wang, Y.J., Computer simulation and experimental studies of SAR distributions of interstitial arrays of sleeved-slot microwave antennas for hyperthermia treatment of brain tumors, *IEEE Trans. Microwave Theory Technol.*, 48, 2191, 2000.
 277. Camart, J.C., Fabre, J.J., Prevost, B., Pribetich, J., and Chive, M., Coaxial antenna array for 915 interstitial hyperthermia: design and modelization—power deposition and heating pattern—phased array, *IEEE Trans. Microwave Theory Technol.*, 40, 2243, 1992.
 278. Clibbon, K.L., McCowen, A., and Hand, J.W., SAR distribution in interstitial microwave antenna arrays with a single dipole displacement, *IEEE Trans. Biomed. Eng.*, 40, 925, 1993.
 279. Cherry, P.C. and Iskander, M.F., FDTD analysis of power deposition patterns of an array of interstitial antennas for use in microwave hyperthermia, *IEEE Trans. Microwave Theory Technol.*, 40, 1692, 1992.
 280. Cherry, P.C. and Iskander, M.F., Calculations of heating patterns of an array of microwave interstitial antennas, *IEEE Trans. Biomed. Eng.*, 40, 771, 1993.
 281. Gentili, G.B., Leoncini, M.L., Trembly, B.S., and Schweizer, S.F., FDTD electromagnetic and thermal analysis of interstitial hyperthermic applicators, *IEEE Trans. Biomed. Eng.*, 42, 973, 1995.
 282. Pisa, S., Cavagnaro, M., Piuzzi, E., Bernardi, P., and Lin, J.C., Power density and temperature distributions produced by interstitial arrays of sleeved-slot antennas for hyperthermic cancer therapy, *IEEE Trans. Microwave Theory Technol.*, 5, 2418, 2003.
 283. Lin, J.C. and Wang, Y.J., Interstitial microwave antennas for thermal therapy, *Int. J. Hyperthermia*, 3, 37, 1987.
 284. Chou, C.-K., Therapeutic heating applications of radio frequency energy, *Biological and Medical Aspects*, Barnes, F.S. and Greenebaum, B., Eds., Taylor & Francis, Boca Raton, FL, 2006, Chapter 12.
 285. Black, D., Thermoregulation in the presence of radiofrequency fields, in *Biological and Medical Aspects*, Barnes, F.S. and Greenebaum, B., Eds., Taylor & Francis, Boca Raton, FL, 2006, Chapter 5.

11

Experimental EMF Exposure Assessment

Sven Kühn and Niels Kuster

CONTENTS

11.1	Objectives and Limitations.....	381
11.1.1	Dosimetry.....	382
11.1.2	Densitometry or Incident Exposure Assessment	383
11.2	Fundamental Quantities of EMF.....	384
11.2.1	Primary Quantities: Basic Restrictions	385
11.2.2	Derived Quantities: Reference Levels or Maximum Permissible Exposure.....	386
11.3	Experimental Techniques	386
11.3.1	Field Probes	386
11.3.1.1	Broadband E Field Probes.....	386
11.3.1.2	Electro-Optical Sensors	389
11.3.2	Temperature Instrumentations	391
11.3.2.1	Temperature Probes	391
11.3.2.2	Infrared Photography.....	392
11.3.2.3	Microcapsulated Thermo-Chromic Liquid Crystals	393
11.3.2.4	Calorimeters.....	393
11.3.3	Measurement Antennas.....	393
11.4	Near-Field Scanners	394
11.4.1	Scanners for Dosimetric Compliance Testing	394
11.4.2	Fast Dosimetric Scanners.....	395
11.4.3	Incident Near-Field Scanners.....	397
11.5	Incident Field Evaluations in the Far Field of Transmitters.....	398
11.5.1	Broadband Measurements.....	399
11.5.2	Frequency-Selective Measurements.....	401
11.5.3	Code-Selective Measurements	402
11.6	Typical Maximum Peak Spatial SAR Exposures.....	402
11.7	Typical Far-Field Exposures	404
Acknowledgment.....		405
References		405

11.1 Objectives and Limitations

Experimental electromagnetic field (EMF) exposure assessments can be divided into two categories: (1) densitometry, that is, quantification of the incident EMF or the field characteristics at the location of exposed bodies but without their presence, and (2)

dosimetry, that is, quantification of the EMF induced in biological tissues or bodies. In most cases of compliance evaluation, verification that the actual exposure is below a certain value is paramount to accurate determination of the individual exposure. However, highly accurate predictions are needed for some medical applications, for instance, hyperthermia. The focus of this chapter is on dosimetry for frequencies above 10 MHz, often referred to as radio frequency (RF) dosimetry. At lower frequencies, experimental dosimetry is usually limited to measurement of the incident magnetic fields.

11.1.1 Dosimetry

Dosimetry is the science of quantifying the three-dimensional (3-D) distribution of EMF inside tissues and organs of biological bodies. The term is also applied with media having dielectric characteristics similar to biological bodies, for example, cell cultures, tissue-simulating liquids, etc. The induced field is the only field parameter that can interact with biological processes and therefore is referred to as the primary quantity.

Dosimetry usually refers to the assessment of the induced fields on a macro level, that is, the averaged induced fields across cells. Microdosimetry refers to the evaluation of fields across membranes, proteins, etc. This is a new field facing various basic problems such as material models and transitions between classical and quantum electrodynamics. Since the field of microdosimetry has not yet matured and since microdosimetry can be directly developed from locally averaged induced fields in the frequency range considered (<300 MHz), the term dosimetry in this chapter refers to microdosimetry only.

The distribution of induced fields, particularly at RF, is a complex function of numerous parameters such as frequency, incident field strength, incident angle, field impedance, incident field distribution, polarization, size and shape (posture) of the biological body, tissue distribution, dielectric characteristics of the tissues, etc. In general, the dynamics of the induced field strength range over several orders of magnitude. In other words, the strength and distributions of the fields induced by the same incident exposure greatly vary with anatomy and body orientation with respect to the field and posture.

It is practically impossible to measure the fields noninvasively or *in vivo*; thus, measurements can only be obtained postmortem. The limitations [1] associated with postmortem evaluations include (1) accessibility to only certain tissues, (2) dielectric changes (e.g., lower tissue temperature and decreased blood content), (3) field distortions by the invasively introduced probe, and (4) large uncertainties associated with obtaining accurate measurements near and across tissue boundaries [2,3]. Only the integrated, totally absorbed power can be determined relatively easily by the calorimeter method (see [Section 11.3.2.4](#)).

Progress in computational electromagnetics along with the exponential growth of computational power and memory have facilitated determination of the field distributions in full anatomical human bodies with resolutions much smaller than 1 mm³ ([see Chapter 10](#) on RF modeling by Lin). The lossy and low-resonance properties of complex anatomical structures pose no special challenges for numerical methods ([Figure 11.1](#)). Limitations are only due to inadequate phantoms providing insufficient spatial resolution, for example, to accurately represent the scull [3].

Nevertheless, experimental dosimetry is often superior to numerical approaches for the compliance testing of commercial devices. Sources usually consist of highly resonant structures tightly assembled with other electronic and metallic structures. It is difficult to predict with reasonable and known uncertainty whether and how distortion of resonances and excitations of secondary structures might occur through simulations, especially when also considering the scattered fields of biological bodies. Small differences can

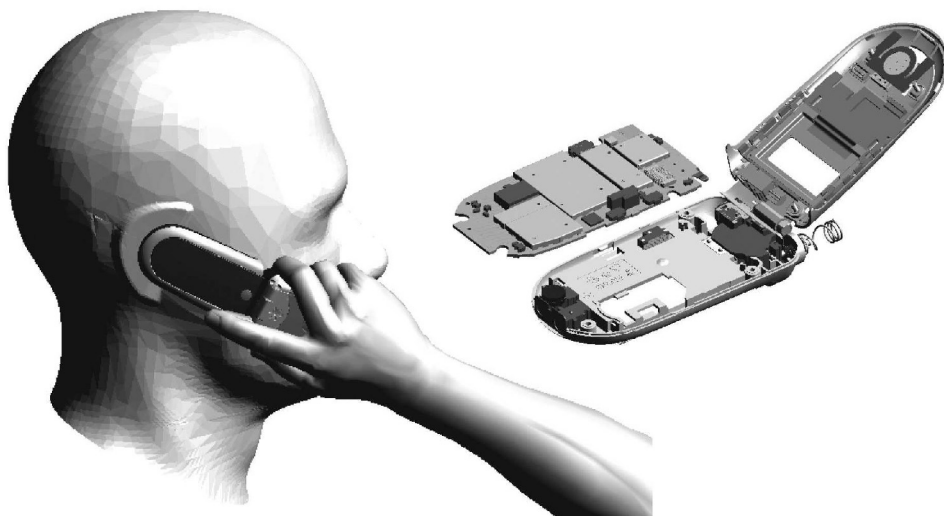


FIGURE 11.1

The latest advances in numerical techniques enable the computation of realistic scenarios without restrictions regarding spatial resolution and material description. The remaining difficulties are material parameters and manufacturing tolerances.

easily result in deviations of more than a factor of 2 from reality. Only when the structure is electromagnetically well-defined can good correspondence between simulations and measurement generally be achieved, that is, with an uncertainty smaller than 20% [4]. On the other hand, experimental techniques allow testing of the physical device under test (DUT) and do not require verification of the computational model.

The detailed information of the field distributions inside anatomical bodies obtainable by numerical methods is often irrelevant, since it cannot be generalized. For safety considerations, the upper boundary of exposure for the entire population rather than individual exposure is relevant. Hence, worst-case phantoms are often applied to assess the upper exposure boundary for specific exposure conditions, for example, from mobile transmitters. Since the degree of freedom for these phantoms is relatively large, they can be chosen homogenously (see Section 11.4.1). Recent evaluation of the procedures for mobile phone compliance testing has confirmed that conservative assessments are possible with a simplified experimental technique using homogenous phantoms [4–6].

During the past decade, considerable progress has been achieved in experimental dosimetric assessment. Since the late 1990s, experimental techniques have been routinely applied for evaluating transmitters operating in the closest vicinity of the body. They have proven to be more reliable, cheaper, and faster. A summary of these techniques and procedures is provided in this chapter. However, dosimetric assessments are limited to homogenous phantoms or to a few tissues in biological bodies. These assessments are normally applied for testing compliance with the basic restrictions or for the validation of results obtained by computational techniques.

11.1.2 Densitometry or Incident Exposure Assessment

Experimental dosimetry requires sophisticated instrumentation, significant expertise, and time. It is impractical for *in situ* exposure assessments. Therefore, easy to apply techniques and methods using a worst-case approach have been developed to determine compliance

with potentially hazardous induced fields by determining the incident fields. The worst-case concept derives the conditions for maximum induced fields inside the human body for an incident field strength in terms of the polarization, field distribution (plane wave), field impedance (plane wave), size, and posture of the human body and its dielectric properties. The induced fields are lower than a value X if the local maximum incident field strength of the E field and H field is below the value Y . Attempts to alter this conservative approach have yielded alternatives with an insufficient scientific and engineering basis (see [Section 11.5](#)).

Assessment of the incident exposure is simple for plane wave or far-field conditions. Under these conditions, the E field vector is perpendicular to the H field vector, and both are orthogonal to the direction of propagation. The ratio of the E and H fields is equal to the wave impedance Z at any location:

$$Z = \frac{E}{H} \quad (11.1)$$

and in free space

$$Z_0 = 377 \Omega \quad (11.2)$$

Furthermore, the amplitude is constant over the entire volume of the absent exposed body. In these cases, it is necessary to measure only one component (E or H field) at one location in space. Unfortunately, far-field conditions rarely occur. However, far-field conditions are approximately met locally by changing the amplitude in space at distances larger than the extension of the reactive near-field zone:

$$r > \frac{2D^2}{\lambda}, \quad D \sim \frac{\lambda}{2} \quad (11.3)$$

$$r > \frac{\lambda}{2\pi}, \quad D \ll \frac{\lambda}{2} \quad (11.4)$$

where r is the radius or distance from the transmitting antenna/structure, λ the wavelength, and D the largest antenna dimension.

In other words, for distances meeting the requirements of Equation 11.3 and Equation 11.4, only the maximum of the field components must be determined to demonstrate compliance.

For any distance smaller than the requirements of Equation 11.3 and Equation 11.4, the maximum of both components must be spatially scanned to reliably predict that the maximal induced fields are below a certain limit. Fine volume scanning of transmitter antennas in the very near field yields greater uncertainty and is more time-consuming than dosimetric measurement in homogenous phantoms. Since such near-field assessments are more conservative than specific absorption rate (SAR) evaluations, they are rarely conducted in the context of exposure assessments.

11.2 Fundamental Quantities of EMF

The basic quantities necessary for electromagnetic exposure assessment are summarized in [Table 11.1](#).

TABLE 11.1

Quantities, Symbols, and Units Used in Experimental Exposure Assessment

Symbol	Quantity	Unit
\vec{E}	E field (vector)	V/m
\vec{H}	H field (vector)	A/m
S	Power density (scalar)	W/m ²
\vec{S}	Pointing vector, $\vec{S} = \vec{E} \times \vec{H}$	W/m ²
W	Energy density	W/m ³
SAR	Specific absorption rate	W/kg
ΔT	Temperature increase	K
J	Current density	A/m ²
$\bar{\epsilon}$	Complex permittivity, $\bar{\epsilon} = \epsilon_0 \cdot \bar{\epsilon}_r$	F/m
ϵ_0	Permittivity of free space, $\epsilon_0 = 8.854 \times 10^{-12}$	F/m
$\bar{\epsilon}_r$	Complex relative permittivity, $\bar{\epsilon}_r = \epsilon_r' - j\epsilon_r''$	F/m
σ	Conductivity	S/m
μ	Permeability, $\mu = \mu_r \cdot \mu_0$	H/m
μ_0	Permeability of free space, $\mu_0 = 4\pi \times 10^{-7}$	H/m
μ_r	Relative permeability	
c	Specific heat capacity	J/(kg K)
ρ	Mass density	kg/m ³

11.2.1 Primary Quantities: Basic Restrictions

Restrictions on exposure to time-varying electric fields, magnetic fields, and EMF that are based directly on established health effects are termed basic restrictions (see Chapter 8 on standards by Van Deventer et al. [68]). Depending on the frequency of the field, the physical quantities used to specify these restrictions are either the current density (J) or the SAR. The dosimetric quantities used in current guidelines [7–10] are J for frequencies up to 10 MHz and the SAR for the frequency range from 100 kHz to 10 GHz. J is related to the internal electric field by Ohm's law:

$$J = \sigma E \quad (11.5)$$

E is the internal electric field, and σ is the complex conductivity of the tissue.

SAR is the ratio of the average rate of the absorbed power to the absorbing mass. It is defined as follows:

$$\text{SAR} = \frac{d}{dt} \left(\frac{dW}{dm} \right) = \frac{d}{dt} \left(\frac{dW}{\rho dV} \right) \quad (11.6)$$

where dW is the incremental energy dissipated in an incremental mass dm included in an incremental volume dV and ρ is the mass density. SAR can also be calculated directly from the electrical loss, which is proportional to the mean square of the locally induced electric field strength E :

$$\text{SAR} = \frac{\sigma E^2}{\rho} = \frac{J^2}{\sigma \rho} \quad (11.7)$$

and to a temperature increase by:

$$\text{SAR} = c \frac{dT}{dt} \quad (11.8)$$

where c is the local specific heat capacity of the tissue. [Equation 11.8](#) is valid only if the exposed body is in thermal equilibrium or in a steady thermal state at the beginning of the exposure, and either heat exchange processes can be neglected during the measurement interval or the processes are known to correct dT correspondingly. Current safety standards [7–10] for limiting EMF exposure provide maximum limits for basic restrictions for the uncontrolled/general public as well as for controlled/occupational exposure over the whole considered frequency range. The standards are ambivalent with respect to the quantity SAR. The debate among experts is whether SAR is a dosimetric quantity only relevant as a surrogate for thermally based models of EMF interaction or whether it can describe effects in addition to those related to temperature. SAR is directly related to the induced internal E fields as well as to the current density ([Equation 11.7](#)) but only directly related to the induced H fields for special cases.

11.2.2 Derived Quantities: Reference Levels or Maximum Permissible Exposure

The derived quantities are the electric field strength (E), magnetic field strength (H), magnetic flux density (B), and power density (S). As discussed in the previous sections, these quantities were derived from the basic restrictions using experimental or computational methods and represent conservative limits for worst-case exposure scenarios. Derived limits are called reference [7] or maximum permissible exposure levels [8,9]. Compliance with these quantities implies compliance with the basic restrictions. However, if the reference quantities exceed the derived limits, the relevant basic restrictions are not necessarily exceeded. In such cases, compliance can be demonstrated by dosimetric means.

In summary, reference levels are easy to assess if the plane wave or far-field conditions are met ([see Section 11.1.2](#)) and the resulting SAR and induced current densities are below the corresponding basic restrictions under all circumstances. Typical reference limits for occupational/controlled and general public/uncontrolled exposure are given in Refs. [7–10].

11.3 Experimental Techniques

11.3.1 Field Probes

E field probes have been used for microwave measurement since the early 1970s. The first power meters were developed by Aslan [11] and Rudge [12]. Aslan used a thermocoupling model consisting of two pairs of thin-film, vacuum-evaporated electrothermic elements that functioned as both an antenna and a detector. Rudge employed two small diode-loaded dipoles as sensor elements. The first prototype of an isotropic, miniature field probe was introduced by Bassen et al. [13] in 1975. Additionally, fiber optic field probes had already been proposed in the 1970s [14]. Comprehensive overviews of field probes are reported in Refs. [2,15].

11.3.1.1 Broadband E Field Probes

Diode-based field probes are well established and commonly used for dosimetric assessment. These probes consist of an appropriate field sensor, a detector, transmission lines, and read-out electronics ([Figure 11.2](#)). Three mutually orthogonal diode-loaded dipoles with an isotropic receiving pattern constitute the probe. To achieve good spatial resolution and broadband performance, electrically short dipoles are employed:

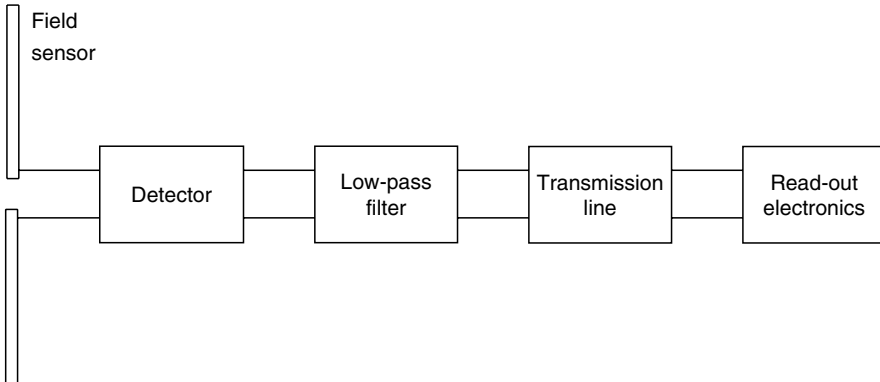


FIGURE 11.2
Simplified schematic of a broadband field probe.

$$\beta h = \frac{2\pi h}{\lambda} \ll 1 \quad (11.9)$$

where h is the length of a dipole arm, β the propagation constant, and λ the wavelength [15]. A flat frequency dependence cannot be achieved if the length of the probe is larger than a fraction of the wavelength ($< 0.05\lambda$). However, this limitation can be overcome by gradually resistive dipoles [16].

Typical isotropic E field probe sensors are shown in Figure 11.3. An RF detector diode (usually Schottky type) is located in the center of the dipole arms. If the detector diode is operated in the square-root law region, the diode current is proportional to the RF power delivered over the dipole to the detector diode. The detector diode is connected with a highly resistive line to the data acquisition electronics. The transmission lines must be designed precisely to eliminate distortions, such as parasitic sensor elements and scattering, which cause degradation of the pattern and unwanted polarization characteristics of the actual receiving antenna. High-resistive transmission lines are ideal for minimizing field perturbation and pickup effects. A detailed investigation of transmission line design

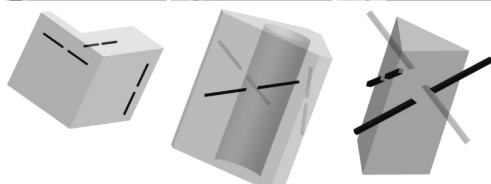
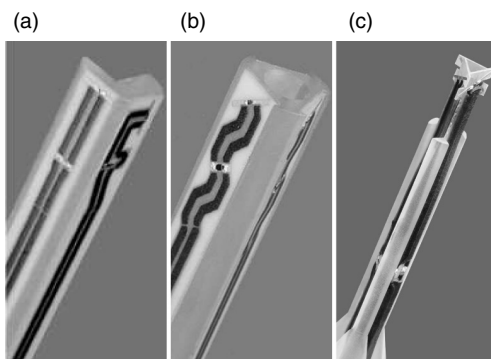


FIGURE 11.3
 E field probe configurations: (a) E field probe for measurements in air with one sensor aligned to the probe axis and two orthogonally, (b) dosimetric probe for E field measurements in tissue-simulating liquids allowing integration of an optical proximity sensor in its center, and (c) miniature dosimetric probe with interleaved dipoles. (From IT'IS Foundation. With permission.)

can be found in Smith [17]. Current probe designs apply either thin-film ($R \sim 10 \text{ M}\Omega/\text{m}$) [14] or thick-film ($R \sim 500 \text{ M}\Omega/\text{m}$) [18] techniques.

The induced fields are recorded by the read-out electronics. The electronics typically consist of a measurement amplifier and an analog digital converter. The read-out field values are then optically forwarded. The optical transmission provides a galvanic decoupling and reduction of field-perturbing conductive parts near the DUT.

In addition to E field probes, H field probes are also available, the basic theory of which can be found in Whiteside and King [19]. H field probes and E field probes are basically similar, except for the field sensor element, that is, H field probes employ a small loop element instead of a dipole sensor. The disadvantages of loop-based sensors include a strong frequency dependence and currents induced by both H and E fields. Different methods for flattening the frequency dependence of loop probes have been proposed in Refs. [2,20]. The ratio of the voltage induced in a circular loop with diameter d by the E field and the H field is [19]:

$$\frac{V_E}{V_H} \simeq -j2\pi \frac{d}{\pi} \quad (11.10)$$

Therefore, for electrically small loops only, that is, $d/\lambda \ll 0.01$, the current will mainly be determined by the magnetic field. In Poković [2], lossy covers were proposed to suppress the E field sensitivity of the loop.

In contrast to dipole-based sensors, thermocouple probes are true square-root law [a1]detectors. Such sensors are, for example, used in free space field probes by Narda [21]. These sensors are, however, impractical for dosimetric and near-field applications because of their generally lower sensitivity and dynamic range.

Thermistors are also true square-root law detectors and also small. They can have higher resolution than thermocouples but need more frequent calibration.

Based on the setup of these isotropic field probes, the measured field magnitude is yielded from the root sum square of the three orthogonal components:

$$|X| = \sqrt{|X_1|^2 + |X_2|^2 + |X_3|^2} \quad X \in \{E,H\} \quad (11.11)$$

This summation is carried out regardless of any phase differences between the respective components. Hence, if maximum hold peak detectors are applied, the field reading represents the upper bound of the field magnitude.

The output signal of the probes just described is dependent on the following parameters:

- Frequency, modulation, and field strength
- Polarization, direction, and field gradients
- Material boundaries near the probe sensors
- Sources of interference (noise, static and low-frequency fields, vibration, temperature, etc.).

Therefore, it is necessary to quantify the influence of these parameters. Calibration under well-defined conditions is carried out to characterize the most crucial parameters for each probe individually. A detailed summary of different calibration methods for field probes and characterization of the parameters contributing to the measurement uncertainty is given in Poković [2]. All possible influences must be included in the resulting uncertainty assessment, since the conditions during the actual application of the probes differ

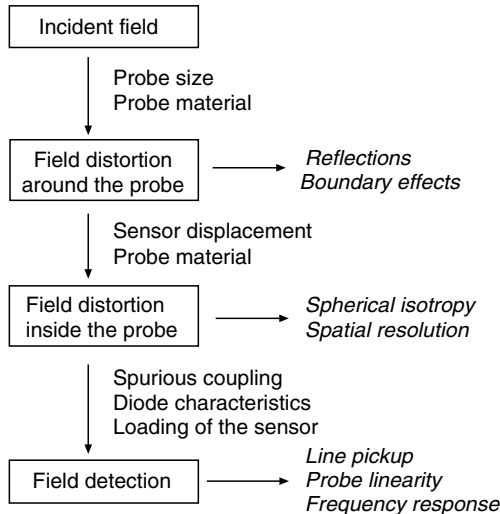


FIGURE 11.4
Impact of the constructional details on the probe characteristics.

considerably from the calibration scenario. Figure 11.4 provides an overview of different probe construction parameters that contribute to the probe characteristics.

Modern dosimetric field probes are available in the frequency range from 10 MHz up to 6 GHz. They have an isotropy error lower than ± 0.5 dB and sensitivities in the range of 1–10 $\mu\text{W/g}$ [22]. Modern probes have very small sensor tip dimensions (2.5 mm) and high spatial resolution, allowing measurements very close to material boundaries. A probe with reduced size (tip diameter 1.0 mm) was introduced by Poković et al. [23] and enables accurate dosimetric measurements for frequencies exceeding 10 GHz. Although this probe consists of only a single sensor element, isotropy is obtained by 120° rotation around the probe axis and an appropriately aligned sensor element. Probes for determining both the electrical and the magnetic field vector information are presented by Poković et al. [24]. This technique is based on measurements of five or more field components in space and reconstruction of the ellipse parameters by a combination of a downhill simplex and a Givens updating algorithm.

11.3.1.2 Electro-Optical Sensors

In contrast to RMS sensors, it is possible to measure fields over a broad frequency band in the time domain by exploiting electro-optic methods. Recent advances in semiconductor and photonic crystal research have provided the foundation for the next generation of near-field measurement equipment based on electro-optical methods. The basic concept of electro-optic probes is shown in Figure 11.5.

The most important electro-optic effects for measuring EMF are the Pockels effect and the quantum confined Stark effect (QCSE). The Pockels effect describes the refraction index dependence on the induced E field of anisotropic dielectric crystals such as cadmium telluride (CdTe) [25] or lithium nobiat (LiNbO_3) [26,27]. H field-sensitive crystals have also been determined, for example, cadmium manganese telluride (CdMnTe) [25]. The QCSE is based on the change of the absorption spectrum of a semiconductor structure under the influence of the electric field. Sensors exploiting the Pockels effect are reported in Refs. [25–27]. A detailed summary of electro-optic phenomena, materials, and applications can be found in Agullo-Lopez et al. [28]. Alternatively, the signal from the field sensor can modulate a small laser diode rather than the external electro-optical modulation.

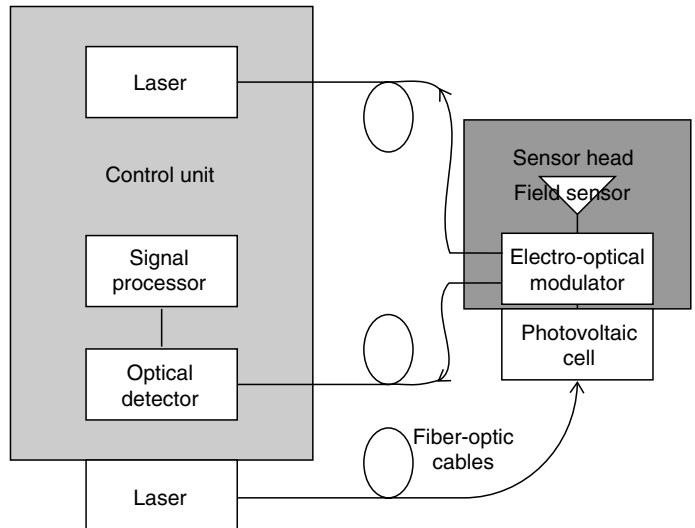


FIGURE 11.5
Principle of an electro-optic probe for EMF measurements.

The most common modulators are the Mach-Zehnder interferometer (MZI) as well as the already mentioned method of the direct modulation of the laser-diode current. The MZI (Figure 11.6) splits the light of a single-mode fiber into two parallel branches of LiNbO_3 waveguides. The feedpoints of the dipole are connected to electrodes that are located between the parallel branches, resulting in the antipodal modulation of the phase of the light. For recombined light, the phase modulation results in an intensity modulation. Sensitivities of $1\text{--}10 \text{ mV}/(\text{m Hz})$ can be reached. The upper cutoff frequency of these sensors is primarily determined by the length of the branches. For high sensitivity, the transit time through the interferometer must be much lower than the periodic time of the signal being measured. In Refs. [26,27], interferometers with a 3-dB bandwidth of 10 GHz were realized. A possibility to overcome this limitation could be the application of traveling wave modulation [29].

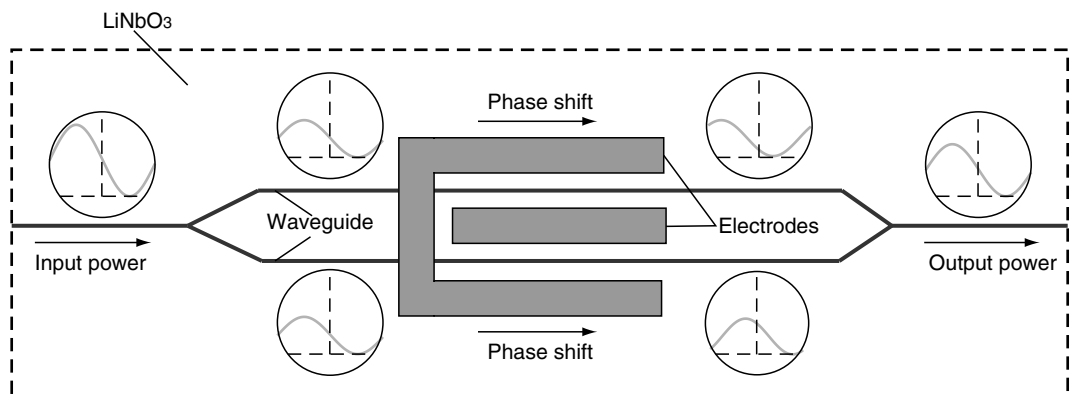


FIGURE 11.6
Schematic of an MZI. The light through the waveguide is modulated antipodally by the electrodes by changing the refractive index of the LiNbO_3 substrate.

Another approach reported in Ref. [25] uses only nonconductive parts in the sensor tip. Different types of crystals that are sensitive to electric and magnetic fields are used. Linear polarized light passing through the electro-optic crystal is reflected on a dielectric mirror and passes through the crystal again, where the polarization is changed. A beam-split polarizer transduces the ellipticity change into a change of the optical intensity. Sensors with a sensitivity of 10–400 V/m and 0.1–0.8 A/m in the frequency range from DC to 2 GHz were realized.

For modulation using QCSE, semiconductors with pn- or pin-junction structures are used. A varying reverse bias over the junction modulates the electric field and consequently the absorption and reflection spectra of the semiconductor as well. If the modulator is operated at a constant frequency, different reflection and transmission characteristics of the light and an intensity modulation result.

In addition to passive modulation (QCSE), direct modulation of a vertical cavity surface emitting laser (VCSEL) [30–32] has recently been applied. The current through the laser is directly modulated by the measurement signal. The VCSEL is especially suitable for modulation because of its high bandwidth, low threshold current, and low noise.

The MZI is the most popular modulation method among the three mentioned, and several commercial products are available based on this technology. Disadvantages include the limited ability to reduce its size as well as the bandwidth limitations. Passive modulators are relatively simple to manufacture as integrated circuits. Although passive modulators are inferior to MZI regarding sensitivity, the development of miniature field probes applying the VSCEL technology is currently the most promising approach.

11.3.2 Temperature Instrumentations

11.3.2.1 Temperature Probes

The locally induced SAR can also be assessed by temperature measurements, as summarized in [Equation 11.8](#). A typical temperature rise curve as applied for SAR measurements is shown in [Figure 11.7](#). Two types of temperature probes exist: those based on thermistors and those based on optical effects. The requirements for temperature probes for SAR assessments are:

- *Small size:* The probe must be small to resolve high temperature gradients, without disturbing the temperature distribution as well as the RF field.
- *Nonconductive materials:* Only electrically nonconductive materials prevent heating of the probe by induced currents and are transparent to EMF.
- *Low noise level:* Especially for dynamic temperature measurements, for example, SAR, small differences must be detected accurately. Therefore, the noise level should be much smaller than 10 mK.
- *Short reaction time:* A short reaction time is essential for SAR measurements, since the temperature rise (dT/dt) is only proportional to the SAR if heat diffusion does not occur. An appropriate probe must have reaction times much lower than 100 msec [33].

Temperature probes for SAR measurement using thermistors were first described by Bowman [34]. These probes utilize high-resistance thermistors that are connected through high-resistance lines to the read-out electronics. In Burkhardt et al. [35], a temperature probe based on a VITEK thermistor (BSD Medical Devices, U.S.A.) is presented. This probe has a noise level of 5 mK, a sensitivity of 5 mK/sec, and a tip diameter of

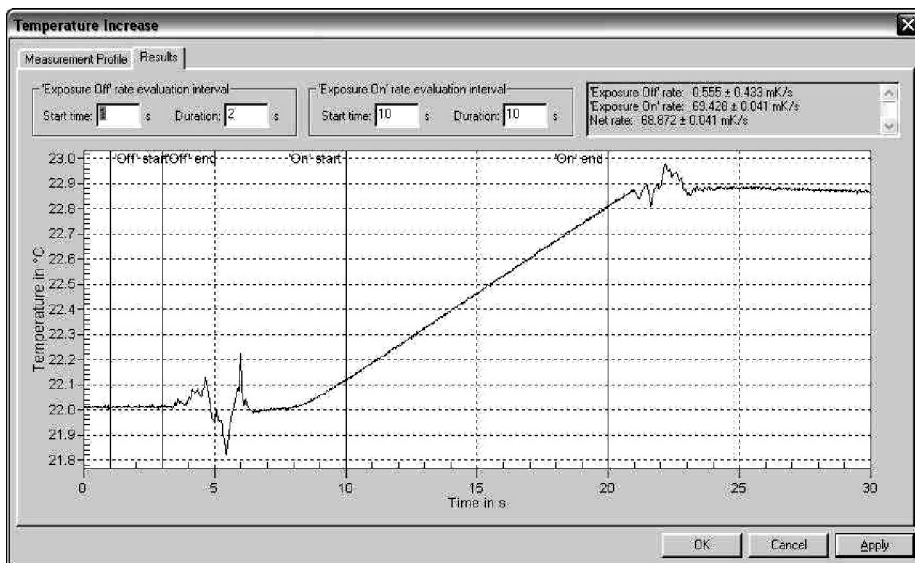


FIGURE 11.7

Typical temperature rise curve for SAR assessment. The linear part of the rise curve is applied for the calculation of the SAR. (Acquired using DASY4 from SPEAG, Switzerland.)

1 mm; however, it has a relatively slow response time of 240 msec. In Schuderer et al. [36], a novel temperature probe design for dosimetric assessments was introduced. The probe provides a spatial resolution of 0.02 mm^3 , noise level of 4 mK, a sensitivity of 0.5 mK/sec, as well as a response time of only 10 msec.

In addition to the thermistor concept, temperature probes based on thermo-optical effects are also available. These probes are applied in high-voltage transformers, industrial microwave ovens, and hyperthermia treatment. One of the exploited effects is the decay rate of a phosphorescent layer at the tip of a fiber optic cable [37]. These modern commercially available probes have a noise level of 0.1 K and reaction times of 250 msec. Another exploited effect is the interferometric application of a cavity that is filled with materials that have highly temperature-dependent refraction indices. These probes reach sensitivities of 2–3 mK/sec [35].

11.3.2.2 *Infrared Photography*

The measurement of temperature by black body-equivalent radiation (infrared photography) is an alternative to invasive measurements using temperature probes. The resolution of infrared thermographs can be very high (<1 mm), and the sensitivity of affordable systems has continuously improved over the years. This was also one of the first methods to measure SAR [38], since the surface radiation can be recorded quickly using infrared cameras without perturbation of the incident field. Infrared cameras were also used to measure the temperature of Global System for Mobile Communications (GSM) mobile phones [39]. The technique has several disadvantages:

- It has limited sensitivity compared to temperature or dosimetric probes.
- It is limited to surfaces.

- The thermal radiation characteristics of the materials must be determined accurately.
- The background radiation must be homogenous.
- Evaporation and convection can cause substantial errors and must be controlled.
- Different aspect angles of the camera can cause different results.

11.3.2.3 Microcapsulated Thermo-Chromic Liquid Crystals

A novel idea to assess 3-D temperature distributions optically and in quasi real time was proposed by Suzuki et al. [40]. Microcapsulated thermo-chromic liquid crystals are suspended uniformly in a gel with the dielectric properties of human muscle tissue. The temperature of the gel is determined by measuring the light scattered from a laser beam that scans through the liquid. The technique has a limited dynamic range and sensitivity.

11.3.2.4 Calorimeters

Calorimetry specifies methods for measuring heat due to biological, chemical, or physical processes that are endothermic or exothermic. Calorimetric methods are suitable for determining average whole-body SAR, but they cannot reveal SAR distributions.

Calorimetry can be subdivided into two types:

- *Direct calorimetry*: The heat is determined directly using calorimeters.
- *Indirect calorimetry*: The amount of expressed heat is determined indirectly by measuring the amount of oxygen consumption and relating it to the oxicaloric equivalent of the reaction.

Basically, calorimetric dosimetry analyzes the heating and cooling processes of an exposed sample. Typical calorimeters used in microwave dosimetry are the Dewer flask calorimeter and the twin-well calorimeter [41].

11.3.3 Measurement Antennas

Different types of broadband matched antennas are usually applied for the frequency-selective exposure assessment of external fields. These measurement antennas are matched to 50Ω to be compatible with standard RF measurement equipment. They are usually applied for far-field measurements of emissions by cellular telephony base stations, broadcast services, etc. Common broadband RF measurement antennas such as horn or logarithmic periodic antennas have a certain directivity. For example, for an antenna with a 45° beam width, more than 18 measurement directions are necessary for each polarization, since the receiving patterns do not have the shapes of square sectors. This reduces the applicability of these antennas for complex propagation scenarios, that is, locations where the received field is not dominated by a direct line of sight propagation path but by multipath reception. Tuned dipole antennas do not show a directivity in the radial direction, but they lack broadband operation. Conical [42] and biconical [43] antennas have the advantage of nondirectiveness in the radial direction and generally good broadband characteristics. If, for example, the ADD3D method [44] is applied in combination with a conical dipole antenna, the measurement orientations for a fully isotropic scan can be reduced to three different directions. In this case, the

isotropy is obtained by an antenna alignment similar to near-field probes, such that the resulting field is:

$$|E| = \sqrt{|E_1|^2 + |E_2|^2 + |E_3|^2} = \sqrt{|U_1|^2 + |U_2|^2 + |U_3|^2} \cdot AF \quad (11.12)$$

where AF is the frequency-dependent antenna factor in linear quantities ($1/\text{m}$) and U_i is the antenna output voltage at the three different antenna orientations. To obtain the antenna output voltages, a measurement receiver (see Section 11.5.1) connected via a well-characterized cable is applied. The antenna output voltage is:

$$|U_{i_{\text{antenna}}}| = |U_{i_{\text{receiver}}}| \cdot \text{ATT}_{\text{cable}} \quad (11.13)$$

where $|U_{i_{\text{receiver}}}|$ is the voltage measured with the receiver and $\text{ATT}_{\text{cable}}$ the attenuation of the cable in linear units. Other sources of attenuation, for example, attenuators to reduce the Voltage standing wave ratio (VSWR) of the measurement antenna, must be similarly considered.

11.4 Near-Field Scanners

11.4.1 Scanners for Dosimetric Compliance Testing

In dosimetric compliance tests, exposures from RF transmitters operating in close proximity to the body, for example, mobile phones or body-worn wireless devices, are compared to the basic restrictions (see Section 11.2.1). This is a complex task, since the exposure greatly depends on the device design, the position of the device with respect to the body, the external and internal anatomy, as well as the effect of the backscattered field on the device (Figure 11.8). In order to obtain a reliable assessment with acceptable effort, the standards must determine the maximum or 90th percentile exposure for the entire

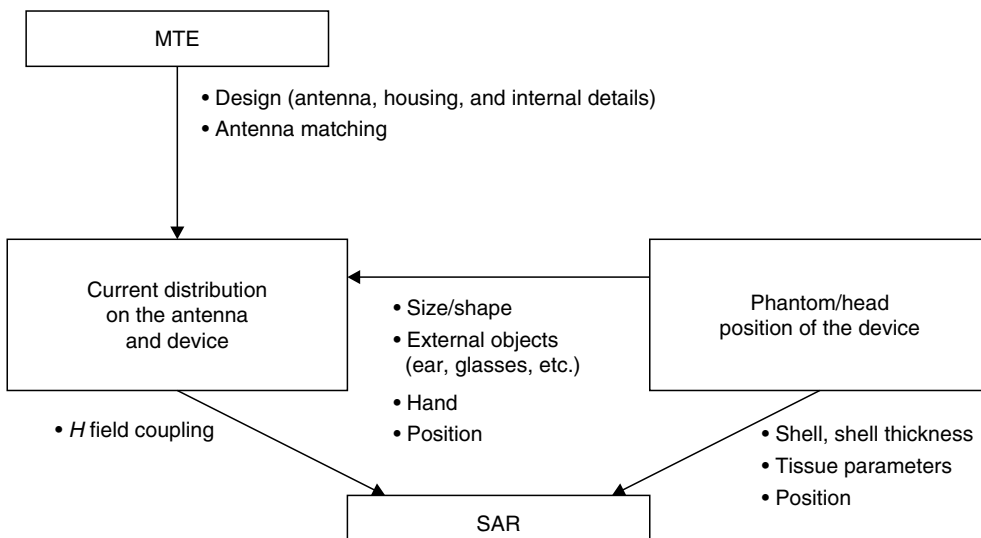


FIGURE 11.8

Overview of impact parameters for dosimetric compliance testing of mobile terminal equipment (MTE).

population that may be operating the DUT. Measurement standards have been developed by different organizations, for example, by the International Electrotechnical Commission (IEC), the Institute of Electrical and Electronics Engineers (IEEE), the Association of Radio Industries and Businesses (ARIB), Korea Electromagnetic Engineering Society (KEES), and others.

In general, a dosimetric evaluation requires the measurement of several hundreds of points distributed over a complex 3-D phantom. The task is divided into (1) searching for the location of the maximum absorption on a 2-D grid and (2) determining the peak spatial SAR value on a fine 3-D grid. Especially at high frequencies, these points must be determined with high accuracy to achieve low measurement uncertainty despite high attenuation and large spatial field variations. Automated dosimetric assessment systems are utilized to perform these compliance tests. A typical configuration of a dosimetric assessment system is shown in Figure 11.9 and [Figure 11.10](#). A computer-controlled six-axis positioner with excellent positioning repeatability of ± 0.2 mm is used to move the dosimetric E field probe within the scanning grid, which can be adaptive, for example, along a surface that is being detected during the scanning job. The different field probe designs have already been discussed in [Section 11.3.1](#). Phantoms, for example, the specific anthropomorphic mannequin (SAM) phantom, elliptical phantom, etc., and tissue-simulating liquids (see [Table 11.2](#)) have been developed and validated with respect to the 90th percentile requirements [45]. A detailed description is provided by Schmid et al. [18]. Because of the strong curvature of the SAM phantom, sufficient accuracy can be obtained only when the measurements are taken with the probes aligned normal to the phantom boundary. The most elaborated components, procedures, and algorithms are employed (Figure 11.10), and an expanded total uncertainty ($k = 2$) for the compliance test of less than 20% can be achieved with even better repeatability.

It should be noted that this approach provides reliable conservative estimates of the maximum peak spatial SAR that might occur in the user population but little information about the exposure of specific tissues.

11.4.2 Fast Dosimetric Scanners

Dosimetric compliance tests of near-field sources are extremely time-consuming, especially as all configurations with all accessories must be evaluated. SAR patterns provide

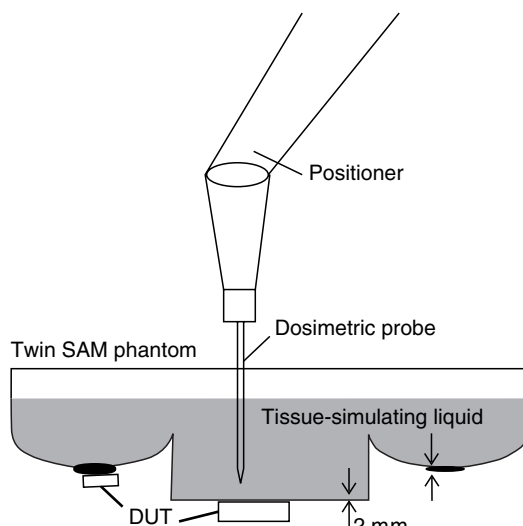


FIGURE 11.9

A dosimetric assessment system consists of a computer-controlled positioner, a dosimetric field probe, and a phantom (left and right head, flat region for system validation) filled with tissue-simulating liquid.



FIGURE 11.10
DASY4 dosimetric assessment system. (From SPEAG, Switzerland.)

further valuable information such as (1) the output power under loaded conditions as indicated by a different peak spatial SAR if the absorption pattern is not altered and (2) changes in the internal RF path, for instance, by poor contacts, as indicated by a modified SAR pattern. Therefore, fast SAR scanners are desirable for precompliance testing as well as for research and development. Such scanners would also be greatly beneficial for

TABLE 11.2

Electric Parameters of Head and Body Tissue Equivalent Liquids at Various Frequencies

Frequency (MHz)	Head		Body	
	ϵ_r	σ (S/m)	ϵ_r	σ (S/m)
150	52.3	0.76	61.9	0.80
300	45.3	0.87	58.2	0.92
450	43.5	0.87	56.7	0.94
835	41.5	0.90	55.2	0.97
900	41.5	0.97	55.0	1.05
915	41.5	0.98	55.0	1.06
1450	40.5	1.20	54.0	1.30
1610	40.3	1.29	53.8	1.40
1800–2000	40.0	1.40	53.3	1.52
2450	39.2	1.80	52.7	1.95
3000	38.5	2.40	52.0	2.73
5800	35.3	5.27	48.2	6.00

quality assurance purposes, when integrated into production lines (every device tested for compliance, output power, and RF performance).

An algorithm to extrapolate peak spatial SAR values from the 2-D area scan performed at the phantom surface was presented by Kanda et al. [46]. Another algorithm reducing the measurement time of an area scan lasting 5–10 min was proposed by Merckel and Fleury [47].

Two additional approaches have been presented to further accelerate the assessment. The first approach, using a scanner based on incident H field measurements, is described in the next section. The second approach is based on a sensor array implanted in a solid flat phantom (Figure 11.11). The phantom is filled with a broadband tissue-simulating gel (300 MHz up to 6 GHz), with sensors located 4 mm below the surface. The density of the sensor array (15 mm) is sufficient to reliably assess the exposure. The measured SAR values of all sensors are acquired and integrated in parallel, such that the total assessment time is less than 3 sec, even for TDMA (Time Division Multiple Access) signals with complicated frame structures.

11.4.3 Incident Near-Field Scanners

In the reactive near field, field gradients are generally very high, and the field impedance differs greatly from the far-field impedance and rapidly changes over short distances. Hence, both E and H fields must be assessed, based on requirements regarding spatial resolution and isotropy that are similar to those of dosimetric scanners. In addition, distortions by reflections from instrumentation must also be carefully evaluated and included in the uncertainty budget.

General purpose scanner systems are equal or similar to those used for dosimetric evaluations, except that E and H field probes optimized for free space are used instead of

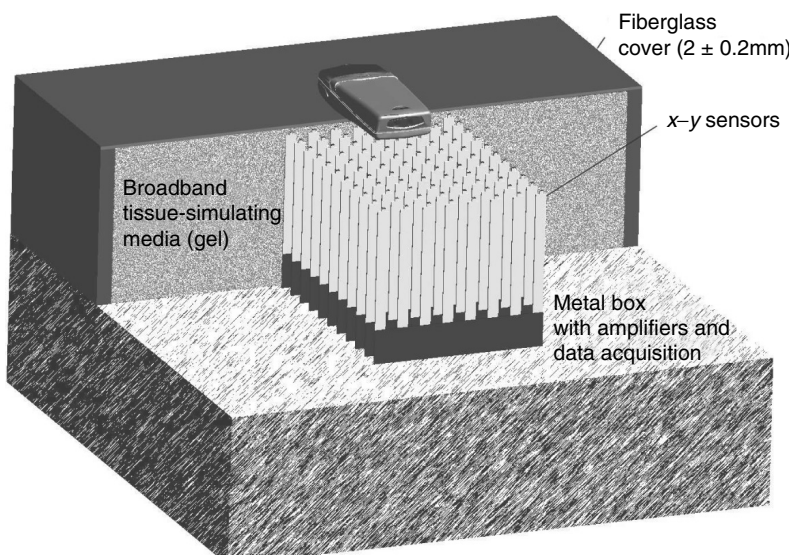


FIGURE 11.11

The concept of a fast dosimetric scanner based on a dense array of sensors completely immersed in a broadband tissue-simulating medium. In order to provide a quick response, the signals of all sensors must be amplified and integrated in parallel for the frame structure and to increase the signal-to-noise ratio. The high-resistive sensor leads are vertical to minimize field distortions.

dosimetric probes. Since the scan procedures do not need to follow complex surfaces, three-axis systems [48] are also suitable. However, such evaluations are rarely used to test compliance with safety limits, since the limits are significantly more conservative and the measurement resources, time required, and uncertainty budget are higher than for dosimetric assessments. Nevertheless, such measurements are valuable for the validation of numerical results [49] or to test compliance with interference limits in the close near field, for example, for hearing aids [50].

A specialized near-field scanner was proposed and developed to test the precompliance of mobile handsets with safety limits [51]. Its underlining concept is based on the primary interaction mechanism of near-field exposure [52], that is, the local SAR is approximately proportional to the square of the incident magnetic field at the surface of the phantom:

$$\text{SAR} = \alpha H_s^2 \quad (11.14)$$

The magnetic field is scanned in a reference plane above the DUT using a loop antenna array. The factor α is determined by relating a traditional compliance measurement inside the phantom to the magnetic field scan in free space for a certain DUT. The system can predict the SAR within 30 sec. The main disadvantage of such a system is that it does not simulate a realistic load to the antenna of the DUT.

11.5 Incident Field Evaluations in the Far Field of Transmitters

Evaluation of the exposure in the far field of a transmitter is usually conducted for fixed transmitters such as radio and TV broadcast antennas, radar sites, or cellular base stations. Exposure assessments are carried out in areas that are generally accessible or restricted to qualified working personnel. Compliance is tested with the reference limits by assuming free space field impedance, that is, by E field evaluation. As described in [Section 11.1.2](#), only one measurement point is required under real far-field conditions. However, actual environments usually involve nearby reflectors, that is, a scanning procedure or statistical knowledge about the field distribution is needed to determine the maximum exposure.

Broadband instant measurements are often insufficient, since the evaluated transmitters do not always operate at maximum power, for example, in the case of base stations, the transmitted power is dependent on the traffic. In such cases, information on the maximum exposure with respect to the measured exposure must be available and soundly applied to extrapolate the worst-case exposure. [Table 11.3](#) lists the parameters that are necessary to extrapolate the worst-case exposure and to reduce the uncertainty of the actual measurement campaign. It is easier to determine the measurement methods when additional parameters are known. General sources of error are:

- Field perturbation by measurement personnel, for instance, reflection and absorption of EMF due to the body of the measurement engineer
- Application of the measurement antenna, for example, nonobservance of antenna directivity and polarization
- Application of ineffectively decoupled cables, for instance, acting as secondary antennas

TABLE 11.3

Important Parameters of RF Transmitter Sites Assessed in the Far Field

Site Parameter	Explanation
Location	The location of the transmitter with respect to the measurement point
Line of sight/nonline of sight	Determines if a prevalent propagation path may be expected
Type of site	Single- or multiple-antenna site
Antenna directivity	Antenna beam characteristics
Antenna radiation direction	The direction the transmitter radiates
Antenna power at measurement	The antenna input power at the time the measurement takes place
Maximum antenna input power	Maximum permissible antenna input power
Frequency	Frequencies at which the site transmits
Communication system	Communication system that is used, that is, which signal characteristics are expected
Other sources of radiation	The field at the measurement point if the assessed transmitter is switched off

- Application of the measurement receiver, for example, incorrect measurement settings
- Selection of the measurement point, for example, measurement points that are not feasible to give the maximum EMF exposure, measurement points close to bodies that influence the measurement antenna's calibration.

Different methods for assessing EMF exposure in the far field have been proposed. One approach is the scanning method. This method requires the engineer to slowly move the measurement antenna with varying polarizations and directions through the volume of interest [53]. The measurement receiver operates in maximum hold mode during the assessment, that is, the maximum field value is determined and compared to the reference values. Another method is based on the examination of several well-defined points in the area of interest. In this case, the antenna is mounted on a tripod, and the different directions and polarizations are examined at the considered points [54]. The first method is conservative but sensitive to the position of the measurement operator with respect to the antenna. The second method can be performed with the measurement engineer further away, but the number of measurements in the volume is small. A combination of both methods is presented in Coray et al. [55], that is, first the region is scanned for the field maximum in the area of interest, and then an isotropic and frequency-selective measurement is performed at the location of the maximum.

Far-field techniques are also often employed in the near field of transmitters, for example, on transmitter towers. Some standards allow a spatial averaging of E field evaluations [9], the rationale of which is based on the whole-body SAR limit. However, this constitutes a relaxation of the safety concept, since it does not consider H field coupling as the dominant mechanism in the near field nor the limits of peak spatial SAR. Based on current knowledge, such relaxations do not exclude violations of the basic restrictions.

The advantages and limitations of different measurement techniques to assess exposure from unknown transmitters are discussed below.

11.5.1 Broadband Measurements

Broadband measurements are especially applicable for survey measurements. The field is measured and automatically summed over a broad frequency range. No information on

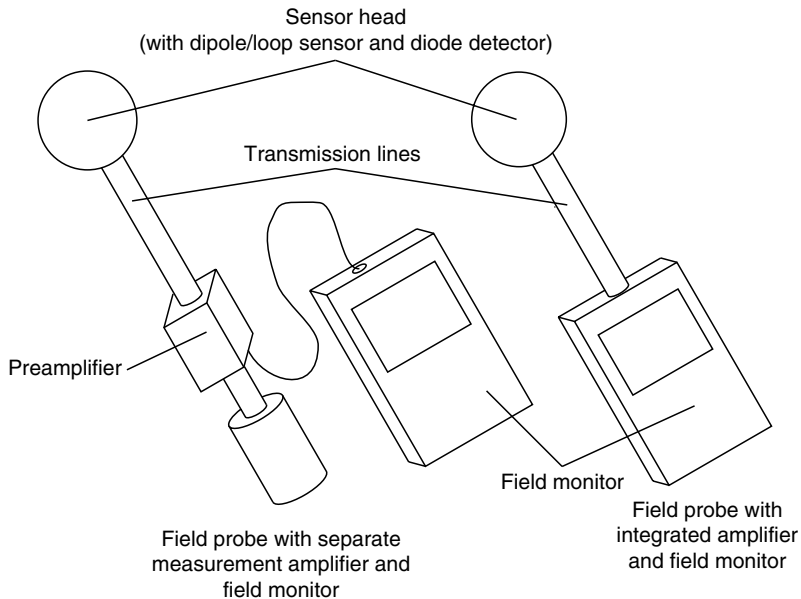


FIGURE 11.12
Schematic of the most common designs of broadband RF survey meters.

the spectral characteristics of the field is available. Therefore, if a broadband meter is used for compliance testing, the measured field value must comply with the lowest permissible limit defined in the measurement range of the meter. Broadband survey meters are relatively inexpensive and easy to apply. Hence, these probes are often used for field measurements.

Figure 11.12 displays typical broadband field survey meter designs. Figure 11.13 displays the frequency response of two broadband probes. The field value measured with probe 1 must comply with the lowest limit in the frequency range from 10 MHz to 1 GHz, whereas probe 2 must comply with the lowest limit between 100 MHz and 10 GHz. The overlapping frequency range is counted twice if the exposure values are added to cover the entire frequency range. Some broadband probes are designed to reflect the frequency dependence of the limits. In all cases, it is advised that the off-band response of

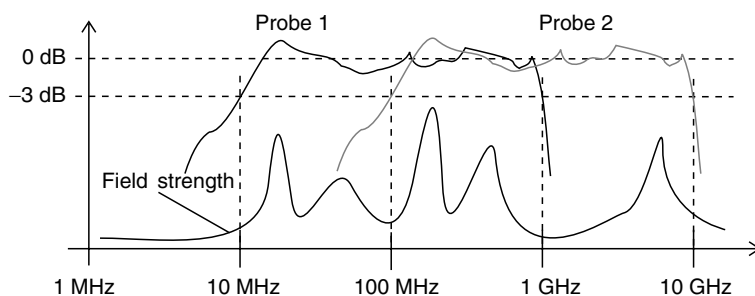


FIGURE 11.13
Frequency response of two broadband field survey meters. The fields in the frequency ranges are summed up. If the fields from probes 1 and 2 are summed again, then the fields in the overlapping frequency range are accounted for twice.

these probe systems be carefully evaluated. If a specific transmitter is the dominant source, compliance testing is greatly simplified [56].

In addition to the frequency response, broadband probes have a certain time-domain transfer function. When pulsed fields are measured, this response must be compensated. However, for this compensation, information on the time-domain characteristics of the measured field is necessary. In summary, the main sources of uncertainty regarding broadband survey meters are:

- Calibration
- Linearity
- Frequency response
- Isotropy
- Time-domain response
- Temperature response

In conclusion, the accuracy of broadband evaluations is significantly limited but generally conservative.

11.5.2 Frequency-Selective Measurements

Frequency-selective measurement techniques can overcome the issue of the unknown spectral composition of the field. However, the execution of the measurement is more complicated, such that insufficiently trained personnel are likely to produce erroneous results.

Measurements in the frequency domain are performed with a measurement antenna, as described in [Section 11.3.3](#), that is connected to a spectrum analyzer (Figure 11.14). The spectrum analyzer mixes the received RF signal down to the base band. A filter is swept in frequency over the considered sweep bandwidth. The signal after the filter is detected using user-definable detectors. Most spectrum analyzers provide video filters for additional filtering (smoothing) of the spectral signal. Setting the sweep and filter parameters can significantly impact the measurement result. Optimal settings for GSM and Universal Mobile Telecommunications System (UMTS) based on a simulation approach were recently presented by Olivier and Martens [57]. The impact of summing up parts of the spectrum because of nonideal filters was investigated by Joseph et al. [58]. Modern analyzers also provide a zero-span mode. The RF signal is mixed down to the base band, and only the time-domain envelope of the signal is displayed afterward. This mode may be applied, for example, to investigate the time-domain characteristics of an unknown communication system. Additionally, it is especially useful to measure pulsed

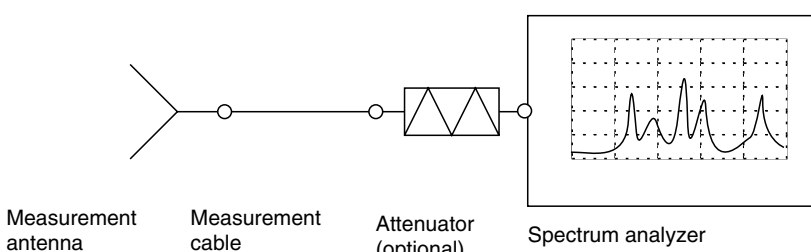


FIGURE 11.14
Schematic of a frequency-selective measurement of EMF.

signal forms, as this signal form is often used in communication systems. In summary, the application of spectrum analyzers is a complex subject. Measurement recommendations dealing with frequency-selective measurements should always describe the spectrum analyzer settings to produce feasible and comparable results. Nevertheless, the measurement engineer should still test the actual applicability of these settings for his particular measurement equipment.

The main sources of uncertainty regarding frequency-selective measurements are:

- Calibration of the spectrum analyzer, cable, and measurement antenna
- Linearity of the spectrum analyzer, cable, and measurement antenna
- Frequency response of the spectrum analyzer, cable, and measurement antenna
- Demodulation method of the spectrum analyzer (detector type)
- Temperature response of the spectrum analyzer, cable, and measurement antenna
- Mismatch between measurement equipment

Although the frequency-selective measurement method overcomes most of the issues regarding broadband survey meters, it is not sufficient to soundly identify the exposure from different transmitters at the same frequency. In this case, measurement receivers should be applied.

11.5.3 Code-Selective Measurements

Code-selective measurements are especially necessary if the exposure from a specific transmitter applies code division multiple access (CDMA), for example, if a UMTS is to be assessed. In the case of UMTS, all base stations usually transmit in a single-frequency band. With a frequency-selective receiver, it is not possible to discriminate between exposure from different base stations, since a single-frequency band is used and the channels are multiplexed in the code domain. Code-selective receivers decode the signal received from a base station, that is, the receiver is able to discriminate between a field strength received from the base station of interest and other noise-like sources. The receiver measures the field received from the base station of interest only if the particular scrambling code is used for decoding. Basically, the same sources of uncertainty must be considered for code- and frequency-selective measurements. However, in contrast to frequency-selective measurements, the modulation of the signal does not increase the uncertainty but rather the possible nonorthogonality of the respective scrambling codes. Many of the typical measurement receivers for UMTS base station measurements (e.g., Rohde and Schwarz TSMU [59], Anritsu ML8720B [60]) provide insufficient sampling rates for swept scanning. Others overcome this limitation, for example, Narda-STS SRM-3000 [61].

11.6 Typical Maximum Peak Spatial SAR Exposures

The daily local RF exposure of the general public has increased by several orders of magnitude with the introduction and proliferation of mobile handsets. This has triggered concern among health agencies and the public, since the highest exposed tissue is the brain. [Figure 11.15](#) and [Figure 11.16](#) display the frequency of worst-case SAR from mobile phones measured according to Refs. [62,63]. Figure 11.15 represents the typical SAR

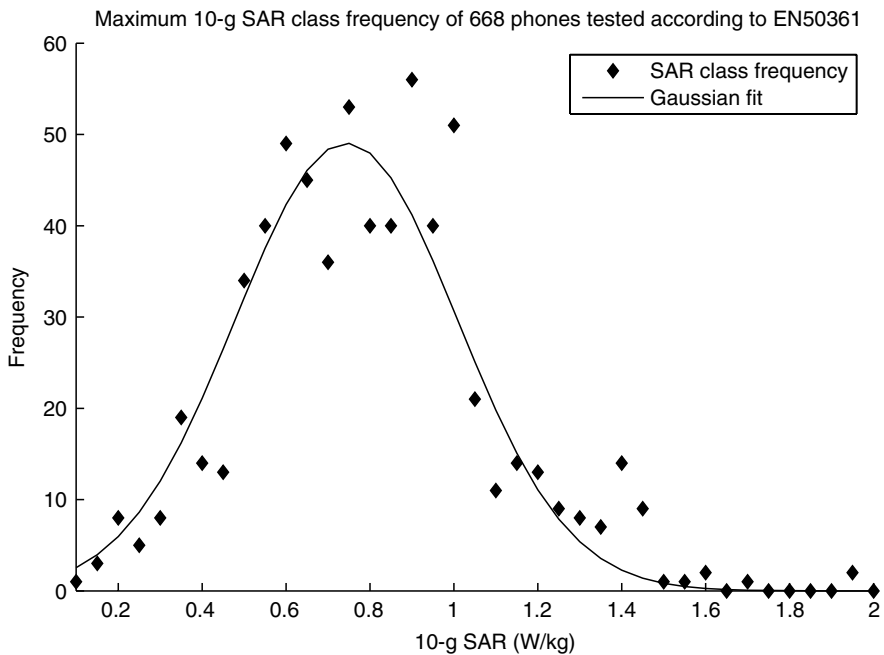


FIGURE 11.15

Statistical distribution of maximum 10-g SAR measured for 668 mobile phones according to EN50361. (From German Federal Office for Radiation Protection, <http://www.bfs.de/elektro/hff/oekolabel.html>, 2005.)

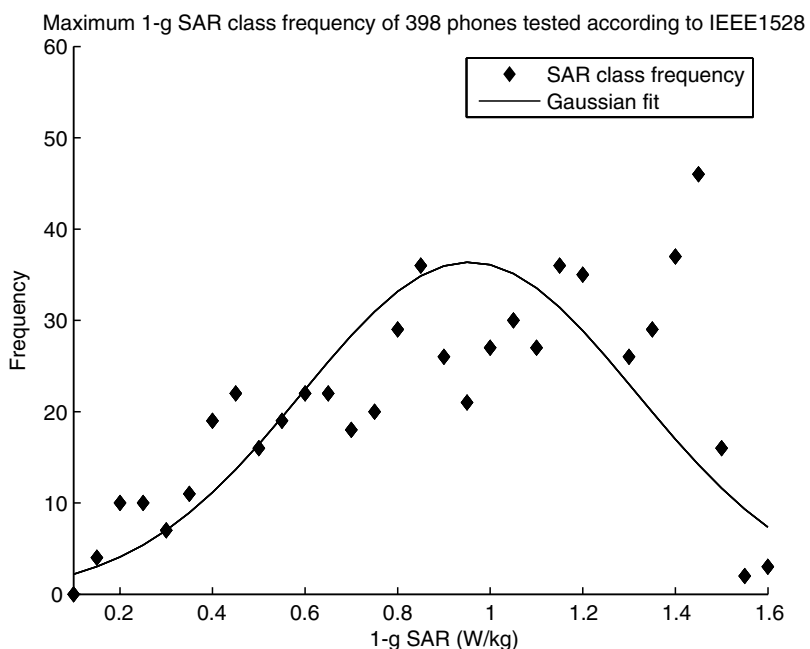


FIGURE 11.16

Statistical distribution of maximum 1-g SAR measured for 687 mobile phones according to IEEE-1528. (From Federal Communications Commission, <http://www.fcc.gov/cgb/sar/>, 2005.)

TABLE 11.4

Worst-Case Peak Spatial SAR of a Set of Wireless Indoor Devices

Device Class	Frequency Range (MHz)	Worst-Case 10-g SAR (W/kg)
Baby surveillance	40–863	0.077
DECT	1880–1900	0.055
WLAN	2400–2484	0.81
Bluetooth	2402–2480	0.49
PC peripherals	27–40	≤ 0.005

Note: An absolute worst case for all commercially available products cannot be estimated based on these data.

values for Europe (mean 10-g SAR: 0.74) [64] and [Figure 11.16](#) for North America (mean 1-g SAR: 0.96) [65]. The different averaging masses are due to different legal regulations in Europe and the United States. These values are a considerable percentage of the limits. A recent statistical analysis of the Federal Communications Commission (FCC) SAR database found that the SAR values of newer phones are typically lower than of older phones despite their greatly reduced size.

SAR measurements of devices operated in home and office environments were reported by Kramer et al. [66]. A summary of the maximum SAR values determined in this study for several types of transmitters is given in Table 11.4. It should be noted that under worst-case scenarios, the SAR values measured for WLAN and Bluetooth communication systems are in the same range as those for mobile phones.

11.7 Typical Far-Field Exposures

A study regarding indoor incident field exposure from cellular base station sites was conducted by ARCS (Austria) [55] in the city of Salzburg. Table 11.5 shows two

TABLE 11.5Results from Indoor Incident *E* Field Measurements Conducted in an Austrian City [55]

Base Station	Distance to Base Station (m)	Cumulative Incident <i>E</i> Field (V/m)	Distance to Base Station (m)	Cumulative Incident <i>E</i> Field (V/m)
1	196	0.37	374	0.35
2	88	0.51	108	0.89
3	9	0.034	15	0.037
4	16	0.62	8	1.00
5	85	0.94	152	0.75
6	81	1.8	85	1.71
7	4	3.7	25	1.02
8	93	0.19	208	0.19
9	34	0.40	55	0.63
10	39	1.9	76	2.8
11	174	0.59	220	0.45
12	41	0.70	107	0.67
13	2.5	0.67	5.5	0.15

Note: Two cumulative incident field exposure values (sum of incident field exposures from multiple transmitters at one site) at different distances are shown as exemplary for each base station site.

TABLE 11.6Worst-Case E Field of Typical Wireless Indoor Devices at 20-cm and 1-m Distance

Device Class	Frequency Range (MHz)	Worst-Case E Field (V/m) (20 cm)	Worst-Case E Field (V/m) (1 m)
Baby surveillance	40–863	8.5	3.2
DECT	1880–1900	11.5	2.9
WLAN	2400–2484	3.9	1.1
Bluetooth	2402–2480	3.1	1.0
PC peripherals	27–40	≤ 1.5	≤ 1.5

cumulative incident field exposure values (sum of incident field exposures from multiple transmitters at one site) measured at different distances from the considered base station sites. The values are within 0.1 to 1 V/m for distances up to several hundreds of meters. These data also underline that the distance to the base station site has a poor correlation for the incident exposure.

Similar results were reported by Bornkessel and Schubert [67]. This study also included outdoor measurement points and addressed the time dependence, that is, traffic dependence of the exposure from cellular base stations. The results showed a significant time dependence for base stations with multiple traffic channels. In these cases, clearly lower exposure can be expected at night and on weekends.

The incident field exposures from typical devices used in home and office environments were assessed by Kramer et al. [66]. The maximum E field exposure values for different device categories are summarized in Table 11.6. The incident field exposure from cellular base stations may be exceeded by the exposure from these devices because of the generally closer distances.

Additionally, an incident exposure of 1 V/m translates to a peak spatial SAR value in the brain that is approximately a factor 10,000 times lower than the maximum exposure by a handset. Thus, exposure by handsets is by far the most dominant source of RF exposure for the general population.

Acknowledgment

The authors wish to thank Prof. Dr. Quirino Balzano, Dr. Urs Lott, and Dr. Katja Pokovic for their critical review of this manuscript. The dosimetric research at the IT'IS Foundation is supported by many institutions, the most significant of which are European and Swiss Funding Agencies, Motorola Inc. (USA), the Mobile Manufacturers Forum (Belgium), MTT (Japan), and Schmid & Partner Engineering AG (SPEAG, Switzerland).

References

- Schmid, G., Neubauer, G., Illievich, U.M., and Alesch, F., "Dielectric properties of porcine brain tissue in the transition from life to death at frequencies from 800 to 1900 MHz," *Bioelectromagnetics*, Vol. 24, No. 6, Sept. 2003, pp. 413–422.

2. Poković, K., Advanced Electromagnetic Probes for Near-Field Evaluations, Ph.D. thesis, Diss. ETH Nr. 13334, Zurich, Switzerland, 1999.
3. Schönborn, F., Poković, K., and Kuster, N., "Dosimetric analysis of the carousel setup for the exposure of rats at 1.62 GHz," *Bioelectromagnetics*, Vol. 25, No. 1, Jan. 2004, pp. 16–26.
4. Christ, A., Chavannes, N., Nikoloski, N., Gerber, H.-U., Poković, K., and Kuster, N., "A numerical and experimental comparison of human head phantoms for compliance testing of mobile telephone equipment," *Bioelectromagnetics*, Vol. 26, No. 2, Feb. 2005, pp. 125–137.
5. Kainz, W., Christ, A., Kellom, T., Seidman, S., Nikoloski, N., Beard, B., and Kuster, N., "The specific anthropomorphic mannequin (SAM) compared to 14 anatomical head models using a novel definition for the mobile phone positioning," *Physics in Medicine and Biology*, Vol. 50, No. 14, July. 2005, pp. 3423–3445.
6. Kuster, N., Schuderer, J., Christ, A., Futter, P., and Ebert, S., "Guidance for exposure design of human studies addressing health risk evaluations of mobile phones," *Bioelectromagnetics*, Vol. 25, No. 7, Oct. 2004, pp. 524–529.
7. ICNIRP, "Guidelines for limiting exposure to time-varying electric, magnetic, and electromagnetic fields (up to 300 GHz)," *Health Physics*, Vol. 74, No. 4, 1998, pp. 494–522.
8. ANSI/IEEE, C95.6–2002, *IEEE Standard for Safety Levels with Respect to Human Exposure to Electromagnetic fields, 0–3 kHz*, The Institute of Electrical and Electronics Engineers, Inc., New York, 2002.
9. ANSI/IEEE, C95.1–2001, *IEEE Standard for Safety Levels with Respect to Human Exposure to Radio Frequency Electromagnetic Fields, 3 kHz to 300 GHz*, The Institute of Electrical and Electronics Engineers, Inc., New York, 2001.
10. National Council on Radiation Protection and Measurements (NCRP), Ed., *Biological Effects and Exposure Criteria for Radiofrequency Electromagnetic Fields*, NCRP, 1986.
11. Aslan, E., "Electromagnetic radiation survey meter," *IEEE Transactions on Instrumentation and Measurement*, Vol. IM-19, No. 4, 1970, pp. 368–372.
12. Rudge, A.W., "An electromagnetic radiation probe for near-field measurements at microwave frequencies," *Journal of Microwave Power*, Vol. 5, No. 3, 1970, pp. 155–174.
13. Bassen, H., Swicord, M., and Abita, J., "A miniature broad-band electric field probe," *Annals of the New York Academy of Sciences, Biological Effects of Nonionizing Radiation*, Vol. 247, No. 2, Feb. 1975, pp. 481–493.
14. Bassen, H., Herman, W., and Hoss, R., "EM probe with fiber optic telemetry system," *Microwave Journal*, Vol. 20, No. 4, Apr. 1977, pp. 35–47.
15. Bassen, H.I. and Smith, G.S., "Electric field probes—a review," *IEEE Transactions on Antennas and Propagation*, Vol. 31, No. 5, 1983, pp. 710–718.
16. Hopfer, S., "The design of broad-band resistive radiation probes," *IEEE Transactions on Instrumentation and Measurements*, Vol. IM-21, No. 4, Nov. 1972, pp. 416–421.
17. Smith, G., "Analysis of miniature electric field probes with resistive transmission lines," *IEEE Transactions on Microwave Theory and Techniques*, Vol. MTT-29, No. 11, Nov. 1981, pp. 1213–1224.
18. Schmid, T., Egger, O., and Kuster, N., "Automated E-field scanning system for dosimetric assessments," *IEEE Transactions on Microwave Theory and Techniques*, Vol. 44, No. 1, Jan. 1996, pp. 105–113.
19. Whiteside, H. and King, R., "The loop antenna as a probe," *IEEE Transactions on Antennas and Propagation*, Vol. AP-12, No. 5, May 1964, pp. 291–297.
20. Kanda, M., "Standard probes for electromagnetic field measurement," *IEEE Transactions on Antennas and Propagation*, Vol. AP-41, No. 10, Oct. 1993, pp. 1349–1364.
21. Narda Safety Test Solutions, "Electric field probe for EMR-200 and EMR-300," <http://www.narda-sts.com>, 2005, accessed Dec. 16, 2005.
22. SPEAG Switzerland, "SPEAG dosimetric near-field probes (product flyer)," <http://www.dasy4.com/flyers/probes.pdf>, 2005, accessed Dec. 16, 2005.
23. Poković, K., Schmid, T., and Kuster, N., "Millimeter-resolution E-field probe for isotropic measurement in lossy media between 100 MHz and 20 GHz," *IEEE Transactions on Instrumentation and Measurements*, Vol. 49, No. 4, Aug. 2000, pp. 873–878.

24. Poković, K., Schmid, T., Fröhlich, J., and Kuster, N., "Novel probes and evaluation procedures to assess field magnitude and polarization," *IEEE Transactions on Electromagnetic Compatibility*, Vol. 42, No. 2, May 2000, pp. 240–245.
25. Cecelja, F. and Balachandran, W., "Optimized CdTe sensors for measurement of electric and magnetic fields in the near-field region," *IEEE Transactions on Instrumentation and Measurements*, Vol. 49, No. 3, June 2000, pp. 483–487.
26. Tokano, Y., Kobayashi, H., and Miyakawa, T., Houjyo, Y. "A gigahertz-range micro optical electric field sensor," in *Electromagnetic Compatibility 2001*, Zurich, Switzerland, 2001, p. 127.
27. Tajima, K., Kobayashi, R., Kuwabara, N., and Tokuda, M., "Development of optical isotropic E-field sensor operating more than 10 GHz using Mach-Zehnder interferometers," *IEICE Transactions on Electronics*, Vol. 85, 2002, p. 961.
28. Agullo-Lopez, F., Cabrera, J., and Agullo-Rueda, F., *Electrooptics*, Academic Press, New York, 1994.
29. Rigrod, W.W. and Kaminow, I.P., "Wide-band microwave light modulation," *IEEE*, Vol. 51, Jan. 1963, pp. 137–140.
30. Lei, C. and Kilcoyne, S., Eds., "Vertical-cavity surface-emitting lasers VI," in *Proceedings of SPIE*, SPIE—The international society for optical engineering, 2002.
31. Choquette, K. and Lei, C., Eds., "Vertical-cavity surface-emitting lasers V," in *Proceedings of SPIE*, SPIE—The international society for optical engineering, 2001.
32. Wilmsen, C., Temkin, H., and Coldren, L., *Vertical-Cavity Surface-Emitting Lasers*, Cambridge University Press, The Edinburgh Building, Cambridge CB2 2RU, U.K. 1999.
33. Schuderer, J., EMF Risk Assessment: In Vitro Research and Sleep Studies, Ph.D. thesis, Diss. ETH Nr. 15347, Zurich, Switzerland, 2003.
34. Bowman, R.-R., "A probe for measuring temperature in radio-frequency heated material," *IEEE Transactions on Microwave Theory and Techniques*, Vol. 24, 1976, pp. 43–45.
35. Burkhardt, M., Poković, K., Gnos, M., Schmid, T., and Kuster, N., "Numerical and experimental dosimetry of petri dish exposure setups," *Journal of the Bioelectromagnetic Society*, Vol. 17, No. 6, 1996, pp. 483–493.
36. Schuderer, J., Schmid, T., Urban, G., Samaras, T., and Kuster, N., "Novel high resolution temperature probe for RF dosimetry," *Physics in Medicine and Biology*, Vol. 49, No. 6, Mar. 2004, pp. N83–N92.
37. Wickersheim, K.-A. and Sun, M.-H., "Fiberoptic thermometry and its application," *Journal of Microwave Power*, Vol. 22, 1987, pp. 85–93.
38. Guy, A.W., "Analyses of electromagnetic fields induced in biological tissue by thermographic studies on equivalent phantom models," *IEEE Transactions on Microwave Theory and Techniques*, Vol. 34, No. 6, June 1971, pp. 671–680.
39. Taurisano, M.D. and Vorst, A.V., "Experimental thermographic analysis of thermal effects induced on a human head exposed to 900 MHz fields of mobile phones," *IEEE Transactions on Microwave Theory and Techniques*, Vol. 48, No. 11, Nov. 2000, pp. 2022–2032.
40. Baba, M., Suzuki, Y., Taki, M., Fukunaga, K., and Watanabe, S., "Three dimensional visualization of the temperature distribution in a phantom for the assessment of localized exposure to microwaves," in *Bioelectromagnetic Society 2005 Annual Meeting*, Bioelectromagnetic Society, Dublin, Ireland, June 2005, pp. 250–251.
41. Durney, C.H., Massoudi, H., and Iskander, M.F., *Radiofrequency Radiation Dosimetry Handbook*, 4th ed. Brooks Air Force, Brooks Air Force Base, TX, 1997.
42. Seibersdorf Research, Austria, "Precision conical dipole PCD 8250," http://www.seibersdorf-rf.com/docs/leaflet/W_Products_PCD8250_engl.pdf, 2005, accessed Dec. 16, 2005.
43. Seibersdorf Research, Austria, "Precision biconical antenna PBA 320," http://www.seibersdorf-rf.com/docs/leaflet/W_Products_PBA320_engl.pdf, 2005, accessed Dec. 16, 2005.
44. Müller, W. and Georg Neubauer, H.H., "ADD3D, a new technique for precise power flux density measurements at mobile communications base stations," http://www.seibersdorf-rf.com/docs/pubdl/Pub4_Add3Denglish.pdf, 2000, accessed Dec. 16, 2005.

45. Drossos, A., Santomaa, V., and Kuster, N., "The dependence of electromagnetic energy absorption upon human head tissue composition in the frequency range of 300–3000 MHz," *IEEE Transactions on Microwave Theory and Techniques*, Vol. 48, No. 11, Nov. 2000, pp. 1988–1995.
46. Kanda, M.Y., Douglas, M.G., Mendivil, E.D., Ballen, M., Gessner, A.V., and Chou, C.-K., "Faster determination of mass-averaged SAR from 2-D area scans," *IEEE Transactions on Microwave Theory and Techniques*, Vol. 52, No. 8, 2004, pp. 2013–2020.
47. Merckel, O. and Fleury, G., "Rapid SAR measurement of mobile phones," *International Symposium on International Journal of Applied Electromagnetics and Mechanics*, Vol. 19, 2004, pp. 183–186.
48. TEM Consulting, "Near field RF scanner," http://www.temconsulting.com/Products/ScanningPositioner/RF_Scanner.htm, 2005, accessed Dec. 16, 2005.
49. Chavannes, N., Tay, R., Nikoloski, N., and Kuster, N., "Suitability of FDTD based TCAD tools for RF design of mobile phones," *IEEE Antennas and Propagation Magazine*, Vol. 45, Dec. 2003, pp. 52–66.
50. ANSI C63.19, "American National Standard for Methods of Measurement of Compatibility between Wireless Communications Devices and Hearing Aids (Revision Draft 3.8)," Oct. 2005.
51. Ogawa, K., Ozaki, A., Kajiwara, S., Yamamoto, A., Koyanagi, Y., and Saito, Y., "High-speed SAR prediction for mass production stages in a factory by H-field measurements," *IEEE Antennas and Propagation Society Symposium*, 2004, Vol. 2, June 2004, pp. 1843–1846.
52. Kuster, N. and Balzano, Q., "Experimental and numerical dosimetry," in *Mobile Communications Safety*, Kuster, N., Balzano, Q., and Lin, J.C., Eds. Chapman & Hall, London, 1996, pp. 13–64.
53. Abteilung Nichtionisierende Strahlung, Mobilfunk Basisstationen (GSM) Messempfchlung, Technical report, BUWAL, Switzerland, 2002.
54. ANFR, Protocol de mesure *in situ*, Technical Report 2.1, Agence National des Frequences, France, May 2004.
55. Coray, R., Krähenbühl, P., Riederer, M., Stoll, D., Neubauer, G., and Szentkuti, B., Immissionen in Salzburg, Technical Report, BAKOM, Switzerland, 2002.
56. CENELEC EN 50400, "Basic standard to demonstrate the compliance of fixed equipment for radio transmission (110 MHz–40 GHz) intended for use in wireless telecommunication networks with the basic restrictions or the reference levels related to general public exposure to radio frequency electromagnetic fields, when put into service," Sept. 2005.
57. Olivier, C. and Martens, L., "Optimal settings for frequency selective electromagnetic field measurements for exposure assessment around base stations," In *Bioelectromagnetic Society 2005 Annual Meeting*, Bioelectromagnetic Society, Dublin, Ireland, June 2005, pp. 466–468.
58. Joseph, W., Olivier, C., and Martens, L., "A robust, fast and accurate deconvolution algorithm for EM-field measurements around GSM and UMTS base stations with a spectrumanalyser," *IEEE Transactions on Instrumentation and Measurements*, Vol. 51, No. 6, Feb. 2003, pp. 1163–1169.
59. Rohde and Schwarz, Germany, "Radio network analyzer R&S TSMU," [http://www.rohde-schwarz.com/www/download_files.nsf/file/TSMU_en.pdf/\\$file/TSMU_en.pdf](http://www.rohde-schwarz.com/www/download_files.nsf/file/TSMU_en.pdf/$file/TSMU_en.pdf), 2004, accessed Dec. 16, 2005.
60. Anritsu, Japan, "ML8720B UMTS/W-CDMA field strength area tester," http://www.eu.anritsu.com/files/ML8720B_E11000.pdf, 2005, accessed Dec. 16, 2005.
61. Narda Safety Test Solutions, "SRM-3000 frequency-selective field strength measuring system for rapid, reliable safety assessments," <http://www.narda-sts.com>, 2005, accessed Dec. 16, 2005.
62. CENELEC EN 50361, "Basic standard for the measurement of specific absorption rate related to human exposure to electromagnetic fields from mobile phones (300 MHz–3 GHz)," 2001.
63. IEEE SC34, Recommended Practice for Measurements and Computations with Respect to Human Exposure to Radio Frequency Electromagnetic Fields, 100kHz to 300 GHz (IEEE Standard C95.3), Technical report, IEEE, 2002.
64. German Federal Office for Radiation Protection, "Strahlenschutzkriterien für ein Mobiltelefon-Ökolabel," <http://www.bfs.de/elektro/hff/oekolabel.html>, 2005, accessed Dec. 16, 2005.
65. Federal Communications Commission, "FCC SAR database," <http://www.fcc.gov/cgb/sar/>, 2005, accessed Dec. 16, 2005.
66. Kramer, A., Kühn, S., Lott, U., and Kuster, N., Development of Procedures for the Assessment of Human Exposure to EMF from Wireless Devices in Home and Office Environments, Technical

- report, IT'IS Foundation for Research on Information Technologies in Society, Zurich, Switzerland, Jan. 2005.
- 67. Bornkessel, C. and Schubert, M., Zwischenbericht: Analyse der Immissionsverteilung, Technical report, IMST GmbH Kamp-Lintfort, 2004.
 - 68. van Deventer, E., Simunic, D., and Repacholi, M., EMF Standards for human health, in *Biological and Medical Aspects*, Barnes, F.S. and Greenebaum, B., Eds., Taylor & Francis, Boca Raton, FL, 2006, [Chapter 8](#).

12

Electromagnetic Imaging of Biological Systems

William T. Joines, Qing H. Liu, and Gary Ybarra

CONTENTS

12.1	Introduction	411
12.2	Development of MWI	413
12.2.1	Frequency Dependence.....	413
12.2.2	Scattering Parameters.....	414
12.2.3	Scattering-Parameter Imaging of Tissue Permittivity.....	415
12.2.4	Power, Signal Attenuation, and Signal-to-Noise Ratio	417
12.3	Three-Dimensional Formulation	418
12.4	Wave Equation and VIE	419
12.4.1	Microwave Imaging.....	421
12.4.2	Electrical Impedance Tomography	422
12.5	Three-Dimensional Images Reconstructed from Simulated Three-Dimensional MWI Data	423
12.6	Two-Dimensional Images Reconstructed from Measured Two-Dimensional EIT Data.....	423
12.6.1	Case 1: One Insulator Object Inside the Container.....	423
12.6.2	Case 2: Two Insulator Objects Inside the Container.....	425
12.6.3	Case 3: One Conductive and One Resistive Object Inside the Container.....	426
12.7	Summary and Conclusions	428
	Acknowledgment.....	428
	References	428

12.1 Introduction

Two emerging types of electromagnetic imaging are presented: electrical impedance imaging (or tomography, EIT) and microwave imaging (MWI). Both techniques rely on the contrast in electromagnetic properties (complex permittivity) of the tissues to be imaged with that of the neighboring tissue region. Both techniques use an array of sensors

around the region to be imaged. For EIT, a current due to a known voltage is passed between all electrodes within an array to determine the electrical impedance (or admittance) of the imaged tissue. For MWI, a microwave signal is sequentially transmitted through the imaged tissue to all antennas within an array to determine the scattering parameters (ratio of reflected and transmitted signals to the incident signal) of the imaged region. EIT uses a lower frequency (in the kHz or MHz range) so that the imaged region is small compared with the signal wavelength. MWI uses a higher frequency (in the GHz range) so that the imaged region is comparable to the signal wavelength. The MWI frequency is chosen to be low enough to yield an adequate depth of penetration into the imaged tissue, but high enough to allow the use of a number of small, closely spaced antennas in the array. Since antenna size is also comparable to signal wavelength, micro-strip patches or waveguide apertures on high-permittivity substrates are often used to reduce the wavelength at the antenna.

Once MWI and electrical impedance imaging are fully developed for clinical use, they have great potential for the early detection of breast cancer. Other imaging methods are now available, but they have certain disadvantages that limit their acceptance as the method of choice for breast cancer screening. Magnetic resonance imaging (MRI) relies on large electrical currents in cryogenically cooled conductors to produce a strong magnetic field. Hardware and safety requirements may continue to make MRI too expensive for widespread use in breast cancer screening. X-ray imaging is now used fairly extensively, but many women dread the discomfort or pain associated with having their breast sandwiched between two hard, flat surfaces in preparation for the screening, and their aversion to this test may prevent them from participating.

For testing patients in the clinic, both MWI and EIT will most likely use the same arrangement as far as the patient is concerned. The patient will lie face down in a comfortable position on a cot or gurney, as illustrated in Figure 12.1. The breast to be screened extends into an opening containing body-temperature liquid that has approximately the same electrical properties as the normal female breast. This liquid is held within a cylindrical or rectangular thin-walled plastic container that is attached beneath the cot. For MWI, numerous small antennas are attached to the entire outer surface of the plastic container. For EIT, numerous small metal electrodes are attached on the inside surface of the plastic container so that the electrodes can flow current through the liquid and the breast tissue under test. These are the techniques, along with numerical modeling,



FIGURE 12.1
Breast imaging arrangement with patient lying comfortably face down.

that we are now using in the laboratory to obtain the results reported herein. Although we describe how we obtain the breast cancer images using phantom (artificial) tissues, we have not yet moved our imaging systems into the clinic to image breast cancer in real patients. The research and development we are now doing are necessary steps that must be taken before successful clinical applications can occur.

12.2 Development of MWI

Active MWI is an emerging technique for several biomedical imaging applications. Besides being economical and easily portable, MWI takes advantage of the high contrast in electrical properties that exists between anomalous and normal tissue over certain ranges of frequency [1–7]. Fortunately for breast cancer imaging, the contrast between normal and malignant tissue appears to be greatest over the approximate frequency range of 600 to 1000 MHz. This frequency range is both low enough and high enough to meet most of the requirements cited earlier.

While the high contrast is advantageous, it does make multiple scattering in the region more pronounced, and this adds to the difficulty of image formation. Although the specific contrasts vary with frequency, there is now a general belief that these contrasts are substantial, especially near 800 MHz (see the references cited in Refs. [8,9] and the review in Fear et al. [10]). For example, according to Joines et al. [6], at 800 MHz, the permittivity relative to air (ϵ_r) and the electrical conductivity (σ) for malignant breast tissue are approximately $\epsilon_r \cong 57.2$ and $\sigma \cong 1.08$ S/m, respectively, while they are $\epsilon_r \cong 16$ and $\sigma \cong 0.16$ S/m, respectively, for normal mammary tissue. The contrast is 3.75 for the relative permittivity and 6.75 for the electrical conductivity. Over the past few years, several research groups have been working on both hardware and software aspects of microwave breast imaging [8,9,11–15] to take advantage of the high contrast in applications of near-field MWI. The reason for the high contrast between malignant and normal tissue may be better understood through a brief examination of the frequency-dependent electrical properties of biological tissue.

12.2.1 Frequency Dependence

The frequency dependence of ϵ and σ is directly related to the polarization of molecules and structural interfaces caused by an applied electric field within the biological tissue. A specific polarization effect is important in determining ϵ and σ up to a relaxation frequency, f_r . Above this frequency the induced polarization can no longer change as fast as the applied field. Thus, above f_r the energy storage term (ϵ) is less, and the energy dissipation term (σ) is greater. Structural or Maxwell–Wagner relaxation, because of cellular membranes and other layered structures within the tissue, is of importance at frequencies below about 100 MHz [16]. Polar or Debye relaxation, because of the rotation of molecules or molecular groups by the applied field, is of importance in determining ϵ and σ at all frequencies above about 30 MHz. In the 30- to 2000-MHz range, the values of ϵ and σ versus frequency are highly dependent on the free-water content ($f_r \cong 25,000$ MHz) of the tissue. However, bound water (f_r in the 100- to 1000-MHz range) and protein molecules (f_r in the 40- to 300-MHz range) also make significant contributions to ϵ and σ .

Because most types of polarization can be described formally in the same qualitative manner, the Debye equations often apply very well, even though they were derived for the case of molecular rotation. For a given relaxation frequency, the Debye relations for ϵ and σ are [17]:

$$\epsilon = \epsilon_H + \frac{\epsilon_L - \epsilon_H}{1 + \left(\frac{f}{f_r}\right)^2} \quad (12.1)$$

and

$$\sigma = \sigma_L + \frac{(\epsilon_L - \epsilon_H)2\pi f_r}{1 + (f_r/f)^2} \quad (12.2)$$

where $\epsilon = \epsilon_H$ at f well above f_r and $\sigma = \sigma_L$, $\epsilon = \epsilon_L$ at f well below f_r .

Two tissues having different constituencies (e.g., normal and malignant tissues) most likely will have different relaxation frequencies (f_{r1} and f_{r2}). If the operating frequency of an applied electromagnetic wave is between f_{r1} and f_{r2} , then an examination of the Debye equations shows that this is the frequency where the greatest contrast occurs between ϵ and σ for the two tissues [5].

12.2.2 Scattering Parameters

As stated earlier, to achieve MWI an electromagnetic wave is sequentially transmitted through the tissue region to be imaged and to all antennas within an array surrounding the region in order to determine the scattering parameters (ratio of reflected and transmitted signals to the incident signal) of the imaged region. This is important because the scattering parameters may be measured as well as calculated.

Taking just two antennas in the array, one transmitting and one receiving, the scattering parameters may be simply expressed. The electric field intensity on the transmitter side (E_1) of the region is made up of incident and reflected (scattered) components and likewise, for the electric field intensity on the receiver side (E_2) of the imaged region. This relationship is expressed as

$$E_1 = E_{1i} + E_{1r} \quad (12.3)$$

and

$$E_2 = E_{2i} + E_{2r} \quad (12.4)$$

where E_{1i} is a wave incident from antenna 1 into the imaged region, E_{1r} is reflected into antenna 1 from the region, E_{2i} is incident from antenna 2 into the region, and E_{2r} passes from the region and into antenna 2. Since the incident and scattered fields completely determine the transmitted and received signals, it is convenient to express the scattered fields as functions of the incident fields, as

$$E_{1r} = S_{11}E_{1i} + S_{12}E_{2i} \quad (12.5)$$

and

$$E_{2r} = S_{21}E_{1i} + S_{22}E_{2i} \quad (12.6)$$

where the scattering parameters are defined as:

$$S_{11} = E_{1r}/E_{1i} \mid_{E_{2i}=0}, S_{12} = E_{1r}/E_{2i} \mid_{E_{1i}=0}, S_{21} = E_{2r}/E_{1i} \mid_{E_{2i}=0}, S_{22} = E_{2r}/E_{2i} \mid_{E_{1i}=0} \quad (12.7)$$

Thus, S_{11} is the reflection coefficient at antenna 1, under the condition that antenna 2 is terminated in the impedance of its connecting cable (usually 50Ω), so that no signal enters the region from antenna 2. Under the same condition at antenna 2, S_{21} is the forward transmission coefficient of signals from antenna 1 to antenna 2. Likewise, S_{22} is the reflection coefficient at antenna 2, under the condition that antenna 1 is terminated in the impedance of its connecting cable (usually 50Ω), so that no signal enters the region from antenna 1. Under the same condition at antenna 1, S_{12} is the reverse transmission coefficient of signals from antenna 2 to antenna 1.

Using the very same concepts and definitions, the scattering parameters for N antennas are expressed as

$$\begin{aligned} E_{1r} &= S_{11}E_{1i} + S_{12}E_{2i} + S_{13}E_{3i} + \cdots + S_{1N}E_{Ni} \\ E_{2r} &= S_{21}E_{1i} + S_{22}E_{2i} + S_{23}E_{3i} + \cdots + S_{2N}E_{Ni} \\ E_{3r} &= S_{31}E_{1i} + S_{32}E_{2i} + S_{33}E_{3i} + \cdots + S_{3N}E_{Ni} \\ &\vdots \\ E_{Nr} &= S_{N1}E_{1i} + S_{N2}E_{2i} + S_{N3}E_{3i} + \cdots + S_{NN}E_{Ni} \end{aligned} \quad (12.8)$$

12.2.3 Scattering-Parameter Imaging of Tissue Permittivity

This method of imaging relies on the propagation of electromagnetic waves into and through the region of interest as shown in Figure 12.2. The reflected and transmitted electric fields are referenced to the incident electric field to determine the magnitude and phase delay of the reflection coefficient at the n th port ($S_{nn} = |S_{nn}| \angle \phi_R = E_r/E_i$) and the transmission coefficient from port n to m ($S_{mn} = |S_{mn}| \angle \phi_T = E_t/E_i$) at multiple transmitter-receiver sites around the circumference of the region.

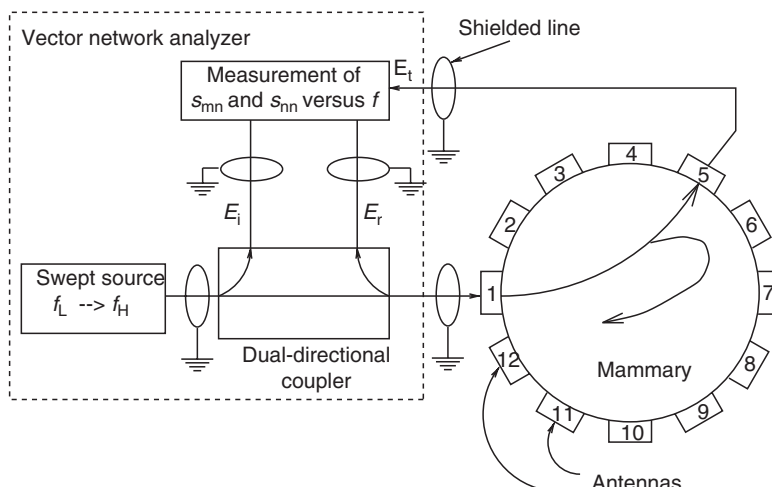


FIGURE 12.2
S-parameter measurement system.

A further visualization of the transmission–reflection method is shown in Figure 12.3, where each antenna on the circumference is a transmitter–receiver and the lines between antennas may be considered average ray paths for transmitted waves. Thus, position 1 in Figure 12.3 transmits to all other receivers at the same time and also receives reflected signals from various points within the target region. Next, position 2 transmits to all positions, and so on around the circumference. Both the amplitude and phase delay of transmitted and reflected signals are functions of the complex permittivity that the particular ray path encounters in traversing or partially traversing the normal and malignant breast tissue regions. The data collected with this method are processed by computer to produce images of subregions of differing permittivity and conductivity within the mammary tissue.

At present, we use a vector network analyzer (HP 8753A, 0.3 MHz to 3 GHz) to perform the measurement functions in Figure 12.2. In a fully developed MWI system, the network analyzer will be replaced with lower-cost, application-specific, individual components.

As an example to illustrate the transmission–reflection imaging method, we use a simplified multiport network theory; a more rigorous full-wave theory will be summarized in Section 12.4. Let d be the distance of an average ray path from a transmitter at port 1 to a receiver at port 7 in Figure 12.3, let Z_0 be the receiver or transmitter impedance, and let Z_M be the intrinsic impedance that the rays encounter in the bulk tissue between transmitter and receiver. From two-port network theory, the reflection coefficient (S_{11}) looking from the transmitter antenna into the bulk tissue is

$$S_{11} = \frac{(Z_M^2 - Z_0^2) \tanh \gamma d}{2Z_0 Z_M + (Z_M^2 - Z_0^2) \tanh \gamma d} = \frac{E_r}{E_i} \quad (12.9)$$

and the transmission coefficient (S_{71}) from port 1 to port 7 is

$$S_{71} = \frac{2Z_0 Z_M \sqrt{1 - \tanh^2 \gamma d}}{2Z_0 Z_M + (Z_M^2 - Z_0^2) \tanh \gamma d} = \frac{E_t}{E_i} \quad (12.10)$$

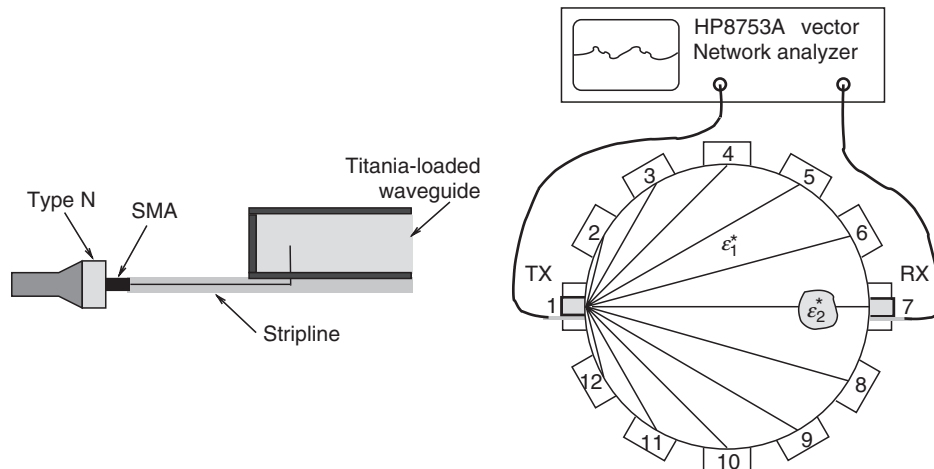


FIGURE 12.3

Top view of the cylindrical plastic container showing some of the antennas in the total array.

where $\gamma = j\omega\sqrt{\mu_0\epsilon^*}$ is the propagation constant of the bulk tissue, and $\omega = 2\pi f$, where f is the frequency in hertz. Let $Z_M = \sqrt{\mu_0/\epsilon^*} = 377/\sqrt{\epsilon_r^*}$ and $Z_0 = 50 \Omega$, then $Z_0/Z_M = \sqrt{\epsilon_r^*}/7.54$, and S_{11} and S_{71} become

$$S_{11} = \frac{(56.85 - \epsilon_r^*)j \tan(2\pi f \sqrt{\epsilon_r^*} d/c)}{15.08\epsilon_r^* + (56.85 + \epsilon_r^*)j \tan(2\pi f \sqrt{\epsilon_r^*} d/c)} = \frac{E_r}{E_i} \quad (12.11)$$

$$S_{71} = \frac{15.08\sqrt{\epsilon_r^*}\sqrt{1 - j \tan^2(2\pi f \sqrt{\epsilon_r^*} d/c)}}{15.08\epsilon_r^* + (56.85 + \epsilon_r^*)j \tan(2\pi f \sqrt{\epsilon_r^*} d/c)} = \frac{E_t}{E_i} \quad (12.12)$$

where $c = 3 \times 10^8 \text{ m/s}$. For example, if $d = 0.1 \text{ m}$, $f = 800 \text{ MHz}$, and the measured values are

$$S_{11} = 0.200 \angle 81.76^\circ = -13.94 \text{ dB} \angle 81.76^\circ \quad (12.13)$$

$$S_{71} = 0.011 \angle 86.49^\circ = -39.17 \text{ dB} \angle 86.49^\circ \quad (12.14)$$

then the complex permittivity of the bulk tissue medium at $f = 800 \text{ MHz}$ is determined as

$$\epsilon_r^* = 36 - j36 = \frac{\epsilon}{\epsilon_0} - j\frac{\sigma}{\omega\epsilon_0} \quad (12.15)$$

where $\epsilon = 36\epsilon_0$ and $\sigma = 1.60 \text{ S/m}$. From our previous measurements [6], normal mammary tissue at 800 MHz would yield $\epsilon_r^* = 17 - j4$, or $\epsilon = 17\epsilon_0$ and $\sigma = 0.18 \text{ S/m}$. Thus, $\epsilon_r^* = 36 - j36$ would represent a very large difference in expected tissue properties along the path from port 1 to port 7, which passes through the region occupied by ϵ_2^* in Figure 12.3. This example is intended to illustrate how the contrast in complex permittivity of a region can not only be measured but also located by coordinate position.

12.2.4 Power, Signal Attenuation, and Signal-to-Noise Ratio

At an operating frequency of 800 MHz, the free space wavelength is $\lambda_0 = 37.5 \text{ cm}$. In normal breast tissue the wavelength is reduced to $\lambda_{\text{normal}} = \frac{\lambda_0}{\sqrt{\epsilon_r}} = 9.375 \text{ cm}$, assuming that the dielectric constant is 16 for normal breast tissue. The distance between any pair of transmitting and receiving antennas is less than 20 cm. Therefore, all measurements are made within a region comparable to the wavelength. The propagation loss between transmitting and receiving antennas is typically in the range of 8 to 16 dB. A typical dielectrically loaded waveguide antenna used for MWI has a $3 \times 3 \text{ cm}$ aperture. If the transmitting antenna is operated at a transmitted power of 0 dB m or 1 mW, it results in a transmitted power density of 0.11 mW/cm^2 , nine times below the ANSI safety level. The received power is -16 to -8 dB m or 25 to $158 \mu\text{W}$. The scattered signal from the tumor is typically 0.01% of the incident wave. Since the network analyzer's noise level is approximately -90 dB m , the signal-to-noise ratio (SNR) at the receiving antenna is on the order of 30 dB.

12.3 Three-Dimensional Formulation

Currently, there are few methods developed for MWI in three dimensions because of the large computational demand in both forward and inverse problems of inhomogenous media. While two-dimensional (2-D) and 3-D imaging techniques based on the scalar-wave approximation have been developed with some success, breast cancer imaging is inherently a 3-D problem and requires the full 3-D inverse scattering algorithms based on the vectorial Maxwell's equations. In our imaging research we have developed a fast inverse scattering method based on the combination of the contrast source inversion and the fast Fourier transform (FFT) algorithms.

Because of the volumetric inhomogeneities in biological tissues, surface integral equation methods become impractical. Methods based on volumetric techniques are more appealing. We focus on the frequency-domain solution of a volume integral equation (VIE) for inhomogenous media. In a typical inhomogenous tissue medium, both the forward and the inverse scattering problems can be formulated using VIEs. The conventional forward scattering method for VIEs is the method of moments (MoM) [18], but the computational cost is prohibitively high; several 3-D forward problems have been solved in a number of articles [19–22] using this approach. If the VIE involves N unknowns, the MoM has a memory requirement of $O(N^2)$, and a CPU time requirement of $O(N^2)$ or $O(N^3)$ depending on whether the resulting matrix equation is solved iteratively or by direct inversion.

An important improvement over the MoM is a variant of Bojarski's k -space method (see references in Ref. [23]), the so-called conjugate-gradient fast Fourier transform (CG-FFT) method proposed during the 1980s [24,25], which uses iterative the Krylov subspace method [26] combined with FFT or nonuniform FFT [27]. Zhang and Liu [28] recently developed a biconjugate-gradient FFT method based on the weak-form discretization of Zwamborn and van den Berg and showed a significant improvement over the CG-FFT method for wave scattering problems. This method has been further accelerated by the stabilized biconjugate-gradient fast Fourier transform (BCGS-FFT) method for wave scattering by Xu et al. [29]. Recently, the adaptive integral method developed for surface integral equations [30] has been further developed for VIEs to accelerate MoM by using two sets of basis functions to represent near-field and far-field interactions [31].

In the present work, we apply the BCGS-FFT method to MWI by solving the VIE. The problem under consideration is schematically shown in Figure 12.4, where an arbitrary

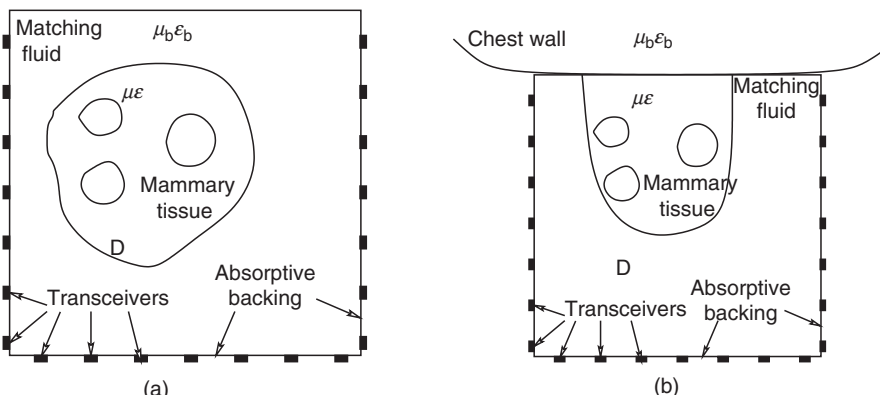


FIGURE 12.4
Imaging chamber from above (a) and from the side (b).

number of antennas are mounted on the plastic container surrounding the phantom model of breast tissue. Specific configurations for simulation will be described in a later section. We calculate the electromagnetic fields both inside the tissue medium and at the receiver array for any source locations. For MWI of breast tissue, the excitation sources (antennas) are in the near-field zone, and the incident field cannot be approximated as a plane wave. Therefore, we include the effects of the finite sources in the near-field zone.

In the following section, we derive from the vectorial Maxwell's equations the VIE for 3-D MWI in the discretized form that we use. Iterative methods for the solution of this discretized linear system are then described. Numerical results are shown to validate the method for MWI.

12.4 Wave Equation and VIE

From Maxwell's equations with an assumed time dependence $e^{j\omega t}$,

$$\nabla \times \mathbf{E} = -j\omega\mu\mathbf{H} \quad (12.16)$$

$$\nabla \times \mathbf{H} = (\sigma + j\omega\epsilon)\mathbf{E} + \mathbf{J} = j\omega\left(\epsilon - j\frac{\sigma}{\omega}\right)\mathbf{E} + \mathbf{J} = j\omega\epsilon^*\mathbf{E} + \mathbf{J} \quad (12.17)$$

$$\nabla \cdot \mathbf{D} = \rho \quad (12.18)$$

$$\nabla \cdot \mathbf{B} = 0 \quad (12.19)$$

we may let

$$\mathbf{B} = \nabla \times \mathbf{A} \quad (12.20)$$

since $\nabla \cdot \nabla \times \mathbf{A} \stackrel{\Delta}{=} 0$ maintains $\nabla \cdot \mathbf{B} = 0$, where \mathbf{A} is the vector potential. Substituting Equation 12.20 into Equation 12.16 yields

$$\nabla \times \mathbf{E} = -j\omega(\nabla \times \mathbf{A}) \quad (12.21)$$

or

$$\nabla \times (\mathbf{E} + j\omega\mathbf{A}) = 0 \quad (12.22)$$

Since $\nabla \times (\nabla\phi) \stackrel{\Delta}{=} 0$, we may let the term in parentheses in Equation 12.22 be the negative gradient of the scalar potential ϕ , and express \mathbf{E} as

$$\mathbf{E} = -\nabla\phi - j\omega\mathbf{A} \quad (12.23)$$

Note that if $\omega = 0$, then $\mathbf{E} = -\nabla\phi$, as expected for static fields. We now invoke the Lorenz condition, which defines the divergence of \mathbf{A} as

$$\nabla \cdot \mathbf{A} = -j\omega\mu\epsilon^*\phi \quad (12.24)$$

Substituting this condition into [Equation 12.23](#) yields

$$\mathbf{E} = -j\omega \left[1 + \frac{\nabla \nabla \cdot}{k^2} \right] \mathbf{A} \quad (12.25)$$

where $k^2 = \omega^2 \mu \epsilon^*$. Since \mathbf{E} and \mathbf{H} are propagating field intensities that satisfy a wave equation, then \mathbf{A} must satisfy a wave equation obtained as follows. Substitute [Equation 12.20](#) and [Equation 12.23](#) into [Equation 12.17](#) to yield

$$\nabla \times \nabla \times \mathbf{A} \stackrel{\Delta}{=} \nabla(\nabla \cdot \mathbf{A}) - \nabla^2 \mathbf{A} = j\omega \mu \epsilon^*(-\nabla \phi + j\omega \mathbf{A}) + \mu \mathbf{J} \quad (12.26)$$

or (again using the Lorenz condition),

$$\nabla^2 \mathbf{A} = -\omega^2 \mu \epsilon^*(\mathbf{r}) \mathbf{A} - \mu \mathbf{J} \quad (12.27)$$

A solution to [Equation 12.27](#) is in general not available in a closed form because $\epsilon^*(\mathbf{r})$ is inhomogenous. However, for a homogenous medium with constant complex permittivity ϵ_b^* , one can find the solution in closed form

$$\mathbf{A}^{inc}(\mathbf{r}) = \mu \int_V \mathbf{J}(\mathbf{r}') g(\mathbf{r}, \mathbf{r}') dV' \quad (12.28)$$

where \mathbf{r} , \mathbf{r}' , and $\mathbf{R} = \mathbf{r} - \mathbf{r}'$ are vectors from the origin to the field point, from the origin to the source point, and from the source point to the field point, respectively. Green's function in [Equation 12.28](#) for the homogenous medium is given by $g(\mathbf{r}, \mathbf{r}') = e^{-jk_b R} / 4\pi R$, where $k_b = \omega \sqrt{\mu \epsilon_b^*}$ is the complex wavenumber of the medium. We call this solution \mathbf{A}^{inc} , the vector potential for the incident field in a homogenous background medium. The corresponding incident electric field can be found from [Equation 12.25](#) as

$$\mathbf{E}^{inc} = -j\omega \left[1 + \frac{\nabla \nabla \cdot}{k_b^2} \right] \mathbf{A}^{inc} \quad (12.29)$$

For an inhomogenous medium, even though a closed form solution is not available, one can express the solution in terms of an integral equation through the equivalence principle, as discussed below.

In order to introduce the equivalence principle, the key is to rewrite Maxwell's equations into a second-order partial differential equation for the electric field:

$$\nabla^2 \mathbf{E} + k_b^2 \mathbf{E} = j\omega \mu [\mathbf{J} + \mathbf{J}_{eq}] \quad (12.30)$$

where

$$\mathbf{J}_{eq} = j\omega [\epsilon^*(\mathbf{r}) - \epsilon_b] \mathbf{E} \quad (12.31)$$

is the volume equivalent electric current density induced in the inhomogenous medium.

Thus, from [Equation 12.30](#), the total field \mathbf{E} can be written as the superposition of the incident field \mathbf{E}^{inc} due to the primary source \mathbf{J} and the scattered field \mathbf{E}^{scat} due to the induced source \mathbf{J}_{eq} . Similar to the incident vector potential and incident electric field, the scattered vector potential and scattered electric fields are

$$\mathbf{A}^{\text{sct}}(\mathbf{r}) = \mu \int_V \mathbf{J}_{\text{eq}}(\mathbf{r}') g(\mathbf{r}, \mathbf{r}') dV' \quad (12.32)$$

$$\mathbf{E}^{\text{sct}} = -j\omega \left[1 + \frac{\nabla \nabla \cdot}{k_b^2} \right] \mathbf{A}^{\text{sct}} \quad (12.33)$$

The total electric field $\mathbf{E}(\mathbf{r})$ is composed of an incident field plus a scattered field, and it is the scattered field that we need to determine. Thus, combining [Equation 12.31](#) through [Equation 12.33](#), we have

$$\mathbf{E}(\mathbf{r}) - \mathbf{E}^{\text{inc}} = \omega^2 \mu \left(1 + \frac{\nabla \nabla \cdot}{k_b^2} \right) \int_V \mathbf{E}(\mathbf{r}') g(\mathbf{r}, \mathbf{r}') [\epsilon^*(\mathbf{r}') - \epsilon_b^*] dV' \quad (12.34)$$

where the subscript b denotes a parameter of the background medium (normal tissue and liquid with the same properties). [Equation 12.34](#) is the integral equation representation of the scattered electric field everywhere in space. In particular, for $\mathbf{r} \in V$, [Equation 12.34](#) is a Fredholm integral equation of the second kind. This is the integral equation we solve for the internal electric field \mathbf{E} for $\mathbf{r} \in V$, from which the field everywhere in the region can be obtained. This type of VIE has been solved by using the MoM [18,20,21]. In our work we will use an alternative discretization method coupled with the Krylov subspace iterative technique to significantly speed up the numerical solution of the problem.

12.4.1 Microwave Imaging

In MWI, scattering parameters are measured using the antennas mounted on the surface of the plastic container in [Figure 12.4](#). The objective of MWI is to reconstruct the distribution of the complex permittivity inside the tissue given the measured scattering parameters.

First, for the MWI system design optimization, the forward problem must be solved. This is to calculate the electric field distribution, given a set of antennas and known distribution of the complex permittivity. In the general problem of microwave interaction with a tissue medium shown in [Figure 12.4](#), an inhomogenous medium with a finite volume V is embedded in an isotropic, homogenous background medium with constant permittivity ϵ_b , electric conductivity σ_b , and permeability μ_b . This background medium may be air or a matching fluid that is designed to approximately match the electrical properties of the tissue to enhance the SNR in the measurement of the scattered field [9]. The inhomogenous volume V is characterized by nonuniform distributions of permittivity $\epsilon(\mathbf{r})$ and conductivity $\sigma(\mathbf{r})$; and permeability is assumed constant, that is, $\mu = \mu_b$. The objective is to solve for the electric field everywhere in space due to a finite antenna (usually electrically small because a large array of antennas is needed in an array imaging system). For more details of the BCGS-FFT method, the reader is referred to Refs. [9,28,29,32].

The above discussion is for the forward problem where the distribution of the complex permittivity is known. In reality, for the clinic application of MWI and electrical impedance tomography, we need to solve the inverse scattering problem where the complex permittivity is an unknown distribution. From some limited measurement data collected on the surface of the container, we infer such unknown permittivity distribution by solving the inverse problem through [Equation 12.34](#). In our work, we apply both the distorted Born iterative method and the contrast source inversion method to solve this inverse problem. For details of such inverse solvers, the reader is referred to Refs. [9,33–35].

12.4.2 Electrical Impedance Tomography

This imaging method uses multiple planar electrodes positioned around the region to be imaged, as in Figure 12.5. Impedance or admittance measurements are made between all electrodes, two at a time. Thus, in a parallel-plate capacitor sense, the admittance between any pair of electrodes is the ratio of current to voltage as:

$$Y = \frac{I}{V} = \frac{\frac{\int J \cdot dS}{d}}{\frac{\int E \cdot dl}{0}} = \frac{\int (\sigma + j\omega\epsilon)E \cdot dS}{\int E \cdot dl} = (\sigma + j\omega\epsilon) \frac{A}{d} = j\omega\epsilon^* \frac{A}{d} \quad (12.35)$$

or $Y = G + j\omega C$, where $G = \sigma (A/d)$, $C = \epsilon (A/d)$, and $\epsilon^* = \epsilon - j\frac{\sigma}{\omega}$ is the measured complex permittivity if A/d is known from calibration data. The real and imaginary parts of ϵ^* , the permittivity ϵ , and the conductivity σ are the electrical properties of the composite tissue between pairs of electrodes. The factor (A/d) is an effective area-to-distance ratio that may be different for each electrode pair, but this ratio is determined by measuring a material with known electrical properties (such as 0.15 M NaCl at 24°C).

In general, the electric field will be nonuniform but most intense in the region between the electrode pair selected for measurement. The fields between adjacent electrodes will measure properties near the tissue surface, while more diametrically opposed electrodes will measure the composite properties across the tissue region. Such a sequence of measurements is stepped around to include all electrode pairs surrounding the region in 3-D, so that the next set of measurements would be between electrode 2 and all the other electrodes, and so on. Thus, the mapping and imaging of a region are done based on the differing electrical properties within the region.

Impedance imaging is a subject that has been under continuing investigation [36–40]. Research into impedance imaging in our research group began in 1975. We used an open-ended coaxial probe that produced a nonradiating, fringing field to measure the admittance of the material against which the probe was held. This was essentially a two-electrode system that measured the admittance between the inner and outer conductors as given in Zhang and Liu [35]. Moving this noninvasive probe to different positions on the surface of the body, we were able to locate and map out the tumors lying near the skin surface on the bodies of two cancer patients. This work indicated that even

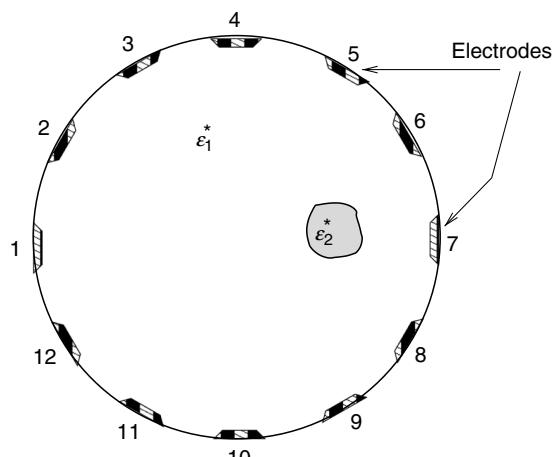


FIGURE 12.5
Configuration of electrical impedance tomography.

when measured through the intact skin, cancerous tissue generally has greater electrical conductivity and permittivity than normal surrounding tissue [41].

The forward and inverse problems of EIT can also be formulated in the same way as for the MWI, that is, using the volume integral [Equation 12.34](#). This is especially convenient if the electrodes are small and can be considered as point electrodes. For finite-size electrodes, in order to apply the boundary conditions on the electrode surface, we use the high-order finite element and spectral element methods to solve the partial differential equations directly in the forward problem. For the inverse problem, we use the distorted Born iterative method [42,43].

12.5 Three-Dimensional Images Reconstructed from Simulated Three-Dimensional MWI Data

Figure 12.6 shows the measurement setup to image two identical spherical anomalies both with $\epsilon_r = 48$ and $\sigma = 0.8$. The sources and receivers are evenly distributed over the six surfaces of the cuboid. The two spheres of radius 1.1 cm are located at $(3.9,0,0)$ and $(-3.9,0,0)$ cm, respectively. The imaged domain is discretized into $31 \times 31 \times 31$ voxels. The reconstructed ϵ_r and σ are displayed on three orthogonal slices in [Figure 12.7](#), showing a high fidelity to the ground truth.

12.6 Two-Dimensional Images Reconstructed from Measured Two-Dimensional EIT Data

This section presents three examples of images reconstructed from measured data obtained from a Two-Dimensional EIT system.

12.6.1 Case 1: One Insulator Object Inside the Container

The first example is Case 1, shown in the left panel of [Figure 12.9](#). The difference between the total field and the background field in the right panel of Figure 12.9 is the measured

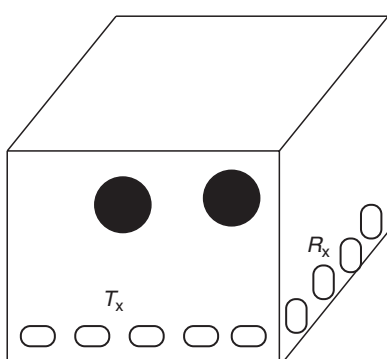


FIGURE 12.6
The setup of Three-Dimensional imaging of two spherical anomalies separated by 7 cm.

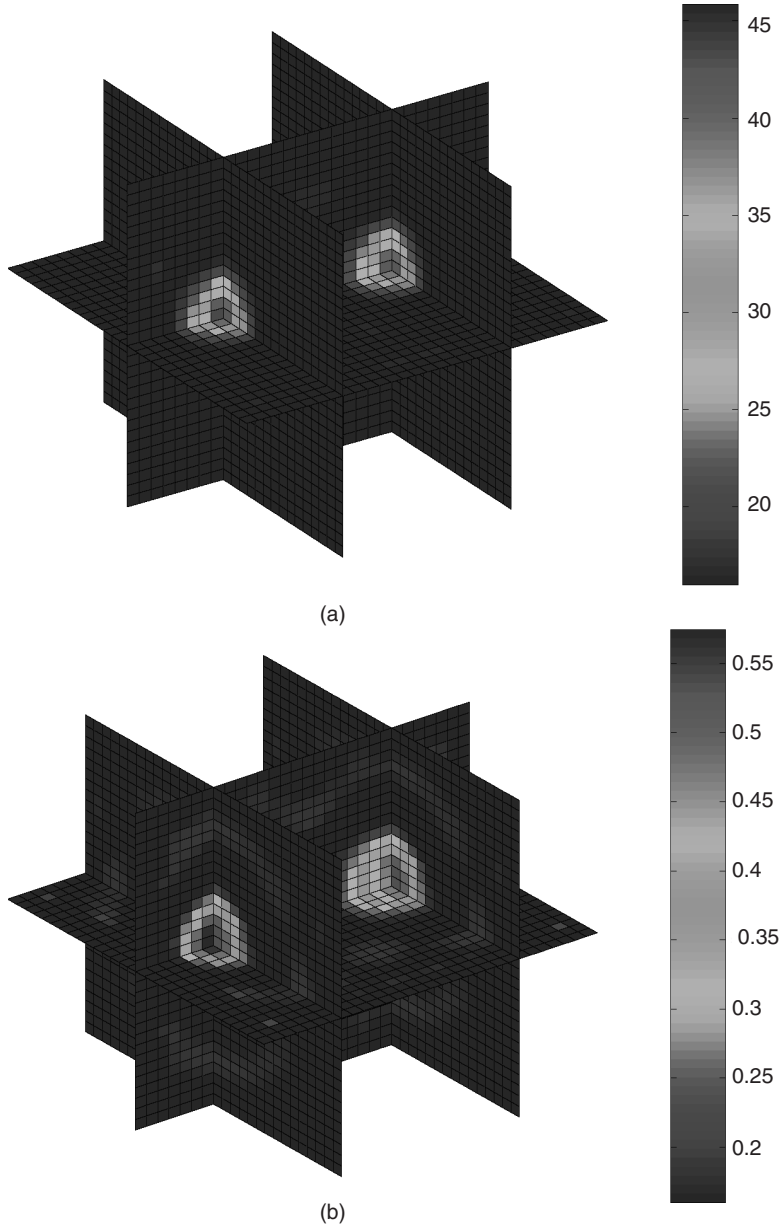


FIGURE 12.7 (See color insert following page 380.)

Inversion for Figure 12.6 on three orthogonal slices through the center of the anomalies. Inverted dielectric constant ϵ_r (a) and conductivity σ (b).

secondary field. The reconstructed image from this secondary field is shown in the left panel of Figure 12.8. The dotted circle in this figure indicates the ground truth of the object. It is observed that the reconstructed image matches well with the ground truth, although the absolute values of the conductivity of the highly resistive object are not well recovered because of the extreme contrast.

In order to show the misfit between the reconstructed data and the measured data, we take the reconstructed 2-D conductivity map in the left panel of Figure 12.8 and use the

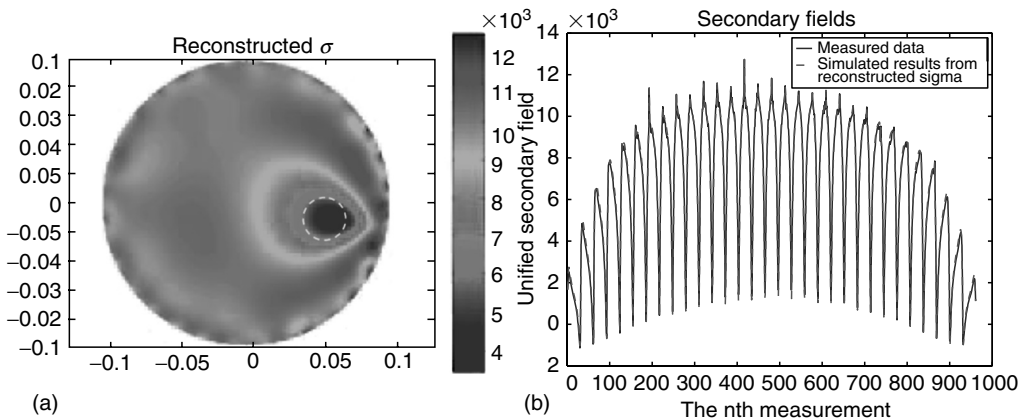


FIGURE 12.8 (See color insert following page 380.)

Left: Image reconstructed from the measured data in Case 1. The dashed circle indicates the ground truth. Right: Comparison of the secondary field between measurements and simulated by forward solver with the reconstructed σ in Case 1.

forward simulator to predict the data corresponding to this image. The comparison between the measured data (blue curve) and the simulated data (red curve) using the reconstructed image is shown in the right panel of Figure 12.8. We observe that these two sets of results have excellent agreement, indicating small data misfit from the reconstructed data.

12.6.2 Case 2: Two Insulator Objects Inside the Container

The setup of the second example (Case 2) is shown in the left panel of Figure 12.10. It is similar to Case 1, except that two insulators (beakers) are inserted into the container. The measured total field and background field are shown in the right panel of Figure 12.10. From the secondary field, the distorted Born iterative method (DBIM) reconstructs the

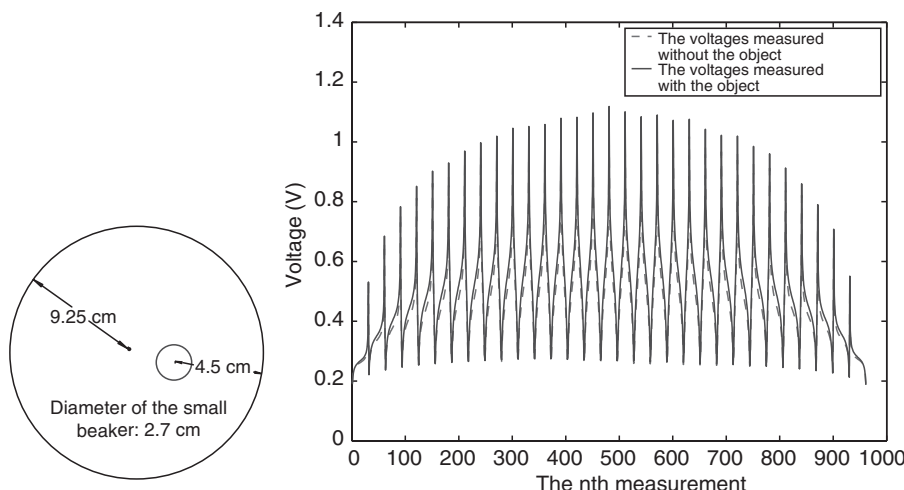


FIGURE 12.9

Left: The setup of Case 1 with one insulator object (beaker). Right: The measured voltage with and without the object in Case 1.

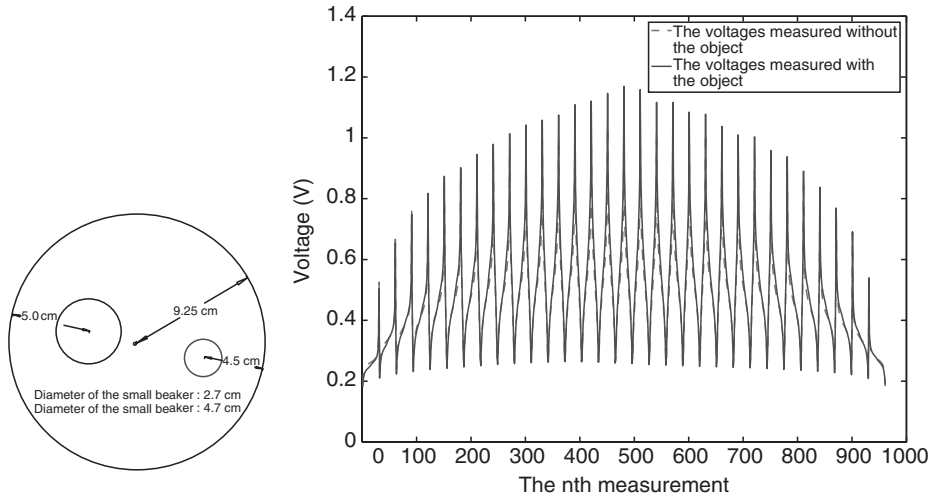


FIGURE 12.10

Left: The setup of Case 2 with two nonconducting circular objects (beakers). Right: The measured voltage with and without the objects in Case 2.

image shown in the left panel of Figure 12.11. The dotted circles in this figure indicate the ground truth of the objects. It is observed that the reconstructed image matches well with the ground truth, although the absolute values of the conductivity of the highly resistive objects are again not well recovered because of the extreme contrasts.

From the reconstructed conductivity image, we use the forward simulator to predict the secondary field data. This simulated result is then compared with the measured secondary field in the right panel of Figure 12.11. Again, we observe that these two sets of results have excellent agreement, indicating small data misfit from the reconstructed data.

12.6.3 Case 3: One Conductive and One Resistive Object Inside the Container

The third case, shown in the left panel of Figure 12.12, consists of two objects in the container. The bigger object is a conductive metal cylinder, while the smaller

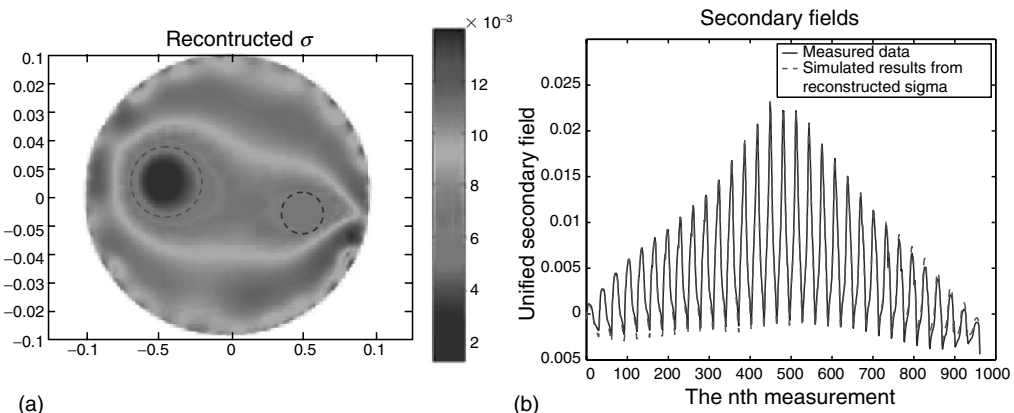


FIGURE 12.11 (See color insert following page 380.)

Left: Image reconstructed from the measured data in Case 2. The dashed circles indicate the ground truth. Right: Comparison of the secondary field between measurements and simulated by forward solver with the reconstructed σ in Case 2.

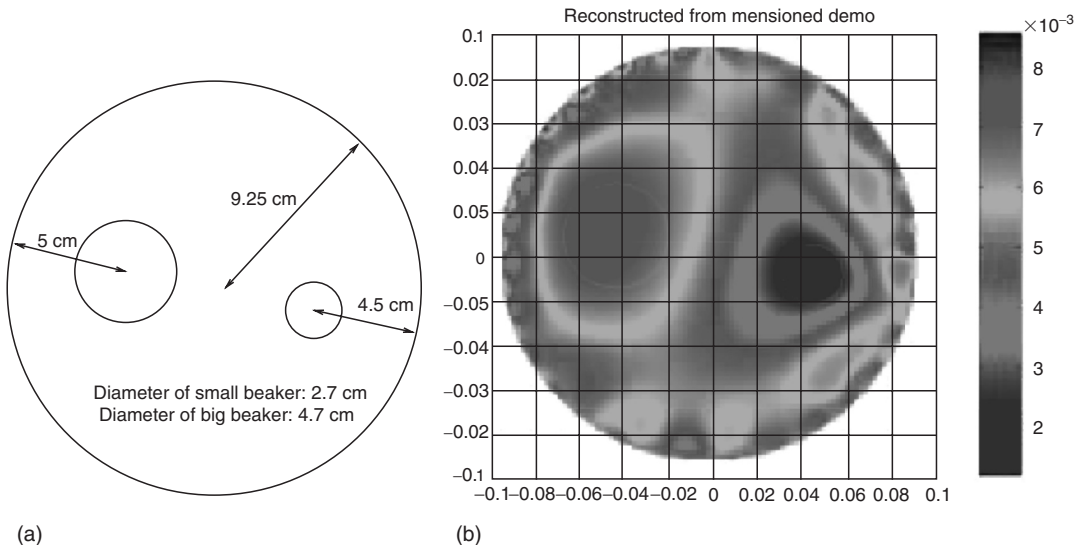


FIGURE 12.12 (See color insert following page 380.)

Left: The setup for Case 3 with one larger metal object and one smaller insulator object. Right: The reconstructed σ . The two circles denote the locations of the objects.

object is a resistive beaker (an insulator). This represents a more interesting case for reconstruction as the conductivity contrast is positive in one region and negative in another.

The reconstructed σ is shown in the right panel of Figure 12.12. The anomalies reconstructed match well with the original objects in location. However, the size of both objects has been somewhat overestimated. The conductivity value of the bigger object is indeed greater than the background, and the smaller object has conductivity values smaller than the background. These indeed match with the original setting that one object is a conductor and another is an insulator, although again the exact values of conductivity are not obtained because of the large contrasts. Nevertheless, the reconstructed images show high-quality reconstruction.

The CPU time for the above image reconstruction examples is less than 3 min on a Pentium IV computer. We emphasize that this speed is expected to be greatly reduced once the program is optimized. Furthermore, in clinical application, the image reconstruction will be performed offline, and thus the computation time of a few minutes is not a concern.

Observations—There are some artifacts in the areas close to the electrodes, perhaps caused by the surface resistance at the interface between the saline solution and the electrodes. However, the overall reconstructed images are excellent. The size and shape of the objects can be well predicted by the reconstructed images. Our future work is to extend the methodology reported here to a full 3-D EIT system. In such a system, we will further improve the sensitivity and resolution of the system by incorporating higher-precision multimeters and by placing a denser 3-D electrode array in the system. Furthermore, to match the higher sensitivity and resolution requirements, we will improve the accuracy of the forward and inverse solvers by incorporating higher-order and spectral methods. From the successful data acquisition and image reconstruction with our 2-D EIT system, it is believed that the 3-D EIT system is highly promising for breast cancer detection.

12.7 Summary and Conclusions

This chapter is a brief summary of MWI and electrical impedance tomography projects ongoing at Duke University. The modeled and measured results presented herein on artificial materials show the kinds of clear images one would fully expect to generate in the clinic using the same techniques. Other research groups are also developing improved MWI and impedance imaging systems, and some breast cancer images derived from clinical data have been published [14,44,45]. Because of 2-D artifacts or algorithm limitations, the earlier clinical images are not as clear as the ones that can be generated with the improved techniques now available. While improvements in current prototypes are encouraging, more work remains before MWI and EIT systems are integrated into clinical applications to produce the high-resolution breast cancer images that are now obtained in the laboratory.

Acknowledgment

We wish to thank the students and postdoctoral research associates involved in the work. Rebecca Willett, Adam Bryan, Erika Ward, Patrick Mathias, John Stang, and Rodger Dalton made significant contributions to the development of MWI hardware. Zhong Qing Zhang helped to develop the forward and inverse scattering algorithms for MWI. Jim Di Sarro, Jackie Hu, Guining Shi, Gang Ye, and Kyle McCarter made significant contributions to the development of electrical impedance tomography hardware. Kim Hwa Lim and Jun Ho Lee developed the forward and inverse solvers for electrical impedance tomography.

References

1. W.T. Joines, R.L. Jirtle, M.D. Rafal, and D.J. Schaefer, "Microwave power absorption differences in normal and malignant tissue," *Int. J. Radiat. Oncol. Biol. Phys.*, Vol. 6, No. 6, 681–687, June 1980.
2. W.T. Joines, S. Shrivastav, and R.L. Jirtle, "A comparison using tissue electrical properties and temperature rise to determine relative absorption of microwave power in malignant tissue," *Med. Phys. J.*, Vol. 16, No. 3, 840–844, Dec. 1989.
3. R. Pethig, "Dielectric properties of biological materials," *IEEE Trans. Elect. Insul.*, Vol. 19, 453–474, 1984.
4. S.S. Chaudhary, R.K. Mishra, A. Swarup, and J.M. Thomas, "Dielectric properties of normal and malignant human breast tissues at radiowave and microwave frequencies," *Indian J. Biochem. Biophys.*, Vol. 21, 76–79, 1984.
5. W.T. Joines, "Frequency dependent absorption of electromagnetic energy in biological tissue," *IEEE Trans. Biomed. Eng.*, Vol. 31, 215–222, Jan. 1984.
6. W.T. Joines, Y. Zhang, C. Li, and R.L. Jirtle, "The measured electrical properties of normal and malignant human tissues from 50 to 900 MHz," *Med. Phys. J.*, Vol. 21, No. 4, 547–550, Apr. 1994.
7. A.M. Campbell and D.V. Land, "Dielectric properties of female human breast tissue measured at 3.2 GHz," *Phys. Med. Biol.*, Vol. 37, No. 1, 193–210, June 1992.
8. L. Jofre, M.S. Hawley, A. Broquetas, E. de los Reyes, M. Ferrando, and A.R. Elias-Fuste, "Medical imaging with a microwave tomographic scanner," *IEEE Trans. Biomed. Eng.*, Vol. 37, No. 3, 303–312, 1990.

9. Q.H. Liu, Z.Q. Zhang, T. Wang, G. Ybarra, L.W. Nolte, J.A. Bryan, and W.T. Joines, "Active microwave imaging I: 2-D forward and inverse scattering methods," *IEEE Trans. Microwave Theory Technol.*, Vol. 50, No. 1, 123–133, Jan. 2002.
10. E.C. Fear, S.C. Hagness, P.M. Meaney, M. Okoniewski, and M.A. Stuchly, "Enhancing breast tumor detection with near-field imaging," *IEEE Microwave Mag.*, 48–56, Mar. 2002.
11. P.M. Meaney, K.D. Paulsen, A. Hartov, and R.K. Crane, "An active microwave imaging system for reconstruction of 2-D electrical property distributions," *IEEE Trans. Biomed. Eng.*, Vol. 42, No. 10, 1017–1025, 1995.
12. S.C. Hagness, A. Taflove, and J.E. Bridges, "Two-dimensional FDTD analysis of a pulsed microwave confocal system for breast cancer detection: fixed-focus and antenna-array sensors," *IEEE Trans. Biomed. Eng.*, Vol. 45, No. 12, 1470–1479, 1998.
13. S.C. Hagness, A. Taflove, and J.E. Bridges, "Three-dimensional FDTD analysis of a pulsed microwave confocal system for breast cancer detection: design of an antenna-array element," *IEEE Trans. Antennas Propagat.*, Vol. 47, No. 5, 783–791, 1999.
14. P.M. Meaney, M.W. Fanning, D. Li, P. Poplack, and K.D. Paulsen, "A clinical prototype for active microwave imaging of the breast," *IEEE Trans. Microwave Theory Technol.*, Vol. 48, No. 11, 1841–1853, 2000.
15. E.C. Fear and M.A. Stuchly, "Microwave detection of breast cancer," *IEEE Trans. Microwave Theory Tech.*, Vol. 48, No. 11, 1854–1863, 2000.
16. Pethig R., *Dielectric and Electronic Properties of Biological Materials*, Wiley, New York, 1979.
17. P. Debye, *Polar Molecules*, Chemical Catalog Co., New York, 1929.
18. R.F. Harrington, *Field Computation by Moment Methods*, Macmillan, New York, 1968.
19. D.E. Livesay and K.M. Chen, "Electromagnetic fields induced inside arbitrarily shaped biological bodies," *IEEE Trans. Microwave Theory Technol.*, Vol. 22, 1273–1280, Dec. 1974.
20. D.H. Schaubert, D.R. Wilton, and A.W. Glisson, "A tetrahedral modeling method for electromagnetic scattering by arbitrarily shaped inhomogeneous dielectric bodies," *IEEE Trans. Antennas Propagat.*, Vol. 32, 77–85, Jan. 1984.
21. C.T. Tsai, H. Massoudi, C.H. Durney, and M.F. Iskander, "A procedure for calculating fields inside arbitrarily shaped, inhomogeneous dielectric bodies using linear basis functions with the moment method," *IEEE Trans. Microwave Theory Technol.*, Vol. 34, 1131–1139, Nov. 1986.
22. H. Massoudi, C.H. Durney, and M.F. Iskander, "Limitations of the cubical block model of man in calculating SAR distributions," *IEEE Trans. Microwave Theory Technol.*, Vol. 32, 746–751, Aug. 1984.
23. N.N. Bojarski, "*k*-Space formulation of the scattering problem in the time domain," *J. Acous. Soc. Am.*, Vol. 72, 570–584, 1982.
24. T.K. Sarkar, E. Arvas, and S.M. Rao, "Application of fast Fourier transform and the conjugate gradient method for efficient solution of electromagnetic scattering from both electrically large and small conducting bodies," *Electromagnetics*, Vol. 5, 99–122, 1985.
25. H. Gan, and W.C. Chew, "A discrete BCG-FFT algorithm for solving 3D inhomogeneous scatterer problems," *J. Electromagn. Waves Appl.*, Vol. 9, 1339–1357, 1995.
26. C. Lanczos, "An iteration method for the solution of the eigenvalue problem of linear differential and integral operators," *J. Res. Nat. Bur. Stand.*, Vol. 45, 255–282, 1950.
27. Q.H. Liu, X.M. Xu, B. Tian, and Z.Q. Zhang, "Applications of nonuniform fast transform algorithms in numerical solutions of differential and integral equations," *IEEE Trans. Geosci. Remote Sensing*, Vol. 38, 1551–1560, 2000.
28. Z.Q. Zhang and Q.H. Liu, "Three-dimensional weak-form conjugate- and bi-conjugate FFT methods for volume integral equations," *Microwave Opt. Technol. Lett.*, Vol. 5, 350–356, 2001.
29. X. Xu, Q.H. Liu, and Z.Q. Zhang, "The stabilized biconjugate gradient fast Fourier transform method for electromagnetic scattering," *J. Appl. Computat. Electromagn. Soc.*, Vol. 17, No. 1, 97–103, Mar. 2002.
30. E. Bleszynski, M. Bleszynski, and J. Jaroszewicz, "Adaptive integral method for solving large-scale electromagnetic scattering and radiation problems," *Radio Sci.*, Vol. 31, 1225–1251, 1996.
31. Z.Q. Zhang and Q.H. Liu, "A volume adaptive integral method (VAIM) for 3D inhomogeneous objects," *IEEE Antennas Wireless Propagat. Lett.*, Vol. 1, No. 6, 102–105, 2002.
32. Z.Q. Zhang, Q.H. Liu, and X.M. Xu, "RCS computation of large inhomogeneous objects using a fast integral equation solver," *IEEE Trans. Antennas Propagat.*, Vol. 51, No. 3, 613–618, Mar. 2003.

33. Z.Q. Zhang, and Q.H. Liu, "Two nonlinear inverse methods for electromagnetic induction measurements," *IEEE Trans. Geosci. Remote Sensing*, Vol. 39, No. 6, 1331–1339, June 2001.
34. Z.Q. Zhang, Q.H. Liu, C. Xiao, E. Ward, G. Ybarra, and W.T. Joines, "Microwave breast imaging: 3-D forward scattering simulation," *IEEE Trans. Biomed. Eng.*, Vol. 50, No. 10, 1180–1189, Oct. 2003.
35. Z.Q. Zhang and Q.H. Liu, "3-D nonlinear image reconstruction for microwave biomedical imaging," *IEEE Trans. Biomed. Eng.*, Vol. 51, No. 3, 544–548, 2004.
36. L.E. Baker, "Principles of the impedance technique," *IEEE Eng. Med. Biol. Mag.*, 11–15, Mar. 1989.
37. S. Caorsi, G.L. Gragnani, and M. Pastorino, "Redundant electromagnetic data for microwave imaging of three-dimensional dielectric objects," *IEEE Trans. Antennas Propagat.*, Vol. 42, No. 5, 581–589, May 1994.
38. M. Cheney and D. Isaacson, "Distinguishability in impedance imaging," *IEEE Trans. Biomed. Eng.*, Vol. 39, No. 8, 852–860, Aug. 1992.
39. B.M. Eyuboglu, B.H. Brown, and D.C. Barber, "*In vivo* imaging of cardiac related impedances changes," *IEEE Eng. Med. Biol. Mag.*, 39–45, Mar. 1989.
40. A.D. Seagar, D.C. Barber, and B.H. Brown, "Electrical impedance imaging," *IEEE Proc.*, Vol. 134, Pt. A, 201–210, 1987.
41. W.T. Joines, E. Tanabe, and Raymond U, "Determining the electrical properties of biological tissue *in vivo*," *IEEE Proc. Southeast. Conf.*, 382–385, Apr. 1976.
42. W.C. Chew, *Waves and Fields in Inhomogeneous Media*, Van Nostrand Reinhold, New York, 1990.
43. Q.H. Liu, "Nonlinear inversion of electrode-type resistivity measurements," *IEEE Trans. Geosci. Remote Sensing*, Vol. 32, No. 3, 499–507, 1994.
44. T.E. Kerner, K.D. Paulsen, A. Hartov, S.K. Soho, and S.P. Poplack, "Electrical impedance spectroscopy of the breast: clinical imaging results in 26 subjects," *IEEE Trans. Med. Imaging*, Vol. 21, No. 6, 638–645, June 2002.
45. A. Malich, T. Fritsch, R. Anderson, T. Boehm, M.G. Freesmeyer, M. Fleck, and W.A. Kaiser, "Electrical impedance scanning for classifying suspicious breast lesions: first results," *Eur. Radiol.*, Vol. 10, No. 10, 1555–1561, 2000.